
# Multi-Omics for the Understanding of Brain Diseases

Edited by
Jong Hyuk Yoon and Chiara Villa

Printed Edition of the Special Issue Published in *Life*

wwww.mdpi.com/journal/life

# Multi-Omics for the Understanding of Brain Diseases

# Multi-Omics for the Understanding of Brain Diseases

Editors

**Chiara Villa**
**Jong Hyuk Yoon**

MDPI • Basel • Beijing • Wuhan • Barcelona • Belgrade • Manchester • Tokyo • Cluj • Tianjin

*Editors*
Chiara Villa
University of Milano-Bicocca
Italy

Jong Hyuk Yoon
Korea Brain Research Institute
Korea

*Editorial Office*
MDPI
St. Alban-Anlage 66
4052 Basel, Switzerland

This is a reprint of articles from the Special Issue published online in the open access journal *Life* (ISSN 2075-1729) (available at: https://www.mdpi.com/journal/life/special_issues/Brain_Disease).

For citation purposes, cite each article independently as indicated on the article page online and as indicated below:

LastName, A.A.; LastName, B.B.; LastName, C.C. Article Title. *Journal Name* **Year**, *Volume Number*, Page Range.

**ISBN 978-3-0365-2602-7 (Hbk)**
**ISBN 978-3-0365-2603-4 (PDF)**

Cover image courtesy of Chiara Villa

# Contents

# About the Editors

**Chiara Villa** is currently Assistant Professor in Pathology at University of Milano-Bicocca. She started her research activity in 2006 at the Department of Neurological Sciences, University of Milan, Fondazione Cà Granda IRCCS Ospedale Maggiore Policlinico, where she obtained her Ph.D. in Molecular Medicine in 2009. Her research activity was mainly focused on the study of novel biomarkers (e.g., microRNAs, pro-inflammatory cytokines) and genetic risk factors in key genes for early detection and/or progression of two neurodegenerative diseases: Alzheimer's disease and frontotemporal lobar degeneration. In 2014, she moved to the University of Milano-Bicocca and joined a research group working on the study of molecular bases of autism spectrum disorders and sleep disorders, including restless legs syndrome and nocturnal frontal lobe epilepsy. Her work is now carried out applying her previous research experience in this field through a molecular approach.

At the moment, she is co-author of 64 research articles published in peer-reviewed journals with a personal H-index of 20.

**Jong Hyuk Yoon** is currently Principal Researcher at the Korea Brain Research Institute. He started his research activity in 2005 at the Department of Life Sciences, Gwangju Institute of Science and Technology (GIST), then he obtained his Ph.D. degree in Life Sciences in 2012 at Pohang University of Science and Technology(POSTECH). His research activity was mainly focused on the study of Omics-based target discovery and characterization of molecular mechanisms in diseases including metabolic diseases, cancers. In 2016, he settled at the Korea Brain Research Institute and his work is now carried out applying his previous research experience to brain diseases. At the moment, he is the author of 35 research articles published in peer-reviewed journals with a personal H-index of 18.

life

*Editorial*

# Multi-Omics for the Understanding of Brain Diseases

**Chiara Villa [1,*] and Jong Hyuk Yoon [2,*]**

[1] School of Medicine and Surgery, University of Milano-Bicocca, 20900 Monza, Italy
[2] Neurodegenerative Diseases Research Group, Korea Brain Research Institute, Daegu 41062, Korea
* Correspondence: chiara.villa@unimib.it (C.V.); jhyoon@kbri.re.kr (J.H.Y.)

Brain diseases, including both neurodegenerative diseases and mental disorders, represent the third largest healthcare problem in developed countries, after cardiovascular disorders and cancer [1]. The majority of human brain diseases have a multifactorial etiology and are characterized by different molecular alterations that act in synergy during the disease development [2]. In the last decade, the advancement of omics technologies, such as genomics, transcriptomics, proteomics, epigenomics, metabolomics, miRNomics, and lipidomics, offers a great contribution to the identification of novel molecular pathways, and to understand pathophysiological alterations underlying brain diseases. However, molecular profiling, which makes it possible to deepen the understanding of these disorders, has shown some limitations. Therefore, the analysis and integration of data derived from massively parallel technologies will allow the simultaneous identification of molecular alterations at different levels (transcript, gene, microRNA, protein, lipid, cellular metabolic processes), incorporating the available information, and thus contributing to providing novel insights into the mechanisms underlying human brain diseases [3].

This Special Issue gathers four reviews and six original research articles highlighting the potentialities of omics approaches in different brain diseases. Some authors reviewed the applications and impact of microfluidics technology on research in Alzheimer's disease (AD), as an alternative platform to understand disease-associated pathways and mechanisms [4]. Regarding age-related disorders, another outstanding review discussed the emerging field of NADomics, the high-throughput study of nicotinamide adenine dinucleotide (NAD+) and its related metabolites. As the NADome (NAD+ metabolome) represents an important biomarker for aging and neurodegenerative diseases, the authors suggested that NADomics can be used to elucidate the pathobiology of these disorders and identify potential therapeutic strategies [5]. Moreover, Perrone and collaborators aimed to review the most recent advancements in genomics, metabolomics, and proteomics related to sudden infant death syndrome (SIDS), which is characterized by an unexpected death during the sleeping period, typically occurring in infants under 1 year of age, and is associated with defects in the portion of the brain that controls breathing. These authors suggested that a model integrating different data from biomarkers and omics analyses may represent a valuable tool to identify a risk profile of SIDS in newborns [6]. Finally, another review addressed the role of zinc and its related proteins as important modulators of the epigenome in different chronic diseases, discussing their interaction with the chromatin [7].

Concerning neuropsychiatric disorders, an integrative multi-omics analysis identified four categories of key genes involved in the pathogenesis of schizophrenia (SCZ), thus offering new insights to better understand the complexity and regional heterogeneity of SCZ [8]. Moreover, another study suggested that the disruption of DGCR8-dependent microRNA biogenesis is crucial for the 22q11.21 copy number variant (CNV) genes involved in psychiatric disorders for late fetal cortical development [9]. MiRNomics has also been analyzed by some authors who described a panel of CSF-enriched miRNAs as a possible tool to identify and characterize new molecular signatures in different neurological diseases [10].

**Citation:** Villa, C.; Yoon, J.H. Multi-Omics for the Understanding of Brain Diseases. *Life* **2021**, *11*, 1202. https://doi.org/10.3390/life11111202

Received: 30 October 2021
Accepted: 5 November 2021
Published: 7 November 2021

In regards to proteomics, Drastichova and collaborators performed a study in a rat brain after withdrawal from morphine, revealing that alterations in protein expression and phosphorylation are associated with synaptic plasticity and cytoskeleton organization, thus contributing to long-term neuroadaptations induced by drug use and withdrawal [11]. Additionally, another study used a combined approach of mass spectrometry-based label-free quantitative proteomics (LFQ) and bioinformatics to investigate the protective effect of *Orthosiphon stamineus* leaf proteins (OSLPs) in SH-SY5Y cells induced by $H_2O_2$ insults that have been prevalently reported in different neurological disorders [12]. Finally, some authors demonstrated the utility of chloride adducts for the examination of human brain lipidomics, as no single platform can evaluate lipidomics as a whole [13].

In conclusion, brain diseases, such as neurodegenerative diseases and mental disorders, need integrative understanding that draws a more reliable hypothesis for pathology, which can be accomplished by an in-depth study of molecular information [14–16]. However, molecular profiling, which makes it possible to understand brain diseases, has been relatively insufficient [17–20]. This Special Issue can provide important information to help gain an in-depth understanding of the molecular aspects of diverse brain diseases. Furthermore, it is believed that multi-omics analysis should be used for brain diseases because multi-omics technology includes multiple molecular profiling, metadata, and big data processing with informatics and computer science, so it is possible to provide new macroscopic, as well as microscopic, insights for understanding brain diseases [21–23].

**Funding:** This research was supported by KBRI basic research program through the Korea Brain Research Institute funded by the Ministry of Science and ICT (21-BR-02-08).

**Institutional Review Board Statement:** Not applicable.

**Data Availability Statement:** Not applicable.

**Conflicts of Interest:** The authors declare no conflict of interest.

## References

1. Deuschl, G.; Beghi, E.; Fazekas, F.; Varga, T.; Christoforidi, K.A.; Sipido, E.; Bassetti, C.L.; Vos, T.; Feigin, V.L. The burden of neurological diseases in Europe: An analysis for the Global Burden of Disease Study 2017. *Lancet Public Health* **2020**, *5*, e551–e567. [CrossRef]
2. La Cognata, V.; Morello, G.; Cavallaro, S. Omics Data and Their Integrative Analysis to Support Stratified Medicine in Neurodegenerative Diseases. *Int. J. Mol. Sci.* **2021**, *22*, 4820. [CrossRef]
3. Manzoni, C.; Kia, D.A.; Vandrovcova, J.; Hardy, J.; Wood, N.W.; Lewis, P.A.; Ferrari, R. Genome, transcriptome and proteome: The rise of omics data and their integration in biomedical sciences. *Brief Bioinform.* **2018**, *19*, 286–302. [CrossRef]
4. Prasanna, P.; Rathee, S.; Rahul, V.; Mandal, D.; Chandra Goud, M.S.; Yadav, P.; Hawthorne, S.; Sharma, A.; Gupta, P.K.; Ojha, S.; et al. Microfluidic Platforms to Unravel Mysteries of Alzheimer's Disease: How Far Have We Come? *Life* **2021**, *11*, 1022. [CrossRef]
5. Braidy, N.; Villalva, M.D.; Grant, R. NADomics: Measuring NAD+ and Related Metabolites Using Liquid Chromatography Mass Spectrometry. *Life* **2021**, *11*, 512. [CrossRef]
6. Perrone, S.; Lembo, C.; Moretti, S.; Prezioso, G.; Buonocore, G.; Toscani, G.; Marinelli, F.; Nonnis-Marzano, F.; Esposito, S. Sudden Infant Death Syndrome: Beyond Risk Factors. *Life* **2021**, *11*, 184. [CrossRef] [PubMed]
7. Yusuf, A.P.; Abubakar, M.B.; Malami, I.; Ibrahim, K.G.; Abubakar, B.; Bello, M.B.; Qusty, N.; Elazab, S.T.; Imam, M.U.; Alexiou, A.; et al. Zinc Metalloproteins in Epigenetics and Their Crosstalk. *Life* **2021**, *11*, 186. [CrossRef]
8. Chen, M.; Wang, W.; Song, W.; Qian, W.; Lin, G.N. Integrative Analysis Identified Key Schizophrenia Risk Factors from an Abnormal Behavior Mouse Gene Set. *Life* **2021**, *11*, 172. [CrossRef] [PubMed]
9. Chen, L.; Cai, W.; Wang, W.; Liu, Z.; Lin, G.N. Spatiotemporal 22q11.21 Protein Network Implicates DGCR8-Dependent MicroRNA Biogenesis as a Risk for Late Fetal Cortical Development in Psychiatric Diseases. *Life* **2021**, *11*, 514. [CrossRef] [PubMed]
10. Muñoz-San Martín, M.; Gomez, I.; Miguela, A.; Belchí, O.; Robles-Cedeño, R.; Quintana, E.; Ramió-Torrentà, L. Description of a CSF-Enriched miRNA Panel for the Study of Neurological Diseases. *Life* **2021**, *11*, 594. [CrossRef]
11. Drastichova, Z.; Hejnova, L.; Moravcova, R.; Novotny, J. Proteomic Analysis Unveils Expressional Changes in Cytoskeleton- and Synaptic Plasticity-Associated Proteins in Rat Brain Six Months after Withdrawal from Morphine. *Life* **2021**, *11*, 683. [CrossRef] [PubMed]
12. Chung, Y.S.; Ahmed, P.K.; Othman, I.; Shaikh, M.F. *Orthosiphon stamineus* Proteins Alleviate Hydrogen Peroxide Stress in SH-SY5Y Cells. *Life* **2021**, *11*, 585. [CrossRef] [PubMed]

13. Wood, P.L.; Hauther, K.A.; Scarborough, J.H.; Craney, D.J.; Dudzik, B.; Cebak, J.E.; Woltjer, R.L. Human Brain Lipidomics: Utilities of Chloride Adducts in Flow Injection Analysis. *Life* **2021**, *11*, 403. [CrossRef] [PubMed]
14. Südhof, T.C. Molecular Neuroscience in the 21st Century: A Personal Perspective. *Neuron* **2017**, *96*, 536–541. [CrossRef]
15. Buffalo, E.A.; Movshon, J.A.; Wurtz, R.H. From basic brain research to treating human brain disorders. *Proc. Natl. Acad. Sci. USA* **2019**, *116*, 26167–26172. [CrossRef]
16. Iturria-Medina, Y.; Carbonell, F.; Assadi, A.; Adewale, Q.; Khan, A.F.; Baumeister, T.R.; Sanchez-Rodriguez, L. Integrating molecular, histopathological, neuroimaging and clinical neuroscience data with NeuroPM-box. *Commun. Biol.* **2021**, *4*, 614. [CrossRef]
17. Beach, T.G. Alzheimer's disease and the "Valley Of Death": Not enough guidance from human brain tissue? *J. Alzheimers Dis.* **2013**, *33* (Suppl. 1), S219–S233. [CrossRef]
18. Sproul, A.A.; Jacob, S.; Pre, D.; Kim, S.H.; Nestor, M.W.; Navarro-Sobrino, M.; Santa-Maria, I.; Zimmer, M.; Aubry, S.; Steele, J.W.; et al. Characterization and molecular profiling of PSEN1 familial Alzheimer's disease iPSC-derived neural progenitors. *PLoS ONE* **2014**, *9*, e84547. [CrossRef] [PubMed]
19. Mellick, G.D.; Silburn, P.A.; Sutherland, G.T.; Siebert, G.A. Exploiting the potential of molecular profiling in Parkinson's disease: Current practice and future probabilities. *Expert Rev. Mol. Diagn.* **2010**, *10*, 1035–1050. [CrossRef]
20. Egervari, G.; Kozlenkov, A.; Dracheva, S.; Hurd, Y.L. Molecular windows into the human brain for psychiatric disorders. *Mol. Psychiatry* **2019**, *24*, 653–673. [CrossRef] [PubMed]
21. Merelli, I.; Pérez-Sánchez, H.; Gesing, S.; D'Agostino, D. High-performance computing and big data in omics-based medicine. *BioMed Res. Int.* **2014**, *2014*, 825649. [CrossRef] [PubMed]
22. Leon-Mimila, P.; Wang, J.; Huertas-Vazquez, A. Relevance of Multi-Omics Studies in Cardiovascular Diseases. *Front. Cardiovasc. Med.* **2019**, *6*, 91. [CrossRef] [PubMed]
23. Yu, X.T.; Zeng, T. Integrative Analysis of Omics Big Data. *Methods Mol. Biol.* **2018**, *1754*, 109–135. [CrossRef] [PubMed]

life

MDPI

*Review*

# Microfluidic Platforms to Unravel Mysteries of Alzheimer's Disease: How Far Have We Come?

**Pragya Prasanna [1,*], Shweta Rathee [2], Vedanabhatla Rahul [3], Debabrata Mandal [4], Macherla Sharath Chandra Goud [1], Pardeep Yadav [5], Susan Hawthorne [6], Ankur Sharma [7], Piyush Kumar Gupta [7], Shreesh Ojha [8], Niraj Kumar Jha [5], Chiara Villa [9] and Saurabh Kumar Jha [5,*]**

1 School of Applied Sciences, KK University, Nalanda 803115, Bihar, India; mscgoud1234@gmail.com
2 Department of Food Science and Technology, National Institute of Food Technology, Entrepreneurship and Management, Sonipat 131028, Haryana, India; shweta.r@niftem.ac.in
3 Department of Mechanical Engineering, National Institute of Technology, Rourkela 769008, Odisha, India; vrahul1803@gmail.com
4 Department of Biotechnology, National Institute of Pharmaceutical Education and Research, Hajipur 844101, Bihar, India; debabrataman@gmail.com
5 Department of Biotechnology, School of Engineering and Technology (SET), Sharda University, Greater Noida 201310, Uttar Pradesh, India; par.yadav2011@gmail.com (P.Y.); niraj.jha@sharda.ac.in (N.K.J.)
6 School of Pharmacy and Pharmaceutical Sciences, Ulster University, Cromore Road, Coleraine, Co., Londonderry BT52 1SA, UK; s.hawthorne@ulster.ac.uk
7 Department of Life Sciences, School of Basic Science and Research (SBSR), Sharda University, Greater Noida 201310, Uttar Pradesh, India; ankur.sharma7@sharda.ac.in (A.S.); dr.piyushkgupta@gmail.com (P.K.G.)
8 Department of Pharmacology and Therapeutics, College of Medicine and Health Sciences, P.O. Box 17666, United Arab Emirates University, Al Ain 15551, United Arab Emirates; shreeshojha@uaeu.ac.ae
9 School of Medicine and Surgery, University of Milano-Bicocca, 20900 Monza, Italy; chiara.villa@unimib.it
* Correspondence: pragyaprasanna36@gmail.com or pragyaprasanna2019@gmail.com (P.P.); Saurabh.jha@sharda.ac.in (S.K.J.)

**Citation:** Prasanna, P.; Rathee, S.; Rahul, V.; Mandal, D.; Chandra Goud, M.S.; Yadav, P.; Hawthorne, S.; Sharma, A.; Gupta, P.K.; Ojha, S.; et al. Microfluidic Platforms to Unravel Mysteries of Alzheimer's Disease: How Far Have We Come? *Life* **2021**, *11*, 1022. https://doi.org/10.3390/life11101022

Academic Editor: Ramón Cacabelos

Received: 21 August 2021
Accepted: 20 September 2021
Published: 28 September 2021



**Abstract:** Alzheimer's disease (AD) is a significant health concern with enormous social and economic impact globally. The gradual deterioration of cognitive functions and irreversible neuronal losses are primary features of the disease. Even after decades of research, most therapeutic options are merely symptomatic, and drugs in clinical practice present numerous side effects. Lack of effective diagnostic techniques prevents the early prognosis of disease, resulting in a gradual deterioration in the quality of life. Furthermore, the mechanism of cognitive impairment and AD pathophysiology is poorly understood. Microfluidics exploits different microscale properties of fluids to mimic environments on microfluidic chip-like devices. These miniature multichambered devices can be used to grow cells and 3D tissues in vitro, analyze cell-to-cell communication, decipher the roles of neural cells such as microglia, and gain insights into AD pathophysiology. This review focuses on the applications and impact of microfluidics on AD research. We discuss the technical challenges and possible solutions provided by this new cutting-edge technique to understand disease-associated pathways and mechanisms.

**Keywords:** Alzheimer's disease; microfluidics; lab-on-chip; 3D culture; organ-on-chip

## 1. Introduction

Alzheimer's disease (AD) is a chronic neurodegenerative condition in which cognition and memory formation decline progressively due to an irreversible loss of neurons in the hippocampus and cortex regions [1]. It is characterized by the extracellular formation of senile plaque mainly constituted by amyloid-beta 42 (Aβ42)peptide and intracellular neurofibrillary tangles (NFTs), composed of hyper-phosphorylated paired helical filaments of the microtubule-associated protein tau (MAPT) [2–4]. Apart from Aβ and tau pathology, processes such as impaired synaptic functions, neurotransmission dysfunction, and

microglia-mediated inflammation play a key role in AD pathogenesis [5]. Primary symptoms of the disease comprise memory deterioration, apathy, depression, and changes in personality and behavior that finally require full-time medical care [6]. The majority of AD cases present as a late-onset sporadic form (SAD) occurring in individuals aged 65 or older. SAD shows a complex etiology and results from a combination of genetic and environmental influences. To date, the only confirmed genetic risk is represented by the presence of the ε4 allele of Apolipoprotein E (ApoE), the main carrier of cholesterol in the central nervous system (CNS). This variant accelerates the onset of AD by enhancing the Aβ deposition into plaques and reducing its clearance from the cerebral tissue [7]. On the contrary, the rare early-onset forms of AD are familiar with FAD with an autosomal dominant pattern of inheritance in one of the known genes, *APP*, *PSEN1*, and *PSEN2*, encoding the Aβ precursor protein (APP), presenilin-1, and presenilin-2, respectively. As all of these are involved in the maturation and processing of APP, mutations in these genes result in increased production or aggregation of Aβ peptides [8]. The 'World Alzheimer Report 2019' shows that AD accounts for more than 70% of the total dementia cases diagnosed worldwide [9,10], therefore an early diagnosis of AD is crucial for disease management [11].

Despite AD prevalence and many years of research, several aspects of its complex etiology remain unexplored [12,13]. Moreover, the current therapeutic strategies are merely symptomatic, attenuating only behavioral symptoms but presenting several side-effects such as confusion, dizziness, depression, constipation, and diarrhea, reported in most medications [14]. Therefore, a more in-depth understanding of the molecular mechanisms underlying AD pathogenesis, revisiting numerous existing concepts, and effective screening for therapies aimed at halting or preventing neurodegeneration in AD is required [15,16]. The lack of suitable experimental models has also presented a bottleneck in understanding the AD pathological mechanism. Moreover, widely accepted notions such as the deposition of Aβ and hyperphosphorylation of microtubular protein tau also lack a direct correlation between the deposition or phosphorylation and the disease progression [17,18].

In recent years, microfluidics is emerging as an economical and versatile platform for biologists to mimic and control the cellular microenvironment in order to model diseases, study cell behavior from single- to multi-cellular organism level, and develop multiple experiments in miniaturized devices suitable for diagnostics, biomedical analysis, pathological studies of neural degeneration and drug developments [19,20]. These devices are popular, especially for their flexibility of design, experimental flexibility, leverage of a sufficient number of controls, handling single cells, controlled co-culture, reduced reagent consumption, reduced contamination risk, and efficient high throughput experimentation.

The past decade has witnessed a surge in the use of microfluidics technology in neurodegenerative diseases to gradually minimize biomedical research dependence on in vivo models [21]. These platforms have been widely implicated in growing 3D gels that could be further applied in producing a three-dimensional tissue representative of human organs. With the help of these miniaturized devices, the growth of neurons, astrocytes, and microglia have also been facilitated in the form of triculture models [22]. This review describes the latest advances in the progress of microfluidics technologies and elaborates various ways through which the domain of microfluidics presents solutions to the management of neurodegenerative disease, with a particular focus on AD. First, we emphasized the applications of microfluidics in the study of disease pathophysiology and the early detection of AD with the help of known biomarkers at a miniaturized level. Subsequently, we examined the impact of microfluidics on accelerating AD research. We then discussed the possible challenges that this field needs to overcome and the directions to be taken before realizing its full-fledged application in the AD field.

## 2. Revisiting Alzheimer's Disease: What Is Known?

### *2.1. History*

AD was first diagnosed by a German psychiatrist and neuropathologist, Alois Alzheimer, in 1906 [16]. However, after 1907, the behavioral and physiological changes in AD and

naturally occurring senility and dementia were differentiated [23]. Symptoms such as failure of storage and retrieval of memory, confusion, and poor judgment have been categorized as characteristic features of AD. Other symptoms include language disturbance, agitation, withdrawal, and hallucinations followed by occasional seizures, increased muscle tone, and mutism [1,9,10,12]. Even after decades of research, the social and economic impact of the disease has not decreased, and the projections of the World Alzheimer Report 2019 predict more than 150 million cases by 2050 [9,10,12]. Due to remarkable advances in science and technology, increased understanding of the disease pathophysiology and causes has led to improved diagnosis and treatment [13,24].

### *2.2. Causes*

Several hypotheses have been proposed to define the etiology of AD based on observed clinical, neuropathological features: cholinergic hypothesis, amyloid cascade hypothesis, and tau propagation hypothesis [25]. Some other potential hallmarks of Alzheimer's dementia are mitochondrial dysfunction, calcium deregulation, neurovascular disintegration, neuroinflammation, metal ion dyshomeostasis, and defective lymphatic system [9,26–28]. However, the most well-known and defining features representing AD are Aβ accumulation, phosphorylated tau aggregation, and neuroinflammation [1,29,30]. In Figure 1, we have summarized the various AD hallmarks in the Alzheimer's brain and have shown how excessive amyloid deposition leads to neuronal disease. As mentioned above, the amyloid cascade hypothesis postulates that APP metabolism and Aβ42 accumulation are the most important triggering factors for AD pathogenesis [31]. This hypothesis holds the accumulation of Aβ peptide responsible for the eventual loss of synapses and neuronal cell death [3,28]. An increasing body of evidence supports toxic Aβ as the primary cause of pathology, which can initiate neuronal dysfunction by inducing granulovacuolar degeneration, astrocytosis, microgliosis, and deficient endosomal transport when deposited extracellularly [32]. Moreover, the Aβ can also deposit around the small blood vessels of the brain, leading to the development of cerebral amyloid angiopathy (CAA), a common neuropathological condition usually occurring in AD patients, probably caused by the failure of Aβ clearance [33].

Tau hypothesis correlates AD pathology with the hyperphosphorylation and intracellular deposition of neurofibrillary tangles (NFTs) of microtubular protein tau [17]. It further elucidates that the propagation of the pathological form of tau protein from one neuron to another may drive the disease aggressively. Few studies linking both the above hypotheses highlight that aggregation of amyloid plaques leads to the activation of vaious kinases, causing hyperphosphorylation of the tau protein [18]. The deposition of plaques and NFTs initiate a neuroinflammatory response by activating microglia and astrocytes that detect aggregated proteins and promote the release of pro-inflammatory cytokines such as interleukin (IL)-1β, IL-6, and tumor necrosis factor (TNF)-α, as well as reactive oxygen species (ROS), giving rise to a chronic inflammatory process [34–37]. The link between Aβ and tau aggregation may be related to microglia activation. Indeed, it has been reported that soluble Aβ oligomers can activate microglial cells that in turn promote the hyperphosphorylation of tau with the subsequent formation of NFTs via cytokine release [38]. In addition to microglia and astrocytes, recent evidence has suggested that oligodendrocytes can also play a role in AD pathogenesis. Several cellular processes such as neuroinflammation and oxidative stress may trigger oligodendrocyte dysfunction and Aβ can impair the maturation of oligodendrocyte progenitor cells and the consequent formation of the myelin sheath [39]. Furthermore, the neuroinflammation and dysfunction of the blood–brain barrier (BBB) resulting from enhanced permeability and reduced expression of tight junction proteins due to increased production of Aβ, overexpression of matrix metalloproteinases (MMP)-2/-9, and ApoE, are also often independently linked with AD pathogenesis [40–44].

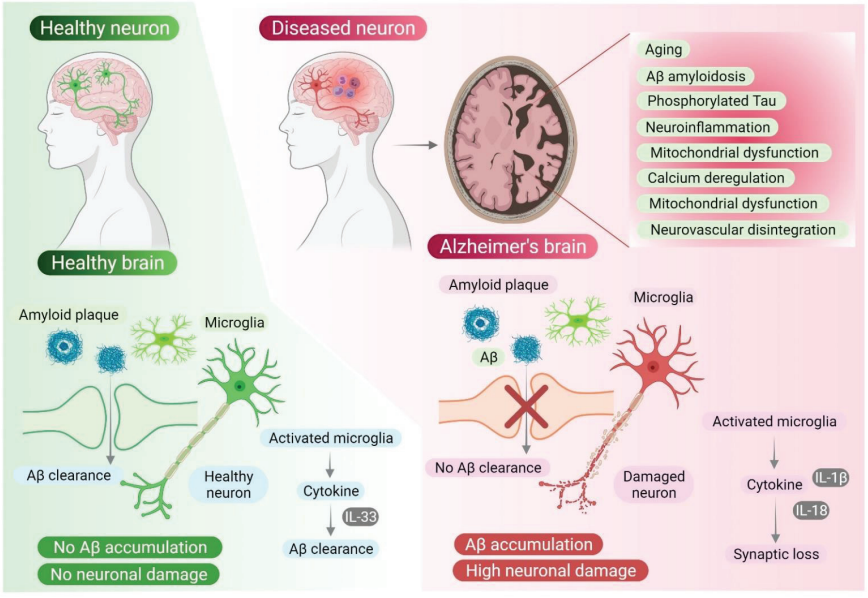


**Figure 1.** The pathophysiology of Alzheimer's disease is very complex. Major pathological hallmarks of Alzheimer's disease are provided. Among all the hallmarks, Aβ accumulation is considered the major cause of neurodegeneration in Alzheimer's disease. It has been found that all other causes such as tau pathology and/or neuroinflammation ultimately converge to Aβ accumulation. For instance, microglia, the innate immune system of the nervous system, mediates neuroinflammation by the production of cytokines such as IL33, IL-8 and IL-1β. Microglial activation initiates inflammation of the neural tissues. The cytokines (IL-33) produced in the due process help in Aβ clearance whereas IL-8 and IL-1β cause synaptic dysfunction. This molecular mechanism reflects the complex.

### *2.3. Diagnostic Biomarkers and Therapeutics*

The definitive diagnosis of AD is only possible by post-mortem histopathological assessment of extracellular Aβ plaques and intraneuronal NFTs [45]. Although the treatment is mainly supportive with symptoms managed on an individual basis, some of the therapeutic options approved for AD from the FDA include the cholinesterase inhibitors such as donepezil, rivastigmine, galantamine (reversible AChEIs), and memantine (NMDA inhibitor) [14,46–49]. However, the effectiveness of these drugs is often questioned [50]. As the pathological changes silently occur in the brain over years before the onset of symptoms, the current challenge is the search for novel biomarkers for an easy and accurate diagnosis of the disease in its initial stages. The actual diagnostic methods rely on the measures of Aβ42, phosphorylated (p-tau), and total tau (t-tau) protein levels in the cerebrospinal fluid (CSF) of patients, in combination with advanced neuroimaging techniques such as magnetic resonance imaging (MRI) and positron emission tomography [51]. Different reliable biomarkers comprising several signaling proteins in blood plasma have also been discovered that can detect Alzheimer's with approximately 90% accuracy even in patients with a mild cognitive impairment (MCI) which may later progress to AD [52]. A similar study with serum proteins, including a disintegrin and metalloprotease 10 (ADAM10), also retained diagnostic accuracy for the early diagnosis of AD [53]. Several blood-based microRNAs (Let-7b and microRNA-206) have also been found to have a strong correlation with cognitive decline and may be used as predictive biomarkers for AD [54]. Although promising, the use of these blood biomarkers in the clinical setting requires validation in further studies and standardization of pre-analytical sample processing and different methods.

## 3. Unsolved Mysteries in Alzheimer's Disease Research

There are long-standing differences in opinion regarding the roles of soluble Aβ fibrils and tau tangles in ameliorating neurotoxicity, inflammation, and AD initiation. Due to the overrated role of amyloids in AD pathology, immunization against Aβ was presumed to be an effective strategy, which unfortunately failed to deliver expected outcomes in clinical trials [30,55]. In subsequent studies, failure to reverse AD pathology following Aβ42 targeting or delaying plaque formation led researchers to believe that Aβ42 deposition is not the sole reason for AD pathogenesis [56]. Nonetheless, this observation and other findings, such as genetic mutations in presenilin-1/-2 and abnormal APP processing in AD, emphasized a significant shift in the focus towards alternative theories [57,58].

The believers in tauopathy also have found challenges in establishing the correlation between the biochemical observations of tau tangles and the clinical progression of the disease in the patients [59]. The specific tau species involved in neurotoxicity are ambiguous and arduous to decipher from the results obtained in the macroscopic experimental setup [60]. Recent evidence indicates that it is not only the amyloid plaques but also the intermediate amyloidic species and oligomeric assemblies that are neurotoxic and may exaggerate the disease pathology [61,62]. The major drawback experienced in the current laboratory practices is that it is incapable of assessing these deleterious oligomeric assemblies due to the problems associated with its separation from the Aβ.

The absence of validated biomarkers, probably due to the inconsistent results produced due to analytical hindrances such as epitope masking and lack of reproducibility, prevents early detection of disease symptoms and poses additional challenges [63,64]. More robust investigation of genetic risk factors, the mechanism of receptor-mediated transport of Aβ and the role of interstitial fluid in regulating the metabolism of Aβ in vitro models need to be determined.

Activation of astrocytes leads to an exacerbated immune response causing neuronal damage and degeneration [65]. Contemporary experimental approaches involve mutant or transgenic animals with disease pathology leading to immense animal mortality [66].

Recently, exosomes have gained considerable attention both as a drug delivery system and a significant biomarker for diagnostics by offering prognostic information [67,68]. These small membrane-bound extracellular vesicles are ubiquitously released from eukaryotic cells to carry and deliver proteins, lipids, and nucleic acids, to the target cells [67]. Though most studies substantiate the benefits of exosomes in the clearance of proteotoxic burden by transferring neuroprotective substances between neural cells, recent findings revealed that exosomes are also involved in the transportation of protein aggregates involved in different neurodegenerative diseases [67,69]. Furthermore, these loaded moieties play a crucial role in AD pathology by spreading Aβ and hyperphosphorylated tau, inducing oxidative/proteotoxic stresses, neuroinflammation, and neuronal loss [68–70]. Since exosomes may prove to be a significant biomarker, better techniques are required to isolate exosomes at a large scale and perform experiments at a co-culture level. However, for the successful implication of these nanovesicles in the domain of exosomes, extensive research is required to ascertain the probable route of administration and safety aspects for clinical application.

## 4. Cellular and Animal Models of AD

### *4.1. In Vitro Models*

The study of AD in vitro has been largely used to elucidate disease pathogenesis at molecular and cellular levels as well as for drug screening and discovery. Different cellular models have been developed to study various aspects of AD, including primary cultures, cancer cell lines, and induced pluripotent stem cells (iPSCs). However, cell culture systems cannot recapitulate the complex environment of the human brain and the interactions with other non-neuronal cells [71].

#### 4.1.1. Primary Cell Lines

Primary cell lines can be derived from transgenic animal or human patients. The major advantages in the use of these cultures rely on their easy availability and the potential to obtain different cell types, including specific neuron subtypes. Primary cultures have been extensively used to investigate the role of Aβ pathology both in astrocytes [72] and microglia [73]. Primary neurons, mainly derived from the hippocampus and cortex, were also employed to examine the neuroprotection mechanisms and the effect of Aβ oligomers on neuron function and apoptosis [74], as well as to reproduce the pathophysiological events occurring in AD, such as inflammation, altered signal pathways or epigenetic changes.

#### 4.1.2. Human Neuroblastoma (SH-SY5Y) Cell Lines

Originally isolated from human bone marrow with neuroblastoma, SH-SY5Y cells are derived from a neuronal lineage in its immature stage. According to the treatment, this cell line can differentiate into several various neural lineages which phenotypically resemble mature neuron-like features, including decreased proliferation rate, neuronal morphology, and expression of neuron-specific markers [75]. In regard to AD, SH-SY5Y cells can be modified to model some pathological aspects of the disease, such as neurodegeneration after exposure to Aβ oligomers [76], oxidative stress [77] and apoptosis [78], as well as to better understand the role of ApoE in AD [79]. Although this model has the potential to study the known molecular mechanisms associated with AD, it cannot fully recapitulate specific characteristics of the sporadic forms of the disease and age-dependent risk factors.

#### 4.1.3. iPSCs-Based Models of AD

Recent advances in iPSC technology have revolutionized the study of neurodegenerative disorders, given the limited access to living cells from brain patients. Reprogrammed from mature somatic cells of both familial (FAD) and sporadic AD (SAD) individuals, iPSCs can be differentiated into different disease-relevant cell types, maintaining the patient's precise genome. The majority of studies performed on iPSC-derived neurons from fibroblasts of FAD and SAD patients showed high levels of Aβ42 and response to β- and γ-secretase inhibitors [80–82], as well as increased hyperphosphorylated tau, the two main pathological hallmarks of AD [81,83]. Regarding other cell types, iPSC-derived astrocytes from AD patients displayed severe pathology and dysfunction [84]. Additionally, iPSCs have also been used to investigate the role of the ApoE ε4 allele in different cell types, including neurons, astrocytes and microglia [85]. The inherent limitations of iPSC-derived two-dimensional (2D) cultures can be partially overcome by the generation of three-dimensional (3D) organoids, complex self-organized aggregates of different cell types derived from iPSCs that closely mimic the complexity of the brain's architecture. Regarding AD, 3D cerebral organoids successfully recapitulate Aβ deposits, tau pathology and neuroinflammation [86,87].

### *4.2. In Vivo Models*

In recent decades, different experimental models in various species have been generated to replicate AD pathology. Invertebrate animal models, including Caenorhabditis elegans, Danio rerio, or Drosophila melanogaster, have been selected for their short lifespan, well-characterized development and behavior [71]. However, mammalian models, especially mice, have been commonly used in AD research due to their similar anatomy to humans and easy manipulation [71].

#### 4.2.1. Transgenic Animal Models of AD

Since the discovery of AD-associated genes, different transgenic animal models have been generated by introducing the human mutant gene into the animal genome or by deleting a specific gene from the animal genome to develop the pathological hallmarks of AD. Many transgenic mouse models have been developed so far, harboring mutations in the

APP, presenilin (PSEN1, PSEN2), MAPT genes or in combination (APP/Tau, APP/PSEN1 double transgenic mice, APP/Tau/PSEN1 triple transgenic mice (3xTg-AD) and five transgenic mice (5xFAD). However, these models do not reproduce all AD pathological features, as they mimic the genetic forms of AD without giving any information on sporadic AD. Single transgenic mouse overexpressing different mutations in APP gene and APP/PSEN1 double transgenic mice exhibited Aβ plaques and cognitive deficits but failed to develop NFTs, whereas the tau transgenic model showed NFTs, neuronal loss, and behavioral and motor impairments without developing Aβ plaques [88]. The two features of AD pathology were recapitulated with the generation of the APP/Tau double transgenic mice that displayed Aβ deposition, NFTs and motor deficits, representing a candidate tool to investigate the interaction between Aβ and tau protein. Compared to single and double transgenic models, the 3xTg-AD harboring mutations in APP, PSEN1 and MAPT genes exhibited more severe pathology but slow development of Aβ [89]. To accelerate the plaque formation, 5xFAD mice co-expressed five AD-linked mutations in human APP and PSEN1 genes, showing thus an early amyloid pathology, but lacking NFTs [90].

As ApoE represents the genetic risk factor for sporadic AD, transgenic, knock-in and knock-out mice expressing human APOE genes have been generated to investigate the mechanisms occurring in SAD. Knock-in mice expressing the human form of ApoE ε4 allele exhibited cognitive deficits [91] and high deposition of plaque or exacerbated tau-mediated neurodegeneration when crossed with APP or tau transgenic mice, respectively [92,93].

#### 4.2.2. Non-Transgenic Animal Models of AD

Non-transgenic animal models are used not only to study the classical AD hallmarks but also to model other pathological mechanisms, including oxidative stress, apoptosis, synaptic dysfunction, neuroinflammation, alterations in gut microbiota–brain axis, or autophagy [94]. As memory deficits and cognition loss are common traits of aged animals ranging from rodents to non-human primates, they can be used as a natural model of AD. Among them, the senescence-accelerated mouse-prone 8 (SAMP8) displayed age-related learning and memory decline as well as most features related to AD pathogenesis, such as oxidative stress, inflammation, Aβ plaques, NFTs, altered autophagy activity, and intestinal flora disruption, representing thus an ideal model to study this disorder [95]. Alternatively, animals can also be induced to develop AD by cerebral injection with Aβ synthetic peptide or other chemicals, by administering a high-fat diet to resemble metabolic abnormalities associated with AD, or generating radiofrequency lesions to the brain to induce cognitive deficiencies [88].

## 5. Microfluidics: An Overview and Biological Applications

The interdisciplinary field of microfluidics, derived from molecular biology, molecular analysis, and microelectronics, emerged in the late 1980s [96]. A timeline of the development of microfluidics from these physical and chemical innovations to its application in biological research has been provided in Figure 2. The emergence of this field began after discovering physical techniques such as photolithography and soft-lithography, later used for the fabrication of chips, and is still evolving with further technological advancements. The emergence of fabrication techniques facilitated the design and fabrication of chip-like 3D structures from solid substrates such as glass, silica, thermoplastics, etc. [96–99]. The first microfluidic devices or chips were made of silicon and glass. Still, due to their brittle nature, low gas permeability, and costly fabrication methods, they have never been considered an attractive option in microfluidics. Investigating alternative materials that could be optically transparent, easy to process, flexible, and comparatively cheap resulted in the discovery of several materials, which have been examined to date for the making of microfluidic devices (Table 1).

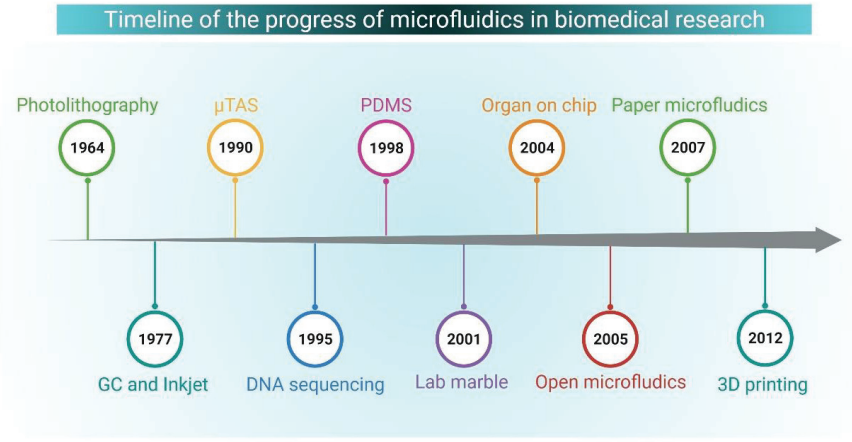


**Figure 2.** Timeline of the progress of microfluidics in biomedical research. Abbreviations: GC, gas chromatography; μTAS, micro total analysis system; PDMS, Polydimethylsiloxane.

For the materials used in designing microfluidic devices, polydimethylsiloxane (PDMS), an elastomer introduced in the 1990s, is a material of choice for cell co-cultures [99–102]. As PDMS is compatible with cells, microfluidic devices made from it started to be used for cell biology applications and studies of co-cultures [98,103]. Technology is usually characterized as an engineering subject. Still, the implementation of the proof-of-concept experiments in the domain of microfluidics serves biologists and clinicians in enhancing capabilities in their everyday research. This technology allows the manipulation of small fluid volumes in a fabricated microscale system and has emerged as an excellent tool in modern biology. These microscale, multichambered tiny devices can grow cells and 3D tissues for biology research [20] and has enabled us to recreate experimental conditions at microscopic levels. This allows manipulation of biological specimens and cells at extraordinary spatiotemporal resolution and reveals otherwise hidden mechanistic insights, leading to a range of biological applications [104]. Properties such as rapid sample processing and precise control of fluids in microfluidic technologies have presented an attractive way to replace traditional experimental approaches. The microliter volumes of reagents mobile in laminar flow match with the biological microenvironments. Multiple diverse biochemical assays can be performed in a small volume, and the flow control feature at the micron level allows for improvement over the traditional macroscale assays. This is widely used in the imaging, bioinformatics, and molecular biology approaches [105,106]. Integration of fluid handling and signal detection features in microfluidics has allowed us to design cheaper yet sensitive point-of-care assay devices for different infectious diseases such as cancer, AIDS, malaria, SARS, dengue, etc. [107–109]. Even paper-based microfluidics such as DNA diagnostics have been developed in recent years, which are low-cost, multiplexed diagnostics [110].

Liquid marble (LM) is also a new type of digital microfluidics (DMF) that can be employed in a variety of biological applications. Cryoprotectant-free cryopreservation of mammalian cells using LM-based digital microfluidics is a potential method. This opens up new ways to cryopreserve rare biological samples without the risk of cryoprotectants causing toxicity [111]. LM can also be utilized for diagnostic testing, cell culture, and drug screening in the biomedical area [112]. DMF, a novel multifunctional microfluidics technology, offers a great deal of potential in the automation and miniaturization fields. In DMF, discrete droplets containing samples and reagents are controlled to implement a series of operations via electrowetting-on-dielectric. This process works by applying electrical potentials to an array of electrodes coated with a hydrophobic dielectric layer. DMF, unlike microchannels, allows for exact control of various reaction processes without

the need for complicated pump, microvalve, and tubing networks. Other distinguishing characteristics of DMF include portability, lower sample consumption, faster chemical reaction time, versatility, and better integration with other technology types. DMF has been used in a wide range of fields (including chemistry, biology, medicine, and the environment) due to its distinct advantages [113]. Droplet-based microfluidics, which can be employed in drug discovery, transcriptomics, and high-throughput molecular genetics, has recently been reported. This enables researchers to work with relatively limited materials, such as primary cells, patient biopsies, or expensive reagents, and to perform tests at very high throughput (up to thousands of samples per second). The ability to undertake large-scale genotypic or phenotypic screens at the single-cell level is another advantage of the technology [114].

Isolated brain tissue, particularly brain slices, can be used to investigate neuronal function at the network, cellular, synaptic, and single channel levels. Neuroscientists have perfected ways for maintaining brain slice viability and function, settling on principles that are strikingly similar to the engineers' approach to building microfluidic devices. With respect to brain slices, microfluidic technology may (1) provide better spatiotemporal control over solution flow/drug delivery to specific slice regions; (2) overcome the traditional limitations of conventional interface and submerged slice chambers and improve oxygen/nutrient penetration into slices; and (3) permit successful integration with modern optical and electrophysiological techniques [115]. Tissue culture (brain tissue slice) and drug screening have recently been performed using microfluidic platforms. In a study, microfluidic tissue culture system has been utilized to enable culturing of brain tissue slices for a sufficiently long period (up to 3 weeks) to facilitate studies on integration of neuronal stem cells into brain tissue and differentiation into dopaminergic neurons. This also allows for long-term culturing on a microscope stage for real-time microscopic imaging during neural stem cell integration experiments in brain slices [116]. This method has the potential to improve treatment success rates by identifying possible responders earlier in the treatment process and allowing direct drug testing on patient tissues during the early stages of drug development [117].

Cell-patterning techniques are also useful for neuron function and activity investigation and are one of the clear advantages of using microfluidics. So far, many neuron patterning techniques, such as in-mold patterning (iMP), and gel micropatterning by micro-casting, or by laser or protein patterning, have been reported. Many applications, ranging from neurodegenerative research to neural computation, require oriented neuronal networks with controlled connectivity. An efficient, directed, and long-lasting guidance of axons toward their target is required to establish such networks in vitro. However, the best guidance achieved so far relies on confining axons in enclosed micro-channels, making them difficult to investigate further. iMP improves axon confinement efficiency on the tracks by 10 to 100 times, resulting in mm-long, highly regular, and fully accessible on-chip axon arrays. iMP also enables well-defined axon guidance from small populations of multiple neurons confined at predefined places in μm-sized wells, thereby opening up new avenues for the construction of complex and precisely regulated neural networks [118]. Gel micropatterning by micro-casting is another neuron patterning approach. By using the repellency of agarose gel toward cell adhesion, patterned cultures of myoblasts and cortical neurons can be prepared. This technology is said to be beneficial for repellency-guided cell patterning in a variety of cell types, with applications in cell–cell interactions and axon guidance. With the repellency of agarose and no specific molecules for cell adherence, this technology is user-friendly and useful not just for micro-molding but also for cellular patterning [119]. Further, Stripe assays have been frequently used as in vitro test systems to investigate the responses of developing axons, as well as migrating cells, to established or novel guidance molecules. Silicon matrices are used to produce striped patterns of active molecules on a surface (referred as a "carpet"), which are then used to culture neurons or any other cell type. Purified proteins were utilized to produce stripe patterns on a silicon matrix [120].

**Table 1.** Properties of materials used in microfluidic chips.

| Properties | Inorganic Materials | Elastomers | Thermoset | Thermoplastics | Hydrogel | Paper |
|---|---|---|---|---|---|---|
| **Examples** | Silicon/Glass | PDMS | Polyester | Polyethylene, Polystyrene Polycarbonate Polyurethane, Teflon, Cyclic Olefin Co-polymer (COC/COP) | Hyaluronic Acid, Agarose, PEG-DA, Alginate, PMMA, And Chitosan | - |
| **Biological Use** | Drug Screening, Assays | Assays, Cell Culture | Capillary | Electrophoresis, DNA Sequencing, PCR | Study Cell-Cell and Cell-Matrix Interaction | Diagnostics |
| **Young's Modulus** | 130–180/50–90 | ~0.0005 | 2.0–2.7 | 1.4–4.1 | Low | 0.0003–0.0025 |
| **Fabrication Technique** | Photolithography | Casting, 3D Printing | Casting/ Photopolymerization | Thermomoulding | Casting/Photopolymerization | Photolithography, Printing |
| **Valving** | Yes | Yes | No | No | Yes | Yes |
| **Channel Dimension/Profile** | <100 nm/3D | <1 µm/3D | <100 nm/Arbitrary 3D | ~100 nm/3D | ~10 µm/3D | ~200 µm/2D |
| **Thermostability** | Very High | Medium | High | Medium-High | Low | Medium |
| **Oxygen Permeability** | <0.01 | ~500 | 0.03-1 | 0.05–5 | >1 | >1 |
| **Solvent Compatibility** | Very High | Low | High | Medium-High | Low | Medium |
| **Hydrophobicity** | Hydrophobic | Hydrophobic | Hydrophobic | Hydrophobic | Hydrophilic | Amphiphilic |
| **Surface Charge** | Very Stable | Stable | Stable | Stable | - | - |
| **Transparency** | No/High | High | High | Medium-High | Low-Medium | Low |
| **Cost** | High | Low | High | Low | Medium | Low |
| **Disadvantage** | High Cost, Brittle | Protein Adsorption, Permeability, Autofluorescence | Rigid, Poor Conductivity, Non-Recyclable | Low Melting Point, Brittle | Non-Adherent, Low Mechanical Strength | Porous, Sample Consumption |
| **Reference(s)** | [121,122] | [123,124] | [125] | [126–128] | [129,130] | [131] |

Abbreviations: PEG-DA, Polyethylene Glycol Diacrylate.

Since the 2000s, organ-on-a-chiptechnology has been widely proposed and engineered on the structure and function of tissues and organs 2000 [132]. However, this has evolved rapidly in the past decade due to advancement in rapid prototyping methods such as 3D printing, widely used to produce 3D scaffolds for tissue engineering and devices mimicking a complex microfluidic environment [133]. The first "human-on-a-chip" cell culture systems to investigate physiological processes and "physiome-on-a-chip" systems to investigate novel compounds and their side effects on the human body have emerged [132,134–136]. The emulation of the pathophysiology of several neurodegenerative diseases in vitro through microfluidic devices has also risen rapidly [137,138]. A comprehensive study of the application of microfluidics in the study of neurodegeneration has been provided in the following sections. Several microfluidic tools available to date are shown in Figure 3.

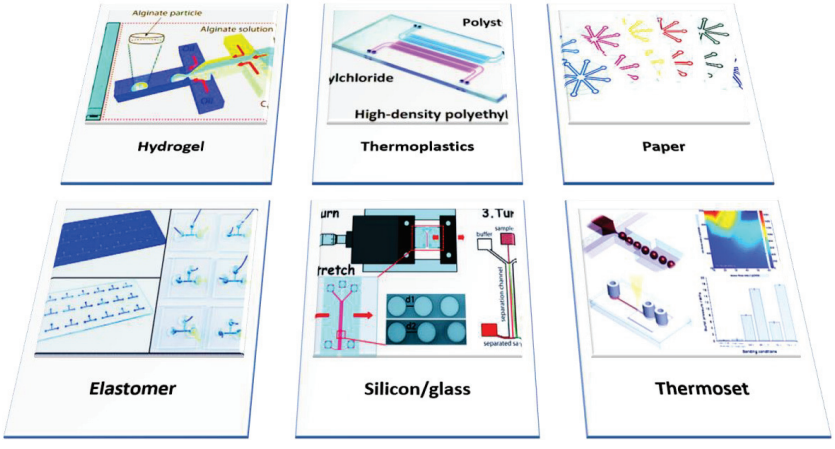


**Figure 3.** Schematic representation of the materials used for the fabrication of microfluidic chips. Hydrogels made up of natural materials, i.e., alginate, serve as matrices for culturing of cells in microfluidic chips. Thermoplastics such as polyvinyl chloride, polystyrene and high-density polyethylene are commonly used in fabrication. Moreover, the typical white color of paper makes it well suited for color-based detection methods in most assays and used for multiple bioassays in the form of origami-inspired folding devices. Elastomer is generally made up of PDMS. The glass-based microfluidic channel is made by the laser direct writing method. Thermoset, polyester-based, is a droplet-based device that can be used at different flow rates with three different oils.

## 6. Application of Microfluidics in Neurodegenerative Studies

Convergence of biology with engineering is evident in microfluidic devices used extensively nowadays in different domains of biomedical research contributing to a more powerful tool for drug delivery, point of care devices, and medical diagnostics [139]. Using microfluidics, a multichambered device can be readily prepared and used to grow neurites, glial cells, endothelial cells, and skeletal muscle cells, along with the maintenance of fluid isolation [140]. These devices can recapitulate organ-like structures and provide an opportunity to investigate organogenesis and disease etiology, accelerate drug discovery, screening, and toxicology studies by mimicking pathological conditions [141]. Utilizing hydrostatic pressure and chemical gradient profiles, localized areas of neurons grown in different compartments could be exposed to different kinds of insults applied insoluble form. A vast amount of literature exists highlighting applications of microfluidics in neurodegenerative diseases along with several neurodegenerative-disease-on-a-chip models focusing on AD, Parkinson's disease, and amyotrophic lateral sclerosis [137,138,142–145]. Furthermore, the microfluidic system has been implicated in the study of regulated cell-cell interactions, elucidating the complexity of intercellular interactions in the neuroinflammation of growing primary brain cells.

It is well known that many brain cells interact with each other under varied conditions to cause neuroinflammation. The microfluidic devices facilitate cell culture, e.g., astrocytes in separate chambers exposed to varied situations. These chambers can be independently regulated and monitored for analyzing morphology, vitality, calcium dynamics, and electrophysiology parameters [146]. It has provided a platform to study neuronal cell death within the brain through simultaneous observation of neuronal connectivity and tau pathology [147]. Unlike 2D culture systems, these 3D cell cultures and microfluidic lab-on-a-chip technologies with in vitro microfluidics systems do not lack the mobility of the cultured cells allowing a better physiological extracellular environment, for examining, neuron-glia interactions minimizing animal morbidity and mortality [148–150]. With the help of 3D culture techniques, the discrepancies in the results of in vitro culture systems and animal models in drug discovery can be avoided [151].

Studying brain development and degeneration at the cellular level suffers several limitations due to the inability to isolate cell culture systems, the absence of an organized physiological neuron connection architecture, and so forth. In this regard, microfluidic systems present an irreplaceable tool to simulate the BBB microenvironment, study axonal functions' construction of neuronal networks, and develop drug delivery systems through devices such as axonal diodes and minimized wireless devices [22,145,152–155]. Furthermore, the technology has led to the minimization of animal models in the study of neurodegenerative diseases, drastically cutting down labor-intensive efforts, time, and animal mortality. Besides, the discrepancies that arise due to species differences between humans and animal models can also be minimized.

The lab-on-chip technologies, with features on a similar physical scale to that of cells, have facilitated the study of complex neural signaling pathways to detect abnormalities, and check whether the application of inhibitors can reverse these without the requirement of animals [156,157]. The microfluidic entities can replicate complicated cell biological processes that control synaptic function, visualize them and manipulate synaptic regions and presynaptic and postsynaptic compartments independently under in vitro conditions, and manipulate synapses and presynaptic and postsynaptic cell bodies independently [101]. Studies show that synapses lose native circuitry and order due to the dissociating of neurons for in vitro studies. The organization of cultured neurons and their connections can be improved and restored by mimicking the natural circuitry in vivo conditions through microfluidic approaches [101]. With the help of microfluidic culture devices, two distinct micro-environments can be established, which may be maintained in fluidic isolation to allow for targeted investigation and treatment.

A compartmented kind of setup to co-culture a wide variety of cells is required to understand the mechanisms of a range of neurodegenerative diseases and model neuromuscular signaling [158,159]. The microfluidic devices fulfill all these requirements and mimic the unique anatomical and cellular interactions of this circuit [159,160]. 3D assay systems have been developed, human brain models allowing the measurement of action potential and velocity, monitoring cell growth, drug discovery, and study of neural–glial interactions and various neurotrophic factors [156,161]. Furthermore, microfluidic neuromuscular co-culture enables innervation by axons crossing from the neuronal to the muscle compartment [162]. The same setup can be used to decipher the impact of genetic alterations on the synaptic function of CNS disorders [163]. Therefore, microfluidics applied widely in various studies of disease, including neurodegeneration. Similarly, its impact on the research and development of AD is overwhelming and promising.

## 7. Impact of Microfluidic Tools in Alzheimer's Disease Research: Recent Developments

Advancements in microfluidic technology have played a significant role in accelerating the research dedicated to the field of AD, as with other diseases, in terms of both drug discovery, exploring novel drug targets, understanding the pathophysiology, or discovering novel biomarker-based diagnostics. A list of such initiatives has been provided in Table 2. Novel AD models, which are more helpful in mimicking the complex features of

AD pathology, have started to replace the traditional models. The 3D culture platforms are more suitable for studying AD pathophysiological mechanisms involving cell–cell interactions, controlled flow dynamics, circulating blood cells, and a brain-specific microenvironment. In a study, distinct roles of Aβ on microglial accumulation have been elucidated by quantifying microglial responses in order to gain insights into the pathophysiological role of microglial migration [164].

Similarly, the effects of axonal trauma on the neuronal networks of primary brain cells and the role of astrocytes were studied on a microfluidic platform [165,166]. The ease, accuracy, and reproducibility of the experiments encouraged a more significant number of studies. Apart from basic research, many disposable biosensors for early detection of AD biomarker ADAM10 and Aβ peptide in the serum have also been developed (limit of detection ~0.35 fg/mL) [167,168]. These low-cost diagnostic kits exhibit better accuracy and sensitivity than the well-established enzyme-linked immunosorbent assay test.

The emerging role of exosomes in the detection and study of AD has created the need for large-scale separation of exosomes, which is cumbersome and challenging with traditional techniques like ultra-centrifugation. Microfluidic devices are emerging as an ideal tool for exosome separation and have also started to gain recognition as excellent exosome detection tools [169]. These miniaturized platforms enable quick and cheap processing of nanovesicles even in the small volumes of liquid samples. Several microfluidic chips based on 3D neuro spheroids have been developed to mimic in vivo brain microenvironment [143]. These kinds of 3D culture-based microfluidic chip provide in vivo microenvironments for high-throughput drug screening and allow the investigation of dendrite-to-nucleus signaling [170]. Synthetic models with AD features such as aggregation of Aβ, and accumulation of phosphorylated tau protein with neuroinflammatory activities have been produced to emulate pathological states. A triculture in vitro model comprising the combination of neurons, astrocytes, and microglia has evolved to address the physiological features and study the durotactic behavior of cells [171]. The human AD triculture model provides an opportunity to learn about microglial recruitment, neurotoxic activities, and astrocytes [171]. A co-culture system with segregated cell bodies, while simultaneously forming myelin sheaths, could also be obtained through a microfluidics approach [172].

These studies claim to reverse the demyelination of axons which can recover the loss of sensory and motor function with the help of co-cultures. The microfluidic devices allow the study of AD-derived tau propagation from neuron to neuron. Application of microfluidic cell culture must be undergone only upon testing the cell lines with the PDMS formulations, checking for leaching of toxic compounds, and examining that the medium composition is well adjusted to suit the device and cells. Microfluidic systems present a reliable method to mimic in vivo fluid conditions of neural tissues by generating gradients to allow the diffusion of two separate fluid phases at the interface [36]. The microfluidic technology facilitates understanding of the mechanism of Aβ under interstitial fluid flow conditions. These kinds of 3D culture-based microfluidic chips provide in vivo microenvironments for high-throughput drug screening [106,132]. These devices have also been used to isolate axons and the cell body to study the targets of excitotoxicity observed in neurodegeneration. In another study, the distal axon is the main target. These models can be widely used for basic mechanistic studies involved in the interaction between neural-glial cells and drug discovery. The microfluidic approach has also been used to grow a 3D human neural cell culture wherein a BBB-like phenotype was developed. The generation of such a phenotype helps in screening novel drugs capable of passing through the BBB to reach deeper neural tissues [148]. This technology facilitates the culturing of cortical neurons in two distinct cell compartments of the same microfluidic device to generate neuronal networks [173]. This setup can bring axonal degeneration in the distal axon chamber without degenerative changes in the untreated somal section [174]. Insults to the selective areas of neurons can be obtained without affecting other neurons by applying hydrostatic pressure [142].

**Table 2.** Details of microfluidic devices and their application in the AD research.

| Cells/Peptide | Flow Control Device | Flow Surface | Active/Passive | Application | Reference(s) |
|---|---|---|---|---|---|
| Axon | NA | Glass | P | Study axonal function | [154] |
| Neural Progenitor Cell | Osmotic micropump | - | A | Study the neurotoxicity of amyloid beta | [36] |
| Neuron | Osmotic micropump | Glass | A & P | in vitro brain model, high-throughput drug screening | [143] |
| Brain Cells | Pneumatically-driven pumps | Polysulfone | P | To provide MPSs for in vitro drug discovery | [175] |
| Aβ42 Peptide | Precision pump | Glass | A | Aβ (1–42) detection | [168] |
| Aβ Peptide | Syringe | - | A | - | [176] |
| Axons | N/A | Glass | P | Study impaired axonal deficit | [156] |
| Axons | N/A | MEA | P | Investigate axonal signals in developmental stage | [177] |
| Neurites | Syringe | Glass | A | Study durotactic behavior of cells and neurite growth | [161] |
| Axons | Gravity/Hydrostatic pressure | PCB/Glass | P | Study axonal physiology and modeling CNS injury | [178] |
| Soma and Axon | N/A | Glass | P | Compartmentalizing the network structure into interconnected sub-populations | [179] |
| Hippocampal Neuronal/Glia Cells | Pressure gradient | Glass | P | Probing the functional synaptic connectivity between mixed primary hippocampal co-cultures | [163] |
| Dendrite | N/A | PDMS | NM | Investigate dendrite-to-nucleus signaling | [170] |
| Oligodendrocyte | N/A | Glass | P | - | [172] |
| Drg/Mc3t3-E1 | N/A | Glass | NM | Mimicking the in vivo scenario to study the interaction between the peripheral nervous system and bone cells | [160] |
| Nmj | Pipette | Glass | N/A | Study subcellular microenvironments, NMJ formation, maintenance, and disruption | [162] |
| Axons | Pipette | Glass | P | Perform drug screening assays | [180] |
| Dendrites and Somata | Syringe | Glass | A | Manipulate synaptic regions and presynaptic and postsynaptic compartments in vitro | [101] |
| Glial Cells/Motor Neurons | N/A | Glass | P | Study interactions with glial cells and other skeletal cells in the chamber | [159] |

**Table 2.** *Cont.*

| Cells/Peptide | Flow Control Device | Flow Surface | Active/Passive | Application | Reference(s) |
|---|---|---|---|---|---|
| Astrocyte | N/A | acrylic plate | P | AD triculture model showing beta-amyloid aggregation, phosphorylated tau accumulation, and neuroinflammatory activity | [144] |
| Tau | N/A | Glass | P | Study effects of tau on mitochondrial transport | [181] |
| (Aβ) Peptides | N/A | Glass | P | Study effects of local Aβ stress on neuronal sub-compartments and networks | [182] |
| ADAM10 | Syringe | N/A | A | ADAM10 biomarker detection in plasma and cerebrospinal fluid | [167] |
| Tau | N/A | Glass | P | Quantify AD-derived Tau propagation | [147] |
| Aβ | N/A | Glass | P | Study roles of Aβ on microglial accumulation | [183] |
| Aβ | Syringe | Overflow microfluidic networks | A | Study cell-to-cell communication, role of astrocytes derived from cortex and hippocampus on neuronal viability | [146] |
| Axons | - | Glass | - | Study mechanisms of indirect axonal excitotoxicity | [174] |
| Neurites | Hydrostatic pressure | Glass and Polystyrene | P | Grow neuronal culture | [142] |
| Cortical Neurons | Pressure difference | Glass | P | Synthesize experimental models emulating pathological states | [173] |
| Ren-WT/Ren-AD Cells | N/A | Glass | P | Grow 3D human neural cell culture, screen novel drugs capable of passing through the BBB to reach deeper neural tissues | [148] |
| Protein | N/A | Glass | P | Detect protein aggregation | [184] |
| Axons | Hydrostatic pressure | Glass or Polystyrene | P | Study localized axon-glia interaction and signaling | [185] |
| Axons | N/A | Glass | P | Examine axonal trauma in neuronal networks | [166] |
| Axons-glia | Hydrostatic pressure | Glass | P | Study axon-glia interactions | [186] |
| Neurites | Syringe | Glass | A | Investigating chemotaxis of neutrophils | [187] |

Abbreviations: MPSs, Micro-physiological systems; DRG, Dorsal root ganglion; NMJ, Neuromuscular junction; MEA, Microelectrode arrays.

## 8. Challenges in the Application of Microfluidics in the Alzheimer's Disease Research

Although microfluidics provides a state-of-the-art facility that enables investigations in biomedical research, there are many challenges that need to be addressed before the optimal utilization of this field's potential. Experts believe that the area of microfluidics

research needs to grow further in order to outperform existing laboratory methods and overcome barriers that hinder researchers from adopting microfluidic-based devices as a common research tool.

First of all, the lack of precise fluid handling techniques at such a microscopic level poses great difficulty in attaining the exact quantity of reagents for performing molecular experiments. Though achieved once, it becomes difficult to replicate the experiments with acceptable accuracy. The second major problem is that it is difficult to scale up the experiments under the same experimental conditions with the same volume of reagents. This is because of inability in fluid handling and duplicating culture or reaction conditions. Often cells may respond differently toa change in the substrate of microfluidic devices. Thirdly, the majority of the culture protocols have been optimized on polystyrene culture plates, a significant component in macroscale devices, unlike microfluidic cell culture devices that use PDMS. New production techniques favoring mass production such as microfluidic hot embossing in polystyrene have been found useful in minimizing the risk of translation failure in microfluidic devices, yet PDMS is the most commonly used substrate for fabricating these devices [188].

Any variation in the reagent volume or reaction conditions leads to inaccurate results and protocols. Moreover, a direct comparison with the macroscale experiments become very difficult as a change in the substrate may hinder the transition of the protocols to the microscale levels. Studies indicate that PDMS may absorb or adsorb the biomolecules from the medium, causing biased experimental conditions [189,190]. Absorption and/or adsorption of reagents will alter the reaction volumes, which is another demerit that microfluidic devices currently face. In addition, we do not know whether PDMS, a material known for its transparency and gas permeability, has any impact on cellular behavior. Since it is the material of choice at present, ascertaining its effect on cellular behavior is essential.

Excessive permeability, technical robustness, and other properties might lead to sample drying and change in osmolarity, posing a considerable obstruction. Samples collected on chips/microfluidic channels for analysis using chip-based PCR, histochemistry, western blots, or MS-Spectrometry will fail to give accurate results upon a slight change in the volume of reaction constituents [104,191]. Additionally, these experiments require the reagents to be properly mixed, but microfluidics produces slow diffusive mixing due to laminar flows, posing a major limitation for these systems wherein fast homogenization is required [192].

The lack of a universal blood substitute or standard culture media that supports all types of tissue is an additional setback. Other drawbacks that must be addressed in the future for the optimal application of microfluidics in Alzheimer's research is its interdisciplinary nature, wherein standardized protocols are generally absent. A combined effort of engineers and molecular biologists is required to fabricate new device designs and carry out biologically relevant experiments [36]. As a range of cell lines are cultured in these devices, generalization in device designs is difficult.

It is well known that physical parameters such as flow, pressure, temperature, pH, and real-time monitoring are equally important in carrying out biological experiments with accuracy. To ascertain these parameters, newly designed chips are now well integrated with the in-line sensors and microfluorimetric imaging facilities, but the chip still lacks features such as feedback control, continuous monitoring, and experimental sample processing. Unlike macroscopic laboratory practices, an automated control system is required to expand the domain of users and replace the 2D or 3D culture systems. The 3D tri culture AD model is gaining popularity as it is undoubtedly advanced over in vitro human AD models. Nonetheless, physiologically relevant in vivo studies are still required to confirm its clinical utility [144].

## 9. Conclusions

Even after a century of extensive research, the field of AD requires more work in the appropriate direction to come up with effective diagnostics and therapeutic cures [12,56,193].

The crucial research problems are challenging with current macroscopic laboratory equipment and practices. The research is at a crossroads where rigor is required to determine the right direction and appropriate focus. Microfluidic systems facilitate work on functional organs at the level of molecular analysis, significantly minimizing the complications involved in handling in vivo systems. These devices outperform age-old methodologies through features such as rapid sample processing, fluid control, flexibility of design, controlled co-culture, reduced reagent consumption, low contamination risk, and efficient high throughput experimentation. Undoubtedly, these novel neurotechnological tools are very useful in gaining an in-depth understanding of the brain's functions and discovering novel therapeutic strategies for neurological disorders like AD. However, the extent to which this technology can serve in AD detection and management is still in a nascent phase. This is because the technology has not been developed to recapitulate biological responses to various stimuli such as chemicals or toxins. Although organs-on-chips may lead to the identification of biomarkers and validation of lead drug candidates, clinically relevant PK/PD models are required to determine the drug doses. In this regard, better scaling approaches to keep an account of fluid flows and volumes of distribution would ensure functional PK/PD models. It is doubtful that organs-on-chips will replace animal testing anytime soon, as the organ function and regulatory requirements are highly complex. Nonetheless, these low-cost techniques are up-and-coming and have accelerated the pace of AD research.

**Author Contributions:** Conceptualization, supervision, writing—original draft preparation, data curation; Reviewing and editing, P.P.; Visualization, S.R.; Data curation, writing—original draft preparation; visualization, V.R.; Reviewing and editing, D.M.; Reviewing and editing, M.S.C.G.; Reviewing and editing, P.Y.; Reviewing and editing, S.H.; Reviewing and editing, A.S.; Reviewing and editing, P.K.G.; Reviewing and editing, S.O.; Artwork and schemes, N.K.J.; Reviewing and editing, C.V.; Conceptualization, supervision, writing—original draft preparation, data curation; Reviewing and editing, S.K.J. All authors have read and agreed to the published version of the manuscript.

**Funding:** The present work did not receive any specific grant from funding agencies in the public, commercial, or not-for-profit sectors.

**Institutional Review Board Statement:** Not Applicable.

**Informed Consent Statement:** Not Applicable.

**Data Availability Statement:** Not Applicable.

**Conflicts of Interest:** The authors have no conflict of interest to declare.

## Abbreviations

| | |
|---|---|
| AD | Alzheimer's disease |
| ADAM10 | A Disintegrin and Metalloprotease 10 |
| Apo E | Apolipoprotein E |
| Aβ | Amyloid-beta |
| CD33 | Complementary determinant 33 |
| IL | Interleukin |
| MMP | Matrix metallopeptidase 9 |
| NMJ | Neuromuscular junction |
| PCR | Polymerase chain reaction |
| PDMS | Polydimethylsiloxane |
| PK/PD | Pharmacokinetic/Pharmacodynamic |
| TNF-α | Tumor necrosis factor-alpha |
| TREM2 | Triggering receptor expressed on myeloid cells2 |

## References


1. Jha, N.K.; Jha, S.K.; Kar, R.; Nand, P.; Swati, K.; Goswami, V.K. Nuclear factor-kappa β as a therapeutic target for Alzheimer's disease. *J. Neurochem.* **2019**, *150*, 113–137. [CrossRef]
2. Crimins, J.L.; Pooler, A.; Polydoro, M.; Luebke, J.I.; Spires-Jones, T.L. The Intersection of Amyloid Beta and Tau in Glutamatergic Synaptic Dysfunction and Collapse in Alzheimer's Disease. *Ageing Res. Rev.* **2013**, *12*, 757–763. [CrossRef]
3. Kumar, P.; Jha, N.K.; Jha, S.K.; Ramani, K.; Ambasta, R.K. Tau phosphorylation, molecular chaperones, and ubiquitin E3 ligase: Clinical relevance in Alzheimer's disease. *J. Alzheimers Dis.* **2015**, *43*, 341–461. [CrossRef]
4. Lee, J.C.; Kim, S.J.; Hong, S.; Kim, Y.S. Diagnosis of Alzheimer's Disease Utilizing Amyloid and Tau as Fluid Biomarkers. *Exp. Mol. Med.* **2019**, *51*, 1–10. [CrossRef] [PubMed]
5. Jha, S.K.; Jha, N.K.; Kumar, D.; Sharma, R.; Shrivastava, A.; Ambasta, R.K.; Kumar, P. Stress-Induced Synaptic Dysfunction and Neurotransmitter Release in Alzheimer's Disease: Can Neurotransmitters and Neuromodulators be Potential Therapeutic Targets? *J. Alzheimers Dis.* **2017**, *57*, 1017–1039. [CrossRef] [PubMed]
6. Jha, N.K.; Jha, S.K.; Kumar, D.; Kejriwal, N.; Sharma, R.; Ambasta, R.K.; Kumar, P. Impact of Insulin Degrading Enzyme and Neprilysin in Alzheimer's Disease Biology: Characterization of Putative Cognates for Therapeutic Applications. *J. Alzheimers Dis.* **2015**, *48*, 891–917. [CrossRef]
7. Liu, C.-C.; Kanekiuo, T.; Xu, H.; Bu, G. Apolipoprotein E and Alzheimer Disease: Risk, Mechanisms and Therapy. *Nat. Rev. Neurol.* **2013**, *9*, 106–118. [CrossRef]
8. D'Argenio, V.; Sarnataro, D. New Insights into the Molecular Bases of Familial Alzheimer's Disease. *J. Pers. Med.* **2020**, *10*, 26. [CrossRef]
9. Lynch, C. World Alzheimer Report 2019: Attitudes to Dementia, a Global Survey. *Alzheimers Dement.* **2020**, *16*, e038255. [CrossRef]
10. 2021 Alzheimer's Disease Facts and Figures. *Alzheimers Dement.* **2021**, *17*, 327–406. [CrossRef]
11. International, D. World Alzheimer Report 2020–Design Dignity Dementia: Dementia-Related Design and the Built Environment. *Alzheimers Dis. Int.* **2020**, *1*, 106–113.
12. Holtzman, D.M.; Morris, J.C.; Goate, A.M. Alzheimer's Disease: The Challenge of the Second Century. *Sci. Transl. Med.* **2011**, *3*, 77. [CrossRef] [PubMed]
13. Kocahan, S.; Doğan, Z. Mechanisms of Alzheimer's Disease Pathogenesis and Prevention: The Brain, Neural Pathology, N-Methyl-D-Aspartate Receptors, Tau Protein and Other Risk Factors. *Clin. Psychopharmacol. Neurosci.* **2017**, *15*, 1–8. [CrossRef]
14. Yiannopoulou, K.G.; Papageorgiou, S.G. Current and Future Treatments for Alzheimer's Disease. *Ther. Adv. Neurol. Disord.* **2013**, *6*, 19. [CrossRef]
15. Guo, T.; Zhang, D.; Zeng, Y.; Huang, T.Y.; Xu, H.; Zhao, Y. Molecular and Cellular Mechanisms Underlying the Pathogenesis of Alzheimer's Disease. *Mol. Neurodegener.* **2020**, *15*, 1–37. [CrossRef] [PubMed]
16. Strassnig, M.; Ganguli, M. About a Peculiar Disease of the Cerebral Cortex: Alzheimer's Original Case Revisited. *Psychiatry* **2005**, *2*, 30–33. [PubMed]
17. You, Y.; Perkins, A.; Cisternas, P.; Muñoz, B.; Taylor, X.; You, Y.; Garringer, H.J.; Oblak, A.L.; Atwood, B.K.; Vidal, R.; et al. Tau as a Mediator of Neurotoxicity Associated to Cerebral Amyloid Angiopathy. *Acta Neuropathol. Commun.* **2019**, *7*, 26. [CrossRef] [PubMed]
18. Huang, H.C.; Jiang, Z.F. Accumulated Amyloid-β Peptide and Hyperphosphorylated Tau Protein: Relationship and Links in Alzheimer's Disease. *J. Alzheimers Dis.* **2009**, *16*, 15–27. [CrossRef]
19. Li, Y.; Li, D.; Zhao, P.; Nandakumar, K.; Wang, L.; Song, Y. Microfluidics-Based Systems in Diagnosis of Alzheimer's Disease and Biomimetic Modeling. *Micromachines* **2020**, *11*, 787. [CrossRef]
20. Velve-Casquillas, G.; Le Berre, M.; Piel, M.; Tran, P.T. Microfluidic Tools for Cell Biological Research. *Nano Today* **2010**, *5*, 28–47. [CrossRef]
21. Edmondson, R.; Broglie, J.J.; Adcock, A.F.; Yang, L. Three-Dimensional Cell Culture Systems and Their Applications in Drug Discovery and Cell-Based Biosensors. *ASSAY Drug Dev. Technol.* **2014**, *12*, 207–218. [CrossRef] [PubMed]
22. Lam, D.; Enright, H.A.; Cadena, J.; Peters, S.K.; Sales, A.P.; Osburn, J.J.; Soscia, D.A.; Kulp, K.S.; Wheeler, E.K.; Fischer, N.O. Tissue-specific extracellular matrix accelerates the formation of neural networks and communities in a neuron-glia co-culture on a multi-electrode array. *Sci. Rep.* **2019**, *9*, 1–5.
23. Goedert, M.; Spillantini, M.G. A Century of Alzheimer's Disease. *Science* **2006**, *314*, 777–781. [CrossRef] [PubMed]
24. Deture, M.A.; Dickson, D.W. The Neuropathological Diagnosis of Alzheimer's Disease. *Mol. Neurodegener.* **2019**, *14*, 32. [CrossRef]
25. Li, H.; Liu, C.C.; Zheng, H.; Huang, T.Y. Amyloid, Tau, Pathogen Infection and Antimicrobial Protection in Alzheimer's Disease -Conformist, Nonconformist, and Realistic Prospects for AD Pathogenesis. *Transl. Neurodegener.* **2018**, *7*, 34. [CrossRef]
26. De-Paula, V.J.; Radanovic, M.; Diniz, B.S.; Forlenza, O.V. Alzheimer's Disease. *Subcell. Biochem.* **2012**, *65*, 329–352.
27. Jack, C.R., Jr.; Holtzman, D.M. Biomarker modeling of Alzheimer's disease. *Neuron* **2013**, *80*, 1347–1358. [CrossRef]
28. Sinha, S.M.; Ansell-Schultz, A.; Civitelli, L.; Hildesjö, C.; Larsson, M.; Lannfelt, L.; Ingelsson, M.; Hallbeck, M. Alzheimer's Disease Pathology Propagation by Exosomes Containing Toxic Amyloid-Beta Oligomers. *Acta Neuropathol.* **2018**, *136*, 41–56. [CrossRef]
29. Murphy, M.P.; LeVine, H., III. Alzheimer's Disease and the $β$-Amyloid Peptide. *J. Alzheimers Dis.* **2010**, *19*, 311. [CrossRef]
30. Sengupta, U.; Nilson, A.N.; Kayed, R. The Role of Amyloid-β Oligomers in Toxicity, Propagation, and Immunotherapy. *EBioMedicine* **2016**, *6*, 42–49. [CrossRef]

31. Tanzi, R.E.; Bertram, L. Twenty Years of the Alzheimer's Disease Amyloid Hypothesis: A Genetic Perspective. *Cell* **2005**, *120*, 545–555. [CrossRef] [PubMed]
32. Chen, X.Q.; Mobley, W.C. Exploring the Pathogenesis of Alzheimer Disease in Basal Forebrain Cholinergic Neurons:Converging Insights from Alternative Hypotheses. *Front. Neurosci.* **2019**, *13*, 446. [CrossRef] [PubMed]
33. Brenowitz, W.D.; Nelson, P.T.; Besser, L.M.; Heller, K.B.; Kukull, W.A. Cerebral Amyloid Angiopathy and Its Co-Occurrence with Alzheimer's Disease and Other Cerebrovascular Neuropathologic Changes. *Neurobiol. Aging* **2015**, *36*, 2702–2708. [CrossRef]
34. Hansen, D.V.; Hanson, J.E.; Sheng, M. Microglia in Alzheimer's Disease. *J. Cell Biol.* **2018**, *217*, 459–472. [CrossRef] [PubMed]
35. Mandrekar-Colucci, S.; Landreth, G.E. Microglia and Inflammation in Alzheimers Disease. *CNS Neurol Disord. Drug Targets* **2012**, *9*, 156–167. [CrossRef] [PubMed]
36. Choi, Y.J.; Chae, S.; Kim, J.H.; Barald, K.F.; Park, J.Y.; Lee, S.H. Neurotoxic Amyloid Beta Oligomeric Assemblies Recreated in Microfluidic Platform with Interstitial Level of Slow Flow. *Sci. Rep.* **2013**, *3*, 1921. [CrossRef]
37. Wang, W.-Y.; Tan, M.-S.; Yu, J.T.; Tan, L. Role of Pro-Inflammatory Cytokines Released from Microglia in Alzheimer's Disease. *Ann. Transl. Med.* **2015**, *3*, 136.
38. Ismail, R.; Parbo, P.; Madsen, L.S.; Hansen, A.K.; Hansen, K.V.; Schaldemose, J.L.; Kjeldsen, P.L.; Stokholm, M.G.; Gottrup, M.G.; Eskildsen, S.F.; et al. The Relationships between Neuroinflammation, Beta-Amyloid and Tau Deposition in Alzheimer's Disease: A Longitudinal PET Study. *J. Neuroinflammation* **2020**, *17*, 151. [CrossRef]
39. Ardura-Fabregat, A.; Boddeke, E.W.G.M.; Boza-Serrano, A.; Brioschi, S.; Castro-Gomez, S.; Ceyzeriat, K.; Dansokho, C.; Dierkes, T.; Gelders, G.; Heneka, M.T.; et al. Targeting Neuroinflammation to Treat Alzheimer's Disease. *CNS Drugs* **2017**, *31*, 1057–1082. [CrossRef]
40. Yamazaki, Y.; Kanekiyo, T. Blood-Brain Barrier Dysfunction and the Pathogenesis of Alzheimer's Disease. *Int. J. Mol. Sci.* **2017**, *18*, 1956. [CrossRef]
41. Sweeney, M.D.; Sagare, A.P.; Zlokovic, B.V. Blood-Brain Barrier Breakdown in Alzheimer Disease and Other Neurodegenerative Disorders. *Nat. Rev. Neurol.* **2018**, *14*, 133–150. [CrossRef] [PubMed]
42. Calsolaro, V.; Edison, P. Neuroinflammation in Alzheimer's Disease: Current Evidence and Future Directions. *Alzheimers Dement.* **2016**, *12*, 719–732. [CrossRef] [PubMed]
43. Rempe, R.G.; Hartz, A.M.S.; Bauer, B. Matrix Metalloproteinases in the Brain and Blood–Brain Barrier: Versatile Breakers and Makers. *Br. J. Pharmacol.* **2016**, *36*, 1481. [CrossRef] [PubMed]
44. Fernandez, C.G.; Hamby, M.E.; McReynolds, M.L.; Ray, W.J. The Role of APOE4 in Disrupting the Homeostatic Functions of Astrocytes and Microglia in Aging and Alzheimer's Disease. *Front. Aging Neurosci.* **2019**, *11*, 14. [CrossRef]
45. Bird, T.D. Genetic Aspects of Alzheimer Disease. *Genet. Med.* **2009**, *10*, 231–239. [CrossRef]
46. Birks, J.S.; Chong, L.Y.; Evans, J.G. Rivastigmine for Alzheimer's Disease. *Cochrane Database Syst. Rev.* **2015**, *9*, CD001191.
47. Woodruff-Pak, D.S.; Vogel, R.W.; Wenk, G.L. Galantamine: Effect on Nicotinic Receptor Binding, Acetylcholinesterase Inhibition, and Learning. *Proc. Natl. Acad. Sci. USA* **2001**, *98*, 2089–2094. [CrossRef]
48. Lilienfeld, S. Cholinesterase Inhibitors for Alzheimer Disease. *JAMA* **2003**, *289*, 2359. [CrossRef]
49. Govind, N. Donepezil for Dementia Due to Alzheimer's Disease. *Br. J. Community Nurs.* **2020**, *25*, 148–149. [CrossRef] [PubMed]
50. Casey, D.A.; Antimisiaris, D.; O'Brien, J. Drugs for Alzheimer's Disease: Are They Effective? *Pharm. Ther.* **2010**, *35*, 208–211.
51. Villa, C. Biomarkers for Alzheimer's Disease: Where Do We Stand and Where Are We Going? *J. Pers. Med.* **2020**, *10*, 238. [CrossRef]
52. Ray, S.; Britschgi, M.; Herbert, C.; Takeda-Uchimura, Y.; Boxer, A.; Blennow, K.; Friedman, L.F.; Galasko, D.R.; Jutel, M.; Karydas, A.; et al. Classification and Prediction of Clinical Alzheimer's Diagnosis Based on Plasma Signaling Proteins. *Nat. Med.* **2007**, *13*, 1359–1362. [CrossRef] [PubMed]
53. O'Bryant, S.E.; Xiao, G.; Barber, R.; Reisch, J.; Hall, J.; Cullum, C.M.; Doody, R.; Fairchild, T.; Adams, P.; Wilhelmsen, K.; et al. A Blood-Based Algorithm for the Detection of Alzheimer's Disease. *Dement. Geriatr. Cogn. Disord.* **2011**, *32*, 55–62. [CrossRef] [PubMed]
54. Galimberti, D.; Villa, C.; Fengolio, C.; Serpente, M.; Ghezzi, L.; Cioffi, S.M.G.; Arighi, A.; Fumagalli, G.; Scrapini, E. Circulating MiRNAs as Potential Biomarkers in Alzheimer's Disease. *J. Alzheimers Dis.* **2014**, *42*, 1261–1267. [CrossRef] [PubMed]
55. Wisniewski, T.; Konietzko, U. Amyloid-β Immunisation for Alzheimer's Disease. *Lancet Neurol.* **2008**, *7*, 805. [CrossRef]
56. Ricciarelli, R.; Fedele, E. The Amyloid Cascade Hypothesis in Alzheimer's Disease: It's Time to Change Our Mind. *Curr. Neuropharmacol.* **2017**, *15*, 926–935. [CrossRef]
57. Wu, Y.Y.; Cheng, I.H.; Lee, C.C.; Chiu, M.J.; Lee, M.J.; Chen, T.F.; Hsu, J.L. Clinical phenotype of G206D mutation in the presenilin 1 gene in pathologically confirmed familial Alzheimer's disease. *J. Alzheimers Dis.* **2011**, *25*, 145–150. [CrossRef]
58. Liu, P.P.; Xie, Y.; Meng, X.Y.; Kang, J.S. History and Progress of Hypotheses and Clinical Trials for Alzheimer's Disease. Signal Transduct. *Target. Ther.* **2019**, *4*, 1–22.
59. Takeda, S. Tau Propagation as a Diagnostic and Therapeutic Target for Dementia: Potentials and Unanswered Questions. *Front. Neurosci.* **2019**, *13*, 1274. [CrossRef]
60. Ballatore, C.; Lee, V.M.Y.; Trojanowski, J.Q. Tau-Mediated Neurodegeneration in Alzheimer's Disease and Related Disorders. *Nat. Rev. Neurosci.* **2007**, *8*, 663–672. [CrossRef]
61. Marshall, K.E.; Vadukul, D.M.; Dahal, L.; Theisen, A.; Fowler, M.W.; Al-Hilaly, Y.; Ford, L.; Kemenes, G.; Day, I.J.; Staras, K.; et al. A Critical Role for the Self-Assembly of Amyloid-B1-42 in Neurodegeneration. *Sci. Rep.* **2016**, *6*, 30182. [CrossRef] [PubMed]

62. Broersen, K.; Rousseau, F.; Schymkowitz, J. The Culprit behind Amyloid Beta Peptide Related Neurotoxicity in Alzheimer's Disease: Oligomer Size or Conformation? *Alzheimers Res. Ther.* **2010**, *2*, 12. [CrossRef] [PubMed]
63. Rabbito, A.; Dulewicz, M.; Kulczyńska-Przybik, A.; Mroczko, B. Biochemical Markers in Alzheimer's Disease. *Int. J. Mol. Sci.* **2020**, *21*, 1989. [CrossRef]
64. O'Bryant, S.E.; Mielke, M.M.; Rissman, R.A.; Lista, S.; Vanderstichele, H.; Zetterberg, H.; Lewczuk, P.; Posner, H.; Hall, J.; Johnson, L.; et al. Blood-Based Biomarkers in Alzheimer Disease: Current State of the Science and a Novel Collaborative Paradigm for Advancing from Discovery to Clinic. *Alzheimers Dement.* **2017**, *13*, 45–58. [CrossRef] [PubMed]
65. Kwon, H.S.; Koh, S.-H. Neuroinflammation in Neurodegenerative Disorders: The Roles of Microglia and Astrocytes. *Transl. Neurodegener.* **2020**, *9*, 42. [CrossRef] [PubMed]
66. Dawson, T.M.; Golde, T.E.; Lagier-Tourenne, C. Animal Models of Neurodegenerative Diseases. *Nat. Neurosci.* **2018**, *21*, 1370–1379. [CrossRef] [PubMed]
67. Zhang, Y.; Liu, Y.; Liu, H.; Tang, W.H. Exosomes: Biogenesis, Biologic Function and Clinical Potential. *Cell Biosci.* **2019**, *9*, 19. [CrossRef]
68. Yin, Q.; Ji, X.; Lv, R.; Pei, J.J.; Du, Y.; Shen, C.; Hou, X. Targetting Exosomes as a New Biomarker and Therapeutic Approach for Alzheimer's Disease. *Clin. Interv. Aging* **2020**, *15*, 195–205. [CrossRef]
69. Howitt, J.; Hill, A.F. Exosomes in the Pathology of Neurodegenerative Diseases. *J. Biol. Chem.* **2016**, *291*, 26589–26597. [CrossRef]
70. Thompson, A.G.; Gray, E.; Heman-Ackah, S.M.; Mäger, I.; Talbot, K.; El Andaloussi, S.; Wood, M.J.; Turner, M.R. Extracellular Vesicles in Neurodegenerative Disease-Pathogenesis to Biomarkers. *Nat. Rev. Neurol.* **2016**, *12*, 346–357. [CrossRef]
71. Saraceno, C.; Musardo, S.; Marcello, E.; Pelucchi, S.; Luca, M.D. Modeling Alzheimer's Disease: From Past to Future. *Front. Pharmacol.* **2013**, *4*, 77. [CrossRef]
72. Grolla, A.A.; Sim, J.A.; Lim, D.; Rodriguez, J.J.; Genazzani, A.A.; Verkhratsky, A. Amyloid-β and Alzheimer's Disease Type Pathology Differentially Affects the Calcium Signalling Toolkit in Astrocytes from Different Brain Regions. *Cell Death Dis.* **2013**, *4*, e623. [CrossRef]
73. Krabbe, G.; Halle, A.; Matyash, V.; Rinnenthal, J.L.; Eom, G.D.; Bernhardt, U.; Miller, K.R.; Prokop, S.; Kettenmann, H.; Heppner, F.L. Functional Impairment of Microglia Coincides with Beta-Amyloid Deposition in Mice with Alzheimer-like Pathology. *PLoS ONE* **2013**, *8*, e60921. [CrossRef]
74. Nguyen, T.L.X.; Kim, C.K.; Cho, J.-H.; Lee, K.-H.; Ahn, J.-Y. Neuroprotection Signaling Pathway of Nerve Growth Factor and Brain-Derived Neurotrophic Factor against Staurosporine Induced Apoptosis in Hippocampal H19-7/IGF-IR [Corrected]. *Exp. Mol. Med.* **2010**, *42*, 583–595. [CrossRef] [PubMed]
75. Medeiros, L.M.D.; Bastiani, M.A.D.; Rico, E.P.; Schonhofen, P.; Pfaffenseller, B.; Wollenhaupt-Aguiar, B.; Grun, L.; Barbe-Tuana, F.; Zimmer, E.R.; Castro, M.A.A.; et al. Cholinergic Differentiation of Human Neuroblastoma SH-SY5Y Cell Line and Its Potential Use as an In vitro Model for Alzheimer's Disease Studies. *Mol. Neurobiol.* **2019**, *56*, 7355–7367. [CrossRef] [PubMed]
76. Zhang, L.; Yu, H.; Zhao, X.; Lin, X.; Tan, C.; Cao, G.; Wang, Z. Neuroprotective Effects of Salidroside against Beta-Amyloid-Induced Oxidative Stress in SH-SY5Y Human Neuroblastoma Cells. *Neurochem. Int.* **2010**, *57*, 547–555. [CrossRef] [PubMed]
77. Forster, J.I.; Koglsberger, S.; Trefois, C.; Boyd, O.; Baumuratov, A.S.; Buck, L.; Balling, R.; Antony, P.M.A. Characterization of Differentiated SH-SY5Y as Neuronal Screening Model Reveals Increased Oxidative Vulnerability. *J. Biomol. Screen.* **2016**, *21*, 496–509. [CrossRef]
78. Song, G.; Li, Y.; Lin, L.; Cao, Y. Anti-Autophagic and Anti-Apoptotic Effects of Memantine in a SH-SY5Y Cell Model of Alzheimer's Disease via Mammalian Target of Rapamycin-Dependent and -Independent Pathways. *Mol. Med. Rep.* **2015**, *12*, 7615–7622. [CrossRef]
79. Dafnis, I.; Argyri, L.; Sagnou, M.; Tzinia, A.; Tsilibary, E.C.; Stratikos, E.; Chroni, A. The Ability of Apolipoprotein E Fragments to Promote Intraneuronal Accumulation of Amyloid Beta Peptide 42 Is Both Isoform and Size-Specific. *Sci. Rep.* **2016**, *6*, 30654. [CrossRef]
80. Yagi, T.; Ito, D.; Okada, Y.; Akamatsu, W.; Nihei, Y.; Yoshizaki, T.; Yamanaka, S.; Okano, H.; Suzuki, N. Modeling Familial Alzheimer's Disease with Induced Pluripotent Stem Cells. *Hum. Mol. Genet.* **2011**, *20*, 4530–4539. [CrossRef]
81. Muratore, C.R.; Rice, H.C.; Srikanth, P.; Callahan, D.G.; Shin, T.; Benjamin, L.N.P.; Walsh, D.M.; Selkoe, D.J.; Young-Pearse, T. The Familial Alzheimer's Disease APPV717I Mutation Alters APP Processing and Tau Expression in IPSC-Derived Neurons. *Hum. Mol. Genet.* **2014**, *23*, 3523–3536. [CrossRef]
82. Kondo, T.; Asai, M.; Tsukita, K.; Kutoku, Y.; Ohsawa, Y.; Sunda, Y.; Imamura, K.; Egawa, N.; Yahata, N.; Okita, K.; et al. Modeling Alzheimer's Disease with IPSCs Reveals Stress Phenotypes Associated with Intracellular Aβ and Differential Drug Responsiveness. *Cell Stem Cell* **2013**, *12*, 487–496. [CrossRef]
83. Israel, M.A.; Yuan, S.H.; Bardy, C.; Reyna, S.M.; Mu, Y.; Herrera, C.; Hefferan, M.P.; Gorp, S.V.; Nazor, K.L.; Boscolo, F.S.; et al. Probing Sporadic and Familial Alzheimer's Disease Using Induced Pluripotent Stem Cells. *Nature* **2012**, *482*, 216–220. [CrossRef]
84. Jones, V.C.; Atkinson, R.-D.; Verkharatsky, A.; Mohamet, L. Aberrant IPSC-Derived Human Astrocytes in Alzheimer's Disease. *Cell Death Dis.* **2017**, *8*, e2696. [CrossRef]
85. Lin, Y.-T.; Seo, J.; Gao, F.; Feldman, H.M.; Wen, H.-L.; Penney, J.; Cam, H.P.; Gjoneska, E.; Raja, W.K.; Cheng, J.; et al. APOE4 Causes Widespread Molecular and Cellular Alterations Associated with Alzheimer's Disease Phenotypes in Human IPSC-Derived Brain Cell Types. *Neuron* **2018**, *98*, 1141–1154. [CrossRef] [PubMed]

86. Gerakis, Y.; Hetz, C. Brain Organoids: A next Step for Humanized Alzheimer's Disease Models? *Mol. Psychiatry* **2019**, *24*, 474–478. [CrossRef] [PubMed]
87. Zeng, X.; Hunsberger, J.G.; Simeonov, A.; Malik, N.; Pei, Y.; Rao, M. Concise review: Modeling central nervous system diseases using induced pluripotent stem cells. *Stem Cells Transl. Med.* **2014**, *3*, 1418–1428. [CrossRef] [PubMed]
88. Li, X.; Bao, X.; Wang, R. Experimental Models of Alzheimer's Disease for Deciphering the Pathogenesis and Therapeutic Screening (Review). *Int. J. Mol. Med.* **2016**, *37*, 271–283. [CrossRef] [PubMed]
89. Oddo, S.; Caccamo, A.; Shepherd, J.D.; Murphy, M.P.; Golde, T.E.; Kayed, R.; Metherate, R.; Mattson, M.P.; Akbari, Y.; LaFerla, F.M. Triple-Transgenic Model of Alzheimer's Disease with Plaques and Tangles: Intracellular Abeta and Synaptic Dysfunction. *Neuron* **2003**, *39*, 409–421. [CrossRef]
90. Oakley, H.; Cole, S.L.; Logan, S.; Maus, E.; Shao, P.; Craft, J.; Guillozet, A.-B.; Ohno, M.; Disterhoft, J.; Eldik, L.V.; et al. Intraneuronal Beta-Amyloid Aggregates, Neurodegeneration, and Neuron Loss in Transgenic Mice with Five Familial Alzheimer's Disease Mutations: Potential Factors in Amyloid Plaque Formation. *J. Neurosci.* **2006**, *26*, 10129–10140. [CrossRef]
91. Grootendorst, J.; Bour, A.; Vogel, E.; Kelche, C.; Sullivan, P.M.; Dodart, J.-C.; Bales, K.; Mathis, C. Human ApoE Targeted Replacement Mouse Lines: H-ApoE4 and h-ApoE3 Mice Differ on Spatial Memory Performance and Avoidance Behavior. *Behav. Brain Res.* **2005**, *159*, 1–14. [CrossRef]
92. Shi, Y.; Yamada, K.; Liddelow, S.A.; Smith, S.T.; Zhao, L.; Luo, W.; Tsai, R.M.; Spina, S.; Grinberg, L.T.; Rojas, J.C.; et al. ApoE4 Markedly Exacerbates Tau-Mediated Neurodegeneration in a Mouse Model of Tauopathy. *Nature* **2017**, *549*, 523–527. [CrossRef]
93. Bales, K.R.; Liu, F.; Wu, S.; Lin, S.; Koger, D.; DeLong, C.; Hansen, J.C.; Sullivan, P.M.; Paul, S.M. Human APOE Isoform-Dependent Effects on Brain β-Amyloid Levels in PDAPP Transgenic Mice. *J. Neurosci.* **2009**, *29*, 6771–6779. [CrossRef]
94. Flores, J.A.-C.; Madrid, A.; Fernandez, P.L.; Perez, A.R.-L.; Oviedo, D.C.; Britton, G.B.; Carreira, M. Critical Review of the Alzheimer's Disease Non-Transgenic Models: Can They Contribute to Disease Treatment? *J. Alzheimers Dis.* **2021**, *82*, S227–S250. [CrossRef] [PubMed]
95. Liu, B.; Liu, J.; Shi, J.-S. SAMP8 Mice as a Model of Age-Related Cognition Decline with Underlying Mechanisms in Alzheimer's Disease. *J. Alzheimers Dis.* **2020**, *75*, 385–395. [CrossRef]
96. Whitesides, G.M. The Origins and the Future of Microfluidics. *Nat. Cell Biol.* **2006**, *442*, 368–373. [CrossRef]
97. Xia, Y.; Whitesides, G.M. Soft Lithography. *Angew. Chem. Int. Ed.* **1998**, *37*, 550–575. [CrossRef]
98. Whitesides, G.M.; Ostuni, E.; Takayama, S.; Jiang, X.; Ingber, D.E. Soft Lithography in Biology and Biochemistry. *Annu. Rev. Biomed. Eng.* **2001**, *3*, 335–373. [CrossRef] [PubMed]
99. Folch, A.; Toner, M. Cellular Micropatterns on Biocompatible Materials. *Biotechnol. Prog.* **1998**, *14*, 388–392. [CrossRef]
100. Duffy, D.C.; McDonald, J.C.; Schueller, O.J.A.; Whitesides, G.M. Rapid Prototyping of Microfluidic Systems in Poly(Dimethylsiloxane). *Anal. Chem.* **1998**, *70*, 4974–4984. [CrossRef]
101. Taylor, A.M.; Dieterich, D.C.; Ito, H.T.; Kim, S.A.; Schuman, E.M. Microfluidic Local Perfusion Chambers for the Visualization and Manipulation of Synapses. *Neuron* **2010**, *66*, 57–68. [CrossRef] [PubMed]
102. Van Midwoud, P.M.; Janse, A.; Merema, M.T.; Groothuis, G.M.M.; Verpoorte, E. Comparison of Biocompatibility and Adsorption Properties of Different Plastics for Advanced Microfluidic Cell and Tissue Culture Models. *Anal. Chem.* **2012**, *84*, 3938–3944. [CrossRef] [PubMed]
103. Kim, S.M.; Lee, S.H.; Suh, K.Y. Cell Research with Physically Modified Microfluidic Channels: A Review. *Lab Chip* **2008**, *8*, 1015–1023. [CrossRef] [PubMed]
104. Sonnen, K.F.; Merten, C.A. Microfluidics as an Emerging Precision Tool in Developmental Biology. *Dev. Cell* **2019**, *48*, 293–311. [CrossRef] [PubMed]
105. Duncombe, T.A.; Tentori, A.M.; Herr, A.E. Microfluidics: Reframing Biological Enquiry. Nat. Rev. Mol. *Cell Biol.* **2015**, *16*, 554–567.
106. Dittrich, P.S.; Manz, A. Lab-on-a-Chip: Microfluidics in Drug Discovery. *Nat. Rev. Drug Discov.* **2006**, *5*, 210–218. [CrossRef] [PubMed]
107. Ying, L.; Wang, Q. Microfluidic Chip-Based Technologies: Emerging Platforms for Cancer Diagnosis. *BMC Biotechnol.* **2013**, *13*, 76. [CrossRef]
108. Chin, C.D.; Laksanasopin, T.; Cheung, Y.K.; Steinmiller, D.; Linder, V.; Parsa, H.; Wang, J.; Moore, H.; Rouse, R.; Umviligihozo, G.; et al. Microfluidics-Based Diagnostics of Infectious Diseases in the Developing World. *Nat. Med.* **2011**, *17*, 1015–1019. [CrossRef] [PubMed]
109. Tay, A.; Pavesi, A.; Yazdi, S.R.; Lim, C.T.; Warkiani, M.E. Advances in Microfluidics in Combating Infectious Diseases. *Biotechnol. Adv.* **2016**, *34*, 404–421. [CrossRef]
110. Reboud, J.; Xu, G.; Garrett, A.; Adriko, M.; Yang, Z.; Tukahebwa, E.M.; Rowell, C.; Cooper, J.M. Paper-Based Microfluidics for DNA Diagnostics of Malaria in Low Resource Underserved Rural Communities. *Proc. Natl. Acad. Sci. USA* **2019**, *116*, 4834–4842. [CrossRef]
111. Vadivelu, R.; Kashaninejad, N.; Sreejith, K.R.; Bhattacharjee, R.; Cock, I.; Nguyen, N.T. Cryoprotectant-Free Freezing of Cells Using Liquid Marbles Filled with Hydrogel. *ACS Appl. Mater. Interfaces* **2018**, *10*, 43439–43449. [CrossRef]
112. Avrămescu, R.E.; Ghica, M.V.; Dinu-Pîrvu, C.; Udeanu, D.I.; Popa, L. Liquid Marbles: FromIndustrial to Medical Applications. *Molecules* **2018**, *23*, 1120. [CrossRef] [PubMed]
113. Wang, H.; Chen, L.; Sun, L. Digital microfluidics: A promising technique for biochemical applications. *Front. Mech. Eng.* **2017**, *12*, 510–525. [CrossRef]

114. Shembekar, N.; Chaipan, C.; Utharala, R.; Merten, C.A. Droplet-based microfluidics indrug discovery, transcriptomics and high-throughput molecular genetics. *Lab Chip* **2016**, *16*, 1314–1331. [CrossRef]
115. Huang, Y.; Williams, J.C.; Johnson, S.M. Brain slice on a chip: Opportunities and challenges of applying microfluidic technology to intact tissues. *Lab Chip* **2012**, *12*, 2103–2117. [CrossRef]
116. Vedarethinam, I.; Avaliani, N.; Tonnesen, J.; Hansen, L.; Sabourin, D.; Dimaki, M.; Kokaia, M.; Dufva, M.; Svendsen, W.E.; Emneus, J.; et al. Long-term brain slice culturing in a microfluidic platform. In Proceedings of the 15th International Conference on Miniaturized Systems for Chemistry and Life Sciences, Seattle, WA, USA, 2–6 October 2011.
117. Astolfi, M.; Péant, B.; Lateef, M.A.; Rousset, N.; Kendall-Dupont, J.; Carmona, E.; Monet, F.; Saad, F.; Provencher, D.; Mes-Masson, A.M.; et al. Micro-dissected tumor tissues on chip: An ex vivo method for drug testing and personalized therapy. *Lab Chip* **2016**, *16*, 312–325. [CrossRef]
118. Yamada, A.; Vignes, M.; Bureau, C.; Mamane, A.; Venzac, B.; Descroix, S.; Viovy, J.L.; Villard, C.; Peyrin, J.M.; Malaquin, L. In-mold patterning and actionable axo-somatic compartmentalization for on-chip neuron culture. *Lab Chip* **2016**, *16*, 2059–2068. [CrossRef] [PubMed]
119. Tanaka, N.; Moriguchi, H.; Sato, A.; Kawai, T.; Shimba, K.; Jimbo, Y.; Tanaka, Y. Microcasting with agarose gel via degassed polydimethylsiloxane molds for repellency-guided cell patterning. *RSC Adv.* **2016**, *6*, 54754–54762. [CrossRef]
120. Knöll, B.; Weinl, C.; Nordheim, A.; Bonhoeffer, F. Stripe assay to examine axonal guidance and cell migration. *Nat. Protoc.* **2007**, *2*, 1216–1224. [CrossRef] [PubMed]
121. Qi, Z.B.; Xu, L.; Xu, Y.; Zhong, J.; Abedini, A.; Cheng, X.; Sinton, D. Disposable Silicon-Glass Microfluidic Devices: Precise, Robust and Cheap. *Lab Chip* **2018**, *18*, 3872–3880. [CrossRef]
122. Qian, J.Y.; Hou, C.W.; Li, X.J.; Jin, Z.J. Actuation Mechanism of Microvalves: A Review. *Micromachines* **2020**, *11*, 172. [CrossRef] [PubMed]
123. Friend, J.; Yeo, L. Fabrication of Microfluidic Devices Using Polydimethylsiloxane. *Biomicrofluidics* **2010**, *4*, 026502. [CrossRef] [PubMed]
124. Fujii, T. PDMS-Based Microfluidic Devices for Biomedical Applications. *Microelectron. Eng.* **2002**, *61–62*, 907–914. [CrossRef]
125. Fiorini, G.S.; Jeffries, G.D.M.; Lim, D.S.W.; Kuyper, C.L.; Chiu, D.T. Fabrication of Thermoset Polyester Microfluidic Devices and Embossing Masters Using Rapid Prototyped Polydimethylsiloxane Molds. *Lab Chip* **2003**, *3*, 158–163. [CrossRef]
126. Wu, W.I.; Sask, K.N.; Brash, J.L.; Selvaganapathy, P.R. Polyurethane-Based Microfluidic Devices for Blood Contacting Applications. *Lab Chip* **2012**, *12*, 960–970. [CrossRef]
127. Liu, K.; Fan, Z.H. Thermoplastic Microfluidic Devices and Their Applications in Protein and DNA Analysis. *Analyst* **2011**, *136*, 1288–1297. [CrossRef]
128. Gencturk, E.; Mutlu, S.; Ulgen, K.O. Advances in microfluidic devices made fromthermoplastics used in cell biology and analyses. *Biomicrofluidics* **2017**, *11*, 051502. [CrossRef] [PubMed]
129. Ertl, P. Recent Advances of Biologically Inspired 3D Microfluidic Hydrogel Cell Culture Systems. *Cell Biol. Cell Metab.* **2015**, *2*, 1–14. [CrossRef]
130. Morteza, B.; Mohseni, N.; Moghtader, M. *An Introduction to Hydrogels and Some Recent Applications*; IntechOpen, 2016.
131. Li, X.; Ballerini, D.R.; Shen, W. A Perspective on Paper-Based Microfluidics: Current Status and Future Trends. *Biomicrofluidics* **2012**, *6*, 011301. [CrossRef]
132. Esch, E.W.; Bahinski, A.; Huh, D. Organs-on-Chips at the Frontiers of Drug Discovery. *Nat. Rev. Drug Discov.* **2015**, *14*, 248–260. [CrossRef]
133. Bhattacharjee, N.; Urrios, A.; Kang, S.; Folch, A. The Upcoming 3D-Printing Revolution in Microfluidics. *Lab Chip* **2016**, *16*, 1720–1742. [CrossRef] [PubMed]
134. Luni, C.; Serena, E.; Elvassore, N. Human-on-Chip for Therapy Development and Fundamental Science. *Curr. Opin. Biotechnol.* **2014**, *25*, 45–50. [CrossRef]
135. Zhang, C.; Zhao, Z.; Abdul Rahim, N.A.; Van Noort, D.; Yu, H. Towards a Human-on-Chip: Culturing Multiple Cell Types on a Chip with Compartmentalized Microenvironments. *Lab Chip* **2009**, *9*, 3185–3192. [CrossRef] [PubMed]
136. Baudoin, R.; Corlu, A.; Griscom, L.; Legallais, C.; Leclerc, E. Trends in the Development of Microfluidic Cell Biochips for in vitro Hepatotoxicity. *Toxicol. Vitr.* **2007**, *21*, 535–544. [CrossRef] [PubMed]
137. Osaki, T.; Shin, Y.; Sivathanu, V.; Campisi, M.; Kamm, R.D. In vitro Microfluidic Models for Neurodegenerative Disorders. *Adv. Healthc. Mater.* **2018**, *7*, 1700489. [CrossRef] [PubMed]
138. Kane, K.I.W.; Jarazo, J.; Moreno, E.L.; Fleming, R.M.T.; Schwamborn, J.C. Passive Controlled Flow for Parkinson's Disease Neuronal Cell Culture in 3D Microfluidic Devices. *Org. Chip* **2020**, *2*, 100005. [CrossRef]
139. Perestrelo, A.R.; Águas, A.C.P.; Rainer, A.; Forte, G. Microfluidic Organ/Body-on-a-Chip Devices at the Convergence of Biology and Microengineering. *Sensors* **2015**, *15*, 31142–31170. [CrossRef]
140. Haring, A.P.; Sontheimer, H.; Johnson, B.N. Microphysiological Human Brain and Neural Systems-on-a-Chip: Potential Alternatives to Small Animal Models and Emerging Platforms for Drug Discovery and Personalized Medicine. *Stem Cell Rev. Rep.* **2017**, *13*, 381–406. [CrossRef]
141. Zheng, F.; Fu, F.; Cheng, Y.; Wang, C.; Zhao, Y.; Gu, Z. Organ-on-a-Chip Systems: Microengineering to Biomimic Living Systems. *Small* **2016**, *12*, 2253–2282. [CrossRef]

142. Taylor, A.M.; Rhee, S.W.; Tu, C.H.; Cribbs, D.H.; Cotman, C.W.; Jeon, N.L. Microfluidic Multicompartment Device for Neuroscience Research. *Langmuir* **2003**, *19*, 1551–1556. [CrossRef]
143. Park, J.; Lee, B.K.; Jeong, G.S.; Hyun, J.K.; Lee, C.J.; Lee, S.H. Three-Dimensional Brain-on-a-Chip with an Interstitial Level of Flow and Its Application as an in vitro Model of Alzheimer's Disease. *Lab Chip* **2015**, *15*, 141–150. [CrossRef] [PubMed]
144. Park, J.; Wetzel, I.; Marriott, I.; Dréau, D.; D'Avanzo, C.; Kim, D.Y.; Tanzi, R.E.; Cho, H. A 3D Human Triculture System Modeling Neurodegeneration and Neuroinflammation in Alzheimer's Disease. *Nat. Neurosci.* **2018**, *21*, 941–951. [CrossRef] [PubMed]
145. Teixeira, M.I.; Amaral, M.H.; Costa, P.C.; Lopes, C.M.; Lamprou, D.A. Recent Developments in Microfluidic Technologies for Central Nervous System Targeted Studies. *Pharmaceutics* **2020**, *12*, 1–37. [CrossRef]
146. McDonald, J.C.; Whitesides, G.M. Poly(dimethylsiloxane) as a material for fabricating microfluidic devices. *Acc. Chem. Res.* **2002**, *35*, 491–499. [CrossRef]
147. Katsikoudi, A.; Ficulle, E.; Cavallini, A.; Sharman, G.; Guyot, A.; Zagnoni, M.; Eastwood, B.J.; Hutton, M.; Bose, S. Quantitative Propagation of Assembled Human Tau from Alzheimer's Disease Brain in Microfluidic Neuronal Cultures. *J. Biol. Chem.* **2020**, *295*, 13079–13093. [CrossRef]
148. Shin, Y.; Choi, S.H.; Kim, E.; Bylykbashi, E.; Kim, J.A.; Chung, S.; Kim, D.Y.; Kamm, R.D.; Tanzi, R.E. Blood–Brain Barrier Dysfunction in a 3D In vitro Model of Alzheimer's Disease. *Adv. Sci.* **2019**, *6*, 1900962. [CrossRef]
149. Gupta, N.; Liu, J.R.; Patel, B.; Solomon, D.E.; Vaidya, B.; Gupta, V. Microfluidics-based 3D Cell Culture Models: Utility in Novel Drug Discovery and Delivery Research. *Bioeng. Transl. Med.* **2016**, *1*, 63–81. [CrossRef]
150. Natarajan, A.; Sethumadhavan, A.; Krishnan, U.M. Toward Building the Neuromuscular Junction: In vitro Models to Study Synaptogenesis and Neurodegeneration. *ACS Omega* **2019**, *4*, 12969–12977. [CrossRef] [PubMed]
151. Breslin, S.; O'Driscoll, L. Three-dimensional cell culture: The missing link in drug discovery. *Drug Discov. Today* **2013**, *18*, 240–249. [CrossRef] [PubMed]
152. Peyrin, J.M.; Deleglise, B.; Saias, L.; Vignes, M.; Gougis, P.; Magnifico, S.; Betuing, S.; Pietri, M.; Caboche, J.; Vanhoutte, P.; et al. Axon Diodes for the Reconstruction of Oriented Neuronal Networks in Microfluidic Chambers. *Lab Chip* **2011**, *11*, 3663–3673. [CrossRef]
153. Gutruf, P.; Rogers, J.A. Implantable, Wireless Device Platforms for Neuroscience Research. *Curr. Opin. Neurobiol.* **2018**, *50*, 42–49. [CrossRef]
154. Tsantoulas, C.; Farmer, C.; Machado, P.; Baba, K.; McMahon, S.B.; Raouf, R. Probing Functional Properties of Nociceptive Axons Using a Microfluidic Culture System. *PLoS ONE* **2013**, *8*, 80722. [CrossRef] [PubMed]
155. Douville, N.J.; Tung, Y.C.; Li, R.; Wang, J.D.; El-Sayed, M.E.H.; Takayama, S. Fabrication of Two-Layered Channel System with Embedded Electrodes to Measure Resistance across Epithelial and Endothelial Barriers. *Anal. Chem.* **2010**, *82*, 2505–2511. [CrossRef] [PubMed]
156. Poon, W.W.; Blurton-Jones, M.; Tu, C.H.; Feinberg, L.M.; Chabrier, M.A.; Harris, J.W.; Jeon, N.L.; Cotman, C.W. β-Amyloid Impairs Axonal BDNF Retrograde Trafficking. *Neurobiol. Aging* **2011**, *32*, 821–833. [CrossRef] [PubMed]
157. Jackson, E.L.; Lu, H. Three-Dimensional Models for Studying Development and Disease: Moving on from Organisms to Organs-on-a-Chip and Organoids. *Integr. Biol.* **2016**, *8*, 672–683. [CrossRef]
158. Ren, Y.; Kunze, A.; Renaud, P. Compartmentalized microfluidics for in vitro Alzheimer's disease studies. Microfluidic and Compartmentalized Platforms for Neurobiological Research. *Neuromethods* **2015**, *103*, 197–215.
159. Southam, K.A.; King, A.E.; Blizzard, C.A.; McCormack, G.H.; Dickson, T.C. Microfluidic Primary Culture Model of the Lower Motor Neuron-Neuromuscular Junction Circuit. *J. Neurosci. Methods* **2013**, *218*, 164–169. [CrossRef]
160. Neto, E.; Alves, C.J.; Sousa, D.M.; Alencastre, I.S.; Lourenço, A.H.; Leitão, L.; Ryu, H.R.; Jeon, N.L.; Fernandes, R.; Aguiar, P.; et al. Sensory Neurons and Osteoblasts: Close Partners in a Microfluidic Platform. *Integr. Biol.* **2014**, *6*, 586–595. [CrossRef]
161. Sundararaghavan, H.G.; Monteiro, G.A.; Firestein, B.L.; Shreiber, D.I. Neurite Growth in 3D Collagen Gels with Gradients of Mechanical Properties. *Biotechnol. Bioeng.* **2009**, *102*, 632–643. [CrossRef]
162. Ionescu, A.; Zahavi, E.E.; Gradus, T.; Ben-Yaakov, K.; Perlson, E. Compartmental Microfluidic System for Studying Muscle-Neuron Communication and Neuromuscular Junction Maintenance. *Eur. J. Cell Biol.* **2016**, *95*, 69–88. [CrossRef]
163. Robertson, G.; Bushell, T.J.; Zagnoni, M. Chemically Induced Synaptic Activity between Mixed Primary Hippocampal Co-Cultures in a Microfluidic System. *Integr. Biol.* **2014**, *6*, 636–644. [CrossRef]
164. Griciuc, A.; Serrano-Pozo, A.; Parrado, A.R.; Lesinski, A.N.; Asselin, C.N.; Mullin, K.; Hooli, B.; Choi, S.H.; Hyman, B.T.; Tanzi, R.E. Alzheimer's disease risk gene CD33 inhibits microglial uptake of amyloid beta. *Neuron* **2013**, *78*, 631–643. [CrossRef] [PubMed]
165. Bianco, F.; Tonna, N.; Lovchik, R.D.; Mastrangelo, R.; Morini, R.; Ruiz, A.; Delamarche, E.; Matteoli, M. Overflow Microfluidic Networks: Application to the Biochemical Analysis of Brain Cell Interactions in Complex Neuroinflammatory Scenarios. *Anal. Chem.* **2012**, *84*, 9833–9840. [CrossRef] [PubMed]
166. Deleglise, B.; Lassus, B.; Soubeyre, V.; Alleaume-Butaux, A.; Hjorth, J.J.; Vignes, M.; Schneider, B.; Brugg, B.; Viovy, J.L.; Peyrin, J.M. Synapto-Protective Drugs Evaluation in Reconstructed Neuronal Network. *PLoS ONE* **2013**, *8*, e71103. [CrossRef]
167. De Oliveira, T.R.; Erbereli, C.R.; Manzine, P.R.; Magalhães, T.N.C.; Balthazar, M.L.F.; Cominetti, M.R.; Faria, R.C. Early Diagnosis of Alzheimer's Disease in Blood Using a Disposable Electrochemical Microfluidic Platform. *ACS Sens.* **2020**, *5*, 1010–1019. [CrossRef] [PubMed]

168. Islam, K.; Jang, Y.C.; Chand, R.; Jha, S.K.; Lee, H.H.; Kim, Y.S. Microfluidic Biosensor for β-Amyloid(1-42) Detection Using Cyclic Voltammetry. *J. Nanosci. Nanotechnol.* **2011**, *11*, 5657–5662. [CrossRef]
169. Yang, F.; Liao, X.; Tian, Y.; Li, G. Exosome Separation Using Microfluidic Systems: Size-Based, Immunoaffinity-Based and Dynamic Methodologies. *Biotechnol. J.* **2017**, *12*, 12. [CrossRef]
170. Cohen, M.S.; Orth, C.B.; Kim, H.J.; Jeon, N.L.; Jaffrey, S.R. Neurotrophin-Mediated Dendrite-to-Nucleus Signaling Revealed by Microfluidic Compartmentalization of Dendrites. *Proc. Natl. Acad. Sci. USA* **2011**, *108*, 11246–11251. [CrossRef]
171. Jorfi, M.; D'Avanzo, C.; Kim, D.Y.; Irimia, D. Three-Dimensional Models of the Human Brain Development and Diseases. *Adv. Healthc. Mater.* **2018**, *7*, 1002. [CrossRef]
172. Yang, I.H.; Gary, D.; Malone, M.; Dria, S.; Houdayer, T.; Belegu, V.; McDonald, J.W.; Thakor, N. Axon Myelination and Electrical Stimulation in a Microfluidic, Compartmentalized Cell Culture Platform. *NeuroMolecular Med.* **2012**, *14*, 112–118. [CrossRef]
173. Kunze, A.; Meissner, R.; Brando, S.; Renaud, P. Co-Pathological Connected Primary Neurons in a Microfluidic Device for Alzheimer Studies. *Biotechnol. Bioeng.* **2011**, *108*, 2241–2245. [CrossRef]
174. Hosie, K.A.; King, A.E.; Blizzard, C.A.; Vickers, J.C.; Dickson, T.C. Chronic Excitotoxin-Induced Axon Degeneration in a Compartmented Neuronal Culture Model. *ASN Neuro* **2012**, *4*, 47–57. [CrossRef]
175. Edington, C.D.; Chen, W.L.K.; Geishecker, E.; Kassis, T.; Soenksen, L.R.; Bhushan, B.M.; Freake, D.; Kirschner, J.; Maass, C.; Tsamandouras, N.; et al. Interconnected Microphysiological Systems for Quantitative Biology and Pharmacology Studies. *Sci. Rep.* **2018**, *8*, 4530. [CrossRef]
176. Lee, J.S.; Park, C.B. Microfluidic Dissociation and Clearance of Alzheimer's β-Amyloid Aggregates. *Biomaterials* **2010**, *31*, 6789–6795. [CrossRef] [PubMed]
177. Hong, N.; Joo, S.; Nam, Y. Characterization of Axonal Spikes in Cultured Neuronal Networks Using Microelectrode Arrays and Microchannel Devices. IEEE Trans. *Biomed. Eng.* **2017**, *64*, 492–498.
178. Lewandowska, M.K.; Bakkum, D.J.; Rompani, S.B.; Hierlemann, A. Recording Large Extracellular Spikes in Microchannels along Many Axonal Sites from Individual Neurons. *PLoS ONE* **2015**, *10*. [CrossRef] [PubMed]
179. Habibey, R.; Latifi, S.; Mousavi, H.; Pesce, M.; Arab-Tehrany, E.; Blau, A. A Multielectrode Array Microchannel Platform Reveals Both Transient and Slow Changes in Axonal Conduction Velocity. *Sci. Rep.* **2017**, *7*, 8558. [CrossRef] [PubMed]
180. Dworak, B.J.; Wheeler, B.C. Novel MEA Platform with PDMS Microtunnels Enables the Detection of Action Potential Propagation from Isolated Axons in Culture. *Lab Chip* **2009**, *9*, 404–410. [CrossRef] [PubMed]
181. Stoothoff, W.; Jones, P.B.; Spires-Jones, T.L.; Joyner, D.; Chhabra, E.; Bercury, K.; Fan, Z.; Xie, H.; Bacskai, B.; Edd, J.; et al. Differential Effect of Three-Repeat and Four-Repeat Tau on Mitochondrial Axonal Transport. *J. Neurochem.* **2009**, *111*, 417–427. [CrossRef]
182. Deleglise, B.; Magnifico, S.; Duplus, E.; Vaur, P.; Soubeyre, V.; Belle, M.; Vignes, M.; Viovy, J.L.; Jacotot, E.; Peyrin, J.M.; et al. β-Amyloid Induces a Dying-Back Process and Remote Trans-Synaptic Alterations in a Microfluidic-Based Reconstructed Neuronal Network. *Acta Neuropathol. Commun.* **2014**, *2*, 145.
183. Cho, H.; Hashimoto, T.; Wong, E.; Hori, Y.; Wood, L.B.; Zhao, L.; Haigis, K.M.; Hyman, B.T.; Irimia, D. Microfluidic Chemotaxis Platform for Differentiating the Roles of Soluble and Bound Amyloid-β on Microglial Accumulation. *Sci. Rep.* **2013**, *3*, 1823. [CrossRef]
184. Choi, I.; Huh, Y.S.; Erickson, D. Size-Selective Concentration and Label-Free Characterization of Protein Aggregates Using a Raman Active Nanofluidic Device. *Lab Chip* **2011**, *11*, 632–638. [CrossRef]
185. Park, J.; Koito, H.; Li, J.; Han, A. Microfluidic Compartmentalized Co-Culture Platform for CNS Axon Myelination Research. *Biomed. Microdevices* **2009**, *11*, 1145–1153. [CrossRef]
186. Hosmane, S.; Yang, I.H.; Ruffin, A.; Thakor, N.; Venkatesan, A. Circular Compartmentalized Microfluidic Platform: Study of Axon-Glia Interactions. *Lab Chip* **2010**, *10*, 741–747. [CrossRef]
187. Taylor, A.M.; Rhee, S.W.; Jeon, N.L. Microfluidic Chambers for Cell Migration and Neuroscience Research. *Methods Mol. Biol.* **2006**, *321*, 167–177. [PubMed]
188. Goral, V.; Hsieh, Y.-C.; Petzold, O.; Faris, R.; Yuen, P.K. Hot Embossing of Plastic Microfluidic Devices Using Poly(Dimethylsiloxane) Molds. *J. Micromech. Microeng.* **2011**, *21*, 017002. [CrossRef]
189. Chumbimuni-Torres, K.Y.; Coronado, R.E.; Mfuh, A.M.; Castro-Guerrero, C.; Silva, M.F.; Negrete, G.R.; Bizios, R.; Garcia, C.D. Adsorption of Proteins to Thin-Films of PDMS and Its Effect on the Adhesion of Human Endothelial Cells. *RSC Adv.* **2011**, *1*, 706–714. [CrossRef] [PubMed]
190. Gomez-Sjoberg, R.; Leyrat, A.; Houseman, B.; Shokat, K.; Quake, S. Biocompatibility and Reduced Drug Absorption of Sol-Gel-Treated Poly(Dimethyl Siloxane) for Microfluidic Cell Culture Applications. *Anal. Chem.* **2010**, *82*, 8954–8960. [CrossRef]
191. Wang, X.; Yi, L.; Mukhitov, N.; Schrell, A.M.; Dhumpa, R.; Roper, M.G. Microfluidics-to-Mass Spectrometry: A Review of Coupling Methods and Applications. *J. Chromatogr. A* **2015**, *1382*, 98–116. [CrossRef]
192. Ward, K.; Fan, Z.H. Mixing in Microfluidic Devices and Enhancement Methods. *J. Micromech. Microeng.* **2015**, *25*, 094001. [CrossRef] [PubMed]
193. Oxford, A.E.; Stewart, E.S.; Rohn, T.T. Clinical Trials in Alzheimer's Disease: A Hurdle in the Path of Remedy. *Int. J. Alzheimers Dis.* **2020**, *2020*, 5380346. [CrossRef] [PubMed]

life

MDPI

*Review*

# NADomics: Measuring NAD$^+$ and Related Metabolites Using Liquid Chromatography Mass Spectrometry

**Nady Braidy [1,2,*], Maria D. Villalva [1] and Ross Grant [3,4]**

[1] Centre for Healthy Brain Ageing, School of Psychiatry, University of New South Wales, Sydney, NSW 2052, Australia; m.villalva@unsw.edu.au
[2] Euroa Centre, UNSW School of Psychiatry, NPI, Prince of Wales Hospital, Barker Street, Randwick, Sydney, NSW 2031, Australia
[3] School of Medical Sciences, University of New South Wales, Sydney, NSW 2052, Australia; r.grant@unsw.edu.au
[4] Australasian Research Institute, Sydney Adventist Hospital, Sydney, NSW 2076, Australia
* Correspondence: n.braidy@unsw.edu.au; Tel.: +61-2-9382-3763; Fax: +61-2-9382-3774

**Abstract:** Nicotinamide adenine dinucleotide (NAD$^+$) and its metabolome (NADome) play important roles in preserving cellular homeostasis. Altered levels of the NADome may represent a likely indicator of poor metabolic function. Accurate measurement of the NADome is crucial for biochemical research and developing interventions for ageing and neurodegenerative diseases. In this mini review, traditional methods used to quantify various metabolites in the NADome are discussed. Owing to the auto-oxidation properties of most pyridine nucleotides and their differential chemical stability in various biological matrices, accurate assessment of the concentrations of the NADome is an analytical challenge. Recent liquid chromatography mass spectrometry (LC-MS) techniques which overcome some of these technical challenges for quantitative assessment of the NADome in the blood, CSF, and urine are described. Specialised HPLC-UV, NMR, capillary zone electrophoresis, or colorimetric enzymatic assays are inexpensive and readily available in most laboratories but lack the required specificity and sensitivity for quantification of human biological samples. LC-MS represents an alternative means of quantifying the concentrations of the NADome in clinically relevant biological specimens after careful consideration of analyte extraction procedures, selection of internal standards, analyte stability, and LC assays. LC-MS represents a rapid, robust, simple, and reliable assay for the measurement of the NADome between control and test samples, and for identifying biological correlations between the NADome and various biochemical processes and testing the efficacy of strategies aimed at raising NAD$^+$ levels during physiological ageing and disease states.

**Keywords:** NAD$^+$; nicotinamide; ageing; plasma; biomarker

**Citation:** Braidy, N.; Villalva, M.D.; Grant, R. NADomics: Measuring NAD$^+$ and Related Metabolites Using Liquid Chromatography Mass Spectrometry. *Life* **2021**, *11*, 512. https://doi.org/10.3390/life11060512

Academic Editors: Chiara Villa and Jong-Hyuk Yoon

Received: 11 April 2021
Accepted: 24 May 2021
Published: 31 May 2021



## 1. Introducing NADomics as a Tool for Quantification of the NADome in Biological Samples

NADomics is the high-throughput study of nicotinamide adenine dinucleotide (NAD$^+$) and its related metabolites. NAD$^+$ is an essential coenzyme that is present in all organisms [1]. NAD$^+$ serves as a major coenzyme for enzymatic reduction–oxidation reactions and ATP production. More recently, NAD$^+$ has also been shown to be a crucial co-substrate for numerous enzymes (i.e., sirtuins, NAD$^+$ glycohydrolase (CD38), poly(adenosine diphosphate–ribose) polymerases (PARPs)) [2–4]. The term NADomics is an analogy to metabolomics, the study of the metabolome. The word NADome is a portmanteau of NAD$^+$ and its related metabolome. The NADome is the entire set of NAD$^+$ metabolites that are anabolised or catabolised by an organism or system (Figure 1). The emerging field of NADomics has enabled the identification and quantification of ever-increasing numbers of NAD-related metabolites.

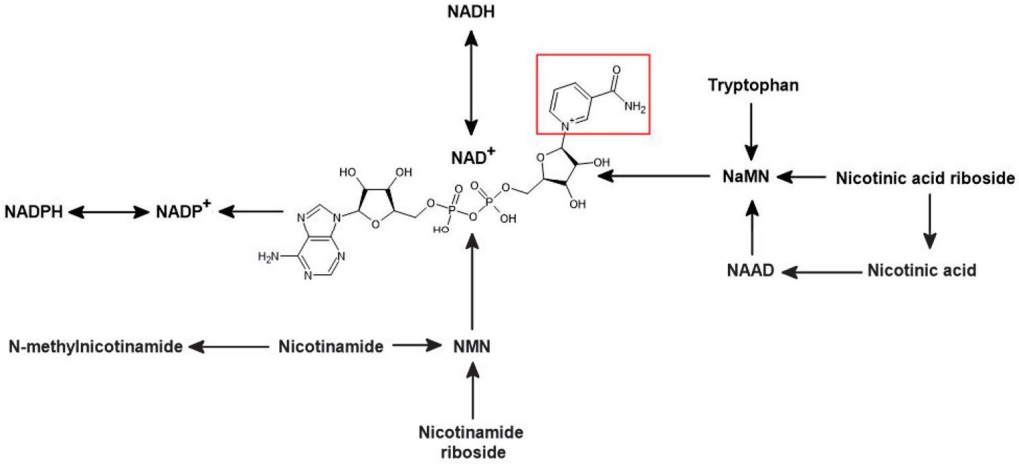


**Figure 1.** $NAD^+$ metabolism in eukaryotic cells. $NAD^+$ anabolism from tryptophan occurs by the de novo kynurenine pathway (KP). $NAD^+$ precursors via the salvage pathway include nicotinamide (NAM), nicotinic acid (NA), nicotinamide riboside (NR), and nicotinic acid riboside (NAR). The enzyme nicotinamide phosphoribosyltransferase (NAMPT) converts NAM to nicotinamide mononucleotide (NMN). Nicotinamide mononucleotide adenylyltransferase (NMNAT1-3) converts NMN to $NAD^+$. NAM can be methylated to N-methyl-nicotinamide (MeNAM) by the action of nicotinamide N-methyltransferase (NNMT). NADH represents the reduced form of $NAD^+$. $NADP^+$ is the phosphorylated form of $NAD^+$. $NADP^+$ can be reduced to NADPH by NAD kinases (NADK1,2). PARPs, Sirtuins, and CD38 $NAD^+$ glycohydrolases are known as $NAD^+$ consumers, leading to the generation of NAM. Nicotinic acid phosphoribosyltransferase (NAPRT) converts NA to nicotinic acid mononucleotide (NAMN), which is then converted to $NAD^+$ by NMNAT1-3. NAR needs to be converted to NAMN to yield $NAD^+$ synthesis via nicotinamide riboside kinases (NRK1,2). NRK1,2 also convert NR to NMN. NAR can form NA via purine nucleoside phosphorylase (PNP). PNP are also capable of converting NR to NAM.

$NAD^+$ and its reduced form NADH can be phosphorylated to $NADP^+$ and NADPH, which serve as major coenzymes in over 400 oxidoreductase enzymes [5]. $NAD^+$ serves as a hydrogen acceptor allowing the transfer of electrons for oxidation–reduction (i.e., redox) reactions leading to ATP production in the mitochondria [1]. $NAD^+$ glycohydrolases (CD38, CD157) are involved in the production of calcium-mobilising messengers, ADP-ribose (ADPR) and its cyclic form (cADPR) [6]. PARP-mediated ADP-ribosylation uses the ADPR moiety of $NAD^+$ to repair DNA, leading to the breakdown $NAD^+$ to nicotinamide (NAM) and an ADP-ribosyl product [7]. Sirtuins are a family of class III $NAD^+$-dependent histone deacetylases that exhibit protein lysine deacetylase, and partial ADPR transferase activities [8]. Deacetylation occurs when the modified lysine side chain is coupled to the cleavage of the glycosidic bonds in $NAD^+$, leading to the generation of the deacetylated lysine, acetylated ADPR, and NAM as by-products [9]. These processes are dependent on $NAD^+$ availability, and NAM is an endogenous inhibitor of CD38, PARP, and sirtuins [5].

Continuous replenishment of cellular $NAD^+$ levels is important for normal cellular survival [10]. The de novo $NAD^+$ biosynthesis pathway in most cells is dependent on the amino acid tryptophan via the kynurenine pathway. When the availability of dietary tryptophan is limited, the efficiency of the conversion of tryptophan to $NAD^+$ decreases below the well-established conversion ratio of 60:1 [11,12]. Nicotinic acid (NA), NAM, NAM riboside (NR), or NA riboside (NAR) can also be used to synthesise $NAD^+$ via the $NAD^+$ salvage pathway [5]. NAM can be methylated to N-methyl-nicotinamide (MeNAM) by the action of NAM N-methyltransferase [13]. The enzymes nicotinamide phosphoribosyltransferase (NAMPT) and nicotinic acid phosphoribosyltransferase (NAPRT) convert NAM and NA to nicotinamide mononucleotide (NMN) and nicotinic acid mononucleotide (NAMN), respectively [5]. Additionally, the phosphorylation of nicotinamide riboside (NR) and nicotinic acid riboside (NAR) via nicotinamide riboside kinase (NRK) also leads

to the production of NMN and NAMN, which can be converted to nicotinic acid adenine dinucleotide (NAAD) and $NAD^+$ by nicotinamide mononucleotide adenyltransferase (NMNAT) [14]. NAAD can be amidated to $NAD^+$ by NAD synthetase (NADS) [5].

The NADome is important in physiological processes such as energy production, transcriptional regulation, DNA repair, protein modification, and secondary messenger signalling [5]. Therefore, the application of NADomics in the clinic provides an essential indicator of nutritional status, redox function, and incidence and progression of age-related diseases [15]. A decline in cellular $NAD^+$ levels has been associated with mitochondrial impairments, immune dysfunction, and reduced histone deacetylase activity, which can interfere with several transcription factors and affect gene expression levels [5]. Reduced $NAD^+$ levels also have a dramatic impact on the activity of PARPs, thus impairing DNA repairing. We and others have demonstrated that intracellular $NAD^+$ levels decline in conditions of metabolic stress in muscle, brain, heart [2], lung [2], liver [2], kidney [2], skin [16], and plasma [17,18] in humans and rats. $NAD^+$ levels are reduced in tissues and cells exposed to oxidative stress and DNA damage, the overfed liver, the failing heart, the damaged peripheral neuron, and the injured brain [5], and correlate with disease severity of multiple sclerosis [19]. However, it remains unclear whether a depressed NADome is a function of age, although ageing is a major risk factor for the accumulation of metabolic stress.

Promotion of cellular $NAD^+$ anabolism has been shown to restore $NAD^+$ levels and reverse some phenotypes of ageing by enhancing cellular repair and stress resistance. Recent studies have shown that administration of the $NAD^+$ precursors, nicotinamide riboside (NR) and nicotinamide mononucleotide (NMN), can attenuate pathology in several murine models of age-related disorders [20]. Additionally, oral administration of NR has been reported to increase whole blood $NAD^+$ levels in humans [21]. A 6-week randomised, double-blind, placebo-controlled crossover clinical trial reported that NR supplementation was well-tolerated and effectively promoted $NAD^+$ metabolism in healthy middle-aged and elderly adults [22]. However, another randomised, placebo-controlled, double-blinded trial showed that NR supplementation had no effect on insulin sensitivity and lipid mobilising effects, and no adverse events due to NR were reported [23]. We also demonstrated that intravenous (I.V) injection of $NAD^+$ increased plasma and urine $NAD^+$ levels and exhibited differential effects on the NADome in healthy middle-aged humans. Thus, while it can be argued that there are several strategies to increase $NAD^+$ levels, understanding the endogenous intracellular and extracellular levels of the NADome are of emerging interest.

## 2. Clinical Relevance for Detection of the NADome in Biological Fluids

The NADome is an essential mediator of metabolic pathways that have been associated with ageing and age-related disorders. Several published methods have identified the NADome in whole blood and various cells or tissues, however, very few studies have examined changes in the NADome extracellularly [17,18,24]. A previous study reported that $NAD^+$ is predominantly an intracellular nucleotide, and only phosphorylated metabolites could be detected using LC-MS/MS [21]. However, emerging evidence suggests that exogenous $NAD^+$ may cross the plasma membrane and replenish intracellular $NAD^+$ levels in mammalian cells [25,26]. The discrepancy is likely to be related to the differences in the LC-MS/MS methodology and sample extraction. For example, Trammell et al. [27] used a double extraction method and two different chromatographic runs for reduced and oxidised forms of adenine and pyridine nucleotides, extending the analysis time per sample.

Owing to the clinical significance of increasing $NAD^+$ levels, and the role of $NAD^+$ in several age-related degenerative diseases, analytical methods for quantification of the NADome can be applied to clinically relevant biological samples, including whole human blood, urine, and CSF. This is because: (1) $NAD^+$ is released from cells at low amounts, (2) $NAD^+$ catabolism is an immediate process that leads to production of biologically active products, including NAM and consequently, MeNAM, (3) $NAD^+$ can act directly

on cell surface receptors such as connexin 43 channels and purinergic P2 receptors and therefore must be present extracellularly (Figure 2) [28], (4) MeNAM is the main metabolite of pyridine nucleotide catabolism and is cleared by urinary excretion [29], and (5) there is a lack of NAD-consuming enzymes in the urine compared to plasma.

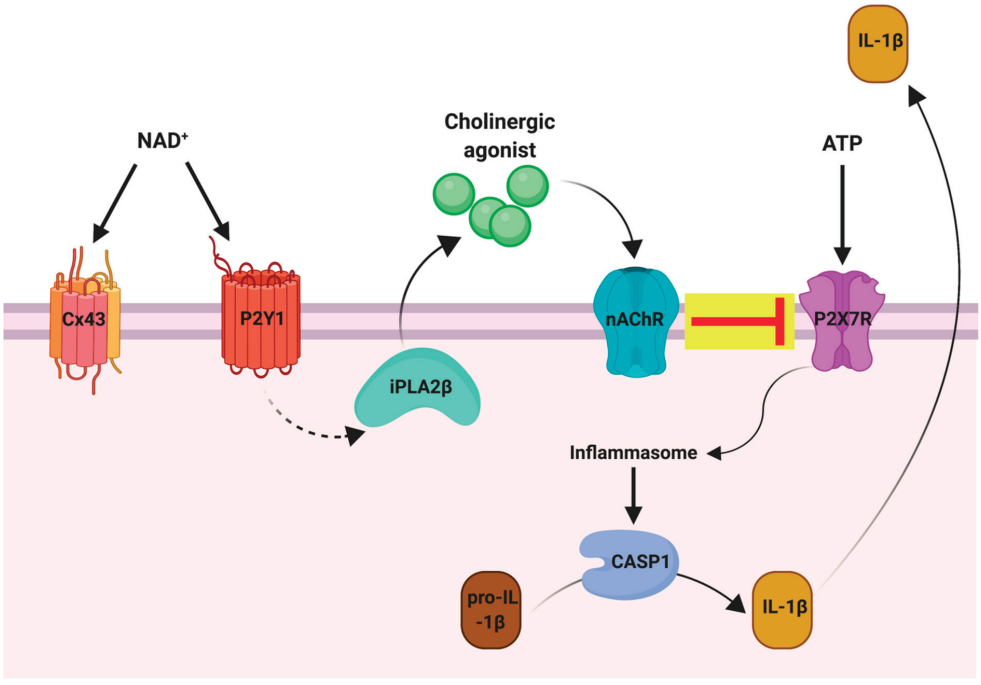


**Figure 2.** Schematic representation of the role of $NAD^+$ in purinergic signalling. Extracellular $NAD^+$ and ATP are released from damaged cells. ATP binds to the ATP-sensitive P2X7 receptor of monocytic cells. Activation of inflammasomes and caspase-1 induces cleavage of pro-IL-1β and release of bioactive IL-1β. $NAD^+$ binds to P2Y receptors and activates iPLA2β, leading to the production and release of bioactive mediators which serve as nicotinic agonists.

$NAD^+$ and related metabolites present in the blood will be filtered at the glomerulous and will be present in at least the renal filtrate of the proximal tubule. Recent studies have shown that CD38-mediated cADPR production in renal arteries and the distal tubule is necessary for Ca2+-mediated regulation of renal function [30]. Thus, the presence of CD38, as a NAD-dependent ectoenzyme in the distal renal tubule, and which its activity is critical for normal renal function and dependent on the availability of $NAD^+$ as a substrate, strongly supports the view that intact $NAD^+$ is still present in the renal filtrate after most of the tubular reabsorption has occurred.

A unique element of the central nervous system (CNS) is its high oxygen consumption and energy requirements relative to size (i.e., 2% of body weight and uses 20% of oxygen). This high energy demand is vital to sustaining the complex metabolic activities of the CNS and is achieved through accelerated mitochondrial activity using readily available $NAD^+$ in its redox couple. Importantly, elevated mitochondrial activity also results in significant superoxide production and nuclear damage [31], necessitating DNA repair through PARP activity, a $NAD^+$ catabolising process. In addition to its role in intracellular metabolism, extracellular $NAD^+$ also exerts direct synaptic effects, reducing synaptic excitotoxicity [32], and may also act as a neurotransmitter [33]. In order to act at the synapse, extracellular $NAD^+$ is clearly present in the CNS, as recently reported [33].

$NAD^+$ is also a central player in the maintenance and control of biological rhythms coordinated through the 20,000 pacemaker neurons in the suprachiasmatic nucleus in the CNS, where NAMPT/NAD+ drives the circadian clock feedback cycle through SIRT1 and CLOCK:BMAL1 [34]. Numerous NADPH-diaphorase (i.e., nitric oxide-producing) neurites are present on the free surface of the ependymal layer in direct contact with the cerebrospinal fluid (CSF) [35], thus suggesting that NADPH must also be present in the CSF to engage with this enzyme. Additionally, nicotinamide N-methyltransferase is present in the CSF and actively converts CSF NAM into its N-methylated metabolite [36], further highlighting both the presence and potential importance of NAM for the CNS.

## 3. Analysis of the NADome Using Traditional Techniques

Several methodologies have been previously used to quantify the NADome. These include specialised HPLC-UV, NMR [37], capillary zone electrophoresis, or colorimetric enzymatic assays [38]. While commonly available biochemical assays are readily available and relatively inexpensive, they provide indirect measurements and require tedious enzymatic manipulation [39,40], limiting their use in the clinic. Moreover, these assays are only available for $NAD^+$, NADH, and ATP, and thus are unable to provide an accurate reflection of changes in other metabolites in the NADome, such as $NADP^+$ and NADPH. For instance, the intracellular levels of $NAD^+$ have been shown to vary between 1 μM to 1 mM [16]. In addition, the ratio of NADPH:$NADP^+$ was reported to be ~100 using an enzymatic assay which measures the substrate concentration of malic and isocitrate dehydrogenase enzymes [41]. However, direct measurement of these metabolites suggests that the ratio of NADPH:$NADP^+$ may be significantly lower, i.e., 3.3 and 0.04 in the rat liver and heart [42]. Although multiple values are missing in the current literature and biological variability may indeed play a role, it is more likely that analytical variation represents a major contributory factor to the reported differences.

NMR-based experimental approaches have been developed to quantify the NADome in human cells. $^1$H NMR spectroscopy has been previously used to quantify the NADome in human platelets and erythrocytes [43]. While the relative concentration can be quantified directly from the NMR spectrum for each metabolite, irrespective of the complexity of the sample, this approach may require up to 2 h of data acquisition to achieve a signal-to-noise ratio of at least 5 for a sample containing approximately 2 μM of metabolite [43]. This can limit the application of NMR for the quantification of the NADome in some biological specimens, where some metabolites may be present in very low nanomolar levels [15].

Liquid chromatography (LC) techniques using absorbance for detection provide some advantages for quantifying multiple metabolites in the NADome relatively fast, i.e., within 10 to 60 min. However, HPLC-UV methods are limited due to low sensitivity and the presence of co-eluting contaminants [16]. For example, in a complex biological sample, a single peak may represent the metabolite of interest and other related metabolites that share identical retention times. Some studies have used mass spectrometry to non-quantitatively confirm the nature of the metabolite(s) present in any given fraction [16]. However, this strategy is time-consuming and costly. Since many metabolites in the NADome can be converted into other metabolites either by oxidation/reduction or enzymatic reactions, accurate quantification of $NAD^+$, NMN, NAM, and other metabolites without examination of the entire NADome may be misleading.

## 4. Quantification of the NADome Using Liquid Chromatography-Mass Spectrometry

LC coupled to tandem mass spectrometry (LC-MS/MS) has been recently developed for the quantitation of the NADome in biological specimens (Figure 3) [16]. In line with HPLC assays, LC allows the separation of individual metabolites and must be optimised in a similar manner to HPLC methods. The data collected from LC-MS is two-dimensional, i.e., retention time and mass-charge ratio, thus increasing specificity and sensitivity and allowing for the separation of closely related metabolites such as $NAD^+$ and NADH. Additionally, most LC-MS assays have a limit of quantification in the femtomole range [16].

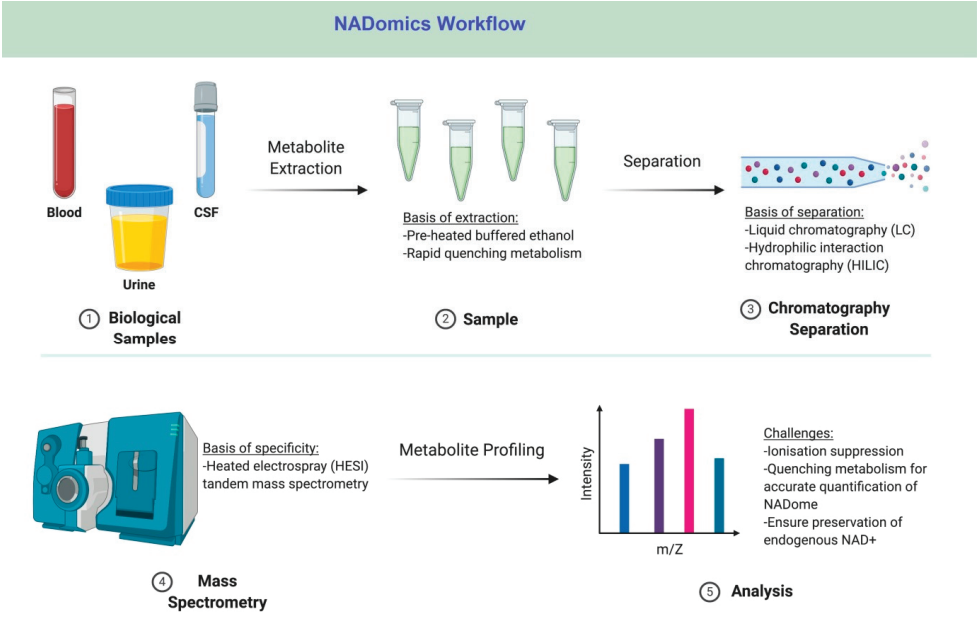


**Figure 3.** NADomics workflow. The NADomics workflow involves profiling the NADome with statistically significant variations in biological samples, e.g., blood, urine, and CSF. The specific $NAD^+$ metabolite ID including chemical structure and concentrations can be elucidated using LC-MS/MS. Analysis is the final step to elucidate associations between the identified metabolite and its role in physiology and disease.

Hydrophilic interaction liquid chromatography (HILIC) is an emerging separation mode of LC that suits well for the quantification of the NADome. The variant uses polar columns with a stationary phase, whereby polar analytes are eluted from the column by increasing water content of the mobile phase (typically acetonitrile with low amounts of water). HILIC also allows for hydrogen donor interactions between neutral polar species, and weak electrostatic mechanisms under high organic solvent conditions [44]. The retention of the analytes, peak shape, and chromatographic tailing is regulated by the pH of the mobile phase and ion strength attributed to ionic additives such as ammonium acetate and ammonium formate. HILIC allows for a high flow rate due to very low column backpressure by the high organic mobile phase [44].

HILIC separation has been previously used for the quantification of AMP, GMP, UMP, CMP, and IMP in infant formula [45,46]. It has also been adapted for quantitative analysis of cAMP, ATP, and other nucleosides, and mono-, di-, and tri-phosphate nucleotides, thus allowing for the simultaneous analysis of a large number of metabolites in a single run [45,46]. A volatile additive in mobile phase enables smooth hyphenation with mass spectrometry detection and has recently been optimised for the detection of at least 17 different metabolites in the NADome in astrocytes and oocytes [47].

## 5. Challenges of NADomics in Biological Specimens

Accurate quantification of the NADome is crucial for evaluating the cellular redox status. In this section, we discuss potential challenges and solutions that have affected previous methods.

### *5.1. Extraction*

Extraction of the NADome is a major source of analytical variation. Immediate extraction of the NADome in biological samples is ideal. Extraction methods which fail to

inactivate enzyme activities following cell lysis can limit the accurate quantitation of the NADome. For example, the levels of $NAD^+$ in a biological sample can be degraded to 1% of the anticipated value, while the levels of NAM can increase more than 10-fold. The most common method of extraction for most $NAD^+$ metabolites is boiled buffered ethanol [16]. We previously demonstrated that ice-cold 80% methanol was suitable for the extraction and maintaining molecular integrity of the NADome in murine oocytes [47].

A recent study compared the quenching and extraction efficiency of 7 different solvents on the NADome in mammalian cells and mouse tissue [42]. The solvents included a cold aqueous buffer with/without detergent, hot aqueous buffer, cold organic mixtures such as 80% methanol, buffered 75% acetonitrile, and acidic 40:40:20 acetonitrile:methanol:water with 0.02 or 0.1 M formic acid. The study found that extraction with acidic 40:40:20 acetonitrile:methanol:water was most efficient at maintaining the NADome for measurement using LC-MS. However, inclusion of detergent may also be useful, albeit to a lesser extent [42].

Human plasma, serum, urine, and cerebrospinal fluid (CSF) require only the removal of proteins, which can be performed using pre-heated buffered ethanol solution (ethanol:HEPES 1 mM, pH 7.1) [24], ice-cold methanol [17], methanol:acetonitrile, or centrifugal filtration apparatus. Additionally, a recent method quantified the NADome in human cell cultures, erythrocytes, CSF, and primate skeletal muscle without drying steps (using steam drying or speed vac), thus increasing NADome stability [24].

### *5.2. Internal Standards*

Ionisation suppression is a major problem that should be considered when measuring the NADome. This phenomenon refers to the ability of some sample components to influence the ionisation and detectability of certain analytes [16]. Therefore, the peak height or peak area may not be a true reflection of the peak size in the original complex mixture. Hence, internal standards are necessary to minimise ionisation suppression errors [16]. Optimisation of internal standards is also important to minimise inaccuracies in the quantification of the NADome due to interconversion of some metabolites, i.e., non-enzymatic degradation limits the accurate measurement of the $NAD^+$:NADH and $NADP^+$:NADPH ratios. Spiking with internal standards can monitor interconversion of these metabolites [42].

Previous studies that quantified the NADome using LC-MS/MS assays used internal standards derived from yeast cultured in $^{13}$C-glucose-supplemented ($^{13}$C $^{15}$N)-labelled medium [48] or in $^{13}$C-glucose with excellent correlation results [16]. However, yeast cell culture facilities may not always be available in-house. Isotopic labels for some $NAD^+$ metabolite isotopic labels are not commercially available. In the absence of the exact isotypic label, a closely related molecule (structural analog) is recommended [49]. Evans [50] quantified 18 metabolites of the NADome with excellent correlation coefficients using external standards.

We previously used the following internal standards for the quantification of selected $NAD^+$ metabolites in human and murine cells: $^2H^4$-NAM (MeNAM, NAM, NA, NAMN, NADPH, NAAD, ADPR, cADPR), $^{13}C^5$-Adenosine (adenosine), $^{13}C^5$-Cyclic AMP (cAMP, $NAD^+$, NMN), $^{13}C^{10}{}^{15}N^5$-ATP (NADH, ATP), $^{13}C^5$-AMP (AMP), and $^{15}N^5$-ADP ($NADP^+$, ADP). Most of these internal standards displayed correlation coefficients ($r^2 \geq 0.98$) [47].

### *5.3. Analyte Stability*

Instability of pyridine nucleotides is likely to be the biggest challenge when quantifying the NADome in a variety of biological samples. For instance, while reduced forms (i.e., NADH and NADPH) are more stable in alkaline solution, the oxidised forms ($NAD^+$ and $NADP^+$) are more stable in acidic solutions, and this is likely due to acid-catalysed autoxidation of NADH and NADPH [27]. Since time, pH, and temperature are likely to have a major effect on the ability to accurately quantify the NADome, quick quenching of metabolism is essential.

Demarest et al. recently assessed the benchtop stability of the NADome in human red blood cells (RBCs), the epithelial cell line HEK-293T, and primate skeletal muscle [24]. The study demonstrated rapid degradation of NADH and NADH within 30 min in the cellular matrices, whereas $NAD^+$ and ADPR were only stable for 10 min, and only 20% remained after 30 min. On the other hand, NAM and NMN levels increased after 1 h. This may be due to increased catabolism and degradation of $NAD^+$ and other metabolites [24]. Interestingly, NMN levels decreased in RBCs and skeletal muscle, while $NADP^+$ remained stable for 1 h in both RBCs and HEK-293T cells. In the CSF, only $NAD^+$ and NMN could be detected in the linear range. $NAD^+$ demonstrated greater stability in the CSF compared to the cellular matrices and this was attributed to a reduced NADome in the CSF and/or limited availability of $NAD^+$ 'consumers', e.g., PARPs and Sirtuins [24].

Therefore, optimising sample collection, storage, and availability of suitable testing protocols is essential to retain and accurately report changes to the NADome in intervention studies. In addition, quenching of samples should be completed without delay to minimise degradation of metabolites by active enzymes and preserve the endogenous NADome.

### *5.4. Liquid Chromatography*

Perhaps the most well-described LC-MS assay for quantification of the NADome is based on hydrophilic interaction liquid chromatography. One method to quantify the NADome uses two different mobile phases on two porous graphitic carbon reversed phases (Hypercarb, Thermo) in alkaline (NMN, NAMN, ADP, ATP, $NAD^+$, NADH, NAAD, $NADP^+$) and acid separation (NA, NAM, and NR) [16]. We previously demonstrated that an amino column using a dual HILIC-RP gradient with heated electrospray (HESI) tandem mass spectrometry detection in mixed polarity multiple reactions monitoring (MRM) mode could be simultaneously used for the quantification of the NADome in a single chromatographic run in biological specimens [47]. Recently, another study using an Accucore HILIC column identified some metabolites in multiple transitions [24]. For instance, $NAD^+$ was observed in the NAAD transition. Additionally, NAM was observed in the NA transition, but these metabolites could not be resolved. Picolinic acid, a metabolite in the de novo $NAD^+$ synthesis pathway and an isomer of NA, also co-eluted with NA [24].

Our refined method is an application of hydrophilic interaction chromatography (HILIC)—a major chromatographic system used in metabolic profiling [50]. The retention mechanism is based on partitioning and water is used as the eluent. An amino-modified HILIC Phenomenex Luna $NH_2$ column has been previously shown to demonstrate good retention and chromatographic resolution of water-soluble metabolites, including the NADome, with good peak shape, compared to cyano and/or silica columns, and none of the selected metabolites were observed in multiple MRM transitions [47,50].

## 6. Concluding Remarks

It is well-established that concentrations of the NADome represent a useful marker for elucidating the current status of cells, and may likely be an important biomarker in several metabolic and age-related disorders. Thus, accurate quantification of the NADome may be beneficial for researchers in understanding the pathobiology of metabolic disorders and effects of drug candidates. LC-MS/MS represents a rapid, robust, simple, and reliable assay for the measurement of the NADome in clinically relevant biological tissue. LC-MS/MS requires minimal sample processing. Using the amino phase chromatographic separation and commercially available internal standards eliminates cost, and requirement for yeast cultures for labelled metabolites, which are likely to represent major obstacles for measurement of the NADome to be applied in clinical diagnosis. NADomics can be used to provide renewed insights on physiological and pathological processes and may assist in identifying and evaluating potential therapeutic strategies.

**Author Contributions:** Conceptualisation, N.B and R.G. Methodology, N.B. and R.G. Writing draft preparation, N.B. and R.G. Writing review and editing, N.B. and R.G. Visualisation, M.D.V. Supervision, N.B. All authors have read and agreed to the published version of the manuscript.

**Funding:** This research received no external funding.

**Institutional Review Board Statement:** Not applicable.

**Informed Consent Statement:** Not applicable.

**Data Availability Statement:** Not applicable.

**Conflicts of Interest:** The authors declare no conflict of interest.

## References


1. Massudi, H.; Grant, R.; Guillemin, G.J.; Braidy, N. $NAD^+$ metabolism and oxidative stress: The golden nucleotide on a crown of thorns. *Redox Rep.* **2012**, *17*, 28–46. [CrossRef]
2. Braidy, N.; Guillemin, G.J.; Mansour, H.; Chan-Ling, T.; Poljak, A.; Grant, R. Age Related Changes in $NAD^+$ Metabolism Oxidative Stress and Sirt1 Activity in Wistar Rats. *PLoS ONE* **2011**, *6*, e19194. [CrossRef]
3. Braidy, N.; Poljak, A.; Grant, R.; Jayasena, T.; Mansour, H.; Chan-Ling, T.; Guillemin, G.J.; Smythe, G.; Sachdev, P. Mapping NAD+ metabolism in the brain of ageing Wistar rats: Potential targets for influencing brain senescence. *Biogerontology* **2014**, *15*, 177–198. [CrossRef]
4. Braidy, N.; Poljak, A.; Grant, R.; Jayasena, T.; Mansour, H.; Chan-Ling, T.; Smythe, G.; Sachdev, P.; Guillemin, G.J. Differential expression of sirtuins in the aging rat brain. *Front. Cell. Neurosci.* **2015**, *9*, 167. [CrossRef] [PubMed]
5. Braidy, N.; Berg, J.; Clement, J.; Khorshidi, F.; Poljak, A.; Jayasena, T.; Grant, R.; Sachdev, P. NAD+ Precursors as Therapeutic Agents for Age-related Degenerative Diseases. *Antioxid. Redox Signal.* **2019**, *30*, 251–294. [CrossRef]
6. Horenstein, A.L.; Sizzano, F.; Lusso, R.; Besso, F.G.; Ferrero, E.; Deaglio, S.; Corno, F.; Malavasi, F. CD38 and CD157 Ectoenzymes Mark Cell Subsets in the Human Corneal Limbus. *Mol. Med.* **2009**, *15*, 76–84. [CrossRef]
7. Surjana, D.; Halliday, G.M.; Damian, D.L. Role of Nicotinamide in DNA Damage, Mutagenesis, and DNA Repair. *J. Nucleic Acids* **2010**, *2010*, 157591. [CrossRef]
8. Vaquero, A.; Sternglanz, R.; Reinberg, D. $NAD^+$ -dependent deacetylation of H4 lysine 16 by class III HDACs. *Oncogene* **2007**, *26*, 5505–5520. [CrossRef]
9. Fan, J.; Krautkramer, K.A.; Feldman, J.L.; Denu, J.M. Metabolic Regulation of Histone Post-Translational Modifications. *ACS Chem. Biol.* **2015**, *10*, 95–108. [CrossRef]
10. Braidy, N.; Guillemin, G.; Grant, R. Promotion of cellular $NAD^+$ anabolism: Therapeutic potential for oxidative stress in ageing and Alzheimer's disease. *Neurotox. Res.* **2008**, *13*, 173–184. [CrossRef]
11. Fu, C.S.; Swendseid, M.E.; Jacob, R.A.; McKee, R.W. Biochemical Markers for Assessment of Niacin Status in Young Men: Levels of Erythrocyte Niacin Coenzymes and Plasma Tryptophan. *J. Nutr.* **1989**, *119*, 1949–1955. [CrossRef] [PubMed]
12. Jacob, R.A.; Swendseid, M.E.; McKee, R.W.; Fu, C.S.; Clemens, R.A. Biochemical Markers for Assessment of Niacin Status in Young Men: Urinary and Blood Levels of Niacin Metabolites. *J. Nutr.* **1989**, *119*, 591–598. [CrossRef]
13. Sartini, D.; Santarelli, A.; Rossi, V.; Goteri, G.; Rubini, C.; Ciavarella, D.; Muzio, L.L.; Emanuelli, M. Nicotinamide N-methyltransferase upregulation inversely correlates with lymph node metastasis in oral squamous cell carcinoma. *Mol. Med.* **2007**, *13*, 415–421. [CrossRef]
14. Bogan, K.L.; Brenner, C. Nicotinic Acid, Nicotinamide, and Nicotinamide Riboside: A Molecular Evaluation of $NAD^+$ Precursor Vitamins in Human Nutrition. *Annu. Rev. Nutr.* **2008**, *28*, 115–130. [CrossRef]
15. Liu, Y.; Clement, J.; Grant, R.; Sachdev, P.; Braidy, N. Quantitation of $NAD^+$: Why do we need to measure it? *Biochim. Biophys. Acta Gen. Subj.* **2018**, *1862*, 2527–2532. [CrossRef]
16. Trammell, S.; Brenner, C. Targeted, LCMS-Based Metabolomics for Quantitative Measurement Of $NAD^+$ Metabolites. *Comput. Struct. Biotechnol. J.* **2013**, *4*, e201301012. [CrossRef]
17. Clement, J.; Wong, M.; Poljak, A.; Sachdev, P.; Braidy, N. The Plasma $NAD^+$ Metabolome Is Dysregulated in "Normal" Aging. *Rejuvenation Res.* **2018**, *22*, 121–130. [CrossRef]
18. Seyedsadjadi, N.; Berg, J.; Bilgin, A.A.; Braidy, N.; Salonikas, C.; Grant, R. High protein intake is associated with low plasma $NAD^+$ levels in a healthy human cohort. *PLoS ONE* **2018**, *13*, e0201968. [CrossRef]
19. Braidy, N.; Lim, C.K.; Grant, R.; Brew, B.J.; Guillemin, G.J. Serum nicotinamide adenine dinucleotide levels through disease course in multiple sclerosis. *Brain Res.* **2013**, *1537*, 267–272. [CrossRef]
20. Long, A.N.; Owens, K.; Schlappal, A.E.; Kristian, T.; Fishman, P.S.; Schuh, R.A. Effect of nicotinamide mononucleotide on brain mitochondrial respiratory deficits in an Alzheimer's disease-relevant murine model. *BMC Neurol.* **2015**, *15*, 19. [CrossRef]
21. Trammell, S.; Schmidt, M.; Weidemann, B.J.; Redpath, P.; Jaksch, F.; Dellinger, R.W.; Philip, R.; Abel, E.D.; Migaud, M.E.; Brenner, C. Nicotinamide riboside is uniquely and orally bioavailable in mice and humans. *Nat. Commun.* **2016**, *7*, 12948. [CrossRef]
22. Martens, C.R.; Denman, B.A.; Mazzo, M.R.; Armstrong, M.L.; Reisdorph, N.; McQueen, M.B.; Chonchol, M.; Seals, D.R. Chronic nicotinamide riboside supplementation is well-tolerated and elevates $NAD^+$ in healthy middle-aged and older adults. *Nat. Commun.* **2018**, *9*, 1286. [CrossRef]
23. Dollerup, O.L.; Christensen, B.; Svart, M.; Schmidt, M.; Sulek, K.; Ringgaard, S.; Stødkilde-Jørgensen, H.; Møller, N.; Brenner, C.; Treebak, J.T.; et al. A randomized placebo-controlled clinical trial of nicotinamide riboside in obese men: Safety, insulin-sensitivity, and lipid-mobilizing effects. *Am. J. Clin. Nutr.* **2018**, *108*, 343–353. [CrossRef]

24. Demarest, T.G.; Truong, G.T.D.; Lovett, J.; Mohanty, J.G.; Mattison, J.A.; Mattson, M.P.; Ferrucci, L.; Bohr, V.A.; Moaddel, R. Assessment of $NAD^+$ metabolism in human cell cultures, erythrocytes, cerebrospinal fluid and primate skeletal muscle. *Anal. Biochem.* **2019**, *572*, 1–8. [CrossRef] [PubMed]
25. Billington, R.A.; Travelli, C.; Ercolano, E.; Galli, U.; Roman, C.B.; Grolla, A.A.; Canonico, P.L.; Condorelli, F.; Genazzani, A.A. Characterization of NAD Uptake in Mammalian Cells. *J. Biol. Chem.* **2008**, *283*, 6367–6374. [CrossRef] [PubMed]
26. Kulikova, V.; Shabalin, K.; Nerinovski, K.; Dölle, C.; Niere, M.; Yakimov, A.; Redpath, P.; Khodorkovskiy, M.; Migaud, M.E.; Ziegler, M.; et al. Generation, Release, and Uptake of the NAD Precursor Nicotinic Acid Riboside by Human Cells. *J. Biol. Chem.* **2015**, *290*, 27124–27137. [CrossRef]
27. Airhart, S.E.; Shireman, L.M.; Risler, L.J.; Anderson, G.D.; Gowda, G.A.N.; Raftery, D.; Tian, R.; Shen, D.D.; O'Brien, K. An open-label, non-randomized study of the pharmacokinetics of the nutritional supplement nicotinamide riboside (NR) and its effects on blood $NAD^+$ levels in healthy volunteers. *PLoS ONE* **2017**, *12*, e0186459. [CrossRef]
28. Alefishat, E.; Alexander, S.P.H.; Ralevic, V. Effects of NAD at purine receptors in isolated blood vessels. *Purinergic Signal.* **2014**, *11*, 47–57. [CrossRef] [PubMed]
29. Adriouch, S.; Haag, F.; Boyer, O.; Seman, M.; Koch-Nolte, F. Extracellular $NAD^+$: A danger signal hindering regulatory T cells. *Microbes Infect.* **2012**, *14*, 1284–1292. [CrossRef] [PubMed]
30. Boini, K.M.; Xia, M.; Xiong, J.; Li, C.; Payne, L.P.; Li, P.-L. Implication of CD38 gene in podocyte epithelial-to-mesenchymal transition and glomerular sclerosis. *J. Cell. Mol. Med.* **2012**, *16*, 1674–1685. [CrossRef]
31. Sasaki, T.; Yamanaka, M.; Kagami, N. WITHDRAWN: Superoxide generation in different brain regions of rats during normoxia and hypoxia-reoxygenation. *Neurosci. Res.* **2012**, *74*, 261–268. [CrossRef]
32. Liang, M.; Yin, X.-L.; Wang, L.-Y.; Yin, W.-H.; Song, N.-Y.; Shi, H.-B.; Li, C.-Y.; Yin, S.-K. $NAD^+$ Attenuates Bilirubin-Induced Hyperexcitation in the Ventral Cochlear Nucleus by Inhibiting Excitatory Neurotransmission and Neuronal Excitability. *Front. Cell. Neurosci.* **2017**, *11*, 21. [CrossRef]
33. Durnin, L.; Dai, Y.; Aiba, I.; Shuttleworth, C.W.; Yamboliev, I.A.; Mutafova-Yambolieva, V.N. Release, neuronal effects and removal of extracellular β-nicotinamide adenine dinucleotide (β-$NAD^+$) in the rat brain. *Eur. J. Neurosci.* **2012**, *35*, 423–435. [CrossRef]
34. Imai, S.-I. "Clocks" in the NAD World: NAD as a metabolic oscillator for the regulation of metabolism and aging. *Biochim. Biophys. Acta Proteins Proteom.* **2010**, *1804*, 1584–1590. [CrossRef] [PubMed]
35. Sancesario, G.; Morello, M.; Massa, R.; Fusco, F.R.; D'Angelo, V.; Bernardi, G. NADPH-Diaphorase Neurons Contacting the Cerebrospinal Fluid in the Ventricles of Rat Brain. *Br. J. Pharmacol.* **1996**, *16*, 517–522. [CrossRef] [PubMed]
36. Aoyama, K.; Matsubara, K.; Kondo, M.; Murakawa, Y.; Suno, M.; Yamashita, K.; Yamaguchi, S.; Kobayashi, S. Nicotinamide-N-methyltransferase is higher in the lumbar cerebrospinal fluid of patients with Parkinson's disease. *Neurosci. Lett.* **2001**, *298*, 78–80. [CrossRef]
37. Casabona, G.; Sturiale, L.; L'Episcopo, M.R.; Raciti, G.; Fazzio, A.; Sarpietro, M.G.; A Genazzani, A.; Cambria, A.; Nicoletti, F. HPLC analysis of cyclic adenosine diphosphate ribose and adenosine diphosphate ribose: Determination of $NAD^+$ metabolites in hippocampal membranes. *Ital. J. Biochem.* **1995**, *44*, 258–268.
38. Bernofsky, C.; Swan, M. An improved cycling assay for nicotinamide adenine dinucleotide. *Anal. Biochem.* **1973**, *53*, 452–458. [CrossRef]
39. Helenius, M.; Jalkanen, S.; Yegutkin, G.G. Enzyme-coupled assays for simultaneous detection of nanomolar ATP, ADP, AMP, adenosine, inosine and pyrophosphate concentrations in extracellular fluids. *Biochim. Biophys. Acta Bioenergy* **2012**, *1823*, 1967–1975. [CrossRef]
40. Romanova, N.; Ugarova, N.; Brovko, L. Bioluminescent Assay of Bacterial Intracellular AMP, ADP, and ATP with the Use of a Coimmobilized Three-Enzyme Reagent (Adenylate Kinase, Pyruvate Kinase, and Firefly Luciferase). *Anal. Biochem.* **1994**, *220*, 410–414. [CrossRef]
41. Veech, R.L.; Eggleston, L.V.; Krebs, H.A. The redox state of free nicotinamide–adenine dinucleotide phosphate in the cytoplasm of rat liver. *Biochem. J.* **1969**, *115*, 609–619. [CrossRef]
42. Lu, W.; Wang, L.; Chen, L.; Hui, S.; Rabinowitz, J.D. Extraction and Quantitation of Nicotinamide Adenine Dinucleotide Redox Cofactors. *Antioxid. Redox Signal.* **2018**, *28*, 167–179. [CrossRef] [PubMed]
43. Shabalin, K.; Nerinovski, K.; Yakimov, A.; Kulikova, V.; Svetlova, M.; Solovjeva, L.; Khodorkovskiy, M.; Gambaryan, S.; Cunningham, R.; Migaud, M.E.; et al. NAD Metabolome Analysis in Human Cells Using 1H NMR Spectroscopy. *Int. J. Mol. Sci.* **2018**, *19*, 3906. [CrossRef] [PubMed]
44. Kiyokawa, E.; Hayama, T.; Yoshida, H.; Yamaguchi, M.; Nohta, H. Fluorous-assisted metal chelate affinity extraction for nucleotides followed by HILIC-MS/MS analysis. *J. Chromatogr. B* **2018**, *1074–1075*, 86–90. [CrossRef] [PubMed]
45. Inoue, K.; Dowell, D. HILIC-MS/MS Method for the Quantitation of Nucleotides in Infant Formula and Adult Nutritional Formula: First Action 2011.21. *J. AOAC Int.* **2012**, *95*, 603–605. [CrossRef] [PubMed]
46. Inoue, K.; Obara, R.; Hino, T.; Oka, H. Development and Application of an HILIC-MS/MS Method for the Quantitation of Nucleotides in Infant Formula. *J. Agric. Food Chem.* **2010**, *58*, 9918–9924. [CrossRef]
47. Bustamante, S.; Jayasena, T.; Richani, D.; Gilchrist, R.; Wu, L.E.; Sinclair, D.A.; Sachdev, P.; Braidy, N. Quantifying the cellular $NAD^+$ metabolome using a tandem liquid chromatography mass spectrometry approach. *Metabolomics* **2018**, *14*, 15. [CrossRef] [PubMed]

48. Evans, J.; Wang, T.-C.; Heyes, M.P.; Markey, S. LC/MS analysis of NAD biosynthesis using stable isotope pyridine precursors. *Anal. Biochem.* **2002**, *306*, 197–203. [CrossRef]
49. Yamada, K.; Hara, N.; Shibata, T.; Osago, H.; Tsuchiya, M. The simultaneous measurement of nicotinamide adenine dinucleotide and related compounds by liquid chromatography/electrospray ionization tandem mass spectrometry. *Anal. Biochem.* **2006**, *352*, 282–285. [CrossRef]
50. Evans, C.; Bogan, K.L.; Song, P.; Burant, C.F.; Kennedy, R.T.; Brenner, C. $NAD^+$ metabolite levels as a function of vitamins and calorie restriction: Evidence for different mechanisms of longevity. *BMC Chem. Biol.* **2010**, *10*, 2. [CrossRef] [PubMed]

life

MDPI

*Review*

# Sudden Infant Death Syndrome: Beyond Risk Factors

**Serafina Perrone [1,*], Chiara Lembo [2], Sabrina Moretti [1], Giovanni Prezioso [1], Giuseppe Buonocore [2], Giorgia Toscani [1], Francesca Marinelli [1], Francesco Nonnis-Marzano [3] and Susanna Esposito [1]**

[1] Department of Medicine and Surgery, University Hospital of Parma, 43126 Parma, Italy; smoretti@ao.pr.it (S.M.); gprezioso@ao.pr.it (G.P.); giorgia.toscani@studenti.unipr.it (G.T.); francesca.marinelli@studenti.unipr.it (F.M.); susannamariaroberta.esposito@unipr.it (S.E.)
[2] Department of Molecular and Developmental Medicine, University of Siena, 53100 Siena, Italy; Chiara.lembo@student.unisi.it (C.L.); giuseppe.buonocore@unisi.it (G.B.)
[3] Department of Chemistry, Life Sciences and Environmental Sustainability, University of Parma, 43126 Parma, Italy; francesco.nonnismarzano@unipr.it
* Correspondence: serafina.perrone@unipr.it; Tel.: +39-0521-703518

**Abstract:** Sudden infant death syndrome (SIDS) is defined as "the sudden death of an infant under 1 year of age which remains unexplained after thorough investigation including a complete autopsy, death scene investigation, and detailed clinical and pathological review". A significant decrease of SIDS deaths occurred in the last decades in most countries after the beginning of national campaigns, mainly as a consequence of the implementation of risk reduction action mostly concentrating on the improvement of sleep conditions. Nevertheless, infant mortality from SIDS still remains unacceptably high. There is an urgent need to get insight into previously unexplored aspects of the brain system with a special focus on high-risk groups. SIDS pathogenesis is associated with a multifactorial condition that comprehends genetic, environmental and sociocultural factors. Effective prevention of SIDS requires multiple interventions from different fields. Developing brain susceptibility, intrinsic vulnerability and early identification of infants with high risk of SIDS represents a challenge. Progress in SIDS research appears to be fundamental to the ultimate aim of eradicating SIDS deaths. A complex model that combines different risk factor data from biomarkers and omic analysis may represent a tool to identify a SIDS risk profile in newborn settings. If high risk is detected, the infant may be referred for further investigations and follow ups. This review aims to illustrate the most recent discoveries from different fields, analyzing the neuroanatomical, genetic, metabolic, proteomic, environmental and sociocultural aspects related to SIDS.

**Keywords:** SIDS; newborn infant; genetic polymorphism; neurotransmitter

**Citation:** Perrone, S.; Lembo, C.; Moretti, S.; Prezioso, G.; Buonocore, G.; Toscani, G.; Marinelli, F.; Nonnis-Marzano, F.; Esposito, S. Sudden Infant Death Syndrome: Beyond Risk Factors. *Life* **2021**, *11*, 184. https://doi.org/10.3390/life11030184

Academic Editor: Jong Hyuk Yoon

Received: 24 December 2020
Accepted: 22 February 2021
Published: 26 February 2021



## 1. Definition and Epidemiology

Sudden infant death syndrome (SIDS) is defined as "the sudden death of an infant under 1 year of age which remains unexplained after thorough investigation including a complete autopsy, death scene investigation, and detailed clinical and pathological review" [1,2]. SIDS is characterized by an unexpected death during the sleeping period and it typically occurs in the first 12 months of age in a previously healthy infant. Most events take place in the child's home; the out-of-home deaths are most frequent at a relative's home or a child-care setting, especially if the child sleeps in prone position and in a stroller and/or car seat [3]. SIDS is a subcategory of Sudden Unexpected Infant Deaths (SUID) and represents nearly half of these cases; SUID includes SIDS of unknown cause and also events of strangulation in bed or accidental suffocation [4]. The peak of incidence of SIDS is around two to four months of age and 90% of cases occur before six months of age; prevalence of SIDS is higher in boys than girls, at a 3:2 ratio [5].

In the late 1980s prone sleep has been documented as a major risk factor for SIDS, leading in the 1990s to "back-to-sleep" campaigns which have had a great impact on reduction of SIDS rates [6]. SIDS infant mortality has decreased well over 50% for most

countries, especially in the first few years after the beginning of national campaigns [7]. Alongside the SIDS prevention recommendations, perinatal care has experienced numerous other improvements, so it's difficult to attribute the SIDS incidence drop to only the supine sleep practice [6]. Furthermore, the increasing rates of other causes of death such as strangulation in bed and accidental suffocation may represent another explanation of the decline in SIDS rates [8]. Over the first decade of this century, infant mortality from SIDS has experienced a continuous drop in some countries such as Australia, Canada, England and Wales, Germany, Japan and the Netherlands, while it has remained stationary in others, notably the USA and New Zealand [9]. Despite continuous public health efforts concentrating on the improvement of sleep conditions with a special focus on the high-risk groups [10,11], incidence of SIDS still continues to be high. In fact, SIDS still represents a prominent cause of infant death, occurring at a rate of 27/100,000 live births in the United Kingdom and 38/100,000 the United States [12,13]. In Italy incidence is about 1 out of 1000 live births [14]. Therefore, continuous research on the cause and prevention of SIDS is needed.

## 2. Pathogenesis and Risk Factors

The most recent evidence suggests that SIDS pathogenesis is a multifactorial condition that comprehends genetic, environmental and sociocultural factors [8]. The Triple-Risk Model, first described in 1994, affirms that SIDS occurs in infants with latent biological vulnerability (brainstem abnormality or genetic pattern), who is exposed to a trigger event or extrinsic risk factor (prone sleeping, airway obstruction) during a critical phase of development [15]. The combination of intrinsic and extrinsic factors which overlap during a period of respiratory, autonomic and cardiac development, usually occurring between two to four months of age, leads to a life-threatening event during a period of sleep. Failure of protective mechanisms during these episodes finally concludes with unexpected death. On the contrary, SIDS is less likely to occur with the removal of one of these factors [16,17].

Multiple extrinsic risk factors for SIDS in the sleep environment of the infants have been examined. Prone sleeping appears to be the most significant risk factor for SIDS. In fact, it is likely to be associated with re-breathing expired gases, suffocation, overheating and decreased arousal [18]. Infants in side lying position are also at high risk to roll into prone position while sleeping [19]. Other factors related to the sleeping environment involve soft bedding, sleeping with blankets, pillows, soft objects, bumper pads, head or face covered during sleep, bedsharing (especially co-sleeping on a couch or sofa) and room or infant overheating [20]. Maternal smoking during pregnancy is associated with a fivefold increase in SIDS events, and postnatal smoking exposure further increases the risk [21–23]. In fact, it's been demonstrated that smoking during pregnancy contributes to the risk due to the disruption of arousal patterns in the sleeping baby along with impairment of autonomic system and cardiovascular response: uterine exposure reduces lung compliance and volume, alters arousal mechanisms and decreases heart rate variability in response to stress, all factors that can negatively affect a baby's ability to respond appropriately to the environment [24,25]. A recent study showed a linear correlation between number of cigarettes smoked daily during pregnancy and the risk of a SUID event. Furthermore, quitting smoking over the three trimesters is strongly associated with great reduction of SUID risk but also diminution of cigarettes smoked daily contributes to a small decrease in risk [26]. Additional risk factors include maternal alcohol use, young maternal age (under 20 years) and poor prenatal care [27]. The combined exposure of alcohol and tobacco beyond the first trimester of pregnancy appears to have a synergistic effect on the risk for SIDS events [28]. Co-sleeping associated with recent use of alcohol or drugs by the parents also increases the risk significantly [29]. The strong association between smoking, alcohol consumption and drugs utilization may also explain, in part, the interaction described between co-sleeping and smoking [29–32]. Bottle-feeding is associated with increased risk, while the use of a pacifier and breastfeeding appear to be protective factors [27,33,34]. Some studies suggest that a significant part of SIDS cases may be closely related to sub-clinical

infection processes [35,36]. In a study conducted by Goldwater et al. in 2020, significantly heavier thymus and brain were found in SIDS victims compared to non-SIDS controls. This finding is related to immune responses in the brain and thymus associated with possible subclinical infections [37].

Intrinsic risk factors are male gender, population subgroups such as non-Hispanic black infants, American Indian or Alaska Native infants [8,38] and prematurity. Preterm birth or low birth weight increases the risk of SIDS events three to four times, suggesting that altered intrauterine environment may contribute to the pathogenesis [39]. Additionally, smoking during pregnancy increases the risk of premature delivery [40]. Furthermore, research suggests that disorders of homeostasis, neuroregulation and cardiorespiratory function associated with brain and brainstem anomalies play an important role in SIDS [16]. In particular, serotonin brainstem abnormalities have been identified in up to 70% of infants who have died of SIDS [16]. Since the serotonin system is associated with several homeostatic functions, these anomalies may possibly lead to a network dysfunction that affects arousal and cardiorespiratory functions [41,42]. In addition to brain vulnerabilities, research has focused on identifying genetic variants related to defects involving autonomic and metabolic functions, neurotransmission and cardiac repolarization, suggested to contribute to SIDS infant's "underlying vulnerability" [2,43,44]. Thus, certain infants may have a genetic predisposition to SIDS or an underlying abnormality in the brainstem, which becomes manifest when the infant experiences environmental challenges (hypoxia, asphyxia, hypercarbia, overheating) during sleep and differentiates a SIDS infant from a healthy infant. In fact, infants without the underlying conditions present an efficient protective brainstem response to homeostatic challenges which promptly manage to avoid SIDS occurrence [2]. The combination of multiple extrinsic and intrinsic factors leads to asphyxia. Vulnerable infants are not able to respond with arousal that prevents re-breathing or apnea. Consequently, asphyxia leads to bradycardia and insufficient gasping breathing, which eventually terminate with death [45].

Most of these life-threatening events occur during the sleep period. In fact, sleep is associated with a reduction of blood pressure, heart rate, respiratory rate and muscle tone, especially in the upper airways. During sleep phases protective reflexes to hypoxia and hypercapnia are also depressed. Blood pressure, cerebral oxygenation and cerebral vascular homeostasis are decreased in the prone position [46,47]. In fact, term infants between two to four months of age show a depressed baroreflex response and decreased arousal in the prone position [48,49]. In premature babies these characteristics in prone position are mostly marked [50,51]. These considerations highlight, indeed, the increased risk of SIDS occurring during sleeping, mainly in the prone position during specific infant development windows.

## 3. The Brainstem Hypothesis in SIDS

Neural research in SIDS has concentrated efforts to define the existence and eventual location of a pathological lesion in the brain. No major anatomic signs of neural pathology have been revealed by standard autopsy.

Impairment of the brainstem has been related to sudden death. The brainstem is the primary anatomic site of homeostatic control and sleep/waking regulation in the brain [52]. The brainstem hypothesis in SIDS suggests that developmental abnormalities in specific brainstem regions lead to a failure of protective mechanisms against exogenous stressors associated with asphyxia, hypoxia, hypercapnia, or thermal imbalance during sleep. Defense functions, as central chemosensitivity to carbon dioxide ($CO_2$) and peripheral and central chemosensitivity to oxygen ($O_2$), activate an autoresuscitation mechanism with arousal accompanied by head lifting to avoid asphyxia. Defects in this system include impaired arousal, ineffective respiratory pattern, episodes of obstructive apnea during sleep and autonomic dysfunction [53,54].

Additional evidence of the possible brainstem role in SIDS was reported by Naeye et al. who described astrogliosis in the medullary reticular formation in 50% of SIDS cases.

This scarring lesion was interpreted as the result of chronic alveolar hypoventilation and hypoxemia [55]. Further studies confirmed the presence of reactive gliosis in different brainstem regions such as inferior olivary nuclei of the brainstem [56,57]. Gliosis is thought to be a sign of brainstem function impairment, as a result of hypoxia and chronic underventilation [58]. Finding a gliosis marker in the brainstem in SIDS cases supported the validity of brainstem hypothesis [59].

Furthermore, an immature developmental pattern in the SIDS brainstem has also been reported, with brainstem neurons presenting an augmented dendritic spine number [60]. These findings have been recently supported by proteomic investigations that showed abnormalities related to neuronal/glial/axonal growth, metabolism and apoptosis in some brainstem areas such as raphe, hypoglossal nuclei and medullary pyramids. These considerations suggest that brainstem immaturity, as well as gliosis, may be involved in the abnormal central respiratory and arousal control [61].

Multiple neurotransmitter networks anomalies are thought to be responsible for the underlying vulnerability in SIDS infants. These defects involve different brainstem neurochemicals such as catecholamines, neuropeptides, acetylcholinergic metabolites, amines, aminoacids (primarily glutamate), growth factors and some cytokines [62]. A defective binding of peptide neurotransmitter substance P to its receptor neurokinin-1 has been described in nuclei involved in cardiorespiratory and autonomic control. In fact, a defect of medullary substance P network with cerebellar sites may result in failure to activate respiratory and motor responses. In particular, low levels of substance P have been found in the olivary nuclei that control head and neck movements. As a consequence, failure of the protective mechanism such as head lifting or tilting to escape hypoxia may occur in SIDS infants [63]. Another study highlighted the interactions of GABA neurons in the medulla oblongata with the medullary serotonergic system in the regulation of homeostasis [64]. Data suggest that deficits of GABAergic and serotoninergic systems cooperate to generate medullary dysfunction in SIDS [65]. SIDS was also associated with low levels of tryptophan hydroxylase enzyme, which is involved in serotonin synthesis, resulting in decreased serotonin production [66].

However, researches have been mostly focused on the role of the brainstem serotoninergic system. The brainstem serotonin network in the rostral medulla is involved in the activation of the protective respiratory and autonomic reactions in response to exogenous stressors during sleep. According to the serotonin brainstem hypothesis, a defect in the serotonin system leads to failure of the autoresuscitation and arousal reaction that ultimately causes SIDS. A study conducted by Kinney et al. identified a serotonergic impairment in the medullary reticular formation of the brainstem as a "core" lesion in SIDS [65]. The affected serotonin brainstem network is supposed to involve serotonin neurons interconnected among arcuate nucleus, paragigantocellularis lateralis, gigantocellularis, intermediate reticular zone and caudal raphe [65]. These regions have been identified using a quantitative autoradiography which has demonstrated a decreased serotonergic receptor binding in these nuclei in SIDS cases compared to controls [67]. The ascending serotoninergic arousal system is also implicated. In fact, the rostral reticular formation dysfunction is postulated to be transmitted to median raphe and dorsal raphe of the ascending serotonergic arousal system that results in failure of the metabolic challenge response, leading to death [65]. In particular, an alteration of Pet-1 expressing neurons located in the serotonergic raphe system has been related to the impaired recovery system. This suggests a role of Pet-1 neuron activity in the neonatal survival mechanism responding to hypoxia [68]. Furthermore, recent findings by Haynes et al. have described increased serum serotonin levels in SIDS cases compared to controls. Therefore, a high serum serotonin may be utilized as a biomarker in SIDS autopsies to distinguish deaths caused by serotonin-related anomalies [69].

As potential causes of serotonin brainstem disruption in SIDS, the role of maternal and pregnancy factors has been discussed. In fact, analysis of the placentas of newborns

who subsequently died of SIDS suggests that an infant's vulnerability originates in the gestational period.

In fact, some maternal factors associated with fetal hypoxia, such as placenta vascular hypoperfusion, maternal anemia and cigarette smoking generate a suboptimal intrauterine environment. These maternal factors are hypothesized to be responsible, in part, for impaired brain development, particularly in the central serotonin system, as the basis of vulnerability in sudden postnatal death [70–72]. Furthermore, some gene polymorphisms of the promoter region of a serotonin transporter protein ("L" allele and "LL" genotype variants) are responsible for increased activity of the serotonin transporter protein, resulting in reduced concentration of serotonin. These genetic variants have been frequently found in SIDS victims [16,62,73,74]. Interestingly, the same variants were also found in additional predisposing conditions [75]. However, some studies reported no association between LL genotype or L allele and SIDS in Caucasians [76,77].

Yet, the role of this polymorphism in other ethnicities as a risk factor in SIDS still needs to be clarified [78]. Additional studies should be carried out to assess the role of population genetics influencing serotonin transporter protein alleles and genotypes distribution in different ethnicities [74]. Different ethnic groups sharing the same social conditions show different SIDS rates [79,80]. Recently, a nearly fivefold variation in high risk of SIDS has been found between ethnic groups in England and Wales [81]. Authors speculated that cultural differences play an important role in infant care rather than genetic factors. Further research into infant-care practices in low-risk ethnic groups might enable more effective prevention of SIDS in the general population. While there is some evidence of how genetic differences might influence susceptibility to certain factors (e.g., inflammatory responses) [82], the knowledge about the functional impact of these differences is still lacking. As a matter of fact, there is no evidence that genetic influences outside of social and environmental factors pose a risk for SIDS.

Brainstem dysfunction is not limited to only one neurochemical network, such as the serotoninergic system. In fact, recent studies conducted by Hunt at al. have reported abnormal expression in nine different proteins within some brainstem nuclei, mainly the raphe nuclei and pyramids, that may relate to developmental and neurological cyto-architecture abnormalities in SIDS cases [61]. A study by Lavezzi et al. recently described low tyrosine hydroxylase expression in SIDS cases associated with a delayed development of Substantia Nigra pars compacta (SNpc). Moreover, nicotine absorption in the uterus was related to decreased neuron density in SN [83]. SNpc represents the major dopamine brain center with an important role in regulation of the sleep-arousal cycle [84]. Therefore, the deficit of dopaminergic neurons, alongside with smoking exposure, may explain SIDS occurrence in the awakening phase in a significant number of cases [83].

## 4. Metabolic Predisposition

Inborn errors of metabolism (IEM) have been described as possible causes of SIDS [85–87]. Metabolomics analysis enables characterization of metabolites produced by cells, tissues and microorganisms, their quantification and interpretation [88]. A study conducted by Graham et al. analyzed data of Nuclear Magnetic Resonance and Mass Spectrometry from the medulla oblongata of infants who died from SIDS. This analysis revealed that fatty acid metabolism was the principal metabolic pathway altered in the brain of infants with SIDS occurrence, thus fatty acids oxidation disorders may represent one of many causes of SIDS. Furthermore, this analysis identified one metabolite (octadecenoyl-L-carnitine) that could be potentially used as a diagnostic tool for early screening to detect infants at greatest risk of SIDS occurrence. Further studies should determine if the same diagnostic biomarkers identified in this study can also be found in blood samples [89].

A recent study conducted a postmortem analysis of short chain fatty acids (SCFAs) values in babies who experienced SIDS or death for causes not related to SIDS. It's described that a SFCAs quantitative profile, involving isobutyric, butyric, hexanoic, valeric, and acetic acids, allows identification of the risk of SIDS [90].

## 5. Proteomics

Proteomic analysis has also been conducted with the aim to identify different expression of proteins in SIDS [61]. A recent study applied proteomic techniques to characterize changes in the proteome related to hypoxia, inflammation and apoptosis of SIDS compared to age-matched controls, analyzing heart, medulla tissues and blood samples. Results showed differentially regulated proteins, especially APOA1, GAPDH, S100B, zyxin and complement component C4A in SIDS cases as compared to the controls. All of them appeared up-regulated in SIDS except C4A, which was down-regulated. These findings suggest the role of these proteins as potentially diagnostic biomarkers for SIDS [91]. Using proteomics as a discovery tool, a study by Broadbelt et al. described a significant reduction levels of isoforms of the 14-3-3 protein family, associated with anomalies in TPH2 and serotonin levels and serotonin receptor (5-HT1A) binding in SIDS cases [92]. In fact, findings suggested that the deficit of 14-3-3, necessary for TPH2 modulation [93–95], may lead to TPH2 deficiency and consequently to medullary serotonin system impairment, resulting in SIDS [92].

## 6. Genetic Predisposition

Genetic studies have mostly focused on the ion channels of heart mutations. Polymorphism in sodium and potassium channel genes have been reported, including the sodium channel gene SCN5A, which is associated with prolonged QT intervals and may also be responsible for altered autonomic system development [96]. In fact, initial findings have showed that 2% of SIDS cases carried gain-of-function mutations in the sodium channel encoded by SCN5A gene [97]. Studies also described some inherited cardiac diseases such as Long and short QT syndrome, Brugada syndrome, catecholaminergic polymorphic ventricular Tachycardia and hypertrophic cardiomyopathy as monogenic causes in some SIDS cases [44,98–102]. It's been suggested that long QT syndrome (LQTS) could explain 10% of all current SIDS cases [98,103].

With the development of next-generation sequencing (NGS), the analysis of the whole exome is expanding the identification of mutations and also potential pathogenic sequence variations responsible for underlying vulnerability in SIDS deaths. Many researches have described pathogenic mutations in genes associated with cardiac channelopathies responsible for SIDS occurrence in up to 30% of cases as monogenic cause of death [44,101,102]. In a study of variant analysis conducted by Tester et al., only 4.3% of the European SIDS cases possessed pathogenic variations in one of the 90 genetic heart disease genes analyzed [104]. Another recent study by Köffer et al. assessed the percentage of rare and ultrarare variants (respectively minor allele frequency $\leq$0.2% and $\leq$0.005%) in genetic heart disease genes. In only 6% of these cases, gene ultrarare variants were considered potentially pathogenic. Therefore, still rare variant interpretations associated with inherited cardiac diseases need to be standardized [105]. A recent study by Liebrechts-Akkerman et al. published in 2020 conducted an analysis using a targeted massively parallel sequencing exon screening, differently from other targeted genotyping SIDS studies. This analysis allowed detecting either novel or previously known exonic DNA variants in selected arrhythmia genes. These findings provided further evidence for cardiac arrhythmias as partial genetic explanation of SIDS. Thus, the authors stress the importance of standardized DNA testing for LQTS and other cardiac arrhythmia genes as an essential element in the ordinary SIDS diagnostic protocol. Furthermore, it's proposed as an additional preventive measure to perform a standard ECG testing in newborns during the first two weeks of life [106]. Another recent study of 2020 by Simma et al. proposed performing standardized neonatal ECG screening in the first days of life with the aim of detecting neonates with a significant transient form of prolonged QT intervals and helping the diagnosis of congenital LQTS. This study suggests applying genetic testing as a second step in case of abnormal ECG results. Furthermore, in this study pathological cases were treated with a beta blocking agent for the first years of life [107].

Implementation of such a strategy would place considerable strain on the health care system. It might also result in increased financial costs and could influence parental behavior. Many questions remain opened: how many lives will ECG save? What do we know about 'normal' and 'abnormal' results that may influence what we do next? Will parents with a 'normal' result be less likely to follow safer sleep advice? Will parents with an 'abnormal' result become very anxious? In absence of clear answers, this topic needs to be carefully thought by planning much more research.

Other studies examined the potential role of noncardiac genes in the pathogenesis of SIDS. According to these studies, 61 genes were identified as potential "SIDS-susceptibility" genes, in the variant analysis typically in the promoter region. Yet, only around 55% of these genes have been involved on a monogenic basis in SIDS [108–112]. Of note, it has been described as a significant overrepresentation of functionally disruptive variants in the SCN4A gene. This gene encodes skeletal muscle voltage-gated sodium channel (Nav1.4), involved in the skeletal respiratory muscle contraction which have a key role in SIDS pathogenesis [113]. A recent study also reported SCN1A variants from exome sequencing in two infants who died of SIDS [114]. A study conducted by Gray et al. performed a SIDS-susceptibility variant analysis of these 61 previously published noncardiac SIDS-susceptibility genes. According to the findings of this research, there is very limited evidence that these specific genes are implicated in SIDS susceptibility in a monogenic basis with autosomal dominant and recessive inheritance. Therefore, it still needs to be investigated whether infant vulnerability to sudden death may be supported by a more complex polygenic inheritance model [115].

The involvement of additional genes regulating the metabolism of neurotransmitters (mainly serotonin and dopamine) has already been described in the previous chapter "The brainstem hypothesis in SIDS" [41,73,74,77].

Finally, genetic predisposition has also been related to increased vulnerability to smoke exposure. In fact, a recent study analyzed the contribution of GSTs (enzymes of glutathione-S-transferase supergene family), involved in detoxification of xenobiotics [116]. A significant correlation has been described between the GSTM1 deletion characterizing the gene polymorphism, resulting in a lack of metabolic activity, and SIDS exposed to smoking. These findings highlight the role of smoking exposure as an important SIDS risk factor connected with a biological predisposition [117].

## 7. Recommendations on Safe Infant Sleeping Environment

In November 2016, the American Academy of Pediatrics task force published updated recommendations to reduce risk of SIDS and sleep-related infant deaths. These recommendations are addressed to infants up to one year of age. The strength of the guidelines is based on case-controlled studies as randomized trials cannot be performed for SIDS [16].

The sleeping position is the "strongest modifiable risk factor for SIDS" [16,32]. Infants should sleep in the supine position until one year of age or until the infant is able to roll from back to supine position, unassisted. Of note, supine position has not been related to increased risk of choking or aspiration, even in infants with gastroesophageal reflux disease [118]. Supine position is also recommended for premature infants either in NICU and home settings [40].

A firm flat surface covered only by a thin, fitted sheet should be used. Soft items such as toys, crib bumpers, positioners and pillows should be avoided, as well as loose sheets and blankets, due to risk of suffocation or airway obstruction [16]. Car seats, infants swings or strollers should not be used for routine sleep. The infant who fell asleep in such equipment should be repositioned to on an appropriate surface as soon as possible, due to the risk of head flexion resulting in obstruction of the upper airways [119]. The sleep surface must be located in a hazard-free location, without dangling cords or electric wires [16].

Overheating of infants by overwrapping, head coverings and excessive clothing must be avoided [120]. Room sharing is encouraged at least during the first six months of age,

but bed sharing is prohibited until one year of age. In fact, sleeping in the caregiver's bed, couch or chairs put the infant at risk of overheating, sleeping on a soft surface and being rolled over by adults. Conversely, room sharing has been shown to decrease SIDS risk by 50% [27].

Breastfeeding appeared to be one of the strongest protective measures against SIDS. Breastfeeding benefit is stronger when breastfeeding is exclusive, reducing the risk of SIDS by approximately 50% if conducted over the first month of life [121]. Furthermore, it was shown that any breastfeeding, exclusive or with formula supplementation, was able significantly protect against SIDS. In addition, the protective effect increases proportionally to the duration of breastfeeding [121].

The pacifier use for naps or bedtime is also considered a protective factor against SIDS. The exact protective mechanism is still unclear; it is assumed that the use of the pacifier may increase autonomic control and cardiovascular stability which help to maintain a patency of the airways. No adverse effect was found of breastfeeding with the use of the pacifier [33,34]. However, it is recommended to introduce pacifiers to infants only after breastfeeding is well established. The pacifier should not be attached to any strings or cords as these might present a risk of strangulation [33,34,122].

The routine use of home apnea monitors is not recommended in infants, including preterm and infants at risk of SIDS. In fact, cardiorespiratory monitors have not been demonstrated to decrease incidence of SIDS [123]. Furthermore, the usage of these tools may distract from adoption of other effective measures or give false alarms that could lead to overdiagnosis with consequential unnecessary analysis and caregiver anxiety [124].

Prenatal care should be endorsed from early pregnancy. Smoking, alcohol consumption and illicit drugs should be avoided by women during pregnancy, after delivery and during breastfeeding, as these factors significantly increase the risk of SIDS occurrence [16,22,23].

Regular immunization in accordance with Centers for Disease Control and Prevention schedule should be followed as it has been demonstrated to be protective and not associated with SIDS risk [16].

Prone position or "tummy time" is recommended only if supervised, when infants are awake and alert, as its benefits motor development and helps minimize positional plagiocephaly [125]. There is no evidence that suggests that swaddling used as a strategy to promote sleep and calm the infant reduces the risk of SIDS. When swaddling practice is performed, infants should be positioned on their back. In fact, recent studies described an increased risk of SIDS in case the swaddled infants are placed in or rolls to the prone position [126].

Finally, education by health care professionals and implementation of safe sleep practices should be based on the model of SIDS risk-reduction recommendations. A recent study described a functional use of smartphone technology for prevention, by assessing infant sleep safety practices among at-risk communities. It's been observed that photographs processed by coders provide a cost and timesaving assessment that may support safe sleep interventions in clinical and community settings [127].

Ongoing research into the etiology of SIDS and other sleep-related infants' deaths is encouraged to help achieve the ultimate goal of completely eradicating SIDS deaths [16].

## 8. Conclusions

SIDS occurrence is associated with multifactorial conditions. While extrinsic factors have been largely recognized and significantly reduced through recommendations on safe sleep worldwide, understanding the underlying intrinsic vulnerability to SIDS still represents a challenge.

Biomarkers such as proteins, metabolites and neurotransmitters have been proposed for early identification of cases at risk. To eliminate SIDS cases related to cardiac channelopaties, it has been also proposed that an ECG is performed on all neonates within two

weeks of life with subsequent genetic analysis if some alterations are detected, but the implementation of such a strategy requires further research.

New "omic" technologies provide a large amount of data that can be analyzed independently and combined, allowing detection of multiple system alterations.

A complex model that combines different risk factors data from biomarkers and omic analysis may represent a tool to identify a SIDS risk profile in newborn settings. If high risk is detected, the infant may be soon referred for further investigations and follow up.

Whole exome sequencing of newborns in NICUs is another promising area to reveal susceptibility to SIDS. [128]. This new technology opens the possibility of extending the concept of precision medicine to an early stage of life.

**Author Contributions:** Conceptualization, S.P., F.N.-M. and S.E.; writing—original draft preparation, C.L., S.M., G.P., F.M., F.N.-M.; writing—review and editing, C.L., S.P., G.B., and G.T.; visualization and supervision, S.P., G.B. and S.E. All authors have read and agreed to the published version of the manuscript.

**Funding:** This research was supported by Department of Medicine and Surgery, University of Parma, Project "Realizzazione della Rete regionale sulla prevenzione e lotta alla "Sudden Infant Death Sindrome" (SIDS)".

**Institutional Review Board Statement:** Not applicable.

**Informed Consent Statement:** Not applicable.

**Data Availability Statement:** Data is contained within the article.

**Acknowledgments:** We thank Daniela They, President of Colibri Association and Allegra Bonomi, President of SEMI per SIDS Association for their support.

**Conflicts of Interest:** The authors declare no conflict of interest.

## Abbreviations

| | |
|---|---|
| LQTS | Long QT syndrome |
| SIDS | Sudden Infant Death Syndrome |
| SNpc | Substantia Nigra pars compacta |
| SP | Substance P |
| SUID | Sudden Unexpected Infant Death |
| TPH | tryptophan hydroxylase gene |

## References

1. Krous, H.F.; Beckwith, J.B.; Byard, R.W.; Rognum, T.O.; Bajanowski, T.; Corey, T.; Cutz, E.; Hanzlick, R.; Keens, T.G.; Mitchell, E.A. Sudden Infant Death Syndrome and Unclassified Sudden Infant Deaths: A Definitional and Diagnostic Approach. *Pediatrics* **2004**, *114*, 234–238. [CrossRef] [PubMed]
2. Kinney, H.C.; Richerson, G.B.; Dymecki, S.M.; Darnall, R.A.; Nattie, E.E. The Brainstem and Serotonin in the Sudden Infant Death Syndrome. *Annu. Rev. Pathol. Mech. Dis.* **2009**, *4*, 517–550. [CrossRef] [PubMed]
3. Kassa, H.; Moon, R.Y.; Colvin, J.D. Risk Factors for Sleep-Related Infant Deaths in In-Home and Out-of-Home Settings. *Pediatrics* **2016**, *138*, e20161124. [CrossRef]
4. Behnam-Terneus, M.; Clemente, M. SIDS, BRUE, and Safe Sleep Guidelines. *Pediatr. Rev.* **2019**, *40*, 443–455. [CrossRef] [PubMed]
5. Shapiro-Mendoza, C.K.; Tomashek, K.M.; Anderson, R.N.; Wingo, J. Recent National Trends in Sudden, Unexpected Infant Deaths: More Evidence Supporting a Change in Classification or Reporting. *Am. J. Epidemiol.* **2006**, *163*, 762–769. [CrossRef] [PubMed]
6. Goldstein, R.D.; Trachtenberg, F.L.; Sens, M.A.; Harty, B.J.; Kinney, H.C. Overall Postneonatal Mortality and Rates of SIDS. *Pediatrics* **2016**, *137*, e20152298. [CrossRef]
7. Hauck, F.R.; Tanabe, K.O. International Trends in Sudden Infant Death Syndrome: Stabilization of Rates Requires Further Action. *Pediatrics* **2008**, *122*, 660–666. [CrossRef]
8. Moon, R.Y.; Fu, L. Sudden Infant Death Syndrome: An Update. *Pediatr. Rev.* **2012**, *33*, 314–320. [CrossRef]
9. Taylor, B.J.; Garstang, J.; Engelberts, A.; Obonai, T.; Cote, A.; Freemantle, J.; Vennemann, M.; Healey, M.; Sidebotham, P.; A Mitchell, E.; et al. International comparison of sudden unexpected death in infancy rates using a newly proposed set of cause-of-death codes. *Arch. Dis. Child.* **2015**, *100*, 1018–1023. [CrossRef] [PubMed]

10. National Institute of Child Health and Human Development, National Institutes of Health. Safe to Sleep Campaign. Available online: https://safetosleep.nichd.nih.gov (accessed on 27 October 2020).
11. Heron, M. Deaths: Leading Causes for 2014. *Natl. Vital Stat. Rep.* **2016**, *65*, 1–96.
12. Matthews, T.J.; MacDorman, M.F. Infant mortality statistics from the 2010 period linked birth/infant death data set. *Natl. Vital Stat. Rep.* **2013**, *62*, 1–26.
13. Patel, V. Unexplained Deaths in Infancy, England and Wales: 2018. Available online: https://www.ons.gov.uk/peoplepopulationandcommunity/birthsdeathsandmarriages/deaths/bulletins/unexplaineddeathsininfancyenglandandwales/2018 (accessed on 27 October 2020).
14. Sindrome Della Morte in Culla. Epidemiologia. Available online: https://www.epicentro.iss.it/sids/epidemiologia (accessed on 27 October 2020).
15. Filiano, J.J.; Kinney, H.C. A Perspective on Neuropathologic Findings in Victims of the Sudden Infant Death Syndrome: The Triple-Risk Model. *Neonatology* **1994**, *65*, 194–197. [CrossRef] [PubMed]
16. Moon, R.Y.; Task Force on Sudden Infant Death Syndrome. SIDS and Other Sleep-Related Infant Deaths: Evidence Base for 2016 Updated Recommendations for a Safe Infant Sleeping Environment. *Pediatrics* **2016**, *138*, e20162940. [CrossRef]
17. Goldstein, R.D.; Kinney, H.C.; Willinger, M. Sudden Unexpected Death in Fetal Life Through Early Childhood. *Pediatrics* **2016**, *137*. [CrossRef]
18. Groswasser, J.; Simon, T.; Scaillet, S.; Franco, P.; Kahn, A. Reduced Arousals Following Obstructive Apneas in Infants Sleeping Prone. *Pediatr. Res.* **2001**, *49*, 402–406. [CrossRef]
19. Li, D.-K.; Petitti, D.B.; Willinger, M.; McMahon, R.M.; Odouli, R.; Vu, H.; Hoffman, H.J. Infant Sleeping Position and the Risk of Sudden Infant Death Syndrome in California, 1997-2000. *Am. J. Epidemiol.* **2003**, *157*, 446–455. [CrossRef] [PubMed]
20. Ruys, J.H.; De Jonge, G.A.; Brand, R.; Engelberts, A.C.; A Semmekrot, B. Bed-sharing in the first four months of life: A risk factor for sudden infant death. *Acta Paediatr.* **2007**, *96*, 1399–1403. [CrossRef] [PubMed]
21. Mitchell, E.; Milerad, J. Smoking and the Sudden Infant Death Syndrome. *Rev. Environ. Health* **2006**, *21*, 81–104. [CrossRef]
22. Dietz, P.M.; England, L.J.; Shapiro-Mendoza, C.K.; Tong, V.T.; Farr, S.L.; Callaghan, W.M. Infant Morbidity and Mortality Attributable to Prenatal Smoking in the U.S. *Am. J. Prev. Med.* **2010**, *39*, 45–52. [CrossRef]
23. MacDorman, M.F.; Cnattingius, S.; Hoffman, H.J.; Kramer, M.S.; Haglund, B. Sudden Infant Death Syndrome and Smoking in the United States and Sweden. *Am. J. Epidemiol.* **1997**, *146*, 249–257. [CrossRef]
24. Fifer, W.P.; Fingers, S.T.; Youngman, M.; Gomez-Gribben, E.; Myers, M.M. Effects of alcohol and smoking during pregnancy on infant autonomic control. *Dev. Psychobiol.* **2009**, *51*, 234–242. [CrossRef] [PubMed]
25. Richardson, H.L.; Walker, A.M.; Horne, R.S.C. Maternal smoking impairs arousal patterns in sleeping infants. *Sleep* **2009**, *32*, 515–521. [CrossRef]
26. Anderson, T.M.; Ferres, J.M.L.; Ren, S.Y.; Moon, R.Y.; Goldstein, R.D.; Ramirez, J.-M.; Mitchell, E.A. Maternal Smoking Before and During Pregnancy and the Risk of Sudden Unexpected Infant Death. *Pediatrics* **2019**, *143*, e20183325. [CrossRef]
27. Hauck, F.R.; Thompson, J.M.D.; O Tanabe, K.; Moon, R.Y.; Vennemann, M.M. Breastfeeding and Reduced Risk of Sudden Infant Death Syndrome: A Meta-analysis. *Pediatrics* **2011**, *128*, 103–110. [CrossRef]
28. Elliott, A.J.; Kinney, H.C.; Haynes, R.L.; Dempers, J.D.; Wright, C.; Fifer, W.P.; Angal, J.; Boyd, T.K.; Burd, L.; Burger, E.; et al. Concurrent prenatal drinking and smoking increases risk for SIDS: Safe Passage Study report. *EClinicalMedicine* **2020**, *19*, 100247. [CrossRef] [PubMed]
29. Blair, P.S.; Sidebotham, P.; Evason-Coombe, C.; Edmonds, M.; Heckstall-Smith, E.M.A.; Fleming, P. Hazardous cosleeping environments and risk factors amenable to change: Case-control study of SIDS in south west England. *BMJ* **2009**, *339*, b3666. [CrossRef]
30. Scragg, R.; Mitchell, E.A.; Taylor, B.J.; Stewart, A.W.; Ford, R.P.; Thompson, J.M.; Allen, E.M.; Becroft, D.M. Bed sharing, smoking, and alcohol in the sudden infant death syndrome. New Zealand Cot Death Study Group. *BMJ* **1993**, *307*, 1312–1318. [CrossRef]
31. Blair, P.S.; Fleming, P.J.; Smith, I.J.; Platt, M.W.; Young, J.; Nadin, P.; Berry, P.J.; Golding, J.; The CESDI SUDI Research Group. Babies sleeping with parents: Case-control study of factors influencing the risk of the sudden infant death syndrome. *BMJ* **1999**, *319*, 1457–1461. [CrossRef]
32. Carpenter, R.G.; Irgens, L.M.; Blair, P.S.; England, P.D.; Fleming, P.; Huber, J.; Jorch, G.; Schreuder, P. Sudden unexplained infant death in 20 regions in Europe: Case control study. *Lancet* **2004**, *363*, 185–191. [CrossRef]
33. Hauck, F.R.; Omojokun, O.O.; Siadaty, M.S. Do Pacifiers Reduce the Risk of Sudden Infant Death Syndrome? A Meta-analysis. *Pediatrics* **2005**, *116*, e716–e723. [CrossRef] [PubMed]
34. Moon, R.Y.; Tanabe, K.O.; Yang, D.C.; Young, H.A.; Hauck, F.R. Pacifier Use and Sids: Evidence for a Consistently Reduced Risk. *Matern. Child Health J.* **2012**, *16*, 609–614. [CrossRef] [PubMed]
35. Goldwater, P.N. Sudden Infant Death Syndrome, Infection, Prone Sleep Position, and Vagal Neuroimmunology. *Front. Pediatr.* **2017**, *5*. [CrossRef] [PubMed]
36. Moscovis, S.M.; Gordon, A.E.; Al Madani, O.M.; Gleeson, M.; Scott, R.J.; Hall, S.T.; Burns, C.; Blackwell, C. Genetic and Environmental Factors Affecting TNF-α Responses in Relation to Sudden Infant Death Syndrome. *Front. Immunol.* **2015**, *6*, 374. [CrossRef]
37. Goldwater, P.N.; Kelmanson, I.A.; Little, B.B. Increased thymus weight in sudden infant death syndrome compared to controls: The role of sub-clinical infections. *Am. J. Hum. Biol.* **2020**, e23528. [CrossRef]

38. Maged, M.; Rizzolo, D. Preventing sudden infant death syndrome and other sleep-related infant deaths. *J. Am. Acad. Physician Assist.* **2018**, *31*, 25–30. [CrossRef] [PubMed]
39. Bigger, H.R.; Silvestri, J.M.; Shott, S.; Weese-Mayer, D.E. Influence of increased survival in very low birth weight, low birth weight, and normal birth weight infants on the incidence of sudden infant death syndrome in the United States: 1985–1991. *J. Pediatr.* **1998**, *133*, 73–78. [CrossRef]
40. Ostfeld, B.M.; Schwartz-Soicher, O.; Reichman, N.E.; Teitler, J.O.; Hegyi, T. Prematurity and Sudden Unexpected Infant Deaths in the United States. *Pediatrics* **2017**, *140*, e20163334. [CrossRef]
41. Weese-Mayer, D.E.; Berry-Kravis, E.M.; Zhou, L.; Maher, B.S.; Curran, M.E.; Silvestri, J.M.; Marazita, M.L. Sudden Infant Death Syndrome: Case-Control Frequency Differences at Genes Pertinent to Early Autonomic Nervous System Embryologic Development. *Pediatr. Res.* **2004**, *56*, 391–395. [CrossRef]
42. Jacobs, B.L.; Azmitia, E.C. Structure and function of the brain serotonin system. *Physiol. Rev.* **1992**, *72*, 165–229. [CrossRef] [PubMed]
43. Weese-Mayer, D.E.; Ackerman, M.J.; Marazita, M.L.; Berry-Kravis, E.M. Sudden Infant Death Syndrome: Review of implicated genetic factors. *Am. J. Med. Genet. Part A* **2007**, *143A*, 771–788. [CrossRef] [PubMed]
44. Van Norstrand, D.W.; Ackerman, M.J. Genomic risk factors in sudden infant death syndrome. *Genome Med.* **2010**, *2*, 86. [CrossRef] [PubMed]
45. Sridhar, R.; Thach, B.T.; Kelly, D.H.; Henslee, J.A. Characterization of successful and failed autoresuscitation in human infants, including those dying of SIDS. *Pediatr. Pulmonol.* **2003**, *36*, 113–122. [CrossRef] [PubMed]
46. Yiallourou, S.R.; Walker, A.M.; Horne, R.S.C. Effects of sleeping position on development of infant cardiovascular control. *Arch. Dis. Child.* **2008**, *93*, 868–872. [CrossRef] [PubMed]
47. Wong, F.Y.; Witcombe, N.B.; Yiallourou, S.R.; Yorkston, S.; Dymowski, A.R.; Krishnan, L.; Walker, A.M.; Horne, R.S.C. Cerebral oxygenation is depressed during sleep in healthy term infants when they sleep prone. *Pediatrics* **2011**, *127*, e558–e565. [CrossRef]
48. Horne, R.S.; Ferens, D.; Watts, A.-M.; Vitkovic, J.; Lacey, B.; Andrew, S.; Cranage, S.M.; Chau, B.; Adamson, T. The prone sleeping position impairs arousability in term infants. *J. Pediatr.* **2001**, *138*, 811–816. [CrossRef]
49. Yiallourou, S.R.; Walker, A.M.; Horne, R.S.C. Prone sleeping impairs circulatory control during sleep in healthy term infants: Implications for SIDS. *Sleep* **2008**, *31*, 1139–1146.
50. Fyfe, K.L.; Yiallourou, S.R.; Wong, F.Y.; Odoi, A.; Walker, A.M.; Horne, R.S.C. Cerebral oxygenation in preterm infants. *Pediatrics* **2014**, *134*, 435–445. [CrossRef]
51. Witcombe, N.B.; Yiallourou, S.R.; Walker, A.M.; Horne, R.S.C. Blood pressure and heart rate patterns during sleep are altered in preterm-born infants: Implications for sudden infant death syndrome. *Pediatrics* **2008**, *122*, e1242–e1248. [CrossRef] [PubMed]
52. Brown, R.E.; Basheer, R.; McKenna, J.T.; Strecker, R.E.; McCarley, R.W. Control of Sleep and Wakefulness. *Physiol. Rev.* **2012**, *92*, 1087–1187. [CrossRef]
53. Franco, P.; Szliwowski, H.; Dramaix, M.; Kahn, A. Decreased autonomic responses to obstructive sleep events in future victims of sudden infant death syndrome. *Pediatr. Res.* **1999**, *46*, 33–39. [CrossRef]
54. Schechtman, V.L.; Lee, M.Y.; Wilson, A.J.; Harper, R.M. Dynamics of Respiratory Patterning in Normal Infants and Infants Who Subsequently Died of the Sudden Infant Death Syndrome. *Pediatr. Res.* **1996**, *40*, 571–577. [CrossRef]
55. Naeye, R.L. Brain-stem and adrenal abnormalities in the sudden-infant-death syndrome. *Am. J. Clin. Pathol.* **1976**, *66*, 526–530. [CrossRef] [PubMed]
56. Kinney, H.C.; McHugh, T.; Miller, K.; Belliveau, R.A.; Assmann, S.F. Subtle Developmental Abnormalities in the Inferior Olive: An Indicator of Prenatal Brainstem Injury in the Sudden Infant Death Syndrome. *J. Neuropathol. Exp. Neurol.* **2002**, *61*, 427–441. [CrossRef] [PubMed]
57. Kinney, H.C.; Burger, P.C.; E Harrell, F.; Hudson, R.P. "Reactive gliosis" in the medulla oblongata of victims of the sudden infant death syndrome. *Pediatrics* **1983**, *72*, 181–187.
58. Takashima, S.; Armstrong, D.; Becker, L.; Bryan, C. Cerebral hypoperfusion in the sudden infant death syndrome? brainstem gliosis and vasculature. *Ann. Neurol.* **1978**, *4*, 257–262. [CrossRef] [PubMed]
59. Becker, L.; Takashima, S. Chronic Hypoventilation and Development of Brain Stem Gliosis. *Neuropediatrics* **1985**, *16*, 19–23. [CrossRef]
60. Takashima, S.; Becker, L. Delayed Dendritic Development of Catecholaminergic Neurons in the Ventrolateral Medulla of Children Who Died of Sudden Infant Death Syndrome. *Neuropediatrics* **1991**, *22*, 97–99. [CrossRef]
61. Hunt, N.J.; Phillips, L.; Waters, K.A.; Machaalani, R. Proteomic MALDI-TOF/TOF-IMS examination of peptide expression in the formalin fixed brainstem and changes in sudden infant death syndrome infants. *J. Proteom.* **2016**, *138*, 48–60. [CrossRef]
62. Bright, F.M.; Vink, R.; Byard, R.W. Neuropathological Developments in Sudden Infant Death Syndrome. *Pediatr. Dev. Pathol.* **2018**, *21*, 515–521. [CrossRef] [PubMed]
63. Bright, F.M.; Vink, R.; Byard, R.W.; Duncan, J.R.; Krous, H.F.; Paterson, D.S. Abnormalities in substance P neurokinin-1 receptor binding in key brainstem nuclei in sudden infant death syndrome related to prematurity and sex. *PLoS ONE* **2017**, *12*, e0184958. [CrossRef]
64. Broadbelt, K.G.; Paterson, D.S.; Belliveau, R.A.; Trachtenberg, F.L.; Haas, E.A.; Stanley, C.; Krous, H.F.; Kinney, H.C. Decreased $GABA_A$ receptor binding in the medullary serotonergic system in the sudden infant death syndrome. *J. Neuropathol. Exp. Neurol.* **2011**, *70*, 799–810. [CrossRef]

65. Kinney, H.C.; Haynes, R.L. The Serotonin Brainstem Hypothesis for the Sudden Infant Death Syndrome. *J. Neuropathol. Exp. Neurol.* **2019**, *78*, 765–779. [CrossRef]
66. Duncan, J.R.; Paterson, D.S.; Hoffman, J.M.; Mokler, D.J.; Borenstein, N.S.; Belliveau, R.A.; Krous, H.F.; Haas, E.A.; Stanley, C.; Nattie, E.E.; et al. Brainstem serotonergic deficiency in sudden infant death syndrome. *JAMA* **2010**, *303*, 430–437. [CrossRef]
67. Panigrahy, A.; Filiano, J.; Sleeper, L.A.; Mandell, F.; Valdes-Dapena, M.; Krous, H.F.; Rava, L.A.; Foley, E.; White, W.F.; Kinney, H.C. Decreased Serotonergic Receptor Binding in Rhombic Lip-Derived Regions of the Medulla Oblongata in the Sudden Infant Death Syndrome. *J. Neuropathol. Exp. Neurol.* **2000**, *59*, 377–384. [CrossRef]
68. Dosumu-Johnson, R.T.; E Cocoran, A.; Chang, Y.; Nattie, E.; Dymecki, S.M. Acute perturbation of Pet1-neuron activity in neonatal mice impairs cardiorespiratory homeostatic recovery. *eLife* **2018**, *7*, 7. [CrossRef]
69. Haynes, R.L.; Frelinger, A.L., 3rd; Giles, E.K.; Goldstein, R.D.; Tran, H.; Kozakewich, H.P.; Haas, E.A.; Gerrits, A.J.; Mena, O.J.; Trachtenberg, F.L.; et al. High serum serotonin in sudden infant death syndrome. *Proc. Natl. Acad. Sci. USA* **2017**, *114*, 7695–7700. [CrossRef]
70. Klonoff-Cohen, H.S.; Srinivasan, I.P.; Edelstein, S.L. Prenatal and intrapartum events and sudden infant death syndrome. *Paediatr. Perinat. Epidemiol.* **2002**, *16*, 82–89. [CrossRef] [PubMed]
71. Getahun, D.; Amre, D.; Rhoads, G.G.; Demissie, K. Maternal and Obstetric Risk Factors for Sudden Infant Death Syndrome in the United States. *Obstet. Gynecol.* **2004**, *103*, 646–652. [CrossRef]
72. Li, D.-K.; Wi, S. Maternal placental abnormality and the risk of sudden infant death syndrome. *Am. J. Epidemiol.* **1999**, *149*, 608–611. [CrossRef] [PubMed]
73. Nonnis Marzano, F.; Maldini, M.; Filonzi, L.; Lavezzi, A.M.; Parmigiani, S.; Magnani, C.; Bevilacqua, G.; Matturri, L. Genes regulating the serotonin metabolic pathway in the brain stem and their role in the etiopathogenesis of the sudden infant death syndrome. *Genomics* **2008**, *91*, 485–491. [CrossRef] [PubMed]
74. Weese-Mayer, D.E.; Zhou, L.; Berry-Kravis, E.M.; Maher, B.S.; Silvestri, J.M.; Marazita, M.L. Association of the serotonin transporter gene with sudden infant death syndrome: A haplotype analysis. *Am. J. Med. Genet. A* **2003**, *122A*, 238–245. [CrossRef] [PubMed]
75. Filonzi, L.; Magnani, C.; Nosetti, L.; Nespoli, L.; Borghi, C.; Vaghi, M.; Marzano, F.N.; Dell, M.; Lewin, L.; Gigante, J. Serotonin Transporter Role in Identifying Similarities between SIDS and Idiopathic ALTE. *Pediatrics* **2012**, *130*, 130–138. [CrossRef] [PubMed]
76. Haas, C.; Braun, J.; Bär, W.; Bartsch, C. No association of serotonin transporter gene variation with sudden infant death syndrome (SIDS) in Caucasians. *Leg. Med.* **2009**, *11* (Suppl. 1), S210–S212. [CrossRef]
77. Paterson, D.S.; Rivera, K.D.; Broadbelt, K.G.; Trachtenberg, F.L.; Belliveau, R.A.; Holm, I.A.; Haas, E.A.; Stanley, C.; Krous, H.F.; Kinney, H.C.; et al. Lack of Association of the Serotonin Transporter Polymorphism with the Sudden Infant Death Syndrome in the San Diego Dataset. *Pediatr. Res.* **2010**, *68*, 409–413. [CrossRef]
78. Paterson, D.S. Serotonin gene variants are unlikely to play a significant role in the pathogenesis of the sudden infant death syndrome. *Respir. Physiol. Neurobiol.* **2013**, *189*, 301–314. [CrossRef] [PubMed]
79. Centers for Disease Control. Linked Birth/Infant Death Records on CDC WONDER Online Database. Available online: https://wonder.cdc.gov/lbd.html (accessed on 27 October 2020).
80. Child and Youth Mortality Review Committee. *Fifth Report to the Minister of Health: Reporting Mortality 2002–2008*; Child and Youth Mortality Review Committee: Wellington, New Zealand, 2009.
81. Kroll, M.E.; Quigley, M.A.; Kurinczuk, J.J.; Dattani, N.; Li, Y.; Hollowell, J. Ethnic variation in unexplained deaths in infancy, including sudden infant death syndrome (SIDS), England and Wales 2006–2012: National birth cohort study using routine data. *J. Epidemiol. Community Health* **2018**, *72*, 911–918. [CrossRef]
82. Cox, A.J.; Moscovis, S.M.; Blackwell, C.C.; Scott, R.J. Cytokine gene polymorphism among Indigenous Australians. *Innate Immun.* **2014**, *20*, 431–439. [CrossRef]
83. Lavezzi, A.M.; Mehboob, R.; Alfonsi, G.; Ferrero, S. Substantia Nigra Abnormalities Provide New Insight on the Neural Mechanisms Underlying the Sleep-Arousal Phase Dysfunctions in Sudden Infant Death Syndrome. *ASN Neuro* **2020**, *12*. [CrossRef]
84. Lima, M.M.S.; Andersen, M.L.; Reksidler, A.B.; Vital, M.A.B.F.; Tufik, S. The Role of the Substantia Nigra Pars Compacta in Regulating Sleep Patterns in Rats. *PLoS ONE* **2007**, *2*, e513. [CrossRef]
85. Keppen, L.D.; Randall, B. Inborn defects of fatty acid oxidation: A preventable cause of SIDS. *South Dak. J. Med.* **1999**, *52*, 187–189.
86. Harpey, J.P.; Charpentier, C.; Paturneau-Jouas, M. Sudden infant death syndrome and inherited disorders of fatty acid beta-oxidation. *Biol. Neonate* **1990**, *58* (Suppl. 1), 70–80. [CrossRef] [PubMed]
87. Villoria, J.G.; Pajares, S.; López, R.M.; Marin, J.L.; Ribes, A. Neonatal Screening for Inherited Metabolic Diseases in 2016. *Semin. Pediatr. Neurol.* **2016**, *23*, 257–272. [CrossRef] [PubMed]
88. Wishart, D.S.; Knox, C.; Guo, A.C.; Eisner, R.; Young, N.; Gautam, B.; Hau, D.D.; Psychogios, N.; Dong, E.; Bouatra, S.; et al. HMDB: A knowledgebase for the human metabolome. *Nucleic Acids Res.* **2009**, *37*, D603–D610. [CrossRef]
89. Graham, S.F.; Turkoglu, O.; Kumar, P.; Yilmaz, A.; Bjorndahl, T.C.; Han, B.; Mandal, R.; Wishart, D.S.; Bahado-Singh, R.O. Targeted Metabolic Profiling of Post-Mortem Brain from Infants Who Died from Sudden Infant Death Syndrome. *J. Proteome Res.* **2017**, *16*, 2587–2596. [CrossRef] [PubMed]

90. Galván-Tejada, C.E.; Villagrana-Bañuelos, K.E.; Zanella-Calzada, L.A.; Moreno-Báez, A.; Luna-García, H.; Celaya-Padilla, J.M.; Galván-Tejada, J.I.; Gamboa-Rosales, H. Univariate Analysis of Short-Chain Fatty Acids Related to Sudden Infant Death Syndrome. *Diagnostics* **2020**, *10*, 896. [CrossRef]
91. El-Kashef, N.; Gomes, I.; Mercer-Chalmers-Bender, K.; Schneider, P.M.; Rothschild, M.A.; Juebner, M. Comparative proteome analysis for identification of differentially abundant proteins in SIDS. *Int. J. Leg. Med.* **2017**, *131*, 1597–1613. [CrossRef]
92. Broadbelt, K.G.; Rivera, K.D.; Paterson, D.S.; Duncan, J.R.; Trachtenberg, F.L.; Paulo, J.A.; Stapels, M.D.; Borenstein, N.S.; Belliveau, R.A.; Haas, E.A.; et al. Brainstem Deficiency of the 14-3-3 Regulator of Serotonin Synthesis: A Proteomics Analysis in the Sudden Infant Death Syndrome. *Mol. Cell. Proteom.* **2012**, *11*. [CrossRef]
93. Furukawa, Y.; Ikuta, N.; Omata, S.; Yamauchi, T.; Isobe, T.; Ichimura, T. Demonstration of the Phosphorylation-Dependent Interaction of Tryptophan Hydroxylase with the 14-3-3 Protein. *Biochem. Biophys. Res. Commun.* **1993**, *194*, 144–149. [CrossRef]
94. Banik, U.; Wang, G.-A.; Wagner, P.D.; Kaufman, S. Interaction of Phosphorylated Tryptophan Hydroxylase with 14-3-3 Proteins. *J. Biol. Chem.* **1997**, *272*, 26219–26225. [CrossRef]
95. Winge, I.; McKinney, J.A.; Ying, M.; D'Santos, C.S.; Kleppe, R.; Knappskog, P.M.; Haavik, J. Activation and stabilization of human tryptophan hydroxylase 2 by phosphorylation and 14-3-3 binding. *Biochem. J.* **2008**, *410*, 195–204. [CrossRef] [PubMed]
96. Plant, L.D.; Bowers, P.N.; Liu, Q.; Morgan, T.; Zhang, T.; State, M.W.; Chen, W.; Kittles, R.A.; Goldstein, S.A. A common cardiac sodium channel variant associated with sudden infant death in African Americans, SCN5A S1103Y. *J. Clin. Investig.* **2006**, *116*, 430–435. [CrossRef] [PubMed]
97. Ackerman, M.J.; Siu, B.L.; Sturner, W.Q.; Tester, D.J.; Valdivia, C.R.; Makielski, J.C.; Towbin, J.A. Postmortem Molecular Analysis of SCN5A Defects in Sudden Infant Death Syndrome. *JAMA* **2001**, *286*, 2264–2269. [CrossRef] [PubMed]
98. Schwartz, P.J.; Stramba-Badiale, M.; Segantini, A.; Austoni, P.; Bosi, G.; Giorgetti, R.; Grancini, F.; Marni, E.D.; Perticone, F.; Rosti, D.; et al. Prolongation of the QT Interval and the Sudden Infant Death Syndrome. *N. Engl. J. Med.* **1998**, *338*, 1709–1714. [CrossRef]
99. Cronk, L.B.; Ye, B.; Kaku, T.; Tester, D.J.; Vatta, M.; Makielski, J.C.; Ackerman, M.J. Novel mechanism for sudden infant death syndrome: Persistent late sodium current secondary to mutations in caveolin-3. *Hear. Rhythm.* **2007**, *4*, 161–166. [CrossRef]
100. Brion, M.; Allegue, C.; Santori, M.; Gil, R.; Blanco-Verea, A.; Haas, C.; Bartsch, C.; Poster, S.; Madea, B.; Campuzano, O.; et al. Sarcomeric gene mutations in sudden infant death syndrome (SIDS). *Forensic Sci. Int.* **2012**, *219*, 278–281. [CrossRef]
101. Tester, D.J.; Ackerman, M.J. Sudden infant death syndrome: How significant are the cardiac channelopathies? *Cardiovasc. Res.* **2005**, *67*, 388–396. [CrossRef] [PubMed]
102. Tester, D.J.; Dura, M.; Carturan, E.; Reiken, S.; Wronska, A.; Marks, A.R.; Ackerman, M.J. A mechanism for sudden infant death syndrome (SIDS): Stress-induced leak via ryanodine receptors. *Hear. Rhythm.* **2007**, *4*, 733–739. [CrossRef]
103. Arnestad, M.; Crotti, L.; Rognum, T.O.; Insolia, R.; Pedrazzini, M.; Ferrandi, C.; Vege, A.; Wang, D.W.; Rhodes, T.E.; George, A.L.; et al. Prevalence of Long-QT Syndrome Gene Variants in Sudden Infant Death Syndrome. *Circulation* **2007**, *115*, 361–367. [CrossRef]
104. Tester, D.J.; Wong, L.C.; Chanana, P.; Jaye, A.; Evans, J.M.; Fitzpatrick, D.R.; Evans, M.J.; Fleming, P.; Jeffrey, I.; Cohen, M.C.; et al. Cardiac Genetic Predisposition in Sudden Infant Death Syndrome. *J. Am. Coll. Cardiol.* **2018**, *71*, 1217–1227. [CrossRef] [PubMed]
105. Köffer, J.; Scheiper-Welling, S.; Verhoff, M.A.; Bajanowski, T.; Kauferstein, S. Post-mortem genetic investigation of cardiac disease–associated genes in sudden infant death syndrome (SIDS) cases. *Int. J. Leg. Med.* **2021**, *135*, 207–212. [CrossRef]
106. Liebrechts-Akkerman, G.; Liu, F.; Van Marion, R.; Dinjens, W.N.; Kayser, M. Explaining sudden infant death with cardiac arrhythmias: Complete exon sequencing of nine cardiac arrhythmia genes in Dutch SIDS cases highlights new and known DNA variants. *Forensic Sci. Int. Genet.* **2020**, *46*, 102266. [CrossRef] [PubMed]
107. Simma, A.; Potapow, A.; Brandstetter, S.; Michel, H.; Melter, M.; Seelbach-Göbel, B.; Apfelbacher, C.; Kabesch, M.; Gerling, S.; The KUNO Kids Study Group. Electrocardiographic Screening in the First Days of Life for Diagnosing Long QT Syndrome: Findings from a Birth Cohort Study in Germany. *Neonatology* **2020**, *117*, 756–763. [CrossRef] [PubMed]
108. Yamamoto, T.; Tanaka, H.; Emoto, Y.; Umehara, T.; Fukahori, Y.; Kuriu, Y.; Matoba, R.; Ikematsu, K. Carnitine palmitoyltransferase 2 gene polymorphism is a genetic risk factor for sudden unexpected death in infancy. *Brain Dev.* **2014**, *36*, 479–483. [CrossRef] [PubMed]
109. Lahrouchi, N.; Lodder, E.M.; Mansouri, M.; Tadros, R.; Zniber, L.; Adadi, N.; Clur, S.-A.B.; Van Spaendonck-Zwarts, K.Y.; Postma, A.V.; Sefiani, A.; et al. Exome sequencing identifies primary carnitine deficiency in a family with cardiomyopathy and sudden death. *Eur. J. Hum. Genet.* **2017**, *25*, 783–787. [CrossRef]
110. Läer, K.; Dörk, T.; Vennemann, M.; Rothämel, T.; Klintschar, M. Polymorphisms in genes of respiratory control and sudden infant death syndrome. *Int. J. Leg. Med.* **2015**, *129*, 977–984. [CrossRef]
111. Fard, D.; Läer, K.; Rothämel, T.; Schürmann, P.; Arnold, M.; Cohen, M.; Vennemann, M.; Pfeiffer, H.; Bajanowski, T.; Pfeufer, A.; et al. Candidate gene variants of the immune system and sudden infant death syndrome. *Int. J. Leg. Med.* **2016**, *130*, 1025–1033. [CrossRef]
112. Cutz, E. Whole Exome Sequencing Reveals CLCNKB Mutations in a Case of Sudden Unexpected Infant Death. *Pediatr. Dev. Pathol.* **2015**, *18*, 339–340. [CrossRef]
113. Männikkö, R.; Wong, L.; Tester, D.J.; Thor, M.G.; Sud, R.; Kullmann, D.M.; Sweeney, M.G.; Leu, C.; Sisodiya, S.M.; Fitzpatrick, D.R.; et al. Dysfunction of NaV1.4, a skeletal muscle voltage-gated sodium channel, in sudden infant death syndrome: A case-control study. *Lancet* **2018**, *391*, 1483–1492. [CrossRef]

114. Brownstein, C.A.; Goldstein, R.D.; Thompson, C.H.; Haynes, R.L.; Giles, E.; Sheidley, B.; Bainbridge, M.; Haas, E.A.; Mena, O.J.; Lucas, J.; et al. SCN1A variants associated with sudden infant death syndrome. *Epilepsia* **2018**, *59*, e56–e62. [CrossRef] [PubMed]
115. Gray, B.; Tester, D.J.; Wong, L.C.; Chanana, P.; Jaye, A.; Evans, J.M.; Baruteau, A.-E.; Evans, M.; Fleming, P.; Jeffrey, I.; et al. Noncardiac genetic predisposition in sudden infant death syndrome. *Genet. Med.* **2018**, *21*, 641–649. [CrossRef] [PubMed]
116. Filonzi, L.; Nosetti, L.; Magnani, C.; Vaghi, M.; Fenjiep, A.F.N.; Marzano, F.N. ALTE and smoking exposure: Which role of detoxification genes polymorphisms? *Clin. Genet.* **2016**, *90*, 383–384. [CrossRef]
117. Filonzi, L.; Magnani, C.; Lavezzi, A.M.; Vaghi, M.; Nosetti, L.; Marzano, F.N. Detoxification genes polymorphisms in SIDS exposed to tobacco smoke. *Gene* **2018**, *648*, 1–4. [CrossRef]
118. Tablizo, M.A.; Jacinto, P.; Parsley, D.; Chen, M.L.; Ramanathan, R.; Keens, T.G. Supine Sleeping Position Does Not Cause Clinical Aspiration in Neonates in Hospital Newborn Nurseries. *Arch. Pediatr. Adolesc. Med.* **2007**, *161*, 507–510. [CrossRef] [PubMed]
119. Batra, E.K.; Midgett, J.D.; Moon, R.Y. Hazards Associated with Sitting and Carrying Devices for Children Two Years and Younger. *J. Pediatr.* **2015**, *167*, 183–187. [CrossRef] [PubMed]
120. Ponsonby, A.-L.; Dwyer, T.; Gibbons, L.E.; Cochrane, J.A.; Wang, Y.-G. Factors Potentiating the Risk of Sudden Infant Death Syndrome Associated with the Prone Position. *N. Engl. J. Med.* **1993**, *329*, 377–382. [CrossRef]
121. Thompson, J.M.; Tanabe, K.; Moon, R.Y.; Mitchell, E.A.; McGarvey, C.; Tappin, D.; Blair, P.S.; Hauck, F.R. Duration of Breastfeeding and Risk of SIDS: An Individual Participant Data Meta-analysis. *Pediatrics* **2017**, *140*, e20171324. [CrossRef] [PubMed]
122. Schnitzer, P.G.; Covington, T.M.; Dykstra, H.K. Sudden Unexpected Infant Deaths: Sleep Environment and Circumstances. *Am. J. Public Health* **2012**, *102*, 1204–1212. [CrossRef] [PubMed]
123. Ramanathan, R.; Corwin, M.J.; Hunt, C.E.; Lister, G.; Tinsley, L.R.; Baird, T.; Silvestri, J.M.; Crowell, D.H.; Hufford, D.; Martin, R.J.; et al. Cardiorespiratory Events Recorded on Home Monitors: Comparison of Healthy Infants with Those at Increased Risk for SIDS. *JAMA* **2001**, *285*, 2199–2207. [CrossRef] [PubMed]
124. Committee on Fetus and Newborn; American Academy of Pediatrics. Apnea, sudden infant death syndrome, and home monitoring. *Pediatrics* **2003**, *111*, 914–917. [CrossRef]
125. Laughlin, J.; Luerssen, T.G.; Dias, M.S. Prevention and Management of Positional Skull Deformities in Infants. *Pediatrics* **2011**, *128*, 1236–1241. [CrossRef]
126. Pease, A.S.; Fleming, P.J.; Hauck, F.R.; Moon, R.Y.; Horne, R.S.; L'Hoir, M.P.; Ponsonby, A.-L.; Blair, P.S. Swaddling and the Risk of Sudden Infant Death Syndrome: A Meta-analysis. *Pediatrics* **2016**, *137*, e20153275. [CrossRef] [PubMed]
127. Nabaweesi, R.; Whiteside-Mansell, L.; Mullins, S.H.; Rettiganti, M.R.; Aitken, M.E. Field assessment of a safe sleep instrument using smartphone technology. *J. Clin. Transl. Sci.* **2019**, *4*, 451–456. [CrossRef] [PubMed]
128. Petrikin, J.E.; Willig, L.K.; Smith, L.D.; Kingsmore, S.F. Rapid whole genome sequencing and precision neonatology. *Semin. Perinatol.* **2015**, *39*, 623–631. [CrossRef] [PubMed]

life

MDPI

*Review*

# Zinc Metalloproteins in Epigenetics and Their Crosstalk

**Abdurrahman Pharmacy Yusuf [1], Murtala Bello Abubakar [1,2,*], Ibrahim Malami [1,3], Kasimu Ghandi Ibrahim [1,2], Bilyaminu Abubakar [1,4], Muhammad Bashir Bello [1,5], Naeem Qusty [6], Sara T. Elazab [7], Mustapha Umar Imam [1,8], Athanasios Alexiou [9,10,*] and Gaber El-Saber Batiha [11,*]**

1 Centre for Advanced Medical Research and Training, Usmanu Danfodiyo University, P.M.B. 2346 Sokoto, Nigeria; yusuf.abdurrahman@udusok.edu.ng (A.P.Y.); almalki.a@tu.edu.sa (I.M.); ghandi.kasimu@udusok.edu.ng (K.G.I.); abubakar.bilyaminu@udusok.edu (B.A.); muhammad.bello@udusok.edu.ng (M.B.B.); mustapha.imam@udusok.edu.ng (M.U.I.)
2 Department of Physiology, Faculty of Basic Medical Sciences, College of Health Sciences, Usmanu Danfodiyo University, P.M.B. 2254 Sokoto, Nigeria
3 Department of Pharmacognosy and Ethnopharmacy, Faculty of Pharmaceutical Sciences, Usmanu Danfodiyo University, P.M.B. 2346 Sokoto, Nigeria
4 Department of Pharmacology and Toxicology, Faculty of Pharmaceutical Sciences, Usmanu Danfodiyo University, P.M.B. 2346 Sokoto, Nigeria
5 Department of Veterinary Microbiology, Faculty of Veterinary Medicine, Usmanu Danfodiyo University, P.M.B. 2346 Sokoto, Nigeria
6 Medical Laboratories Department, Faculty of Applied Medical Sciences, Umm Al-Qura University, Mecca 21955, Saudi Arabia; nfqusty@uqu.edu.sa
7 Department of Pharmacology, Faculty of Veterinary Medicine, Mansoura University, Mansoura, Dakahlia 35516, Egypt; sarataha1@mans.edu.eg
8 Department of Medical Biochemistry, Faculty of Basic Medical Sciences, College of Health Sciences, Usmanu Danfodiyo University, P.M.B. 2254 Sokoto, Nigeria
9 Novel Global Community Educational Foundation, Hebersham, NSW 2770, Australia
10 AFNP Med, Haidingergasse 29, 1030 Vienna, Austria
11 Department of Pharmacology and Therapeutics, Faculty of Veterinary Medicine, Damanhour University, Damanhour, AlBeheira 22511, Egypt
* Correspondence: murtala.bello@udusok.edu.ng (M.B.A.); alexiou@ngcef.net (A.A.); dr_gaber_batiha@vetmed.dmu.edu.eg (G.E.-S.B.)

**Citation:** Yusuf, A.P.; Abubakar, M.B.; Malami, I.; Ibrahim, K.G.; Abubakar, B.; Bello, M.B.; Qusty, N.; Elazab, S.T.; Imam, M.U.; Alexiou, A.; et al. Zinc Metalloproteins in Epigenetics and Their Crosstalk. *Life* **2021**, *11*, 186. https://doi.org/10.3390/life11030186

Academic Editor: Jong Yoon

Received: 5 February 2021
Accepted: 23 February 2021
Published: 26 February 2021



**Abstract:** More than half a century ago, zinc was established as an essential micronutrient for normal human physiology. In silico data suggest that about 10% of the human proteome potentially binds zinc. Many proteins with zinc-binding domains (ZBDs) are involved in epigenetic modifications such as DNA methylation and histone modifications, which regulate transcription in physiological and pathological conditions. Zinc metalloproteins in epigenetics are mainly zinc metalloenzymes and zinc finger proteins (ZFPs), which are classified into writers, erasers, readers, editors, and feeders. Altogether, these classes of proteins engage in crosstalk that fundamentally maintains the epigenome's modus operandi. Changes in the expression or function of these proteins induced by zinc deficiency or loss of function mutations in their ZBDs may lead to aberrant epigenetic reprogramming, which may worsen the risk of non-communicable chronic diseases. This review attempts to address zinc's role and its proteins in natural epigenetic programming and artificial reprogramming and briefly discusses how the ZBDs in these proteins interact with the chromatin.

**Keywords:** epigenetics; epigenome; zinc finger domain; zinc finger motif; zinc finger proteins; zinc metalloproteins

## 1. Introduction

Zinc is an omnipresent micronutrient essential for healthy prenatal and postnatal developments in humans and the growth and development of plants, animals, and microorganisms [1,2]. In silico data suggest that about 10% of the human proteome potentially binds zinc [3]. Zinc is present in all body tissues and fluids as a component of over

2000 proteins (including epigenetically active enzymes) [4–7]. A group of writers, erasers, and readers of epigenetic marks are zinc-dependent [8]. Some of these are enzymes such as histone deacetylases (HDACs) having the zinc itself incorporated in their active sites; thus, it directly partakes in the catalytic process [9]. Others are proteins containing zinc within a zinc-binding domain (ZBD). These domains are important in substrate recognition, self-regulation, integrity, crosstalk, and sometimes catalysis [10,11]. With intracellular zinc within the normal range, these proteins work together in a coordinated manner to shape the plastic epigenome. In contrast, fluctuations in zinc levels or its deficiency and loss of function mutations in the ZBDs of these proteins affect their expression and function and may lead to epigenetic perturbations. [12,13]. These aberrant epigenetic changes may increase the risk of non-communicable chronic diseases such as cancer, diabetes, and cardiovascular diseases with possible multigenerational or transgenerational consequences. Intracellular zinc homeostasis is under the tight regulation of two families of zinc transporters and the zinc-binding proteins metallothionines (MTs) [14,15]. In addition to their zinc homeostasis roles, zinc transporters are also emerging as important modulators of the epigenome [4].

The significance of zinc, its deficiency, its transporters, and some of its enzymes in epigenetics has been partly reviewed [4,8,16]. However, these reviews are not all-inclusive and did not cover other ZBD-containing proteins involved in epigenome programming and editing. Here, we attempt to provide a comprehensive overview of zinc metalloproteins' roles in natural and synthetic epigenetics. We also try to explore how the ZBDs in these proteins interact with the chromatin. Of note, in the context of this article, the term "zinc metalloproteins" encompasses zinc finger proteins (ZFPs), zinc metalloenzymes, and enzymes requiring zinc activation for catalysis.

## 2. Molecular Bases of Epigenetic Modifications

Since the late 1980s, epigenetics has been one of the critical areas of research in molecular biology. From the late twentieth century to date, the meaning of the term "Epigenetics" has been evolving, and its exact definition remains elusive [17]. However, this review focuses on the most common definition (the molecular mechanism of transcription regulation) derived from the root words "epi+genetics", which means in addition to or "on the top" of genetics. Based on this concept, it has been defined as the mitotically and meiotically heritable layer of chemical code beyond the deoxyribonucleic acid (DNA) sequence, which regulates the genome, leading to various transcriptional outcomes in different cell types [17–19]. The four basic mechanisms involved in epigenetic regulations include DNA methylation, histone post-translational modifications, remodeling of the chromatin architecture, and gene silencing associated with noncoding RNAs such as microRNA [20–22]. Discussing the detailed molecular mechanisms of these epigenetic events is indeed beyond the scope of this review. Therefore, here, we focus only on zinc's role and that of its proteins in DNA methylation, histone modifications, chromatin remodeling, epigenome editing, and their crosstalk.

### *2.1. DNA Methylation*

DNA methylation is the physical addition of a methyl ($-CH_3$) group to a DNA sequence. The most common form of this modification in eukaryotes is adding a methyl group to the 5th carbon of cytosine in a DNA sequence to form 5′-methylcytosine (5′-mC) [23–25]. This modification predominantly occurs at cytosine-phospho-guanine dinucleotide-rich regions called CpG islands, which are mainly present around the promoter regions of genes and have been implicated in transcription regulation [26]. Moreover, DNA methylation occurs harmoniously and proportionately on both strands of the methylated DNA [27]. In most cases, cytosine methylation promotes gene silencing principally via the gene promoter's CpG islands' hypermethylation. Meanwhile, the promoter regions of transcriptionally active genes remain hypomethylated [26]. Thus, the methylation status of a gene could affect its expression level.

In mammals, two sets of enzymes regulate the DNA methylation status of the genome. They include the zinc-dependent DNA methyltransferases (DNMTs), which facilitate 5′C methylation and its passive demethylation, and the iron-dependent members of the ten-eleven translocases (TETs), which catalyze the active demethylation of DNA coupled to base excision repair [23,28,29]. So far, DNMT1, DNMT3a, and DNMT3b are the three known DNMTs that directly add methyl groups from S-adenosyl methionine (SAM) to the human genome [30]. DNMT1 catalyzes the maintenance or restoration of DNA methylation patterns of a hemimethylated double-stranded DNA in somatic cells following replication; therefore, it is called maintenance DNMT (Figure 1) [31]. On the other hand, DNMT3a and DNMT3b establish new methylation tasks on a newly synthesized (unmethylated) double-stranded DNA in the germline and the embryo; they are named de novo DNMTs (Figure 1) [30]. These three enzymes are not mutually exclusive catalytically, as Ren et al. (2018) [31] have reported more evidence suggesting the involvement of each enzyme in de novo and maintenance DNA methylation.

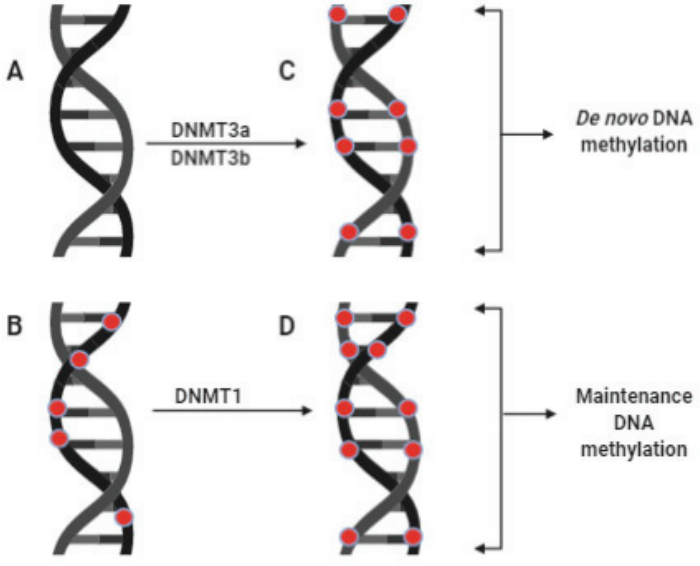


**Figure 1.** Comparison between de novo DNA methylation and maintenance DNA methylation. The figure compares de novo DNA methylation and maintenance DNA methylation. The two forms of DNA methylation catalyzed by DNMTs. (**A**) = unmethylated DNA; (**B**) = hemimethylated DNA; (**C**) and (**D**) = fully methylated DNA; DNMT3a/DNMT3b = DNA methyltransferases 3a/3b, both catalyze de novo DNA methylation (methylation of a newly formed double-stranded DNA during gametogenesis and embryogenesis). DNMT1 = DNA methyltransferase 1: It catalyzes replication-dependent maintenance of DNA methylation existing on hemimethylated DNA. Red dots stand for methyl groups. Source: Icons were obtained and customized in BioRender (biorender.com (accessed on 23 February 2021)).

### *2.2. Histone Post-Translational Modifications and Chromatin Remodeling*

Histones are highly conserved basic proteins with a net positive charge. They have variable structures and amino acid composition that form the chromatin core. In eukaryotes, the chromatin core comprises a spherical octamer of four pairs of histone variants, namely H2A, H2B, H3, and H4, on which the DNA binds. Additionally, a fifth variant (H1) connects the DNA-bound octamers at regular intervals [32]. Each of the histone variants has an extended tail of amino acids at its N-terminus, which supports epigenetic modifications such as methylation, acetylation, phosphorylation, ubiquitination, ribosylation,

citrullination, and SUMOylation [33–36]. Chromatin organization is achieved due to the tight winding of DNA around the histone octamers to form condensed structures called nucleosomes. Tightly packed nucleosomes form a higher-order structural organization called chromatin [22,37,38]. Based on the degree of packaging, chromatin can be heterochromatin or euchromatin. Heterochromatin is tightly packed and inaccessible to transcription factors, while euchromatin is loose and accessible [26].

Mechanistically, histone modifications regulate transcription in two ways: one is by facilitating the transition between heterochromatin and euchromatin (chromatin remodeling), and the other is by serving as scaffolds or binding sites for reader proteins, which in turn recruit other proteins that write or erase epigenetic marks [37,39,40]. It is conceivable that modifications that strengthen DNA–histone interactions to form tight chromatin usually lead to gene silencing, while those that disrupt this interaction promote gene expression [38]. Interestingly, histone modifications work in a coordinated manner. Different histone marks engage in unique crosstalk or interaction that maintains the chromatin's highly dynamic state. This interaction will be discussed further under this review's subsequent headings, describing zinc's role in the various forms of histone modifications.

## 3. Molecular Bases of Epigenome Regulation Associated with Zinc Metalloproteins

Some of the epigenetically active enzymes identified so far are zinc metalloenzymes. Zinc is essential for the catalysis and autoregulation of enzymes such as DNMTs, histone methyltransferases/methylases (HMTs), histone demethylases (HDMs), histone acetyltransferases/acetylases (HATs), histone deacetylases (HDACs), histone E3-ubiquitin ligases (EUBLs), and histone deubiquitinating module (DUBm) complexes [4,41]. Interestingly, zinc is not only required for the integrity, catalysis, and self-regulation of these enzymes but also in recognition of their substrates and their recruitment to binding sites by other zinc-binding proteins [31,42–44]. Furthermore, the methionine synthase and betaine–homocysteine methyltransferase essential in DNA and histone methylation are zinc-dependent [45]. Additionally, zinc finger proteins (ZFPs) are also involved in epigenetic regulations, especially in epigenome editing [46]. ZFPs are the largest group of transcription factors with diverse structures that commonly have a zinc finger domain (ZFD) housing structural arrays of amino acids coordinated by one or more zinc atoms called zinc finger motifs (ZFMs) [10,47].

### *3.1. Role of Zinc in DNA Methylation*

Each of the three DNMTs is composed of complex multi-functional domains categorized into a C-terminal catalytic domain and an N-terminal regulatory domain [31]. DNMT1 contains approximately 1620 amino acid residues [48]. About 78 of the total amino acids (about 4.83%), which comprises residues 621–698, form a ZBD called the CXXC domain (C for Cysteine and X for any amino acid) [49]. The domain is part of the N-terminal regulatory region, which interacts with the unmethylated CpG islands of a hemimethylated DNA to facilitate the self-inhibition of DNMT1 through an autoinhibitory linker. In this way, the enzyme is prevented from de novo DNA methylation [31,50,51]. Furthermore, the interaction between the ZBD and the catalytic domain of DNMT1 is essential for the enzyme's allosteric activation [4]. Thus, the ZBD forms part of the N-terminal regulatory domain that controls the enzyme's catalytic activity. Additionally, the ability of DNMT1 to recognize hemimethylated DNA is dependent on its interaction with a ZFP called the ubiquitin-like protein 1, containing plant homeodomain (PHD) and a really interesting new gene (RING) finger domains (UHRF1). This protein senses DNMT1 and reads methylation patterns on a hemimethylated DNA with the aid of its PHD and SRA (SET and RING associated) domains [43]. Thus, it recognizes the methylation marks on the DNA and directs the enzyme to those marked regions [44,52]. Similarly, the N-terminal regulatory domains of both DNMT3a and DNMT3b harbor a cysteine-rich complex multi-subunit domain called the "alpha thalassemia mental retardation x-linked DNA methyltransferase3 DNA methyltransferase3L" related domain abbreviated as *ATRX-DNMT3-DNMT3L* or simply ADD

domain. The domain encloses two ZFDs, namely a Guanine-Alanine-Thymine-Alanine-like (GATA-like) and a PHD together with a C-terminal alpha-helix [42,53]. ADD domain facilitates the autoinhibition and allosteric activation of both enzymes [31]. In addition to DNMT3a and b, DNMT3-like protein (DNMT3L) is another member of the DNMT3 family identified in humans [54]. This protein also contains the ADD domain but lacks the catalytic domain and helps in the allosteric regulation of both DNMT3a and DNMT3b [27,42]. In 2001, Bourc'his and co-researchers reported that some offspring of a homozygous knockout (DNMT3L-/-) model of female mice died before midgestation [55]. According to these researchers, the dead fetuses had hypomethylated maternally imprinted genes. This finding suggests the role of DNM3L in the de novo methylation of maternally imprinted regions of the DNA. A year later, Chedin et al. (2002) [54] co-expressed DNMT3L with DNMT3a in a human cell line. Their intervention enhanced the de novo methylation activity of DNMT3a at the targeted DNA sequences irrespective of which sequence is involved, but with little or no effect on DNMT3b. However, studies reviewed by Suetake et al. (2004) [56] have reported similar results for DNMT3b. These observations entail that DNMT3L has a stimulatory role on both DNMT3a and DNMT3b. Mechanistically, the stimulatory role of DNMT3L on DNMT3a/b may not involve their recruitment to the targeted regions. Instead, it may depend on the allosteric interaction between the C-terminal half of DNMT3L, and these enzymes' catalytic domains [56]. Moreover, DNMT3L could bind to DNMT3a/b but not the DNA itself [56], further emphasizing the lack of the protein's catalytic domain. Furthermore, a more recent study indicated that DNMT3L exerts its regulatory function through its PHD-like ZFD (the ADD domain) [57]. In a nutshell, these findings imply that the ZFD (ADD) in the DNMT3 family dictates the enzymes' catalytic domains.

Emerging evidence suggests a strong correlation between cellular zinc levels and the expression and activities of DNMTs in different experimental models. For instance, studies have shown a significant increase in the protein expression levels and activities of DNMT1 and DNMT3A in zinc-deficient human esophageal cancer (EC) cell lines compared to similar cell lines without zinc deficiency [58,59]. Consequently, zinc deficiency improved these cells' radiosensitivity by enhancing the hypermethylation of the microRNA 193b gene promoter via the upregulation of DNMTs. MiR-193b induces radioresistance in EC cells by arresting their cell cycle through the downregulation of Cyclin D1 mRNA [58]. One possible mechanism by which zinc deficiency could upregulate DNMT1 activity is by distorting the N-terminal CXXC domain's integrity due to lack of zinc, which may result in loss of its autoinhibitory function.

Moreover, in another study on hypozincemia-induced cognitive dysfunction in rats, zinc deficiency led to the upregulation of DNMT1 transcription in their hippocampus and subsequent hypermethylation of the brain-derived neurotrophic factor (BDNF) gene and its downregulation [60]. BDNF is highly expressed in the mammalian brain's hippocampus and is one of the critical regulators of learning and memory [61,62]. In contrast, no significant change in DNMT3B gene expression was reported in the study, while DNMT3A expression was downregulated [60]. Furthermore, a more recent study on the effect of zinc supplementation on offspring's cognitive function in rats reported a significant downregulation of DNMT1 and BDNF as well as the upregulation of DNMT3A protein levels in the hippocampus of the F1 neonates of zinc-deficient dams; however, all three proteins were downregulated in the lactating offspring of these rats [63]. According to the researchers, there was no significant hypermethylation of the BDNF gene in the offspring throughout the experiment. Its downregulation at the developmental stage correlates with the neonatal upregulation of DNMT3A, which may be due to the deformation of its regulatory ZBD (the ADD domain).

Additionally, this observation further illustrates the enzyme's de novo methyltransferase activity described earlier. However, there were no significant changes in the protein expression levels of DNMTs and BDNF following post-weaning zinc supplementation, although DNMT3A and BDNF showed an increasing trend [63]. This finding implies that zinc supplementation in offspring could restore the expression of DNMTs and DNA methy-

lation changes in some genes, which an early life zinc deficiency might have perturbed in parents. Thus, it is conceivable from these observations that zinc deficiency affects the DNA methylation statuses of genes through different pathways involving DNMTs in vivo. It is also noteworthy that hypozincemia-induced perturbations in the DNA methylation status depend on the cell's physiological or pathological state.

Role of Zinc in Folate-Mediated One-Carbon Metabolism

Zinc indirectly affects DNA and histone methylation through one-carbon metabolism, which is a term used to describe the relationship between folate and methionine metabolic pathways [64]. One carbon unit (such as methyl and formyl groups) is transferred to folic acid from amino acids and then redistributed to other molecules through SAM to facilitate methylation reactions, including DNA and histone methylations [65].

The methyl groups added to DNA and histones usually come from amino acids, such as serine and betaine/trimethylglycine (obtained from choline). Serine donates a 1C unit to form glycine and 5, 10-methylenetetrahydrofolate. Then, the latter is reduced to 5-methyltetrahydrofolate by methylenetetrahydrofolate reductase (MHTR). Then, the activated folate donates its methyl group to homocysteine to form methionine, and thus, THF is regenerated for another cycle. This reaction is catalyzed by 5-methyltetrahydrofolate-homocysteine methyltransferase (MTR), which is also known as methionine synthase [65,66]. MTR is dependent on zinc and biotin [16]. In the active site of MTR, the zinc ion is coordinated by three cysteine residues, namely C217, C272, and C273, in a trigonal bipyramidal structure [67], which is critical for the catalytic activity of this enzyme. Following synthesis, methionine reacts with ATP to generate SAM, which facilitates DNA, RNA, and histone methylation, among other methylation reactions, and homocysteine is regenerated for another cycle. A study has shown that MTR gene expression was significantly downregulated in the liver and kidney of zinc-deficient rats compared to control. These changes could not be reversed by zinc supplementation [68]. The study also reported elevated levels of homocysteine (an immediate substrate of MTR) in the serum of zinc-deficient rats, further indicating the enzyme's downregulation. One possible consequence of this finding is the depletion of SAM (a cofactor of DNMTs and HMTs), thus affecting DNA and histone methylation (Figure 2).

Alternatively, methionine is generated from homocysteine and betaine in another reaction catalyzed by betaine–homocysteine methyltransferase (BHMT) [64,65,69]. This enzyme also requires zinc for its activity [16] (Figure 2). In the active site of BHMT, the zinc atom is coordinated by the thiol groups of three cysteine residues, namely C217, C299, and C300 tetrahedrally, in addition to a fourth, which is coordinated by the OH of tyrosine (Y77). This coordination is also critical for the enzyme's catalytic activity [70]. In a study involving mice initially fed with a high-fat diet and later treated with either a zinc diet (containing 30 g zinc) or a no-added zinc diet, there was a significant downregulation of the BHMT gene and protein expression, lower methionine levels, and reduced homocysteine clearance in the liver of zinc-deficient mice; the mRNA and protein levels of Specificity protein 1/Sp1 (a ZF transcription factor that regulates the transsulfuration pathway of methionine metabolism) were also suppressed in the same group of mice [71]. Notably, these observations reaffirm the vital role of zinc in methionine and SAM synthesis as well as homocysteine clearance, which is mechanistically due to its ability to regulate the expression and function of MTR, BHMT, Sp1, and perhaps other unidentified zinc metalloproteins involved in the various pathways linking homocysteine to SAM. Thus, the findings explain zinc's role in maintaining DNA and histone methylation facilitated by SAM, which is a product of one carbon metabolism and a cofactor of DNMTs and HMTs.

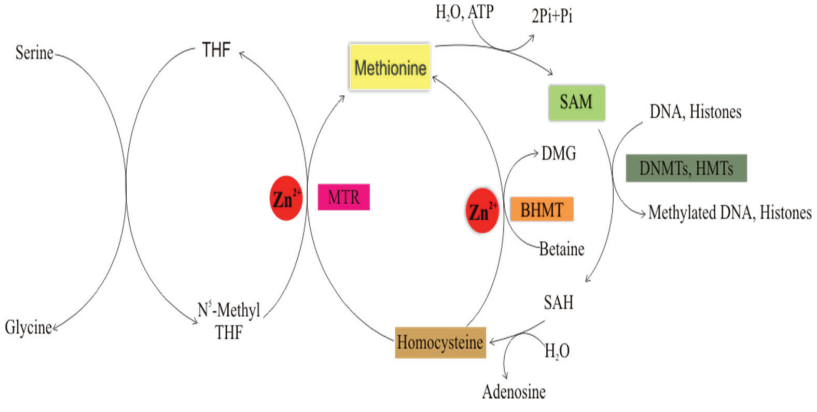


**Figure 2.** Role of zinc in DNA and histone methylation through the folate-mediated one-carbon metabolism. This figure summarizes the pathways linking one-carbon metabolism with DNA and histone methylation. Zinc-dependent enzymes and key intermediates are highlighted in different colors. BHMT (**orange**) = Betaine homocysteine methyltransferase: A zinc-dependent enzyme, which catalyzes the alternate reaction of methionine synthesis; DMG = Dimethylglycine; DNMTS (**dark green**) = DNA methyltransferases: Catalyze DNA methylation and have zinc-binding domains that regulate their activities; HMTs (**dark green**) = histone methyltransferases: Catalyze histone, lysine, and arginine methylation; MTR (**pink**) = Methionine synthase: It is zinc-dependent and catalyzes the direct synthesis of methionine (the direct precursor of SAM) from homocysteine and $N^5$-methyl THF; SAH = S-Adenosylhomocysteine; SAM (**light green**) = S-Adenosylmethionine: The activated methyl donor for methylation reactions; THF = Tetrahydrofolate: The active form of folate that supplies methyl groups to homocysteine to form methionine. Zn2+ (**red**) = Zinc ion. Source: Image was created in Corel Draw X3 Graphics Suite (Pixmantec Rawshooter essentials 2005. Version 1.1.3).

### *3.2. Role of Zinc in Histone Methylation*

Histone methylation is the addition of one, two, or three methyl groups on the ε-nitrogen of lysine or the guanidino nitrogen of arginine residues of mainly H3 and H4 tails, which is catalyzed by HMTs [72,73]. Histone arginine methylation is catalyzed by protein arginine methyltransferases (PRMTs). In contrast, histone lysine methylation is catalyzed by lysine-specific histone methyltransferases containing or not containing the evolutionarily conserved SET domain (suppressor of variegation, enhancer of zeste, and trithorax) [72,74]. SET is a catalytic domain initially discovered in the expression product of some genes responsible for heterochromatin formation and the white eye phenotype in Drosophila melanogaster [75]. In some SET domain-containing HMTs, the domain harbors either post-SET only or pre-SET and post-SET cysteine-rich ZFDs. These domains interact with the SET domain to maintain its integrity and regulate its catalytic activity [73,74]. For instance, the two yeast HMTs, cryptic loci regulator 4 and histone-lysine N-methyltransferase dim-5 (Clr4 and Dim-5) are SET domain-containing HMTs, and both have pre-SET and post-SET ZFDs flanking their SET domain [76,77]. Clr4 is a reader and a writer of histone 3 lysine 9 (H3K9) methylation mark and facilitates chromatin condensation in Schizosaccharomyces pombe [76]. On the other hand, Dim-5 methylates H3 at K9 and facilitates DNA methylation in Neurospora crassa [78]. The pre-SET ZFD of both enzymes exerts a structural function and encloses three zinc ions in trigonal coordination with nine cysteine residues. Each zinc ion bonds to four cysteine residues tetrahedrally such that three are individually attached while it shares the fourth one with the neighboring zinc atom [76,79]. The post-SET domain in both proteins appears to be a cysteine-rich ZFD enclosing a zinc ion in tetrahedral coordination. It seems to be involved in SAM binding, although its exact function remains elusive [74,79]. Histone lysine methyltransferases are very diverse in eukaryotes, including humans. About seven families and a few orphan

members have been identified in humans. SUV39H1 and SUV39H2 are examples of human homologs of the yeast Clr4 harboring the pre-SET and post-SET ZFMs [79,80]. SET domain-containing HMTs catalyzes the methylation of H3, mainly at K9 and K4 [45,76]. Interestingly, histone lysine methylation does not disrupt the lysine residues positive charge and has fewer effects on DNA–histone interaction. However, unlike DNA methylation that often leads to gene silencing, histone lysine methylation activates or represses genes either by providing a binding site for methyl reader proteins, which in turn recruit the transcription machinery to the targeted genes or by remodeling the chromatin architecture, thus affecting the ability of transcriptional complexes to access DNA [23,52,81]. Generally, the methylation of H3 at K4, K36, and K79 leads to gene activation, whereas methylation at K9 and K27 of H3, as well as K20 of H4, altogether leads to gene repression [45].

### *3.3. Role of Zinc in Histone Demethylation*

Histone demethylation is the reverse of histone methylation catalyzed by HDMs. It involves the removal of methyl groups from the lysine and arginine residues of histone tails. Histone demethylases are of two types: lysine demethylases (KDMs) and peptidyl-arginine demethylases (PADs) [82]. KDMs are the class of histone demethylases with ZBDs. Based on their catalytic mechanisms, they are subdivided into two groups of six families: a flavin adenine dinucleotide-dependent amine oxidases (AOF/KDM1) and an iron (ii) and alpha-ketoglutarate-dependent Jumonji-containing (JmjC) dioxygenases (KDMs 2-6) [4,83]. Two members of the KDM1 family, lysine-specific demethylases 1 and 2 (LSD1 and LSD 2), have been identified [80]. LSD2, also known as KDM1B or AOF1, has approximately 822 amino acids, some of which form an N-terminal ZFD with C4H2C2-type and CW-type classes of ZFMs, and specifically demethylates H3K4me1 and H3K4me2 marks [84]. The N-terminal ZFD (residues 50–264) facilitates substrate specificity and maintains the enzyme's active conformation [85]. Mutations in the genes transcribing the ZF components of this domain induce conformational changes in the amine oxidase domain, with subsequent loss of the demethylase activity [86]. This observation suggests its role in the catalytic mechanism of the enzyme. The second family of lysine demethylases encompasses more than 30 proteins, all of which contain the JmjC domain [82]. A typical example of a KDM in this family is KDM2B, also known as *JHDM1B/FBXL10/NDY1*, which demethylates H3K4me3 and H3K36me2. In addition to the JmjC domain, the enzyme contains two other zinc finger domains: the CXXC and the PHD domains, together with an F-box domain. The JmjC domain erases the H3K36me2 mark, the CXXC is for unmethylated DNA binding and recruitment of transcription factors, and the PHD serves as a histone modificatison reader domain [83]. A study has reported the enrichment of the H3K4me3 mark in the thymus of hematopoietic cell-specific knockout mice model of the CXXC domain of KDM2B [87]. This observation supports the earlier mentioned role of this domain in the demethylation of the H3K4me3 mark.

### *3.4. Role of Zinc in Histone Acetylation*

Histone acetylation is the transfer of a negatively charged two-carbon unit, the acetyl group ($CH_3CO^-$), from acetyl-CoA to specific N-terminal lysine residues of histone tails [88]. Being negatively charged, the acetyl group neutralizes the positive charge on the acetylated lysine residues and hence reduces the overall positive charge on the histone protein. Consequently, this leads to the disruption of DNA–histone interactions (electrostatic interactions between negatively charged DNA and the positively charged histones), making the DNA more accessible to the transcription machinery. Therefore, histone acetylation favors euchromatin formation and activates gene expression [4,88–90]. Histone acetylation is catalyzed by HATs, some of which are zinc-dependent. Several families of HATs have been identified in eukaryotes, including humans [91]. Examples of ZBD-containing HATs are the members of the MYST family, which is an acronym derived from the names of two human genes and two yeast genes: human monocytic leukemia ZFP (MOZ), yeast bf2, also known as ySas3 or KAT6 (histone lysine acetyltransferase 6),

yeast Sas2 (KAT8), and human Tip60 (KAT5). The defining feature of this class of HATs is the N-terminal MYST domain, which has an intrinsic HAT activity [92]. Some MYST family members contain zinc within a C2HC-type ZFM and a PHD-linked ZFD, which helps in the identification of and interaction with substrates [91,93]. Five members of the MYST family have been identified in humans: two important ones are MOZ and its paralog MORF (MOZ Related Factor), which are also known as KAT6A and KAT6B (previously MYST3 and MYST4), respectively; both catalyze the acetylation of H3 at K9 and K14 [94]. Similarly, the N-terminals of both enzymes enclose two tandem PHD ZFs that enable H3 recognition and binding and regulate the HAT domain [93,94].

### *3.5. Role of Zinc in Histone Deacetylation*

Histone deacetylation is the hydrolytic removal of an acetyl group from N-acetyl lysine residues on histone tails, which are catalyzed by HDACs. A total of eighteen HDACs hydrolyze the amide bond of N-acetyl lysine residues of histone tails in mammals, including humans [95]. These enzymes are of four categories or classes, which require either zinc or NAD+ for catalysis. Class I (HDACs 1-3, 8), class II (IIa: HDACs 4, 5, 7, 9 and IIb: HDACs 6, 10) and class IV (HDAC 11) are zinc-dependent, while class III (sirtuins 1-7) depend on NAD+ [96–99]. The zinc ion in the active sites of zinc-dependent HDACs coordinates an aspartate-histidine (D-H) dyad and a tyrosine (Y) residue (except in class IIa HDACs, in which the Y residue has been replaced by another H). The coordination maintains the appropriate positioning of the functional groups required for the catalytic process [9,97,100]. In this catalytic mechanism, the zinc ion launches an initial nucleophilic attack on the water molecule (an essential step in the catalytic mechanism common to numerous zinc metalloenzymes, including carboxypeptidase A and carbonic anhydrase). Then, the zinc ion induces a polarity on the carbonyl oxygen of N-acetyl lysine on the histone tail and thus facilitates a broad base nucleophilic attack (on the carbonyl carbon) by the zinc-bound water molecule [9,100,101]. In addition to the central zinc atom typical to all the eleven zinc-dependent HDACs, class IIa HDACs also enclose another zinc atom within a unique and highly conserved (among members of this class IIa) CCHC-type ZFM found adjacent to the entrance of their active sites [102]. Although this motif's exact function is not clear, it may be critical for maintaining these enzymes' catalytic activity and stability and may serve as a potential allosteric site to develop their inhibitors. HDAC inhibitors have been employed in the management of diabetes mellitus (DM) [103–105] and cancer [100,106,107]. Interestingly, some of these drugs' inhibitory mechanism is based on their ability to chelate the zinc ion in their active sites [9].

### *3.6. Role of Zinc in Histone Ubiquitination*

Ubiquitination is the covalent attachment of one or a chain of ubiquitin molecules. It is one of the diverse post-translational medications of proteins, including histones [108]. Histone ubiquitination (mostly monoubiquitination) occurs predominantly at specific lysine residues of H2A and H2B. It is involved in transcription regulation and DNA repair [42]. This modification regulates transcription by three primary mechanisms: (1) direct remodeling of the chromatin architecture to increase or decrease DNA accessibility to transcriptional complexes, (2) recruitment of proteins that facilitate chromatin remodeling, and (3) as a prerequisite for other histone modifications such as methylation and acetylation [109]. Generally, protein ubiquitination occurs in three stages: activation, conjugation, and ligation catalyzed by ubiquitin-activating enzymes (E1), ubiquitin-conjugating enzymes (E2), and ubiquitin ligases (E3) [110].

The zinc-dependent class of E3 ubiquitin ligases (EUBLs) are the RING domain-containing proteins that catalyze the monoubiquitination of H2A at K13, K15, K119, K127, and K129 as well as H2B at K34, K120, and K125, respectively [41]. The RING domain harbors two zinc atoms in tetrahedral coordination with a histidine ring and seven cysteine side chains. This arrangement creates a C3HC4-type ZFM with 40–60 amino acid residues arranged in the sequence, Cys-X2-Cys-X [9-39]-Cys-X[1-3]-His-X[2-3]-Cys-X2-Cys-X[4-48]-

Cys-X2-Cys, where "X" represents any amino acid [111]. Histone ubiquitination marks are associated with transcription silencing, activation, and DNA repair or participate in crosstalk that regulates other histone marks, such as histone methylation, which is essential in maintaining the dynamic nature of the chromatin [41,112].

In humans, H2A monoubiquitination is catalyzed by three enzymes or enzyme complexes: (1) RING finger 168 (RNF168), which adds a unit of ubiquitin on H2A at K13 or K15 and promotes the non-homologous end-joining pathway in the DNA damage repair response; (2) members of the polycomb repressor complex 1 (RING1A, RING1B and RNF51), which ubiquitinate H2A at K119 and lead to transcriptional repression; (3) the BRCA1/BARD1 complex (BReast CAncer type-1 susceptibility protein/BRCA1-Associated RING Domain protein 1) ubiquitinates H2A at K127 K129 and promotes the homologous recombination pathway in the DNA damage repair response [112]. On the other hand, several RING finger families of enzymes and enzyme complexes that catalyze H2B monoubiquitination have been identified in humans. The RNF20–RNF40 complex, which mainly catalyzes H2BK120ub1, appears to be the predominant writer of H2Bub1 marks [41,112]. Another important class is the MOF–MSL (MOZ-related Factor–Male Specific Lethal homolog) complex comprising MOF, MSL1, MSL2, and MSL3. The MSL1/2 component catalyzes the monoubiquitination of H2B at K34, while the MOF component (a member of the MYST family of HATs discussed earlier) catalyzes H4K16 acetylation [113]. Of note, H2Bub1 at K120 and K34 has been linked to transcriptional upregulation. In contrast, H2Aub1 at K34 and K120 and H4K31ub1 are collectively involved in crosstalk that facilitates H3K4 and H3K79 methylation [41].

### *3.7. Role of Zinc in Histone Deubiquitination*

Histone deubiquitination is the removal of the ubiquitin moieties attached to lysine residues of histone tails by hydrolysis. H2A/B deubiquitination is catalyzed by the *Spt-Ada-Gcn5-Acetyltransferase* (SAGA) coactivator complex, which is a multi-subunit complex with both histone acetylase and deubiquitinase activity that is structurally and functionally conserved from yeast to humans [114]. In both yeast and humans, the SAGA complex is organized into a functional unit called the deubiquitinating module (DUBm), comprising of four functional subunits: three of them form an N-terminal regulatory region, and the fourth one creates the catalytic domain [115]. The four components in the yeast DUBm are the ubiquitin-specific protease 8 (Ubp8), which is the catalytic domain, and the three N-terminal subunits, namely the SAGA-associated factor 11 (Sgf11), the transcription and mRNA export factor (Sus1), and the SAGA-associated factor 73 (Sgf73). These units altogether serve as a scaffold that maintains the catalytic domain's active form [115]. Of note, Sgf11 and Sgf73 are ZFDs required for the DUBm function and stability, respectively [116]. In humans, the ubiquitin-specific protease 22 (USP22) is the ZFD-containing component of the human SAGA complex that deubiquitinates both H2A and H2B in vitro [114]. Moreover, similar to the yeast complex, this module also contains hATXN7 (human ataxin 7), hATXN7L3 (human ataxin 7 like 3), and hENY2 (human enhancer of yellow 2 transcription factor homolog, which are the ZBD-containing protein orthologs of the yeast Sgf73, Sgf11, and Sus1, respectively. The units interact to allosterically regulate its activity [114].

### *3.8. Zinc Finger Proteins That Read Epigenetic Modifications*

Apart from enzymes, a plethora of proteins containing ZBDs (collectively referred to as transcription factors) is also involved in epigenetics. These proteins can read/recognize and bind to methylation patterns on the CpG islands of DNA or the various modifications on the N-terminal lysine/arginine residues of histone tails and then recruit other proteins that alter chromatin conformation, leading to varying transcriptional consequences [10,11,117].

#### 3.8.1. DNA Methylation Readers and Their Binding Mechanisms

Based on the commonalities in their methyl binding domains (MBDs) and the binding mechanism, methyl binding proteins (MBPs) are of two types: readers of double (fully)

methylated DNA and readers of hemimethylated DNA. The first group (readers of double-methylated DNA) comprises the best-characterized families of MBPs [10]. The most typical feature uniting these diverse families of transcription factors is the presence of two or more Cys2His2 (C2H2) ZFMs. Each ZFM has approximately 30 amino acid residues arranged in a simple structure: a central zinc atom coordinating two histidine rings protruding from the α-helix and two cysteine side chains extending from the β-sheets (Figure 3). Then, these motifs form binding domains harboring a set of two, three, or more zinc fingers arranged in tandem repeats. Examples include the Broad-complex, Tramtrack, and Bric-a-brac, which are also known as POxvirus and Zinc finger (BTB/POZ) domains containing families such as Kaiso (ZBTB33), ZBTB4, and ZBTB38 [10,117,118].

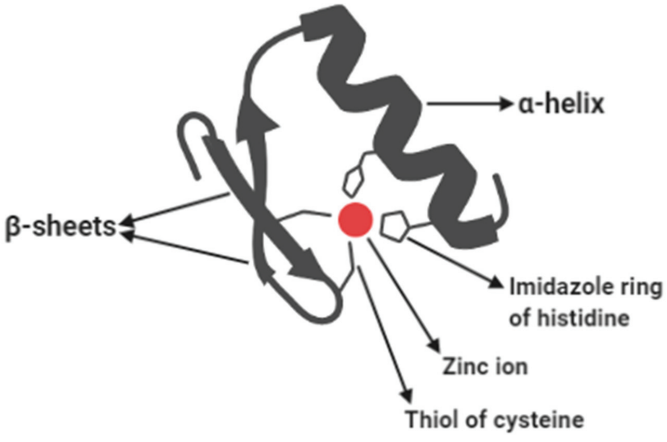


**Figure 3.** Labeled cartoon representation of a Cys2His2 zinc finger motif. A C2H2 zinc finger is an essential structural component of fully methylated DNA reader proteins with methyl binding domains. The red dot represents the zinc atom; the spiral structure denotes the alpha-helix; the two antiparallel arrows are the beta-sheets. The two five-membered rings extending from the alpha helix are the imidazole rings of histidine; the two curves extending from the beta-sheets and pointing toward the red dot are the thiols of the two cysteine residues. Source: Icon was obtained and customized in BioRender (biorender.com (accessed on 23 February 2021)).

More members of ZF MBPs reviewed by Hodges et al. (2020) [10] include zinc finger protein 57 (ZFP57), a member of the Krüpple-associated box (KRAB) domain family; Krüppel-like factor 4 (KLF4), a member of the Krüppel-like factor family, Wilm's Tumor Gene 1 (WT1); Early Growth Response Protein 1 (EGR1); and CCCTC-binding factor (CTCF), which is also known as 11-ZFP.

These proteins' binding mechanisms are complex and transcription factor-dependent due to variable structures and amino acid composition. However, they generally present a unique interaction model. Here, the arginine residue that precedes the first histidine ring in the C2H2 ZFM forms a hydrogen bond with the 3′-G ring and a Van der Waals interaction with the 5′-mC of the CpG dinucleotide. This interaction creates a 5-methylCytosine/Thymine-Arginine-Guanine triad typical of fully methylated DNA readers [119]. Additionally, a conserved glutamate residue (among the readers of double methylated DNA) also interacts with the 5′-mC via an OHN-type and an OHC-type hydrogen bonds [10]. This mechanism has been extensively reviewed recently [117,120]. Moreover, a conserved lysine residue in ZBTB38 and other ZFPs (whose ZFM sequences were aligned) substitutes the arginine in methylated DNA binding [117]. Thus, this finding demonstrates another possible mechanism for CpG methylation recognition by ZFPs.

On the other hand, the hemimethylated DNA readers are mainly the SRA domain-containing families of MBPs [121]. UHRF1 and UHRF2 are the members of this family

identified in humans. In addition to the SRA domain, both contain a ubiquitin-like (UBL), a tandem Tudor, a PHD, and a RING domain. Studies have shown that the ability of UHRF1 to recruit DNMT1 to the replication foci depends on the interaction between its SRA domain and hemimethylated DNA [31,43,44]. UHRF2 is also known to read the 5-hydroxymethyl cytosine (5 hmC) mark on DNA through its SRA domain and recruit DNMT1 to replicate foci [122]. 5 hmC is an oxidation product of 5 mC generated by the members of the TET family of proteins in the mammalian DNA demethylation pathway; it is found at the proximity of transcription factor binding sites and is also involved in the regulation of transcription [123,124].

#### 3.8.2. Histone Modifications Readers and Their Binding Mechanisms

Readers of histone modifications are numerous, very diverse, and histone mark specific. The best characterized ZF readers include bromodomain, chromodomain, and PHD readers. They recognize modified and unmodified lysine and arginine residues [125]. The chromodomain and bromodomain proteins recognize methylated lysine and acetylated lysine, respectively. In contrast, the PHD readers acknowledge both modified and unmodified lysine and arginine residues. Thus, PHD proteins are considered versatile readers of histone modifications [40].

The predominant readers of lysine methylation are the chromodomain containing members of chromatin modifiers (collectively referred to as the Royal family), which recognize methylated lysine mainly at H3 and participate in chromatin remodeling. A critical member of this family is the heterochromatin protein 1 (HP1). It binds to H3 methylations primarily at K9 and, to some extend K27, and it facilitates heterochromatin condensation [126]. Another important example of a methylated lysine reader is the Bromodomain PHD finger Transcription Factor (BPTF). This protein is a PHD containing a bromodomain reader considered the largest subunit of the ATP-dependent chromatin remodeling complex called the nucleosome remodeling factor (NURF) in humans. This protein has a preference for H3K4me2/me3 (the marks associated with the transcription start site of active genes) and thus remodels the chromatin state of those genes to enable their expression [127].

Due to their diversity, the binding mechanisms of methyl lysine readers differ from one reader to another. However, most of these proteins form an aromatic pocket with the side chains of tryptophan and tyrosine residues, which help them recognize and bind to various histone methylation marks. On the other hand, readers of unmodified lysine such as the PHD do not form an aromatic pocket; instead, they form hydrogen bonds between the ε-nitrogen of the lysine residue and the hydroxyl hydrogen of either aspartate or a glutamate residue in the PHD domain [125]. Table 1 summarizes the significant ZBDs discussed in this review; their functions and examples of human proteins containing these domains are given.

**Table 1.** Summary of zinc-binding domains and their functions.

| ZBD | Function | Example(s) | References |
|---|---|---|---|
| ADD | Allosteric control of the catalytic domain | DNMT3a/3b/3L | [31,41,57] |
| BTB/POZ | Readers of fully methylated DNA (double methylated CpG islands) | Kaiso (ZBTB33), ZBTB4, ZBTB38. | [10,117] |
| CXXC | Substrate recognition and self-regulation | DNMT1. | [49,50] |
| JmjC | H3K36me2 demethylation | KDM2B | [82] |
| KRAB | Reads fully methylated DNA (double methylated CpG islands) | ZFP57 | [10] |
| MYST | HAT activity (H3K9/K14 acetylation) | MOZ, MORF | [94] |
| PHD | Reads a broad range of histone marks and has E3-ubiquitin ligase activity. | UHRF1, UHRF2, BPTF | [11,40] |
| RING | E3-ubiquitin ligase | RNF168, PRC1, RNF20-RNF40 complex | [41] |
| SET | H3K4 methyltransferase activity | SET1A, SET1B | [45,76] |
| SRA | Reads hemimethylated DNA. | UHRF1, UHRF2. | [121,122] |

### *3.9. Role of Zinc in Epigenome Editing*

Due to their ability to recognize epigenetic marks, zinc finger proteins (especially the Cys2His2 class of ZFs) are also involved in synthetic epigenetics. It is a popular concept known as epigenome editing [128]. This synthetic form of epigenetic modification entails writing or erasing epigenetic marks on the DNA or histones via the recruitment of the natural catalytic activity of the chromatin-modifying enzymes [46]. Two basic techniques have been employed to achieve this purpose. One of them involves using artificially customized epigenetic mark readers (the Cys2His2 ZFs) to recruit these catalytic domains to the predetermined targeted regions on the DNA and histones [20]. The ZFs are coupled to the chromatin-modifying enzymes, and the resultant machinery is employed to add or erase epigenetic marks.

The abbreviations used in the table are defined hereunder, and the respective letters in each acronym are capitalized. ADD—Alpha thalassemia mental retardation x-linked DNA methyltransferase3 DNA methyltransferase3L; BTB/POZ—Broad-complex, Tramtrack, and Bric-a-brac, also known as POxvirus and Zinc finger; BPTF—Bromodomain PHD finger Transcription Factor; CXXC—C for Cysteine and X for any amino acid; DNMT1—DNA methyltransferase1; DNMT3a/3b/3L—DNA methyltransferase3a/3b/3L; HAT—Histone acetyltransferase; H3K36me2—Histone 3 lysine 36 dimethyl; H3K4—Histone 3 lysine4; H3K9/K14—Histone 3 lysine 9/lysine14; JmjC—Jumonji-containing; KDM2B—lysine demethylase 2B; KRAB—KRüpple-Associated Box; MORF—MOZ-Related Factor; MOZ—human MOnocytic leukemia Zinc finger protein; MYST—MOZ, Ybf2 (Sas3), Sas2, and Tip60; PHD—Plant HomeoDomain; RING—Really Interesting New Gene; RNF168—Ring Finger168; PRC1—Polycomb Repressor Complex1; RNF20–RNF40—Ring Finger20–Ring Finger40; SET—Suppressor of variegation 3-9, Enhancer-of-zeste and Trithorax; SET1A—Suppressor of variegation 3-9, Enhancer-of-zeste and Trithorax 1A; SET1B—Suppressor of variegation 3-9, Enhancer-of-zeste and Trithorax 1B; SRA—SET and RING finger Associated domain; UHRF1—Ubiquitin-like, containing PHD and RING finger domains, 1; UHRF2—Ubiquitin-like, containing PHD and RING finger domains, 2; ZFP57—Zinc finger protein 57.

#### Role of Zinc in DNA Methylation Editing

DNMTs coupled to zinc fingers are used to introduce or delete DNA methylations at specific predetermined targeted regions. This technique has been used to alter the DNA methylation statuses of genes, affecting gene expression. For example, a customized array of seven ZFs coupled to the catalytic domain of DNMT3a was employed to induce DNA methylation on the p16 promoter of immunodeficient mice. Consequently, this led to increased metastasis and cancer cells' proliferation due to the p16 gene suppression [129]. P16 is a tumor-suppressor protein that was found to be associated with improved prognosis and early survival of patients with oropharyngeal cancer in China [130]. In ZF arrays, each unit of a ZF recognizes three nucleotide bases. Hence, the customized collection of zinc fingers used in chromatin recognition can bind to about nine to 18 DNA bases as each array has three to six ZFMs (Figure 4).

On the other hand, oxidative (active) DNA demethylation at targeted promoters of specific genes has been induced by the ten-eleven-translocases (TET) family members. This task was achieved by coupling these enzymes with specially designed ZFs that target those genes' promoters. For example, in a study conducted to induce oxidative DNA demethylation on human intracellular adhesion molecule 1 (ICAM-1) gene promoter, a hexameric ZF array was coupled to the TET-2 enzyme and used to target the promoter [131]. This intervention led to demethylation of the ICAM promoter and subsequent reactivation of the expression of the gene.

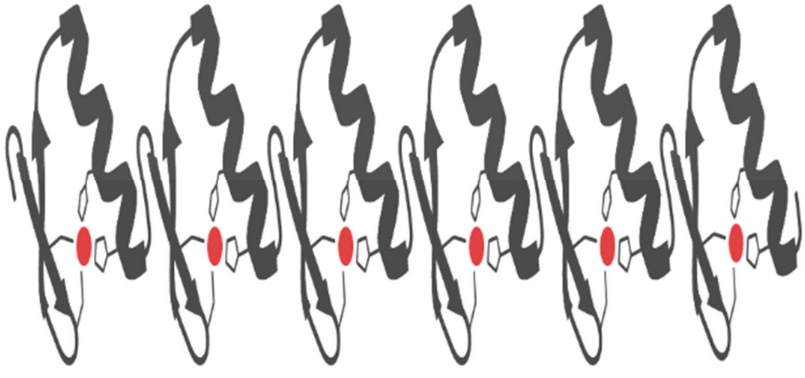

**Figure 4.** Cartoon representation of the zinc finger (ZF) array. A customized sequential array of six Cys2His2 ZFs: each of the six units containing a red dot surrounded by a coiled strand and two antiparallel arrows represent a Cys2His2 ZF. The red dot is the zinc ion coordinated by the side chains of two cysteines and two histidine residues. ZF arrays are employed in synthetic epigenetics to edit (add or delete) epigenetic marks at predetermined DNA or histone regions. They are usually coupled with writers or erasers to achieve this purpose. Source: Icons were obtained and customized in BioRender (biorender.com (accessed on 23 February 2021)).

## 4. Summary of Zinc Metalloproteins in Epigenetics and Their Crosstalk

Zinc metalloproteins involved in epigenetics are summarily classified into five main classes. Class I are the writers or markers: they include zinc metalloenzymes that establish epigenetic marks such as DNA methylation, histone methylation acetylation, and ubiquitination. Examples are DNMTs, HMTs, HATs, and EUBLs. Class II is nicknamed erasers due to their ability to erase or remove epigenetic marks such as histone methylation, acetylation, and ubiquitination. Examples include enzymes such as KDMs, HDACs, and DUBm complexes. Class III is made up of a large family of ZFPs that read epigenetic marks such as DNA methylation and histone modifications and subsequently generate signaling pathways by recruiting an array of proteins involved in the signal transduction process, which ultimately lead to the activation or silencing of genes [39,40,112]. This class is termed readers, and their examples include Kaiso, UHRF1, UHRF2, ZFP57, HP1, BPTF, etc. Class IV is made up of a customized combination of readers coupled with writers or erasers. These assemblies are employed in epigenome editing and are referred to as editors.

A classic example is the hexameric Cys2His2 ZF array associated with the TET-2 enzyme and used for the ICAM gene promoter [128]. Class V are zinc-dependent enzymes nicknamed feeders due to their ability to catalyze critical reactions in the folate-mediated one-carbon metabolism, which is a term used to describe the group of metabolic pathways involved in the supply of one-carbon units such as activated methyl group (in the form of SAM) from folate to DNA, histones, and other biomolecules. In other words, they feed the methylation pathways with active methyl groups for various methylation reactions, including DNA and histone methylations (Figure 5).

Interestingly, readers are involved in crosstalk with writers and erasers, and this interplay regulates the human epigenome, leading to various transcriptional outcomes in both health and disease conditions. For instance, a PHD protein such as UHRF1 can read modified or unmodified histones and then recruit a writer such as DNMT1 to the replication foci. The latter establish epigenetic marks on hemimethylated DNA.

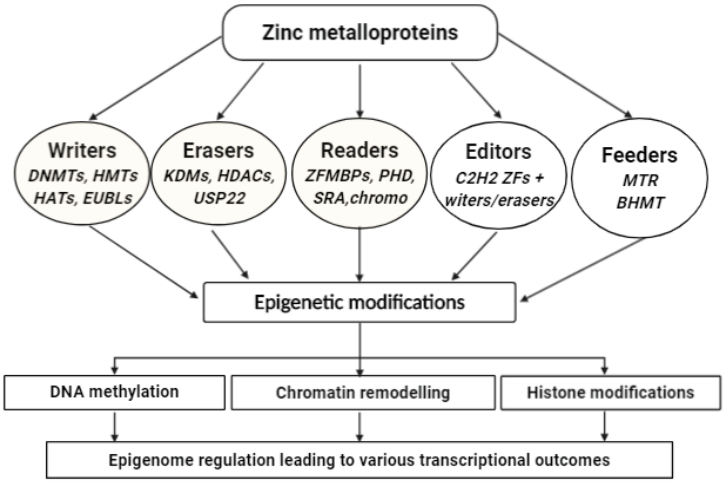


**Figure 5.** Summary of zinc metalloproteins and their roles in epigenome regulation. Figure 5 summarizes the various classes of zinc metalloproteins that come together to regulate the epigenome. Writers, erasers, readers, editors, and feeders represent the names of the types. These classes of proteins work together in a coordinated manner to regulate the epigenome. Examples of enzymes/proteins in each category are given in abbreviations. BHMT = Betaine homocysteine methyltransferase: a zinc metalloenzyme that catalyzes the formation of methionine from homocysteine and betaine, an essential reaction in DNA and histone methylation; chromo = Chromodomain containing proteins such as heterochromatin protein 1 (HP1), an H3K9 methyl reader that facilitates heterochromatin condensation; C2H2 ZFs = 2-Cysteine-2-Histidine-type of zinc fingers, critical readers of fully methylated DNA; DNMTS = DNA methyltransferases, enzymes that catalyze de novo and maintenance DNA methylation at the CpG islands of fully methylated or hemimethylated DNA; HATs = Histone acetyltransferases, enzymes that catalyze histone lysine acetylation; HDACs = Histone deacetylases, enzymes that catalyze removal acetyl groups from acetyl-lysine residues of histone tails; HMTs = Histone methyltransferases, enzymes that catalyze the methylation of histones on lysine residues; KDMs = Histone lysine demethylases, enzymes that remove methyl groups from the methylated lysine residues of histones; MTR = Methionine synthase, an enzyme that catalyzes the synthesis of methionine from homocysteine and tetrahydrofolate, an essential reaction for DNA and histone acetylation; PHD = Plant homeodomain containing zinc finger proteins, they serve as versatile readers of histone modifications; SRA = SET and RING finger Associated domain-containing proteins: they read hemimethylated DNA. USP22 = Ubiquitin-specific protease 22: the catalytic component of the human deubiquitinating module complex that catalyzes histone deubiquitination. ZF MBPs = Zinc finger methyl binding proteins: readers of fully methylated DNA. Source: Image was created in BioRender (biorender.com (accessed on 23 February 2021)).

## 5. Conclusions and Future Perspectives

This paper reviewed zinc's epigenetics role, which depends on zinc metalloproteins' involvement in epigenome programming. We also discussed here that these proteins contain ZBDs critical for substrate recognition, self-regulation, and catalysis. Most importantly, we demonstrated that an interplay involving the ZBDs of these proteins maintains the highly plastic epigenome in a dynamic state. Therefore, we conclude that zinc is an essential trace metal in epigenetics. However, despite the plethora of ZBD-containing proteins identified and still being discovered, only a few of them have been employed to manipulate the epigenome. Non-communicable chronic diseases such as cancers, diabetes mellitus, and cardiovascular diseases have been associated with aberrant epigenetic changes in the genes related to these diseases; targeting these genes with customized ZBDs could make a remarkable difference in minimizing their burden. For instance, the hypermethylation of

oncogenes or demethylation of tumor suppressor genes by epigenetic editors could help control various cancers. Furthermore, studies on transgenerational epigenetic effects at different doses of parental zinc exposure on offspring could unveil how zinc deficiency affects future generations' health. Thus, the epigenetic burden of diseases could be minimized.

**Author Contributions:** Conceptualization, A.P.Y., M.B.A., M.U.I.; writing—original draft preparation, A.P.Y.; writing—review and editing, M.B.A., I.M., K.G.I., B.A., M.B.B., N.Q., S.T.E., M.U.I., A.A., G.E.-S.B.; project administration, M.U.I.; funding acquisition, A.A. and M.U.I. All authors contribute to the writing—review and editing. All authors have read and agreed to the published version of the manuscript.

**Funding:** This study was supported by a grant from the Center for Advanced Medical Research and Training (CAMRET), Usmanu Danfodio University Sokoto, Sokoto, Nigeria. Abdurrahman Pharmacy, Yusuf is a recipient of CAMRET research funded scholarship.

**Institutional Review Board Statement:** Not applicable.

**Informed Consent Statement:** Not applicable.

**Data Availability Statement:** Not applicable.

**Conflicts of Interest:** The authors declare no conflict of interest.

## References

1. Chasapis, C.T.; Loutsidou, A.C.; Spiliopoulou, C.A.; Stefanidou, M.E. Zinc and human health: An update. *Arch. Toxicol.* **2012**, *86*, 521–534. [CrossRef]
2. Hambidge, K.M.; Krebs, N.F. Zinc Deficiency: A Special Challenge. *J. Nutr.* **2007**, *137*, 1101–1105. [CrossRef] [PubMed]
3. Andreini, C.; Banci, L.; Bertini, I.; Rosato, A. Counting the Zinc-Proteins Encoded in the Human Genome. *J. Proteome Res.* **2006**, *5*, 196–201. [CrossRef]
4. Brito, S.; Lee, M.-G.; Bin, B.-H.; Lee, J.-S. Zinc and Its Transporters in Epigenetics. *Mol. Cells* **2020**, *43*, 323–330. [PubMed]
5. Chasapis, C.T.; Ntoupa, P.-S.A.; Spiliopoulou, C.A.; Stefanidou, M.E. Recent aspects of the effects of zinc on human health. *Arch. Toxicol.* **2020**, *94*, 1443–1460. [CrossRef]
6. Roohani, N.; Hurrell, R.; Kelishadi, R.; Schulin, R. Zinc and its importance for human health: An integrative review. *J. Res. Med. Sci.* **2013**, *18*, 144–157. [CrossRef]
7. Foster, M.; Samman, S. Zinc and Regulation of Inflammatory Cytokines: Implications for Cardiometabolic Disease. *Nutrients* **2012**, *4*, 676–694. [CrossRef] [PubMed]
8. Blanquart, C.; Linot, C.; Cartron, P.-F.; Tomaselli, D.; Mai, A.; Bertrand, P. Epigenetic Metalloenzymes. *Curr. Med. Chem.* **2019**, *26*, 2748–2785. [CrossRef]
9. Porter, N.J.; Christianson, D.W. Structure, mechanism, and inhibition of the zinc-dependent histone deacetylases. *Curr. Opin. Struct. Biol.* **2019**, *59*, 9–18. [CrossRef] [PubMed]
10. Hodges, A.J.; Hudson, N.O.; Buck-Koehntop, B.A. Cys2His2 Zinc Finger Methyl-CpG Binding Proteins: Getting a Handle on Methylated DNA. *J. Mol. Biol.* **2020**, *432*, 1640–1660. [CrossRef] [PubMed]
11. Matthews, J.M.; Bhati, M.; Lehtomaki, E.; Mansfield, R.E.; Cubeddu, L.; Mackay, J.P. It Takes Two to Tango: The Structure and Function of LIM, RING, PHD and MYND Domains. *Curr. Pharm. Des.* **2009**, *15*, 3681–3696. [CrossRef] [PubMed]
12. Wessels, I.; Maywald, M.; Rink, L. Zinc as a Gatekeeper of Immune Function. *Nutrients* **2017**, *9*, 1286. [CrossRef] [PubMed]
13. Coneyworth, L.J.; Jackson, K.A.; Tyson, J.; Bosomworth, H.J.; Van Der Hagen, E.; Hann, G.M.; Ogo, O.A.; Swann, D.C.; Mathers, J.C.; Valentine, R.A.; et al. Identification of the human zinc transcriptional regulatory element (ZTRE): A palindromic protein-binding DNA se-quence responsible for zinc-induced transcriptional repression. *J. Biol. Chem.* **2012**, *287*, 36567–36581. [CrossRef]
14. Bin, B.-H.; Seo, J.; Kim, S.T. Function, Structure, and Transport Aspects of ZIP and ZnT Zinc Transporters in Immune Cells. *J. Immunol. Res.* **2018**, *2018*, 9365747. [CrossRef] [PubMed]
15. Myers, S.A.; Nield, A.; Myers, M. Zinc Transporters, Mechanisms of Action and Therapeutic Utility: Implications for Type 2 Diabetes Mellitus. *J. Nutr. Metab.* **2012**, *2012*, 1–13. [CrossRef]
16. Gu, H.F.; Zhang, X. Zinc Deficiency and Epigenetics. In *Handbook of Famine, Starvation, and Nutrient Deprivation: From Biology to Policy*; Preedy, V., Patel, V.B., Eds.; Springer: New York City, NY, USA, 2017; pp. 1–18. [CrossRef]
17. Lappalainen, T.; Greally, J.M. Associating cellular epigenetic models with human phenotypes. *Nat. Rev. Genet.* **2017**, *18*, 441–451. [CrossRef]
18. Greally, J.M. A user's guide to the ambiguous word 'epigenetics'. *Nat. Rev. Mol. Cell Biol.* **2018**, *19*, 207–208. [CrossRef] [PubMed]
19. Felsenfeld, G. A Brief History of Epigenetics. *Cold Spring Harb. Perspect. Biol.* **2014**, *6*, a018200. [CrossRef]
20. Kungulovski, G.; Jeltsch, A. Epigenome Editing: State of the Art, Concepts, and Perspectives. *Trends Genet.* **2016**, *32*, 101–113. [CrossRef]

21. Van Otterdijk, S.D.; Michels, K.B. Transgenerational epigenetic inheritance in mammals: How good is the evidence? *FASEB J.* **2016**, *30*, 2457–2465. [CrossRef] [PubMed]
22. Kanherkar, R.R.; Bhatia-Dey, N.; Csoka, A.B. Epigenetics across the human lifespan. *Front. Cell Dev. Biol.* **2014**, *2*, 49. [CrossRef] [PubMed]
23. Zhang, W.; Qu, J.; Liu, G.-H.; Belmonte, J.C.I. The ageing epigenome and its rejuvenation. *Nat. Rev. Mol. Cell Biol.* **2020**, *21*, 137–150. [CrossRef] [PubMed]
24. Moore, L.D.; Le, T.; Fan, G. DNA Methylation and Its Basic Function. *Neuropsychopharmacology* **2013**, *38*, 23–38. [CrossRef] [PubMed]
25. Mohamed, M.A.; Greif, P.A.; Diamond, J.; Sharaf, O.; Maxwell, P.; Montironi, R.; Young, R.A.; Hamilton, P.W. Epigenetic events, remodelling enzymes and their relationship to chromatin organization in prostatic intraepithelial neoplasia and prostatic adenocarcinoma. *BJU Int.* **2007**, *99*, 908–915. [CrossRef]
26. Korkmaz, A.; Manchester, L.; Topal, T.; Ma, S.; Tan, D.; Reiter, R. Epigenetic mechanisms in human physiology and diseases. *J. Exp. Integr. Med.* **2011**, *1*, 139–147. [CrossRef]
27. Lin, C.-C.; Chen, Y.-P.; Yang, W.-Z.; Shen, J.C.K.; Yuan, H.S. Structural insights into CpG-specific DNA methylation by human DNA methyltransferase 3B. *Nucleic Acids Res.* **2020**, *48*, 3949–3961. [CrossRef]
28. Maret, W. Zinc Biochemistry: From a Single Zinc Enzyme to a Key Element of Life. *Adv. Nutr.* **2013**, *4*, 82–91. [CrossRef]
29. An, J.; Rao, A.; Ko, M. TET family dioxygenases and DNA demethylation in stem cells and cancers. *Exp. Mol. Med.* **2017**, *49*, e323. [CrossRef] [PubMed]
30. Gowher, H.; Jeltsch, A. Mammalian DNA methyltransferases: New discoveries and open questions. *Biochem. Soc. Trans.* **2018**, *46*, 1191–1202. [CrossRef]
31. Ren, W.; Gao, L.; Song, J. Structural Basis of DNMT1 and DNMT3A-Mediated DNA Methylation. *Genes* **2018**, *9*, 620. [CrossRef]
32. Venkatesh, S.; Workman, J.L. Histone exchange, chromatin structure and the regulation of transcription. *Nat. Rev. Mol. Cell Biol.* **2015**, *16*, 178–189. [CrossRef]
33. Ebrahimi, V.; Soleimanian, A.; Ebrahimi, T.; Azargun, R.; Yazdani, P.; Eyvazi, S.; Tarhriz, V. Epigenetic modifications in gastric cancer: Focus on DNA methylation. *Gene* **2020**, *742*, 144577. [CrossRef]
34. Furukawa, A.; Wakamori, M.; Arimura, Y.; Ohtomo, H.; Tsunaka, Y.; Kurumizaka, H.; Umehara, T.; Nishimura, Y. Acetylated histone H4 tail enhances histone H3 tail acetylation by altering their mutual dynamics in the nucleosome. *Proc. Natl. Acad. Sci. USA* **2020**, *117*, 19661–19663. [CrossRef] [PubMed]
35. Zhou, Y.; Dun, Y.; Fu, H.; Wang, L.; Pan, X.; Yang, X.; Fang, H. Design, synthesis, and preliminary bioactivity evaluation of *N*-benzylpyrimidin-2-amine derivatives as novel histone deacetylase inhibitor. *Chem. Biol. Drug Des.* **2017**, *90*, 936–942. [CrossRef] [PubMed]
36. Moosavi, A.; Ardekani, A.M. Role of Epigenetics in Biology and Human Diseases. *Iran. Biomed. J.* **2016**, *20*, 246–258.
37. Hayashi-Takanaka, Y.; Kina, Y.; Nakamura, F.; Becking, L.; Nakao, Y.; Nagase, T.; Nozaki, N.; Kimura, H. Histone mod-ification dynamics as revealed by a multicolor immunofluorescence-based single-cell analysis. *J. Cell Sci.* **2020**, *133*. [CrossRef]
38. Obri, A.; Serra, D.; Herrero, L.; Mera, P. The role of epigenetics in the development of obesity. *Biochem. Pharmacol.* **2020**, *177*, 113973. [CrossRef]
39. Blum, R. Stepping inside the realm of epigenetic modifiers. *Biomol. Concepts* **2015**, *6*, 119–136. [CrossRef]
40. Sánchez, R.; Zhou, M.-M. The PHD finger: A versatile epigenome reader. *Trends Biochem. Sci.* **2011**, *36*, 364–372. [CrossRef]
41. Marsh, D.J.; Dickson, K.A. Writing Histone Monoubiquitination in Human Malignancy—The Role of RING Finger E3 Ubiquitin Ligases. *Genes* **2019**, *10*, 67. [CrossRef] [PubMed]
42. Jeltsch, A.; Jurkowska, R.Z. Allosteric control of mammalian DNA methyltransferases—A new regulatory paradigm. *Nucleic Acids Res.* **2016**, *44*, 8556–8575. [CrossRef] [PubMed]
43. Bronner, C.; Krifa, M.; Mousli, M. Increasing role of UHRF1 in the reading and inheritance of the epigenetic code as well as in tumorogenesis. *Biochem. Pharmacol.* **2013**, *86*, 1643–1649. [CrossRef] [PubMed]
44. Rothbart, S.B.; Krajewski, K.; Nady, N.; Tempel, W.; Xue, S.; Badeaux, A.I.; Barsyte-Lovejoy, D.; Martinez, J.Y.; Bedford, M.T.; Fuchs, S.M.; et al. Association of UHRF1 with methylated H3K9 directs the maintenance of DNA methylation. *Nat. Struct. Mol. Biol.* **2012**, *19*, 1155–1160. [CrossRef] [PubMed]
45. Gu, B.; Lee, M.G. Histone H3 lysine 4 methyltransferases and demethylases in self-renewal and differentiation of stem cells. *Cell Biosci.* **2013**, *3*, 39. [CrossRef]
46. Thakore, P.I.; Black, J.B.; Hilton, I.B.; Gersbach, C.A. Editing the epigenome: Technologies for programmable transcription and epigenetic modulation. *Nat. Methods* **2016**, *13*, 127–137. [CrossRef]
47. Laity, J.H.; Lee, B.M.; Wright, P.E. Zinc finger proteins: New insights into structural and functional diversity. *Curr. Opin. Struc. Biol.* **2011**, *11*, 39–46. [CrossRef]
48. Cui, D.; Xu, X. DNA Methyltransferases, DNA Methylation, and Age-Associated Cognitive Function. *Int. J. Mol. Sci.* **2018**, *19*, 1315. [CrossRef]
49. Pradhan, M.; Estève, P.-O.; Chin, H.G.; Samaranayke, M.; Kim, G.-D.; Pradhan, S. CXXC Domain of Human DNMT1 Is Essential for Enzymatic Activity. *Biochem.* **2008**, *47*, 10000–10009. [CrossRef] [PubMed]
50. Zhang, Z.-M.; Liu, S.; Lin, K.; Luo, Y.; Perry, J.J.; Wang, Y.; Song, J. Crystal Structure of Human DNA Methyltransferase 1. *J. Mol. Biol.* **2015**, *427*, 2520–2531. [CrossRef]

51. Dhe-Paganon, S.; Syeda, F.; Park, L. DNA methyl transferase 1: Regulatory mechanisms and implications in health and disease. *Int. J. Biochem. Mol. Boil.* **2011**, *2*, 58–66.
52. Niinuma, T.; Kitajima, H.; Kai, M.; Yamamoto, E.; Yorozu, A.; Ishiguro, K.; Sasaki, H.; Sudo, G.; Toyota, M.; Hatahira, T.; et al. UHRF1 depletion and HDAC inhibition reactivate epigenetically silenced genes in colorectal cancer cells. *Clin. Epigenet.* **2019**, *11*, 1–13. [CrossRef]
53. Argentaro, A.; Yang, J.-C.; Chapman, L.; Kowalczyk, M.S.; Gibbons, R.J.; Higgs, D.R.; Neuhaus, D.; Rhodes, D. Structural consequences of disease-causing mutations in the ATRX-DNMT3-DNMT3L (ADD) domain of the chromatin-associated protein ATRX. *Proc. Natl. Acad. Sci. USA* **2007**, *104*, 11939–11944. [CrossRef] [PubMed]
54. Chédin, F.; Lieber, M.R.; Hsieh, C.-L. The DNA methyltransferase-like protein DNMT3L stimulates de novo methylation by Dnmt3a. *Proc. Natl. Acad. Sci. USA* **2002**, *99*, 16916–16921. [CrossRef]
55. Bourc'His, D.; Xu, G.-L.; Lin, C.-S.; Bollman, B.; Bestor, T.H. DNMT3L and the Establishment of Maternal Genomic Imprints. *Science* **2001**, *294*, 2536–2539. [CrossRef]
56. Suetake, I.; Shinozaki, F.; Miyagawa, J.; Takeshima, H.; Tajima, S. DNMT3L Stimulates the DNA Methylation Activity of DNMT3a and DNMT3b through a Direct Interaction. *J. Biol. Chem.* **2004**, *279*, 27816–27823. [CrossRef]
57. Vlachogiannis, G.; Niederhuth, C.E.; Tuna, S.; Stathopoulou, A.; Viiri, K.; de Rooij, D.G.; Jenner, R.G.; Schmitz, R.J.; Ooi, S.K. The Dnmt3L ADD Domain Controls Cytosine Methylation Establishment during Spermatogenesis. *Cell Rep.* **2015**, *10*, 944–956. [CrossRef]
58. Jin, J.; Guo, Y.; Dong, X.; Liu, J.; He, Y. Methylation-associated silencing of miR-193b improves the radiotherapy sensitivity of esophageal cancer cells by targeting cyclin D1 in areas with zinc deficiency. *Radiother. Oncol.* **2020**, *150*, 104–113. [CrossRef]
59. Mahmood, N.; Rabbani, S.A. DNA Methylation Readers and Cancer: Mechanistic and Therapeutic Applications. *Front. Oncol.* **2019**, *9*, 489. [CrossRef]
60. Hu, Y.-D.; Pang, W.; He, C.-C.; Lu, H.; Liu, W.; Wang, Z.-Y.; Liu, Y.-Q.; Huang, C.-Y.; Jiang, Y.-G. The cognitive impairment induced by zinc deficiency in rats aged 0~2 months related to BDNF DNA methylation changes in the hippocampus. *Nutr. Neurosci.* **2016**, *20*, 519–525. [CrossRef] [PubMed]
61. Dandi, E.; Kalamari, A.; Touloumi, O.; Lagoudaki, R.; Nousiopoulou, E.; Simeonidou, C.; Spandou, E.; Tata, D.A. Beneficial effects of environmental enrichment on behavior, stress reactivity and synaptophysin/BDNF expression in hippocampus following early life stress. *Int. J. Dev. Neurosci.* **2018**, *67*, 19–32. [CrossRef] [PubMed]
62. Miranda, M.; Morici, J.F.; Zanoni, M.B.; Bekinschtein, P. Brain-Derived Neurotrophic Factor: A Key Molecule for Memory in the Healthy and the Pathological Brain. *Front. Cell. Neurosci.* **2019**, *13*, 363. [CrossRef] [PubMed]
63. Jiang, Y.-G.; Wang, Y.-H.; Zhang, H.; Wang, Z.-Y.; Liu, Y.-Q. Effects of early-life zinc deficiency on learning and memory in offspring and the changes in DNA methylation patterns. *Nutr. Neurosci.* **2020**, 1–10. [CrossRef]
64. Asai, A.; Konno, M.; Koseki, J.; Taniguchi, M.; Vecchione, A.; Ishii, H. One-carbon metabolism for cancer diagnostic and therapeutic approaches. *Cancer Lett.* **2020**, *470*, 141–148. [CrossRef] [PubMed]
65. Clare, C.E.; Brassington, A.H.; Kwong, W.Y.; Sinclair, K.D. One-Carbon Metabolism: Linking Nutritional Biochemistry to Epigenetic Programming of Long-Term Development. *Annu. Rev. Anim. Biosci.* **2019**, *7*, 263–287. [CrossRef]
66. Choi, S.-W.; Friso, S. Epigenetics: A New Bridge between Nutrition and Health. *Adv. Nutr.* **2010**, *1*, 8–16. [CrossRef]
67. Koutmos, M.; Pejchal, R.; Bomer, T.M.; Matthews, R.G.; Smith, J.L.; Ludwig, M.L. Metal active site elasticity linked to activation of homocysteine in methionine synthases. *Proc. Natl. Acad. Sci. USA* **2008**, *105*, 3286–3291. [CrossRef] [PubMed]
68. Jing, M.; Rech, L.; Wu, Y.; Goltz, D.; Taylor, C.G.; House, J.D. Effects of zinc deficiency and zinc supplementation on homocysteine levels and related enzyme expression in rats. *J. Trace Elem. Med. Biol.* **2015**, *30*, 77–82. [CrossRef] [PubMed]
69. Danchin, A.; Sekowska, A.; You, C. One-carbon metabolism, folate, zinc and translation. *Microb. Biotechnol.* **2020**, *13*, 899–925. [CrossRef]
70. Castro, C.; Millian, N.S.; Garrow, T.A. Liver betaine-homocysteine S-methyltransferase activity undergoes a redox switch at the active site zinc. *Arch. Biochem. Biophys.* **2008**, *472*, 26–33. [CrossRef]
71. Wu, L.; Zhou, X.; Linli, H.; He, J.; Huang, L.; Ouyang, Z.; He, L.; Wei, T.; He, Q. Improved Sp1 and Betaine Homocysteine-S-Methyltransferase Expression and Homocysteine Clearance Are Involved in the Effects of Zinc on Oxidative Stress in High-Fat-Diet-Pretreated Mice. *Biol. Trace Elem. Res.* **2018**, *184*, 436–441. [CrossRef] [PubMed]
72. Sawan, C.; Herceg, Z. Histone modifications and cancer. *Adv. Genet.* **2010**, *70*, 57–85. [CrossRef] [PubMed]
73. Wood, A.; Shilatifard, A. Posttranslational Modifications of Histones by Methylation. *Adv. Protein Chem.* **2004**, *67*, 201–222. [CrossRef]
74. Qian, C.; Zhou, M.-M. SET domain protein lysine methyltransferases: Structure, specificity and catalysis. *Cell. Mol. Life Sci. CMLS* **2006**, *63*, 2755–2763. [CrossRef]
75. Elgin, S.C.; Reuter, G. Position-Effect Variegation, Heterochromatin Formation, and Gene Silencing in Drosophila. *Cold Spring Harb. Perspect. Biol.* **2013**, *5*, a017780. [CrossRef] [PubMed]
76. Min, J.; Zhang, X.; Cheng, X.; Grewal, S.I.; Xu, R.-M. Structure of the SET domain histone lysine methyltransferase Clr4. *Nat. Struct. Biol.* **2002**, *9*, 828–832. [CrossRef]
77. Zhang, X.; Tamaru, H.; Khan, S.I.; Horton, J.R.; Keefe, L.J.; Selker, E.U.; Cheng, X. Structure of the Neurospora SET Domain Protein DIM-5, a Histone H3 Lysine Methyltransferase. *Cell* **2002**, *111*, 117–127. [CrossRef]

78. Ruesch, C.E.; Ramakrishnan, M.; Park, J.; Li, N.; Chong, H.S.; Zaman, R.; Joska, T.M.; Belden, W.J. The Histone H3 Lysine 9 Methyltransferase DIM-5 Modifies Chromatin atfrequencyand Represses Light-Activated Gene Expression. *G3 Genes Genomes Genet.* **2015**, *5*, 93–101. [CrossRef]
79. Dillon, S.C.; Zhang, X.; Trievel, R.C.; Cheng, X. The SET-domain protein superfamily: Protein lysine methyltransferases. *Genome Biol.* **2005**, *6*, 227. [CrossRef]
80. Li, B.; Zheng, Y.; Yang, L. The Oncogenic Potential of SUV39H2: A Comprehensive and Perspective View. *J. Cancer* **2019**, *10*, 721–729. [CrossRef] [PubMed]
81. Hublitz, P.; Albert, M.; Hfmpeters, A. Mechanisms of transcriptional repression by histone lysine methylation. *Int. J. Dev. Biol.* **2009**, *53*, 335–354. [CrossRef] [PubMed]
82. Hosseini, A.; Minucci, S. A comprehensive review of lysine-specific demethylase 1 and its roles in cancer. *Epigenomics* **2017**, *9*, 1123–1142. [CrossRef]
83. Yan, M.; Yang, X.; Wang, H.; Shao, Q. The critical role of histone lysine demethylase KDM2B in cancer. *Am. J. Transl. Res.* **2018**, *10*, 2222–2233.
84. Karytinos, A.; Forneris, F.; Profumo, A.; Ciossani, G.; Battaglioli, E.; Binda, C.; Mattevi, A. A Novel Mammalian Flavin-dependent Histone Demethylase. *J. Biol. Chem.* **2009**, *284*, 17775–17782. [CrossRef] [PubMed]
85. Burg, J.M.; Link, J.E.; Morgan, B.S.; Heller, F.J.; Hargrove, A.E.; McCafferty, D.G. KDM1 class flavin-dependent protein lysine demethylases. *Biopolymers* **2015**, *104*, 213–246. [CrossRef]
86. Zhang, Q.; Qi, S.; Xu, M.; Yu, L.; Tao, Y.; Deng, Z.; Wu, W.; Li, J.; Chen, Z.; Wong, J. Structure-function analysis reveals a novel mechanism for regulation of histone demethylase LSD2/AOF1/KDM1b. *Cell Res.* **2012**, *23*, 225–241. [CrossRef] [PubMed]
87. Isshiki, Y.; Nakajima-Takagi, Y.; Oshima, M.; Aoyama, K.; Rizk, M.; Kurosawa, S.; Saraya, A.; Kondo, T.; Sakaida, E.; Nakaseko, C.; et al. KDM2B in polycomb repressive complex 1.1 functions as a tumor suppressor in the initiation of T-cell leukemogenesis. *Blood Adv.* **2019**, *3*, 2537–2549. [CrossRef]
88. Chrun, E.S.; Modolo, F.; Daniel, F.I. Histone modifications: A review about the presence of this epigenetic phenomenon in carcinogenesis. *Pathol. Res. Pract.* **2017**, *213*, 1329–1339. [CrossRef]
89. Calcagno, D.Q.; Wisnieski, F.; Mota, E.R.D.S.; De Sousa, S.B.M.; Da Silva, J.M.C.; Leal, M.F.; Gigek, C.O.; Santos, L.C.; Rasmussen, L.T.; Assumpção, P.P.; et al. Role of histone acetylation in gastric cancer: Implications of dietetic compounds and clinical perspectives. *Epigenomics* **2019**, *11*, 349–362. [CrossRef]
90. Zhou, Z.; Lin, Z.; Pang, X.; Tariq, M.A.; Ao, X.; Li, P.; Wang, J. Epigenetic regulation of long non-coding RNAs in gastric cancer. *Oncotarget* **2017**, *9*, 19443–19458. [CrossRef] [PubMed]
91. Yuan, H.; Marmorstein, R. Histone acetyltransferases: Rising ancient counterparts to protein kinases. *Biopolymers* **2012**, *99*, 98–111. [CrossRef]
92. Yang, X.-J.; Ullah, M.F. MOZ and MORF, two large MYSTic HATs in normal and cancer stem cells. *Oncogene* **2007**, *26*, 5408–5419. [CrossRef]
93. Katsumoto, T.; Yoshida, N.; Kitabayashi, I. Roles of the histone acetyltransferase monocytic leukemia zinc finger protein in normal and malignant hematopoiesis. *Cancer Sci.* **2008**, *99*, 1523–1527. [CrossRef] [PubMed]
94. Yang, X.-J. MOZ and MORF acetyltransferases: Molecular interaction, animal development and human disease. *Biochim. Biophys. Acta (BBA) Mol. Cell Res.* **2015**, *1853*, 1818–1826. [CrossRef]
95. Seto, E.; Yoshida, M. Erasers of Histone Acetylation: The Histone Deacetylase Enzymes. *Cold Spring Harb. Perspect. Biol.* **2014**, *6*, a018713. [CrossRef]
96. D'Mello, S.R. Histone deacetylases 1, 2 and 3 in nervous system development. *Curr. Opin. Pharmacol.* **2020**, *50*, 74–81. [CrossRef] [PubMed]
97. Asfaha, Y.; Schrenk, C.; Avelar, L.A.A.; Hamacher, A.; Pflieger, M.; Kassack, M.U.; Kurz, T. Recent advances in class IIa histone deacetylases research. *Bioorg. Med. Chem.* **2019**, *27*, 115087. [CrossRef]
98. Athanasopoulos, D.; Karagiannis, G.; Tsolaki, M. Recent Findings in Alzheimer Disease and Nutrition Focusing on Epigenetics. *Adv. Nutr.* **2016**, *7*, 917–927. [CrossRef] [PubMed]
99. Michan, S.; Sinclair, D. Sirtuins in mammals: Insights into their biological function. *Biochem. J.* **2007**, *404*, 1–13. [CrossRef]
100. Lombardi, P.M.; Cole, K.E.; Dowling, D.P.; Christianson, D.W. Structure, mechanism, and inhibition of histone deacetylases and related metalloenzymes. *Curr. Opin. Struct. Biol.* **2011**, *21*, 735–743. [CrossRef] [PubMed]
101. Lindskog, S. Structure and mechanism of carbonic anhydrase. *Pharmacol. Ther.* **1997**, *74*, 1–20. [CrossRef]
102. Liu, H.; Zhang, F.; Wang, K.; Tang, X.; Wu, R. Conformational dynamics and allosteric effect modulated by the unique zinc-binding motif in class IIa HDACs. *Phys. Chem. Chem. Phys.* **2019**, *21*, 12173–12183. [CrossRef]
103. Yahaya, T. Role of Epigenetics in the Pathogenesis and Management of Type 2 Diabetes Mellitus. *Transl. Univ. Toledo J. Med. Sci.* **2019**, *6*, 20–28. [CrossRef]
104. Yamato, E. High dose of histone deacetylase inhibitors affects insulin secretory mechanism of pancreatic beta cell line. *Endocr. Regul.* **2018**, *52*, 21–26. [CrossRef] [PubMed]
105. Christensen, D.P.; Dahllöf, M.; Lundh, M.; Rasmussen, D.N.; Nielsen, M.D.; Billestrup, N.; Grunnet, L.G.; Mandrup-Poulsen, T. Histone Deacetylase (HDAC) Inhibition as a Novel Treatment for Diabetes Mellitus. *Mol. Med.* **2011**, *17*, 378–390. [CrossRef]
106. Chen, J.; Li, D.; Li, W.; Yin, J.; Zhang, Y.; Yuan, Z.; Gao, C.; Liu, F.; Jiang, Y. Design, synthesis and anticancer evaluation of acridine hydroxamic acid derivatives as dual Topo and HDAC inhibitors. *Bioorg. Med. Chem.* **2018**, *26*, 3958–3966. [CrossRef]

107. Yuan, Z.; Sun, Q.; Li, D.; Miao, S.; Chen, S.; Song, L.; Gao, C.; Chen, Y.; Tan, C.; Jiang, Y. Design, synthesis and anticancer potential of NSC-319745 hydroxamic acid derivatives as DNMT and HDAC inhibitors. *Eur. J. Med. Chem.* **2017**, *134*, 281–292. [CrossRef] [PubMed]
108. Heaton, S.M.; Borg, N.A.; Dixit, V.M. Ubiquitin in the activation and attenuation of innate antiviral immunity. *J. Exp. Med.* **2016**, *213*, 1–13. [CrossRef] [PubMed]
109. Hammond-Martel, I.; Yu, H.; Affar, E.B. Roles of ubiquitin signaling in transcription regulation. *Cell. Signal.* **2012**, *24*, 410–421. [CrossRef]
110. Callis, J. The Ubiquitination Machinery of the Ubiquitin System. *Arab. Book* **2014**, *12*, e0174. [CrossRef] [PubMed]
111. Borden, K.L.; Freemont, P.S. The RING finger domain: A recent example of a sequence—Structure family. *Curr. Opin. Struct. Biol.* **1996**, *6*, 395–401. [CrossRef]
112. Uckelmann, M.; Sixma, T.K. Histone ubiquitination in the DNA damage response. *DNA Repair* **2017**, *56*, 92–101. [CrossRef] [PubMed]
113. Wu, L.; Zee, B.M.; Wang, Y.; Garcia, B.A.; Dou, Y. The RING Finger Protein MSL2 in the MOF Complex Is an E3 Ubiquitin Ligase for H2B K34 and Is Involved in Crosstalk with H3 K4 and K79 Methylation. *Mol. Cell* **2011**, *43*, 132–144. [CrossRef] [PubMed]
114. Lang, G.; Bonnet, J.; Umlauf, D.; Karmodiya, K.; Koffler, J.; Stierle, M.; Devys, D.; Tora, L. The Tightly Controlled Deubiquitination Activity of the Human SAGA Complex Differentially Modifies Distinct Gene Regulatory Elements. *Mol. Cell. Biol.* **2011**, *31*, 3734–3744. [CrossRef]
115. Morgan, M.T.; Haj-Yahya, M.; Ringel, A.E.; Bandi, P.; Brik, A.; Wolberger, C. Structural basis for histone H2B deubiquitination by the SAGA DUB module. *Science* **2016**, *351*, 725–728. [CrossRef]
116. Koehler, C.; Bonnet, J.; Stierle, M.; Romier, C.; Devys, D.; Kieffer, B. DNA Binding by Sgf11 Protein Affects Histone H2B Deubiquitination by Spt-Ada-Gcn5-Acetyltransferase (SAGA). *J. Biol. Chem.* **2014**, *289*, 8989–8999. [CrossRef]
117. Hudson, N.O.; Buck-Koehntop, B.A. Zinc Finger Readers of Methylated DNA. *Molecules* **2018**, *23*, 2555. [CrossRef]
118. Cassandri, M.; Smirnov, A.; Novelli, F.; Pitolli, C.; Agostini, M.; Malewicz, M.; Melino, G.; Raschellà, G. Zinc-finger proteins in health and disease. *Cell Death Discov.* **2017**, *3*, 17071. [CrossRef] [PubMed]
119. Liu, Y.; Zhang, X.; Blumenthal, R.M.; Cheng, X. A common mode of recognition for methylated CpG. *Trends Biochem. Sci.* **2013**, *38*, 177–183. [CrossRef]
120. Kribelbauer, J.F.; Lu, X.-J.; Rohs, R.; Mann, R.S.; Bussemaker, H.J. Toward a Mechanistic Understanding of DNA Methylation Readout by Transcription Factors. *J. Mol. Biol.* **2020**, *432*, 1801–1815. [CrossRef]
121. Shimbo, T.; Wade, P.A. Proteins That Read DNA Methylation. *Adv. Exp. Med. Biol.* **2016**, *945*, 303–320. [CrossRef] [PubMed]
122. Zhou, T.; Xiong, J.; Wang, M.; Yang, N.; Wong, J.; Zhu, B.; Xu, R.-M. Structural Basis for Hydroxymethylcytosine Recognition by the SRA Domain of UHRF2. *Mol. Cell* **2014**, *54*, 879–886. [CrossRef] [PubMed]
123. Yu, M.; Hon, G.C.; Szulwach, K.E.; Song, C.-X.; Zhang, L.; Kim, A.; Li, X.; Dai, Q.; Shen, Y.; Park, B.; et al. Base-Resolution Analysis of 5-Hydroxymethylcytosine in the Mammalian Genome. *Cell* **2012**, *149*, 1368–1380. [CrossRef] [PubMed]
124. Wu, H.; D'Alessio, A.C.; Ito, S.; Wang, Z.; Cui, K.; Zhao, K.; Sun, Y.E.; Zhang, Y. Genome-wide analysis of 5-hydroxymethylcytosine distribution reveals its dual function in transcriptional regulation in mouse embryonic stem cells. *Genes Dev.* **2011**, *25*, 679–684. [CrossRef] [PubMed]
125. Yun, M.; Wu, J.; Workman, J.L.; Li, B. Readers of histone modifications. *Cell Res.* **2011**, *21*, 564–578. [CrossRef] [PubMed]
126. Yap, K.L.; Zhou, M.-M. Structure and Mechanisms of Lysine Methylation Recognition by the Chromodomain in Gene Transcription. *Biochemistry* **2011**, *50*, 1966–1980. [CrossRef]
127. Li, H.; Ilin, S.; Wang, W.; Duncan, E.M.; Wysocka, J.; Allis, C.D.; Patel, D.J. Molecular basis for site-specific read-out of histone H3K4me3 by the BPTF PHD finger of NURF. *Nat. Cell Biol.* **2006**, *442*, 91–95. [CrossRef]
128. Jurkowski, T.P.; Ravichandran, M.; Stepper, P. Synthetic epigenetics—Towards intelligent control of epigenetic states and cell identity. *Clin. Epigenet.* **2015**, *7*, 18. [CrossRef]
129. Cui, C.; Gan, Y.; Gu, L.; Wilson, J.; Liu, Z.; Zhang, B.; Deng, D. P16-specific DNA methylation by engineered zinc finger methyltransferase inactivates gene transcription and promotes cancer metastasis. *Genome Biol.* **2015**, *16*, 1–12. [CrossRef] [PubMed]
130. Meng, H.-X.; Miao, S.-S.; Chen, K.; Li, H.-N.; Yao, G.; Geng, J.; Wang, H.; Shi, Q.-T.; He, J.; Mao, X.; et al. Association of p16 as Prognostic Factors for Oropharyngeal Cancer: Evaluation of p16 in 1470 Patients for a 16 Year Study in Northeast China. *BioMed Res. Int.* **2018**, *2018*, 1–8. [CrossRef]
131. Chen, H.; Kazemier, H.G.; De Groote, M.L.; Ruiters, M.H.J.; Xu, G.-L.; Rots, M.G. Induced DNA demethylation by targeting Ten-Eleven Translocation 2 to the human ICAM-1 promoter. *Nucleic Acids Res.* **2014**, *42*, 1563–1574. [CrossRef] [PubMed]

life

MDPI

*Article*

# Integrative Analysis Identified Key Schizophrenia Risk Factors from an Abnormal Behavior Mouse Gene Set

**Miao Chen [1], Weidi Wang [1], Weicheng Song [1], Wei Qian [1] and Guan Ning Lin [1,2,*]**

[1] School of Biomedical Engineering, Shanghai Jiao Tong University, Shanghai 200030, China; chenmiao95@sjtu.edu.cn (M.C.); wwd@smhc.org.cn (W.W.); goubegou@sjtu.edu.cn (W.S.); kentergav@sjtu.edu.cn (W.Q.)

[2] Engineering Research Center of Digital Medicine and Clinical Translational, Ministry of Education of China, Shanghai 200030, China

* Correspondence: nickgnlin@sjtu.edu.cn

**Abstract:** Schizophrenia (SCZ) is a severe chronic psychiatric illness with heterogeneous symptoms. However, the pathogenesis of SCZ is unclear, and the number of well-defined SCZ risk factors is limited. We hypothesized that an abnormal behavior (AB) gene set verified by mouse model experiments can be used to better understand SCZ risks. In this work, we carried out an integrative bioinformatics analysis to study two types of risk genes that are either differentially expressed (DEGs) in the case-control study data or carry reported SCZ genetic variants (MUTs). Next, we used RNA-Seq expression data from the hippocampus (HIPPO) and dorsolateral prefrontal cortex (DLPFC) to define the key genes affected by different types (DEGs and MUTs) in different brain regions (DLPFC and HIPPO): DLPFC-kDEG, DLPFC-kMUT, HIPPO-kDEG, and HIPPO-kMUT. The four hub genes (SHANK1, SHANK2, DLG4, and NLGN3) of the biological functionally enriched terms were strongly linked to SCZ via gene co-expression network analysis. Then, we observed that specific spatial expressions of DLPFC-kMUT and HIPPO-kMUT were convergent in the early stages and divergent in the later stages of development. In addition, all four types of key genes showed significantly larger average protein–protein interaction degrees than the background. Comparing the different cell types, the expression of four types of key genes showed specificity in different dimensions. Together, our results offer new insights into potential risk factors and help us understand the complexity and regional heterogeneity of SCZ.

**Keywords:** schizophrenia; abnormal behavior gene set; region; differentially expressed genes; *de novo* mutation; copy number variant

**Citation:** Chen, M.; Wang, W.; Song, W.; Qian, W.; Lin, G.N. Integrative Analysis Identified Key Schizophrenia Risk Factors from an Abnormal Behavior Mouse Gene Set. *Life* **2021**, *11*, 172. https://doi.org/10.3390/life11020172

Academic Editors: Jong Hyuk Yoon and Chiara Villa

Received: 17 December 2020
Accepted: 20 February 2021
Published: 23 February 2021



## 1. Introduction

Schizophrenia (SCZ) is a severe chronic psychiatric disorder with a prevalence of <1% [1] and a heritability of 0.8 to 0.85 [2]. SCZ is characterized by positive symptoms, including delusions, hallucinations, and abnormal behavior, as well as negative symptoms, including social dysfunction, lack of motivation, and disorganized speech [3,4]. However, the genetic basis of SCZ remains largely undetermined, and the associations between SCZ's clinical manifestation and genetics are unclear. Thus, identifying a potential genetic basis for SCZ is needed to understand how these complex components contribute to the disorder.

One of the primary goals of genomic medicine is to identify genetic risk factors for diseases. An important method used for discovering the genetic basis of diseases is based on using experimental mouse models to translate information from animals to humans. The abnormal behavior gene set (MP:0004924) derived from the Mouse Genome Informatics (MGI) database [5] is defined as any anomaly in the actions, reactions, or performance of an organism in response to external or internal stimuli compared to the controls. It is still a challenge to elucidate SCZ genes based on the evidence indicated by the abnormal behavior (AB) gene set.

To our knowledge, limited research has been carried out to systematically investigate which genes in the AB gene set are truly associated with SCZ. Today, the incremental growth of genetic studies provides another chance for using multi-omics integrative analysis to understand the etiology of SCZ, which has already resulted in hundreds of genetic loci being associated with SCZ [6]. Meanwhile, the links between psychiatric disorders and mutations, including copy number variants (CNVs) and *de novo* mutations (DNMs), have also been firmly established [7,8]. The Schizophrenia Exome Sequencing Meta-analysis (SCHEMA) consortium made an extensive effort to identify 10 exome-wide significant genes, with 24,248 cases and 97,322 controls [9]. Since the 22q11.2 deletion syndrome was first linked with SCZ [10], the research on SCZ and associated mutations has rapidly progressed. So far, the evidence for the roles of CNVs and DNMs in SCZ is overwhelming [11–15], as summarized in mutation databases such as PsyMuKB [16]. In addition, numerous SCZ transcriptome studies have identified various differentially expressed genes (DEGs) between patients and healthy controls [17,18], especially in brain regions such as the hippocampus (HIPPO) [17] and dorsolateral prefrontal cortex (DLPFC) [18,19]. However, determining the biological significance behind different brain regions is still a challenging task for SCZ research. In summary, both types of identified genes—genes with genetic variants (MUTs) and those with differentially expressed genes—may have different contributions to SCZ and may involve convergent or divergent biological functions. Analysis using the two types of gene sets could serve as a viable investigation method for identifying potential disorder risk factors based on the AB genes.

To better understand (1) which AB genes are the key genes of SCZ, (2) how the disruptions of these key genes in different brain regions are involved in SCZ, and (3) whether DEGs and MUTs are involved in convergent or divergent biological functions, we performed an integrative analysis (Figure 1). Two types of risk genes (DEGs and MUTs) were separately overlapped with AB genes from the PsyMuKB database. Then, we constructed the co-expression networks separately in DLPFC and HIPPO using the RNA-Seq expression data from BrainSeq Phase 2 [17]. Consequently, we identified four types of key genes affected by different types (DEGs and MUTs) in different brain regions (DLPFC and HIPPO): DLPFC-kDEG, DLPFC-kMUT, HIPPO-kDEG, and HIPPO-kMUT. Four types of key genes from the AB gene set were identified for subsequent analysis, including brain function, the protein–protein interaction (PPI) network, and spatial and cell-type-specific expression patterns, to uncover all possible underlying genetic links. Together, our results indicate that the key genes found by our integrative analysis could help in understanding and studying the potential risk genes in SCZ.

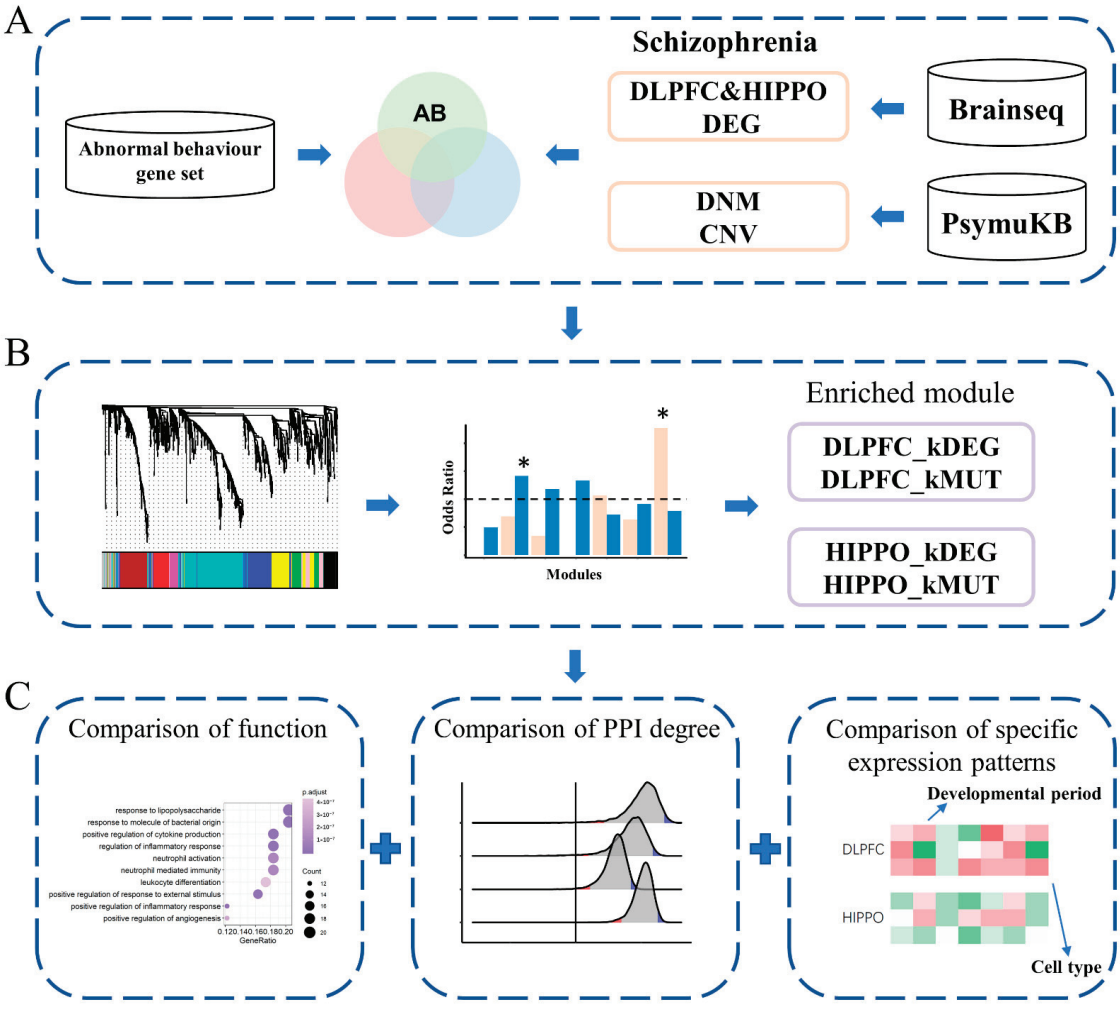


**Figure 1.** Flowchart of the study. (**A**) Data collection and filtration. RNA-Seq data analyzed in this study were obtained from BrainSeq Phase 2, which was also used to identify differentially expressed genes (DEGs). Copy number variants (CNVs) and *de novo* mutations (DNMs) associated with schizophrenia (SCZ) and the abnormal behavior (AB) gene set were collected from PsymuKB. DEGs and MUTs separately overlapped with the AB set. (**B**) The two co-expression networks were constructed from the AB gene expression profiles of two different brain regions separately (DLPFC and HIPPO). A star * with a significant *p*-value marks the identified module. (**C**) The integrative analyses pipeline, including protein–protein interaction (PPI) analysis, brain function, spatial-specific and cell-type-specific expression patterns, was followed. DLPFC, dorsolateral prefrontal cortex; HIPPO, hippocampus.

## 2. Materials and Methods

### *2.1. Data Collection and Filtration*

The RNA-Seq data analyzed in this study were obtained from BrainSeq Phase 2 [17], downloaded from http://eqtl.brainseq.org/phase2 (accessed on 17 December 2020) and consisting of 286 SCZ cases and 614 control samples. We used all 284 SCZ cases and 460 control samples over 18 years of age for subsequent analysis. Then, we chose genes that were expressed in the brain (defined as the average RPKM > 0.1 in BrainSeq Phase 2 [17])

for further analysis. The AB gene set (Table S1), CNV (Table S2), and DNM (Table S3) data for SCZ were collected from the PsyMuKB [16] in-house database (URL: http://www.psymukb.net/, accessed on 17 December 2020). AB genes with an average RPKM < 0.1 in BrainSeq were also removed.

### *2.2. Detection of Differentially Expressed Genes*

Differential expression was assessed using the DESeq2 [20] package in R between SCZ cases and control samples separately by tissue from 2 brain regions: HIPPO and DLPFC. The significance threshold was an adjusted *p*-value of <0.05 and a $\log_2$ fold change (FC) value of >1.2.

### *2.3. Weighted Co-Expression Network Construction and Key Module Identification*

The weighted co-expression network was built using the WGCNA [21] package in R. The networks were constructed separately by tissues, and AB genes with evidence of robust expression (see above) were included in the network. Then, network construction was performed using the blockwiseModules function. The soft-thresholding power was chosen based on the smallest threshold that resulted in a scale-free R2 fit of 0.9. We also set the minimum module size to 30 genes and the minimum height for merging modules to 0.25. Key modules were identified by the odds ratio. The module of each tissue with the highest odds ratio and *p*-value of <0.01 (Chi-square test) was chosen as the significant module for subsequent analysis.

### *2.4. Gene Ontology and Gene Set Enrichment Analyses*

Unless otherwise noted, we used the enrichGO function from clusterProfiler [22] for gene ontology [23] enrichment analyses with a pvalueCutoff of 0.01 and a qvalueCutoff of 0.05. The gene-concept network was plotted using the cnetplot function of clusterProfiler.

### *2.5. Analysis of Spatial/Cell-type Specific Expression of Genes*

We applied the Expression Weighted Celltype Enrichment (EWCE) R package [24], a bootstrap enrichment tool based on the specificity matrix, to conduct an enrichment analysis on two datasets: Brainspan [25] for the period and region analyses and Dronc [26] data for the adult brain cell type analysis. Specificity used the definition described by Saunders et al. (2018) [27]. We first calculated the specificity matrix of 2 single-cell datasets with the "generate.celltype.data" R function. Next, enrichment of all 4 types of genes was tested with the "bootstrap.enrichment.test" R function. The background gene list was defined by all genes annotated in the tested single-cell dataset.

### *2.6. Brain-Expressed PPI Statistics for Disease Genes*

We calculated the numbers of PPI partners with other brain-expressed genes (bPPI) in the BioGRID [28] database for all brain-expressed genes. We then compared the average number of PPI partners for each gene type with other brain-expressed genes referred to as the background by bootstrapping 10,000 times. *p*-values were calculated using a 2-tailed hypothesis test. For example, DLPFC-kDEG contained 99 genes with an average of 35.93 PPI partners. We randomly chose 99 genes from among all the brain-expressed genes and calculated their average number of partners 10,000 times. In 9962 bootstraps, the average number was smaller than 35.93. Since the average number was larger than 35.93 in only 38 bootstraps, the *p*-value was 0.0038 for the alternative hypothesis "larger."

## 3. Results

### *3.1. Abnormal Behavior Genes Were Significantly Enriched in SCZ Gene Sets*

We focused on genes harboring mutations and differentially expressed genes in SCZ patients' brains to define the subsets of different kinds of functional genes in SCZ. We first collected genes with genetic variants (MUTs), including CNVs and the DNMs of SCZ from PsyMuKB [16], as well as 2363 and 2981 genes that were identified to be differentially

expressed between an adult with schizophrenia and a healthy control in DLPFC and HIPPO, respectively, with p.adj <0.05 and fold changes >1.2. Next, we extracted the AB gene set from PsyMuKB [16]. We observed a significant overlap between the AB gene set and the DNM gene (p.adj = $4.04 \times 10^{-38}$ calculated using a hypergeometric test and adjusted with a Bonferroni test) but no significant overlap between the AB gene set and the CNV gene (p.adj = 0.138 calculated by a hypergeometric test and adjusted by a Bonferroni test) (Figure 2A). For DEGs, significant results were found for both overlaps between the AB gene set and DEGs in HIPPO (p.adj = $3.36 \times 10^{-11}$ calculated by a hypergeometric test and adjusted by a Bonferroni test) and DLPFC (p.adj = $1.11 \times 10^{-4}$ calculated by a hypergeometric test and adjusted by a Bonferroni test) (Figure 2B). In summary, except for the overlap between the AB gene set and the CNV gene, the other three overlaps were all significant.

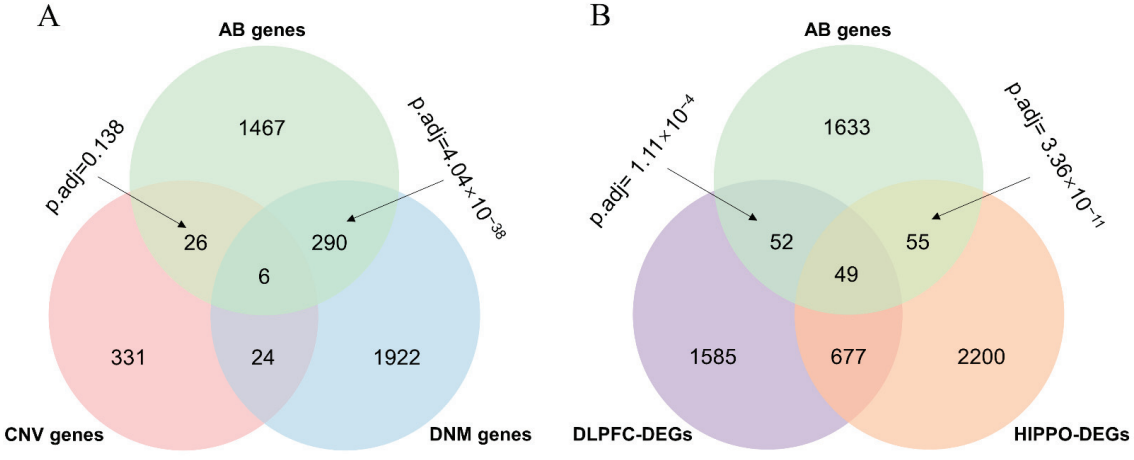


**Figure 2.** Overlaps between the AB gene set and different types of SCZ risk genes. (**A**) Venn diagram of AB and MUT by different types (CNV and DNM). (**B**) Venn diagram of AB and DEGs by brain region (DLPFC and HIPPO). The *p*-value was calculated by a hypergeometric test and adjusted by the Bonferroni method. AB genes, abnormal behavior gene set; CNV genes, genes associated with copy number variation; DNM genes, genes associated with *de novo* mutation; DLPFC-DEGs, differentially expressed genes detected in dorsolateral prefrontal cortex; HIPPO-DEGs, differentially expressed genes detected in hippocampus.

### *3.2. Two Significant Modules Were Identified in DLPFC*

We performed a weighted gene co-expression network analysis (WGCNA) [21] to extract the biological information embedded in the multidimensional transcriptome dataset, which allowed us to identify modules of co-expressed genes. To identify discrete groups of co-expressed genes showing transcriptional differences between SCZ and the controls, we constructed a co-expression network using RNA-Seq data composed of both SCZ and control samples. Using a combination of SCZ cases (N = 152) and controls (N = 222) with the RNA-Seq expression data in the DLPFC from BrainSeq Phase 2 [17], 10 modules were identified, which were first examined for enrichment of DEGs and MUTs (Figure 3A). We found that DEGs overlapping with the AB gene set were significantly enriched in the black module (odds ratio (OR) = 5.189, Chi-square test $p = 1.889 \times 10^{-19}$) (Figure 3B). The MUTs of SCZ overlapped with the AB gene set and were significantly enriched in the pink module (OR = 1.768, $p = 0.006$) (Figure 3B). No significance was observed for any of the other modules. Thus, we defined genes within the black module as the keys of differentially expressed genes in DLPFC (DLPFC-kDEG) Likewise, genes within the pink module were considered the key genes affected by mutations in DLPFC (DLPFC-kMUT).

We next explored whether DLPFC-kDEG and DLPFC-kMUT diverged in their biological or neuronal functions. We performed Gene Ontology–Biological Pathway (GO-BP) analysis on DLPFC-kDEG and DLPFC-kMUT alone using the clusterProfiler [22] R package. DLPFC-kDEG was significantly enriched with gene ontology terms related to its response to lipopolysaccharides, positive regulation of cytokine production, and inflammatory response, among other factors. (Figure 3C). It was reported that stimulation of the peripheral blood mononuclear cells by lipopolysaccharides leads to the release of cytokines and other inflammatory mediators [29]. Schizophrenic patients featured an inflammatory cytokine profile and regulatory cytokines. The severity of symptoms may affect abnormal cytokine levels in these patients [30]. DLPFC-kMUT, on the other hand, was enriched in gene ontology categories related to the synapses, including modulation of chemical synaptic transmission, regulation of trans-synaptic signaling, and synapse organization (Figure 3D). We also found that 28 genes of DLPFC-kMUT overlapped with a synaptic gene group associated with SCZ, as identified by Lips et al. [31].

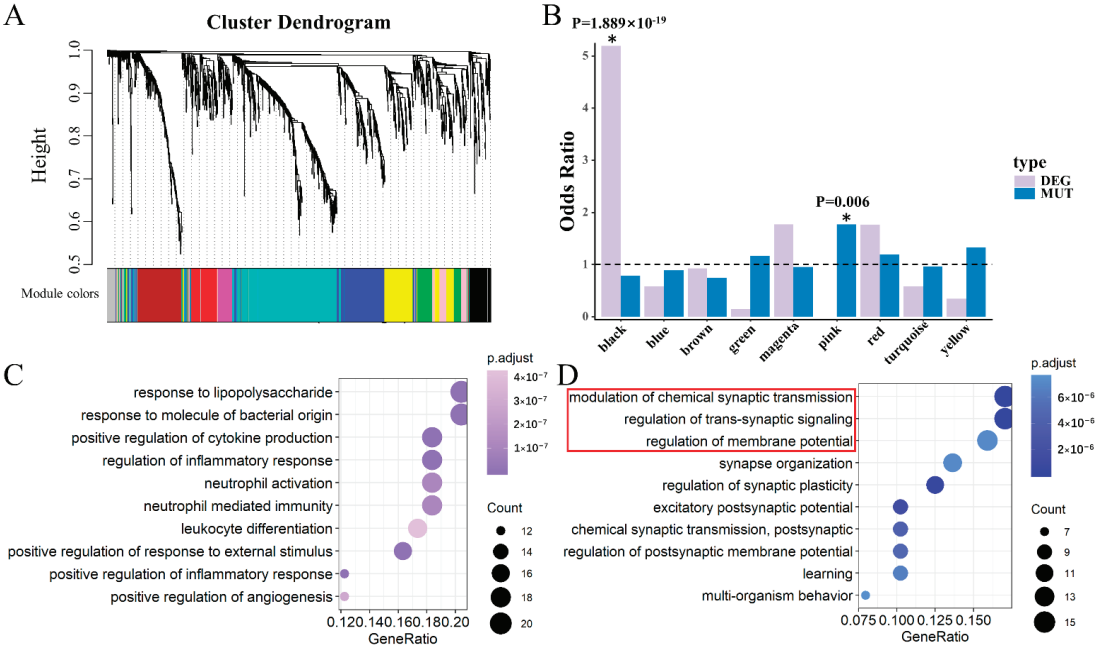


**Figure 3.** Module identification and functional enrichment in DLPFC. (**A**) Clustering dendrograms of the AB gene set according to gene expression data in DLPFC, with dissimilarity based on the topological overlap. Each colored row represents a color-coded module that contains a group of highly connected genes. In total, 10 modules were identified. (**B**) Modules are listed on the *x*-axis, and the *y*-axis indicates the odds ratio. The horizontal line indicates the threshold of y = 1, which distinguishes the modules enriched in a greater proportion by the target genes. The *p*-value was calculated by a Chi-square distribution test. A star with a significant *p*-value marks two identified modules. (**C**) GO-BP analysis for the black module genes (DLPFC-kDEG) showing the top 10 enriched gene ontology categories. Pathway names are shown on the left, and the color of dots on the right represents the adjusted *p*-value of the corresponding pathway. (**D**) Gene Ontology–Biological Pathway (GO-BP) analysis for pink module genes (DLPFC-kMUT) showing the top 10 enriched gene ontology categories. The red box indicates the GO terms that were the same as those in the blue module in HIPPO.

### *3.3. Two Significant Modules Were Identified in HIPPO*

To identify the key genes in HIPPO, we also constructed a co-expression network using similar analyses in DLPFC. With a combination of SCZ cases (N = 132) and controls (N = 238)

using RNA-Seq data in the HIPPO from BrainSeq Phase 2 [17], eight modules were identified (Figure 4A). The yellow module was enriched in genes identified as DEGs overlapping with the AB gene set between the SCZ cases and controls, reflected by a significant odds ratio (OR = 2.272, $p = 7.086 \times 10^{-6}$) (Figure 4B). For the MUTs of SCZ overlapping with the AB gene set, the blue module was identified to be significantly enriched (OR = 1.415, $p = 0.005$) (Figure 4B). Genes of the yellow module were defined as the key for differentially expressed genes in HIPPO (HIPPO-kDEG). Likewise, the blue module genes were defined as the key genes affected by mutation in HIPPO (HIPPO-kMUT).

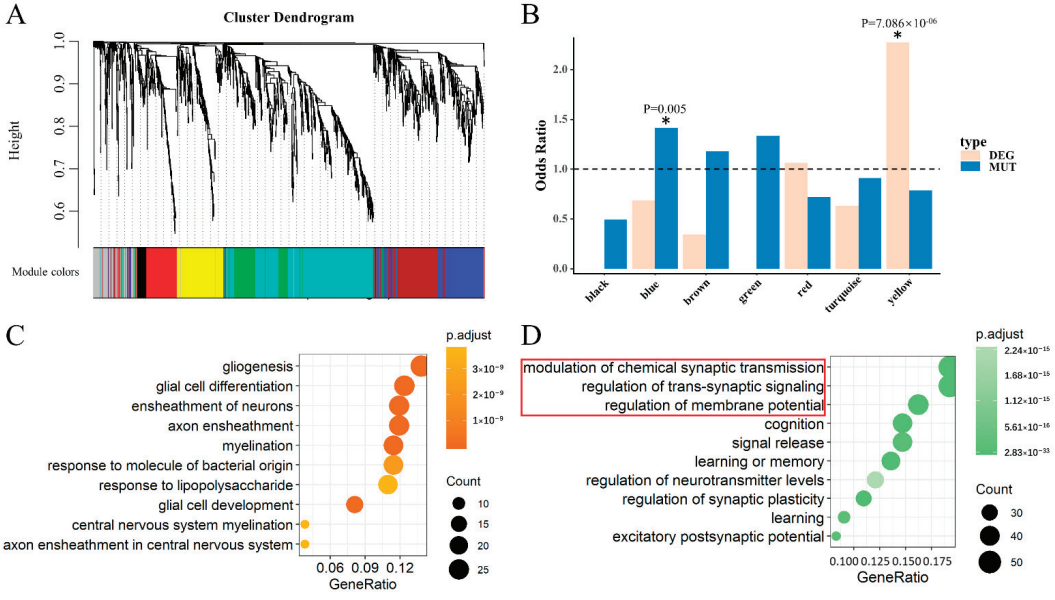


**Figure 4.** Module identification and functional enrichment in HIPPO. (**A**) Clustering dendrograms of the AB gene set by gene expression data in HIPPO with dissimilarity based on the topological overlap. A total of eight modules were identified. (**B**) The histogram shows significant modules. A star with a significant *p*-value marks two identified modules. (**C**) GO-BP analysis for yellow module genes (HIPPO-kDEG) showing the top 10 enriched gene ontology categories. (**D**) GO-BP analysis for blue module genes (HIPPO-kMUT) showing the top 10 enriched gene ontology categories. The red box indicates the GO terms that were same as those in the pink module in DLPFC.

To determine whether there is a difference in biological or neuronal functions, we also performed a GO-BP analysis on HIPPO-kDEG and HIPPO-kMUT alone. We observed that the enrichment of HIPPO-kDEG was associated with gene ontology terms related to gliogenesis, glial cell differentiation, and the ensheathment of neurons, among other factors (Figure 4C). As observed, the top three gene ontology categories of HIPPO-kMUT were consistent with those of DLPFC-kMUT (Figure 4D). This result indicates that the MUTs of SCZ featured unified biological functions in both DLPFC and HIPPO based on the modulation of chemical synaptic transmission, the regulation of trans-synaptic signaling, and the regulation of membrane potential. Many studies have noted that subjects with SCZ appear to share a common abnormality in synaptic transmission control [32].

### *3.4. Comparison between DLPFC-kMUT and HIPPO-kMUT*

Considering the consistency of the top 3 GO terms of DLPFC-kMUT and HIPPO-kMUT, we compared the genes of the 2 categories and found that 42 genes were overlapped. Moreover, the overlap ratio of genes accounted for 15.2% of HIPPO-kMUT and reached 47.7% of DLPFC-kMUT (Figure 5A).

Considering that DLPFC-kMUT and HIPPO-kMUT converged in their biological functions, we combined these two categories of genes to perform the functional enrichment analysis. As shown in Figure 5B, the five most significant GO terms were the modulation of chemical synaptic transmission (p.adj = $5.93 \times 10^{-33}$), the regulation of trans-synaptic signaling (p.adj = $5.93 \times 10^{-33}$), cognition (p.adj = $5.87 \times 10^{-23}$), regulation of membrane potential (p.adj = $2.01 \times 10^{-22}$), and learning or memory (p.adj = $2.84 \times 10^{-24}$). The two terms (modulation of chemical synaptic transmission and regulation of trans-synaptic signaling) shared the exact same genes. In the same way, cognition and learning or memory nearly shared the same genes. We observed that 13 genes connected these 5 GO terms, 4 of which (SHANK1, SHANK2, DLG4, and NLGN3) belonged to the overlap between DLPFC-kMUT and HIPPO-kMUT.

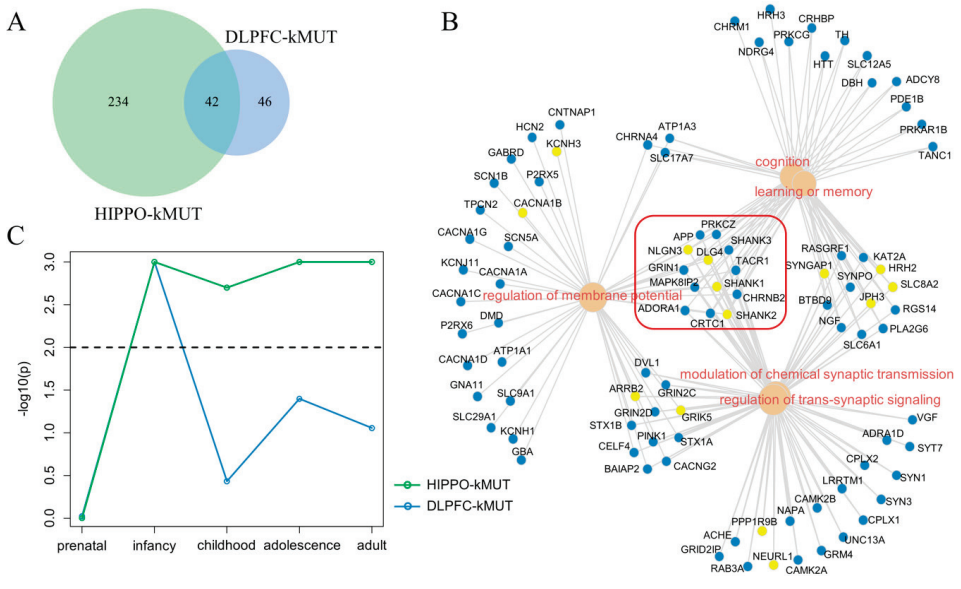


**Figure 5.** Comparison between DLPFC-kMUT and HIPPO-kMUT. (**A**) Overlapping gene counts of DLPFC-kMUT and HIPPO-kMUT. (**B**) GO-BP analysis for a combination of DLPFC-kMUT and HIPPO-kMUT, showing the genes contained in the first five most enriched GO terms. Blue dots show the genes contained in one of DLPFC-kMUT and HIPPO-kMUT, while the yellow dots show genes contained in both categories. The red box refers to genes related to all five GO terms. (**C**) Period-specific expression of DLPFC-kMUT and HIPPO-kMUT. The *p*-values calculated by the Expression Weighted Celltype Enrichment (EWCE) R package are shown. The *x*-axis shows the developmental stage, the *y*-axis shows the -log10 value of the p threshold, and the dashed line shows *p*-value = 0.01.

After determining that DLPFC-kMUT and HIPPO-kMUT converged in GO enrichment, we sought to determine whether they also had specific expression patterns in terms of developmental periods. For this purpose, we applied the Expression Weighted Celltype Enrichment (EWCE) R package [24], a bootstrap enrichment tool based on a specificity matrix, to the Brainspan [25] dataset. The result showed similar trends during the early stages of development (prenatal and infancy) (Figure 5C). However, in childhood, adolescence, and adulthood, DLPFC-kMUT and HIPPO-kMUT diverged in the following trend: HIPPO-kMUT was specifically expressed in the child, adolescent, and adult brains, unlike that of DLPFC-kMUT. Although SCZ usually emerges between ages 18 and 25, several longitudinal population-based studies have indicated that problems appear much earlier [33].

### *3.5. Larger Average PPI Degree Compared with Background*

Furthermore, we explored the roles of our key genes in the gene interaction networks. Protein–protein interactions are a key factor in determining protein function and are a basic component of cellular protein complexes and pathways since proteins rarely act alone. Comprehending PPI is thus crucial to understanding complex molecular relationships. To understand PPI characteristics, we used a bootstrap test (10,000 times) to compare the average degrees of four types of key genes with backgrounds defined by other genes that are expressed in the brain (average RPKM > 0.1 in BrainSeq Phase 2). Four types of key genes all showed a significantly larger average degree than the background (DLPFC-kDEG: $p = 0.0344$; DLPFC-kMUT: $p = 0.0131$; HIPPO-kDEG: $p = 0.0049$; HIPPO-kMUT: $p = 0.0001$) (Figure 6). In DLPFC-kDEG, for example, the P-value of the alternative hypothesis "smaller than the background" was 0.038, indicating that all four types of genes might act as hub genes in the PPI network.

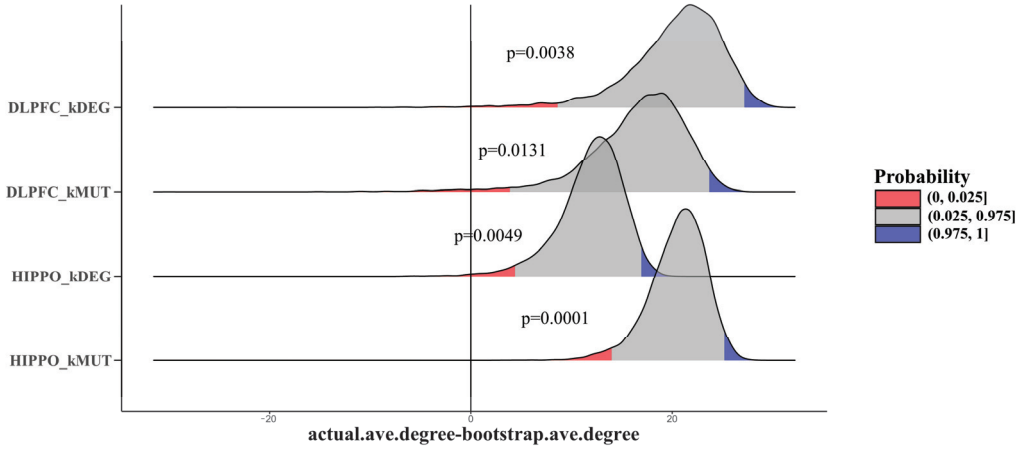


**Figure 6.** Joy plot shows bootstrap results comparing the average degrees of different kinds of key genes with other genes that are expressed in the brain (average RPKM > 0.1 in BrainSeq Phase 2). *x*-axis: The difference between the average degree obtained in the bootstrap tests and the actual average degree of the disease genes. *y*-axis: Density distribution. The horizontal line indicates x = 0, which means that the actual average degree equals the average bootstrap degree. The red and blue areas indicate the two-tailed test *p*-value threshold ($p < 0.025$ and $p > 0.975$).

### *3.6. Different Cell-Type-Specific Expression Patterns*

We also tested the temporally specific expression patterns between DLPFC-kMUT and HIPPO-kMUT. As a result, we explored whether DLPFC-kMUT and HIPPO-kMUT have specific expression patterns in different cell types. We extended this comparison to all four categories via EWCE.

We also tested the brain cell-type-specific expression in Dronc single-cell data [26]. Comparing the different cell types, the expression of four categories of key genes showed specificity in different dimensions. On the one hand, DLPFC-kMUT and HIPPO-kMUT were specifically expressed in neuronal stem cells (NSC), microglia (MG), oligodendrocyte precursor cells (OPC), granule neurons from the hip dentate gyrus region (exDG), and GABAergic interneurons (GABA), while DLPFC-kDEG and HIPPO-kDEG were not specifically expressed. Conversely, DLPFC-kDEG and HIPPO-kDEG were specifically expressed in pyramidal neurons from the hip CA region (exCA1/3) (Table 1). Therefore, the gene types explained cell-type-specific expression patterns better than brain regions.

**Table 1.** Cell-type expression patterns of DLPFC-kDEG, DLPFC-kMUT, HIPPO-kDEG, and DLPFC-kMUT. Cell-type-specific expression of four types of genes. The *p*-values calculated by the EWCE R package are shown. *p*-values < 0.01 are marked as blue. Classes are divided by the number of specific expressions in the four categories. The red boxes indicate categories with similar specific expression patterns. NSC, neuronal stem cell; MG, microglia; OPC, oligodendrocyte precursor cell; exDG, granule neuron from the hip dentate gyrus region; GABA, GABAergic interneuron; exCA1/3, pyramidal neuron from the hip CA region; ODC, oligodendrocyte; ASC, astrocyte; exPFC, glutamatergic neuron from the PFC; END, endotheliocyte.

| Class | Cell Type | *p*-Value | | | |
|---|---|---|---|---|---|
| | | DLPFC-kMUT | HIPPO-kMUT | DLPFC-kDEG | HIPPO-kDEG |
| 2 out of 4 | NSC | 0.003 | 0.001 | 0.999 | 1.000 |
| | MG | 0.001 | 0.001 | 1.000 | 1.000 |
| | OPC | 0.001 | 0.001 | 1.000 | 1.000 |
| | exDG | 0.001 | 0.001 | 1.000 | 1.000 |
| | GAGB | 0.001 | 0.001 | 0.731 | 0.254 |
| | exCA1 | 0.239 | 0.485 | 0.001 | 0.001 |
| | exCA3 | 0.282 | 0.153 | 0.001 | 0.001 |
| 3 out of 4 | ODC | 0.001 | 0.001 | 0.344 | 0.001 |
| | ASC | 0.007 | 0.001 | 0.014 | 0.001 |
| | exPFC | 0.033 | 0.001 | 0.001 | 0.001 |
| 1 out of 4 | END | 0.209 | 0.019 | 0.170 | 0.001 |

## 4. Discussion

In this study, we identified four categories of key genes (DLPFC-kDEG, DLPFC-kMUT, HIPPO-kDEG, and HIPPO-kMUT) in the AB gene set that may be potential SCZ risk factors and analyzed their characteristics. To our knowledge, this study is the first to focus on narrowing the scope of the AB mice gene set to determine the potential SCZ risk factors. These different categories of key genes will provide insights into the functional biology in SCZ.

In the analysis of gene co-expression, we identified a correlation between the SCZ and the AB gene set that strongly depends on the gene type class. In each co-expression network, only one module was found for each type of gene. When considering the same types of genes associated with different brain regions, strong concordance was found. As shown by our analysis and the genetic studies of others [34], different brain regions may share a genetic basis, especially in the early development stages. A study of gene expression patterns in the DLPFC of subjects with SCZ revealed that the gene's encoding proteins involved in presynaptic function regulation were the most consistently altered [35].

The discovery of functional pathways is essential for explaining the biological processes of diseases [36]. Determining the essential regulatory pathways that can affect the brain's molecular structure or function and that can lead to mental illness is an active research topic. Our finding that DLPFC-kMUT and HIPPO-kMUT share precisely the same top three GO terms associated with synaptic functions is worth exploring further. A previous study confirmed that DNMs on SCZ patients are significantly enriched in genes related to synaptic functions [37]. Furthermore, genes shared by the top five GO terms are highly associated with SCZ, including SHANK1/2/3, NLGN3, and DLG4. For the development stage, specific expression patterns of DLPFC-kMUT and HIPPO-kMUT converged in the early stage but diverged in the later stages of the developmental periods, which confirmed the notion that "early neurodevelopmental" injury may cause SCZ.

Post-synaptic neuroglial protein (NLGN) is one of the most well-characterized synaptic cell adhesion molecules, promoting excitatory and inhibitory synapse formation. In humans, there are five NLGN genes with NLGN1/2 located on the autosomes and

NLGN3/4/4Y on the sex chromosomes. Hamilton et al. [38] assessed an Nlgn3 knockout mouse model that exhibited abnormalities in phenotypes, including juvenile play, perseverative behaviors, and sensorimotor gating. In a previous study, 19 genetic variants were identified by sequencing all the exons and promoter regions of the neuroligin-2 (NLGN2) gene with the cohort consisting of 584 SCZ patients and 549 control subjects, and the variant in NLGN2 was identified as a loss-of-function mutant in inducing GABAergic synaptogenesis, which may be an important contributing factor for the onset of SCZ [39]. The mRNA expression levels of NLGN3 and SHANK3 were found to be significantly decreased in individuals with autism spectrum disorder (ASD) compared to the controls [40]. SCZ and ASD are two severe psychiatric disorders that share considerable comorbidities in both clinical and genetic contexts [41]. The genetic influence of NLGN3 and SHANK3 on SCZ is also worth exploring.

Post-synaptic density protein 95 (PSD95) is a member of the synapse-associated protein family of scaffolding molecules that control the organization, composition, and function of synapses [42]. PSD95 is encoded by the disks large homolog 4 (DLG4) gene. Feyder et al. [43] characterized increased repetitive behaviors, abnormal communication and social behaviors, impaired motor coordination, and increased stress reactivity and anxiety-related responses in mice with PSD-95 deletion ($Dlg4^{-/-}$). A family-based association analysis of genetic variants also highlighted a putative role for DLG4 in SCZ pathogenesis [44]. In addition, the linkage between DLG4 and SCZ has been well established through both variant association [45] and expression studies [46,47].

SHANK family members share five main domain regions: N-terminal ankyrin repeats, the SH3 domain, the PDZ domain, the proline-rich region, and a C-terminal SAM domain. Through these functional domains, SHANK interacts with many PSD proteins [48]. This complex has been shown to play an important role in targeting, anchoring, and dynamically regulating the synaptic localization of neurotransmitter receptors and signaling molecules [49]. Several genetic Shank mouse models have been generated, including Shank1 [50], Shank2 [51,52], and Shank3 [51,53–55] knockout mice models. In these studies, assays for detecting behavioral phenotypes in the following domains were included: (I) Social behavior, (II) communication, and (III) repetitive and stereotyped patterns of behavior. Numerous studies have strongly suggested a causative role of rare SHANK1/2/3 variants in SCZ [39,56–58] and have underlined the contribution of these variants in a variety of neuropsychiatric disorders. The genetic influence of SHANK1/2/3, NLGN3, and DLG4 on SCZ needs further experimental verification. In addition, the PSD95/SAPAP/SHANK postsynaptic complex may play an important role in SCZ. This is also worth exploring in subsequent research. SCZ and ASD are two different severe neurodevelopmental disorders with similar phenotypes and high comorbidity. It will be of great significance to study the common pathological mechanisms of the two disorders.

The four types of key genes all showed significantly larger average PPI degrees than the background. The availability of high-throughput PPI datasets has also led to various studies [59,60]. Previous analyses have suggested that an interactive network usually consists of a small number of highly connected "hubs" and many low degree nodes [61]. At the molecular level, highly connected "hub" genes are more sensitive to perturbations. Today, high-degree proteins remain a research hotspot. Our analysis suggests that these key genes involved in the abnormal behavior of experimental mouse models are more likely to be highly connected "hubs" in the network of SCZ.

Through macroscopic research, many remarkable results have been obtained. However, scientists have also begun to focus on the subtle differences between individual cells from the same organ or tissue to determine cell heterogeneity, which plays a vital role in complex neuropsychiatric illnesses. When studying cell-type-specific expression, DLPFC-kMUT and HIPPO-kMUT were found to be specifically expressed in the cells associated with neurons (NSC, MG, GABA, etc.). In SCZ, GABA may play an important role in the pathophysiology of SCZ due to changes in the presynaptic and postsynaptic components of its neurotransmission [62]. Using biological annotations and brain gene expression, we

showed that the mutation class explains specific expression patterns better than specific brain regions.

In summary, although our current study has some limitations, we provided a strategy for discovering the potential genetic basis of diseases using experimental mouse models to translate information from animals to humans. Our strategy provides new insights into the possibility of studying potential risk genes of SCZ. These key genes we discovered may continue to be used to study mental disorders. These four categories of key genes provide new inspiration for follow-up experimental verification. These genes may serve as biomarkers to be applied as potential therapeutic targets for SCZ. Targets identified because they inhabit high-confidence networks related to both risk and the illness state may act better than specific gene candidates. These current findings on key genes likely foreshadow the regional heterogeneity and biological differences in the gene types of SCZ. The present integrative analysis strengthens our understanding of SCZ and enhances our ability to find new ways to improve the lives of individuals affected by this disorder.

## 5. Conclusions

In our study, we identified four categories of key genes in an abnormal behavior gene set that may be potential SCZ risk factors (DLPFC-kDEG, DLPFC-kMUT, HIPPO-kDEG, and HIPPO-kMUT) and analyzed their characteristics. We found a similar synaptic function between DLPFC-kMUT and HIPPO-kMUT. For the development stage, specific expression patterns of DLPFC-kMUT and HIPPO-kMUT converged in the early stage of development and diverged later. The four types of key genes all showed a significantly larger average PPI degree than the background. Through cell-type-specific expression patterns, gene types explained cell-type-specific expression patterns better than brain regions. These different categories of key genes may provide insight for selecting biomarkers of SCZ.

**Supplementary Materials:** The following are available online at https://www.mdpi.com/2075-1729/11/2/172/s1, Table S1: Abnormal behavior gene set used in this study, Table S2. Details of genes with copy number variant uesd in this study from PsyMuKB, Table S3. Details of genes with *de novo* mutation uesd in this study from PsyMuKB.

**Author Contributions:** Conceptualization, G.N.L. and M.C.; Methodology, W.S. and M.C.; Software, W.W. and M.C.; Validation, W.S. and M.C.; Formal analysis, W.W. and W.Q.; Data curation, W.Q.; Writing—original draft preparation, M.C., W.W. and W.S.; Writing—review and editing, G.N.L. and W.W.; Visualization, M.C.; Supervision, G.N.L.; Project administration, M.C.; Funding acquisition, G.N.L. All authors have read and agreed to the published version of the manuscript.

**Funding:** This work was supported by grants from the National Natural Science Foundation of China (No. 81971292); Program for Professor of Special Appointment (Eastern Scholar) at Shanghai Institutions of Higher Learning (No. 1610000043); Medical-industrial intersection program of Shanghai Jiao Tong university (No. YG2019QNA59); Shanghai Mental Health Center (No. 2019-YJ01 and 2019-QH-03).

**Institutional Review Board Statement:** Not applicable.

**Informed Consent Statement:** Not applicable.

**Conflicts of Interest:** The authors declare no conflict of interest.

## References

1. Smeland, O.B.; Frei, O.; Dale, A.M.; Andreassen, O.A. The polygenic architecture of schizophrenia—rethinking pathogenesis and nosology. *Nat. Rev. Neurol.* **2020**, *16*, 366–379. [CrossRef] [PubMed]
2. Craddock, N.; O'Donovan, M.C.; Owen, M.J. The genetics of schizophrenia and bipolar disorder: Dissecting psychosis. *J. Med. Genet.* **2005**, *42*, 193. [CrossRef]
3. Patel, K.R.; Cherian, J.; Gohil, K.; Atkinson, D. Schizophrenia: Overview and treatment options. *Pharm. Ther.* **2014**, *39*, 638–645. [PubMed]
4. Tandon, R.; Nasrallah, H.A.; Keshavan, M.S. Schizophrenia, "just the facts" 4. Clinical features and conceptualization. *Schizophr. Res.* **2009**, *110*, 1–23. [CrossRef]

5. Blake, J.A.; Bult, C.J.; Eppig, J.T.; Kadin, J.A.; Richardson, J.E.; Mouse Genome Database Group. The Mouse Genome Database: Integration of and access to knowledge about the laboratory mouse. *Nucleic Acids Res.* **2014**, *42*, D810–D817. [CrossRef]
6. Lam, M.; Chen, C.-Y.; Li, Z.; Martin, A.R.; Bryois, J.; Ma, X.; Gaspar, H.; Ikeda, M.; Benyamin, B.; Brown, B.C.; et al. Comparative genetic architectures of schizophrenia in East Asian and European populations. *Nat. Genet.* **2019**, *51*, 1670–1678. [CrossRef]
7. Pardiñas, A.F.; Holmans, P.; Pocklington, A.J.; Escott-Price, V.; Ripke, S.; Carrera, N.; Legge, S.E.; Bishop, S.; Cameron, D.; Hamshere, M.L.; et al. Common schizophrenia alleles are enriched in mutation-intolerant genes and in regions under strong background selection. *Nat. Genet.* **2018**, *50*, 381–389. [CrossRef] [PubMed]
8. Avramopoulos, D. Recent Advances in the Genetics of Schizophrenia. *Complex. Psychiatry* **2018**, *4*, 35–51. [CrossRef] [PubMed]
9. Singh, T.; Poterba, T.; Curtis, D.; Akil, H.; Al Eissa, M.; Barchas, J.D.; Bass, N.; Bigdeli, T.B.; Breen, G.; Bromet, E.J.; et al. Exome sequencing identifies rare coding variants in 10 genes which confer substantial risk for schizophrenia. *Med. Rxiv.* **2020**. [CrossRef]
10. Bassett, A.S.; Chow, E.W.C.; AbdelMalik, P.; Gheorghiu, M.; Husted, J.; Weksberg, R. The Schizophrenia Phenotype in 22q11 Deletion Syndrome. *Am. J. Psychiatry* **2003**, *160*, 1580–1586. [CrossRef] [PubMed]
11. Howrigan, D.P.; Rose, S.A.; Samocha, K.E.; Fromer, M.; Cerrato, F.; Chen, W.J.; Churchhouse, C.; Chambert, K.; Chandler, S.D.; Daly, M.J.; et al. Exome sequencing in schizophrenia-affected parent-offspring trios reveals risk conferred by protein-coding de novo mutations. *Nat. Neurosci.* **2020**, *23*, 185–193. [CrossRef]
12. Girard, S.L.; Gauthier, J.; Noreau, A.; Xiong, L.; Zhou, S.; Jouan, L.; Dionne-Laporte, A.; Spiegelman, D.; Henrion, E.; Diallo, O.; et al. Increased exonic de novo mutation rate in individuals with schizophrenia. *Nat. Genet.* **2011**, *43*, 860–863. [CrossRef] [PubMed]
13. Wang, Q.; Li, M.; Yang, Z.; Hu, X.; Wu, H.-M.; Ni, P.; Ren, H.; Deng, W.; Li, M.; Ma, X.; et al. Increased co-expression of genes harboring the damaging de novo mutations in Chinese schizophrenic patients during prenatal development. *Sci. Rep.* **2015**, *5*, 18209. [CrossRef]
14. Xu, B.; Ionita-Laza, I.; Roos, J.L.; Boone, B.; Woodrick, S.; Sun, Y.; Levy, S.; Gogos, J.A.; Karayiorgou, M. De novo gene mutations highlight patterns of genetic and neural complexity in schizophrenia. *Nat. Genet.* **2012**, *44*, 1365–1369. [CrossRef]
15. Guipponi, M.; Santoni, F.A.; Setola, V.; Gehrig, C.; Rotharmel, M.; Cuenca, M.; Guillin, O.; Dikeos, D.; Georgantopoulos, G.; Papadimitriou, G.; et al. Exome Sequencing in 53 Sporadic Cases of Schizophrenia Identifies 18 Putative Candidate Genes. *PLoS ONE* **2014**, *9*, e112745. [CrossRef] [PubMed]
16. Lin, G.N.; Guo, S.; Tan, X.; Wang, W.; Qian, W.; Song, W.; Wang, J.; Yu, S.; Wang, Z.; Cui, D.; et al. PsyMuKB: An Integrative De Novo Variant Knowledge Base for Developmental Disorders. *Genom. Proteom. Bioinform.* **2019**, *17*, 453–464. [CrossRef]
17. Collado-Torres, L.; Burke, E.E.; Peterson, A.; Shin, J.; Straub, R.E.; Rajpurohit, A.; Semick, S.A.; Ulrich, W.S.; Price, A.J.; Valencia, C.; et al. Regional Heterogeneity in Gene Expression, Regulation, and Coherence in the Frontal Cortex and Hippocampus across Development and Schizophrenia. *Neuron* **2019**, *103*, 203–216. [CrossRef]
18. Akbarian, S.; Liu, C.; Knowles, J.A.; Vaccarino, F.M.; Farnham, P.J.; Crawford, G.E.; Jaffe, A.E.; Pinto, D.; Dracheva, S.; Geschwind, D.H.; et al. The PsychENCODE project. *Nat. Neurosci.* **2015**, *18*, 1707–1712. [CrossRef]
19. Schubert, C.R.; O'Donnell, P.; Quan, J.; Wendland, J.R.; Xi, H.S.; Winslow, A.R.; Domenici, E.; Essioux, L.; Kam-Thong, T.; Airey, D.C.; et al. BrainSeq: Neurogenomics to Drive Novel Target Discovery for Neuropsychiatric Disorders. *Neuron* **2015**, *88*, 1078–1083. [CrossRef]
20. Love, M.I.; Huber, W.; Anders, S. Moderated estimation of fold change and dispersion for RNA-seq data with DESeq2. *Genome Biol.* **2014**, *15*, 550. [CrossRef] [PubMed]
21. Langfelder, P.; Horvath, S. WGCNA: An R package for weighted correlation network analysis. *BMC Bioinform.* **2008**, *9*, 559. [CrossRef]
22. Yu, G.; Wang, L.-G.; Han, Y.; He, Q.-Y. ClusterProfiler: An R package for comparing biological themes among gene clusters. *Omics J. Integr. Biol.* **2012**, *16*, 284–287. [CrossRef]
23. Ashburner, M.; Ball, C.A.; Blake, J.A.; Botstein, D.; Butler, H.; Cherry, J.M.; Davis, A.P.; Dolinski, K.; Dwight, S.S.; Eppig, J.T.; et al. Gene Ontology: Tool for the unification of biology. *Nat. Genet.* **2000**, *25*, 25–29. [CrossRef]
24. Skene, N.G.; Grant, S.G.N. Identification of Vulnerable Cell Types in Major Brain Disorders Using Single Cell Transcriptomes and Expression Weighted Cell Type Enrichment. *Front. Neurosci.* **2016**, *10*, 16. [CrossRef]
25. Miller, J.A.; Ding, S.-L.; Sunkin, S.M.; Smith, K.A.; Ng, L.; Szafer, A.; Ebbert, A.; Riley, Z.L.; Royall, J.J.; Aiona, K.; et al. Transcriptional landscape of the prenatal human brain. *Nature* **2014**, *508*, 199–206. [CrossRef]
26. Habib, N.; Avraham-Davidi, I.; Basu, A.; Burks, T.; Shekhar, K.; Hofree, M.; Choudhury, S.R.; Aguet, F.; Gelfand, E.; Ardlie, K.; et al. Massively parallel single-nucleus RNA-seq with DroNc-seq. *Nat. Methods* **2017**, *14*, 955–958. [CrossRef]
27. Saunders, A.; Macosko, E.Z.; Wysoker, A.; Goldman, M.; Krienen, F.M.; de Rivera, H.; Bien, E.; Baum, M.; Bortolin, L.; Wang, S.; et al. Molecular Diversity and Specializations among the Cells of the Adult Mouse Brain. *Cell* **2018**, *174*, 1015–1030.e1016. [CrossRef]
28. Stark, C.; Breitkreutz, B.-J.; Reguly, T.; Boucher, L.; Breitkreutz, A.; Tyers, M. BioGRID: A general repository for interaction datasets. *Nucleic Acids Res.* **2006**, *34*, D535–D539. [CrossRef]
29. Reale, M.; Patruno, A.; De Lutiis, M.A.; Pesce, M.; Felaco, M.; Di Giannantonio, M.; Di Nicola, M.; Grilli, A. Dysregulation of chemo-cytokine production in schizophrenic patients versus healthy controls. *BMC Neurosci.* **2011**, *12*, 13. [CrossRef]
30. Momtazmanesh, S.; Zare-Shahabadi, A.; Rezaei, N. Cytokine Alterations in Schizophrenia: An Updated Review. *Front. Psychiatry* **2019**, *10*, 892. [CrossRef] [PubMed]

31. Lips, E.S.; Cornelisse, L.N.; Toonen, R.F.; Min, J.L.; Hultman, C.M.; Holmans, P.A.; O'Donovan, M.C.; Purcell, S.M.; Smit, A.B.; Verhage, M.; et al. Functional gene group analysis identifies synaptic gene groups as risk factor for schizophrenia. *Mol. Psychiatry* **2012**, *17*, 996–1006. [CrossRef]
32. Lewis, D.A.; Lieberman, J.A. Catching Up on Schizophrenia: Natural History and Neurobiology. *Neuron* **2000**, *28*, 325–334. [CrossRef]
33. Insel, T.R. Rethinking schizophrenia. *Nature* **2010**, *468*, 187–193. [CrossRef]
34. Tierney, A.L.; Nelson, C.A., 3rd. Brain Development and the Role of Experience in the Early Years. *Zero Three* **2009**, *30*, 9–13.
35. Mirnics, K.; Middleton, F.A.; Marquez, A.; Lewis, D.A.; Levitt, P. Molecular characterization of schizophrenia viewed by microarray analysis of gene expression in prefrontal cortex. *Neuron* **2000**, *28*, 53–67. [CrossRef]
36. Moon, A.L.; Haan, N.; Wilkinson, L.S.; Thomas, K.L.; Hall, J. CACNA1C: Association with Psychiatric Disorders, Behavior, and Neurogenesis. *Schizophr. Bull.* **2018**, *44*, 958–965. [CrossRef] [PubMed]
37. Fromer, M.; Pocklington, A.J.; Kavanagh, D.H.; Williams, H.J.; Dwyer, S.; Gormley, P.; Georgieva, L.; Rees, E.; Palta, P.; Ruderfer, D.M.; et al. De novo mutations in schizophrenia implicate synaptic networks. *Nature* **2014**, *506*, 179–184. [CrossRef]
38. Hamilton, S.M.; Green, J.R.; Veeraragavan, S.; Yuva, L.; McCoy, A.; Wu, Y.; Warren, J.; Little, L.; Ji, D.; Cui, X.; et al. Fmr1 and Nlgn3 knockout rats: Novel tools for investigating autism spectrum disorders. *Behav. Neurosci.* **2014**, *128*, 103–109. [CrossRef]
39. Sun, C.; Cheng, M.-C.; Qin, R.; Liao, D.-L.; Chen, T.-T.; Koong, F.-J.; Chen, G.; Chen, C.-H. Identification and functional characterization of rare mutations of the neuroligin-2 gene (NLGN2) associated with schizophrenia. *Hum. Mol. Genet.* **2011**, *20*, 3042–3051. [CrossRef]
40. Yasuda, Y.; Hashimoto, R.; Yamamori, H.; Ohi, K.; Fukumoto, M.; Umeda-Yano, S.; Mohri, I.; Ito, A.; Taniike, M.; Takeda, M. Gene expression analysis in lymphoblasts derived from patients with autism spectrum disorder. *Mol. Autism.* **2011**, *2*, 9. [CrossRef]
41. Meyer, U.; Feldon, J.; Dammann, O. Schizophrenia and autism: Both shared and disorder-specific pathogenesis via perinatal inflammation? *Pediatr. Res.* **2011**, *69*, 26R–33R. [CrossRef]
42. Feng, W.; Zhang, M. Organization and dynamics of PDZ-domain-related supramodules in the postsynaptic density. *Nat. Rev. Neurosci.* **2009**, *10*, 87–99. [CrossRef] [PubMed]
43. Feyder, M.; Karlsson, R.-M.; Mathur, P.; Lyman, M.; Bock, R.; Momenan, R.; Munasinghe, J.; Scattoni, M.L.; Ihne, J.; Camp, M.; et al. Association of Mouse Dlg4 (PSD-95) Gene Deletion and Human DLG4 Gene Variation with Phenotypes Relevant to Autism Spectrum Disorders and Williams' Syndrome. *Am. J. Psychiatry* **2010**, *167*, 1508–1517. [CrossRef]
44. Balan, S.; Yamada, K.; Hattori, E.; Iwayama, Y.; Toyota, T.; Ohnishi, T.; Maekawa, M.; Toyoshima, M.; Iwata, Y.; Suzuki, K.; et al. Population-specific haplotype association of the postsynaptic density gene DLG4 with schizophrenia, in family-based association studies. *PLoS ONE* **2013**, *8*, e70302. [CrossRef]
45. Cheng, M.-C.; Lu, C.-L.; Luu, S.-U.; Tsai, H.-M.; Hsu, S.-H.; Chen, T.-T.; Chen, C.-H. Genetic and Functional Analysis of the DLG4 Gene Encoding the Post-Synaptic Density Protein 95 in Schizophrenia. *PLoS ONE* **2010**, *5*, e15107. [CrossRef]
46. Kristiansen, L.V.; Beneyto, M.; Haroutunian, V.; Meador-Woodruff, J.H. Changes in NMDA receptor subunits and interacting PSD proteins in dorsolateral prefrontal and anterior cingulate cortex indicate abnormal regional expression in schizophrenia. *Mol. Psychiatry* **2006**, *11*, 737–747. [CrossRef]
47. Kristiansen, L.V.; Meador-Woodruff, J.H. Abnormal striatal expression of transcripts encoding NMDA interacting PSD proteins in schizophrenia, bipolar disorder and major depression. *Schizophr. Res.* **2005**, *78*, 87–93. [CrossRef]
48. Zhou, Y.; Kaiser, T.; Monteiro, P.; Zhang, X.; Van der Goes, M.S.; Wang, D.; Barak, B.; Zeng, M.; Li, C.; Lu, C.; et al. Mice with Shank3 Mutations Associated with ASD and Schizophrenia Display Both Shared and Distinct Defects. *Neuron* **2016**, *89*, 147–162. [CrossRef]
49. McAllister, A.K. Dynamic aspects of CNS synapse formation. *Annu. Rev. Neurosci.* **2007**, *30*, 425–450. [CrossRef]
50. Hung, A.Y.; Futai, K.; Sala, C.; Valtschanoff, J.G.; Ryu, J.; Woodworth, M.A.; Kidd, F.L.; Sung, C.C.; Miyakawa, T.; Bear, M.F.; et al. Smaller dendritic spines, weaker synaptic transmission, but enhanced spatial learning in mice lacking Shank1. *J. Neurosci.* **2008**, *28*, 1697–1708. [CrossRef]
51. Schmeisser, M.J.; Ey, E.; Wegener, S.; Bockmann, J.; Stempel, A.V.; Kuebler, A.; Janssen, A.L.; Udvardi, P.T.; Shiban, E.; Spilker, C.; et al. Autistic-like behaviours and hyperactivity in mice lacking ProSAP1/Shank2. *Nature* **2012**, *486*, 256–260. [CrossRef]
52. Won, H.; Lee, H.R.; Gee, H.Y.; Mah, W.; Kim, J.I.; Lee, J.; Ha, S.; Chung, C.; Jung, E.S.; Cho, Y.S.; et al. Autistic-like social behaviour in Shank2-mutant mice improved by restoring NMDA receptor function. *Nature* **2012**, *486*, 261–265. [CrossRef]
53. Peca, J.; Feliciano, C.; Ting, J.T.; Wang, W.; Wells, M.F.; Venkatraman, T.N.; Lascola, C.D.; Fu, Z.; Feng, G. Shank3 mutant mice display autistic-like behaviours and striatal dysfunction. *Nature* **2011**, *472*, 437–442. [CrossRef]
54. Bozdagi, O.; Sakurai, T.; Papapetrou, D.; Wang, X.; Dickstein, D.L.; Takahashi, N.; Kajiwara, Y.; Yang, M.; Katz, A.M.; Scattoni, M.L.; et al. Haploinsufficiency of the autism-associated Shank3 gene leads to deficits in synaptic function, social interaction, and social communication. *Mol. Autism.* **2010**, *1*, 15. [CrossRef] [PubMed]
55. Wang, X.; McCoy, P.A.; Rodriguiz, R.M.; Pan, Y.; Je, H.S.; Roberts, A.C.; Kim, C.J.; Berrios, J.; Colvin, J.S.; Bousquet-Moore, D.; et al. Synaptic dysfunction and abnormal behaviors in mice lacking major isoforms of Shank3. *Hum. Mol. Genet.* **2011**, *20*, 3093–3108. [CrossRef]
56. Peykov, S.; Berkel, S.; Schoen, M.; Weiss, K.; Degenhardt, F.; Strohmaier, J.; Weiss, B.; Proepper, C.; Schratt, G.; Nöthen, M.M.; et al. Identification and functional characterization of rare SHANK2 variants in schizophrenia. *Mol. Psychiatry* **2015**, *20*, 1489–1498. [CrossRef]

57. Lennertz, L.; Wagner, M.; Wölwer, W.; Schuhmacher, A.; Frommann, I.; Berning, J.; Schulze-Rauschenbach, S.; Landsberg, M.W.; Steinbrecher, A.; Alexander, M.; et al. A promoter variant of SHANK1 affects auditory working memory in schizophrenia patients and in subjects clinically at risk for psychosis. *Eur. Arch. Psychiatry Clin. Neurosci.* **2012**, *262*, 117–124. [CrossRef] [PubMed]
58. Gauthier, J.; Champagne, N.; Lafreniere, R.G.; Xiong, L.; Spiegelman, D.; Brustein, E.; Lapointe, M.; Peng, H.; Cote, M.; Noreau, A.; et al. De novo mutations in the gene encoding the synaptic scaffolding protein SHANK3 in patients ascertained for schizophrenia. *Proc. Natl. Acad. Sci. USA* **2010**, *107*, 7863–7868. [CrossRef]
59. Rual, J.-F.; Venkatesan, K.; Hao, T.; Hirozane-Kishikawa, T.; Dricot, A.; Li, N.; Berriz, G.F.; Gibbons, F.D.; Dreze, M.; Ayivi-Guedehoussou, N.; et al. Towards a proteome-scale map of the human protein–protein interaction network. *Nature* **2005**, *437*, 1173–1178. [CrossRef]
60. Li, S.; Armstrong, C.M.; Bertin, N.; Ge, H.; Milstein, S.; Boxem, M.; Vidalain, P.O.; Han, J.D.; Chesneau, A.; Hao, T.; et al. A map of the interactome network of the metazoan C. elegans. *Science* **2004**, *303*, 540–543. [CrossRef] [PubMed]
61. Fox, A.D.; Hescott, B.J.; Blumer, A.C.; Slonim, D.K. Connectedness of PPI network neighborhoods identifies regulatory hub proteins. *Bioinformatics* **2011**, *27*, 1135–1142. [CrossRef] [PubMed]
62. de Jonge, J.C.; Vinkers, C.H.; Hulshoff Pol, H.E.; Marsman, A. GABAergic Mechanisms in Schizophrenia: Linking Postmortem and In Vivo Studies. *Front. Psychiatry* **2017**, *8*, 118. [CrossRef]

life

MDPI

*Article*

# Spatiotemporal 22q11.21 Protein Network Implicates DGCR8-Dependent MicroRNA Biogenesis as a Risk for Late Fetal Cortical Development in Psychiatric Diseases

**Liang Chen, Wenxiang Cai, Weidi Wang, Zhe Liu and Guan-Ning Lin ***

School of Biomedical Engineering, Shanghai Jiao Tong University, Shanghai 200030, China; chenliang66@sjtu.edu.cn (L.C.); caiwenxiang@sjtu.edu.cn (W.C.); wwd-swxx@foxmail.com (W.W.); liuzlm1030@sjtu.edu.cn (Z.L.)
* Correspondence: nickgnlin@sjtu.edu.cn

**Abstract:** The chromosome 22q11.21 copy number variant (CNV) is a vital risk factor that can be a genetic predisposition to neurodevelopmental disorders (NDD). As the 22q11.21 CNV affects multiple genes, causal disease genes and mechanisms affected are still poorly understood. Thus, we aimed to identify the most impactful 22q11.21 CNV genes and the potential impacted human brain regions, developmental stages and signaling pathways. We constructed the spatiotemporal dynamic networks of 22q11.21 CNV genes using the brain developmental transcriptome and physical protein–protein interactions. The affected brain regions, developmental stages, driver genes and pathways were subsequently investigated via integrated bioinformatics analysis. As a result, we first identified that 22q11.21 CNV genes affect the cortical area mainly during late fetal periods. Interestingly, we observed that connections between a driver gene, *DGCR8*, and its interacting partners, *MECP2* and *CUL3*, also network hubs, only existed in the network of the late fetal period within the cortical region, suggesting their functional specificity during brain development. We also confirmed the physical interaction result between DGCR8 and CUL3 by liquid chromatography-tandem mass spectrometry. In conclusion, our results could suggest that the disruption of DGCR8-dependent microRNA biogenesis plays a vital role in NDD for late fetal cortical development.

**Keywords:** CNV; PPI; spatiotemporal network; chromosome 22q11.21; DGCR8

**Citation:** Chen, L.; Cai, W.; Wang, W.; Liu, Z.; Lin, G.-N. Spatiotemporal 22q11.21 Protein Network Implicates DGCR8-Dependent MicroRNA Biogenesis as a Risk for Late Fetal Cortical Development in Psychiatric Diseases. *Life* **2021**, *11*, 514. https://doi.org/10.3390/life11060514

Academic Editors: Jong-Hyuk Yoon and Chiara Villa

Received: 14 May 2021
Accepted: 31 May 2021
Published: 31 May 2021



## 1. Introduction

Copy number variants (CNVs) are duplications or deletions of a genomic fragment ranging from one kilobase (Kb) to five megabases (Mb) [1]. They have often been identified as risk factors for genetic disorders [2]. The chromosome 22q11.2 region includes low copy repeats (LCRs) that mediate nonallelic homologous recombination. More specifically, the most commonly 22q11.2 deleted or duplicated region spans LCR-A to LCR-D, located on chromosome 22q11.21 [3]. Previous studies showed 22q11.21 deletion to be associated with several psychiatric disorders. 22q11.2 deletion syndrome is also known as DiGeorge or velocardiofacial syndrome. An elevated rate of autism spectrum disorder (ASD) has been reported in patients with 22q11.2 deletion syndrome [3]. In addition, deletion of 22q11.21 can cause schizophrenia, intellectual delay or attention deficit hyperactivity disorder [4,5], and duplication of 22q11.21 may lead to learning disability, developmental delay and ASD [3,6].

Previous genetic studies suggested that several 22q11.21 genes might be involved in psychiatric disorders [7,8]. In an attempt to pinpoint the role of 22q11.21 CNV genes in neurodevelopmental disorders, animal models have been established, and the biological functions of these genes have been examined [9]. One clinical phenotype, microcephaly, has often been observed in mental disorder patients with 22q11.21 deletion [10,11]. This phenotype has been reproduced in DGCR8 knockout zebrafish and mouse models [12,13].

Although these phenotypes have been observed, the underlying genetic mechanisms are still unclear. As a component of the microprocessor complex, DGCR8 is responsible for processing long primary miRNAs (pri-miRNAs) into short hairpins called precursor miRNAs (pre-miRNAs). It was reported that microRNAs (miRNAs) play a pivotal role in ASD and schizophrenia. In addition, another 22q11.21CNV gene, Ran-binding protein 1 (RANBP1), plays a critical role in RAN-dependent nucleocytoplasmic transport [14]. Homozygous RANBP1 mutant embryos exhibited microcephaly [15]. Previous studies suggested that RANBP1 is involved in nucleocytoplasmic transport to regulate neuronal polarity [16]. Although the biological functions of the individual gene have been uncovered, little is known about how the 22q11.21 CNV causes neurodevelopmental disorders since these multiple genes play different roles across different anatomic structures during different developmental stages.

Protein–protein interactions (PPIs) play an important role in biological processes. PPI network analysis is especially useful for discovering the underlying molecular mechanism in systems biology [17,18]. Actually, a protein interaction network frequently describes physical PPIs between proteins [19]. Analyses of molecular networks can identify the biological module and complex signaling pathways [20]. Many studies explored the pathogenesis of CNVs in psychiatric disorders by constructing a static topological network [21,22]. However, protein expression is dynamic, which can differ within various anatomical structures and developmental stages, and within the protein interactions as well [23–25].

Previous studies showed strong correlations between higher co-expression and protein interaction [26]. PPIs change along with dynamic expression levels of proteins. For this reason, PPIs could be affirmed by co-expression data. Therefore, integrating PPIs with gene expression data can uncover protein interactions at different developmental periods and in different anatomical areas. Previous works revealed the pathogenesis of candidate genes or CNVs by constructing spatiotemporal PPI networks due to alterations of protein expression patterns in different anatomical areas and during different developmental stages [27,28]. Although significant progress has been made [29], the particular human brain regions, periods, protein networks and signal pathways influenced by the 22q11.21 CNV remain unclear. Thus, in this study, we constructed a spatiotemporal network of the 22q11.21 CNV by integrating data from the human brain developmental transcriptome with physical interactions of 22q11.21 proteins. Our results demonstrate that 22q11.21 proteins interact with their related partners significantly in three particular spatiotemporal intervals, and the interaction patterns alter across these intervals. In particular, we identified that the parietal, temporal and occipital lobes are critical regions for the interactions between 22q11.21 proteins and their partners during early mid-fetal and late fetal periods. Furthermore, we observe that DGCR8 interacts with MECP2 and CUL3 during the late fetal period. Our results suggest that the DGCR8-dependent microRNA biogenesis pathway is crucial for the 22q11.21 CNV genes involved in psychiatric disorders.

## 2. Materials and Methods

### *2.1. Identification of 22q11.21 Genes and the Human Brain Transcriptome Data Collection*

We collected data from previous studies that assessed the 22q11.21 CNV located on chromosome 22 (chr: 22, 17.9–20.5) [3,30]. Twenty-six genes are located on this region (Supplementary Table S1). Human brain transcriptome data were downloaded from BrainSpan (http://www.brainspan.org, RNA-Seq Gencode v3c summarized to genes). BrainSpan provides normalized reads per kilobase per million (RPKM) expression data on 578 developing brain samples across 13 developmental stages. The expression values for samples of the same age and from the same area were averaged. To reduce noise, we removed genes with a log2 intensity of <0.4 in all samples and with a coefficient of variation of <0.07. Therefore, 15,095 genes were retained for analysis.

### *2.2. The Datasets of Physical Protein–Protein Interactions Restricted to Brain-Expressed Genes*

Protein–protein interaction data were downloaded from the BioGRID database (https://downloads.thebiogrid.org/BioGRID/Release-Archive/BIOGRID-3.4.161/) (accessed on 19 May 2018). BIOGRID-ORGANISM-3.4.161.tab2 was downloaded in May 2018. The human PPIs were utilized (BIOGRID-ORGANISM-Homo_sapiens-3.4.161.tab2.txt). We obtained only physical protein–protein interactions. Redundancy and self-interaction data were also removed, leaving 241,123 pairs. Next, the protein–protein interaction (PPI) network was integrated with the human brain transcriptome to assemble a brain-expressed human interactome, termed HIBE.

### *2.3. Construction of Spatiotemporal Protein Network*

We defined eight non-overlapping periods (Supplementary Table S2). Anatomical structures were divided into four areas according to anatomical and functional similarity (Supplementary Table S3). Consequently, we constructed thirty-one spatiotemporal protein networks after removing one region from P3 (P3R4) due to a lack of enough RNA-seq data. CNV genes were mapped to the HIBE network to build a static network. Spatiotemporal expression data were combined with static PPI networks, and the SCC (Spearman correlation coefficient) values were calculated. The interactions were confirmed only if the SCC was >0.5. Thirty-one networks were constructed.

We defined eight developmental periods as previously described (Supplementary Table S2) [28,31]. Anatomical structures were divided into four areas as previously described [28] (Supplementary Table S3) according to anatomical and functional similarity. Consequently, we constructed thirty-one spatiotemporal protein networks after removing one region from P3 (P3R4) due to a lack of enough RNA-seq data. CNV genes were mapped to the HIBE network to build a static network. Spatiotemporal expression data were combined with static PPI networks, and the SCC (Spearman correlation coefficient) was calculated. The interactions were confirmed only if the SCC was >0.5. We used Cytoscape software for network visualization. Thirty-one networks were constructed.

### *2.4. Enrichment Analyses in Three Spatiotemporal Networks*

Fractions of co-expression interacting pairs were calculated from 22q11.21 proteins and three control datasets. The Fisher exact test was used to identify significant enrichment of connectivity for the 22q11.21 CNV. One-way ANOVA tests were performed to analyze the difference between 22q11.21 networks from the same developmental period (P2R1, P2R2) or the same anatomical area (P2R1 and P4R1). Topological features were defined for each 22q11.21 CNV gene: the fraction of interacting partners unique to one network and the fraction of interacting partners shared by two networks (Supplementary Tables S4 and S5). The statistically significant differences were calculated using ANOVA tests, and genes from dynamic networks were analyzed using Metascape [32]. Functional enrichment was performed in three GO categories: biological process, molecular function and cellular component. Terms with $p < 0.01$, a minimum count of 3 and an enrichment factor of >1.5 (the enrichment factor was defined as the observed count's ratio to the count expected by chance) were collected and grouped into clusters based on their membership similarities. Furthermore, *p*-values were calculated based on the cumulative hypergeometric distribution. The Q-value was calculated using Benjamini–Hochberg correction for multiple testing.

ASD risk genes' associated genes were from a previous report. The FMRP target gene set was from a previous publication [33]. Voltage-gated calcium channel complex proteins were from a previous study by Catrin Swantje Müller [34,35]. Developmental delay genes were derived from a previous report [36]. Two gene sets were downloaded from the Mouse Genome Informatics (MGI) database (http://www.informatics.jax.org), abnormal nervous system electrophysiology (MP: 0002272) and abnormal long-term potentiation (MP: 0002207) [34]. Differences between the mutations of proteins from 22q11.21 spatiotemporal networks and mutations from 20,240 genes were analyzed using Fisher's

exact test. The *p*-values were corrected using the Benjamini–Hochberg method. To test whether proteins from 22q11.21 spatiotemporal networks are enriched in two gene sets (MP: 0002272, 0002207), Fisher's exact test was utilized. The Benjamini–Hochberg method was used to correct the *p*-values.

### *2.5. Cell Culture and Transfection*

HEK293T cells were cultured in Dulbecco's Modified Eagle Medium (DMEM) supplemented with 10% Fetal Bovine Serum and 1% penicillin-streptomycin and maintained in a humidified incubator at 37 °C in an atmosphere containing 5% $CO_2$. For cell transfection, $1.5 \times 10^6$ cells were seeded into a 10cm dish until they reached 80–90% confluency. Transfections were undertaken using the jetPRIME Transfection Reagent with pCMV6-entry-HA-DGCR8. HEK293T cells were transfected with pCMV6-entry-HA-DGCR8. A total of 10 µg of DNA and 20 µL of transfection reagent were used per 10cm dish. After 48 h, the cells were rinsed with ice-cold PBS, collected and resuspended in lysis buffer (20 mM Tris-Cl, 5 mM EDTA pH 7.4, 150 mM NaCl, 1% Triton X-100 and 10% (vol/vol) glycerol), supplemented with 1mM PMSF, and complete protease inhibitor cocktail. Of the supernatant, 5% was saved for the input control, and the rest of the cell lysates were immunoprecipitated with either anti-HA or control mouse IgG for 12 h at 4 °C. After that, the cell lysates were added to the protein G beads overnight at 4 °C, and immunocomplexes were washed three times with lysis buffer, boiled in 5 × SDS loading buffer with 20 mM DTT and then resolved by 10% SDS-PAGE gels (Supplementary Figure S2). The gels were stained with Coomassie brilliant blue (CBB). Protein bands were excised at around 88 kDa.

### *2.6. Peptide Preparation and LC-MS/MS*

First, gels were de-stained with 50% (*v*/*v*) methanol and vortexed vigorously for 30 min. Then, gel pieces were washed in water for 15 min. Gel pieces were washed in water for 15 min. Gel pieces were then dehydrated in 100% acetonitrile for 10 min and dried in a vacuum centrifuge. The disulfide bonds of proteins were then reduced with dithiothreitol (10 mM) and alkylated with iodoacetamide (55 mM). Next, gel pieces were washed with 50% (*v*/*v*) acetonitrile and $NH_4HCO_3$ (25 mM) and dehydrated with 100% acetonitrile. Gel pieces were digested with trypsin in $NH_4HCO_3$ (25 mM). Peptides were extracted with 50% (*v*/*v*) acetonitrile and 1% (*v*/*v*) trifluoroacetic acid. Free peptides were dried using a vacuum centrifuge, separated using liquid chromatography (LC) (Easy-nLC 1000; Thermo Fisher, Waltham, MA, USA) and introduced into a Q Exactive mass spectrometer (Thermo Fisher). Finally, peptides were analyzed by MASCOT (www.matrixscience.com).

### *2.7. Proteome Analyses*

Data analyses were undertaken using Proteome Discoverer 1.4 (Thermo Scientific), which incorporates the MASCOT search engine. The Homo sapiens database from Uniprot was downloaded on 15 May 2019, and human protein sequences were searched. Carbamidomethyl was used as the fixed modification, with oxidation as the dynamical modification. The maximum number of missed cleavages considered was two. Immunoprecipitation samples were prepared in three independent experiments. Analyses involved only proteins that were detected by MS at least twice.

## 3. Results

### *3.1. Construction of Spatiotemporal Interaction Network for 22q11.21*

PPIs occur only if proteins express at the same cell component simultaneously [37]. Multiple studies have reported a robust correlation between co-expression and protein interaction [26,38]. Hence, the combination of data from gene expression and protein interaction could uncover protein interactions at different developmental stages and within various anatomical regions. To study the regulatory role of the 22q11.21 CNV during brain development, we extracted 26 genes located in the chromosomal region of 22q11.21 encompassing ~4.3 Mb (chromosome 22: 17.4–21.7 Mb) (Supplementary Table S1) and

constructed dynamic networks by integrating spatiotemporal RNA expression data with 22q11.21 physical PPIs (Figure 1).

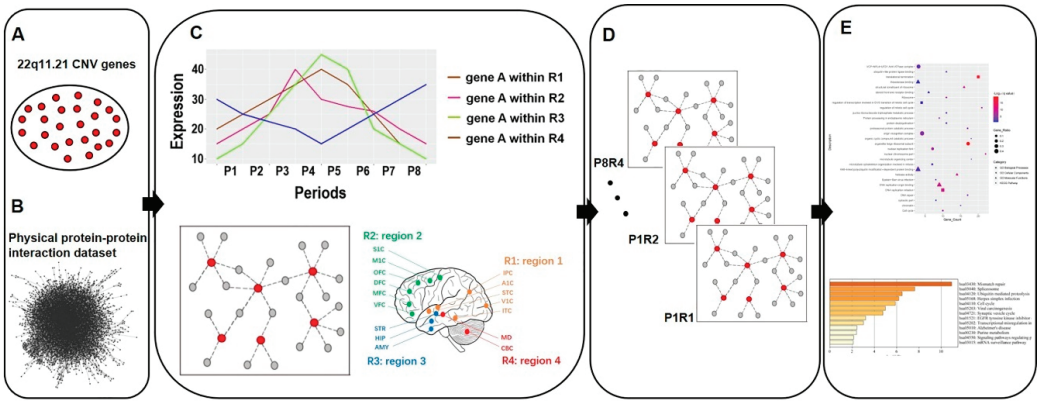


**Figure 1.** The flow chart shows the pipeline of this research study. (**A**) Twenty-six 22q11.21 CNV genes expressed in the brain were identified. (**B**) Physical protein–protein interaction (PPI) dataset was combined with 22q11.21 CNV genes to construct CNV protein–protein interactions (PPIs). (**C**) 22q11.21 CNV PPIs were combined with the human brain transcriptome dataset [28]. (**D**) A 22q11.21 spatiotemporal co-expression PPI network was established. (**E**) Gene Ontology and pathway analysis were performed.

Human developmental brain gene expression data were obtained from BrainSpan (www.brainspan.org). Next, we partitioned the expression data by their developmental periods and brain regions as previously described [28] (Supplementary Tables S2 and S3) and defined 32 spatiotemporal intervals by partitioning eight developmental periods (P1–8) and four brain regions (R1–4), eliminating P3R4 (P3, late mid-fetal; R4, mediodorsal nucleus of the thalamus and cerebella cortex) due to insufficient data (Materials and Methods). We defined three different control datasets to reduce biases: (i) all brain-expressed proteins interacting with their physically interacting partners; (ii) common CNVs' brain-expressed proteins interacting with their physically interacting partners, where the common CNVs were distinguished in the 1000 Genomes Project; (iii) all possible pairs between 22q11.21 CNV genes and human brain-expressed genes. We combined the physical PPI network with the human brain transcriptome to build up a brain-expressed human interactome, termed HIBE. After that, a static network was constructed by mapping CNV genes to the HIBE network. Next, the spatiotemporal expression data were integrated with the network, and the Spearman correlation coefficient (SCC) values were calculated. The interactions were certified only if the SCC was >0.5 (Materials and Methods). Finally, thirty-one networks were established.

### *3.2. 22q11.21 Co-Expressed Interacting Protein Pairs Are Enriched in the Early Mid-Fetal and Late Fetal Periods*

To evaluate the statistically significant enrichment of connectivity for the 22q11.21 CNV, we calculated fractions of co-expression interacting pairs for 22q11.21 proteins and three control datasets (Materials and Methods). We identified that early mid-fetal and late fetal periods were significantly enriched in interacting pairs. After false discovery rate (FDR) correction for multiple testing, we identified significant enrichment in three intervals: P2R1 (P2: early mid-fetal; R1: parietal, temporal and occipital cortex; Fisher's exact test, $p = 0.00146$), P2R2 (P2: early mid-fetal; R2: prefrontal and motor cortex; $p = 6.6 \times 10^{-6}$) and P4R1 (P4: late fetal; R1: parietal, temporal and occipital cortex; $p = 0.018$) (Figure 2).

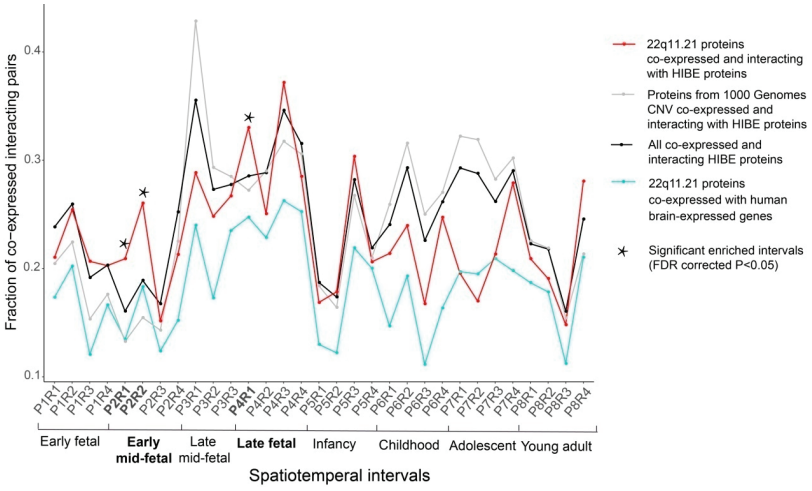


**Figure 2.** The 22q11.21 co-expressed interacting protein pairs are significantly enriched in three spatiotemporal intervals. The fractions of protein pairs from the 22q11.21 CNV co-expressed and interacting with HIBE proteins (red line), all co-expressed and interacting HIBE proteins (black line), proteins from the 1000 Genome Project CNVs co-expressed and interacting with HIBE proteins (dark gray line) and 22q11.21 CNV proteins co-expressed with all brain-expressed human genes (aquamarine line). Thirty-one spatiotemporal intervals of brain development are shown on the x-axis. 22q11.21 co-expressed interacting protein pairs are significantly enriched in spatiotemporal intervals (indicated by a star symbol) compared with the control networks. The statistical enrichments were calculated using Fisher's exact test, and *p*-values were FDR-corrected for multiple comparisons.

### *3.3. Similarities and Differences between the Spatiotemporal 22q11.21 Networks*

To assess the similarities among different spatiotemporal 22q11.21 co-expressed PPI networks, we measured their convergence by calculating the fraction of the shared proteins between these networks, P2R1, P2R2 and P4R1. We observed that 21 of the 26 (80.8%) 22q11.21 CNV proteins and 68 of their 406 (21.7%) co-expressed interacting partners were shared by all three networks (Figure 3, Supplementary Tables S4 and S5). Next, we performed functional enrichment on these shared CNV genes and shared interacting partners using Metascape (http://metascape.org) (Figure 3) and observed that the top three significant terms of the biological process were "mitochondrial translational elongation", "DNA replication initiation" and "regulation of mitotic cell cycle".

Next, we compared the connectivity of co-expressed interacting proteins either within the same developmental period (early mid-fetal P2) or within the same brain region (R1) to identify both topological and functional differences between spatiotemporal 22q11.21 networks. As noted, we identified three spatiotemporal networks with significantly enriched co-expressed PPI pairs across different brain regions (R1 and R2) within the same developmental period (early mid-fetal P2) and also across different developmental periods (early mid-fetal P2 and late fetal P4) within the same region (R1). Network changes were assessed by calculating the fractions of co-expressed interacting partners unique to one network and the fractions of co-expressed interacting partners shared by different networks (Figure 4, Table 1). We found statistically significant differences either between the same region within different developmental periods (P2R1 and P4R1, ANOVA test $p = 2 \times 10^{-16}$) (Table 1, Supplementary Table S6) or between different regions within the same developmental period (P2R1 and P2R2, ANOVA, $p = 0.0186$) (Table 1, Supplementary Table S7). These results demonstrate that the 22q11.21 network changes obviously across different developmental periods or brain regions.

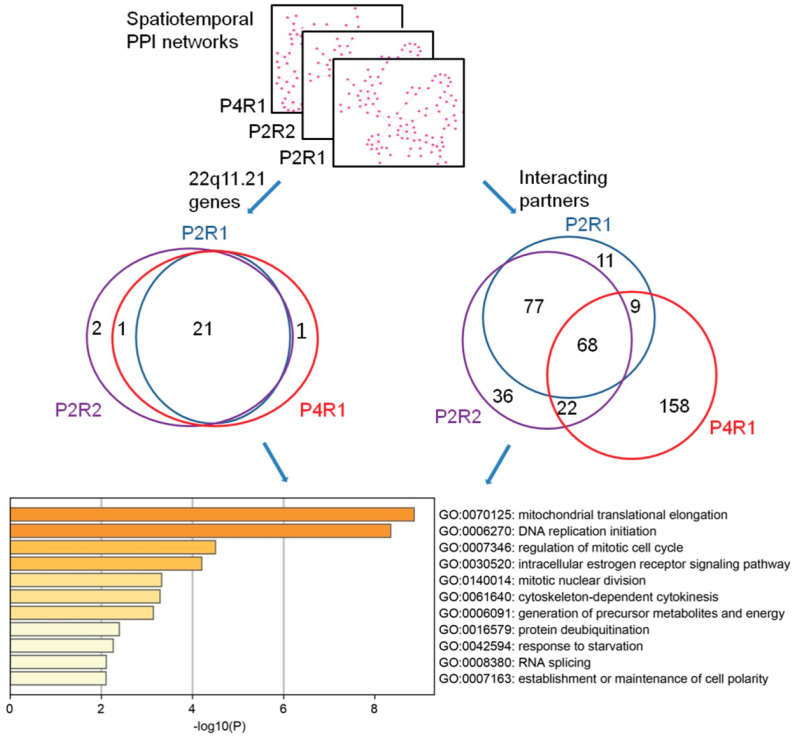


**Figure 3.** Functional convergence of the 22q11.21 spatiotemporal networks. The overlaps of 22q11.21 genes (left Venn diagram) and their co-expressed interacting partners (right Venn diagram) are across three significant spatiotemporal intervals. The top 11 significantly enriched biological processes' GO terms of shared proteins are shown.

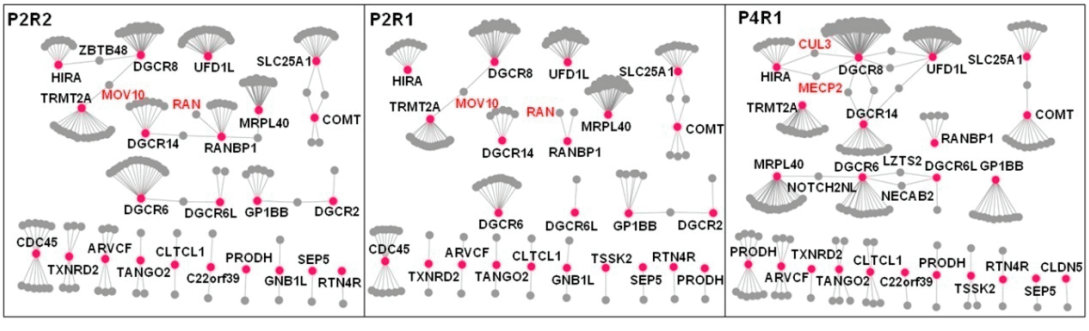


**Figure 4.** Difference between the 22q11.21 spatiotemporal networks. Spatiotemporal networks were compared across different brain regions within the same developmental period (P2R1 and P2R2) and across different development periods within the same brain region (P2R1 and P4R1). 22q11.21 genes are shown as red nodes, their co-expressed interacting partners as gray nodes and the PPIs between co-expressed genes at a particular developmental period as gray edges. The nodes that lost all edges were removed from the corresponding networks. Significant differences are observed across developmental periods and brain regions. The ANOVA statistics are shown in Table 1.

**Table 1.** Summary of ANOVA test statistics.

| ANOVA Tests | Sum of Squares | df | Mean Square | F | *p*-Value |
|---|---|---|---|---|---|
| P2R1 and P2R2 | 0.811 | 1 | 0.8114 | 5.971 | 0.0186 * |
| P2R1 and P4R1 | 7.302 | 1 | 7.302 | 257.8 | $2 \times 10^{-16}$ *** |

*** $p < 0.001$; * $p < 0.05$.

### *3.4. 22q11.21 Networks Involved in the Regulation of Translation and DNA Replication*

Next, we investigated the biological functions of 22q11.21 proteins and their partners within three dynamic 22q11.21 networks, P2R1, P2R2 and P4R1. We used Gene Ontology (GO) and Kyoto Encyclopedia of Genes and Genomes (KEGG) to analyze the enrichment of the functional pathways (Materials and Methods). For 22q11.21 proteins and their partners from the P2R1 network, the top three significant terms of the biological process were "translational termination", "DNA replication initiation" and "regulation of mitotic cell cycle" (Figure 5). Twenty genes were enriched in the term "translational termination". There were ten genes enriched in "DNA replication initiation", for instance, MECP2, CDK2, MCM3 and ORC1. Twenty-one genes, such as MECP2, BRCA2, CDK2 and RCC1, were enriched in "regulation of mitotic cell cycle" (Supplementary Table S8).

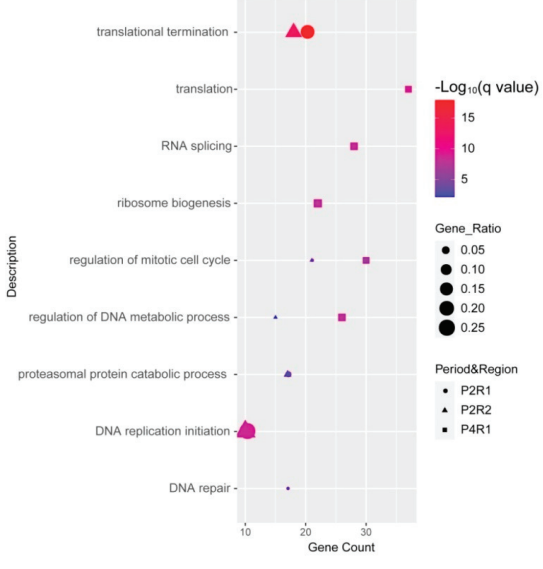


**Figure 5.** Functional analyses of proteins within three significant intervals, P2R1, P2R2 and P4R1. Dot plot shows significantly enriched GO terms of biological process for CNV proteins and their partners within three significant intervals.

The top three significant terms for the biological processes involving 22q11.21 proteins and partners from the P2R2 network were "translational termination", "DNA replication initiation" and "regulation of mitotic cell cycle" (Figure 5). Eighteen genes were enriched in the term "translational termination", such as MRPL58, UPF1 and MRPL15. The term "DNA replication initiation" was enriched by ten genes, for instance, CDK2, MCM3 and CDC45. Twenty-one genes were enriched in "regulation of mitotic cell cycle", such as RANBP1, PCNA and RCC1 (Supplementary Table S9).

For 22q11.21 proteins and their partners from the P4R1 network, the top three significant terms for the biological process were "translation", "RNA splicing" and "ribosome biogenesis" (Figure 5). Thirty-seven genes were enriched in the term "translation", such as

DHX9, EGFR and ELAVL1. Twenty-eight genes, for instance, DDX5, DDX15 and ELAVL2, were enriched in the term "RNA splicing". Twenty-two genes were enriched in the term "ribosome biogenesis", such as DGCR8, DDX10 and DKC1 (Supplementary Table S10).

We observed that 158 co-expressed and interacting partners of CNV proteins were only from the P4R1 network. These 158 co-expressed partners were not found in the P2R1 and P2R2 networks and were associated with "ribonucleoprotein complex biogenesis", "RNA splicing via transesterification reactions" and "translation" (Supplementary Figure S1). Twenty-five genes were enriched in "ribonucleoprotein complex biogenesis", such as DHX9, DDX10 and DKC1. Twenty genes, for instance, DDX5, DHX9 and ELAVL2, were enriched in "RNA splicing, via transesterification reaction".

### *3.5. De novo Mutations Are Significantly Enriched in Spatiotemporal Networks*

De novo mutations have recently been identified by exome sequencing and whole-genome sequencing from patients with psychiatric disorders [39,40] and have been observed to be potential genetic risk factors for psychiatric disorders [41,42]. Thus, we set out to investigate all 22q11.21 proteins and their interacting partners through the perspective of de novo mutations observed in psychiatric disorders (Materials and Methods). Previous studies collected de novo mutations from psychiatric disorders to generate disease- and phenotype-related gene sets [39]. Genes from the dynamic 22q11.21 networks were significantly enriched in ASD genes (FDR-corrected $p = 1.0299 \times 10^{-6}$). These genes were also significantly enriched in fragile X mental retardation protein (FMRP) target genes (FDR-corrected $p = 1.0299 \times 10^{-6}$) and voltage-gated calcium channel complex-related genes (FDR-corrected $p = 1.42 \times 10^{-3}$). There was no significant difference between the entire 22q11.21 network for developmental delay genes (FDR-corrected $p = 0.224$), long-term potentiation-associated genes (FDR-corrected $p = 0.1024$) and electrophysiology genes (FDR-corrected $p$-value = 0.254) (Supplementary Table S11).

### *3.6. Spatiotemporal Networks Identify Oivotal Co-Expression Partners in Developing Cortex*

Within the P4R1 network, DGCR8 possesses the highest value of betweenness centrality among the CNV proteins, thus indicating that DGCR8 is a driver gene and adopts a central position within this network (Figure 4, Supplementary Table S12). Knockout of DGCR8 in zebrafish led to a decrease in brain size, and early developmental defects were observed as well [12]. Thus, we furthered our CNV investigation by focusing on DGCR8 and its interaction patterns across three spatiotemporal networks. Within the P4R1 network, two hub proteins, MECP2 and CUL3, interacted with DGCR8. As previously known, MECP2 interacts with DGCR8 to suppress Drosha-DGCR8-mediated miRNA processing, and it was shown to significantly reduce precursor and mature miRNAs [43]. Another P4R1 hub protein, CUL3, is also a DGCR8 partner and a core component of an E3 ubiquitin–protein ligase complex [44]. CUL3 mediates ubiquitination and degradation of target proteins [45]. Our observation suggested that CUL3 ubiquitin ligase promotes DGCR8 ubiquitination and proteasomal degradation.

DGCR8 interacts with MOV10 within P2R1 and P2R2 networks (Figure 4). As a component of the RNA-induced silencing complex (RISC), MOV10 is required for miRNA-mediated gene silencing [46,47]. In addition, DGCR8 interacted with ZBTB48 (Figure 4), which is a ZNF and BTB-containing protein [48]. Previous studies suggested that DGCR8 involves nucleotide excision repair (NER) to maintain genomic integrity during development [49,50]. ZBTB48 promotes rapid deletion of telomeric sequences to prevent telomeres from extreme elongation to protect genome integrity [48,51].

Within the P4R1 network, DGCR6 interacted with Leucine zipper putative tumor suppressor 2 (LZTS2) (Figure 4). LZTS2 negatively regulates microtubule severing at centrosomes and is necessary for centrosome spindle formation [52]. DGCR6 is involved in neural crest cell migration into the third and fourth pharyngeal pouches [53]. DGCR6 and DGCR6L share 97% identical amino acids [53]. Previous studies suggested that these two genes are candidate genes involved in the pathology of DiGeorge syndrome [54].

DGCR6 and MRPL40 (mitochondrial large ribosomal subunit protein 40) interacted with NOTCH2NL within the P4R1 network (Figure 4). While MRPL40 is involved in short-term synaptic plasticity [55], NOTCH2NL activates the Notch pathway by inhibiting interactions between Delta and Notch.

Within P2R1 and P2R2 networks, RANBP1 interacted with RAN (Figure 4). RAN is regulated by RANBP1 and plays an essential role in nucleocytoplasmic transport and mitosis [56]. A previous study showed that RANBP1 and RAN are involved in regulating axonogenesis [16]. Our results suggest that parietal–temporal–occipital lobes (R1) and the prefrontal and motor-sensory cortex (R2) are the primary regions for RANBP1 to modulate RAN during the early mid-fetal period.

### *3.7. Validation of the Interaction between DRCR8 and CUL3 by Immunoprecipitation and Liquid Chromatography-Tandem Mass Spectrometry (LC-MS/MS)*

To confirm the interaction between DGCR8 and CUL3 in mammalian cells, we performed a co-immunoprecipitation (Co-IP) assay (Methods). The immunocomplexes from Co-IP were then detected by LC-MS/MS. More than five peptides were detected for DGCR8 and CUL3 (Figure 6). Each peptide was detected more than twice with high confidence. The interaction between DGCR8 and CUL3 was validated by LC-MS/MS (Figure 6).

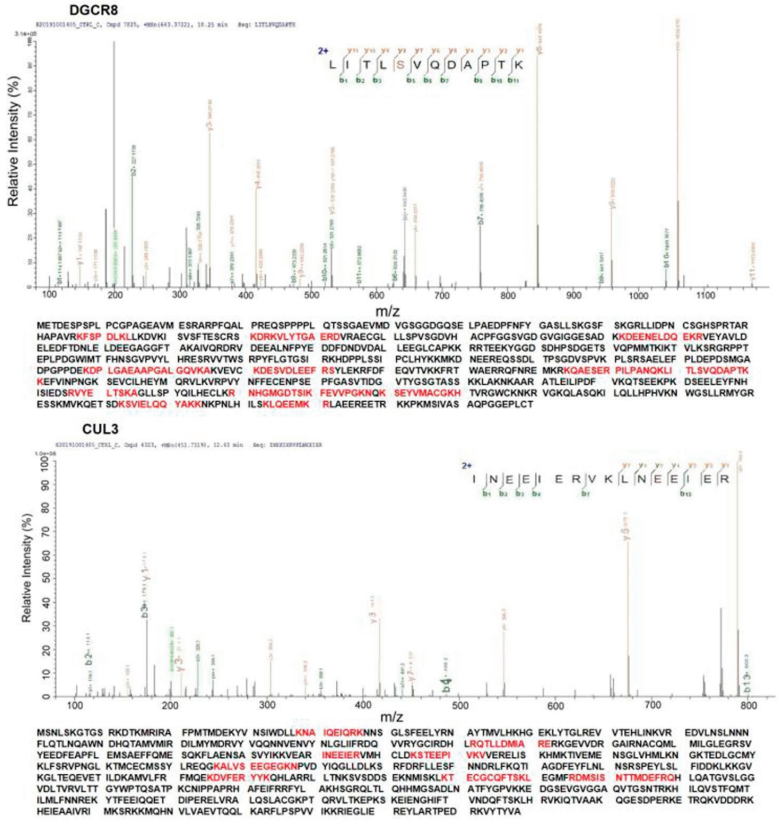


**Figure 6.** Investigation of interaction between DGCR8 and CUL3. DGCR8 and CUL3 were identified, and the amino acids marked with red color are peptides identified by immunoprecipitation (IP) and LC-MS/MS.

## 4. Discussion

In the current study, we constructed a spatiotemporal network for the 22q11.21 CNV, a vital risk factor for psychiatric disorders, and carried out bioinformatics analysis for the CNV to identify the impacted brain regions, developmental stages and potential disease-related genes. Our spatiotemporal network analysis indicated that mid-fetal and late fetal periods were the critical periods for 22q11.21 CNV proteins to affect human brain development. Moreover, our study suggests that the frontal, parietal, temporal and occipital lobes are crucial regions affected by CNV genes. This result is also in accordance with previous reports that the frontal, parietal, temporal and occipital lobes were abnormal in 22q11.21 deletion carriers [57,58]. In sum, these results indicate that the 22q11.21 CNV plays a critical role in developing the human brain's frontal, parietal, temporal and occipital lobes.

We identified that one CNV gene, *DGCR8*, is a driver gene in the parietal, temporal and occipital cortex (R1) during the late fetal period (P4). This result is consistent with the previous finding that homozygote DGCR8 mouse embryos demonstrated abnormal brain development [13]. One hub partner, MECP2, interacted with DGCR8. It was reported that MECP2 binds to methylated DNA, which activates or represses specific genes [59]. Previous studies reported that MECP2 is associated with severe neurodevelopmental disorders, including autism spectrum disorder and Rett syndrome [60,61]. DGCR8 is an essential component of the microRNA processing complex involved in the biogenesis of microRNA, and another work indicates that knockout DGCR8 could induce microcephaly [13]. Furthermore, previous works showed that MECP2 regulates the DGCR8/Drosha complex to suppress nuclear microRNA processing and dendritic growth [43]. Taken together, our results demonstrate that MECP2 interacted with DGCR8 in the parietal, temporal and occipital cortex to affect brain development during the late fetal period.

DGCR8 interacts with another hub partner, Cullin 3 (CUL3). As a core component of the E3 ubiquitin ligase complex, CUL3 mediates proteasomal degradation. Previous studies proved CUL3 is a high-confidence risk factor for autism spectrum disorder and developmental delay [62,63]. CUL3 knockout mice showed autism-associated behavioral phenotypes. CUL3 is a critical component of E3 ubiquitin–protein ligase complexes involved in ubiquitination and degradation of target proteins [64,65]. The protein level of DGCR8 is decreased by ubiquitination [66,67]. Since the PPI interaction can be identified by Co-IP and liquid chromatography-tandem mass spectrometry (LC-MS/MS) [68], we then identified and validated the interaction between DGCR8 and CUL3 with high confidence by Co-IP and LC-MS/MS in our study. Our results suggest CUL3-mediated ubiquitination and degradation of DGCR8 to be involved in primary microRNA processing.

Furthermore, other essential CNV genes and partners were identified from dynamic networks. *MRPL40*, *DGCR6*, *DGCR6L* and *Ranbp1* are 22q11.21 CNV genes. In the parietal, temporal and occipital cortex (R1) during the late fetal period (P4), we observed that MRPL40 interacted with notch 2 N-terminal like A (NOTCH2NL), which is highly expressed in radial glia. NOTCH2NL promotes Notch signaling by interacting directly with NOTCH receptors. Previous works have demonstrated that NOTCH2NL is associated with the differentiation of neuronal progenitors [69,70]. MRPL40 has been shown to affect short-term synaptic plasticity through the regulation of mitochondrial calcium [55]. Our network analysis results indicate that MRPL40 might be involved in the NOTCH signaling pathway. Within the P4R1 network, DGCR6 and DGCR6L interacted with LZTS2. DGCR6 and DGCR6L associate with cell migration. LZTS2 regulates β-Catenin to be involved in microtubule severing, which is a significant mechanism for cell migration. Our results implicate that DGCR6 and DGCR6L may regulate cell migration via modulating LZTS2. Within P2R1 and P2R2 networks, Ranbp1 interacted with Ran. Ran is a Ran GTPase-binding and ras-related nuclear protein. Previous studies demonstrated that Ranbp1 influences the development of the cerebral cortex [16,71]. Ranbp1 interacts with Ran to influence Ran-guanosine triphosphate (GTP) gradients that triggered mitotic spindle assembly [72]. In addition, mice with a homozygous deletion of Ranbp1 also show microcephaly or exencephaly [15]. Our results suggest Ranbp1 affects human brain development in the

parietal–temporal–occipital (R1) and prefrontal and motor-sensory cortexes (R2) during the early mid-fetal period.

After performing disease- and phenotype-related gene set enrichment analysis, we observed that genes from the spatiotemporal 22q11.21 network were significantly enriched in ASD genes, fragile X mental retardation protein (FMRP) target genes and voltage-gated calcium channel complex-related genes. Since Bernard J Crespi and Helen J Crofts showed that the 22q11.21 CNV is associated with ASD and schizophrenia [73], our results agree with previous works that discovered the 22q11.21 CNV as a significant risk factor for ASD [74,75].

## 5. Conclusions

In summary, we constructed dynamic 22q11.21 CNV networks to explore the pathological mechanisms of this CNV associating with psychiatric disorders. We identified that the frontal, parietal, temporal and occipital lobes are crucial regions for 22q11.21 genes to affect brain development during the early mid-fetal and late fetal periods. As a driver gene, *DGCR8* plays an important role in the parietal, temporal and occipital cortex during the late fetal period. Two vital hub partners, MECP2 and CUL3, interact with DGCR8. The physical interaction between DGCR8 and CUL3 was confirmed by liquid chromatography-tandem mass spectrometry (LC-MS/MS). Our results suggest that the DGCR8-dependent microRNA biogenesis pathway is crucial for the 22q11.21 CNV to be involved in psychiatric disorders. In addition, other CNV genes, such as *MRPL40*, *DGCR6*, *DGCR6L* and *Ranbp1*, may affect cortex development during the early mid-fetal or late fetal period.

**Supplementary Materials:** The following are available online at https://www.mdpi.com/article/10.3390/life11060514/s1, Figure S1: The significantly enriched biological process of 158 partners only from the P4R1 network, Figure S2: SDS-PAGE separation of the immunoprecipitated proteins, Table S1: Genes within the 22q11.21 copy number variation, Table S2: Developmental brain period from the BrainSpan related to Figure 1, Table S3: Four brain regions and the anatomical structures, Table S4: Shared 22q11.21 CNV genes for three spatiotemporal networks (P2R1, P2R2 and P4R1), Table S5: Shared co-expression interacting partners for three spatiotemporal networks (P2R1, P2R2 and P4R1), Table S6: Results of ANOVA test for interaction patterns of proteins from P2R1 and P4R1 networks, Table S7: Results of ANOVA test for interaction patterns of proteins from P2R1 and P2R2 networks, Table S8: Top 3 significant terms of biological process for proteins from P2R1 network, Table S9: Top 3 significant terms of biological process for proteins from P2R2 network, Table S10: Top 3 significant terms of biological process for proteins from P4R1 network, Table S11: Enrichment analysis of de novo mutation genes from 22q11.21 spatiotemporal networks, Table S12: Parameters of P4R1 network.

**Author Contributions:** G.-N.L. designed the experiments, interpreted the results and revised and approved the final version of the manuscript. L.C. designed the experiments, performed data analysis, conducted the major experiments, interpreted the results and drafted the manuscript. W.C. conducted part of the experiments. W.W. and Z.L. participated in data collection and revised the manuscript. All authors have read and agreed to the published version of the manuscript.

**Funding:** This work was supported by grants from the National Natural Science Foundation of China (No. 81671328, 81971292); Program for Professor of Special Appointment (Eastern Scholar) at Shanghai Institutions of Higher Learning (No. 1610000043); and Innovation Research Plan supported by Shanghai Municipal Education Commission (ZXWF082101).

**Institutional Review Board Statement:** Not applicable.

**Informed Consent Statement:** Not applicable.

**Data Availability Statement:** The datasets used and/or analyzed during the current study are available from the corresponding author on reasonable request.

**Conflicts of Interest:** The authors declare that they have no conflicts of interest.

## Abbreviations

CNVs: copy number variants; PPI: protein–protein interaction; Co-IP: co-immunoprecipitation; LC-MS/MS: liquid chromatography-tandem mass spectrometry; 22q11.2DS: 22q11.2 deletion syndrome; FDR: false-discovery rate; LCRs: low copy repeats; RANBP1: Ran-binding protein 1; pri-miRNAs: primary miRNAs; ANOVA: analysis of variance; GO: Gene Ontology; KEGG: Kyoto Encyclopedia of Genes and Genomes; ASD: autism spectrum disorder; FMRP: fragile X mental retardation protein; IgG: immunoglobulin G; CBB: Coomassie brilliant blue; LC-MS/MS: liquid chromatography-tandem mass spectrometry.

## References


1. Freeman, J.L.; Perry, G.H.; Feuk, L.; Redon, R.; McCarroll, S.A.; Altshuler, D.M.; Aburatani, H.; Jones, K.W.; Tyler-Smith, C.; Hurles, M.E.; et al. Copy number variation: New insights in genome diversity. *Genome Res.* **2006**, *16*, 949–961. [CrossRef]
2. Zhang, F.; Gu, W.; Hurles, M.E.; Lupski, J.R. Copy number variation in human health, disease, and evolution. *Annu. Rev. Genom. Hum. Genet.* **2009**, *10*, 451–481. [CrossRef] [PubMed]
3. Clements, C.C.; Wenger, T.L.; Zoltowski, A.R.; Bertollo, J.R.; Miller, J.S.; de Marchena, A.B.; Mitteer, L.M.; Carey, J.C.; Yerys, B.E.; Zackai, E.H.; et al. Critical region within 22q11.2 linked to higher rate of autism spectrum disorder. *Mol. Autism* **2017**, *8*, 58. [CrossRef]
4. Bassett, A.S.; Chow, E.W.; AbdelMalik, P.; Gheorghiu, M.; Husted, J.; Weksberg, R. The schizophrenia phenotype in 22q11 deletion syndrome. *Am. J. Psychiatry* **2003**, *160*, 1580–1586. [CrossRef]
5. Burnside, R.D. 22q11.21 Deletion Syndromes: A Review of Proximal, Central, and Distal Deletions and Their Associated Features. *Cytogenet. Genome Res.* **2015**, *146*, 89–99. [CrossRef] [PubMed]
6. Coppinger, J.; McDonald-McGinn, D.; Zackai, E.; Shane, K.; Atkin, J.F.; Asamoah, A.; Leland, R.; Weaver, D.D.; Lansky-Shafer, S.; Schmidt, K.; et al. Identification of familial and de novo microduplications of 22q11.21-q11.23 distal to the 22q11.21 microdeletion syndrome region. *Hum. Mol. Genet.* **2009**, *18*, 1377–1383. [CrossRef] [PubMed]
7. Wang, H.; Duan, S.; Du, J.; Li, X.; Xu, Y.; Zhang, Z.; Wang, Y.; Huang, G.; Feng, G.; He, L. Transmission disequilibrium test provides evidence of association between promoter polymorphisms in 22q11 gene DGCR14 and schizophrenia. *J. Neural Transm.* **2006**, *113*, 1551–1561. [CrossRef]
8. Forsyth, J.K.; Nachun, D.; Gandal, M.J.; Geschwind, D.H.; Anderson, A.E.; Coppola, G.; Bearden, C.E. Synaptic and Gene Regulatory Mechanisms in Schizophrenia, Autism, and 22q11.2 Copy Number Variant-Mediated Risk for Neuropsychiatric Disorders. *Biol. Psychiatry* **2020**, *87*, 150–163. [CrossRef]
9. Ouchi, Y.; Banno, Y.; Shimizu, Y.; Ando, S.; Hasegawa, H.; Adachi, K.; Iwamoto, T. Reduced adult hippocampal neurogenesis and working memory deficits in the Dgcr8-deficient mouse model of 22q11.2 deletion-associated schizophrenia can be rescued by IGF2. *J. Neurosci. Off. J. Soc. Neurosci.* **2013**, *33*, 9408–9419. [CrossRef] [PubMed]
10. Guy, C.; Wang, X.; Lu, X.; Lu, J.; Li, S. Two patients with small chromosome 22q11.21 alterations and central nervous system abnormalities. *Mol. Cytogenet.* **2015**, *8*, 102. [CrossRef]
11. Lindgren, V.; McRae, A.; Dineen, R.; Saulsberry, A.; Hoganson, G.; Schrift, M. Behavioral abnormalities are common and severe in patients with distal 22q11.2 microdeletions and microduplications. *Mol. Genet. Genom. Med.* **2015**, *3*, 346–353. [CrossRef]
12. Liu, Y.; Zhu, Z.; Ho, I.H.T.; Shi, Y.; Xie, Y.; Li, J.; Zhang, Y.; Chan, M.T.V.; Cheng, C.H.K. Germline-specific dgcr8 knockout in zebrafish using a BACK approach. *Cell. Mol. Life Sci.* **2017**, *74*, 2503–2511. [CrossRef]
13. Marinaro, F.; Marzi, M.J.; Hoffmann, N.; Amin, H.; Pelizzoli, R.; Niola, F.; Nicassio, F.; De Pietri Tonelli, D. MicroRNA-independent functions of DGCR8 are essential for neocortical development and TBR1 expression. *EMBO Rep.* **2017**, *18*, 603–618. [CrossRef] [PubMed]
14. Kehlenbach, R.H.; Dickmanns, A.; Kehlenbach, A.; Guan, T.; Gerace, L. A role for RanBP1 in the release of CRM1 from the nuclear pore complex in a terminal step of nuclear export. *J. Cell Biol.* **1999**, *145*, 645–657. [CrossRef] [PubMed]
15. Paronett, E.M.; Meechan, D.W.; Karpinski, B.A.; LaMantia, A.S.; Maynard, T.M. Ranbp1, Deleted in DiGeorge/22q11.2 Deletion Syndrome, is a Microcephaly Gene That Selectively Disrupts Layer 2/3 Cortical Projection Neuron Generation. *Cereb Cortex* **2015**, *25*, 3977–3993. [CrossRef] [PubMed]
16. Mencarelli, C.; Nitarska, J.; Kroecher, T.; Ferraro, F.; Massey, K.; Riccio, A.; Pichaud, F. RanBP1 Couples Nuclear Export and Golgi Regulation through LKB1 to Promote Cortical Neuron Polarity. *Cell Rep.* **2018**, *24*, 2529–2539. [CrossRef]
17. Braun, P.; Gingras, A.C. History of protein-protein interactions: From egg-white to complex networks. *Proteomics* **2012**, *12*, 1478–1498. [CrossRef]
18. Dunn, R.; Dudbridge, F.; Sanderson, C.M. The use of edge-betweenness clustering to investigate biological function in protein interaction networks. *BMC Bioinf.* **2005**, *6*, 39. [CrossRef]
19. Fromont-Racine, M.; Rain, J.C.; Legrain, P. Toward a functional analysis of the yeast genome through exhaustive two-hybrid screens. *Nat. Genet.* **1997**, *16*, 277–282. [CrossRef]
20. Dittrich, M.T.; Klau, G.W.; Rosenwald, A.; Dandekar, T.; Muller, T. Identifying functional modules in protein-protein interaction networks: An integrated exact approach. *Bioinformatics* **2008**, *24*, i223–i231. [CrossRef]

21. Blizinsky, K.D.; Diaz-Castro, B.; Forrest, M.P.; Schürmann, B.; Bach, A.P.; Martin-de-Saavedra, M.D.; Wang, L.; Csernansky, J.G.; Duan, J.; Penzes, P. Reversal of dendritic phenotypes in 16p11. 2 microduplication mouse model neurons by pharmacological targeting of a network hub. *Proc. Natl. Acad. Sci. USA* **2016**, *113*, 8520–8525. [CrossRef]
22. Roth, J.G.; Muench, K.L.; Asokan, A.; Mallett, V.M.; Gai, H.; Verma, Y.; Weber, S.; Charlton, C.; Fowler, J.L.; Loh, K.M.; et al. 16p11.2 microdeletion imparts transcriptional alterations in human iPSC-derived models of early neural development. *eLife* **2020**, *9*. [CrossRef] [PubMed]
23. Tebbenkamp, A.T.; Willsey, A.J.; State, M.W.; Sestan, N. The developmental transcriptome of the human brain: Implications for neurodevelopmental disorders. *Curr. Opin. Neurol.* **2014**, *27*, 149–156. [CrossRef]
24. Khaitovich, P.; Muetzel, B.; She, X.; Lachmann, M.; Hellmann, I.; Dietzsch, J.; Steigele, S.; Do, H.-H.; Weiss, G.; Enard, W. Regional patterns of gene expression in human and chimpanzee brains. *Genome Res.* **2004**, *14*, 1462–1473. [CrossRef] [PubMed]
25. Grigoriev, A. A relationship between gene expression and protein interactions on the proteome scale: Analysis of the bacteriophage T7 and the yeast Saccharomyces cerevisiae. *Nucleic Acids Res.* **2001**, *29*, 3513–3519. [CrossRef]
26. Ge, H.; Liu, Z.; Church, G.M.; Vidal, M. Correlation between transcriptome and interactome mapping data from Saccharomyces cerevisiae. *Nat. Genet.* **2001**, *29*, 482–486. [CrossRef] [PubMed]
27. Taylor, I.W.; Linding, R.; Warde-Farley, D.; Liu, Y.; Pesquita, C.; Faria, D.; Bull, S.; Pawson, T.; Morris, Q.; Wrana, J.L. Dynamic modularity in protein interaction networks predicts breast cancer outcome. *Nat. Biotechnol.* **2009**, *27*, 199–204. [CrossRef]
28. Lin, G.N.; Corominas, R.; Lemmens, I.; Yang, X.; Tavernier, J.; Hill, D.E.; Vidal, M.; Sebat, J.; Iakoucheva, L.M. Spatiotemporal 16p11.2 protein network implicates cortical late mid-fetal brain development and KCTD13-Cul3-RhoA pathway in psychiatric diseases. *Neuron* **2015**, *85*, 742–754. [CrossRef]
29. Toyoshima, M.; Akamatsu, W.; Okada, Y.; Ohnishi, T.; Balan, S.; Hisano, Y.; Iwayama, Y.; Toyota, T.; Matsumoto, T.; Itasaka, N.; et al. Analysis of induced pluripotent stem cells carrying 22q11.2 deletion. *Transl. Psychiatry* **2016**, *6*, e934. [CrossRef]
30. Rozas, M.F.; Benavides, F.; León, L.; Repetto, G.M. Association between phenotype and deletion size in 22q11.2 microdeletion syndrome: Systematic review and meta-analysis. *Orphanet J. Rare Dis.* **2019**, *14*, 1–9. [CrossRef]
31. Willsey, A.J.; Sanders, S.J.; Li, M.; Dong, S.; Tebbenkamp, A.T.; Muhle, R.A.; Reilly, S.K.; Lin, L.; Fertuzinhos, S.; Miller, J.A.; et al. Coexpression networks implicate human midfetal deep cortical projection neurons in the pathogenesis of autism. *Cell* **2013**, *155*, 997–1007. [CrossRef]
32. Zhou, Y.; Zhou, B.; Pache, L.; Chang, M.; Khodabakhshi, A.H.; Tanaseichuk, O.; Benner, C.; Chanda, S.K. Metascape provides a biologist-oriented resource for the analysis of systems-level datasets. *Nat. Commun.* **2019**, *10*, 1523. [CrossRef]
33. Ascano, M., Jr.; Mukherjee, N.; Bandaru, P.; Miller, J.B.; Nusbaum, J.D.; Corcoran, D.L.; Langlois, C.; Munschauer, M.; Dewell, S.; Hafner, M.; et al. FMRP targets distinct mRNA sequence elements to regulate protein expression. *Nature* **2012**, *492*, 382–386. [CrossRef]
34. Pardinas, A.F.; Holmans, P.; Pocklington, A.J.; Escott-Price, V.; Ripke, S.; Carrera, N.; Legge, S.E.; Bishop, S.; Cameron, D.; Hamshere, M.L.; et al. Common schizophrenia alleles are enriched in mutation-intolerant genes and in regions under strong background selection. *Nat. Genet.* **2018**, *50*, 381–389. [CrossRef]
35. Müller, C.S.; Haupt, A.; Bildl, W.; Schindler, J.; Knaus, H.G.; Meissner, M.; Rammner, B.; Striessnig, J.; Flockerzi, V.; Fakler, B.; et al. Quantitative proteomics of the Cav2 channel nano-environments in the mammalian brain. *Proc. Natl. Acad. Sci. USA* **2010**, *107*, 14950–14957. [CrossRef] [PubMed]
36. Deciphering Developmental Disorders Study. Prevalence and architecture of *de novo* mutations in developmental disorders. *Nature* **2017**, *542*, 433–438. [CrossRef]
37. Cheng, L.; Fan, K.; Huang, Y.; Wang, D.; Leung, K.S. Full Characterization of Localization Diversity in the Human Protein Interactome. *J. Proteome Res.* **2017**, *16*, 3019–3029. [CrossRef] [PubMed]
38. Piya, S.; Shrestha, S.K.; Binder, B.; Stewart, C.N., Jr.; Hewezi, T. Protein-protein interaction and gene co-expression maps of ARFs and Aux/IAAs in Arabidopsis. *Front. Plant Sci.* **2014**, *5*, 744. [CrossRef] [PubMed]
39. Fromer, M.; Pocklington, A.J.; Kavanagh, D.H.; Williams, H.J.; Dwyer, S.; Gormley, P.; Georgieva, L.; Rees, E.; Palta, P.; Ruderfer, D.M.; et al. De novo mutations in schizophrenia implicate synaptic networks. *Nature* **2014**, *506*, 179–184. [CrossRef] [PubMed]
40. Vissers, L.E.; de Ligt, J.; Gilissen, C.; Janssen, I.; Steehouwer, M.; de Vries, P.; van Lier, B.; Arts, P.; Wieskamp, N.; del Rosario, M.; et al. A de novo paradigm for mental retardation. *Nat. Genet.* **2010**, *42*, 1109–1112. [CrossRef]
41. Sanders, S.J.; Murtha, M.T.; Gupta, A.R.; Murdoch, J.D.; Raubeson, M.J.; Willsey, A.J.; Ercan-Sencicek, A.G.; DiLullo, N.M.; Parikshak, N.N.; Stein, J.L.; et al. De novo mutations revealed by whole-exome sequencing are strongly associated with autism. *Nature* **2012**, *485*, 237–241. [CrossRef]
42. Michaelson, J.J.; Shi, Y.; Gujral, M.; Zheng, H.; Malhotra, D.; Jin, X.; Jian, M.; Liu, G.; Greer, D.; Bhandari, A.; et al. Whole-Genome Sequencing in Autism Identifies Hot Spots for De Novo Germline Mutation. *Cell* **2012**, *151*, 1431–1442. [CrossRef]
43. Cheng, T.L.; Wang, Z.; Liao, Q.; Zhu, Y.; Zhou, W.H.; Xu, W.; Qiu, Z. MeCP2 suppresses nuclear microRNA processing and dendritic growth by regulating the DGCR8/Drosha complex. *Dev. Cell* **2014**, *28*, 547–560. [CrossRef]
44. Dubiel, W.; Dubiel, D.; Wolf, D.A.; Naumann, M. Cullin 3-Based Ubiquitin Ligases as Master Regulators of Mammalian Cell Differentiation. *Trends Biochem. Sci.* **2018**, *43*, 95–107. [CrossRef] [PubMed]
45. Wimuttisuk, W.; Singer, J.D. The Cullin3 ubiquitin ligase functions as a Nedd8-bound heterodimer. *Mol. Biol. Cell* **2007**, *18*, 899–909. [CrossRef]

46. Robb, G.B.; Rana, T.M. RNA helicase A interacts with RISC in human cells and functions in RISC loading. *Mol. Cell* **2007**, *26*, 523–537. [CrossRef] [PubMed]
47. Fu, K.; Tian, S.; Tan, H.; Wang, C.; Wang, H.; Wang, M.; Wang, Y.; Chen, Z.; Wang, Y.; Yue, Q.; et al. Biological and RNA regulatory function of MOV10 in mammalian germ cells. *BMC Biol.* **2019**, *17*, 39. [CrossRef]
48. Jahn, A.; Rane, G.; Paszkowski-Rogacz, M.; Sayols, S.; Bluhm, A.; Han, C.T.; Draskovic, I.; Londono-Vallejo, J.A.; Kumar, A.P.; Buchholz, F.; et al. ZBTB48 is both a vertebrate telomere-binding protein and a transcriptional activator. *EMBO Rep.* **2017**, *18*, 929–946. [CrossRef]
49. Tulay, P.; Sengupta, S.B. MicroRNA expression and its association with DNA repair in preimplantation embryos. *J. Reprod. Dev.* **2016**, 2015–2167. [CrossRef] [PubMed]
50. Calses, P.C.; Dhillon, K.K.; Tucker, N.; Chi, Y.; Huang, J.W.; Kawasumi, M.; Nghiem, P.; Wang, Y.; Clurman, B.E.; Jacquemont, C.; et al. DGCR8 Mediates Repair of UV-Induced DNA Damage Independently of RNA Processing. *Cell Rep.* **2017**, *19*, 162–174. [CrossRef]
51. Vilas, C.K.; Emery, L.E.; Denchi, E.L.; Miller, K.M. Caught with One's Zinc Fingers in the Genome Integrity Cookie Jar. *Trends Genet. TIG* **2018**, *34*, 313–325. [CrossRef] [PubMed]
52. Sudo, H.; Maru, Y. LAPSER1/LZTS2: A pluripotent tumor suppressor linked to the inhibition of katanin-mediated microtubule severing. *Hum. Mol. Genet.* **2008**, *17*, 2524–2540. [CrossRef] [PubMed]
53. Demczuk, S.; Thomas, G.; Aurias, A. Isolation of a novel gene from the DiGeorge syndrome critical region with homology to Drosophila gdl and to human LAMC1 genes. *Hum. Mol. Genet.* **1996**, *5*, 633–638. [CrossRef] [PubMed]
54. Das Chakraborty, R.; Bernal, A.J.; Schoch, K.; Howard, T.D.; Ip, E.H.; Hooper, S.R.; Keshavan, M.S.; Jirtle, R.L.; Shashi, V. Dysregulation of DGCR6 and DGCR6L: Psychopathological outcomes in chromosome 22q11.2 deletion syndrome. *Transl. Psychiatry* **2012**, *2*, e105. [CrossRef]
55. Devaraju, P.; Yu, J.; Eddins, D.; Mellado-Lagarde, M.M.; Earls, L.R.; Westmoreland, J.J.; Quarato, G.; Green, D.R.; Zakharenko, S.S. Haploinsufficiency of the 22q11.2 microdeletion gene Mrpl40 disrupts short-term synaptic plasticity and working memory through dysregulation of mitochondrial calcium. *Mol. Psychiatry* **2017**, *22*, 1313–1326. [CrossRef]
56. Plafker, K.; Macara, I.G. Facilitated nucleocytoplasmic shuttling of the Ran binding protein RanBP1. *Mol. Cell. Biol.* **2000**, *20*, 3510–3521. [CrossRef]
57. Lin, C.J.; Koh, F.M.; Wong, P.; Conti, M.; Ramalho-Santos, M. Hira-mediated H3.3 incorporation is required for DNA replication and ribosomal RNA transcription in the mouse zygote. *Dev. Cell* **2014**, *30*, 268–279. [CrossRef] [PubMed]
58. Mattiaccio, L.M.; Coman, I.L.; Thompson, C.A.; Fremont, W.P.; Antshel, K.M.; Kates, W.R. Frontal dysconnectivity in 22q11.2 deletion syndrome: An atlas-based functional connectivity analysis. *Behav. Brain Funct.* **2018**, *14*, 2. [CrossRef]
59. Hansen, J.C.; Ghosh, R.P.; Woodcock, C.L. Binding of the Rett syndrome protein, MeCP2, to methylated and unmethylated DNA and chromatin. *IUBMB Life* **2010**, *62*, 732–738. [CrossRef]
60. LaSalle, J.M.; Yasui, D.H. Evolving role of MeCP2 in Rett syndrome and autism. *Epigenomics* **2009**, *1*, 119–130. [CrossRef] [PubMed]
61. Ausió, J. Role of MeCP2 in neurological disorders: Current status and future perspectives. *Epigenomics* **2018**, *10*, 5–8. [CrossRef] [PubMed]
62. Boyden, L.M.; Choi, M.; Choate, K.A.; Nelson-Williams, C.J.; Farhi, A.; Toka, H.R.; Tikhonova, I.R.; Bjornson, R.; Mane, S.M.; Colussi, G.; et al. Mutations in kelch-like 3 and cullin 3 cause hypertension and electrolyte abnormalities. *Nature* **2012**, *482*, 98–102. [CrossRef]
63. Nakashima, M.; Kato, M.; Matsukura, M.; Kira, R.; Ngu, L.H.; Lichtenbelt, K.D.; van Gassen, K.L.I.; Mitsuhashi, S.; Saitsu, H.; Matsumoto, N. De novo variants in CUL3 are associated with global developmental delays with or without infantile spasms. *J. Hum. Genet.* **2020**, *65*, 727–734. [CrossRef]
64. Anderica-Romero, A.C.; Gonzalez-Herrera, I.G.; Santamaria, A.; Pedraza-Chaverri, J. Cullin 3 as a novel target in diverse pathologies. *Redox Biol.* **2013**, *1*, 366–372. [CrossRef]
65. McEvoy, J.D.; Kossatz, U.; Malek, N.; Singer, J.D. Constitutive turnover of cyclin E by Cul3 maintains quiescence. *Mol. Cell. Biol.* **2007**, *27*, 3651–3666. [CrossRef] [PubMed]
66. Zhu, C.; Chen, C.; Huang, J.; Zhang, H.; Zhao, X.; Deng, R.; Dou, J.; Jin, H.; Chen, R.; Xu, M.; et al. SUMOylation at K707 of DGCR8 controls direct function of primary microRNA. *Nucleic Acids Res.* **2015**, *43*, 7945–7960. [CrossRef] [PubMed]
67. Herbert, K.M.; Pimienta, G.; DeGregorio, S.J.; Alexandrov, A.; Steitz, J.A. Phosphorylation of DGCR8 increases its intracellular stability and induces a progrowth miRNA profile. *Cell Rep.* **2013**, *5*, 1070–1081. [CrossRef]
68. Zhang, W.; Zhong, T.; Chen, Y. LC-MS/MS-based targeted proteomics quantitatively detects the interaction between p53 and MDM2 in breast cancer. *J. Proteom.* **2017**, *152*, 172–180. [CrossRef]
69. Fiddes, I.T.; Lodewijk, G.A.; Mooring, M.; Bosworth, C.M.; Ewing, A.D.; Mantalas, G.L.; Novak, A.M.; van den Bout, A.; Bishara, A.; Rosenkrantz, J.L.; et al. Human-Specific NOTCH2NL Genes Affect Notch Signaling and Cortical Neurogenesis. *Cell* **2018**, *173*, 1356–1369.e1322. [CrossRef]
70. Hansen, D.V.; Lui, J.H.; Parker, P.R.; Kriegstein, A.R. Neurogenic radial glia in the outer subventricular zone of human neocortex. *Nature* **2010**, *464*, 554–561. [CrossRef]

71. Meechan, D.W.; Tucker, E.S.; Maynard, T.M.; LaMantia, A.S. Diminished dosage of 22q11 genes disrupts neurogenesis and cortical development in a mouse model of 22q11 deletion/DiGeorge syndrome. *Proc. Natl. Acad. Sci. USA* **2009**, *106*, 16434–16445. [CrossRef] [PubMed]
72. Zhang, M.S.; Arnaoutov, A.; Dasso, M. RanBP1 governs spindle assembly by defining mitotic Ran-GTP production. *Dev. Cell* **2014**, *31*, 393–404. [CrossRef] [PubMed]
73. Crespi, B.J.; Crofts, H.J. Association testing of copy number variants in schizophrenia and autism spectrum disorders. *J. Neurodev. Disord.* **2012**, *4*, 15. [CrossRef] [PubMed]
74. Kanduri, C.; Kantojarvi, K.; Salo, P.M.; Vanhala, R.; Buck, G.; Blancher, C.; Lahdesmaki, H.; Jarvela, I. The landscape of copy number variations in Finnish families with autism spectrum disorders. *Autism Res. Off. J. Int. Soc. Autism Res.* **2016**, *9*, 9–16. [CrossRef]
75. Sanders, S.J.; He, X.; Willsey, A.J.; Ercan-Sencicek, A.G.; Samocha, K.E.; Cicek, A.E.; Murtha, M.T.; Bal, V.H.; Bishop, S.L.; Dong, S.; et al. Insights into Autism Spectrum Disorder Genomic Architecture and Biology from 71 Risk Loci. *Neuron* **2015**, *87*, 1215–1233. [CrossRef] [PubMed]

life

MDPI

*Article*

# Description of a CSF-Enriched miRNA Panel for the Study of Neurological Diseases

**María Muñoz-San Martín, Imma Gomez, Albert Miguela, Olga Belchí, René Robles-Cedeño, Ester Quintana *,† and Lluís Ramió-Torrentà *,†**

Neuroimmunology and Multiple Sclerosis Unit (UNIEM), Girona Biomedical Research Institute (IDIBGI), Doctor Josep Trueta University Hospital, Dr Castany s/n, Salt, 17190 Girona, Spain; mmunoz@idibgi.org (M.M.-S.M.); igomez@idibgi.org (I.G.); amiguela@idibgi.org (A.M.); lgabegui@gmail.com (O.B.); rrobles@idibgi.org (R.R.-C.)

* Correspondence: equintana@idibgi.org (E.Q.); llramio@idibgi.org (L.R.-T.); Tel.: +34-872987087 (E.Q. & L.R.-T.)

† Authors contributed equally as principal investigators.

**Abstract:** Background: The study of circulating miRNAs in CSF has gained tremendous attention during the last years, as these molecules might be promising candidates to be used as biomarkers and provide new insights into the disease pathology of neurological disorders. Objective: The main aim of this study was to describe an OpenArray panel of CSF-enriched miRNAs to offer a suitable tool to identify and characterize new molecular signatures in different neurological diseases. Methods: Two hundred and fifteen human miRNAs were selected to be included in the panel, and their expression and abundance in CSF samples were analyzed. In addition, their stability was studied in order to propose suitable endogenous controls for CSF miRNA studies. Results: miR-143-3p and miR-23a-3p were detected in all CSF samples, while another 80 miRNAs were detected in at least 70% of samples. miR-770-5p was the most abundant miRNA in CSF, presenting the lowest mean Cq value. In addition, miR-26b-5p, miR-335-5p and miR-92b-3p were the most stable miRNAs and could be suitable endogenous normalizers for CSF miRNA studies. Conclusions: These OpenArray plates might be a suitable and efficient tool to identify and characterize new molecular signatures in different neurological diseases and would improve the yield of miRNA detection in CSF.

**Keywords:** CSF; miRNAs; neurological diseases; OpenArray

**Citation:** Muñoz-San Martín, M.; Gomez, I.; Miguela, A.; Belchí, O.; Robles-Cedeño, R.; Quintana, E.; Ramió-Torrentà, L. Description of a CSF-Enriched miRNA Panel for the Study of Neurological Diseases. *Life* **2021**, *11*, 594. https://doi.org/10.3390/life11070594

Academic Editors: Jong Hyuk Yoon and Chiara Villa

Received: 20 May 2021
Accepted: 18 June 2021
Published: 22 June 2021



## 1. Introduction

Neurological disorders are diseases that might affect the peripheral and central nervous system (CNS), affecting hundreds of millions of individuals of all age groups and races worldwide [1,2]. Neurological disorders were responsible for 276 million disability-adjusted life-years and 16.5% of total global deaths in 2016 [3]. Specifically, brain disorders, which include a broad range of different conditions, suchas neurodegenerative diseases, demyelinating and neuroinflammatory diseases, tumors, dementias, infections or mental disorders, are a major public health problem, representing an important economic and social burden [4]. The brain is considered to be the most complex organ of the body, but its inaccessibility hinders the study of pathological processes [5].

Cerebrospinal fluid (CSF) is an ultrafiltrate of plasma that is found around and within the organs of the CNS and maintains an appropriate chemical environment for the neural tissue [6]. In different neurological disorders, the composition of CSF might change [7], highlighting its interesting nature as a fluid, as it might reflect the level of brain damage [8]. Measuring levels of different components of CSF might be a valuable tool to facilitatethe diagnosis and prognosis of neurological conditions [7].

microRNAs (miRNAs) are small non-coding RNAs that are evolutionarily conserved whose mature and biologically active form is 18–25 nucleotides long [9]. miRNAs regulate gene expression by two mutually exclusive posttranscriptional mechanisms: translational

repression or mRNA cleavage [10]. Most miRNAs are located inside cells, but there are also extracellular miRNAs, known as circulating miRNAs, that might be found in different biological fluids such as plasma, serum or CSF [11]. In contrast to cellular miRNAs, circulating miRNAs are remarkably stable despite the existence of RNases in body fluids and unfavorable conditions [12]. It has been suggested that they are delivered to the extracellular fluids by the passive leakage of apoptosis, necrosis or due to active secretion by cells [13]. In 2007, Valadi et al. proposed a novel paracrine mechanism for intercellular communication showing that extracellular miRNAs could be delivered into recipient cells, where they could alter gene expression [14].

CSF circulating miRNA studies in neurological conditions have gained tremendous attention during the last years, as they might be promising candidates to be used as biomarkers and provide new insights into the disease pathology and therapeutic targets of neurological disorders. CSF miRNAs might discriminate between Alzheimer's disease (AD) individuals and controls [15] or distinguish multiple sclerosis (MS) disease phenotypes from each other [16]. The diagnosis of other neurological conditions such as Huntington's disease (HD), temporal lobe epilepsy or CNS injury might be supported by the analysis of CSF miRNAs [17–19]. It is known that CSF miRNA content is less abundant than the content of other biological material such as cells or serum [20], and miRNA composition can vary between tissues and biofluids [21].

miRNA profiling studies show great promise for the biomarker field in neurological disorders, but further research is needed to validate theresults ofdifferent laboratories [22]. Therefore, the main aim of this study was to describe a panel of CSF-enriched miRNAs that might be a suitable and efficient tool to identify and characterize new molecular signatures in different neurological diseases and improve the yield of miRNA detection in CSF. A set of 215 miRNAs was selected to be included in the customized panels, and their expression and abundance in CSF samples were analyzed. In addition, some miRNAs were proposed as suitable endogenous controls for CSF miRNA studies.

## 2. Material and Methods

### *2.1. Biological Samples*

The whole cohort of patients was composed ofspinal anesthesia subjects (SAS), corresponding to neurologically healthy patients with hip/knee impairment undergoing surgical intervention; subjects affected by other neurological diseases (ONDs) ratherthan MS, whose pathologies were of vascular origin, migraines, dementia or dizziness; and MS subjects, including the phenotypes relapsing–remitting MS (RRMS) and primary progressive MS (PPMS). Most individuals were recruited at the Girona Neuroimmunology and Multipe Sclerosis Unit of Dr. Josep Trueta University Hospital (Girona, Spain). All participants signed a written informed consent form. The Ethics Committee and the Committee for Clinical Investigation from Dr. Josep Trueta University Hospital approved the protocol employed.

CSF samples were obtained at the moment of diagnosis by means of a lumbar puncture made by a neurologist. In the case of SAS, an anesthesiologist performed this technique during surgery. After collecting CSF, it was centrifuged at 400× *g* and 19 °C for 15 min in order to obtain cell-free CSF.

### *2.2. Circulating RNA Extraction and Purification*

Circulating RNA from CSF was purified from 300 or 500 µL of starting material using the mirVana PARIS Isolation kit (Applied Biosystems) according to the manufacturer's protocol. Briefly, the initial volume of sample (300 µL in most cases) was mixed with the same volume of 2× Denaturing solution containing 375 µL of 2-mercaptoethanol. At this point, two exogenous miRNAs (cel-miR-39 and cel-miR-54) were added at 5 pM to verify the quality of the extraction process. The same volume of acid-phenol:chloroform was then added, and the upper aqueous phase obtained after centrifugation (17,000× *g*, 10 min, 19 °C) was recovered. This phase was mixed with 100% ethanol and placed into a filter

cartridge provided in the kit. After the RNA washing procedures, total RNA was eluted with 40 µL of nuclease-free water and stored at −80 °C for its lateruse.

### *2.3. Circulating miRNA Retrotranscription and Preamplification*

The Applied BiosystemsTaqMan Advanced miRNA cDNA Synthesis kit (Applied Biosystems, Foster City, CA, USA) was used to obtain miRNA cDNA in this study. This kit has been specially designed to work with materials whose miRNA contents are limited. It employs universal reverse transcription (RT) chemistry to obtain the cDNA template used for mature miRNA detection and quantification with TaqMan Advanced miRNA Assays. Two microliters of RNA eluate were used for the preparation of miRNA cDNA and, after the addition of a poly(A) tail and an adaptor following the manufacturer's instructions, an RT reaction and miRNA amplification reaction were performed.

### *2.4. Circulating miRNA Profiling*

To analyze the miRNA expression ofCSF samples, cDNA templates were subjected to PCR amplification to detect specific miRNAs using TaqMan Advanced miRNA assay technology. These assays were pre-loaded during the manufacturing process in TaqMan OpenArray Human Advanced microRNA plates—the high-throughput screening platforms chosen to carry out the profiling step in this study. Two different formats were used: fixed-content plates (fc-OA) and custom-configured plates (cc-OA). The first werepreloaded with 754 human Advanced miRNA assays and allowed the analysis of three samples per plate. cc-OA plates were designed to analyze specifically 215 CSF-enriched miRNAs for this study (Supplementary Table S1).

cDNA templates were diluted to 1:20 in 0.1X TE buffer to be run in triplicate in TaqMan OpenArray Plates. These diluted cDNA samples were combined with the same volume of TaqMan OpenArray Real-Time PCR Master Mix in tubes. Five microliters of the combined master mix and cDNA sample were added to the determined wells in an OpenArray 384-well Sample Plate. The automated OpenArray AccuFill System was used to load the samples into the TaqMan OpenArray Plate through holes. Then, they were cycled and imaged with the QuantStudio 12 K Flex Real-Time PCR System, resulting in Cq values for each sample and miRNA.

### *2.5. Databases for Cellular/Tissue-Enriched Source Analyses and Disease Associations*

To study the potential sources of the 20 most abundant miRNAs in CSF, the human miRNA tissue atlas, CNS microRNA profiles described by Hoye et al. and FANTOM5 human miRNA atlas were used to identify miRNA expression across tissue, CNS cells and primary cells, respectively [21,23,24]. Version 3.0 of the Human MicroRNA Disease Database was used to explore experimentally supported miRNA–disease associations [25].

### *2.6. Search of Candidate Normalizer miRNAs for CSF Samples*

Three different algorithms were used to identify stable miRNAs in CSF samples: Normfinder [26], geNorm [27] and the coefficient of variation (CV) score. These algorithms generate a score that represents the stability: the smaller the score, the higher the expression stability the miRNA has. The summarized stability score (SSS) for each miRNA was calculated to summarize the results [28].

## 3. Results

### *3.1. Profiling of CSF Samples in fc-OA Plates*

Three samples of CSF were used to extract RNA from an initial volume of 500 µL and 300 µL in order to establish the average miRNA detection in CSF samples using two fc-OA panels containing 754 TaqMan Advanced miRNA assays.

As observed in Figure 1, 500 µL of CSF samples presented an average number of detected miRNAs of 89, whereas 300 µL of CSF samples showed a mean detection of 79 miRNAs, which indicated a percentage of detection of 11.8% and 10.5%, respectively, from the total miRNA set. The detection of 99 miRNAs overlapped for at least one sample from each starting volume. Analyzing each initial volume individually, 23, 60 and 112 miRNAs were detected in 3, 2 or 1 sample/s for 300 µL of CSF, respectively, corresponding to 13.4%, 21.5% and 65.1% of the total set of detected miRNAs. Regarding to 500 µL, 52, 39 and 59 miRNAs were detected in 3, 2 or 1 sample/s, respectively, corresponding to 34.7%, 26.0% and 39.3% of the total detected miRNAs (Supplementary Figure S1). Despite the fact that both initial volumes presented a comparable detection, the intra-volume degree of correlation when working with 300 µL of CSF was less consistent than that observed for 500 µL of CSF. However, as CSF is very valuable and difficult to obtain, henceforth, total RNA from CSF was extracted from 300 µL of sample.

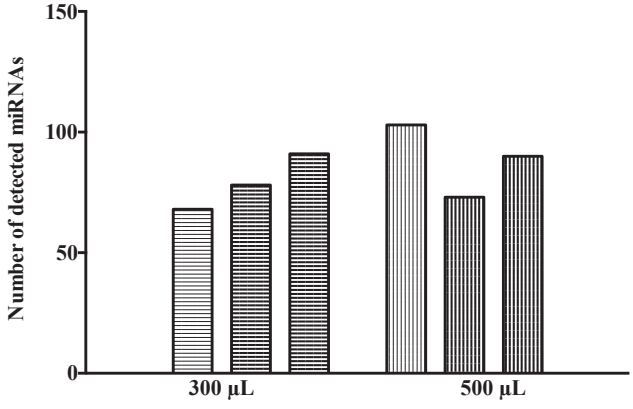


**Figure 1.** miRNA detection in CSF in TaqMan OpenArray Human Advanced microRNA panels. The number of miRNAs with Cq values (range 15–35) detected in each tested sample was represented in each column. Columns with horizontal stripes represent CSF samples whose initial volume was 300 µL and columns with vertical stripes represent CSF samples whose initial volume was 500 µL.

### *3.2. Selection of 215 miRNAs to Be Included in cc-OA Plates*

Due to the low detection presented by CSF samples in fc-OA, cc-OA plates were customized for studying CSF miRNA profiles. The selected 224 format allowed us to analyze 12 samples simultaneously, covering a total of 215 miRNAs plus one mandatory control (miR-16). miRNAs needed to meet at least one of the following criteria to be included in the panel:

1. Previously associated with MS in tissue, serum/plasma or CSF;
2. Particularly brain-enriched;
3. Detectable in CSF based on existing literature and/or our previous experience;
4. Potential endogenous normalizer;
5. Negative control.

The list of 215 miRNA assays included in these cc-OA panels is shown in Supplementary Table S1.

### *3.3. miRNA Classification According to Their Detectability*

To analyze the performance of the detection of miRNAs with these cc-OA plates, 64 CSF samples were used, belonging to SAS, OND, PPMS and RRMS individuals. The clinical characteristics of the cohort are depicted in Table 1.

miRNAs were classified according to the percentage of CSF samples in which they were detectable (Table 2). From the total set of 215 miRNAs, 2 miRNAs, miR-143-3p and miR-23a-3p, were detected in all CSF samples. Another 80 miRNAs, representing 37.2% of miRNAs, were detected in at least 70% of samples. These two categories represented the suitable miRNAs to proceed with further analysis in differential expression studies. When subclassifying the whole cohort in each specific individual group, it could be observed that 80 miRNAs might be detectable in 70% of samples in at least three groups. Other miRNAs might seem to be more detectable in some groups exclusively (Supplementary Figure S2).

**Table 1.** Clinical characteristics of the studied cohort.

| Group | *n* | Age (Mean ± SD) | Sex (F/M) |
|---|---|---|---|
| SAS | 7 | 50.2 ± 5.8 | 5/2 |
| OND | 6 | 51.7 ± 5.5 | 4/2 |
| Vascular origin | 2 | 50.5 ± 0.7 | 2/0 |
| Migraines | 2 | 52 ± 5.7 | 2/0 |
| Dementia | 1 | 60 | 0/1 |
| Dizziness | 1 | 45 | 0/1 |
| PPMS | 11 | 52.6 ± 7.0 | 6/5 |
| RRMS | 40 | 32.1 ± 13.0 | 30/10 |

SAS: spinal anesthesia subjects; OND: other neurological diseases; PPMS: primary progressivemultiple sclerosis; RRMS: relapsing-remitting multiple sclerosis; SD: standard deviation; F: female; M: male.

**Table 2.** miRNA classification according to their detectability.

| Detection | Number of miRNAs (%) | miRNAs |
|---|---|---|
| 100% | 2 (0.9) | miR-143-3p; miR-23a-3p |
| 99–70% | 80 (37.2) | let-7a-5p; let-7b-5p; let-7c-5p; let-7f-5p; let-7g-5p; let-7i-5p; miR-100-3p; miR-100-5p; miR-101-3p; miR-10b-5p; miR-124-3p; miR-125a-5p; miR-125b-5p; miR-1260a; miR-1298-5p; miR-130a-3p; miR-137; miR-142-3p; miR-144-3p; miR-145-5p; miR-146a-5p; miR-148a-3p; miR-148b-3p; miR-150-5p; miR-151a-3p; miR-15a-5p; miR-181a-5p; miR-181c-5p; miR-185-5p; miR-186-5p; miR-195-5p; miR-199a-3p; miR-199a-5p; miR-19a-3p; miR-204-5p; miR-20a-5p; miR-21-5p; miR-219a-5p; miR-22-3p; miR-221-3p; miR-223-3p; miR-23b-3p; miR-24-3p; miR-25-3p; miR-26a-5p; miR-26b-5p; miR-27a-3p; miR-27b-3p; miR-29a-3p; miR-29c-5p; miR-30c-5p; miR-30d-5p; miR-320a; miR-320b; miR-335-5p; miR-338-3p; miR-342-3p; miR-34a-5p; miR-34c-5p; miR-361-5p; miR-374b-5p; miR-376a-3p; miR-378a-3p; miR-423-5p; miR-448; miR-449b-5p; miR-450b-3p; miR-451a; miR-452-3p; miR-497-5p; miR-645; miR-652-3p; miR-653-3p; miR-660-5p; miR-664a-3p; miR-770-5p; miR-885-5p; miR-9-5p; miR-92b-3p; miR-939-5p |
| 69–50% | 31 (14.4) | let-7b-3p; let-7e-5p; miR-1-3p; miR-103a-3p; miR-107; miR-128-3p; miR-133a-3p; miR-133b; miR-135a-5p; miR-151a-5p; miR-15b-5p; miR-17-5p; miR-1911-5p; miR-193a-5p; miR-196a-5p; miR-222-3p; miR-28-5p; miR-30c-2-3p; miR-34b-3p; miR-34b-5p; miR-34c-3p; miR-378a-5p; miR-424-5p; miR-501-3p; miR-516b-5p; miR-525-3p; miR-633; miR-9-3p; miR-93-5p; miR-99a-3p; miR-99b-5p |
| 49–30% | 31 (14.4) | let-7f-2-3p; miR-106b-3p; miR-106b-5p; miR-126-5p; miR-1264; miR-132-3p; miR-155-5p; miR-181b-5p; miR-190a-5p; miR-205-5p; miR-210-3p; miR-302b-3p; miR-302d-3p; miR-31-5p; miR-32-5p; miR-339-5p; miR-361-3p; miR-376c-3p; miR-411-5p; miR-412-3p; miR-425-5p; miR-483-3p; miR-484; miR-502-3p; miR-505-3p; miR-518f-3p; miR-524-3p; miR-576-3p; miR-583; miR-92a-3p; miR-937-3p |

**Table 2.** *Cont.*

| Detection | Number of miRNAs (%) | miRNAs |
|---|---|---|
| 30–1% | 70 (32.6) | miR-103a-2-5p; miR-10a-5p; miR-122-5p; miR-1247-5p; miR-1249-3p; miR-125a-3p; miR-127-3p; miR-129-2-3p; miR-1292-5p; miR-142-5p; miR-145-3p; miR-146b-5p; miR-153-3p; miR-181d-5p; miR-183-3p; miR-191-3p; miR-191-5p; miR-194-5p; miR-19b-3p; miR-200c-3p; miR-203a-3p; miR-206; miR-216a-5p; miR-218-5p; miR-27b-5p; miR-30a-3p; miR-30c-1-3p; miR-30e-3p; miR-323a-3p; miR-325; miR-326; miR-328-3p; miR-34a-3p; miR-363-3p; miR-369-3p; miR-369-5p; miR-373-3p; miR-375; miR-383-5p; miR-410-3p; miR-449a; miR-450b-5p; miR-452-5p; miR-454-3p; miR-455-3p; miR-483-5p; miR-486-5p; miR-487a-3p; miR-489-3p; miR-490-3p; miR-513a-5p; miR-515-3p; miR-518d-3p; miR-518e-3p; miR-520h; miR-523-3p; miR-532-3p; miR-532-5p; miR-548d-5p; miR-548e-3p; miR-548k; miR-548n; miR-551a; miR-570-3p; miR-593-5p; miR-615-3p; miR-628-3p; miR-642a-5p; miR-656-3p; miR-876-3p |
| 0% | 1 (0.5) | miR-211-5p |

### *3.4. miRNA Abundance in CSF Samples and Disease Associations*

Among those miRNAs that were detectable in at least 70% of samples, the 20 most abundant miRNAs (lower Cq values) in CSF were identified by ranking the average Cq values of all samples as shown in Table 3. miR-770-5p presented the lowest mean Cq value (20.9). When subclassifying the whole cohort in each specific patient group, miR-770-5p remained the most abundant miRNA in CSF. From these 20 miRNAs, it should be highlighted that miR-451a and miR-144-3p presented the greatest differences between OND and SAS individuals.

**Table 3.** miRNA abundance in CSF samples.

| miRNA | Mean Cqvalue | Neurologicaldisease | PMID |
|---|---|---|---|
| miR-770-5p | 20.9 | GBM | 27572852 |
| miR-939-5p | 24.1 | Complex regional painsyndrome | 31489147 |
| miR-450b-3p | 24.1 | PD | 23938262 |
| miR-26b-5p | 24.4 | AD, hypoxia/ischemia, diffuseintrinsicpontine glioma, ALS | 23895045, 29937716, 0124166, 29543360, 30210287, 24027266 |
| miR-145-5p | 24.7 | Myastheniagravis, MS, stroke, seizure, GBM | 24043548, 23773985, 26096228, 27833019, 28284220, 23745809, 27752929, |
| miR-204-5p | 25.0 | Frontotemporaldementia, SPI, mesial temporal lobeepilepsy, GBM | 29434051, 29547407, 25410734, 30008822 |
| miR-30c-5p | 25.1 | ALS, MS | 30210287, 29551498 |
| miR-451a | 25.1 | Depression, ALS, GBM | 26343596, 30210287, 18765229 |
| miR-335-5p | 25.4 | Stroke, astrocytoma, neuroblastoma, majordepressiondisorder | 27856935, 21592405, 23806264, 26314506 |
| let-7a-5p | 25.8 | PD, GBM, ALS, MS | 30267378, 23600457, 26502847, 30210287, 25487315 |
| miR-23a-3p | 25.9 | MS, epilepsy, HD, SPI, GBM | 24277735, 26382856, 30359470, 27725128, 27907012, 20711171 |
| miR-221-3p | 26.0 | Stroke, PD, GBM, neuropathicpain | 23860376, 27748571, 28381184, 27059231, 18759060, 24055409 |
| miR-449b-5p | 26.0 | Stroke, PD | 30135469, 29935433 |
| miR-144-3p | 26.0 | Bipolar disorder, GBM, AD | 19849891, 26250785, 23546882 |
| miR-143-3p | 26.2 | AD, GBM | 26078483, 22490015, 23376635, 21211035 |
| miR-137 | 26.2 | AD, schizophrenia, GBM, HD | 22155483, 26899870, 29684772, 26187071, 21926974, 25044277, 18577219, 23965969, 21994399 |

**Table 3.** *Cont.*

| miRNA | Mean Cqvalue | Neurologicaldisease | PMID |
|---|---|---|---|
| miR-150-5p | 26.4 | MS, stroke, HD | 28067602, 27144214, 27246008, 22048026 |
| miR-26a-5p | 26.5 | Migraine, PD, GBM | 26333279, 30267378, 20080666 |
| miR-92b-3p | 27.3 | Neuroblastoma, GBM | 21572098, 22829753 |
| miR-23b-3p | 27.4 | GBM | 22745829, 23152062 |

Disease association established using the Human MicroRNA Disease Database [24]. PMID numbers identify articles referring an association between a miRNA and a neurological disease. GBM: glioblastoma; PD: Parkinson'sdisease; AD: Alzheimer's disease; ALS: amyotrophic lateral sclerosis; MS: multiple sclerosis; SPI: spinal cord injury; HD: Huntington's disease.

Exploring the association of these miRNAs with diseases in the Human MicroRNA Disease Database [25], all of them have been previously related to at least one neurological disorder such as glioblastoma, Parkinson's disease, MS, Alzheimer's disease, stroke or epilepsy.

### *3.5. Cellular/Tissue-Enriched Source Analysis of Most Abundant miRNAs*

The potential tissue and cellular origin of the 20 most abundant miRNAs in CSF was examined using different repositories. First, Ludwig et al. determined the abundance of miRNA in tissue biopsies of two individuals [21]. Using the data from this human miRNA tissue atlas, a heat map of the normalized expression of miRNA in 30 different tissues was constructed (Figure 2). As could be observed, the expression of some miRNAs (let-7a-5p, miR-137, miR-204-5p, miR-221-3p, miR-26a-5p, miR-26b-5p, miR-30c-5p, miR-335-5p, miR-451a, miR-770-5p and miR-939-5p) was higher in brain and spinal cord tissues. Further investigating CNS cell types using the repository of CNS microRNA profiles [24], miR-137, miR-335-5p and miR-770-5p might present an increased expression in motor neurons, whereas miR-221-3p expression might seem to be elevated in astrocytes.

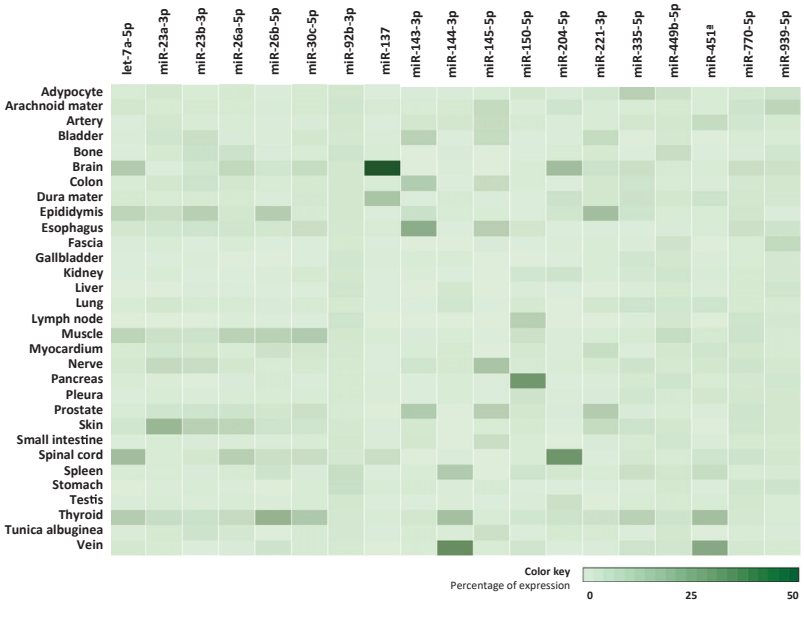


**Figure 2.** Most abundant miRNA expression in tissue biopsies by human miRNA tissue atlas. Normalized expression of the most abundant miRNAs in CSF in 30 tissues was retrieved from the human miRNA tissue atlas [20] and the percentage of expression calculated and represented in a heat map.

After analyzing miRNA expression across primary cells using the FANTOM5 atlas [23], the predominant expression of miR-26a-5p, miR-26b-5p, miR-144-3p, miR-150-5p and miR-450b-3p in different immune cell subsets should be highlighted (Table 4). Specifically, miR-143-3p was highly expressed in circulating cells and neutrophils, miR-150-5p was highly expressed in T cells and circulating cells, and miR-450b-3p was highly expressed in neutrophils. miR-26a-5p and miR-26b-5p were similarly found in the nine immune cells described.

**Table 4.** Percentage of expression of the most abundant miRNAs in primary immune cells.

| Immune Cell Subset | miR-26a-5p | miR-26b-5p | miR-144-3p | miR-150-5p | miR-450b-3p |
|---|---|---|---|---|---|
| Circulating cell | 4.87 | 6.47 | 53.67 | 25.63 | 0.00 |
| Dendritic cell | 1.47 | 3.03 | 0.65 | 0.71 | 0.00 |
| Lymphocyte B lineage | 4.77 | 6.71 | 1.76 | 3.35 | 0.00 |
| Macrophage | 1.69 | 2.84 | 0.00 | 0.03 | 0.00 |
| Mastcell | 3.41 | 7.97 | 0.60 | 0.08 | 0.00 |
| Monocyte | 3.58 | 5.75 | 0.90 | 5.08 | 0.00 |
| Natural Killer cell | 3.65 | 7.26 | 0.24 | 17.09 | 0.00 |
| Neutrophil | 5.91 | 8.69 | 23.93 | 0.28 | 27.95 |
| T cell | 4.25 | 4.85 | 0.23 | 46.94 | 0.00 |

Data obtained from FANTOM5 human miRNAs repository [22]. Percentage of expression in specific primary cells are shown for each miRNA.

### *3.6. Search for Suitable Endogenous Normalizers for CSF Samples*

Although a normalization method based on the mean expression value of all miRNAs has been proposed and validated for qPCR data from array-based approaches (screening phase), the search fora candidate reference endogenous miRNAs is necessary for futurestudies, and thus we evaluated a limited panel of miRNAs in a wider cohort (validation phase) [28]. To date, no study has proposedreliable endogenous controls for CSF using TaqMan Advanced miRNA assay technology. For this reason, a search of endogenous controls for use in qPCR experiments with CSF samples was made using the OpenArray data obtained in this study.

Those miRNAs detected in at least 70% of samples were selected. Three different algorithms were used to identify stable miRNAs: Normfinder [26], geNorm [27] and the CV score. To outline the results, the SSS for each miRNA was also calculated [28]. In Table 5, stability scores obtained for the 17 most stable miRNAs are represented, showing that miR-23a-3p, miR-26b-5p and miR-125a-5p might be suitable endogenous miRNAs for CSF studies. SSS scores were also calculated for these 17 miRNAs in each group of patients (Supplementary Table S2). While miR-26b-5p presented similar scores in each group, miR-23a-3p seemed more stable in PPMS and SAS individuals and miR-125a-5p might not be recommendable for OND. miR-335-5p and miR-92b-3p could also be stable in all groups.

Despite selecting the best endogenous candidates for CSF samples, the establishment ofthe optimum number of reference miRNAs must be experimentally determined. geNorm also generates a pairwise stability measure to determine if adding more reference miRNAs for the normalization process is beneficial. As shown in Figure 3, the recommended cut off value of 0.15 indicates that the use of eight endogenous controls in CSF samples would offer an acceptable stability for the reference miRNA combination [29]. Therefore, we would strongly recommend the use of miR-21-5p, miR-23a-3p, miR-26b-5p, miR-27a-3p, miR-92b-3p, miR-125a-5p, miR-221-3p and miR-335-5p for the normalization of qPCR experiments in CSF samples.

**Table 5.** miRNA stability scores for geNorm, Normfinder and CV algorithms and SSS score for CSF samples.

| miRNA | geNorm | NormFinder | CV Score | SSS Score |
|---|---|---|---|---|
| miR-101-3p | 1.63 (12) | 0.83 (12) | 0.98 (17) | 2.07 (14) |
| miR-125a-5p | 1.46 (4) | 0.63 (3) | 0.59 (3) | 1.69 (3) |
| miR-143-3p | 1.59 (8) | 0.79 (8) | 0.73 (9) | 1.92 (9) |
| miR-151a-3p | 1.71 (15) | 0.90 (15) | 0.85 (12) | 2.11 (15) |
| miR-15a-5p | 1.71 (16) | 0.91 (16) | 0.93 (16) | 2.15 (17) |
| miR-181a-5p | 1.67 (16) | 0.87 (14) | 0.80 (11) | 2.05 (13) |
| miR-186-5p | 1.72 (17) | 0.92 (17) | 0.88 (13) | 2.14 (16) |
| miR-21-5p | 1.66 (6) | 0.74 (6) | 0.62 (5) | 1.82 (6) |
| miR-221-3p | 1.61 (11) | 0.81 (11) | 0.61 (4) | 1.90 (8) |
| miR-23a-3p | 1.43 (1) | 0.61 (1) | 0.65 (6) | 1.68 (2) |
| miR-26b-5p | 1.46 (3) | 0.64 (4) | 0.46 (1) | 1.66 (1) |
| miR-27a-3p | 1.58 (7) | 0.77 (7) | 0.71 (8) | 1.89 (7) |
| miR-335-5p | 1.52 (5) | 0.72 (5) | 0.56 (2) | 1.77 (5) |
| miR-652-3p | 1.60 (10) | 0.79 (9) | 0.91 (15) | 2.00 (12) |
| miR-653-3p | 1.60 (9) | 0.80 (10) | 0.89 (14) | 1.99 (11) |
| miR-9-5p | 1.64 (13) | 0.83 (13) | 0.76 (10) | 1.99 (10) |
| miR-92b-3p | 1.44 (2) | 0.62 (2) | 0.66 (7) | 1.70 (4) |

miRNA stability scores are represented for each algorithm and its ranked position from the total set of 17 miRNAs is in brackets. CV: coefficient of variation; SSS: summarized stability score.

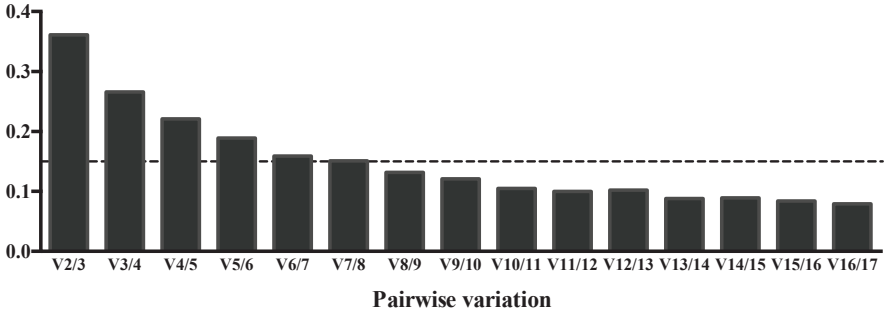


**Figure 3.** Evaluation of the optimum number of reference miRNAs for CSF samples according to the geNorm software. Pairwise variation between samples is reduced by the inclusion of additional reference miRNAs. The magnitude of the change in the normalization factor after the inclusion of a ninth additional reference gene implies a value under the recommended cut off of 0.15, showing that the use of eight endogenous controls is optimum for CSF samples.

## 4. Discussion

CSF is a clear liquid located around and within the CNS, and it maybe analyzed through lumbar puncture [30]. One of its essential functions is the maintenance of an appropriate chemical environment for neural tissue. As the interstitial fluid of the CNS and CSF are in anatomic continuity, this valuable biofluid might mirror the events of the CNS [6]. Even though CSFis a sample that is obtained with a very invasive technique, it might be very useful for the study of the pathogenic mechanisms of neurological diseases as it is a relatively cell and microorganism-free fluid [31].

miRNAs have been detected in different biological fluids as plasma, serum or CSF, where they remain highly stable, unlike the case of cellular miRNAs [32]. For this reason, circulating miRNA profiles have been widely studied in different conditions to exploit their potential as biomarkers. miRNAs have been described to be implicated in different processes such as inflammation, neurogenesis, apoptosis, blood–brain barrier protection and/or remyelination [33,34]. The deregulation of their levels in patients with neurological diseases might represent new potential biomarkers as well as new avenues for research in developing new therapies [33–35].

Some of the unsolved challenges in miRNA profiling studies include the existence of heterogeneous and conflicting results as well as the lack of replication among studies [22]. In fact, as shown in this study, differences in the consistency of results might be observed depending on the initial volume of CSF. As CSF has an important role in diagnosis but its collection might be limited due to the invasiveness of this procedure [31], the use of 300 µL of CSF might still be encouraged, as the detectability was comparable to that observed with 500 µL of CSF, despite presenting a lower intra-volume correlation. High-throughput platforms allow the detection of multiple miRNAs in parallel, which is very useful in biomarker research in order to find molecular signatures [28]. Most published CSF profiling studies have used pre-configured miRNA detection platforms. These platforms have been frequently tested in biological fluids other thanCSF. miRNAs might present different levels of expression and their composition can vary between tissues and biofluids [21], and CSF contains lower levels of miRNA than serum or plasma [20]. It is necessary to analyze and study CSF miRNA profiles to design specific platforms that allow us to extract all the informative potential that CSF could offer more efficiently.

This study presents the first analysis of CSF miRNA levels using TaqMan Advanced miRNA technology from Applied Biosystems with the final aim of designing CSF-enriched miRNA panels to be used in a wide spectrum of neurological diseases. In 2017, Wang et al. defined a specific CSF–miRNA panel to be used in the study of AD [36]. They customized TaqMan low density array (TLDAs) panels containing 47 miRNAs. However, as was explained in Section 3, up to 79 miRNAs were detected in our studied cohort using fc-OA plates. Therefore, to customize OpenArray plates targeting 215 miRNAs, the new TaqMan Advanced miRNA technology was chosen. Among these 215 miRNAs, 41 were present in the panel of Wang et al. [36]. In addition, the utilization of OpenArray instead of TLDAs brings the efficient advantage of analyzing a larger number of samples in a shorter period of time [37], and this new TaqMan Advanced miRNA technology allows a more universal and specific detection of miRNA [38].

The performance of cc-OA plates was tested in order to determine their suitability to be used as a tool to identify new molecular signatures in CSF. First of all, the detectability of each assayed miRNA was measured by calculating the percentage of samples in which it could be detected. This analysis showed that miR-143-3p and miR-23a-3p were present in all samples, while another 80 miRNAs could be detected in at least 70% of samples, representing 38.1% of miRNAs. Second, the 20 most abundant miRNAs in the studied CSF samples were chosen by ranking their mean Cq value. All of them belonged to this 38.1% of miRNAs detected in 70% of samples. Surprisingly, only four of them (let-7a-5p, miR-30c-5p, miR-150-5p and miR-204-5p) were included in the CSF panel described by Wang et al. [36]. It should be mentioned that this discrepancy might be due to the use of different technologies for miRNA detection and the processing of CSF samples with different protocols in both studies. In addition, despite having been analyzed, only nine miRNAs were detected in previous miRNA studies carried out with human CSF samples and TLDAs [39,40]. This highlights the importance of using the newest technologies to increase specificity and sensibility. Although redefining the format by reducing the number of assays might be an option for future work, we would suggest that this format should be maintained to be able to find new miRNA profiles in different neurological disorders, as we could only use a narrow range of available CSF samples.

When examining the potential source of the most abundant miRNAs in CSF, some of them were highly expressed in the brain, spinal cord and different CNS cell types. These miRNAs have been found to be associated with some of the most common CNS disorders in the contexts of tumors (glioblastoma) [41], neurodegenerative aspect (Parkinson's disease) [42], dementia (AD) [43] or long-term disability (stroke) [44]. Another interesting group of miRNAs is those whose expression was found to be increased in specific immune cell subsets such as miR-26a-5p, miR-26b-5p, miR-144-3p, miR-150-5p and miR-450b-3p. Specifically, it should be highlighted that miR-150-5p has been previously related to MS in

CSF [39,40], a chronic inflammatory and neurodegenerative disease of the CNS [45], and its key role in modulating inflammatory responses has been widely recognized [46].

An essential step in qPCR experiments is the normalization procedure, which enables the control of variations in extraction and RT yield, as well as increased efficiency of amplification. It is required before any comparison in miRNA concentrations between different samples and biological groups is performed [47]. The search for candidate endogenous miRNAs will be necessary in later studies [28]. In this study, three different methods were in CSF samples. The NormFinder approach calculated the stability based on the intergroup and intragroup variation, the GeNorm algorithm ranked genes based on pairwise correlation, and CV analysis calculated the variance of a miRNA across all samples taken together [48]. In addition, SSS, as proposed by Marabita et al., was calculated in order to summarize all this information [28].

miR-23a-3p, miR-26b-5p and miR-125a-5p were found to be the most stable miRNAs in the whole cohort of CSF samples. However, when analyzing the stability in the different groups of individuals, miR-26b-5p, miR-92b-3p and miR-335-5p might seem the most promising miRNAs to be used as endogenous normalizers. This reinforces the necessity of the experimental validation of any endogenous miRNAs as normalizers for particular tissues, cell types or biofluids and specific experimental designs [49]. Although miR-23a-3p might have been proposed as an optimal reference miRNA in cervical tissue [50], it has also been found to be involved in some aspects related to melanoma growth and progression [51]. Some other miRNAs previously used as normalizers in CSF in other studies are miR-24 [52], miR-17 [39] and miR-320a [53]. Although the preferred method for the normalization of individual qPCR data is the utilization of a minimum of two endogenous reference miRNAs [54], our analysis determined that eight endogenous miRNAs is the optimum number for CSF samples, with the addition of miR-21-5p, miR-27a-3p and miR-221-3p to be combined with those previously mentioned.

## 5. Conclusions

As the interest in high-throughput platforms is increasing in the field of miRNA biomarkers, a panel of CSF-enriched miRNAs was presented and a set of endogenous controls to be used in neurological diseases was proposed.

These cc-OA plates with 215 loaded miRNA assays allowed the detection of approximately 38.1% of these miRNAs in at least 70% of CSF studied samples, withmiR-770-5p having the lowest Cq values. Although the use of eight endogenous controls in CSF samples is highly recommended, miR-26b-5p, miR-335-5p and miR-92b-3p are the most stable miRNAs in CSF.

These OpenArray plates might be a suitable and efficient tool to identify and characterize new molecular signatures in different neurological diseases and would improve the yield of miRNA detection in CSF.

**Supplementary Materials:** The following are available online at https://www.mdpi.com/article/10.3390/life11070594/s1. Table S1: List of selected miRNA assays included in TaqMan OpenArray Human Advanced microRNA panels, Table S2: SSS scores for CSF samples of each studied group, Figure S1: Venn diagram plot the number of detected miRNAs in different conditions, Figure S2: Venn diagram plot the number of miRNAs detected in at least 70% of samples in each group of patients, Figure S3: Mean Cq value of the most abundant miRNAs in CSF in each specific group of studied samples.

**Author Contributions:** Conceptualization, M.M.-S.M., E.Q. and L.R.-T.; methodology, M.M.-S.M., I.G., O.B., R.R.-C., E.Q. and L.R.-T.; formal analysis, M.M.-S.M., A.M., E.Q. and L.R.-T.; investigation, M.M.-S.M., A.M., E.Q. and L.R.-T.; writing—original draft preparation, M.M.-S.M., E.Q. and L.R.-T.; writing—review and editing, M.M.-S.M., E.Q. and L.R.-T.; project administration, E.Q. and L.R.-T.; funding acquisition, E.Q. and L.R.-T. All authors have read and agreed to the published version of the manuscript.

**Funding:** The author(s) disclose the receipt of the following financial support for the research, authorship and/or publication of this article: this study was supported by a grant from the Instituto Carlos III—Spanish Government (PI13/01782). M.M.-S.M. was supported by a FI-DGR 2016 from AGAUR. A.M. was supported by a grant from Granés Fundació.

**Institutional Review Board Statement:** The study was conducted according to the guidelines of the Declaration of Helsinki, and approved by the Ethics Committee of IDIBGI (approval on 2 December 2013).

**Informed Consent Statement:** Informed consent was obtained from all subjects involved in the study.

**Data Availability Statement:** The data presented in this study are available on request from the corresponding author.

**Acknowledgments:** We want to particularly acknowledge the patients and the IDIBGI Biobank (Biobanc IDIBGI, B. 0000872), integrated in the Spanish National Biobank Network, for their collaboration.

**Conflicts of Interest:** The authors declare no conflict of interest.

## References

1. Misra, M.K.; Damotte, V.; Hollenbach, J.A. The immunogenetics of neurological disease. *Immunology* **2018**, *153*, 399–414. [CrossRef]
2. World Health Organization. Mental Health: Neurological Disorders. Available online: https://www.who.int/news-room/q-a-detail/mental-health-neurological-disorders (accessed on 28 April 2021).
3. Feigin, V.L.; Nichols, E.; Alam, T.; Bannick, M.S.; Beghi, E.; Blake, N.; Culpepper, W.J.; Dorsey, E.R.; Elbaz, A.; Ellenbogen, R.G.; et al. Global, regional, and national burden of neurological disorders, 1990–2016: A systematic analysis for the Global Burden of Disease Study 2016. *Lancet Neurol.* **2019**, *18*, 459–480. [CrossRef]
4. DiLuca, M.; Olesen, J. The cost of brain diseases: A burden or a challenge? *Neuron* **2014**, *82*, 1205–1208. [CrossRef]
5. LeFeber, J. In Vitro Models of Brain Disorders. In *Advances in Neurobiology*; Springer New York LLC: New York, NY, USA, 2019; Volume 22, pp. 19–49. [CrossRef]
6. Vernau, W.; Vernau, K.A.; Sue Bailey, C. Cerebrospinal Fluid. In *Clinical Biochemistry of Domestic Animals*; Elsevier Inc.: Amsterdam, The Netherlands, 2008; pp. 769–819. [CrossRef]
7. Hrishi, A.P.; Sethuraman, M. Cerebrospinal fluid (CSF) analysis and interpretation in neurocritical care for acute neurological conditions. *Indian J. Crit. Care Med.* **2019**, *23* (Suppl. 2), S115–S119. [CrossRef]
8. Jagot, F.; Davoust, N. Is it worth considering circulating microRNAs in multiple sclerosis? *Front. Immunol.* **2016**, *7*, 129. [CrossRef]
9. Sempere, L.F. Celebrating 25 years of microRNA research: From discovery to clinical application. *Int. J. Mol. Sci.* **2019**, *20*, 1987. [CrossRef]
10. Wahid, F.; Shehzad, A.; Khan, T.; Kim, Y.Y. MicroRNAs: Synthesis, mechanism, function, and recent clinical trials. *Biochim. Biophys. Acta Mol. Cell Res.* **2010**, *1803*, 1231–1243. [CrossRef]
11. Zhang, L.; Ding, H.; Zhang, Y.; Wang, Y.; Zhu, W.; Li, P. Circulating MicroRNAs: Biogenesis and Clinical Significance in Acute Myocardial Infarction. *Front. Physiol.* **2020**, *11*, 1088. [CrossRef]
12. Sohel, M.H. Extracellular/Circulating MicroRNAs: Release Mechanisms, Functions and Challenges. *Achiev. Life Sci.* **2016**, *10*, 175–186. [CrossRef]
13. Cui, M.; Wang, H.; Yao, X.; Zhang, D.; Xie, Y.; Cui, R.; Zhang, X. Circulating MicroRNAs in Cancer: Potential and Challenge. *Front. Genet.* **2019**, *10*, 626. [CrossRef] [PubMed]
14. Valadi, H.; Ekström, K.; Bossios, A.; Sjöstrand, M.; Lee, J.J.; Lötvall, J.O. Exosome-mediated transfer of mRNAs and microRNAs is a novel mechanism of genetic exchange between cells. *Nat. Cell Biol.* **2007**, *9*, 654–659. [CrossRef] [PubMed]
15. Lusardi, T.A.; Phillips, J.I.; Wiedrick, J.T.; Harrington, C.A.; Lind, B.; Lapidus, J.A.; Quinn, J.F.; Saugstad, J.A. MicroRNAs in human cerebrospinal fluid as biomarkers for Alzheimer's disease. *J. Alzheimer's Dis.* **2017**, *55*, 1223–1233. [CrossRef] [PubMed]
16. Martinez, B.; Peplow, P. MicroRNAs in blood and cerebrospinal fluid as diagnostic biomarkers of multiple sclerosis and to monitor disease progression. *Neural Regen. Res.* **2020**, *15*, 606–619. [CrossRef]
17. Reed, E.R.; Latourelle, J.C.; Bockholt, J.H.; Bregu, J.; Smock, J.; Paulsen, J.S.; Myers, R.H.; De Soriano, I.; Hobart, C.; Miller, A.; et al. MicroRNAs in CSF as prodromal biomarkers for Huntington disease in the PREDICT-HD study. *Neurology* **2018**, *90*, E264–E272. [CrossRef]
18. Raoof, R.; Jimenez-Mateos, E.M.; Bauer, S.; Tackenberg, B.; Rosenow, F.; Lang, J.; Onugoren, M.D.; Hamer, H.; Huchtemann, T.; Körtvélyessy, P.; et al. Cerebrospinal fluid microRNAs are potential biomarkers of temporal lobe epilepsy and status epilepticus. *Sci. Rep.* **2017**, *7*, 3328. [CrossRef]
19. Yang, Q.; Shi, Q.; Fu, J. Applications of cerebrospinal miRNA in the detection and treatment of acute CNS injury. *Front. Lab. Med.* **2018**, *2*, 83–88. [CrossRef]
20. Weber, J.A.; Baxter, D.H.; Zhang, S.; Huang, D.Y.; Huang, K.H.; Lee, M.J.; Galas, D.J.; Wang, K. The microRNA spectrum in 12 body fluids. *Clin. Chem.* **2010**, *56*, 1733–1741. [CrossRef]

21. Ludwig, N.; Leidinger, P.; Becker, K.; Backes, C.; Fehlmann, T.; Pallasch, C.; Rheinheimer, S.; Meder, B.; Stähler, C.; Meese, E.; et al. Distribution of miRNA Expression Across Human Tissues. *Nucleic Acids Res.* **2016**, *44*, 3865–3877. Available online: https://pubmed.ncbi.nlm.nih.gov/26921406/ (accessed on 3 July 2020). [CrossRef]
22. Mycko, M.P.; Baranzini, S.E. microRNA and exosome profiling in multiple sclerosis. *Mult. Scler. J.* **2020**, *26*, 599–604. [CrossRef]
23. Lizio, M.; Harshbarger, J.; Shimoji, H.; Severin, J.; Kasukawa, T.; Sahin, S.; Abugessaisa, I.; Fukuda, S.; Hori, F.; Ishikawa-Kato, S.; et al. Gateways to the FANTOM5 promoter level mammalian expression atlas. *Genome Biol.* **2015**, *16*, 22. [CrossRef]
24. Hoye, M.L.; Koval, E.D.; Wegener, A.J.; Hyman, T.S.; Yang, C.; O'Brien, D.R.; Miller, R.L.; Cole, T.; Schoch, K.M.; Shen, T.; et al. MicroRNA profiling reveals marker of motor neuron disease in ALS models. *J. Neurosci.* **2017**, *37*, 5574–5586. [CrossRef]
25. Huang, Z.; Shi, J.; Gao, Y.; Cui, C.; Zhang, S.; Li, J.; Zhou, Y.; Cui, Q. HMDD v3.0: A database for experimentally supported human microRNA-disease associations. *Nucleic Acids Res.* **2019**, *47*, D1013–D1017. [CrossRef]
26. Andersen, C.L.; Jensen, J.L.; Ørntoft, T.F. Normalization of real-time quantitative reverse transcription-PCR data: A model-based variance estimation approach to identify genes suited for normalization, applied to bladder and colon cancer data sets. *Cancer Res.* **2004**, *64*, 5245–5250. [CrossRef]
27. Vandesompele, J.; De Preter, K.; Pattyn, F.; Poppe, B.; Van Roy, N.; De Paepe, A.; Speleman, F. Accurate normalization of real-time quantitative RT-PCR data by geometric averaging of multiple internal control genes. *Genome Biol.* **2002**, *3*. [CrossRef]
28. Marabita, F.; de Candia, P.; Torri, A.; Tegnér, J.; Abrignani, S.; Rossi, R.L. Normalization of circulating microRNA expression data obtained by quantitative real-time RT-PCR. *Brief. Bioinform.* **2016**, *17*, 204–212. [CrossRef] [PubMed]
29. Inada, K.; Okoshi, Y.; Cho-Isoda, Y.; Ishiguro, S.; Suzuki, H.; Oki, A.; Tamaki, Y.; Shimazui, T.; Saito, H.; Hori, M.; et al. Endogenous reference RNAs for microRNA quantitation in formalin-fixed, paraffin-embedded lymph node tissue. *Sci. Rep.* **2018**, *8*. [CrossRef] [PubMed]
30. Huff, T.; Tadi, P.; Varacallo, M. Neuroanatomy, Cerebrospinal Fluid.StatPearlsPublishing. 2019. Available online: http://www.ncbi.nlm.nih.gov/pubmed/29262203 (accessed on 14 October 2020).
31. Stoicea, N.; Du, A.; Lakis, C.D.; Tipton, C.; Arias-Morales, C.E.; Bergese, S.D. The miRNA journey from theory to practice as a CNS biomarker. *Front. Genet.* **2016**, *7*, 11. [CrossRef] [PubMed]
32. O'Brien, J.; Hayder, H.; Zayed, Y.; Peng, C. Overview of microRNA biogenesis, mechanisms of actions, and circulation. *Front. Endocrinol.* **2018**, *9*, 402. [CrossRef] [PubMed]
33. Hussein, M.; Magdy, R. MicroRNAs in central nervous system disorders: Current advances in pathogenesis and treatment. *Egypt. J. Neurol. Psychiatry Neurosurg.* **2021**, *57*, 36. [CrossRef]
34. Duffy, C.P.; McCoy, C.E. The Role of MicroRNAs in Repair Processes in Multiple Sclerosis. *Cells* **2020**, *9*, 1711. [CrossRef] [PubMed]
35. Kamal, M.; Mushtaq, G.; Greig, N. Current Update on Synopsis of miRNA Dysregulation in Neurological Disorders. *CNS Neurol. Disord. Drug Targets.* **2015**, *14*, 492–501. [CrossRef]
36. Wang, W.X.; Fardo, D.W.; Jicha, G.A.; Nelson, P.T. A Customized Quantitative PCR MicroRNA Panel Provides a Technically Robust Context for Studying Neurodegenerative Disease Biomarkers and Indicates a High Correlation Between Cerebrospinal Fluid and Choroid Plexus MicroRNA Expression. *Mol. Neurobiol.* **2017**, *54*, 8191–8202. [CrossRef]
37. Farr, R.J.; Januszewski, A.S.; Joglekar, M.V.; Liang, H.; McAulley, A.K.; Hewitt, A.W.; Thomas, H.E.; Loudovaris, T.; Kay, T.W.H.; Jenkins, A.; et al. A comparative analysis of high-throughput platforms for validation of a circulating microRNA signature in diabetic retinopathy. *Sci. Rep.* **2015**, *5*. [CrossRef]
38. Thermo Fisher Scientific. *TaqMan Advanced MiRNA Assays-Superior Performance for MiRNA Detection and Quantification*; Thermo Fisher Scientific: Waltham, MA, USA, 2016.
39. Quintana, E.; Ortega, F.J.; Robles-Cedeño, R.; Villar, M.L.; Buxó, M.; Mercader, J.M.; Alvarez-Cermeño, J.C.; Pueyo, N.; Perkal, H.; Fernández-Real, J.M.; et al. miRNAs in cerebrospinal fluid identify patients with MS and specifically those with lipid-specific oligoclonalIgM bands. *Mult. Scler. J.* **2017**, *23*, 1716–1726. [CrossRef]
40. Bergman, P.; Piket, E.; Khademi, M.; James, T.; Brundin, L.; Olsson, T.; Piehl, F.; Jagodic, M. Circulating miR-150 in CSF is a novel candidate biomarker for multiple sclerosis. *Neurol. Neuroimmunol. Neuroinflamm.* **2016**, *3*, e219. [CrossRef] [PubMed]
41. Li, Y.; Min, W.; Li, M.; Han, G.; Dai, D.; Zhang, L.; Chen, X.; Wang, X.; Zhang, Y.; Yue, Z.; et al. Identification of hub genes and regulatory factors of glioblastomamultiforme subgroups by RNA-seq data analysis. *Int. J. Mol. Med.* **2016**, *38*, 1170–1178. [CrossRef] [PubMed]
42. Ma, W.; Li, Y.; Wang, C.; Xu, F.; Wang, M.; Liu, Y. Serum miR-221 serves as a biomarker for Parkinson's disease. *Cell Biochem. Funct.* **2016**, *34*, 511–515. [CrossRef] [PubMed]
43. Geekiyanage, H.; Jicha, G.A.; Nelson, P.T.; Chan, C. Blood serum miRNA: Non-invasive biomarkers for Alzheimer's disease. *Exp. Neurol.* **2012**, *235*, 491–496. [CrossRef]
44. Zhao, B.; Zhu, Z.; Hao, J.; Wan, Z.; Guo, X. Decreased plasma miR-335 expression in patients with acute ischemic stroke and its association with calmodulin expression. *J. Int. Med. Res.* **2016**, *44*, 1331–1338. [CrossRef]
45. Thompson, A.J.; Baranzini, S.E.; Geurts, J.; Hemmer, B.; Ciccarelli, O. Multiple sclerosis. *Lancet* **2018**, *391*, 1622–1636. [CrossRef]
46. Sang, W.; Wang, Y.; Zhang, C.; Zhang, D.; Sun, C.; Niu, M.; Zhang, Z.; Wei, X.; Pan, B.; Chen, W.; et al. MiR-150 impairs inflammatory cytokine production by targeting ARRB-after blocking CD28/B7 costimulatory pathway. *Immunol. Lett.* **2016**, *172*, 1–10. [CrossRef]

47. Bustin, S.A.; Benes, V.; Garson, J.A.; Hellemans, J.; Huggett, J.; Kubista, M.; Mueller, R.; Nolan, T.; Pfaffl, M.W.; Shipley, G.L.; et al. The MIQE guidelines: Minimum information for publication of quantitative real-time PCR experiments. *Clin. Chem.* **2009**, *55*, 611–622. [CrossRef]
48. Krishnan Sundaram, V.; Kumar Sampathkumar, N.; Massaad, C.; Grenier, J. Optimal use of statistical methods to validate reference gene stability in longitudinal studies. *PLoS ONE* **2019**. [CrossRef]
49. Solayman, M.H.M.; Langaee, T.; Patel, A.; El-Wakeel, L.; El-Hamamsy, M.; Badary, O.; Johnson, J.A. Identification of Suitable Endogenous Normalizers for qRT-PCR Analysis of Plasma microRNA Expression in Essential Hypertension. *Mol. Biotechnol.* **2016**, *58*, 179–187. [CrossRef] [PubMed]
50. Shen, Y.; Li, Y.; Ye, F.; Wang, F.; Wan, X.; Lu, W.; Xie, X. Identification of miR-23a as a novel microRNA normalizer for relative quantification in human uterine cervical tissues. *Exp. Mol. Med.* **2011**, *43*, 358–366. [CrossRef] [PubMed]
51. Ma, M.; Dai, J.; Tang, H.; Xu, T.; Yu, S.; Si, L.; Cui, C.; Sheng, X.; Chi, Z.; Mao, L.; et al. MicroRNA-23a-3p inhibits mucosal melanoma growth and progression through targeting adenylate cyclase 1 and attenuating cAMP and MAPK pathways. *Theranostics* **2019**, *9*, 945–960. [CrossRef]
52. Baraniskin, A.; Kuhnhenn, J.; Schlegel, U.; Maghnouj, A.; Zöllner, H.; Schmiegel, W.; Hahn, S.; Schroers, R. Identification of microRNAs in the cerebrospinal fluid as biomarker for the diagnosis of glioma. *Neuro-Oncology* **2012**, *14*, 29–33. [CrossRef]
53. Sørensen, S.S.; Nygaard, A.-B.; Carlsen, A.L.; Heegaard, N.H.H.; Bak, M.; Christensen, T. Elevation of brain-enriched miRNAs in cerebrospinal fluid of patients with acute ischemic stroke. *Biomark. Res.* **2017**, *5*, 24. [CrossRef]
54. De Ronde, M.W.J.; Ruijter, J.M.; Moerland, P.D.; Creemers, E.E.; Pinto-Sietsma, S.-J. Study Design and qPCR Data Analysis Guidelines for Reliable Circulating miRNA Biomarker Experiments: A Review. *Clin. Chem.* **2018**, *64*, 1308–1318. [CrossRef] [PubMed]

life

MDPI

*Article*

# Proteomic Analysis Unveils Expressional Changes in Cytoskeleton- and Synaptic Plasticity-Associated Proteins in Rat Brain Six Months after Withdrawal from Morphine

**Zdenka Drastichova, Lucie Hejnova, Radka Moravcova and Jiri Novotny ***

Department of Physiology, Faculty of Science, Charles University, 12800 Prague, Czech Republic; zdenka.drastichova@natur.cuni.cz (Z.D.); lucie.hejnova@natur.cuni.cz (L.H.); radka.moravcova@natur.cuni.cz (R.M.)
* Correspondence: jiri.novotny@natur.cuni.cz; Tel.: +420-2-2195-1760

**Abstract:** Drug withdrawal is associated with abstinence symptoms including deficits in cognitive functions that may persist even after prolonged discontinuation of drug intake. Cognitive deficits are, at least partially, caused by alterations in synaptic plasticity but the precise molecular mechanisms have not yet been fully identified. In the present study, changes in proteomic and phosphoproteomic profiles of selected brain regions (cortex, hippocampus, striatum, and cerebellum) from rats abstaining for six months after cessation of chronic treatment with morphine were determined by label-free quantitative (LFQ) proteomic analysis. Interestingly, prolonged morphine withdrawal was found to be associated especially with alterations in protein phosphorylation and to a lesser extent in protein expression. Gene ontology (GO) term analysis revealed enrichment in biological processes related to synaptic plasticity, cytoskeleton organization, and GTPase activity. More specifically, significant changes were observed in proteins localized in synaptic vesicles (e.g., synapsin-1, SV2a, Rab3a), in the active zone of the presynaptic nerve terminal (e.g., Bassoon, Piccolo, Rims1), and in the postsynaptic density (e.g., cadherin 13, catenins, Arhgap35, Shank3, Arhgef7). Other differentially phosphorylated proteins were associated with microtubule dynamics (microtubule-associated proteins, Tppp, collapsin response mediator proteins) and the actin–spectrin network (e.g., spectrins, adducins, band 4.1-like protein 1). Taken together, a six-month morphine withdrawal was manifested by significant alterations in the phosphorylation of synaptic proteins. The altered phosphorylation patterns modulating the function of synaptic proteins may contribute to long-term neuroadaptations induced by drug use and withdrawal.

**Keywords:** morphine; withdrawal; brain; proteomics; synaptic plasticity

**Citation:** Drastichova, Z.; Hejnova, L.; Moravcova, R.; Novotny, J. Proteomic Analysis Unveils Expressional Changes in Cytoskeleton- and Synaptic Plasticity-Associated Proteins in Rat Brain Six Months after Withdrawal from Morphine. *Life* **2021**, *11*, 683. https://doi.org/10.3390/life11070683

Academic Editors: Jong Hyuk Yoon, Chiara Villa and Stefano Gianni

Received: 28 May 2021
Accepted: 10 July 2021
Published: 13 July 2021



## 1. Introduction

Morphine is an opioid drug used as an effective analgesic for the treatment of postoperative and cancer pain. However, medication with morphine can create harmful side effects. Prolonged administration of this drug brings about a high risk of abuse and addiction, which manifests as physical dependence and/or psychological addiction [1]. Physical dependence stems from neuroadaptive changes which occur at the molecular and cellular levels in the central nervous system (CNS) and are associated with the appearance of withdrawal symptoms following the discontinuation of drug use [1–3]. In experimental conditions, the cessation of morphine use is accomplished by abruptly stopping chronic treatment with the drug or by administration of an opioid receptor antagonist which acts as a potent competitive inhibitor and blocks opioid receptors. In animals, this intervention evokes withdrawal symptoms such as jumping, paw tremors, teeth chattering, and diarrhea [1].

During drug administration and withdrawal, neuroadaptations occurring in the brain are associated with alterations in synapses, ion channels and structural compartments. In

this respect, the greatest attention has been focused on neurotransmitter glutamatergic, dopaminergic and GABAergic systems [2–4]. However, it is highly likely that drug administration and withdrawal may induce changes in the expression and function of other proteins involved in the regulation of synaptic plasticity. The synapses, specialized sites capable of mediating communication between neurons in the CNS, are composed of pre- and postsynaptic compartments [5]. The presynaptic terminal contains the active zone (AZ) with proteins involved in the recruitment and exocytosis of synaptic vesicles (SVs), which release neurotransmitters into the synaptic cleft. The postsynaptic site contains the postsynaptic density (PSD) with receptors and signaling components that respond to neurotransmitters released from the presynaptic terminal [5]. Alterations in the expression and posttranslational modifications of synaptic proteins may cause synaptic dysfunction and subsequently lead to neurological disorders [5–7].

The long-lasting brain adaptations connected with compulsive drug use and craving are not limited to only one brain region. Although the ventral tegmental area (VTA) and the nucleus accumbens (NA) are widely recognized as brain regions critical for the development of drug addiction and reward [8,9], it was found that dopaminergic neurons from the VTA project not only to the NA but also to the dorsal striatum, prefrontal cortex and hippocampus and, conversely, the NA receives glutamatergic inputs from the cortex and hippocampus [10]. Dysregulated homeostasis in glutamatergic synapses is implicated in cognitive impairments and cravings associated with opioid use disorder [9]. The dopamine system is also involved in opioid use disorder because low dopamine D2/3 receptor availability and low presynaptic dopamine were found in the striatum of opioid dependent patients [11]. Addictive drugs also modify cerebellar glutamate and endocannabinoid interactions, norepinephrine and dopamine levels, and intracellular signaling transduction pathways [12]. The reduced release of dopamine in the NA may also be driven by increased activity of dynorphin and the κ-opioid receptor system in the ventral striatum, thereby contributing to the negative emotional state associated with withdrawal and protracted abstinence [13]. The hippocampus is critical for the formation of addictive memory and for triggering a relapse [14]. Drug-induced dysregulation of neuronal networks in the cortex contributes to the functional abnormalities of brain reward systems and causes compulsive drug use [13]. The cerebellum has been shown to be involved in emotional memory and experience, language, temporal perception, automatization of rules or decision making, which have all been found to be altered in addicted patients [12,15].

Morphine acts through opioid receptors (ORs). It has a high affinity for μ-OR and a somewhat lower affinity for κ- and δ-ORs [16]. The distribution of ORs differs between different regions of rat brain. The highest number of μ-OR is found in the striatum, a lower number in the hippocampus, and the lowest number in the cortex [17]. Although rat cerebellum was originally believed to be devoid of μ- and κ-ORs [18], some later studies reported opposite results; not only μ- and δ-ORs [19], but also κ-ORs [20] were found there. ORs are apparently less abundant in rat cerebellum when compared to other brain regions. Anyways, there are some indications that morphine can have a huge impact on cerebellar Purkinje cells [21]. Hence, the cerebellum should also be involved in dealing with opioid use disorder.

It has been observed that cytoskeletal dynamics may contribute to synaptic plasticity in addicted animals and the actin filaments were studied in the greatest detail in this respect [22]. The organization and remodeling of the microtubule network are also essential for synapse formation and stability. This network is affected by microtubule dynamic instability, branching, orientation, posttranslational modifications and interactions with microtubule-associated proteins (MAPs) [23,24]. Microtubules are composed of α- and β-tubulin heterodimers, whose posttranslational modifications might facilitate the recruitment of distinct MAPs for local regulation of microtubule function and are critical for neuronal health at all stages of life [24–26]. There are different types of MAPs with various functions and posttranslational modifications which affect their interaction with microtubules, microtubule dynamics and rearrangements of the microtubule network when

neuroplasticity occurs [26]. Phosphorylation mediated by $Ca^{2+}$/calmodulin-dependent kinase II (CaMKII) [26,27], glycogen synthase kinase III β (GSKIIIβ), cdc2 kinase, c-Jun N-terminal kinase 1 (JNK1), cAMP-dependent protein kinase (PKA), protein kinase C (PKC), and serine/threonine-protein kinase MARK [26] is an essential posttranslational modification of tubulins and MAPs. Tubulins and MAPs bind to many other interacting partners. Tubulin directly interacts with synapsin-1, a presynaptic vesicle protein, which is a neuronal phosphoprotein that contributes to the clustering of synaptic vesicles with cytoskeletal elements at the presynaptic terminals and thereby regulates SV cycling and neurotransmitter release [28]. Synapsin-1 can be phosphorylated at different phosphorylation sites by different kinases, and phosphorylation patterns coordinate the interaction of synapsin-1 with actin filaments or microtubules [28]. The other interacting partners of tubulins comprise tubulin polymerization-promoting protein (Tppp) [29] and stathmin [30]. The interacting partners of MAPs include calcium and potassium channels, neurotransmitter receptors, and spectrin [26,31]. Microtubules contribute to the formation, maintenance and function of axons and dendrites. Interestingly, modifications in dendrite branching as well as changed expression of tubulin, tau, stathmin and other cytoskeletal components were observed following chronic morphine treatment and spontaneous withdrawal [32,33].

Small GTPases of the Ras superfamily, which can be divided into several subfamilies such as Ras, Rho, Rab, Arf, and Ran, are important regulators of cytoskeletal reorganization. These GTP-binding proteins are involved in the regulation of cytoskeletal dynamics, vesicle trafficking and synaptic connectivity and plasticity [34–39]. Rab and Arf GTPases mediate coupling between microtubule motor proteins and vesicles, as well as transport of the cargo vesicles along microtubules and actin filaments to specific locations [35]. Rho GTPases play an essential role in changes of intracellular cytoskeleton dynamics [34,37]. Rab GTPases are known to modulate Rho activity to mediate cytoskeleton remodeling [35]. The activity of small GTPases is regulated by guanine nucleotide exchange factors (GEFs) and GTPase activator proteins (GAPs). While GEFs stimulate the exchange of GDP for GTP to activate small GTPases, GAPs promote GTP hydrolysis to inactivate them [34]. Most of the 150 GEFs and GAPs that have been identified so far are expressed in the brain with a specific spatial and temporal distribution pattern, but their function has not yet been elucidated [38]. Small GTPases and their regulators are modified by phosphorylation regulating their stability and activity, subcellular localization, and interactions with binding partners [40–43]. RhoA/Rho kinase signaling was shown to be downregulated in the NA of cocaine-dependent rats and may thus contribute to synaptic changes leading to drug addiction [44]. Rho signaling might also be related to synaptic plasticity in the amygdala and prefrontal cortex, which were identified as regulators of the reward circuitry as well [34].

The present study aimed to explore the long-term impact of morphine withdrawal on proteomic profiling of selected rat brain regions. It is known that drug addiction is associated with dysregulation of the dopamine and glutamate systems [9]. However, it would be too simplistic to assume that this process is mediated only by changes in neurotransmitters and their receptors. It is imaginable that dysregulation of neurotransmitter systems is associated with changes in the synaptic vesicle cycle that is comprised of several individual processes. It is also imaginable that postsynaptic signal transmission depends not only on the number of receptors on the postsynaptic membrane but also on the composition of the postsynaptic density. Likewise, changes in neurotransmitter signaling, which may affect cognitive functions (e.g., memory and learning, addiction, reward, motivation, and habits), are presumably related to changes in protein expression and protein posttranslational modifications determining the protein functions. The comprehensive analysis of the proteome and phosphoproteome can help us determine which of the components of synaptic vesicles, proteins of the presynaptic active zone and the postsynaptic density are affected by morphine, and reveal which synaptic processes could potentially be modulated by pharmacotherapeutic interventions during the withdrawal period.

## 2. Materials and Methods

### *2.1. Materials*

Morphine sulfate was obtained from Saneca Pharmaceutical, Ltd., (Hlohovec, Slovakia) and BCA assay kit was from Thermo Fisher Scientific Inc. (Carlsbad, CA, USA). All other chemicals were purchased from Sigma-Aldrich (St. Louis, MO, USA) and were of the highest purity available.

### *2.2. Animals, Morphine Treatment and Withdrawal*

Male Wistar rats (approximately 8 weeks of age) were purchased from Velaz, Ltd., Prague, Czech Republic. Rats were housed in groups of 3/cage in standard plastic cages containing wood chip bedding. They were maintained at normal ambient temperature ($22 \pm 1$ °C) under a stable light-dark cycle (12 h light and 12 h darkness), and were allowed free access to food and water. All procedures were performed according to national and institutional guidelines for the care and use of animals in laboratory research. The protocols were approved by the Ministry of Education, Youth and Sports of the Czech Republic (license no. MSMT-1479/2019–6). Repeated administration of morphine was performed according to previously established procedures [45,46]. Rats were injected with increasing doses (10–50 mg/kg per day) of morphine dissolved in 0.9% NaCl for 10 consecutive days. Control animals received 0.9% NaCl. After cessation of morphine administration, and throughout the following 6 months of abstinence, rats were kept under standard housing conditions with food and water ad libitum.

### *2.3. Brain Tissue Homogenization and Digestion*

The brains from morphine-treated (MOR; n = 9) and control (CON; n = 9) rats were rapidly removed, dissected and snap frozen in liquid nitrogen and stored at −80 °C until use. In order to obtain a reasonable number of samples for proteomic analyses and, simultaneously, to preserve the effect of the intrinsic biological variation, three pooled samples of prefrontal cortex (Ctx), hippocampus (Hp), striatum (Str) or cerebellum (Cb) were prepared for both MOR and CON groups by mixing equal amounts of respective brain tissues from three trios of randomly selected animals in each group. The pooled brain tissue samples were homogenized in 10 volumes of TMES buffer (20 mM Tris, 3 mM $MgCl_2$, 1 mM EDTA, 250 mM sucrose; pH 7.4) containing protease and phosphatase inhibitors (cOmplete and PhosSTOP) using a glass-Teflon homogenizer (1200 rpm, 10 strokes), mixed 1:1 with 2% SDC (sodium deoxycholate) in 100 mM TEAB (triethylammonium bicarbonate; pH 8.0), and sonicated for $3 \times 10$ s in 2.0 mL Eppendorf tubes using a Bandelin UW 2070 sonicator (40% amplitude), as described previously [46]. Samples were cleared ($14{,}000\times g$, 10 min). Protein concentration was determined using the Pierce BCA protein assay kit with bovine serum albumin as calibration standard and 250 μg of protein per sample were used for MS sample preparation. Proteins were digested by 5 μg of trypsin per sample at 37 °C overnight. Phosphopeptides were enriched using $TiO_2$ according to [47].

### *2.4. nLC-MS2 Analysis*

Nano reversed phase columns (EASY-Spray column, 50 cm × 75 μm ID, PepMap C18, 2 μm particles, 100 Å pore size) were used for LC/MS analysis. Mobile phase buffer A was composed of water and 0.1% formic acid. Mobile phase B was composed of acetonitrile and 0.1% formic acid. Samples were loaded onto the trap column (C18 PepMap100, 5 μm particle size, 300 μm × 5 mm, Thermo Scientific) for 4 min at 18 μL/min loading buffer was composed of water, 2% acetonitrile and 0.1% trifluoroacetic acid. Peptides were eluted with Mobile phase B gradient from 2% to 35% B in 60 min. Eluting peptide cations were converted to gas-phase ions by electrospray ionization and analyzed on a Thermo Orbitrap Fusion (Q-OT- qIT, Thermo Fisher Scientific (Cleveland, OH, USA). Survey scans of peptide precursors from 350 to 1400 m/z were performed in orbitrap at 120K resolution (at 200 $m/z$) with a $1 \times 10^6$ ion count target. Tandem MS was performed by isolation at 1.5 Th with the quadrupole, HCD fragmentation with normalized collision energy of 35, and rapid scan

MS analysis in the ion trap. The MS2 ion count target was set to 104 and the max injection time was 150 ms. Only those precursors with charge state 2–6 were sampled for MS2. The dynamic exclusion duration was set to 30 s with a 10 ppm tolerance around the selected precursor and its isotopes. Monoisotopic precursor selection was turned on. Cycle time was set to 2 s.

### *2.5. Data Analysis*

All data were analyzed and quantified with the MaxQuant software (version 1.6.3.4, Planck Institute of Biochemistry, Munich, Germany) [48]. The false discovery rate (FDR) was set to 1% for both proteins and peptides and we specified a minimum peptide length of seven amino acids. The Andromeda search engine was used for the MS/MS spectra search against the Rattus norvegicus database (Uniprot, https://www.uniprot.org; assessd on 18 August 2020) containing 29,958 entries. Enzyme specificity was set as C-terminal to Arg and Lys, also allowing cleavage at proline bonds and a maximum of two missed cleavages. Carbamidomethylation of cysteine was selected as fixed modification and N-terminal protein acetylation and methionine oxidation as variable modifications. The "match between runs" feature of MaxQuant was used to transfer identifications to other LC-MS/MS runs based on their masses and retention time (maximum deviation 0.7 min) and this was also used in quantification experiments. Quantifications were performed with the label-free algorithm in MaxQuant [49]. Data analysis was performed using Perseus 1.6.1.3 software [50]. For quantification, intensities were determined as the intensity maximum over the retention time profile. To evaluate the degree of uniqueness, unique plus razor peptides were included for quantification. Only those phosphosites with localization probability higher than 0.75 were used for further data analysis.

Gene Ontology (GO) enrichment analysis of proteomic and phosphoproteomic profiles for each brain region was performed using appropriate online annotation tools (ShinyGO v0.61 and gProfiler); the p-value threshold was set to $10^{-5}$ for biological processes.

## 3. Results

### *3.1. GO Enrichment Analysis of Differentially Phosphorylated Proteins after a 6-Month Morphine Withdrawal*

In order to evaluate the differences in phosphoproteomes of selected brain regions from control and morphine-withdrawn rats, bioinformatics analysis of data acquired by bottom-up label-free LC-MS proteomics was conducted using the MaxQuant and Perseus software platforms. A qualitative change was defined as the absence/presence of a protein in one experimental group in pairwise comparison under the condition that the protein was detectable/undetectable at least in two of three biological replicates. A quantitative change was defined as an at least two-fold difference in protein expression level between two experimental groups and concurrently the protein was detected at least in two of three biological replicates. By comparison of control and morphine-withdrawn rats, we identified 185 differentially phosphorylated sites on 109 phosphoproteins in cortex, 454 differentially phosphorylated sites on 256 phosphoproteins in hippocampus, 313 differentially phosphorylated sites on 174 phosphoproteins in striatum and 288 differentially phosphorylated sites on 183 phosphoproteins in cerebellum. The sets of altered phosphoproteins for each brain region were examined by GO enrichment analysis using the gProfiler tool (https://biit.cs.ut.ee/gprofiler_beta/gost; assessed on 12 February 2021) in order to specify biological processes which were affected by a six-month morphine withdrawal. A list of enriched GO terms related to synaptic plasticity, cytoskeleton organization and regulation of GTPase activity for each brain region (Table 1) includes p-values and numbers of differentially phosphorylated proteins. The detailed data of these GO enriched terms are stated in Table S1, including GO term IDs, negative logarithms of p-values, sizes of GO terms, numbers and gene names of altered proteins associated with GO terms.

**Table 1.** Gene Ontology (GO) biological process enrichment analysis of differentially phosphorylated and expressed proteins in four selected rat brain regions six months after withdrawal from morphine (conducted by gProfiler).

| Biological Processes | Ctx | Hp | Str | Cb |
|---|---|---|---|---|
| Synaptic vesicle cycle | P | P | P | P |
| Synapse organization | E | P | - | P |
| Neurotransmitter transport and secretion | P,E | P | P | P |
| Regulation of neurotransmitter level | - | P | P | P |
| Synaptic transmission | E | P | - | P |
| Synaptic signaling | P,E | P,E | P | P |
| Cytoskeleton organization | P | P | P,E | - |
| Regulation of GTPase activity | - | P | P | E |

Ctx, cortex; Hp, hippocampus; Str, striatum; Cb, cerebellum; P, GO biological processes inferred from the differences in protein phosphorylation; E, GO biological processes inferred from the differences in protein expression; -, GO enriched biological process not found.

The GO enriched terms related to synaptic plasticity (e.g., synaptic vesicle cycle, signal release from the synapse, neurotransmitter secretion and transport) and cytoskeleton organization were found in the cortex (Table 1 and Supplementary Table S1) but no altered proteins were found in biological processes followed in this study. The GO terms related to synaptic plasticity, cytoskeleton organization and regulation of GTPase activity were found in the hippocampus and striatum (Table 1 and Supplementary Table S1). In the hippocampus, synaptic processes affected by long-term morphine withdrawal included synaptic signaling, synaptic vesicle cycle, synapse organization and neurotransmitter secretion and transport, actin filament-based processes and microtubule cytoskeleton organization involved in mitosis (Table 1). The altered phosphoproteins Arhgef7, Nf1 and Rgs14 are involved in modulation of synaptic plasticity, cytoskeleton organization and regulation of GTPase activity. The altered phosphoproteins Add2, Mapt, Myh10, Palm and Ppfia1 are associated with cytoskeletal and synaptic processes, proteins Arhgap35 and Stmn3 with cytoskeletal processes and regulation of GTPase activity and proteins Rasgrf1, Sema4d, Stxbp5l and Syngap1 with synaptic processes and regulation of GTPase activity (Supplementary Table S1). In the striatum, similar GO enriched terms were included in the list as in the hippocampus, but the number of GO enriched terms was smaller (Table 1). Only four proteins (Arhgap35, Bcr, Crk and Hdac6) establish associations between synaptic plasticity, cytoskeleton organization and regulation of GTPase activity according to GO enrichment analysis (Supplementary Table S1). In the cerebellum, GO enriched terms were related to synaptic plasticity and similar to those found in the cortex, hippocampus and striatum (Table 1). The most GO enriched terms related to synaptic plasticity, cytoskeleton organization and regulation of GTPase activity were found in the hippocampus, where the largest set of altered phosphoproteins was determined. Moreover, the most extensive relations were observed in this brain region, given that several phosphoproteins were involved at least in two of three biological processes examined in this study.

When comparing the appearance of differentially phosphorylated proteins involved in single biological processes, the greatest similarity between different brain regions was noticed for cytoskeleton organization. Microtubule-associated proteins Map1a, Map1b, Map2 and Mapt, erythrocyte membrane proteins Epb41l1 and Epb41l3, as well as other proteins such as Add2, Cdc42bpb, Dpysl3, Marcks and Palm were found in the list of GO enriched terms related to cytoskeleton organization in all four brain regions (Supplementary Table S1). Regarding synaptic biological processes, phosphoproteins Syn1 and Bsn were identified in all four brain regions (Supplementary Table S1).

### *3.2. GO Enrichment Analysis of Differentially Expressed Proteins after a 6-Month Morphine Withdrawal*

In order to evaluate the differences in proteomes of selected brain regions from control and morphine-withdrawn rats, bioinformatic analysis of data acquired by bottom-up

label-free LC-MS proteomics was conducted using the MaxQuant and Perseus software platforms. A qualitative change was defined as the absence/presence of a protein in one experimental group in pairwise comparison under the condition that the protein was un/detectable at least in two of three biological replicates. A quantitative change was defined as an at least two-fold difference in protein expression level between two experimental groups and concurrently the protein was detected at least in two of three biological replicates. The levels of 79, 51, 78 and 175 proteins were altered by long-term morphine withdrawal in the cortex, hippocampus, striatum and cerebellum, respectively. The sets of differentially expressed proteins for each brain region were assessed by GO enrichment analysis using the ShinyGO v0.61 tool (http://bioinformatics.sdstate.edu/go/; assessed on 9 March 2021) in order to specify biological processes which were affected by a six-month morphine withdrawal. A list of enriched GO terms related to synaptic plasticity, cytoskeleton organization and regulation of GTPase activity for each brain region (Table 1) includes FDR values and numbers of altered proteins. The detailed data of these GO enriched terms are stated in Table S2, including gene names and numbers of altered proteins associated with GO terms.

The most enriched GO terms inferred from the differences in protein expression in cortex were related to synaptic plasticity and signaling, synapse assembly and neurotransmitter receptor transport (Table 1 and Supplementary Table S2). Two GO terms related to synaptic plasticity were found in the hippocampus. While GO enriched terms identified in the striatum were related to cytoskeleton organization and actin filament-based process, those in the cerebellum were linked to signal transduction mediated by small GTPases (Table 1 and Supplementary Table S2).

Using GO enrichment analysis, no association between synaptic plasticity, cytoskeleton organization and regulation of small GTPase activity was found in the proteomic profiles of differentially expressed proteins. Biological processes related to synaptic plasticity were identified in the cortex and hippocampus, biological processes related to cytoskeleton organization in striatum and biological processes related to the regulation of small GTPase activity in the cerebellum. The numbers of differentially expressed proteins in the cortex, hippocampus and striatum were smaller than the numbers of differentially phosphorylated proteins, which might decrease the chance of finding associations between the proteins altered by morphine withdrawal.

### *3.3. Changes in Protein Expression and Phosphorylation Induced by a 6-Month Morphine Withdrawal*

The datasets of differentially phosphorylated proteins associated with synaptic plasticity, cytoskeleton organization and regulation of GTPase activity consist of 78 phosphosites from 42 phosphoproteins in cortex, 188 phosphosites from 95 phosphoproteins in hippocampus, 113 phosphosites from 59 phosphoproteins in striatum, and 96 phosphosites from 49 phosphoproteins in cerebellum (Supplementary Table S3). Long-term morphine withdrawal elicited distinct changes in the phosphorylation of different phosphosites, resulting in the formation of unique phosphorylation profiles in different brain regions. For better clarity and transparency, changes in phosphorylation of some phosphoproteins are listed separately for the cortex (Table 2), hippocampus (Table 3), striatum (Table 4), and cerebellum (Table 5).

**Table 2.** A list of differentially phosphorylated proteins associated with cytoskeletal, synaptic plasticity and GTPase regulatory activity in the cortex six months after withdrawal from morphine.

| Protein ID | Gene | Protein Name | Position, Fold Change |
|---|---|---|---|
| Q5HZA7 | Bin1 | Bin1 protein | S265 (_1) ↑(MW) |
| G3V984 | Bsn | Protein bassoon | S2632 (_2) ↑(2.80); S2634 (_2) ↑(2.80) |
| P11275 | Camk2a | $Ca^{2+}$/calmodulin-dependent protein kinase type II α | S330 (_2) ↓(-4.88); S331 (_3) ↑(2.54); S333 (_3) ↑(2.62); T336 (_3) ↑(3.40); T337 (_3) ↑(4.57) |
| Q7TT49 | Cdc42bpb | Ser/Thr-proteine kinae MRCK β | S1695 (_1) ↓(C) |
| A0A0G2JTD7 | Clasp1 | Cytoplasmic linker-associated protein 1 | S596 (_1) ↑(2.64); S1050 (_1) ↑(MW) |
| F1M787 | Ctnnd2 | Catenin δ2 | T455 (_1) ↑(2.01); S515 (_2) ↑(3.64) |
| Q62952 | Dpysl3 | Dihydropyrimidinase-related protein 3 | T509 (_3) ↑(2.27); T514 (_2) ↑(7.12) |
| D3ZMI4 | Epb41l1 | Band 4.1-like protein 1 | S766 (_2) ↑(2.07); S767 (_2) ↑(2.07); S1337 (_1) ↓(C) |
| A0A0G2K1Q9 | Epb41l3 | Erythrocyte membrane protein band 4.1-like 3 | S94 (_2) ↑(MW); S97 (_2) ↓(−2.99) |
| A0A0G2K527 | Git1 | ARF GTPase-activating protein Git1 | T383 (_1) ↓(C); T383 (_2) ↓(C) |
| A0A0G2K5C6 | Map1a | Microtubule-associated protein 1A | S1518 (_1) ↑(2.76); S2001 (_3) ↑(2.37); S2005 (_3)↑(2.37) |
| P15205 | Map1b | Microtubule-associated protein 1B | S930 (_1) ↑(6.14); T965 (_2) ↓(−2.34); S1315 (_3) ↑(3.62); S1389 (_2) ↑(2.09); S1393 (_2) ↑(2.09) |
| F1MAQ5 | Map2 | Microtubule-associated protein 2 | T1606 (_2) ↑(2.84); S1782 (_2) ↑(2.12); S1784 (_2) ↑(3.20); S1784 (_3) ↓(−3.09) |
| D4A1Q2 | Mapt | Microtubule-associated protein tau | S436 (_2) ([2.95); S440 (_2) ↑(2.74); T648 (_3) ↑(2.00); S661 (_1) ↑(MW) |
| Q920Q0 | Palm | Paralemmin-1 | S112 (_3) ↑(2.11) |
| D3Z9C7 | Pclo | Protein piccolo | S3054 (_1) ↓(C); S3326 (_1) ↑(2.34) |
| Q6IRK8 | Sptan1 | Spectrin α chain 1 | S1029 (_1) ↑(MW) |
| Q9QXY2 | Srcin1 | Src kinase signaling inhibitor 1 | S342 (_2) ↓(C) |
| P61265 | Stx1b | Syntaxin-1B protein | S10 (_1) ↑(6.58) |
| D3ZU84 | Stxbp5l | Syntaxin-binding protein 5-like | S723 (_3) ↑(2.12); S724 (_3) ↑(2.12); S727 (_3) ↑(2.12) |
| P09951 | Syn1 | Synapsin-1 | S430 (_3) ↓(C) |
| D3ZQL7 | Tppp | Tubulin polymerization-promoting protein | S34 (_1) ↑(6.74) |

↑, protein hyperphosphorylation after a 6-month morphine withdrawal; ↓, protein hypophosphorylation after a 6-month morphine withdrawal; C, protein phosphorylation detected only in samples from control rats; MW, protein phosphorylation detected only in samples from morphine-withdrawn rats.

**Table 3.** A list of differentially phosphorylated proteins associated with cytoskeletal, synaptic plasticity and GTPase regulatory activity in the hippocampus six months after withdrawal from morphine.

| Protein ID | Gene | Protein Name | Position, Fold Change |
|---|---|---|---|
| Q5QD51 | Akap12 | A-kinase anchor protein 1 | S614 (_2) ↑(5.04); S616 (_2) ↑(5.04) |
| A0A0G2K6R9 | Ank2 | Ankyrin 2 | S1730 (_3) ↑(4.85); S1731 (_3) ↑(4.85); S1734 (_3) ↑(4.85); S2243 (_2) ↑(MW); S2246 (_2) ↓(C); S2532 (_2) ↑(2.17); T2535 (_2) ↑(2.17) |
| D4A9G6 | Arhgap33 | Rho GTPase-activating protein 33 | T974 (_1) ↓(C) |
| D4AD82 | Arhgap35 | Rho GTPase-activating protein 35 | S1179 (_1) ↑(2.99) |
| A0A1B0GWY | Arhgef2 | Rho guanine nucleotide exchange factor 2 | S916 (_1) ↓(C) |

**Table 3.** *Cont.*

| Protein ID | Gene | Protein Name | Position, Fold Change |
|---|---|---|---|
| D4A1D2 | Arhgef26 | Rho guanine nucleotide exchange factor 26 | S390 (_1) ↑(3.70) |
| A0A0G2QC21 | Arhgef7 | Rho guanine nucleotide exchange factor 7 | S228 (_1) ↓(C) |
| Q5HZA7 | Bin1 | Bin1 protein | S265 (_1) ↑(MW) |
| M9MMM8 | Brsk2 | Ser/Thr-protein kinase BRSK2 | T364 (_2) ↓(C); S398 (_3) ↓(C) |
| G3V984 | Bsn | Protein bassoon | S1098 (_2) ↑(2.48); T1100 (_3) ↑(MW) |
| P11275 | Camk2a | $Ca^{2+}$/calmodulin-dependent protein kinase type II subunit α | S330 (_2) ↑(2.81); S330 (_3) ↑(2.25); S333 (_2) ↑(10.48); S333 (_3) ↑(3.44); T334 (_3) ↓(−2.22); T336 (_1) ↓(C); T336 (_3) ↓(−4.38) |
| P35565 | Canx | Calnexin | S563 (_1) ↑(2.14) |
| Q7TT49 | Cdc42bpb | Ser/Thr-proteine kinae MRCK β | S1692 (_2) ↓(−3.11); S1695 (_2) ↓(−3.11) |
| Q62950 | Crmp1 | Dihydropyrimidinase-related protein 1 | S8 (_1) ↑(2.65) |
| F1M787 | Ctnnd2 | Catenin δ2 | S515 (_2) ↑(4.35) |
| A0A1B0GWS4 | Cttn | Src substrate cortactin | S125 (_2) ↑(2.41); S125 (_3) ↑(2.04); S135 (_3) ↑(2.14) |
| A0A0G2K7F5 | Dlg4 | Disks large homolog 4 | S413 (_2) ↓(C) |
| G3V849 | Dlgap1 | Discs, large homolog-associated protein 1 | S421 (_2) ↑(2.33) |
| A0A0G2JUI3 | Dlgap2 | Discs, large homolog-associated protein 2 | S947 (_2) ↑(MW) |
| A0A0G2JX56 | Dnajc5 | DnaJ (Hsp40) homolog, subfamily C, member 5 | S8 (_1) ↑(MW) |
| D4A0I5 | Dnajc6 | DnaJ (Hsp40) homolog, subfamily C, member 6 | Y750 (_1) ↓(C) |
| Q62952 | Dpysl3 | Dihydropyrimidinase-related protein 3 | T507 (_2) ↓(C); T509 (_2) ↑(MW) |
| D3ZMI4 | Epb41l1 | Band 4.1-like protein 1 | T489 (_1) ↑(2.46); S544 (_2) ↑(2.09); S544 (_3) ↑(10.71); S546 (_2) ↑(2.09); T1252 (_1) ↓(C); S1320 (_2) ↓(−3.09); S1322 (_2) ↓(−3.09); T1324 (_2) ↓(−9.45) |
| A0A0G2K1Q9 | Epb41l3 | Erythrocyte membrane protein band 4.1-like 3 | S91 (_3) ↑(2.44) |
| A0A0G2K5C6 | Map1a | Microtubule-associated protein 1A | S764 (_1) ↑(MW); S1236 (_2) ↑(MW); S1691 (_1) ↑(2.56); S2135 (_1) ↓(-2.55) |
| P15205 | P15205 | Microtubule-associated protein 1B | S14 (_1) ↓(C); S614 (_1) ↓(-4.06); S985 (_1) ↓(C); S1239 (_2) ↓(C); S1244 (_2) ↓(C); S1254 (_2) ↓(−6.20); S1315 (_3) ↑(2.46); S1371 (_1) ↑(2.39); S1382 (_3) ↑(2.05); S1432 (_1) ↓(C); S1465 (_1) ↑(3.69); S1494 (_1) ↑(4.52); S1772 (_3) ↑(2.30); S1775 (_3) ↑(2.30); S1778 (_3) ↑(2.30) |
| F1MAQ5 | Map2 | Microtubule-associated protein 2 | S362 (_2) ↑(2.64); S1064 (_1) ↓(−2.51); S1784 (_3)↑(2.10); S1785 (_3) ↑(2.76); S1793 (_2) ↑(MW); 1793 (_3) ↓(C); S1796 (_3) ↓(C); S1797 (_3) ↓(C) |
| D4A1Q2 | Mapt | Microtubule-associated protein tau | S45 (_2) ↓(C); S423 (_3) ↑(2.15); T426 (_1) ↓(-2.68); T426 (_3) ↑[2.15]; S436 (_2) ↑[2.53]; S436 (_3) ↑(3.39); S440 (_2) ↑(2.42); S444 (_3) ↑(3.39); S447 (_1) ↑(2.39); S447 (_3) ↑(3.39); S480 (_2) ↑(2.04); S661 (_1) ↑(MW) |
| Q920Q0 | Palm | Paralemmin-1 | T141 (_2) ↑(3.52); T145 (_2) ↑(3.52) |
| D3Z9C7 | Pclo | Protein piccolo | S3054 (_1) ↓(−3.58); S3326 (_1) ↓(−2.52) |
| D3ZZ81 | Ppfia1 | PTPRF-interacting protein alpha 1 | S239 (_2) ↓(−2.17); S242 (_2) ↓(−2.17) |

**Table 3.** *Cont.*

| Protein ID | Gene | Protein Name | Position, Fold Change |
|---|---|---|---|
| P63012 | Rab3a | Ras-related protein Rab-3A | S188 (_1) ↓(C) |
| D3ZKQ4 | Rabl6 | RAB, member RAS oncogene family-like 6 | S474 (_2) ↑(5.34) |
| Q5FVT1 | Ralbp1 | RalA-binding protein 1 | S48 (_2) ↓(C); S62 (_2) ↓(C) |
| M0R920 | Ranbp3 | Ran-binding protein 3 | S409 (_1) ↑(MW) |
| F1LM43 | Rasgrf1 | Ras-specific guanine nucleotide releasing factor 1 | S747 (_1) ↑(2.02) |
| O08773 | Rgs14 | Regulator of G-protein signaling 14 | S286 (_1) ↓(−4.28) |
| A0A0G2KAV8 | Rims1 | Regulating synaptic membrane exocytosis protein 1 | S409 (_1) ↑(2.33) |
| A0A0G2K8W9 | Sptbn1 | Spectrin β chain | S2122 (_2) ↑(2.86); S2132 (_2) ↑(2.86); S2155 (_3) ↑(3.20) |
| Q9QXY2 | Srcin1 | Src kinase signaling inhibitor 1 | S342 (_2) ↑(MW); S357 (_2) ↑(MW) |
| D3ZU84 | Stxbp5l | Syntaxin-binding protein 5-like | S503 (_1) ↑(MW) |
| Q02563 | Sv2a | Synaptic vesicle glycoprotein 2A | S127 (_1) ↓(−11.11) |
| P09951 | Syn1 | Synapsin-1 | S436 (_3) ↑(2.15); S518 (_1) ↑(MW); S682 (_2) ↑(MW) |
| D3ZCL8 | Syngap1 | Ras/Rap GTPase-activating protein SynGAP | S1103 (_2) ↑(2.45) |
| P97610 | Syt12 | Synaptotagmin-12 | T103 (_1) ↓(C) |
| D3ZQL7 | Tppp | Tubulin polymerization-promoting protein | S31 (_1) ↓(−4.52) |

↑, protein hyperphosphorylation after a 6-month morphine withdrawal; ↓, protein hypophosphorylation after a 6-month morphine withdrawal; C, protein phosphorylation detected only in samples from control rats; MW, protein phosphorylation detected only in samples from morphine-withdrawn rats.

**Table 4.** A list of differentially phosphorylated proteins associated with cytoskeletal, synaptic plasticity and GTPase regulatory activity in the striatum six months after withdrawal from morphine.

| Protein ID | Gene | Protein Name | Position, Fold Change |
|---|---|---|---|
| F1M2D4 | Arhgap23 | Rho GTPase-activating protein 23 | T560 (_2) ↑(MW) |
| D4A987 | Arhgap31 | Cdc42 GTPase-activating protein | S455 (_2) ↓(-2.11); S459 (_2) ↓(−2.11) |
| D4AD82 | Arhgap35 | Rho GTPase-activating protein 35 | Y1105 (_1) ↑(2.30) |
| Q6TUE6 | Arhgap5 | Rho GTPase-activating protein 5 | T1171 (_2) ↓(C) |
| G3V984 | Bsn | Protein bassoon | S1220 (_1) ↑(MW); S2842 (_1) ↑(MW) |
| P11275 | Camk2a | $Ca^{2+}$/calmodulin-dependent protein kinase type II subunit α | S330 (_2) ↓(−2.83) |
| Q7TT49 | Cdc42bpb | Ser/Thr-proteine kinae MRCK β | S1692 (_1) ↑(MW) |
| F1M787 | Ctnnd2 | Catenin δ2 | S515 (_2) ↓(−2.41) |
| A0A1B0GWS4 | Cttn | Src substrate cortactin | S125 (_2) ↑(6.53) |
| A0A0G2K7F5 | Dlg4 | Disks large homolog 4 | S414 (_2) ↑(2.17); S417 (_2) ↑(2.17) |
| A0A0G2JUI3 | Dlgap2 | Discs, large homolog-associated protein 2 | S557 (_2) ↑(2.33) |
| A0A0G2JX56 | Dnajc5 | DnaJ (Hsp40) homolog, subfamily C, member 5 | S10 (_2) ↑(2.68) |
| P47942 | Dpysl2 | Dihydropyrimidinase-related protein 2 | S537 (_1) ↑(2.12) |
| Q62952 | Dpysl3 | Dihydropyrimidinase-related protein 3 | T518 (_2) ↓(−3.10) |

**Table 4.** *Cont.*

| Protein ID | Gene | Protein Name | Position, Fold Change |
|---|---|---|---|
| D3ZMI4 | Epb41l1 | Band 4.1-like protein 1 | S544 (_3) ↑(2.30); S546 (_3) ↑(2.30); T550 (_3) ↑(2.30); T1324 (_2) ↑(2.53) |
| A0A0G2K1Q9 | Epb41l3 | Erythrocyte membrane protein band 4.1-like 3 | T540 (_2) ↑(MW) |
| A0A0G2K527 | Git1 | ARF GTPase-activating protein Git1 | S379 (_3) ↓(C); T383 (_3) ↓(C) |
| A0A0G2K5C6 | Map1a | Microtubule-associated protein 1A | S1136 (_2) ↑(MW); S1232 (_3) ↓)C); S2432 (_1) ↑(MW) |
| P15205 | Map1b | Microtubule-associated protein 1B | S929 (_2) ↓(-2.52); S930 (_2) ↓(-2.52); S956 (_2) ↓(−2.72); S960 (_2) ↑(MW); S963 (_3) ↓(C); S1239 (_2) ↓(C); S1244 (_1) ↑(MW); S1244 (_2) ↓(C); S1389 (_1) ↑(MW); S1494 (_1) ↓(−2.69); T1496 (_1) ↑(6.78); S1646 (_1) ↑(2.12); S1778 (_2) ↑(2.01); S1781 (_3) ↑(2.05) |
| F1MAQ5 | Map2 | Microtubule-associated protein 2 | S1780 (_3) ↑(6.15); S1784 (_3) ↑(2.32); S1788 (_3) ↑(6.15) |
| D4A1Q2 | Mapt | Microtubule-associated protein tau | S480 (_2) ↑(3.75); Y639 (_3) ↑(MW) |
| Q920Q0 | Palm | Paralemmin-1 | S124 (_1) ↑(MW); T361 (_2) ↓(C); S365 (_2) ↓(C) |
| D3Z9C7 | Pclo | Protein piccolo | S66 (_1) ↓(−2.45); T2103 (_1) ↓(−2.06) |
| F1LSE6 | Ppfia3 | Liprin α3 | T678 (_1) ↓(C) |
| P63012 | Rab3a | Ras-related protein Rab-3A | S190 (_1) ↑(MW) |
| F1M386 | Rapgef2 | Rap guanine nucleotide exchange factor 2 | T1118 (_2) ↑(MW) |
| A0A0G2KAV8 | Rims1 | Regulating synaptic membrane exocytosis protein 1 | S637 (_2) ↑(2.06); S640 (_2) ↑(2.06) |
| A0A0G2K8W9 | Sptbn1 | Spectrin β chain | S2155 (_2) ↑(26.05) |
| Q9QXY2 | Srcin1 | Src kinase signaling inhibitor 1 | T658 (_2) ↑(MW) |
| Q02563 | Sv2a | Synaptic vesicle glycoprotein 2A | S80 (_2) ↑(MW); S81 (_2) ↑(MW); S127 (_1) ↑(2.24) |
| P09951 | Syn1 | Synapsin-1 | S425 (_1) ↑(2.39); S508 (_1) ↑(2.22); S516 (_1) ↑(MW) |
| D3ZZQ0 | Tnik | Similar to Traf2 and NCK interacting kinase, splice variant 4 | S335 (_2) ↑(MW); S766 (_1) ↓(C) |

↑, protein hyperphosphorylation after a 6-month morphine withdrawal; ↓, protein hypophosphorylation after a 6-month morphine withdrawal; C, protein phosphorylation detected only in samples from control rats; MW, protein phosphorylation detected only in samples from morphine-withdrawn rats.

**Table 5.** A list of differentially phosphorylated proteins associated with cytoskeletal, synaptic plasticity and GTPase regulatory activity in the cerebellum six months after withdrawal from morphine.

| Protein ID | Gene | Protein Name | Position, Fold Change |
|---|---|---|---|
| Q5QD51 | Akap12 | A-kinase anchor protein 12 | S273 (_2) ↓(C) |
| A0A0G2K6R9 | Ank2 | Ankyrin 2 | S2698 (_2) ↓(C) |
| Q5HZA7 | Bin1 | Bin1 protein | S265 (_1) ↑(MW) |
| G3V984 | Bsn | Protein bassoon | S1034 (_2) ↑(3.26); S1035 (_2) ↑(3.26); S1098 (_2) ↓(−2.06); T1100 (_3) ↑(MW); S1469 (_2) ↓(C) |
| P35565 | Canx | Calnexin | S582 (_1) ↓(−45.95) |
| Q62950 | Crmp1 | Dihydropyrimidinase-related protein 1 | S566 (_2) ↑(2.64); S570 (_2) ↑(2.64) |
| A0A0G2JT93 | Ctnnb1 | Catenin β1 | T556 (_1) ↑(2.06) |
| F1M787 | Ctnnd2 | Catenin δ2 | S517 (_1) ↑(2.29) |
| A0A1B0GWS4 | Cttn | Src substrate cortactin | S123 (_2) ↓(−4.09); S135 (_3) ↓(C) |
| D4A0I5 | Dnajc6 | DnaJ (Hsp40) homolog, subfamily C, member 6 | S564 (_2) ↑(2.40) |

**Table 5.** *Cont.*

| Protein ID | Gene | Protein Name | Position, Fold Change |
|---|---|---|---|
| P47942 | Dpysl2 | Dihydropyrimidinase-related protein 2 | S542 (_1) ↑(MW) |
| Q62952 | Dpysl3 | Dihydropyrimidinase-related protein 3 | Y499 (_3) ↓(−2.30); T509 (_3) ↓(−2.21); T514 (_2) ↓(C) |
| A0A0G2K1Q9 | Epb41l3 | Erythrocyte membrane protein band 4.1-like 3 | S97 (_3) ↑(MW) |
| A0A0G2K527 | Git1 | ARF GTPase-activating protein Git1 | S376 (_2) ↓(C); S379 (_3) ↑(MW); T383 (_3) ↑(MW) |
| A0A0G2K5C6 | Map1a | Microtubule-associated protein 1A | S1860 (_1) ↑(7.34) |
| P15205 | Map1b | Microtubule-associated protein 1B | S821 (_3) ↓(−2.08); S824 (_2) ↓(−2.28); S824 (_3) ↓(−2.08); S825 (_2) ↑(−2.28); S825 (_3) ↓(−2.08); S963 (_3) ↓(C); S1254 (_3) ↑(MW); S1317 (_3) ↑(MW); S1319 (_3) ↓(C); S1332 (_2) ↓(C); S1393 (_1) ↓(C) |
| F1MAQ5 | Map2 | Microtubule-associated protein 2 | S724 (_2) ↓(C); Y744 (_2) ↓(C) |
| D4A1Q2 | Mapt | Microtubule-associated protein tau | S423 (_3) ↓(C); T426 (_3) ↓(C);S649 (_2) ↓(−5.59); S649 (_3) ↑(3.33) |
| Q920Q0 | Palm | Paralemmin-1 | S244 (_2) ↑(MW); T363 (_2) ↓(C); T367 (_2) ↑(MW]) |
| D3Z9C7 | Pclo | Protein piccolo | S63 (_2) ↓(C); S2337 (_2) ↑(2.56); S2343 (_2) ↑(2.56); S3320 (_2) ↑(2.35); S3326 (_2) ↑(2.35) |
| D3ZKH6 | Rabgap1l | Rab GTPase-activating protein 1-like | S490 (_1) ↑(MW) |
| D3ZKQ4 | Rabl6 | RAB, member RAS oncogene family-like 6 | T606 (_2) ↓(C); S650 (_2) ↑(MW) |
| F1M386 | Rapgef2 | Rap guanine nucleotide exchange factor 2 | S1115 (_2) ↑(MW) |
| P61265 | Stx1b | Syntaxin-1B | S109 (_1) ↓(−2.56) |
| P61765 | Stxbp1 | Syntaxin-binding protein 1 | S594 (_1) ↑(2.66) |
| Q02563 | Sv2a | Synaptic vesicle glycoprotein 2A | S80 (_3) ↓(C); S81 (_3) ↓(C); T84 (_3) ↓(C); S127 (_1) ↑(2.70) |
| P09951 | Syn1 | Synapsin-1 | S430 (_3) ↓(C); S432 (_3) ↑(2.25); S680 (_2) ↑(2.16) |
| P97610 | Syt12 | Synaptotagmin-12 | S93 (_2) ↓(−2.25); S97 (_2) ↓(−2.25); T103 (_1) ↓(C) |
| G3V6M3 | Syt2 | Synaptotagmin-2 | T125 (_1) ↑(299.42) |

↑, protein hyperphosphorylation after a 6-month morphine withdrawal; ↓, protein hypophosphorylation after a 6-month morphine withdrawal; C, protein phosphorylation detected only in samples from control rats; MW, protein phosphorylation detected only in samples from morphine-withdrawn rats.

The datasets of differentially expressed proteins associated with synaptic plasticity, cytoskeletal organization and GTPase regulatory activity comprise 9 proteins in the cortex, 4 proteins in the hippocampus, 8 proteins in the striatum and 10 proteins in the cerebellum (Table 7). The details, including quantification and statistics, QC (quantification control) parameters of identification and samples data binary logarithms, are stated in Supplementary Table S4. In order to determine the associations between differentially phosphorylated and expressed proteins, protein–protein association networks were created for each brain region using the String database (https://string-db.org/; assessed on 22 March 2021) with color depiction of alterations in protein levels (Figures 1–4).

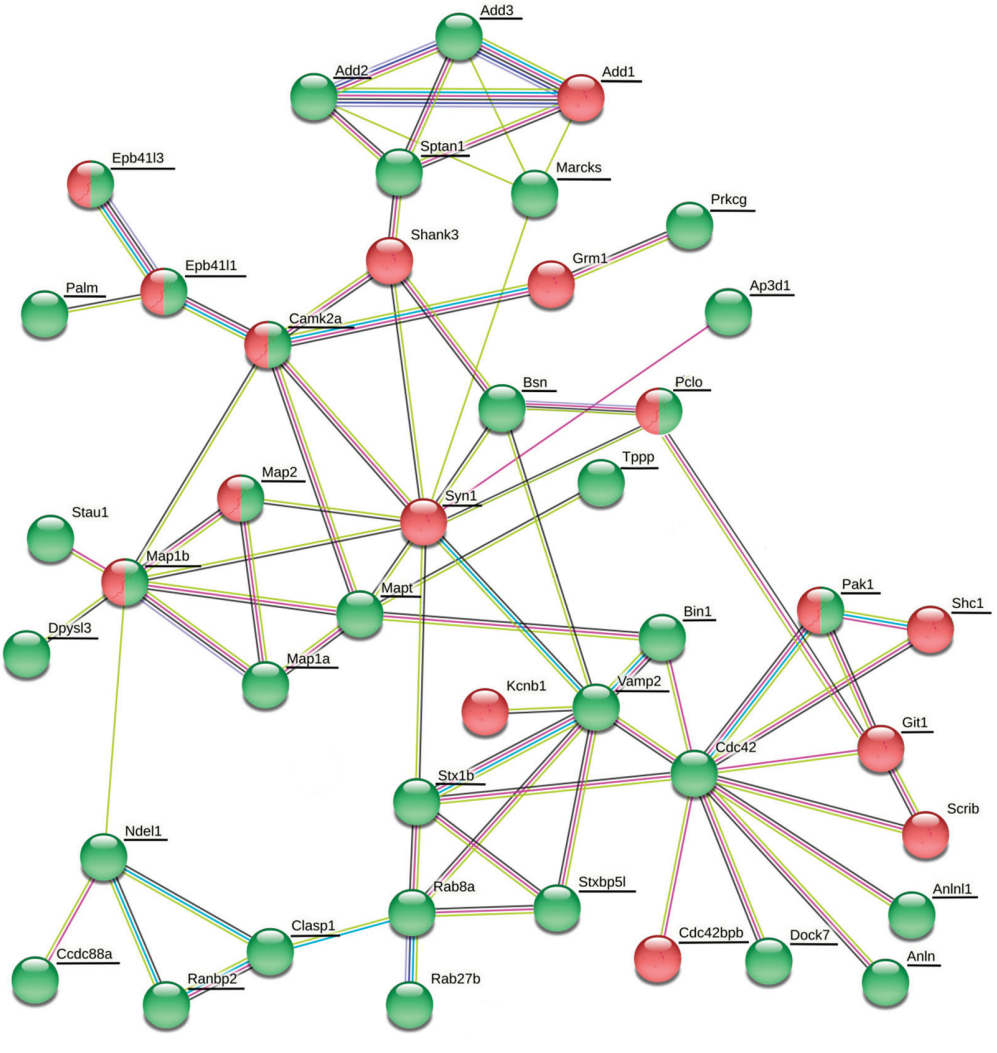


**Figure 1.** Network representation of differentially expressed or phosphorylated proteins in rat cortex six months after morphine withdrawal. Forty-four differentially expressed or phosphorylated proteins were mapped onto the rat String database of protein-protein associations and connected in a tight network with 71 edges. The green and red nodes represent proteins with increased and decreased levels, respectively, in the cortex of morphine-withdrawn rats relative to controls. The names of differentially phosphorylated proteins are underlined. Edges between the nodes represent the connection or relationship between the respective proteins. The average node degree is 3.23 and enrichment *p*-value of protein–protein associations is <1.0e−16.

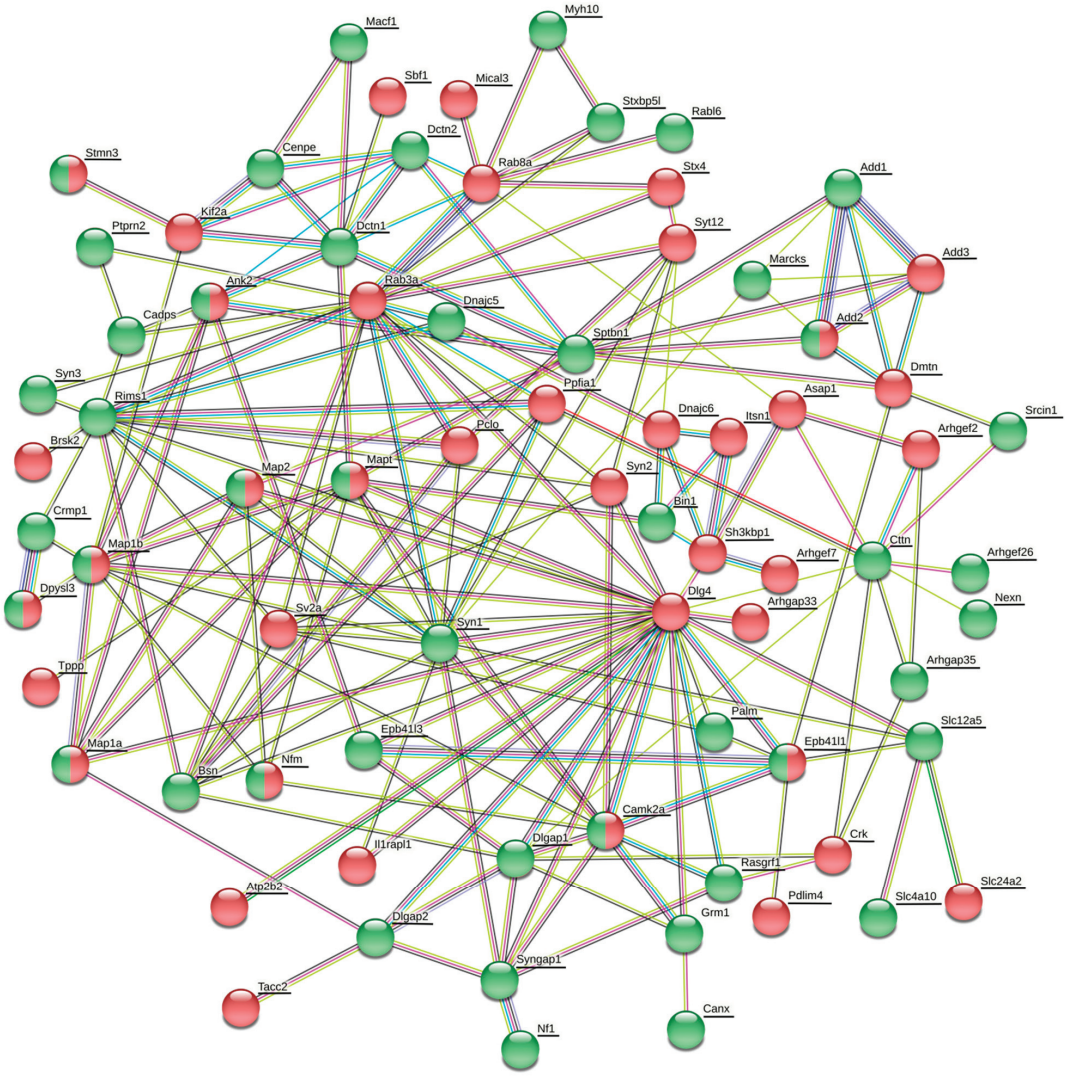


**Figure 2.** Network representation of differentially expressed or phosphorylated proteins in rat hippocampus six months after morphine withdrawal. Seventy-five differentially expressed or phosphorylated proteins were mapped onto the rat String database of protein–protein associations and connected in a tight network with 183 edges. The green and red nodes represent proteins with increased and decreased levels, respectively, in the hippocampus of morphine-withdrawn rats relative to controls. The names of differentially phosphorylated proteins are underlined. Edges between the nodes represent the connection or relationship between the respective proteins. The average node degree is 4.88 and enrichment *p*-value of protein–protein associations is <1.0e−16.

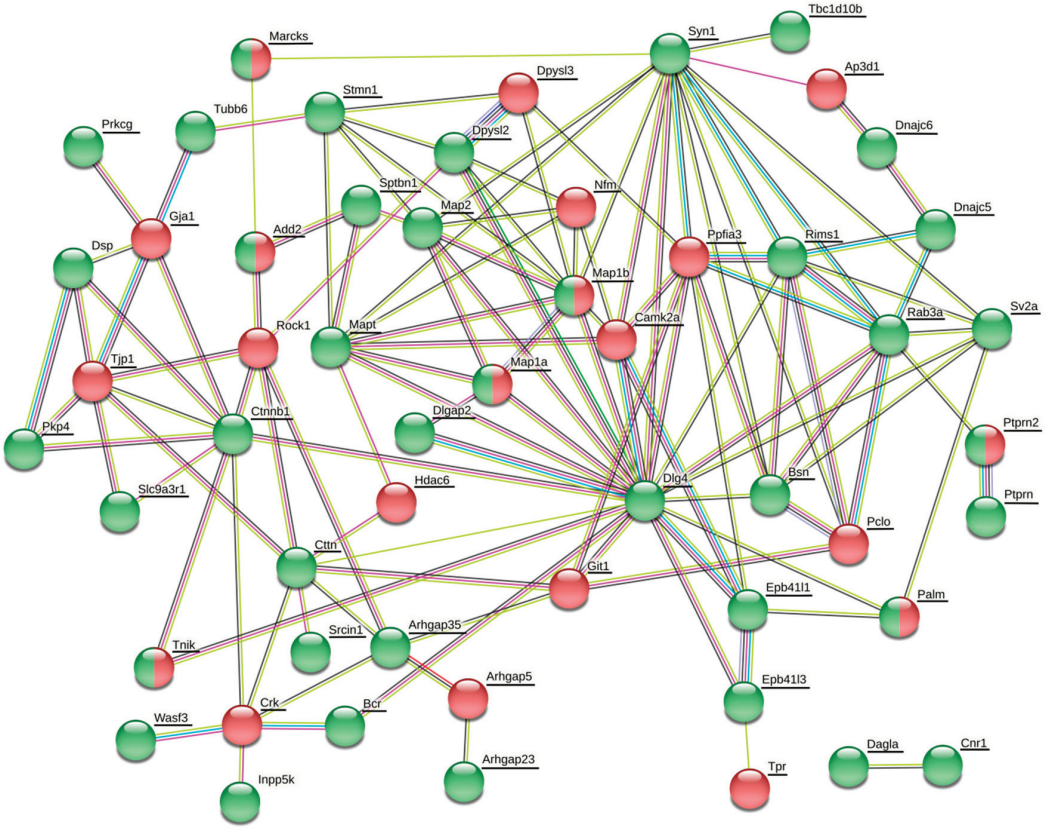


**Figure 3.** Network representation of differentially expressed or phosphorylated proteins in rat striatum six months after morphine withdrawal. Fifty-four differentially expressed or phosphorylated proteins were mapped onto the rat String database of protein–protein associations and connected in a tight network with 124 edges. The green and red nodes represent proteins with increased and decreased levels, respectively, in the striatum of morphine-withdrawn rats relative to controls. The names of differentially phosphorylated proteins are underlined. Edges between the nodes represent the connection or relationship between the respective proteins. The average node degree is 4.59 and enrichment *p*-value of protein–protein associations is <1.0e−16.

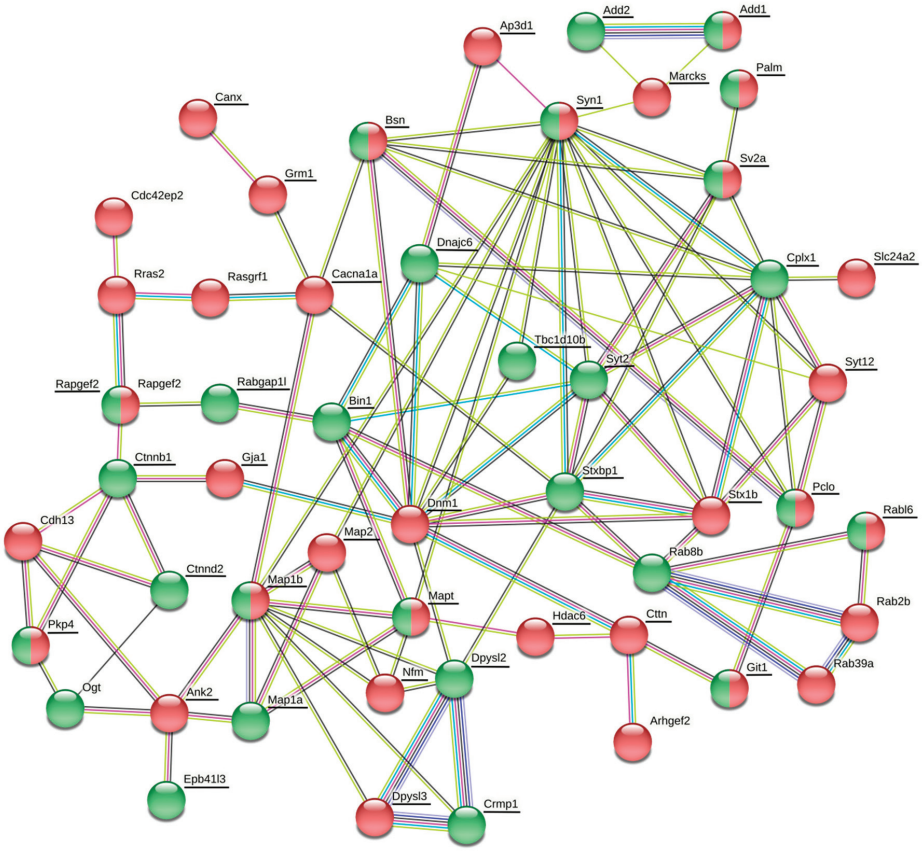


**Figure 4.** Network representation of differentially expressed or phosphorylated proteins in rat cerebellum six months after morphine withdrawal. Fifty-one differentially expressed or phosphorylated proteins were mapped onto the rat String database of protein–protein associations and connected in a tight network with 107 edges. The green and red nodes represent proteins with increased and decreased levels, respectively, in the striatum of morphine-withdrawn rats relative to controls. The names of differentially phosphorylated proteins are underlined. Edges between the nodes represent the connection or relationship between the respective proteins. The average node degree is 4.20 and enrichment *p*-value of protein–protein associations is <1.0e−16.

We observed alterations in phosphorylation of synapsin-1, Bassoon and Piccolo proteins, regulating synaptic membrane exocytosis protein 1 (Rims1), Rab3a, synaptic vesicle glycoprotein SV2A, synaptotagmin-2, syntaxin-1b, syntaxin-binding protein 5-like (Stxbl5l), Bin1 protein, Ppfia proteins, cytoplasmic linker-associated protein 1 (Clasp), MAP1B, Tau, Srcin1, Akap12, Tnik, diydropyrimidinase-related proteins (Dpysl proteins and Crmp1), serine/threonine-protein kinase MRCK beta (Cdc42bpb), serine/threonine-protein kinase Brsk2 and DnaJ homolog 6 (Dnajc6) (Tables 2–5 and Supplementary Table S3), which are either components of synaptic vesicles or participate in synaptic vesicle transport and exocytosis in the active zone [51–54]. In the cortex, we found that a six-month morphine withdrawal increased the level of Rab27b (Table 6), which participates in synaptic vesicle exocytosis and recycling at the presynaptic nerve terminal [55]. Another group of differentially phosphorylated synaptic phosphoproteins included MAP1A, MAP1B, MAP2, tau, Camk2a, Tppp (brain specific protein p25 alpha), SynGAP1, δ-catenin, spectrin alpha chain, spectrin beta chain, cortactin, ankyrin 2, paralemmin-1, band 4.1-like protein 1, band

4.1-like protein 3, calnexin and RGS14 (Tables 2–5). The levels of Shank3 and cadherin 13 were found to be decreased after a six-month morphine withdrawal in cortex and cerebellum, respectively (Table 6). All these proteins represent components of postsynaptic multimeric complexes [51,54,56,57]. The third group differentially phosphorylated or expressed proteins included Cdc42 and regulators of Rho/Cdc42 GTPases, Rho-associated protein kinase 1 (Rock1), Rab proteins and its regulator RabGAP1l, Rras2, and regulators of Ras/Rap GTPases (Tables 2–6, Supplementary Tables S3 and S4). While many Rab GTPases are located in the presynaptic nerve terminal and are involved in biogenesis, transport, docking, exocytosis and recycling of synaptic vesicles [55], Rab8 proteins are involved in GluA1-AMPA receptors trafficking from the endoplasmatic reticulum to the Golgi complex and in their delivery to the postsynaptic membrane [58]. Ras and Rap GTPases contribute to linking NMDA receptor activation and calcium influx with phosphorylation and trafficking of AMPA receptors during the induction of synaptic plasticity [59]. Rho and Cdc42 GTPases are located at the presynaptic nerve terminals as well as in the postsynaptic cells. Cdc42 signaling can induce actin cytoskeleton remodeling and subsequently trafficking or scaffolding of vesicles or key exocytosis molecules to the presynaptic nerve terminal [60]. Cdc42 signaling and RhoA/Rock signaling are both located in the postsynaptic neurons [56].

**Table 6.** A list of differentially expressed proteins associated with cytoskeletal, synaptic plasticity and regulation of GTPase activity in selected brain regions six months after withdrawal of morphine.

| Brain Region | Protein ID | Gene | Proteine Name | Alteration |
|---|---|---|---|---|
| Cortex | A0A0G3JSM8 | Cdc42 | Cell division control protein 42 homolog | ↑ (MW) |
| | P23385; G3V7U1 | Grm1 | Metabotropic glutamate receptor 1 | ↓ (−2.31) |
| | P15387; A0A0H2UI34 | Kcnb1 | Potassium voltage-gated channel subfamily B member1 | ↓ (−2.26) |
| | D4A7P2 | Lrrtm2 | Leucine-rich repeat transmembrane | ↑(2.43) |
| | Q99P74 | Rab27b | Ras-related protein Rab-27B | ↑ (MW) |
| | P35280 | Rab8a | Ras-related protein Rab-8A | ↑ (2.34) |
| | D3ZWS0 | Scrib | Scribble planar cell polarity protein | ↓ (C) |
| | A0A0U1RRP5 | Shank3 | SH3 and multiple ankyrin repeat domains protein 3 | ↓ (C) |
| | Q9ET50 | Stau1 | Staufen double-stranded RNA-binding protein 1 | ↑ (2.08) |
| Hippocampus | F1LLX6 | Cadps | Calcium-dependent secretion activator 1 | ↑ (MW) |
| | P23385;G3V7U1 | Grm1 | Metabotropic glutamate receptor 1 | ↑ (2.16) |
| | P59824; 0A096MJW6 | Il1rapl1 | Interleukin-1 receptor accessory protein-like 1 | ↓ (−2.03) |
| | P35280 | Rab8a | Ras-related protein Rab-8A | ↓ (C) |
| Striatum | F1LMV6 | Dsp | Desmoplakin | ↑ (MW) |
| | Q99PS8 | Hrg | Histidine-rich glycoprotein | ↓ (−2.04) |
| | A0A0G2K2Z2 | Inpp5k | Inositol polyphosphate-5-phosphatase K | ↑ (MW) |
| | D3ZKG5 | Parvb | Parvin, beta | ↓ (2.01) |
| | Q63644 | Rock1 | Rho-associated protein kinase 1 | ↓ (C) |
| | P34901 | Sdc4 | Syndecan-4 | ↑ (2.20) |
| | F1MA97 | Thsd7a | Thrombospondin type 1 domain-containing 7A | ↑ (2.19) |
| | Q4QQV0 | Tubb6 | Tubulin beta chain | ↑ (2.10) |
| Cerebellum | Q5FVC2;A0A1B0GWY5 | Arhgef2 | Rho guanine nucleotide exchange factor 2 | ↓ (−2.38) |
| | Q5PQP4 | Cdc42ep2 | Cdc42 effector protein 2 | ↓ (C) |
| | F1M7X3 | Cdh13 | Cadherin 13 | ↓ (C) |
| | G3V6F4; P56558 | Ogt | O-linked N-acetylglucosamine transferase | ↑ (MW) |
| | Q3B7V5 | Rab2b | Rab2b, member RAS oncogene family | ↓ (C) |
| | D3ZZP2 | Rab39a | Rab39, member RAS oncogene family | ↓ (C) |
| | P70550 | Rab8b | Ras-related protein Rab-8B | ↑ (MW) |
| | A0A0G2JU11;F1M386 | Rapgef2 | Rap guanine nucleotide exchange factor 2 | ↓ (−2.41) |
| | P28818; A0A0G2JZ23 | Rasgrf1 | Ras-specific guanine nucleotide-releasing factor 1 | ↓ (−2.21) |
| | Q5BJU0 | Rras2 | Ras-related 2 | ↓ (C) |

↑, protein hyperphosphorylation after a 6-month morphine withdrawal; ↓, protein hypophosphorylation after a 6-month morphine withdrawal; C, protein phosphorylation detected only in samples from control rats; MW, protein phosphorylation detected only in samples from morphine-withdrawn rats.

3.3.1. Changes in Protein Expression and Phosphorylation in the Cortex

Proteins related to synaptic vesicle arrangement and cycling in cortex were mostly hyperphosphorylated after a six-month morphine withdrawal (Figure 1 and Table 2). Synapsin-1 together with Cdc42bpb and Srcin1 were found to be hypophosphorylated. Piccolo and MAP1B were simultaneously hyper- and hypophosphorylated at different phosphosites. Some other proteins (Bsn, Stx1b, Stxbl5l, Bin1, Clasp, tau, Dpysl3) were hyperphosphorylated. This was accompanied by an increase in the level of Rab27b (Table 6), which is together with Rab3 engaged in synaptic vesicle docking and exocytosis [58]. Likewise, proteins forming postsynaptic complexes were mostly hyperphosphorylated (Figure 1 and Table 2). MAP1A, tau, TPPP, δ-catenin, spectrin α-chain, paralemmin-1, band 4.1-like protein 1 and band 4.1-like protein 3 were hyperphosphorylated and only Git1 was hypophosphorylated. Three proteins (MAP1B, MAP and Camk2a) were simultaneously hyper- and hypophosphorylated. This was accompanied by a decrease in the level of Shank3 (Table 6), which colocalizes with Bassoon in the presynaptic nerve terminal [61], and forms multimeric sheets within the postsynaptic density where they interact with numerous PSD proteins and the actin cytoskeleton [62]. Scribble planar cell polarity protein (Scrib), which acts a scaffold for the recruitment of proteins and directs membrane localization of SVs [63], was downregulated (Table 6). The level of Cdc42 homolog was increased in cortex from morphine-withdrawn rats (Table 6) and Cdc42bpb (MRCK beta kinase) was hyperphosphorylated at Ser1695 phosphosite located in the C-terminus of the protein (Table 2).

3.3.2. Changes in Protein Expression and Phosphorylation in the Hippocampus

There was no clear trend in the level of phosphorylation of proteins related to synaptic vesicle arrangement and cycling in the hippocampus after a six-month morphine withdrawal (Figure 2 and Table 3). Synapsin-1 together with Bassoon, Rims1, Stxbl5l, Bin1, Srcin1, Akap12, Crmp1 and Dnajc5 were hyperphosphorylated (Table 3). Piccolo, Rab3a, SV2a protein, Ppfia1, Cdc42bpb, Brsk2 and Dnajc6 were hypophosphorylated. MAP1B and tau proteins with Dpysl3 were found to be simultaneously hyperphosphorylated at some phosphosites and hypophosphorylated at others (Figure 2 and Table 3). Likewise, proteins forming postsynaptic complexes were mostly hyper- and hypophosphorylated to the same extent (Figure 2 and Table 3). MAPs (MAP1A, MAP1B, MAP2 and tau) together with Camk2a, Ank2, band 4.1-like protein 1 were simultaneously hyper- and hypophosphorylated at different phosphosites. SynGAP1, δ-catenin, spectrin β chain, cortactin, paralemmin-1, band 4.1-like protein 3, calnexin and Dlgap2 were hyperphosphorylated and Tppp, Rgs14 and Dlg4 were hypophosphorylated (Figure 2 and Table 3). The observed changes in phosphoproteome were accompanied by a downregulation of interleukin-1 receptor accessory protein-like 1 (Il1rapl1) (Table 6), which promotes formation of excitatory synapses [64]. Small GTPases were not affected by a six-month morphine withdrawal, except for changed phosphorylation of Rab3a and Rabl6 (Table 3). On the other hand, the level of phosphorylation of regulators of Rho/Cdc42 GTPases, Arhgap and Arhgef, was markedly changed. Arhgap33 was hypophosphorylated at Thr974 and Arhgap35 was hyperphosphorylated at Ser1179 (Table 3). The Ser1179 phosphosite at Arhgap35 is located in the p120RasGAP binding domain [43]. Three Arhgef proteins were differentially phosphorylated (Table 3). Whereas Arhgef26 was hyperphosphorylated, Arhgef7 (β-PIX) was hyperphosphorylated at Ser228 and Arhgef2 (Lfc) at Ser916 (Table 3). Ral and Ran GTPase binding proteins, Ralbp1 and Ranbp3, were hypophosphorylated and hyperphosphorylated, respectively. Rasgrf1 was hyperphosphorylated at Ser747 (Table 3). These data suggest that a six-month morphine withdrawal exerts a great impact on GTPase signaling, mainly on Rho/Cdc42 signaling via its GAP and GEF regulators and on Ras signaling via its releasing factor Rasgrf1 and Ras/Rap GTPase activating protein SynGAP1, and indirectly via phosphorylation of Arhgap35 in its p120RasGAP binding domain.

3.3.3. Changes in Protein Expression and Phosphorylation in the Striatum

Proteins related to synaptic vesicle arrangement and cycling were mostly hyperphosphorylated after a six-month morphine abstinence (Figure 3 and Table 4). Synapsin-1 together with Cdc42bpb, Srcin1, Bassoon, Rims1, Rab3a, SV2a, Tau, Dpysl2 and Dnajc5 were found to be hyperphosphorylated. Piccolo, Ppfia3 and Dpysl3 were hypophosphorylated. MAP1B and Tnik were simultaneously hyper- and hypophosphorylated at different phosphosites. Likewise, proteins forming postsynaptic complexes were mostly hyperphosphorylated (Figure 3 and Table 4). MAP2, tau, β-catenin, spectrin β-chain, cortactin, band 4.1-like protein 1, band 4.1-like protein 3 were hyperphosphorylated and only Git1 and Camk2a were hypophosphorylated. MAP1A, MAP1B and paralemmin-1 were simultaneously hyper- and hypophosphorylated (Figure 3 and Table 4). The β-tubulin isoform Tubb6, belonging to the building blocks of microtubules, was upregulated (Table 6). Long-term morphine withdrawal diversely affected proteins implicated in signaling mediated by small G proteins. Contrary to hyperphosphoryled Rab3a, the other Rab protein, Rabl6, was hypophosphorylated. Interestingly, Arhgap proteins were distinctly phosphorylated (Table 4). Whereas Arhgap23 and Arhgap35 (p190RhoGAP) were hyperphosphorylated, Arhgap31 (Cdc42GAP) and Arhgap5 were hypophosphorylated. Arhgap35 was hyperphosphorylated at Tyr1105; this residue is phosphorylated by Src kinase and is involved in the association of Arhgap35 with p120RasGAP [43]. These changes were accompanied by a decrease in expression of Rock1, Rho-associated protein kinase 1 associated with cadherin/catenin or cortactin/Srcin1 complexes (Figure 2).

3.3.4. Changes in Protein Expression and Phosphorylation in the Cerebellum

There was no clear trend in the level of phosphorylation of proteins related to synaptic vesicle arrangement and cycling in the cerebellum after a six-month morphine withdrawal (Figure 4 and Table 5). Synapsin-1 together with Bassoon, Piccolo, SV2a protein, MAP1B and tau were found to be simultaneously hyperphosphorylated at some phosphosites and hypophosphorylated at others. While the Stx1b, Akap12 and Dpysl3 proteins were only hypophosphorylated, synaptotagmin-2, Bin-1, Dpysl2, Crmp1 and Dnajc 6 were only hyperphosphorylated. Interestingly, phosphorylation of synaptotagmin-2 at Thr125 increased nearly three hundred times (Table 5). Likewise, proteins forming postsynaptic complexes were mostly hyper- and hypophosphorylated to the same extent (Figure 4 and Table 5). MAP1B, tau, paralemmin-1 and Git1 were simultaneously hyper- and hypophosphorylated at different phosphosites. Whereas MAP1A, β- and δ-catenins and band 4.1-like protein 3 were hyperphosphorylated, MAP2, cortactin and calnexin were hypophosphorylated (Figure 4 and Table 5). This was accompanied by a decrease in the expression of cadherin 13 (Table 6). Small GTPases and their regulators were altered mainly at the level of protein expression than phosphorylation. Rab2b, Rab39 and Rras2 were downregulated and Rab8b was upregulated (Table 6). The Rabl6 protein was simultaneously hyper- and hypophosphorylated at different phosphosites (Table 5). The expression levels of four GTPase regulators (Arhgef2, Cdc42ep2, Rapgef2 and Rasgrf1) were decreased (Table 6) suggesting regulation of several GTPase signaling pathways. Interestingly, Rapgef2 and Rabgap1l were simultaneously hyperphosphorylated at Ser1115 and at Ser490, respectively (Table 5).

3.3.5. Comparison of Changes in Pre- and Postsynaptic Protein Clusters between Different Brain Regions

To determine which presynaptic and postsynaptic multimeric complexes were most affected by a six-month morphine withdrawal, some altered proteins were arranged into seven clusters according to their function or interaction with each other (Table 7). Three protein clusters involving components of synaptic vesicles, synaptic vesicle exocytosis and components of the active zone represent multimeric protein complexes located in the presynaptic nerve terminal. The clusters of proteins involved in the cadherin–catenin complex or in a scaffold structure of the postsynaptic density are located in dendritic spines.

Two clusters of proteins were associated with the actin–spectrin network or microtubule dynamics. From presynaptic protein clusters, proteins of the active zone were apparently most affected because alterations in protein phosphorylation frequently occurred in all the four brain regions under scrutiny. The phosphoproteins present in synaptic vesicles were also differentially phosphorylated in all four brain regions. Interestingly, there were fewer changes in the cortex compared with the other three regions. Synaptic vesicle exocytosis was affected only in the cortex and cerebellum, and the observed alterations differed markedly between these two regions.

In general, the cadherin–catenin complex was affected by a six-month morphine withdrawal and changes occurred mainly on the level of catenin phosphorylation in all four brain regions, but some regional differences were observed (Table 7). First, no other protein involved in the cadherin–catenin complex was found to be altered in the cortex. Second, the RhoA signaling pathway was greatly affected in the striatum, where Arhgap35, a negative regulator of RhoA, was phosphorylated at Tyr1105 (Table 4). Importantly, Tyr1105 phosphorylation was shown to be required for RhoA inactivation [43]. The expression of Rock1 kinase, which is activated by RhoA, was decreased. These data indicate that RhoA signaling pathway is suppressed in the striatum after a six-month morphine withdrawal. Third, alteration in the cadherin family was found only in the cerebellum, where the level of cadherin 13 was decreased.

The level of Shank3, a scaffold protein localized in the postsynaptic density, which acts as a modulator of small GTPases and actin dynamics, was decreased in the cortex but not changed in the other three brain regions where its interacting protein, cortactin, was differentially phosphorylated (Table 7). In hippocampus, the Shank3 interacting partner, Arhgef7 (β-PIX), was differentially phosphorylated at Ser228 (Table 3) localized in the Dbl domain outside the domains mediating interaction with Shank3 [65], indicating that the interaction of Shank3 and Arhgef7 was not affected by a six-month morphine withdrawal. The Dbl domain is associated with activation of Rho GTPases [66], suggesting yet another possibility how the Rho signaling pathway could be affected. Shank3 protein and its interacting proteins affect the actin cytoskeleton via formation and stabilization of F actin and subsequently spine morphogenesis via enhancement of spine maturation [67]. Thus, a six-month morphine withdrawal could differently affect spine morphogenesis in all four brain regions under investigation.

Spectrins, ankyrin 2 and adducins, which were found to be differentially phosphorylated (Table 7), together with actin filaments form a membrane-associated periodic skeleton (MPS). They are ubiquitously distributed in mature axons, where F-actin rings are arranged periodically by spectrin tetramer spacers [68]. Adducins and band 4.1-like protein 1 stabilize interaction between actin and spectrin [68], suggesting regional changes in actin-spectrin interactions induced by a six-month morphine withdrawal.

The microtubule-associated proteins belong to a few proteins which were differentially phosphorylated in all four brain regions (Table 7). As a rule, these proteins were altered at several different phosphosites (Tables 2–5). MAP1B, which is localized in the presynaptic nerve terminal as well in postsynaptic cells, is a microtubule-associated protein with the largest number of altered phosphosites in all four brain regions (Tables 2–5). Dihydropyriminase-related proteins Crmp1 and Dpysl2 were found to be differentially phosphorylated in the hippocampus, striatum and cerebellum (Table 7), suggesting that microtubule stability was more affected in these brain three regions than in the cortex.

### *3.4. Changes in Phosphorylation Pattern of Selected Phosphoproteins after a 6-Month Morphine Withdrawal*

Because MAPs, synapsin-1 (Syn1), Bassoon and Piccolo proteins were found to be altered in all the four brain regions (Tables 2–5, Supplementary Table S3) and were frequently present in GO enrichment analysis of altered phosphoproteins after a six-month morphine withdrawal (Supplementary Table S1), we focused on their alterations in detail. Camk2a kinase was found to be differentially phosphorylated in cortex, hippocampus and striatum (Tables 2–4).

**Table 7.** Comparison of changes induced by a six-month morphine withdrawal in protein clusters comprising presynaptic or postsynaptic multimeric complexes in selected brain regions.

| Protein | Function | Alteration | Ctx | H | S | Cb |
|---|---|---|---|---|---|---|
| Synapsin-1 | Components of synaptic vesicles [69] | Phosphorylation | ↓ | ↑ | ↑ | ↑↓ |
| SV2a | Components of synaptic vesicles [69] | Phosphorylation | - | ↓ | ↑ | ↑↓ |
| Synaptotagmin-2 | Components of synaptic vesicles [69] | Phosphorylation | - | - | - | ↑ |
| Rab3a | Components of synaptic vesicles [69] | Phosphorylation | - | ↓ | ↑ | - |
| Rab27b | Synaptic vesicle exocytosis [55] | Expression | ↑ | - | - | - |
| Syntaxin-1B | Component of SNARE complex [70] | Phosphorylation | ↑ | - | - | ↓ |
| Complexin-1 | Interaction with syntaxin-1 [70] | Phosphorylation | - | - | - | ↑ |
| Stxbp1 (Munc18-1) | Interaction with syntaxin-1 [70] | Phosphorylation | - | - | - | ↑ |
| Vamp2 (Synaptobrevin) | Interaction with syntaxin-1 [70] | Phosphorylation | ↑ | - | - | - |
| Bassoon | Protein of active zone [71] | Phosphorylation | ↑ | ↑ | ↑ | ↑↓ |
| Piccolo | Protein of active zone [71] | Phosphorylation | ↑↓ | ↓ | ↓ | ↑↓ |
| Ppfia3 (Liprin α3) | Protein of active zone [71] | Phosphorylation | - | - | ↓ | - |
| Rims1 | Protein of active zone [71] | Phosphorylation | - | ↑ | ↑ | - |
| Git1 | Interaction with liprin α [71] | Phosphorylation | ↓ | - | ↓ | ↑↓ |
| Cadherin 13 | Cadherin–catenin complex [72] | Expression | - | - | - | ↓ |
| Catenin β | Cadherin–catenin complex [72] | Phosphorylation | - | - | ↑ | ↑ |
| Catenin δ2 | Cadherin–catenin complex [72] | Phosphorylation | ↑ | ↑ | - | ↑ |
| Arhgap35 | Interaction with catenin δ, inactivation of RhoA [72] | Phosphorylation | - | ↑ | ↑ | - |
| Rock1 | Activation by RhoA [72] | Expression | - | - | ↓ | - |
| Cortactin | Interaction with catenin δ [72] | Phosphorylation | - | ↑ | ↑ | ↓ |
| Shank3 | Scaffold in postsynaptic density [67] | Expression | ↓ | - | - | - |
| Arhgef7 (β-PIX) | Interaction with Shank3 [67] | Phosphorylation | - | ↓ | - | - |
| Git1 | Interaction with β-PIX [73] | Phosphorylation | ↓ | - | ↓ | ↑↓ |
| Cortactin | Interaction with Shank3 [67] | Phosphorylation | - | ↑ | ↑ | ↓ |
| Spectrin α | Actin–spectrin network [68] | Phosphorylation | ↑ | - | - | - |
| Spectrin β | Actin–spectrin network [68] | Phosphorylation | - | ↑ | ↑ | - |
| Ankyrin 2 | Actin–spectrin network [68] | Phosphorylation | - | ↑↓ | - | ↓ |
| Alpha-adducin | Actin–spectrin network [68] | Phosphorylation | ↓ | ↑ | - | ↑↓ |
| Beta-adducin | Actin–spectrin network [68] | Phosphorylation | ↑ | ↑↓ | ↑↓ | ↑ |
| Gamma-adducin | Actin–spectrin network [68] | Phosphorylation | ↑ | ↓ | - | - |
| Band 4.1-like protein 1 | Actin–spectrin network [68] | Phosphorylation | ↑ | ↑↓ | ↑ | - |
| MAP1A | Microtubule dynamics [26] | Phosphorylation | ↑ | ↑↓ | ↑↓ | ↑ |
| MAP1B | Microtubule dynamics [26] | Phosphorylation | ↑↓ | ↑↓ | ↑↓ | ↑↓ |
| MAP2 | Microtubule dynamics [26] | Phosphorylation | ↑↓ | ↑↓ | ↑ | ↓ |
| Tau (MAPT) | Microtubule dynamics [26] | Phosphorylation | ↑ | ↑↓ | ↑ | ↑↓ |
| Tppp | Microtubule polymerization [74] | Phosphorylation | ↑ | ↓ | - | - |
| Dpysl2 (Crmp2) | Microtubule stability [75] | Phosphorylation | - | - | ↑ | ↑ |
| Crmp1 | Microtubule stability [76] | Phosphorylation | - | ↑ | - | ↑ |

↑, hyperphosphorylation or increased level of protein after a 6-month morphine withdrawal; ↓, hypophosphorylation or decreased level of protein after a 6-month morphine withdrawal; ↑↓, protein with simultaneous hyperphosphorylation at some phosphosites and hypophosphorylation at others in one experimental group; -, no change; Ctx, cortex. H, hippocampus, S, striatum, Cb, cerebellum.

#### 3.4.1. Changes in Phosphorylation Pattern of Selected Phosphoproteins in the Cortex

MAP1A protein was detected to be hyperphosphorylated at Ser1518, Ser2001 and Ser2005 in cortex after a six-month morphine withdrawal (Table 2). All these phosphosites are outside the microtubule-binding domain (MBD) and their function is not known [26]. MAP1B protein was hyperphosphorylated at Ser930, Ser1315, Ser1389 and Ser1393 and hypophosphorylated at Thr965 (Table 2). The phosphosites Ser1389 and Ser1393 have not been yet described, but they match Ser1388 and Ser1392 found in MAP1B purified from neonatal rat brain [77]. They are located in MTA, a microtubule assembly-helping site [78]. Phosphorylation of Ser1392 by DYRK1A kinase was found to prime the subsequent phosphorylation of Ser1388 by GSK3β kinase and both these phosphosites must be concurrently phosphorylated for regulating microtubule stability [77]. MAP2 protein was hyperphosphorylated at Thr1606, Ser1782 and Ser1784 on doubly phosphorylated phosphopeptide and hypophosphorylated at Ser1784 on triply phosphorylated phosphopeptide (Table 2). The phosphosite Thr1606 is located in the proline-rich domain and its phosphorylation is known to reduce microtubule binding by MAP2 [79,80]. By comparing the MAP2 sequence (F1MAQ5) identified in our study with rat sequence of full-length

MAP2 [81], we determined that the phosphosites Ser1782 and Ser1784 are located in the repeat 4a domain. Phosphorylation of Ser1782 may act to dissociate MAP2 from microtubules [79]. Tau protein was hyperphoshorylated at Ser436, Ser440, Thr648 and Ser661 (Table 2). The detected rat tau protein (ID D4A1Q2) has a length of 686 amino acids. The largest human tau isoform has 441 amino acids and its phosphorylation sites have been widely examined [82–84]. By comparing the sequences of rat and human tau isoforms, rat phosphosites Ser436, Ser440, Thr648 and Ser661 were matched to human Ser191, Ser195, Thr403 and Ser416, respectively. The phosphosites Ser436 and Ser440 are located in the proline-rich domain, which is involved in binding to and bundling F-actin [85] and serves as a core tubulin-binding domain with tubulin polymerization capacity [86]. The phosphosites Thr403 and Ser416 are located in the C-terminal domain, in which site-specific phosphorylations may facilitate the process of tau assembly [87]. In the cortex, TPPP protein was hyperphosphorylated at Ser34 in the N-terminal tail after a six-month morphine withdrawal (Table 2). The function of this phosphorylation is not yet known.

Synapsin-1 was found to be hypophosphorylated at Ser430 (Table 2), a phosphosite located in domain D. Basson was hyperphosphorylated at phosphosites Ser2632 and Ser2634 (Table 2). Piccolo was hyperphosphorylated at Ser3326 and hypophosphorylated at Ser3054 (Table 2). The phosphosite Ser3054 is located in CC3 docking site engaged in scaffolding and assembly of a core complex in the cytomatrix at the active zone [88]. Camk2a kinase was hyperphosphorylated at Ser331, Ser333, Thr336 and Thr337 and hypophosphorylated at Ser330 (Table 2). All these phosphosites are located in the C-terminal domain, which mediates holoenzyme formation [89].

#### 3.4.2. Changes in Phosphorylation Pattern of Selected Phosphoproteins in the Hippocampus

MAP1A protein was hyperphosphorylated at Ser764, Ser1236 and Ser1691 and hypophosphorylated at Ser2135 in the hippocampus after a six-month morphine withdrawal (Table 3). All these phosphosites are outside the MBD domain and their function is not known [26]. MAP1B protein was hyperphosphorylated at Ser1315, Ser1371, Ser1382, Ser1465, Ser1494, Ser1772, Ser1775 and Ser1778 and hypophosphorylated at Ser14, Ser614, Ser985, Ser1239, Ser1244, Ser1254 and Ser1432 (Table 3). The phosphosite Ser14 is located in the N-terminal actin-binding domain (ABD), Ser614 in the MTB domain and cluster of phosphosites Ser985, Ser1239, Ser1244, Ser1254, Ser1315, Ser1371 and Ser1382 in MTA site. The phosphosites Ser1432, Ser1465, Ser1494, Ser1772, Ser1775 and Ser1778 are located in the sequence between the MTA site and MBD domain of the C-terminal tail [78]. The most frequent alterations in phosphorylation of MAP1B were found in a microtubule assembly-helping site MTA, suggesting that a six-month morphine withdrawal could affect microtubule assembly. MAP2 protein was hyperphosphorylated at Ser362, Ser1784, Ser1785 and Ser1793 (in doubly phosphorylated phosphopeptide) and hypophosphorylated at Ser1064, Ser1793 (in triply phosphorylated phosphopeptide), Ser1796 and Ser1797 (Table 3). The phosphosites Ser362 and Ser1064 are located in a sequence termed the end of acidic domain [81], Ser1784 in the repeat 4a domain and Ser1785, Ser1793, Ser1796 and Ser1797 in the C-terminal domain. By sequence comparison, the phosphosite Ser1793 in MAP2 (F1MAQ5) with 1825 amino acids matches Ser435 in MAP2c with 476 amino acids [90]. Phosphorylation of this phosphosite is mediated by proteinkinase A (PKA), and has an effect on the binding of 14-3-3 proteins [90], a highly abundant protein family in the brain affecting the activity and localization of substrate proteins [91].

Tau protein was hyperphosphorylated at Ser423, Thr426 (in triply phosphorylated phosphopeptide), Ser 436 (in doubly and triply phosphorylated phosphopeptides), Ser440, Ser444, Ser447 (in doubly and triply phosphorylated phosphopeptides), Ser480 and Ser661, and was hypophosphorylated at Ser45 and Thr426 (in doubly phosphorylated phosphopeptide). The phosphosite Ser45 is located in the N-terminal domain, while the phosphosites Ser423, Thr426, Ser436, Ser440 are in the proline-rich domain P1, and Ser 444, Ser447 and Ser480 in the proline-rich domain P2. The phosphosite Ser661 is located in the C-terminal domain. The most frequent alterations in phosphorylation were found in proline-rich

domains, suggesting that binding of tau with actin and tubulin could have been affected by a six-month morphine withdrawal.

TPPP protein was found to be hypophosphorylated at Ser31 in the N-terminal tail (Table 3). By sequence comparison, this phosphosite in rat TPPP matched Ser32 in human TPPP/p25 [92]. This phosphosite Ser32 was shown to be phosphorylated by PKA [74] and Rock1 [93].

Synapsin-1 was hyperphosphorylated at Ser436, Ser518 and Ser682 (Table 3). The phosphosites Ser436 and Ser518 are located in the proline-rich domain D, while the phosphosite Ser682 is in domain E [94]. Basson was hyperphosphorylated at Ser1098 and Thr1100 (Table 3). Piccolo was hypophosphorylated at Ser3054 and Ser3326 (Table 3). Camk2a was hyperphosphorylated at Ser330 and Ser333 (both in doubly and triply phosphorylated peptides), while it was hypophosphorylated at Thr334 and Thr336 (in singly and triply phosphorylated peptides) (Table 3).

#### 3.4.3. Changes in Phosphorylation Pattern of Selected Phosphoproteins in the Striatum

MAP1A protein was found to be hyperphosphorylated at Ser1136 and Ser2432 and hypophosphorylated at Ser1232 in the striatum after a six-month morphine withdrawal (Table 4). All these phosphosites are outside the microtubule-binding domain and their function is not yet known [26]. MAP1B protein was hyperphosphorylated at Ser960, Ser1244 (in singly phosphorylated peptide), Ser1389, Thr1496, Ser1646, Ser1778 and Ser1781 and hypophosphorylated at Ser929, Ser930, Ser956, Ser963, Ser1239, Ser1244 (in doubly phosphorylated peptide) and Ser1494 (Table 4). The phosphosites Ser930, Ser956, Ser960 and Ser963 are located in a sequence between the C-terminal MBD domain and MTA site, the phosphosites Ser1239, Ser1244 and Ser1389 in MTA site, the phosphosites Ser1494, Thr1496, Ser1646, Ser1778 and Ser1781 in a sequence between the MTA site and the N-terminal MBD domain. The most frequent alterations in phosphorylation of Map1B were found in sequences outside the known binding domain and the function of phosphorylation of these phosphosites has not yet been described. MAP2 protein was hyperphosphorylated at phosphosites Ser1780, Ser1784 and Ser1788 in the C-terminal tail (Table 4). The function of these phosphosites is not known.

Tau protein was hyperphosphorylated only at Ser480 located in proline-rich domain P2 and at Tyr639 located in C-terminal domain (Table 4); these phosphosites match Ser235 and Tyr394 in human tau, respectively. The phosphosite Ser235, together with Ser202, Thr205 and Thr231 in human tau are phosphorylated by CDK2/CycA3 kinase in vitro, and when at least three out of these four positions are phosphorylated, tau loses its capacity to assemble tubulin into microtubules [95]. In our study, the other three phosphosites matched to Ser202, Thr205 and Thr231 in human Tau were not detected or altered (data not shown). The phosphosites Tyr394 and Ser396 in human Tau were proved to weaken the interaction between tau and microtubules and phosphorylation at Tyr394 had a more pronounced effect than phosphorylation at Tyr394 [95]. In our study, Tyr639 matched to Tyr394 in human tau was greatly hyperphosphorylated (Table 4) but phosphorylation at Ser641 matched to Ser396 in human Tau was not altered in striatum after six-month morphine abstinence suggesting only a smaller weakening of interaction between Tau and microtubules.

Synapsin-1 was found to be hyperphosphorylated at Ser425, Ser508 and Ser516 (Table 4); all these phosphosites are located in domain D [94]. Bassoon was hyperphosphorylated at Ser1220 and Ser2842 and Piccolo was hypophorylated at Ser66 and Trh2103 (Table 4). The phosphosite Thr2103 in Piccolo is located in the docking site for Daam1, which is involved in actin cytoskeleton dynamics [88]. Camk2a was hypophosphorylated at Ser330 (Table 4).

#### 3.4.4. Changes in Phosphorylation Pattern of Selected Phosphoproteins in the Cerebellum

MAP1A protein was hyperphosphorylated at Ser1860 in the cerebellum after a six-month morphine withdrawal (Table 5). This phosphosite is outside the microtubule-binding

domain and its function is not known [26]. Map1B protein was hyperphosphorylated at Ser825 (in doubly phosphorylated peptide), Ser1254, Ser1317 and hypophosphorylated at Ser821, Ser824 (in doubly and triply phosphorylated peptides), Ser825 (in triply phosphorylated peptide), Ser963, Ser1319, Ser1332 and Ser1393 (Table 5). The phosphosites Ser821, Ser824, Ser825 are located in MBD domain in the heavy chain near the N-terminus of MAP1A. The phosphosites Ser963, Ser1254, Ser1317, Ser1319, Ser1332 and Ser1393 are located in MTA site. These results suggest alterations in binding of MAP1B to microtubules and microtubule assembly.

MAP2 otein was hypophosphorylated at Ser724 and Tyr744 (Table 5) in the variable central region of the protein [90]; the function of these phosphosites is not yet known. Tau protein was hyperphosphorylated at Ser649 in triply phosphorylated peptide and hypophosphorylated at Ser423, and at Thr426 and Ser649 in doubly phosphorylated peptide (Table 5). The phosphosites Ser423 and Thr426 are located in the proline-rich domain P1 and the phosphosite Ser649 in the C-terminal domain, suggesting alterations in binding of tau to actin and microtubules and in tau assembly.

Synapsin-1 was hyperphosphorylated at Ser432 located in domain D and at Ser680 in domain E and hypophosphorylated at Ser430 located in domain D (Table 5). Bassoon was hyperphosphorylated at Ser1034, Ser1035 and Thr1100 and hypophosphorylated at Ser1098 and Ser1469 (Table 5). The phosphosite Ser1469 is located in the docking site for dynein light chains (DLCs) involved in vesicle trafficking [88]. Piccolo was hyperphosphorylated at Ser2337, Ser2343, Ser3320 and Ser3326 and hypophosphorylated at Ser63 (Table 5). The phosphosites Ser2337 and 2343 are located in the docking site for GTPase-activating protein Git1 [88], which was also differentially phosphorylated after a six-month morphine withdrawal. It was hyperphosphorylated at Ser379 and Thr383 and hypophosphorylated at Ser376 (Supplementary Table S3). By comparing the sequence of rat Git1 (A0A0G2K527) with human Git1 [96], the phosphosites Ser376, Ser379 and Thr383 in rat Git1 were found to match Ser394, Ser397 and Thr401 in human Git1. These phosphosites are located in a synaptic localization domain (SLD), suggesting that the function of Git1 in synapse formation is regulated by phosphorylation [96]. Alterations in phosphorylation of Git1 in SLD domain may suggest changes in synaptic activity.

## 4. Discussion

The present study followed from previous work in which alterations in protein expression and phosphorylation were assessed by 2-D electrophoresis and label-free quantification in selected brain regions of rats three months after cessation of chronic morphine treatment [46]. Here, we observed that cytoskeletal proteins (actin and tubulin) and their binding partners (Tppp, Dpysl2, F-actin capping protein β) were differentially expressed or phosphorylated mainly in the cortex and hippocampus. The tubulin polymerization promoting protein is specifically expressed in oligodendrocytes [29], and has two cellular functions. It promotes microtubule polymerization and regulates HDAC6 activity [93]. Tppp dynamically colocalizes with microtubules and induces microtubule bundling and stabilization followed by increased acetylation of microtubules [97]. The phosphorylation of human Tppp at Ser32, corresponding to Ser31 in rat Tppp, mediated by Rock kinase contributes to inhibition of its binding to HDAC6, subsequent increase in HDAC6 activity and tubulin deacetylation [93]. While the level of Tppp protein was downregulated following a three-month morphine withdrawal in the cortex and hippocampus and hypophosphorylated in the striatum [46], a six-month morphine withdrawal resulted in hyperphosphorylation of Tppp at Ser34 in the cortex and hypophosphorylation at Ser31 in the hippocampus, suggesting that, at least in rat hippocampus, regulation of tubulin acetylation via Tppp expression or phosphorylation at Ser31 might occur over the course of several months after morphine withdrawal.

Dihydropyrimidinase-related protein 2 (Dpysl2) is another protein which was found to be differentially phosphorylated after a three- as well as six-month morphine withdrawal. Whereas this protein was hyperphosphorylated in the cortex and hypophosphorylated

in the hippocampus after a three-month morphine withdrawal [46], it was hyperphosphorylated at Ser537 in the striatum and at Ser542 in the cerebellum after a six-month morphine withdrawal. The other dihydropyrimidinase-related proteins, Crmp1 (collapsin response mediator protein 1) and Dpysl3, were also differentially phosphorylated after a six-month morphine withdrawal. The majority of differentially phosphorylated sites on dihydropyrimidinase-related proteins were located in the C-terminal region, and only one differentially phosphorylated site in Crmp1 was located in the N-terminal region. Whereas the N-terminal dihydropyrimidinase-like domain appears to promote microtubule assembly, the C-terminal region of Crmp1 and Crmp2 (Dpysl2) is sufficient to stabilize the microtubules [76]. The phosphorylation of Crmps at its C-terminal domains causes microtubule destabilization, while inhibition of the C-terminal phosphorylation has a stabilizing effect [98]. The residues Thr509, Thr514 and Ser518 at the C-terminus of collapsin response mediator proteins are phosphorylated by GSK-3β [76]. In the present study, differential phosphorylation patterns at these residues in Dpysl3 (Crmp4) were observed in all four brain regions under scrutiny. Hyperphosphorylation at Thr509 and hypophosphorylation at Ser518 in Dpysl3 were found in the hippocampus and striatum, respectively. The residues Thr509 and Thr514 were simultaneously hyperphosphorylated in the cortex and hypophosphorylated in the cerebellum, indicating an opposing trend in the binding of Dpysl3 to microtubules in the cortex and cerebellum. Taken together, collapsin response mediator proteins are other microtubule-binding phosphoproteins that were affected by protracted morphine withdrawal.

Morphine belongs to addictive opioid pain relievers that are often used in medical care and have a high potential for abuse. Drug abuse is a relapsing brain disease characterized by the adaptations within the mesolimbic reward system and associated neural circuits that may persist a long time after cessation of drug intake [99]. It was demonstrated that morphine-abstinent mice develop low sociability and despair-like behavior detectable up to four weeks after discontinuation of chronic drug exposure [100]. In the cocaine self-administration model of relapse liability, many protein alterations occurring during cocaine self-administration returned to normal levels between 1 and 100 d of abstinence, but some remained altered even after 100 d. On the other hand, some proteins which were not affected during cocaine self-administration altered during the abstinence period. Differentially expressed proteins during the abstinence period may contribute to specific functions related to relapse liability [101]. In that report, proteins associated with synaptic plasticity were altered in the prefrontal cortex, suggesting the importance of synaptic communication in withdrawal-associated behavior. Cocaine administration induced changes in the level of Dpysl2 and the following drug withdrawal was associated with changed expression of SNAP-25, a component of the SNARE complex, and dynamin-1 located in the postsynaptic density [101]. This is consistent with our current results suggesting that alterations in the proteome profiles of synaptic proteins may contribute to molecular neuroadaptations associated with chronic drug exposure and long-term drug abstinence.

Synapsin-1 is one of crucial proteins whose phosphorylation occurs commonly during withdrawal from different drugs. This protein was differentially phosphorylated at Ser9, Ser62 and Ser67 in the NA two hours after cocaine self-administration and phosphorylation at Ser9 was still elevated after 22 h [102]. Phosphorylation at Ser603 of synapsin-1 was increased in the mouse NA after chronic nicotine administration and decreased 24 h after drug cessation [103]. Synapsin acts as a key protein for maintaining SVs within the reserve pool, which is a large SV cluster distal to the active zone. The reserve pool serves as a store that replenishes SVs into a readily-releasable pool following exocytosis of neurotransmitters [104]. The mechanism of maintaining SVs within the reserve pool by synapsin is unclear. The first hypothesis relies on the involvement of synapsin in cross-linking of SVs, thereby anchoring SVs to each other. The cross-linking of SVs follows dimerization and tetramerization of synapsin mediated by its conserved domain C. The second hypothesis relies on creating a liquid phase that allows SVs to float within a synapsin droplet. Such formation of liquid condensate is mediated by the variable IDR domains at

the C-terminal end of the molecule [104]. It is hard to imagine that such process depends on the level of expression of these IDR domains and it should be mediated by posttranslational modifications, including phosphorylation. Interestingly, phosphorylation of synapsin-1 by CaMKII caused a disassembling of the liquid phase of synapsin [105]. In our present study, the phosphorylation of synapsin induced by a six-month morphine withdrawal occurred in phosphorylation sites in domains D and E, which are located in IDR domains at the C-terminal end of synapsin (Tables 2–5). Although these phosphorylation sites are of unknown functions and the protein kinase phosphorylating them is not known as well, they might be proposed as phosphorylation sites of CaMKII in the formation and disassembly of the liquid phase of synapsin.

The vesicle cluster near the active zone has been suggested to be the main source for many other proteins, including Rab3, complexin, synaptobrevin (Vamp2), amphiphysin (Bin1), Rim2 (similar to Rims1), bassoon, cortactin, and tubulin [106]. In our present study, many of these proteins or their isoforms were differentially phosphorylated or expressed (Tables 2–7). The vesicle cluster has been proposed to serve as a buffer for soluble accessory proteins involved in vesicle recycling and to ensure that the soluble recycling proteins are delivered upon demand during synaptic activity and thereby to support neurotransmission indirectly [106]. However, there is yet another possibile way the phosphorylation of synaptic proteins may be employed in the synaptic vesicle cycle. It might contribute to the interaction between vesicles and soluble proteins.

Some proteins from presynaptic and postsynaptic compartments engaged in cell adhesion, scaffolding, exocytosis and neurotransmitter transport may be implicated in several synaptopathies, causing neurological disorders [5]. Not only mutations and deletions in genes producing synaptic proteins, but also aberrant phosphorylation of proteins related to synaptic plasticity and cytoskeleton organization may play an important role in the pathogenesis of neurological diseases. One of the most studied phosphoprotein whose hyperphosphorylation is associated with the pathology of Alzheimer's disease is tau [6,83,84]. Tau hyperphosphorylation alters the ability of tau to stabilize microtubules and subsequently impairs axonal transport [6]. The stabilization of microtubules was shown to improve cognitive function and axonal transport [107,108]. The other neurotoxic effects of tau hyperphosphorylation in Alzheimer's disease include the impairment of long-term depression, NMDA receptor hypofunction, impaired neuronal hyperexcitability and reduced Fyn-induced Src family kinase activity [6]. In our study, tau was hypophosphorylated only in the cerebellum, but hyperphoshorylated in cortex, hippocampus and striatum. The greatest degree of hyperphosphorylation was detected in the hippocampus and most of the hyperphosphorylated phosphosites were located in proline-rich domains involving tubulin-binding site, the motif contributing to the regulation of tau interaction with microtubules and promoting microtubule polymerization [90], suggesting that hyperphosphorylation of tau in the hippocampus induced by long-term morphine withdrawal might affect the stabilization of microtubules associated with alterations in cognitive functions.

MAP1A, MAP1B, MAP2, collapsin response mediator proteins, α- and β-adducins, ankyrin 2, Akap12, Stxbp1, Marcks, and stathmin represent another group of differentially phosphorylated phosphoproteins whose aberrant phosphorylation is associated with neurological diseases [6]. Besides MAPs and collapsing response mediator proteins, stathmins possess microtubule-destabilizing activity, which is mediated by protein phosphorylation [109,110]. This suggests that alterations in microtubule stability can be one of the neuroadaptive mechanisms induced by long-term drug withdrawal which might be associated with changes in cognitive functions. A 30-day withdrawal from cocaine self-administration resulted in changes of Src kinase/Srcin1 signaling together with microtubule and actin remodeling followed by increased dendritic spine density and morphological restructuring of dendritic spines in NA [111]. Our results suggest the Src kinase/Srcin1 signaling as well as microtubule and actin dynamics are affected during morphine withdrawal also in the cortex, hippocampus and striatum by differential phosphorylation of Srcin1 and microtubule- and actin-associated proteins. Repeated morphine treatment elicits changes

in the density of dendrites and dendritic spines in the cortex and hippocampus [112–114], suggesting that Src kinase/Srcin1 signaling and microtubule/actin dynamics should be a common mechanism affecting the morphology of dendrites and dendritic spines during drug withdrawal. The morphology of dendrites and dendritic spines are also regulated by Rho and Ras family of GTPases [115], as well as by some regulators of GTPases such as SynGAP, ArhGEF7, ArhGAP35 [115,116]. Dendrites and dendritic spines have been recognized to be critical for synaptic plasticity related to cognitive processes such as learning and memory. Reward learning is encoded by dendritic spine changes from the first drug exposure to relapse even long into the withdrawal period [111].

Phosphoproteomic analysis revealed the phosphosite Ser331 in CaMKII whose phosphorylation was associated with inhibition of CaMKII activity and memory extinction in the amygdala from rats self-administered with cocaine for ten days [117]. In our study, the phosphosite Ser331 in CaMKII was hyperphoshorylated in the cortex after morphine withdrawal, suggesting memory extinction in cortex associated with opioid-related reward memories [118]. Because the consequences of morphine use are long-lasting, even many months after the cessation of drug administration, it is highly desirable to find novel strategies that could reverse cellular processes leading to drug relapse. Our results suggest that therapeutic agents affecting the phosphorylation state of synaptic proteins and improving the formation of the reserve pool and morphology of dendritic spines might be considered as potential candidates for restoring synaptic function and thus reversing drug seeking and relapse during protracted withdrawal.

## 5. Conclusions

Our results demonstrate for the first time that prolonged administration and subsequent discontinuation of morphine can cause diverse neuroadaptive changes in different regions of rat brain which are detectable even six months after cessation of drug intake. Distinct changes were observed in both protein expression and phosphorylation in the cortex, hippocampus, striatum, and cerebellum. In general, changes in protein phosphorylation were more prominent than those in protein expression. Alterations in protein expression and phosphorylation were found to be associated with synaptic plasticity and cytoskeleton organization. In all four brain regions, a six-month morphine withdrawal strongly affected the phosphorylation of proteins located in the active zone of the presynaptic nerve terminal, which is the site of synaptic vesicle exocytosis. Significant alterations were uncovered in the phosphorylation of proteins engaged in microtubule dynamics and stability, as well as in organization of the spectrin–actin network. The role of many phosphosites with altered phosphorylation is still unclear and needs to be elucidated. The observed changes of the phosphoproteomic profiles of different brain regions elicited by prolonged morphine withdrawal may likely affect cognitive functions. However, this assumption requires further investigation.

**Supplementary Materials:** The following are available online at https://www.mdpi.com/article/10.3390/life11070683/s1, Table S1: The enrichment analysis of differentially phosphorylated proteins in four regions of rat brain after a 6-month morphine withdrawal, Table S2: The enrichment analysis of differentially expressed proteins in four regions of rat brain after a 6-month morphine withdrawal, Table S3: A list of differentially phosphorylated proteins related to cytoskeleton, synaptic plasticity and regulation of small GTPase activity in four regions of rat brain, Table S4: A list of differentially expressed proteins related to cytoskeleton, synaptic plasticity and regulation of small GTPase activity in four regions of rat brain after.

**Author Contributions:** Conceptualization, J.N.; Methodology and Investigation, L.H. and Z.D., Data Analysis and Interpretation, Z.D.; Project Administration and Supervision, J.N. Writing—Original Draft, Z.D. and J.N.; Writing—Review and Editing, J.N., L.H. and R.M. All authors have read and agreed to the published version of the manuscript.

**Funding:** This study was supported by the Czech Science Foundation (no. 19-03295S), by the Charles University Institutional Research Fund (no. SVV-260571/2020), and by the project "BIOCEV–

Biotechnology and Biomedicine Centre of the Academy of Sciences and Charles University" (no. CZ.1.05/1.1.00/02.0109), funded from the European Regional Development Fund.

**Institutional Review Board Statement:** The study was conducted according to the guidelines of the Declaration of Helsinki and approved by the Animal Ethics Committee of the Faculty of Science, Charles University (Prague, Czech Republic), and by the Ministry of Education, Youth and Sports of the Czech Republic (licence no. MSMT-1479/2019–6).

**Data Availability Statement:** Data is contained within the article.

**Acknowledgments:** We thank Karel Harant and Pavel Talacko from the Laboratory of Mass Spectrometry, Biocev, Charles University, Faculty of Science for performing LC/MS analysis.

**Conflicts of Interest:** The authors declare no conflict of interest.

## References

1. Listos, J.; Lupina, M.; Talarek, S.; Mazur, A.; Orzelska-Gorka, J.; Kotlinska, J. The Mechanisms Involved in Morphine Addiction: An Overview. *Int. J. Mol. Sci.* **2019**, *20*, 4302. [CrossRef]
2. Meye, F.J.; Trusel, M.; Soiza-Reilly, M.; Mameli, M. Neural circuit adaptations during drug withdrawal—Spotlight on the lateral habenula. *Pharmacol. Biochem. Behav.* **2017**, *162*, 87–93. [CrossRef]
3. Volkow, N.D.; Koob, G.F.; McLellan, A.T. Neurobiologic Advances from the Brain Disease Model of Addiction. *N. Engl. J. Med.* **2016**, *374*, 363–371. [CrossRef]
4. Gipson, C.D.; Kupchik, Y.M.; Kalivas, P.W. Rapid, transient synaptic plasticity in addiction. *Neuropharmacology* **2014**, *76 Pt B*, 276–286. [CrossRef]
5. Torres, V.I.; Vallejo, D.; Inestrosa, N.C. Emerging Synaptic Molecules as Candidates in the Etiology of Neurological Disorders. *Neural. Plast.* **2017**, *2017*, 8081758. [CrossRef] [PubMed]
6. Perluigi, M.; Barone, E.; Di Domenico, F.; Butterfield, D.A. Aberrant protein phosphorylation in Alzheimer disease brain disturbs pro-survival and cell death pathways. *Biochim. Biophys. Acta Mol. Cell Res.* **2016**, *1862*, 1871–1882. [CrossRef] [PubMed]
7. Tenreiro, S.; Eckermann, K.; Outeiro, T.F. Protein phosphorylation in neurodegeneration: Friend or foe? *Front. Mol. Neurosci.* **2014**, *7*, 42. [CrossRef] [PubMed]
8. Brown, A.L.; Flynn, J.R.; Smith, D.W.; Dayas, C.V. Down-regulated striatal gene expression for synaptic plasticity-associated proteins in addiction and relapse vulnerable animals. *Int. J. Neuropsychopharmacol.* **2011**, *14*, 1099–1110. [CrossRef] [PubMed]
9. Kruyer, A.; Chioma, V.C.; Kalivas, P.W. The Opioid-Addicted Tetrapartite Synapse. *Biol. Psychiatry* **2020**, *87*, 34–43. [CrossRef]
10. Areal, L.B.; Hamilton, A.; Martins-Silva, C.; Pires, R.G.W.; Ferguson, S.S.G. Neuronal scaffolding protein spinophilin is integral for cocaine-induced behavioral sensitization and ERK1/2 activation. *Mol. Brain* **2019**, *12*, 15. [CrossRef]
11. Burns, J.A.; Kroll, D.S.; Feldman, D.E.; Kure Liu, C.; Manza, P.; Wiers, C.E.; Volkow, N.D.; Wang, G.J. Molecular Imaging of Opioid and Dopamine Systems: Insights Into the Pharmacogenetics of Opioid Use Disorders. *Front. Psychiatry* **2019**, *10*, 626. [CrossRef]
12. Miquel, M.; Vazquez-Sanroman, D.; Carbo-Gas, M.; Gil-Miravet, I.; Sanchis-Segura, C.; Carulli, D.; Manzo, J.; Coria-Avila, G.A. Have we been ignoring the elephant in the room? Seven arguments for considering the cerebellum as part of addiction circuitry. *Neurosci. Biobehav. Rev.* **2016**, *60*, 1–11. [CrossRef]
13. Koob, G.F.; Volkow, N.D. Neurobiology of addiction: A neurocircuitry analysis. *Lancet Psychiat.* **2016**, *3*, 760–773. [CrossRef]
14. Han, H.; Dong, Z.; Jia, Y.; Mao, R.; Zhou, Q.; Yang, Y.; Wang, L.; Xu, L.; Cao, J. Opioid addiction and withdrawal differentially drive long-term depression of inhibitory synaptic transmission in the hippocampus. *Sci. Rep.* **2015**, *5*, 9666. [CrossRef]
15. Gould, T.J. Addiction and cognition. *Addict. Sci. Clin. Pract.* **2010**, *5*, 4–14.
16. Chen, J.C.; Smith, E.R.; Cahill, M.; Cohen, R.; Fishman, J.B. The opioid receptor binding of dezocine, morphine, fentanyl, butorphanol and nalbuphine. *Life Sci.* **1993**, *52*, 389–396. [CrossRef]
17. Buzas, B.; Cox, B.M. Quantitative analysis of mu and delta opioid receptor gene expression in rat brain and peripheral ganglia using competitive polymerase chain reaction. *Neuroscience* **1997**, *76*, 479–489. [CrossRef]
18. Mansour, A.; Fox, C.A.; Akil, H.; Watson, S.J. Opioid-receptor mRNA expression in the rat CNS: Anatomical and functional implications. *Trends Neurosci.* **1995**, *18*, 22–29. [CrossRef]
19. Mrkusich, E.M.; Kivell, B.M.; Miller, J.H.; Day, D.J. Abundant expression of mu and delta opioid receptor mRNA and protein in the cerebellum of the fetal, neonatal, and adult rat. *Dev. Brain Res.* **2004**, *148*, 213–222. [CrossRef]
20. Herraez-Baranda, L.A.; Carretero, J.; Gonzalez-Sarmiento, R.; Rodriguez, R.E. Kappa opioid receptor is expressed in the rat cerebellar cortex. *Cell Tissue Res.* **2005**, *320*, 223–228. [CrossRef]
21. Bekheet, S.H.; Saker, S.A.; Abdel-Kader, A.M.; Younis, A.E. Histopathological and biochemical changes of morphine sulphate administration on the cerebellum of albino rats. *Tissue Cell* **2010**, *42*, 165–175. [CrossRef]
22. Rothenfluh, A.; Cowan, C.W. Emerging roles of actin cytoskeleton regulating enzymes in drug addiction: Actin or reactin'? *Curr. Opin. Neurobiol.* **2013**, *23*, 507–512. [CrossRef] [PubMed]
23. Dent, E.W. Dynamic microtubules at the synapse. *Curr. Opin. Neurobiol.* **2020**, *63*, 9–14. [CrossRef]
24. Lasser, M.; Tiber, J.; Lowery, L.A. The Role of the Microtubule Cytoskeleton in Neurodevelopmental Disorders. *Front. Cell. Neurosci.* **2018**, *12*, 165. [CrossRef]

25. Bucher, M.; Fanutza, T.; Mikhaylova, M. Cytoskeletal makeup of the synapse: Shaft versus spine. *Cytoskeleton* **2020**, *77*, 55–64. [CrossRef]
26. Ramkumar, A.; Jong, B.Y.; Ori-McKenney, K.M. ReMAPping the microtubule landscape: How phosphorylation dictates the activities of microtubule-associated proteins. *Dev. Dyn.* **2018**, *247*, 138–155. [CrossRef] [PubMed]
27. Craddock, T.J.A.; Tuszynski, J.A.; Hameroff, S. Cytoskeletal Signaling: Is Memory Encoded in Microtubule Lattices by CaMKII Phosphorylation? *PLoS Comput. Biol.* **2012**, *8*, e1002421. [CrossRef]
28. Bodaleo, F.J.; Gonzalez-Billault, C. The Presynaptic Microtubule Cytoskeleton in Physiological and Pathological Conditions: Lessons from Drosophila Fragile X Syndrome and Hereditary Spastic Paraplegias. *Front. Mol. Neurosci.* **2016**, *9*, 60. [CrossRef]
29. DeBonis, S.; Neumann, E.; Skoufias, D.A. Self protein-protein interactions are involved in TPPP/p25 mediated microtubule bundling. *Sci. Rep.* **2015**, *5*, 13242. [CrossRef] [PubMed]
30. Nouar, R.; Breuzard, G.; Bastonero, S.; Gorokhova, S.; Barbier, P.; Devred, F.; Kovacic, H.; Peyrot, V. Direct evidence for the interaction of stathmin along the length and the plus end of microtubules in cells. *Faseb J.* **2016**, *30*, 3202–3215. [CrossRef]
31. Bakota, L.; Ussif, A.; Jeserich, G.; Brandt, R. Systemic and network functions of the microtubule-associated protein tau: Implications for tau-based therapies. *Mol. Cell. Neurosci.* **2017**, *84*, 132–141. [CrossRef]
32. Robinson, T.E.; Kolb, B. Morphine alters the structure of neurons in the nucleus accumbens and neocortex of rats. *Synapse* **1999**, *33*, 160–162. [CrossRef]
33. Marie-Claire, C.; Courtin, C.; Roques, B.P.; Noble, F. Cytoskeletal genes regulation by chronic morphine treatment in rat striatum. *Neuropsychopharmacology* **2004**, *29*, 2208–2215. [CrossRef]
34. Qu, L.; Pan, C.; He, S.M.; Lang, B.; Gao, G.D.; Wang, X.L.; Wang, Y. The Ras Superfamily of Small GTPases in Non-neoplastic Cerebral Diseases. *Front. Mol. Neurosci.* **2019**, *12*, 121. [CrossRef] [PubMed]
35. Kjos, I.; Vestre, K.; Guadagno, N.A.; Distefano, M.B.; Progida, C. Rab and Arf proteins at the crossroad between membrane transport and cytoskeleton dynamics. *Biochim. Biophys. Acta Mol. Cell Res.* **2018**, *1865*, 1397–1409. [CrossRef]
36. Schoneborn, H.; Raudzus, F.; Coppey, M.; Neumann, S.; Heumann, R. Perspectives of RAS and RHEB GTPase Signaling Pathways in Regenerating Brain Neurons. *Int. J. Mol. Sci.* **2018**, *19*, 4052. [CrossRef] [PubMed]
37. Song, S.; Cong, W.; Zhou, S.; Shi, Y.; Dai, W.; Zhang, H.; Wang, X.; He, B.; Zhang, Q. Small GTPases: Structure, biological function and its interaction with nanoparticles. *Asian. J. Pharm. Sci.* **2019**, *14*, 30–39. [CrossRef]
38. Ba, W.; Nadif Kasri, N. RhoGTPases at the synapse: An embarrassment of choice. *Small GTPases* **2017**, *8*, 106–113. [CrossRef]
39. Mishra, A.K.; Lambright, D.G. Small GTPases and Their GAPs. *Biopolymers* **2016**, *105*, 431–448. [CrossRef]
40. Shirakawa, R.; Horiuchi, H. Ral GTPases: Crucial mediators of exocytosis and tumourigenesis. *J. Biochem.* **2015**, *157*, 285–299. [CrossRef] [PubMed]
41. Patel, M.; Karginov, A.V. Phosphorylation-mediated regulation of GEFs for RhoA. *Cell Adh. Migr.* **2014**, *8*, 11–18. [CrossRef] [PubMed]
42. Walkup, W.G.; Washburn, L.; Sweredoski, M.J.; Carlisle, H.J.; Graham, R.L.; Hess, S.; Kennedy, M.B. Phosphorylation of Synaptic GTPase-activating Protein (synGAP) by Ca2+/Calmodulin-dependent Protein Kinase II (CaMKII) and Cyclin-dependent Kinase 5 (CDK5) Alters the Ratio of Its GAP Activity toward Ras and Rap GTPases. *J. Biol. Chem.* **2015**, *290*, 4908–4927. [CrossRef] [PubMed]
43. Heraud, C.; Pinault, M.; Lagree, V.; Moreau, V. p190RhoGAPs, the ARHGAP35- and ARHGAP5-Encoded Proteins, in Health and Disease. *Cells* **2019**, *8*, 351. [CrossRef] [PubMed]
44. Kim, W.Y.; Shin, S.R.; Kim, S.; Jeon, S.; Kim, J.H. Cocaine regulates ezrin-radixin-moesin proteins and RhoA signaling in the nucleus accumbens. *Neuroscience* **2009**, *163*, 501–505. [CrossRef] [PubMed]
45. Bourova, L.; Vosahlikova, M.; Kagan, D.; Dlouha, K.; Novotny, J.; Svoboda, P. Long-term adaptation to high doses of morphine causes desensitization of mu-OR- and delta-OR-stimulated G-protein response in forebrain cortex but does not decrease the amount of G-protein alpha subunits. *Med. Sci. Monit.* **2010**, *16*, BR260–BR270.
46. Ujcikova, H.; Hejnova, L.; Eckhardt, A.; Roubalova, L.; Novotny, J.; Svoboda, P. Impact of three-month morphine withdrawal on rat brain cortex, hippocampus, striatum and cerebellum: Proteomic and phosphoproteomic studies. *Neurochem. Int.* **2021**, *144*, 104975. [CrossRef]
47. Humphrey, S.J.; Karayel, O.; James, D.E.; Mann, M. High-throughput and high-sensitivity phosphoproteomics with the EasyPhos platform. *Nat. Protoc.* **2018**, *13*, 1897–1916. [CrossRef]
48. Cox, J.; Mann, M. MaxQuant enables high peptide identification rates, individualized p.p.b.-range mass accuracies and proteome-wide protein quantification. *Nat. Biotechnol.* **2008**, *26*, 1367–1372. [CrossRef]
49. Cox, J.; Hein, M.Y.; Luber, C.A.; Paron, I.; Nagaraj, N.; Mann, M. Accurate Proteome-wide Label-free Quantification by Delayed Normalization and Maximal Peptide Ratio Extraction, Termed MaxLFQ. *Mol. Cell. Proteomics* **2014**, *13*, 2513–2526. [CrossRef]
50. Tyanova, S.; Temu, T.; Sinitcyn, P.; Carlson, A.; Hein, M.Y.; Geiger, T.; Mann, M.; Cox, J. The Perseus computational platform for comprehensive analysis of (prote)omics data. *Nat. Methods* **2016**, *13*, 731–740. [CrossRef]
51. Collins, M.O.; Yu, L.; Coba, M.P.; Husi, H.; Campuzano, I.; Blackstock, W.P.; Choudhary, J.S.; Grant, S.G. Proteomic analysis of in vivo phosphorylated synaptic proteins. *J. Biol. Chem.* **2005**, *280*, 5972–5982. [CrossRef]
52. Loscher, W.; Gillard, M.; Sands, Z.A.; Kaminski, R.M.; Klitgaard, H. Synaptic Vesicle Glycoprotein 2A Ligands in the Treatment of Epilepsy and Beyond. *CNS Drugs* **2016**, *30*, 1055–1077. [CrossRef] [PubMed]

53. Yao, J.; Nowack, A.; Kensel-Hammes, P.; Gardner, R.G.; Bajjalieh, S.M. Cotrafficking of SV2 and Synaptotagmin at the Synapse. *J. Neurosci.* **2010**, *30*, 5569–5578. [CrossRef]
54. Engholm-Keller, K.; Waardenberg, A.J.; Muller, J.A.; Wark, J.R.; Fernando, R.N.; Arthur, J.W.; Robinson, P.J.; Dietrich, D.; Schoch, S.; Graham, M.E. The temporal profile of activity-dependent presynaptic phospho-signalling reveals long-lasting patterns of poststimulus regulation. *PLoS Biol.* **2019**, *17*, e3000170. [CrossRef] [PubMed]
55. Binotti, B.; Jahn, R.; Chua, J.J.E. Functions of Rab Proteins at Presynaptic Sites. *Cells* **2016**, *5*, 7. [CrossRef] [PubMed]
56. Boda, B.; Dubos, A.; Muller, D. Signaling mechanisms regulating synapse formation and function in mental retardation. *Curr. Opin. Neurobiol.* **2010**, *20*, 519–527. [CrossRef]
57. Gerber, K.J.; Squires, K.E.; Hepler, J.R. Roles for Regulator of G Protein Signaling Proteins in Synaptic Signaling and Plasticity. *Mol. Pharmacol.* **2016**, *89*, 273–286. [CrossRef]
58. Mignogna, M.L.; D'Adamo, P. Critical importance of RAB proteins for synaptic function. *Small GTPases* **2018**, *9*, 145–157. [CrossRef]
59. Stornetta, R.L.; Zhu, J.J. Ras and Rap signaling in synaptic plasticity and mental disorders. *Neuroscientist* **2011**, *17*, 54–78. [CrossRef]
60. Shen, W.; Wu, B.; Zhang, Z.; Dou, Y.; Rao, Z.R.; Chen, Y.R.; Duan, S. Activity-induced rapid synaptic maturation mediated by presynaptic cdc42 signaling. *Neuron* **2006**, *50*, 401–414. [CrossRef] [PubMed]
61. Halbedl, S.; Schoen, M.; Feiler, M.S.; Boeckers, T.M.; Schmeisser, M.J. Shank3 is localized in axons and presynaptic specializations of developing hippocampal neurons and involved in the modulation of NMDA receptor levels at axon terminals. *J. Neurochem.* **2016**, *137*, 26–32. [CrossRef]
62. Vyas, Y.; Montgomery, J.M. The role of postsynaptic density proteins in neural degeneration and regeneration. *Neural Regen. Res.* **2016**, *11*, 906–907. [CrossRef]
63. Brigidi, G.S.; Bamji, S.X. Cadherin-catenin adhesion complexes at the synapse. *Curr. Opin. Neurobiol.* **2011**, *21*, 208–214. [CrossRef] [PubMed]
64. Pozzi, D.; Menna, E.; Canzi, A.; Desiato, G.; Mantovani, C.; Matteoli, M. The Communication Between the Immune and Nervous Systems: The Role of IL-1 beta in Synaptopathies. *Front. Mol. Neurosci.* **2018**, *11*, 111. [CrossRef]
65. Park, E.; Na, M.; Choi, J.H.; Kim, S.; Lee, J.R.; Yoon, J.Y.; Park, D.; Sheng, M.; Kim, E. The Shank family of postsynaptic density proteins interacts with and promotes synaptic accumulation of the beta PIX guanine nucleotide exchange factor for Rac1 and Cdc42. *J. Biol. Chem.* **2003**, *278*, 19220–19229. [CrossRef] [PubMed]
66. Soisson, S.M.; Nimnual, A.S.; Uy, M.; Bar-Sagi, D.; Kuriyan, J. Crystal structure of the Dbl and pleckstrin homology domains from the human Son of sevenless protein. *Cell* **1998**, *95*, 259–268. [CrossRef]
67. Sarowar, T.; Grabrucker, A.M. Actin-Dependent Alterations of Dendritic Spine Morphology in Shankopathies. *Neural Plast.* **2016**, *2016*, 8051861. [CrossRef] [PubMed]
68. Unsain, N.; Stefani, F.D.; Caceres, A. The Actin/Spectrin Membrane-Associated Periodic Skeleton in Neurons. *Front. Synaptic. Neurosci.* **2018**, *10*, 10. [CrossRef]
69. Li, Y.C.; Kavalali, E.T. Synaptic Vesicle-Recycling Machinery Components as Potential Therapeutic Targets. *Pharmacol. Rev.* **2017**, *69*, 141–160. [CrossRef]
70. Mishima, T.; Fujiwara, T.; Sanada, M.; Kofuji, T.; Kanai-Azuma, M.; Akagawa, K. Syntaxin 1B, but not syntaxin 1A, is necessary for the regulation of synaptic vesicle exocytosis and of the readily releasable pool at central synapses. *PLoS ONE* **2014**, *9*, e90004. [CrossRef]
71. Wong, M.Y.; Liu, C.; Wang, S.S.H.; Roquas, A.C.F.; Fowler, S.C.; Kaeser, P.S. Liprin-alpha3 controls vesicle docking and exocytosis at the active zone of hippocampal synapses. *Proc. Natl. Acad. Sci. USA* **2018**, *115*, 2234–2239. [CrossRef]
72. Spence, E.F.; Soderling, S.H. Actin Out: Regulation of the Synaptic Cytoskeleton. *J. Biol. Chem.* **2015**, *290*, 28613–28622. [CrossRef]
73. Tolias, K.F.; Duman, J.G.; Um, K. Control of synapse development and plasticity by Rho GTPase regulatory proteins. *Prog. Neurobiol.* **2011**, *94*, 133–148. [CrossRef]
74. Hlavanda, E.; Klement, E.; Kokai, E.; Kovacs, J.; Vincze, O.; Tokesi, N.; Orosz, F.; Medzihradszky, K.F.; Dombradi, V.; Ovadi, J. Phosphorylation blocks the activity of tubulin polymerization-promoting protein (TPPP): Identification of sites targeted by different kinases. *J. Biol. Chem.* **2007**, *282*, 29531–29539. [CrossRef] [PubMed]
75. Hensley, K.; Kursula, P. Collapsin Response Mediator Protein-2 (CRMP2) is a Plausible Etiological Factor and Potential Therapeutic Target in Alzheimer's Disease: Comparison and Contrast with Microtubule-Associated Protein Tau. *J. Alzheimers Dis.* **2016**, *53*, 1–14. [CrossRef] [PubMed]
76. Lin, P.C.; Chan, P.M.; Hall, C.; Manser, E. Collapsin Response Mediator Proteins (CRMPs) Are a New Class of Microtubule-associated Protein (MAP) That Selectively Interacts with Assembled Microtubules via a Taxol-sensitive Binding Interaction. *J. Biol. Chem.* **2011**, *286*, 41466–41478. [CrossRef]
77. Scales, T.M.E.; Lin, S.; Kraus, M.; Goold, R.G.; Gordon-Weeks, P.R. Nonprimed and DYRK1A-primed GSK3 beta-phosphorylation sites on MAP1B regulate microtubule dynamics in growing axons. *J. Cell Sci.* **2009**, *122*, 2424–2435. [CrossRef]
78. Villarroel-Campos, D.; Gonzalez-Billault, C. The MAP1B Case: An Old MAP That is New Again. *Dev. Neurobiol.* **2014**, *74*, 953–971. [CrossRef]
79. Grubisha, M.J.; Sun, X.; MacDonald, M.L.; Garver, M.; Sun, Z.; Paris, K.A.; Patel, D.S.; DeGiosio, R.A.; Lewis, D.A.; Yates, N.A.; et al. MAP2 is differentially phosphorylated in schizophrenia, altering its function. *Mol. Psychiatry* **2021**. [CrossRef]

80. Stock, M.F.; Chu, J.; Hackney, D.D. The kinesin family member BimC contains a second microtubule binding region attached to the N terminus of the motor domain. *J. Biol. Chem.* **2003**, *278*, 52315–52322. [CrossRef] [PubMed]
81. Illenberger, S.; Drewes, G.; Trinczek, B.; Biernat, J.; Meyer, H.E.; Olmsted, J.B.; Mandelkow, E.M.; Mandelkow, E. Phosphorylation of microtubule-associated proteins MAP2 and MAP4 by the protein kinase p110(mark)—Phosphorylation sites and regulation of microtubule dynamics. *J. Biol. Chem.* **1996**, *271*, 10834–10843. [CrossRef]
82. Kimura, T.; Sharma, G.; Ishiguro, K.; Hisanaga, S. Phospho-Tau Bar Code: Analysis of Phosphoisotypes of Tau and Its Application to Tauopathy. *Front. Neurosci.* **2018**, *12*, 44. [CrossRef] [PubMed]
83. Simic, G.; Babic Leko, M.; Wray, S.; Harrington, C.; Delalle, I.; Jovanov-Milosevic, N.; Bazadona, D.; Buee, L.; de Silva, R.; Di Giovanni, G.; et al. Tau Protein Hyperphosphorylation and Aggregation in Alzheimer's Disease and Other Tauopathies, and Possible Neuroprotective Strategies. *Biomolecules* **2016**, *6*, 6. [CrossRef]
84. Duka, V.; Lee, J.H.; Credle, J.; Wills, J.; Oaks, A.; Smolinsky, C.; Shah, K.; Mash, D.C.; Masliah, E.; Sidhu, A. Identification of the sites of tau hyperphosphorylation and activation of tau kinases in synucleinopathies and Alzheimer's diseases. *PLoS ONE* **2013**, *8*, e75025. [CrossRef]
85. He, H.J.; Wang, X.S.; Pan, R.; Wang, D.L.; Liu, M.N.; He, R.Q. The proline-rich domain of tau plays a role in interactions with actin. *BMC Cell Biol.* **2009**, *10*, 81. [CrossRef] [PubMed]
86. McKibben, K.M.; Rhoades, E. Independent tubulin binding and polymerization by the proline-rich region of tau is regulated by tau's N-terminal domain. *J. Biol. Chem.* **2019**, *294*, 19381–19394. [CrossRef] [PubMed]
87. Abraha, A.; Ghoshal, N.; Gamblin, T.C.; Cryns, V.; Berry, R.W.; Kuret, J.; Binder, L.I. C-terminal inhibition of tau assembly in vitro and in Alzheimer's disease. *J. Cell Sci.* **2000**, *113 Pt 21*, 3737–3745. [CrossRef]
88. Gundelfinger, E.D.; Reissner, C.; Garner, C.C. Role of Bassoon and Piccolo in Assembly and Molecular Organization of the Active Zone. *Front. Synaptic. Neurosci.* **2015**, *7*, 19. [CrossRef] [PubMed]
89. Griffith, L.C. Regulation of calcium/calmodulin-dependent protein kinase II activation by intramolecular and intermolecular interactions. *J. Neurosci.* **2004**, *24*, 8394–8398. [CrossRef] [PubMed]
90. Melkova, K.; Zapletal, V.; Narasimhan, S.; Jansen, S.; Hritz, J.; Skrabana, R.; Zweckstetter, M.; Ringkjobing Jensen, M.; Blackledge, M.; Zidek, L. Structure and Functions of Microtubule Associated Proteins Tau and MAP2c: Similarities and Differences. *Biomolecules* **2019**, *9*, 105. [CrossRef]
91. Shimada, T.; Fournier, A.E.; Yamagata, K. Neuroprotective function of 14-3-3 proteins in neurodegeneration. *Biomed. Res. Int.* **2013**, *2013*, 564534. [CrossRef]
92. Ovadi, J.; Orosz, F. An unstructured protein with destructive potential: TPPP/p25 in neurodegeneration. *Bioessays* **2009**, *31*, 676–686. [CrossRef] [PubMed]
93. Schofield, A.V.; Steel, R.; Bernard, O. Rho-associated Coiled-coil Kinase (ROCK) Protein Controls Microtubule Dynamics in a Novel Signaling Pathway That Regulates Cell Migration. *J. Biol. Chem.* **2012**, *287*, 43620–43629. [CrossRef] [PubMed]
94. Sudhof, T.C.; Czernik, A.J.; Kao, H.T.; Takei, K.; Johnston, P.A.; Horiuchi, A.; Kanazir, S.D.; Wagner, M.A.; Perin, M.S.; De Camilli, P.; et al. Synapsins: Mosaics of shared and individual domains in a family of synaptic vesicle phosphoproteins. *Science* **1989**, *245*, 1474–1480. [CrossRef] [PubMed]
95. Barbier, P.; Zejneli, O.; Martinho, M.; Lasorsa, A.; Belle, V.; Smet-Nocca, C.; Tsvetkov, P.O.; Devred, F.; Landrieu, I. Role of Tau as a Microtubule-Associated Protein: Structural and Functional Aspects. *Front. Aging Neurosci.* **2019**, *11*, 204. [CrossRef]
96. Webb, D.J.; Mayhew, M.W.; Kovalenko, M.; Schroeder, M.J.; Jeffery, E.D.; Whitmore, L.; Shabanowitz, J.; Hunt, D.F.; Horwitz, A.F. Identification of phosphorylation sites in GIT1. *J. Cell Sci.* **2006**, *119*, 2847–2850. [CrossRef]
97. Tokesi, N.; Lehotzky, A.; Horvath, I.; Szabo, B.; Olah, J.; Lau, P.; Ovadi, J. TPPP/p25 promotes tubulin acetylation by inhibiting histone deacetylase 6. *J. Biol. Chem.* **2010**, *285*, 17896–17906. [CrossRef]
98. Nakamura, F.; Ohshima, T.; Goshima, Y. Collapsin Response Mediator Proteins: Their Biological Functions and Pathophysiology in Neuronal Development and Regeneration. *Front. Cell. Neurosci.* **2020**, *14*, 188. [CrossRef]
99. Le Merrer, J.; Befort, K.; Gardon, O.; Filliol, D.; Darcq, E.; Dembele, D.; Becker, J.A.J.; Kieffer, B.L. Protracted abstinence from distinct drugs of abuse shows regulation of a common gene network. *Addict. Biol.* **2012**, *17*, 1–12. [CrossRef]
100. Goeldner, C.; Lutz, P.E.; Darcq, E.; Halter, T.; Clesse, D.; Ouagazzal, A.M.; Kieffer, B.L. Impaired emotional-like behavior and serotonergic function during protracted abstinence from chronic morphine. *Biol. Psychiatry* **2011**, *69*, 236–244. [CrossRef]
101. Lull, M.E.; Erwin, M.S.; Morgan, D.; Roberts, D.C.S.; Vrana, K.E.; Freeman, W.M. Persistent proteomic alterations in the medial prefrontal cortex with abstinence from cocaine self-administration. *Proteomics Clin. Appl.* **2009**, *3*, 462–472. [CrossRef]
102. Sun, W.L.; Eisenstein, S.A.; Zelek-Molik, A.; McGinty, J.F. A Single Brain-Derived Neurotrophic Factor Infusion into the Dorsomedial Prefrontal Cortex Attenuates Cocaine Self-Administration-Induced Phosphorylation of Synapsin in the Nucleus Accumbens during Early Withdrawal. *Int. J. Neuropsychopharmacol.* **2015**, *18*, pyu049. [CrossRef] [PubMed]
103. Jackson, K.J.; Imad Damaj, M. Beta2-containing nicotinic acetylcholine receptors mediate calcium/calmodulin-dependent protein kinase-II and synapsin I protein levels in the nucleus accumbens after nicotine withdrawal in mice. *Eur. J. Pharmacol.* **2013**, *701*, 1–6. [CrossRef] [PubMed]
104. Zhang, M.; Augustine, G.J. Synapsins and the Synaptic Vesicle Reserve Pool: Floats or Anchors? *Cells* **2021**, *10*, 658. [CrossRef]
105. Milovanovic, D.; Wu, Y.; Bian, X.; De Camilli, P. A liquid phase of synapsin and lipid vesicles. *Science* **2018**, *361*, 604–607. [CrossRef]

106. Denker, A.; Krohnert, K.; Buckers, J.; Neher, E.; Rizzoli, S.O. The reserve pool of synaptic vesicles acts as a buffer for proteins involved in synaptic vesicle recycling. *Proc. Natl. Acad. Sci. USA* **2011**, *108*, 17183–17188. [CrossRef] [PubMed]
107. Guo, B.; Huang, Y.; Gao, Q.; Zhou, Q. Stabilization of microtubules improves cognitive functions and axonal transport of mitochondria in Alzheimer's disease model mice. *Neurobiol. Aging* **2020**, *96*, 223–232. [CrossRef]
108. Fernandez-Valenzuela, J.J.; Sanchez-Varo, R.; Munoz-Castro, C.; De Castro, V.; Sanchez-Mejias, E.; Navarro, V.; Jimenez, S.; Nunez-Diaz, C.; Gomez-Arboledas, A.; Moreno-Gonzalez, I.; et al. Enhancing microtubule stabilization rescues cognitive deficits and ameliorates pathological phenotype in an amyloidogenic Alzheimer's disease model. *Sci. Rep.* **2020**, *10*, 14776. [CrossRef]
109. Goodson, H.V.; Jonasson, E.M. Microtubules and Microtubule-Associated Proteins. *Cold Spring Harb. Perspect. Biol.* **2018**, *10*, a022608. [CrossRef]
110. Uchida, S.; Martel, G.; Pavlowsky, A.; Takizawa, S.; Hevi, C.; Watanabe, Y.; Kandel, E.R.; Alarcon, J.M.; Shumyatsky, G.P. Learning-induced and stathmin-dependent changes in microtubule stability are critical for memory and disrupted in ageing. *Nat. Commun.* **2014**, *5*, 4389. [CrossRef] [PubMed]
111. Calipari, E.S.; Godino, A.; Salery, M.; Damez-Werno, D.M.; Cahill, M.E.; Werner, C.T.; Gancarz, A.M.; Peck, E.G.; Jlayer, Z.; Rabkin, J.; et al. Synaptic Microtubule-Associated Protein EB3 and SRC Phosphorylation Mediate Structural and Behavioral Adaptations During Withdrawal From Cocaine Self-Administration. *J. Neurosci.* **2019**, *39*, 5634–5646. [CrossRef] [PubMed]
112. Beltran-Campos, V.; Silva-Vera, M.; Garcia-Campos, M.L.; Diaz-Cintra, S. Effects of morphine on brain plasticity. *Neurologia* **2015**, *30*, 176–180. [CrossRef] [PubMed]
113. Miller, E.C.; Zhang, L.; Dummer, B.W.; Cariveau, D.R.; Loh, H.; Law, P.Y.; Liao, D. Differential modulation of drug-induced structural and functional plasticity of dendritic spines. *Mol. Pharmacol.* **2012**, *82*, 333–343. [CrossRef]
114. Russo, S.J.; Dietz, D.M.; Dumitriu, D.; Morrison, J.H.; Malenka, R.C.; Nestler, E.J. The addicted synapse: Mechanisms of synaptic and structural plasticity in nucleus accumbens. *Trends Neurosci.* **2010**, *33*, 267–276. [CrossRef] [PubMed]
115. Chidambaram, S.B.; Rathipriya, A.G.; Bolla, S.R.; Bhat, A.; Ray, B.; Mahalakshmi, A.M.; Manivasagam, T.; Thenmozhi, A.J.; Essa, M.M.; Guillemin, G.J.; et al. Dendritic spines: Revisiting the physiological role. *Prog. Neuropsychopharmacol. Biol. Psychiatry* **2019**, *92*, 161–193. [CrossRef]
116. Lee, S.; Zhang, H.Y.; Webb, D.J. Dendritic spine morphology and dynamics in health and disease. *Cell Health Cytoskelet.* **2015**, *7*, 121–131.
117. Rich, M.T.; Abbott, T.B.; Chung, L.; Gulcicek, E.E.; Stone, K.L.; Colangelo, C.M.; Lam, T.T.; Nairn, A.C.; Taylor, J.R.; Torregrossa, M.M. Phosphoproteomic Analysis Reveals a Novel Mechanism of CaMKIIalpha Regulation Inversely Induced by Cocaine Memory Extinction versus Reconsolidation. *J. Neurosci.* **2016**, *36*, 7613–7627. [CrossRef] [PubMed]
118. Sun, N.; Chi, N.; Lauzon, N.; Bishop, S.; Tan, H.; Laviolette, S.R. Acquisition, extinction, and recall of opiate reward memory are signaled by dynamic neuronal activity patterns in the prefrontal cortex. *Cereb. Cortex* **2011**, *21*, 2665–2680. [CrossRef] [PubMed]

life

MDPI

*Article*

# *Orthosiphon stamineus* Proteins Alleviate Hydrogen Peroxide Stress in SH-SY5Y Cells

**Yin-Sir Chung [1], Pervaiz Khalid Ahmed [2,3], Iekhsan Othman [1,4] and Mohd. Farooq Shaikh [1,3,*]**

[1] Neuropharmacology Research Laboratory, Jeffrey Cheah School of Medicine and Health Sciences, Monash University Malaysia, Bandar Sunway 47500, Malaysia; mymycys@gmail.com (Y.-S.C.); Iekhsan.Othman@monash.edu (I.O.)
[2] School of Business, Monash University Malaysia, Bandar Sunway 47500, Malaysia; pervaiz.ahmed@monash.edu
[3] Global Asia in the 21st Century (GA21), Monash University Malaysia, Bandar Sunway 47500, Malaysia
[4] Liquid Chromatography-Mass Spectrometry (LCMS) Platform, Jeffrey Cheah School of Medicine and Health Sciences, Monash University Malaysia, Bandar Sunway 47500, Malaysia
* Correspondence: farooq.shaikh@monash.edu

**Abstract:** The neuroprotective potential of *Orthosiphon stamineus* leaf proteins (OSLPs) has never been evaluated in SH-SY5Y cells challenged by hydrogen peroxide ($H_2O_2$). This work thus aims to elucidate OSLP neuroprotective potential in alleviating $H_2O_2$ stress. OSLPs at varying concentrations were evaluated for cytotoxicity (24 and 48 h) and neuroprotective potential in $H_2O_2$-induced SH-SY5Y cells (24 h). The protective mechanism of $H_2O_2$-induced SH-SY5Y cells was also explored via mass-spectrometry-based label-free quantitative proteomics (LFQ) and bioinformatics. OSLPs (25, 50, 125, 250, 500, and 1000 µg/mL; 24 and 48 h) were found to be safe. Pre-treatments with OSLP doses (250, 500, and 1000 µg/mL, 24 h) significantly increased the survival of SH-SY5Y cells in a concentration-dependent manner and improved cell architecture—pyramidal-shaped cells, reduced clumping and shrinkage, with apparent neurite formations. OSLP pre-treatment (1000 µg/mL, 24 h) lowered the expressions of two major heat shock proteins, HSPA8 (heat shock protein family A (Hsp70) member 8) and HSP90AA1 (heat shock protein 90), which promote cellular stress signaling under stress conditions. OSLP is, therefore, suggested to be anti-inflammatory by modulating the "signaling of interleukin-4 and interleukin-13" pathway as the predominant mechanism in addition to regulating the "attenuation phase" and "HSP90 chaperone cycle for steroid hormone receptors" pathways to counteract heat shock protein (HSP)-induced damage under stress conditions.

**Keywords:** *Orthosiphon stamineus*; plant-derived proteins; neuroprotective; SH-SY5Y cell model; hydrogen peroxide

**Citation:** Chung, Y.-S.; Ahmed, P.K.; Othman, I.; Shaikh, M.F. *Orthosiphon stamineus* Proteins Alleviate Hydrogen Peroxide Stress in SH-SY5Y Cells. *Life* **2021**, *11*, 585. https://doi.org/10.3390/life11060585

Academic Editors: Chiara Villa and Jong Hyuk Yoon

Received: 10 May 2021
Accepted: 17 June 2021
Published: 20 June 2021



## 1. Introduction

Worldwide, central nervous system (CNS) disorders remain one of the greatest threats in public health, and they account for a significant proportion of the global disease burden [1,2]. These disorders may involve a wide variety of mechanisms but share some common themes, including abnormal protein behavior, oxidative stress, mitochondrial dysfunction, excitotoxicity, ion imbalance, cellular inflammation, cytotoxicity, necrosis, apoptosis, and others [3–7].

Neuroprotection has been explored as a possible treatment strategy [6,8] that aims to prevent neuronal injury and loss of various brain functions with the ultimate goal of better preserving brain function [9].

*Orthosiphon stamineus* (OS) or *Orthosiphon aristatus var. aristatus* (OAA) is a medicinal plant belonging to the Lamiaceae family. Often, it is referred to as "cat's whiskers" or "misai kucing". A plethora of studies on the crude extracts or secondary metabolites of OS has shown protective effects, including antioxidative, anti-inflammatory, antiproliferative, cytotoxic, and antiangiogenic effects [10,11]. Added to that, OS has recently been

reported for its neuroprotective effects [12]. In another recent study, OS leaf proteins (OSLPs) alleviated pentylenetetrazol-induced seizures in adult zebrafish [13]. The protein compositions identified with important neuroprotective potential include rosmarinate synthase (transferase family), beta-myrcene synthase and R-linalool synthase (terpene synthase family), baicalein 7-O-glucuronosyltransferase (cytochrome P450 family), and baicalin-beta-D-glucuronidase (glycosyl hydrolase 79 family) [13].

Many biological processes are simultaneously active and coordinated in every living cell. Each of them contains synthesis, catalysis, and regulation functions, which are almost always performed by proteins organized in higher-order structures and networks. For decades, people have been using biochemical and biophysical methods to study the structure and function of selected proteins. However, the properties and behavior of the proteome as an integrated system remain largely elusive. Powerful technology based on mass spectrometry now allows the identification, quantification, and characterization of proteins in terms of the composition, structure, function, and control of the proteome, revealing complex biological processes and phenotypes. Proteomics has been described as an important method for obtaining biological information because most biological activities are attributed to proteins, thus improving our concept of biological systems. [14,15]. Proteomics allows us to visualize the highly dynamic cascades of events with peptide-level information, not limited to a static point, as we can see in the Reactome Database, wherein each reaction, interaction, and pathway that happens throughout a whole biological event is depicted with its proteomics details [16–18].

Human neuroblastoma cell line, SH-SY5Y, with a stable karyotype consisting of 47 chromosomes, is an in vitro model ideal for high-throughput studies on neurobiology [19]. The SH-SY5Y model provides an efficient platform that is essential for preliminary drug testing, protein functionality, and molecular mechanisms in neurological conditions [20]. Hydrogen peroxide ($H_2O_2$) insults have been prevalently reported in different neurological disorders, including neuroexcitation, neuroinflammation, and neurotoxicity, just to name a few [21–23]. This study was commenced to evaluate the neuroprotective potential of OSLPs in SH-SY5Y cells induced by $H_2O_2$.

## 2. Materials and Methods

### *2.1. Materials, Chemicals, and Apparatuses*

Human SH-SY5Y neuroblastoma cells (ATCC®CRL-2266TM) were purchased from the American Type Culture Collection (ATCC, Manassas, VA, USA). Fetal bovine serum (FBS) and penicillin–streptomycin mixture (Pen/Strep) were purchased from PAA Laboratories (Austria). Hemocytometer BLAUBRAND® Neubauer, Dulbecco's modified Eagle's medium (DMEM), 3-(4,5-methylthiazol-2-yl)-2,5-diphenyl-tetrazolium bromide (MTT), complete EDTA-free protease inhibitors, phosphatase inhibitors cocktail 2, hydrogen peroxide ($H_2O_2$), TRIS hydrochloride (TRIS-HCl), dithiothreitol (DTT), iodoacetamide (IAA), HPLC-grade methanol (MeOH), ammonium bicarbonate (ABC), trifluoroethanol (TFE), formic acid (FA), and 2,3,5-triphenyltetrazolium chloride (TTC) were purchased from Sigma-Aldrich (St. Louis, MO, USA). Trypsin/Lys-C Mix (Promega, USA), T-25 flasks (Corning Inc., Tewksbury, MA, USA), 15 mL Falcon tubes (BD Biosciences, Billerica, MA, USA), TrypLE™ Express (Life Technologies, Nærum, Denmark), and phosphate-buffered saline solution (10XPBS) (Abcam, Hangzhou, China) were also purchased. Pierce® trypsin protease, mass spec grade Pierce® radioimmunoprecipitation assay (RIPA) buffer as well as Pierce®C18 mini spin columns were purchased from Thermo Scientific Pierce (Waltham, MA, USA). Protein LoBind microcentrifuge tubes were purchased from Eppendorf (Framingham, MA, USA), a Quick Start™ Bradford Protein Assay Kit from Bio-Rad (Irvine, CA, USA), trifluoroacetic acid (TFA), acetonitrile (ACN), and mass-spec grade CHAPS (Nacailai Tesque, Kyoto, Japan) were all purchased from Sigma-Aldrich (St. Louis, MO, USA). Milli-Q ultrapure water (MQUP) was from Millipore GmbH (Germany); dimethylsulfoxide (DMSO) and 37% formaldehyde solution were purchased from Friendemann Schmidt Chemical (Parkwood, WA, Australia). Refrigerated centrifuge 5415R from Eppendorf AG

(Hamburg, Germany), hydrochloric acid (36%) from Ajax Chemical (Australia), and acetic acid (glacial, 100%) from Merck (Darmstadt, Germany) were also purchased. Purified nitrogen gas (99.999%) was supplied by Merck (Darmstadt, Germany) Iwatani Malaysia S/B, and liquid nitrogen ($LN_2$) was purchased from Linde Malaysia. An ultrasonic cell crusher (JY88-II N, Shanghai, China), an Eyela SpeedVac Vacuum Concentrator (Thermo Scientific Pierce, Waltham, MA, USA), a precision incubator (Memmert INB200, Schwabach, Germany), and a Cole-Parmer™ Stuart™ Orbital Shaker (Thermo Scientific Pierce, Waltham, MA, USA) were also purchased. All the other chemicals used were of analytical grade.

### *2.2. Software and Equipment*

An Olympus CKX41 inverted trinocular microscope (Manila, Philippines) connected to an Olympus UIS2 optical system camera and AnalySIS 1.5 software were used for the microscopic examination of SH-SY5Y cells.

In the protein expression study, an Agilent 1200 series HPLC paired with an Agilent 6550 iFunnel quadrupole time of flight (Q-TOF) LC/MS, a C-18 300Å large capacity chip, and Agilent MassHunter data acquisition software (all from Agilent Technologies, USA) were used to determine the differentially expressed proteins. Additionally, version 8.0 of PEAKS®Studio software (Bioinformatics Solution, Waterloo, ON, Canada) and the UniProtKB database (organism: *Homo sapiens*) were used to analyze the results of the mass-spectrometry-based label-free quantitative proteomics (LFQ). Cytoscape software, with version 3.7.2 of the BiNGO plugin, was used for Gene Ontology (GO)-annotated information (Cytoscape Consortium, California, USA). Reactome Pathway Browser version 3.7 and Reactome Database Release 72 (organism: *Homo sapiens*) were utilized for the investigation into protein–protein interactions, functional annotations, and systemic pathway enrichment analysis.

### *2.3. Experimental Design*

#### 2.3.1. Extraction and Identification of Proteins by Nanoflow Liquid Chromatography Electrospray Ionization Coupled with Tandem Mass Spectrometry/Mass Spectrometry (Nanoflow-ESI-LCMS/MS)

The OS plants, aged about 12 months old (voucher specimen 11,009), were collected from Kampung Repuh, Batu Kurau (GPS coordinates: 4.52° N, 100.48° E; Perak, Malaysia). The fresh leaves were collected, cleaned, flash-frozen using liquid nitrogen, and ground into a fine powder using a pre-chilled grinder and ultrasonic cell crusher. The leaf powder was then weighed (50 mg) and kept in sterile 2.0 mL Eppendorf Protein LoBind® microtubes. The one-tube method was modified from previous studies [24–26]. The supernatants produced were then harvested and subjected to vacuum concentration (300 rpm; 24 h; 40 °C). Next, in-solution protein digestion was carried out based on the manufacturer's instructions (Mass Spec Grade Promega, USA). The digested peptides were loaded onto a C-18 300Å large capacity chip (Agilent, USA) and separated using a binary buffer system. The column was equilibrated by Buffer 1 (0.1% FA in MQUP) and Buffer 2 (60% ACN containing 0.1% FA). The digested peptides were eluted with a linear gradient: 50 min in 0–40% Buffer 2 followed by 40–80% Buffer 2 for an additional 30 min. Quadrupole time of flight (Q-TOF) was set at positive polarity, capillary voltage at 2050 V, fragmentor voltage at 300 V, drying gas flow 5 L/min, and a gas temperature of 300 °C. The peptide spectrum was analyzed in auto MS mode, ranging from 110–3000 m/z for the MS scan and 50–3000 m/z for the MS/MS scan, followed by up to 15 data-dependent MS/MS scans (top 15 approaches), with higher-energy collisional dissociation (HCD) at a resolution of 17,500 at 200 m/z. Dynamic exclusion was set to 30 s. Agilent MassHunter data acquisition software (version B.07.00, Agilent Technologies, Santa Clara, CA, USA) and PEAKS® Studio software (version 7.5, Bioinformatics Solutions Inc., Waterloo, ON, Canada) were used for the spectrum analysis. Next, the Lamiaceae protein databases of UniProtKB (http://www.uniprot.org/uniprot/ accessed on 10 January 2020) and NCBInr (https://www.ncbi.nlm.nih.gov/ accessed on 10 January 2020) were downloaded. Protein identification and homology search by

comparing the de novo sequence tags were assisted by PEAKS® Studio (version B.07.00). The settings applied were as follows: both parent mass and precursor mass tolerance were set at 0.1 Da with monoisotopic as the precursor mass search type; carbamidomethylation was set as a fixed modification, with maximum missed cleavage set at 3; maximum variable post-translational modification was set at 3, and trypsin/Lys-C was selected as the digestion enzyme. The other parameters were set as default by Agilent. The filtration parameters were set at a significant score (−10logP) of protein ≥20 and the number of peptides ≥20 to exclude inaccurate proteins. PEAKS® indicated that a −10logP score of greater than 20 is relatively high in confidence as it targets very few decoy matches above the threshold [27] (see Supplementary Table S1).

#### 2.3.2. SH-SY5Y Cells—Initial Culture, Sub-Culture, and Seeding Conditions

The SH-SY5Y cells obtained were maintained in an initial culture medium (pre-warmed to 37 °C) consisting of DMEM supplemented with 10% FBS and 1% Pen/Strep and kept in an incubator at 37 °C with 5% $CO_2$ and 95% air. The initial culture medium was refreshed every 4–7 days to remove non-adherent cells and to replenish nutrients and was monitored for cell confluence. When the cells reached ≥80% confluence, the sub-culture was performed. The old initial culture medium was aspirated, and the T-25 flask was rinsed with 1 mL of warm 1X PBS (5 s, twice). To lift the cells, 1 mL of TrypLE™ Express was added, and the flask was incubated (5–10 min, 37 °C, 5% $CO_2$, and 95% air). The flask was removed and observed under a microscope to confirm the detachment of cells (SH-SY5Y cells were seen as "floating"). The cell suspension produced was very gently transferred to a sterile 15 mL Falcon tube containing 1 mL of 1X PBS (37 °C). The tube was centrifuged (1000 rpm, 3 min, r.t.). The supernatant produced was gently discarded without disturbing the soft, transparent cell pellet formed at the bottom. The cell pellet was re-suspended in 1 mL fresh growth medium consisting of DMEM supplemented with 1% FBS and 1% Pen/Strep (pre-warmed to 37 °C) and was ready for seeding into the plates. In this study, the cells used for each experiment were of less than 20 passages.

#### 2.3.3. Evaluation of Cytotoxic Effects of OSLPs on SH-SY5Y Cells (24 and 48 h)

SH-SY5Y cells ($5 \times 10^4$) were seeded in 96-well plates ($n = 3$). Vacuum-concentrated OSLP was diluted in the growth medium at a concentration range of 25, 50, 125, 250, 500, 1000, 2000, 4000, and 10,000 µg/mL. The cells were then treated with OSLP at varying concentrations and incubated for 24 and 48 h (37 °C, 5% $CO_2$, 95% air). Upon complete incubation, both treatment groups were evaluated for cytotoxic effects using MTT assays. Absorbance was read at wavelength 570 nm with the reference filter set at 690 nm. All experiments were 3 independent biological replicates performed in triplicate, and the relative cell viability is expressed as a percentage (%) relative to the untreated control cells (normal control). Additionally, the maximal non-toxic dose (MNTD) and minimal toxic dose (MTD) of OSLP at 24 and 48 h were also determined [28].

$$Cell\ viability\ (\%) = \frac{Absorbance\ of\ sample - Absorbance\ of\ blank}{Absorbance\ of\ control - Absorbance\ of\ blank} \times 100 \quad (1)$$

#### 2.3.4. Hydrogen Peroxide ($H_2O_2$) Induction and Determination of Half-Maximal Inhibitory Concentration ($IC_{50}$)

SH-SY5Y cells ($5 \times 10^4$) were seeded in 96-well plates ($n = 3$). SH-SY5Y cells were induced by $H_2O_2$ at concentrations of 0, 50, 100, 150, 200, 250, 300, and 350 µM. All concentrations of $H_2O_2$ were freshly prepared by diluting a 30.2% ($v/v$) stock solution with DMEM. Following that, the $H_2O_2$-induced cells were incubated at 37 °C with 5% $CO_2$ and 95% air for 24 h. Upon completion of incubation, cell viability (%) of the SH-SY5Y cells, the half-maximal inhibitory concentration ($IC_{50}$), and the maximal inhibitory concentration ($IC_{90}$) were determined using an MTT assay. All experiments were 3 independent biological replicates performed in triplicate.

2.3.5. Evaluation of OSLP Protective Effects on SH-SY5Y Cells

SH-SY5Y cells ($5 \times 10^4$) were seeded in 96-well plates ($n = 6$). Vacuum-concentrated OSLP was diluted in the growth medium at a concentration range of 25, 50, 125, 250, 500, and 1000 μg/mL. The cells were assigned to a total of 8 groups, namely, normal control (NC) without $H_2O_2$ induction and OSLP treatments; negative control (Neg C, $H_2O_2$), which was induced by 150 μM of $H_2O_2$; and six OSLP treatment groups that received six different concentrations (25–1000 μg/mL) (Table 1). All six treatment groups were pre-treated with OSLP and incubated for 24 h at 37 °C, with 5% $CO_2$ and 95% air. Following that, all six groups were treated with Eppendorf Protein LoBind®. Upon completion of incubation, all 8 experiment groups were evaluated using MTT assays. All experiments were 6 independent biological replicates performed in triplicate.

**Table 1.** Experiment groups in the evaluation of OSLP protective effects on SH-SY5Y cells.

| Group | Treatment |
|---|---|
| NC | Normal control (untreated cells) |
| $H_2O_2$ | $H_2O_2$ induction (150 μM $H_2O_2$) |
| 25 | OSLP 25 μg/mL + 150 μM $H_2O_2$ |
| 50 | OSLP 50 μg/mL + 150 μM $H_2O_2$ |
| 125 | OSLP 125 μg/mL + 150 μM $H_2O_2$ |
| 250 | OSLP 250 μg/mL + 150 μM $H_2O_2$ |
| 500 | OSLP 500 μg/mL + 150 μM $H_2O_2$ |
| 1000 | OSLP 1000 μg/mL + 150 μM $H_2O_2$ |

Remark: $H_2O_2$, hydrogen peroxide; OSLP, *Orthosiphon stamineus* leaf protein.

2.3.6. Microscopic Examination Using Bright-Field Imaging

Microscopic changes (10×) of the SH-SY5Y cells were studied using bright-field microscopy. The bright-field microscopic images of the normal control (NC), the negative control ($H_2O_2$ induced by 150 μM $H_2O_2$), and three OSLP treatment groups (250, 500, and 1000 μg/mL) were captured with an Olympus CKX41 inverted trinocular microscope connected to an Olympus UIS2 optical system camera and AnalySIS 1.5 software.

*2.4. Protein Expression Study*

2.4.1. Protein Expression Profiling with Mass Spectrometry-Based Label-Free Quantitative Proteomics (LFQ)

OSLP was prepared in a concentration of 10 mg/mL (as mother stock) and was then twofold diluted to 250, 500, and 1000 μg/mL in fresh growth medium (DMEM with 1% FBS and 1% Pen/Strep). SH-SY5Y cells ($1 \times 10^6$) were seeded in 6-well plates. The cells were assigned to 5 groups (Table 2). Three treatment groups were pre-treated with freshly prepared OSLP and incubated for 24 h (37 °C, 5% $CO_2$, 95% air). Following that, they were induced by 150 μM of $H_2O_2$ for another 24 h and returned to incubation (37 °C, 5% $CO_2$, 95% air). Upon complete incubation, all five experiment groups were subject to cell lysis for protein extraction in order to conduct mass-spectrometry-based label-free quantitative proteomics (LFQ). For all experiments, 3 independent biological replicates were performed.

**Table 2.** Experiment groups in the protein expression study.

| Group | Treatment |
|---|---|
| NC | Normal control (untreated cells) |
| $H_2O_2$ | $H_2O_2$ induction (150 μM $H_2O_2$) |
| 250 | OSLP 250 μg/mL + 150 μM $H_2O_2$ |
| 500 | OSLP 500 μg/mL + 150 μM $H_2O_2$ |
| 1000 | OSLP 1000 μg/mL + 150 μM $H_2O_2$ |

Remark: $H_2O_2$, hydrogen peroxide; OSLP, *Orthosiphon stamineus* leaf protein.

2.4.2. Protein Extraction from SH-SY5Y Cells

After aspirating the media, the cells were treated with TrypLE™ Express, incubated, and rinsed with pre-cooled 1X PBS. The content was collected into individual sterile Eppendorf Protein LoBind® microtubes and centrifuged (500× *g*, 4 °C; 10 min). The produced supernatant was discarded, but the soft, transparent pellet was collected and lysed with ice-cold lysis buffer (200 µL of RIPA, protease inhibitor 20% *v*/*v*, phosphatase inhibitor 1% *v*/*v*) and incubated (4 °C; 20 min). Following that, the cell suspension was homogenized using an ultrasonic cell crusher and then briefly centrifuged (2000× *g*, 4 °C; 10 min). The proteins extracted were collected into new, individual, sterile Eppendorf Protein LoBind® microtubes and were concentrated using a speed-vacuum concentrator (300 rpm; 24 h; 60 °C) before storage at −152 °C for subsequent analysis.

2.4.3. Protein Estimation by Bradford Protein Assay

Protein concentration was estimated using a Quick Start™ Bradford protein assay, following the instructions of the manufacturer. Briefly, 5µL of the sample or standard was loaded onto a 96-well plate in triplicate. This was followed by adding 250 µL of dye reagent into each well. The plate was incubated at room temperature (25–27 °C; 5 min). Absorbance was read at 595 nm with a Bio-Rad Benchmark Plus microplate reader with Microplate Manager 5.2.1 software. Protein concentrations were determined from the standard curve.

2.4.4. In-Solution Digestion of Proteins

In-solution protein digestion was performed as instructed (Mass Spec Grade Promega, Madison, WI, USA). Protein samples were solubilized in 6 M urea/50 mM TRIS-HCl (pH 8.02), followed by the addition of 5 mM DTT (freshly prepared) and incubated in the dark (30 min; 37 °C). Next, 15 mM IAA (freshly prepared) was added and incubated in the dark (30 min; r.t.). The reduced and alkylated protein solutions were diluted sixfold with 50 mM TRIS-HCl (pH 8.02). Following that, 20 µg of crude protein was digested by trypsin/Lys-C mix (ratio 25 protein:1 protease; *w*/*w*) buffered in 50 mM TRIS-HCl (pH 8.02) and then incubated in the dark (overnight; 37 °C). Formic acid (1%) was added to halt the enzymatic reaction. Following that, all the samples were subjected to centrifugation (16,000× *g*; 4 °C; 10 min). The supernatant produced was collected and concentrated using a speed-vacuum concentrator (300 rpm; 24 h; 60 °C). Formic acid (10 µL of 0.1%) was added into all the sample tubes, followed by brief vortexing and centrifugation.

2.4.5. De-Salting of Proteins

Each protein biological replicate was independently de-salted using modified instructions for the Pierce®C18 mini spin column. Every mini spin column was firstly activated using a 50% ACN solution (repeated thrice, r.t.) and equilibrated using a 0.5% solution of TFA in 5% ACN (repeated thrice, r.t.). A 90 µL volume of protein was individually added into a 30 µL solution of sample buffer (2% of TFA in 20% of ACN) and momentarily vortexed at a speed of 2200 rpm to ensure proper mixing. This step was repeated individually for each protein biological replicate. Next, each of them was loaded onto individual sterile mini spin columns for de-salting (repeated thrice, r.t.). Subsequently, each protein biological replicate was washed using a 0.5% solution of TFA in 5% ACN (repeated thrice, r.t.). Finally, each protein biological replicate was eluted using a 70% solution of ACN (repeated thrice, r.t.), and all the produced flow-through was collected, vacuum-concentrated (300 rpm; 24 h; 60 °C), and then stored at −20 °C for mass-spectrometry-based LFQ at a later date.

2.4.6. Mass-Spectrometry-Based Label-Free Quantitative Proteomics (LFQ) Using Nanoflow-ESI-LCMS/MS

An Agilent C-18 300Å large capacity chip was used to load the previously de-salted peptides. The column was equilibrated using 0.1% FA in water (Buffer 1), and the peptides were eluted using an increasing gradient of 90% ACN in 0.1% FA (Buffer 2) using the following gradient: 3–50% Buffer 2 from 0–30 min, 50–95% Buffer 2 from 30–32 min, 95%

Buffer 2 from 32–39 min, and 95–3% Buffer 2 from 39–47 min. The Q-TOF settings were as follows: positive polarity, fragmentor voltage at 300 V, capillary voltage at 2050 V, drying gas at a flow rate of 5 L/min, and a 300 °C gas temperature. Auto MS/MS mode was used to analyze the intact protein, with a range of 110–3000 m/z for the MS scan and a 50–3000 m/z range for the MS/MS scan. Agilent MassHunter data acquisition software was used to perform the spectrum analysis.

#### 2.4.7. Peptide and Protein Identification by Automated De Novo Sequencing and LFQ Analysis

The UniProtKB database (Organism: *Homo sapiens*) (https://www.uniprot.org/proteomes/UP000005640, 163,191 proteins; accessed on 13 March 2020) was used to identify the peptides and proteins, as well as conduct homology searching via comparison of the de novo sequence tag, using the following settings: trypsin cleavage, a parent mass and a precursor mass tolerance of 0.1 Da, minimum ratio count of 2, maximum variable post-translational modification of 3, carbamidomethylation as a fixed modification with maximum missed cleavage of 3, mass error tolerance of 20.0 ppm, and other parameters as default settings of Agilent. The false discovery rate (FDR) threshold was set at 1%, and a protein score of $-10\lg P > 20$ was used to filter out proteins that were inaccurate. PEAKS® software indicated that a protein score of $-10\lg P > 20$ has relatively high confidence as it targets very few decoy matches above the threshold.

The differentially expressed proteins were identified using LFQ analysis using the following settings: significance score $\geq 13$, protein fold change $\geq 1$, number of unique peptides $\geq 1$, and an FDR threshold of $\leq 1\%$. PEAKSQ indicated that a significance score of $\geq 13$ is equal to a significance value of $p < 0.05$. All other parameters were kept at the default settings set by Agilent.

### *2.5. Bioinformatics Analysis*

Using bioinformatics analysis (functional annotations, protein–protein interactions, and systemic pathway enrichment analysis) of the identified differentially expressed proteins, the proteins were analyzed and matched using the GO Consortium, Ensemble (http://www.ensembl.org/Homo_sapiens accessed on 13 December 2019), and Reactome Database (Release 72; organism: *Homo sapiens*) online databases.

### *2.6. Statistical Analysis*

Statistical analysis was carried out using version 5.0 of GraphPad Prism. The data obtained from the in vitro assays were expressed using the notation of mean ± standard error of the mean (SEM). One-way ANOVA followed by Dunnett's post hoc test was used to compare data between the control and treated groups using the significance levels of * $p < 0.5$, ** $p < 0.01$, and *** $p < 0.001$. The built-in statistical tool of PEAKS® software (PEAKSQ statistical analysis) was used to analyze the identified differentially expressed proteins. A 13% significance score (which is equal to a significance level of 0.05) and an FDR of $\leq 1\%$ are considered to be statistically significant. In the bioinformatics analysis, the hypergeometric test followed by Benjamini and Hochberg's FDR correction at $p$-value <0.05 (built-in BiNGO statistical tool) was used to correlate the functional annotation of genes with their interacting proteins; overrepresentation analysis of pathways was tested with hypergeometric distribution, following the Benjamani-Hochberg method, corrected at $p$-value <0.05 (Reactome Pathway Browser version 3.7 built-in statistical tool). The overrepresentation analysis of Reactome Pathways was used to predict the possible associations of systemic pathways with their interacting proteins and genes.

## 3. Results

### *3.1. Evaluation of Cytotoxic Effects of OSLP on SH-SY5Y Cells (24 and 48 h)*

After 24 h incubation, no significant cytotoxic effects of OSLP were observed at concentrations below 4000 µg/mL compared to the NC ($F = 251.7$; $p > 0.05$; Figure 1). Cytotoxic effects were apparent when the SH-SY5Y cells were treated with 4000 µg/mL of

OSLP (95 ± 1%). This slight reduction, however, did not attain any statistical significance when compared to the NC (F = 251.7; $p > 0.05$; Figure 1). In contrast, treatment with 10 mg/mL of OSLP was found to result in a significant decrease, about 52 ± 2%, compared to the NC (F = 251.7; ^^^ $p < 0.001$; Figure 1).

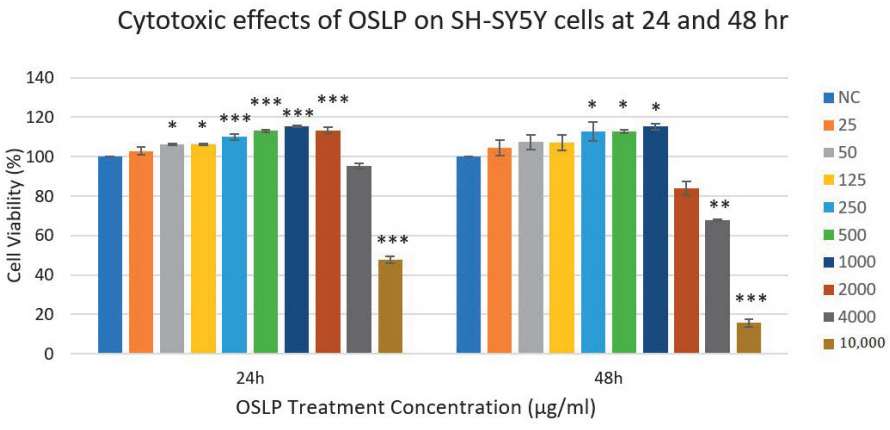


**Figure 1.** Cytotoxic effects of OSLP on SH-SY5Y cells at 24 and 48 h. Data shown are presented as mean ± SEM of 3 independent experiments performed in triplicate. * $p < 0.05$, ** $p < 0.01$ and *** $p < 0.001$ against the normal control group (NC). One-way ANOVA with Dunnett's post hoc test.

After 48 h incubation, no significant cytotoxic effects of OSLP were observed at concentrations below 2000 µg/mL compared to the NC (F = 106.6; $p > 0.05$; Figure 1). Significant cytotoxic effects of OSLP were apparent at concentrations above 2000 µg/mL compared to the NC (F = 106.6; ** $p < 0.01$; Figure 1). At 2000 µg/mL of OSLP, cell viability significantly decreased to 84 ± 4% (F = 106.6; ** $p < 0.01$; Figure 1) and declined further to 68 ± 0.5% at 4000 µg/mL of OSLP (F = 106.6; *** $p < 0.001$; Figure 1). A significant plunge, about 84 ± 2%, in the SH-SY5Y cell population was observed at 10 mg/mL of OSLP treatment (F = 106.6; *** $p < 0.001$; Figure 1). This indicates that 10 mg/mL of OSLP exerted significant cytotoxic effects on the survival of SH-SY5Y cells.

From the graph plotted (Figure 1), the MNTD of OSLP at 24 h treatment was determined as approximately 2000 µg/mL, whilst the MTD of OSLP at 24 h treatment was approximately 4000 µg/mL. In contrast, the MNTD of OSLP at 48 h treatment was determined as approximately 1000 µg/mL, whereas the MTD of OSLP at 48 h treatment was approximately 2000 µg/mL.

### *3.2. Hydrogen Peroxide ($H_2O_2$) Induction and Determination of Half-Maximal Inhibitory Concentration ($IC_{50}$)*

As depicted in Figure 2, exposure from 50 to 350 µM of $H_2O_2$ decreased the cell population in a concentration-dependent manner. Cell viability (%) decreased when $H_2O_2$ concentrations increased. When compared to the NC, 50–100 µM of $H_2O_2$ did not significantly inhibit SH-SY5Y cell growth (F = 105.6; $p > 0.5$; Figure 2) but 150–350 µM of $H_2O_2$ significantly inhibited SH-SY5Y cell growth (F = 105.6; *** $p < 0.001$; Figure 2). At about 150 µM of $H_2O_2$, cell viability was reduced significantly to 42 ± 6% (F = 105.6; *** $p < 0.001$) and further declined significantly to 34 ± 3% (F = 105.6; *** $p < 0.001$) when the concentration increased to 200 µM growth. Following that, cell viability tumbled steeply to 11 ± 0.4%, 3 ± 0.5%, and 5 ± 0.2% when $H_2O_2$ induction increased to 250, 300, and 350 µM, respectively (F = 105.6; *** $p < 0.001$). From the graph plotted (Figure 2), the $IC_{50}$ of $H_2O_2$ was determined as approximately 150 µM whilst the $IC_{90}$ of $H_2O_2$ was determined as 250 µM and above.

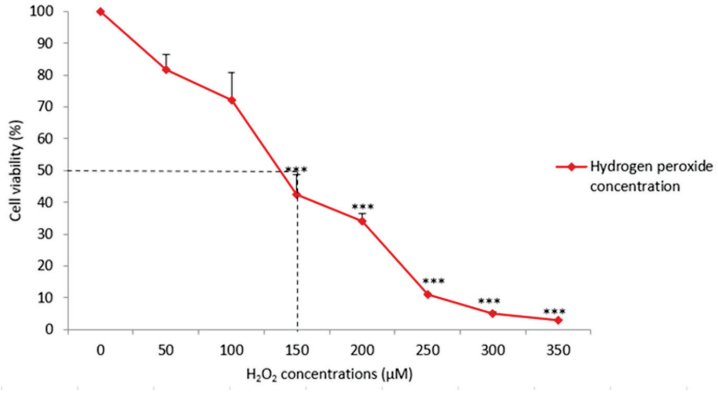


**Figure 2.** Cell viability of SH-SY5Y cells induced by $H_2O_2$. SH-SY5Y cells were treated with 0–350 μM $H_2O_2$. Data shown are presented as mean ± SEM of 3 independent experiments performed in triplicate. *** shows $p < 0.001$ against the untreated group (NC, 24 h). One-way ANOVA with Dunnett's post hoc test.

### *3.3. Evaluation of OSLP Protective Effects on SH-SY5Y Cells*

From the graph plotted (Figure 3), $H_2O_2$ induction (negative control, 150 μM) significantly decreased SH-SY5Y cell viability (43 ± 5%; F = 17.9; *** $p < 0.001$) compared to the NC. OSLP at these two concentrations, 25 μg/mL (38 ± 2%; F = 17.9; $p > 0.5$) and 50 μg/mL (42 ± 5%; F = 17.9; $p > 0.5$), did not show significant protection against $H_2O_2$ induction. At 125 μg/mL, OSLP increased cell viability by about 30% compared to the $H_2O_2$ group (61 ± 9%; F = 17.9; $p > 0.5$). OSLP at 250 μg/mL significantly increased SH-SY5Y cell viability (71 ± 12%; F = 17.9; * $p < 0.01$) compared to the $H_2O_2$ group. An increase of 39% in cell viability was recorded. OSLP at these two concentrations, 500 μg/mL (88 ± 6%; F = 17.9; *** $p < 0.001$) and 1000 μg/mL (101 ± 2%; F = 17.9; *** $p < 0.001$), significantly increased SH-SY5Y cell viability compared to the $H_2O_2$ group. OSLP at 500 μg/mL increased by about 51% whilst OSLP at 1000 μg/mL increased by about 57% in cell viability.

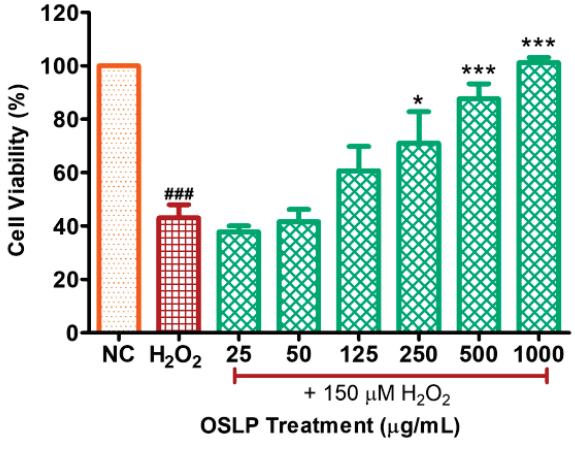


**Figure 3.** OSLP protective effects on $H_2O_2$-induced SH-SY5Y cells. Data shown are presented as mean ± SEM of 3 independent experiments performed in triplicate. * $p < 0.05$ and *** $p < 0.001$ against against the negative control group ($H_2O_2$, 150 μM), whereas ### shows $p < 0.001$ against the normal control group (NC, no OSLP treatment, and $H_2O_2$ induction). One-way ANOVA with Dunnett's post hoc test.

Microscopic Examination Using Bright-Field Imaging

Figure 4 displays the representative bright-field microscopic images of the SH-SY5Y cells. The NC displayed normal cell architecture, with pyramidal-shaped cells having apparent neurites (panel a, blue arrows). SH-SY5Y cells induced by 150 μM of $H_2O_2$ showed disrupted cell architecture, with clusters of clumping cells and reduced neurites (panel b, red arrows) compared to the normal control (NC), which received no OSLP treatment and no $H_2O_2$ induction (panel a, blue arrows). Pre-treatment with OSLP at 250, 500, and 1000 μg/mL improved the cell architecture, with reduced clumping cells and restored neuronal cell shapes with clear neurites (panels c–e, orange arrows) compared to the negative control ($H_2O_2$,150 μM). The cell population was also markedly declined in the negative control, but pre-treatments with OSLP increased cell growth.

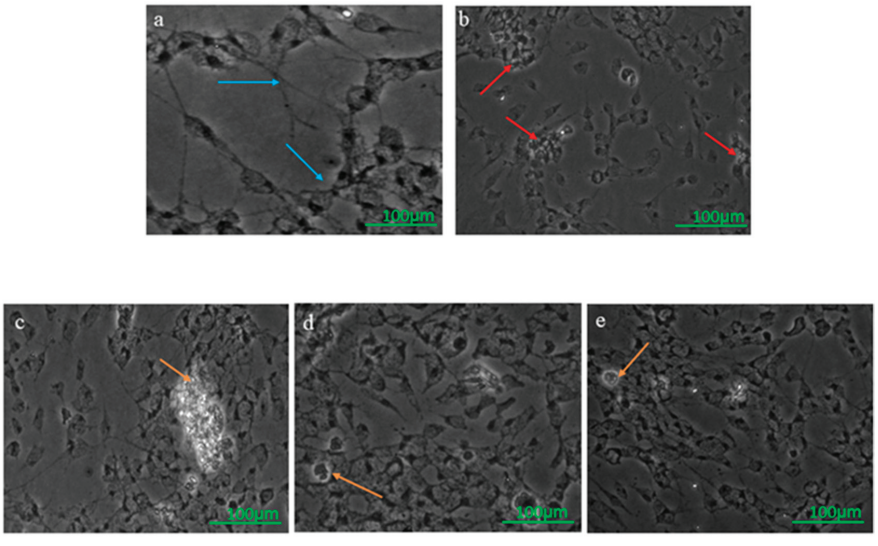


**Figure 4.** Representative bright-field microscopic images of SH-SY5Y cells. Upper row: (**a**) normal control (NC, without OSLP treatment and $H_2O_2$ induction) displays pyramidal-shaped cells, showing clear neurites (blue arrows), and did not cluster; (**b**) $H_2O_2$ (induced by 150 μM of $H_2O_2$) shows disrupted neuronal cell shapes, with many clumping cells (red arrows) and reduced neurites in addition to a declined population. Lower row: (**c**–**e**) OSLP treatment groups, 250, 500 and 1000 μg/mL, respectively. OSLP treatments reduced clumping cells and restored the neuronal cell shapes, with clear neurites seen (orange arrows). Scale bar = 100 μm.

### *3.4. Protein Expression Study*

Proteins were extracted from the normal control (NC, SH-SY5Y cells without OSLP treatment and $H_2O_2$ induction), the negative control, ($H_2O_2$, 150 μM $H_2O_2$ only) and three OSLP treatment groups (250 μg/mL + 150 μM $H_2O_2$, 500 μg/mL + 150 μM $H_2O_2$, and 1000 μg/mL + 150 μM $H_2O_2$). The protein samples were subjected to mass-spectrometry-based label-free quantitative proteomics (LFQ) using nanoflow-ESI-LCMS/MS and subsequent bioinformatics analysis. As to the final results and discussion, only these two pairs were used: Pair A, $H_2O_2$ (150 μM $H_2O_2$ only) versus normal control (without OSLP treatment and $H_2O_2$ induction) and Pair B, $H_2O_2$ (150 μM $H_2O_2$ only) versus OSLP treatment (OSLP 1000 μg/mL + 150 μM $H_2O_2$). The highest dose of OSLP was chosen to elucidate its maximal protective effects on SH-SY5Y cells induced by $H_2O_2$.

3.4.1. Protein Expression Analysis with Mass-Spectrometry-Based Quantitative Label-Free Proteomics (LFQ)

LFQ has profiled 32 differentially expressed proteins, of which 22 were identified in Pair A ($H_2O_2$ vs. NC) and 10 were identified in Pair B ($H_2O_2$ vs. Treatment) (Figure 5, Tables 3 and 4).

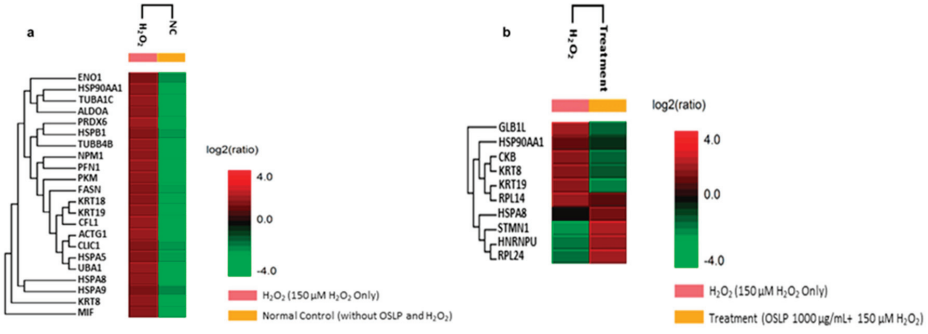


**Figure 5.** Heat map displays the differentially expressed proteins identified from (**a**) Pair A: $H_2O_2$ (150 μM $H_2O_2$ only) versus NC (normal control without OSLP treatment and $H_2O_2$ induction) and (**b**) Pair B: $H_2O_2$ (150 μM $H_2O_2$ only) versus OSLP treatment (OSLP 1000 μg/mL + 150 μM $H_2O_2$), $n = 3$, significance ≥13, FDR ≤ 1%, fold change ≥1, number of unique peptide ≥1. Protein names are listed on the left, while experimental groups are indicated on top. The color key on the bottom right indicates the log2 (ratio) expression levels (green = low, red = high).

**Table 3.** Differentially expressed proteins identified from Pair A ($H_2O_2$ vs. NC).

| Uniprot Accession ID | Uniprot Protein Name | Significance (≥13) | Coverage (%) | #Peptides | #Unique | Avg. Mass | Group Profile (Ratio of NC/$H_2O_2$) | Ensembl Protein |
|---|---|---|---|---|---|---|---|---|
| P11142 | Heat shock cognate 71 kDa protein | 34.31 | 16 | 7 | 5 | 67,980 | 0.34:1.00 | HSPA8 |
| P04075 | Fructose-bisphosphate aldolase A | 24.61 | 25 | 5 | 5 | 39,818 | 0.20:1.00 | ALDOA |
| P68371 | Tubulin beta-4B chain | 24.00 | 15 | 5 | 1 | 49,831 | 0.12:1.00 | TUBB4B |
| P05787 | Keratin, type II cytoskeletal 8 | 23.26 | 63 | 31 | 15 | 53,704 | 0.20:1.00 | KRT8 |
| O00299 | Chloride intracellular channel protein 1 | 23.2 | 8 | 1 | 1 | 26,794 | 0.02:1.00 | CLIC1 |
| P06733 | Alpha-enolase | 22.22 | 23 | 7 | 7 | 47,169 | 0.28:1.00 | ENO1 |
| P05783 | Keratin, type I cytoskeletal 18 | 20.41 | 63 | 19 | 17 | 48,030 | 0.16:1.00 | KRT18 |
| P38646 | Stress-70 protein, mitochondrial | 20.12 | 13 | 6 | 6 | 72,401 | 0.20:1.00 | HSPA9 |
| P04792 | Heat shock protein beta-1 | 19.50 | 40 | 6 | 6 | 22,783 | 0.15:1.00 | HSPB1 |
| P23528 | Cofilin-1 | 18.80 | 28 | 4 | 4 | 22,728 | 0.17:1.00 | CFL1 |
| P07737 | Profilin-1 | 18.10 | 46 | 5 | 5 | 15,054 | 0.25:1.00 | PFN1 |
| P14618 | Pyruvate kinase PKM | 17.35 | 18 | 6 | 3 | 57,937 | 0.23:1.00 | PKM/PK3 |
| P30041 | Peroxiredoxin-6 | 16.95 | 21 | 1 | 1 | 11,161 | 0.18:1.00 | PRDX6 |
| P22314 | Ubiquitin-like modifier-activating enzyme 1 | 16.61 | 3 | 2 | 2 | 117,849 | 0.10:1.00 | UBA1 |
| P63261 | Actin, cytoplasmic 2 | 16.55 | 33 | 11 | 1 | 41,793 | 0.07:1.00 | ACTG1 |
| P49327 | Fatty acid synthase | 16.33 | 3 | 4 | 4 | 273,424 | 0.29:1.00 | FASN |
| Q9BQE3 | Tubulin alpha-1C chain | 15.94 | 18 | 7 | 7 | 57,730 | 0.26:1.00 | TUBA1C |
| P14174 | Macrophage migration inhibitory factor | 14.39 | 10 | 1 | 1 | 12,476 | 0.11:1.00 | MIF |
| P08727 | Keratin, type I cytoskeletal 19 | 13.91 | 34 | 10 | 8 | 44,106 | 0.15:1.00 | KRT19 |
| P07900 | Heat shock protein HSP 90-alpha | 13.79 | 12 | 6 | 3 | 68,372 | 0.36:1.00 | HSP90AA1 |
| P11021 | Endoplasmic reticulum chaperone BiP | 13.35 | 7 | 3 | 2 | 66,914 | 0.17:1.00 | HSPA5 |
| P06748 | Nucleophosmin | 13.27 | 15 | 2 | 2 | 28,400 | 0.21:1.00 | NPM1 |

Remark: The Ensembl Human Database (https://asia.ensembl.org/Homo_sapiens/Info/Index, accessed on 9 November 2019) was used to search for the Ensembl protein nomenclatures.

**Table 4.** Differentially expressed proteins identified from Pair B ($H_2O_2$ vs. Treatment).

| Uniprot Accession ID | Uniprot Protein Name | Significance (≥13) | Coverage (%) | #Peptides | #Unique | Avg. Mass | Group Profile (Ratio of $H_2O_2$/Treatment) | Ensembl Protein |
|---|---|---|---|---|---|---|---|---|
| Q, | Heterogeneous nuclear ribonucleoprotein U | 31.91 | 2 | 1 | 1 | 67,980 | 1.00:1.72 | HNRNPU |
| P05787 | Keratin, type II cytoskeletal 8 | 25.07 | 69 | 41 | 20 | 39,818 | 1.00:0.44 | KRT8 |
| P11142 | Heat shock cognate 71 kDa protein | 18.72 | 21 | 11 | 2 | 49,831 | 1.00:0.94 | HSPA8 |
| P83731 | 60S ribosomal protein L24 | 16.92 | 11 | 1 | 1 | 53,704 | 1.00:2.79 | RPL24 |
| P50914 | 60S ribosomal protein L14 | 16.33 | 6 | 1 | 1 | 26,794 | 1.00:0.58 | RPL14 |
| P16949 | Stathmin | 15.88 | 15 | 2 | 2 | 47,169 | 1.00:2.24 | STMN1 |
| Q6UWU2 | Beta-galactosidase-1-like protein | 15.63 | 2 | 1 | 1 | 48,030 | 1.00:0.38 | GLB1L |
| P08727 | Keratin, type I cytoskeletal 19 | 14.96 | 43 | 14 | 12 | 72,401 | 1.00:0.27 | KRT19 |
| P12277 | Creatine kinase B-type | 14.25 | 12 | 2 | 2 | 22,783 | 1.00:0.41 | CKB |
| P07900 | Heat shock protein HSP 90-alpha | 13.00 | 20 | 11 | 3 | 22,728 | 1.00:0.49 | HSP90AA1 |

Remark: The Ensembl Human Database (https://asia.ensembl.org/Homo_sapiens/Info/Index, accessed on 9 November 2018) was used to search for the Ensembl protein nomenclatures.

In Pair A ($H_2O_2$ vs. NC), all the proteins were found expressed at higher levels in the $H_2O_2$-treated samples than in the NC. In contrast, in Pair B ($H_2O_2$ vs. Treatment), seven proteins were expressed at lower levels in the OSLP-treated group than in the $H_2O_2$-treated group. They were keratin, type II cytoskeletal 8 (KRT8, P05787), heat shock cognate 71 kDa protein (HSPA8, P11142), 60S ribosomal protein L14 (RPL14, P50914), beta-galactosidase-1-like protein (GLB1L, Q6UWU2), keratin, type I cytoskeletal 19 (KRT19, P08727), creatine kinase B-type (CKB, P12277), and heat shock protein HSP 90-alpha (HSP90AA1, P07900). The others, namely, heterogeneous nuclear ribonucleoprotein U (HNRNPU, Q00839), 60S ribosomal protein L24 (RPL24, P83731), and stathmin (STMN1, P16949), were expressed at higher levels in the OSLP-treated group than in the $H_2O_2$-treated group (Figure 5, Tables 3 and 4). Additionally, four proteins were found expressed in both pairs (Figure 6). They were heat shock cognate 71 kDa protein (HSPA8, P11142), keratin, type II cytoskeletal 8 (KRT8, P05787), keratin, type I cytoskeletal 19 (KRT19, P08727), and heat shock protein HSP 90-alpha (HSP90AA1, P07900). Interestingly, these proteins were found expressed at lower levels in both the NC and the OSLP-treated groups (Figure 5).

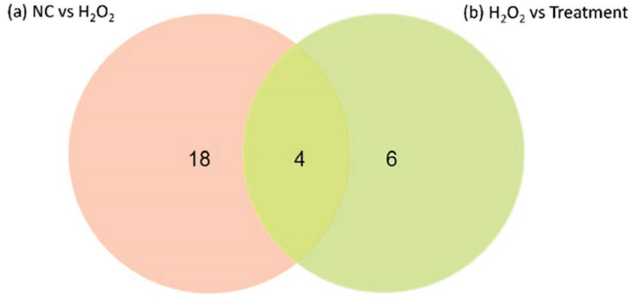


**Figure 6.** A two-way Venn diagram depicts the differentially expressed proteins identified from (**a**) Pair A: $H_2O_2$ (150 μM $H_2O_2$ only) versus NC (normal control without OSLP treatment and $H_2O_2$ induction) and (**b**) Pair B: $H_2O_2$ (150 μM $H_2O_2$ only) versus OSLP treatment (OSLP 1000 μg/mL + 150 μM $H_2O_2$), $n = 3$. As shown, a total of 32 differentially expressed proteins were identified; 4 are overlaps between the two pairs, 18 are identified in Pair A, and 6 are in Pair B.

3.4.2. Bioinformatics Analysis

The differentially expressed proteins were also studied using functional annotation analysis to identify and visualize the cellular components, molecular functions, and biological processes of the differentially expressed proteins. The differentially expressed proteins were found to localize at cellular components, including non-membrane-bound organelle (GO:43228), intracellular non-membrane-bound organelle (GO:43232), cytoskeleton (GO:5856), cytoplasm (GO:5737), cytoplasmic part (GO:44444), intracellular organelle (GO:43229), organelle (GO:43226), cell surface (GO:9986), pigment granule (GO:48770), and melanosome (GO:42470) (Figure 7).

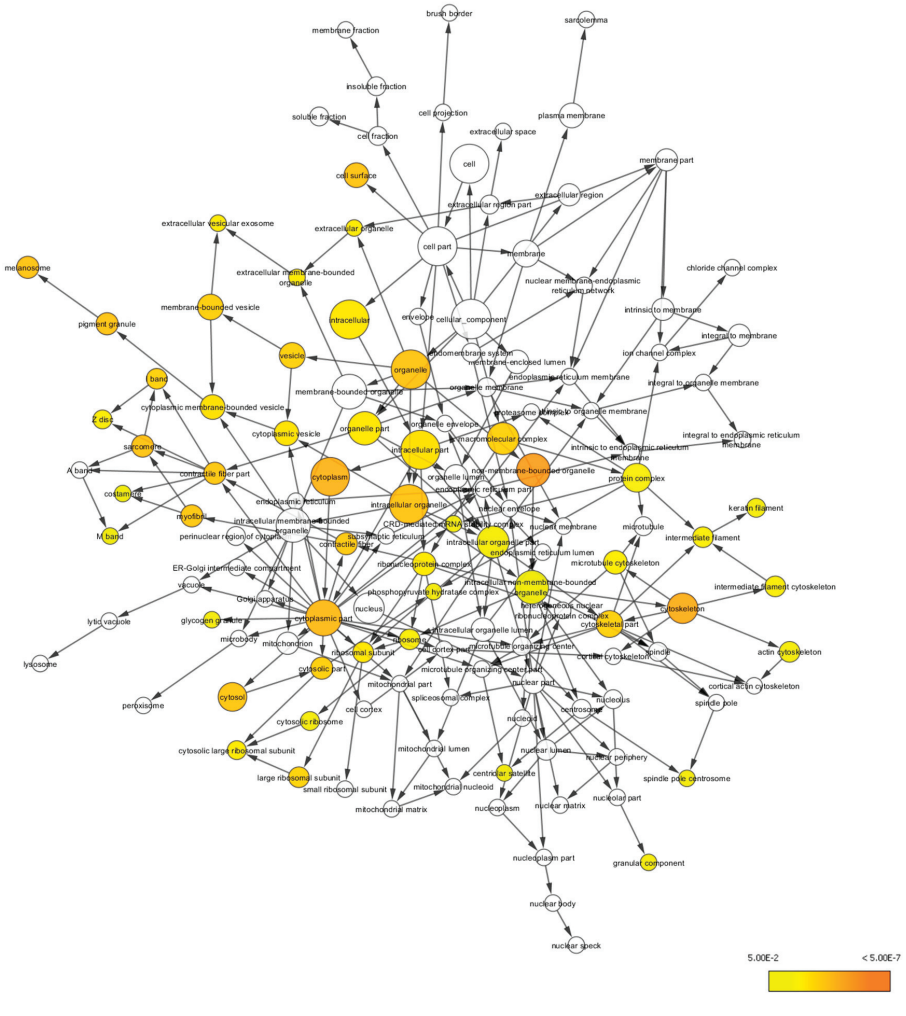


**Figure 7.** BiNGO result for cellular components, as visualized in Cytoscape (organism: *Homo sapiens*). Colored nodes indicate significant overrepresention. White nodes indicate insignificant overrepresention; they are included to show the colored nodes in the context of the GO hierarchy. The color key on the bottom right indicates the significance level of overrepresentation.

At these cellular localizations, the interactions of the differentially expressed proteins have been networked to an array of molecular functions involved in protein binding (GO:5515), unfolded protein binding (GO:51082), structural molecule activity (GO:5198), caspase inhibitor activity (GO:43027), ATP binding (GO:5524), adenyl ribonucleotide binding (GO:32559), ribonucleotide binding (GO:32553), purine ribonucleotide binding (GO:32555), adenyl nucleotide binding (GO:30554), and purine nucleotide binding (GO:17076) (Figure 8).

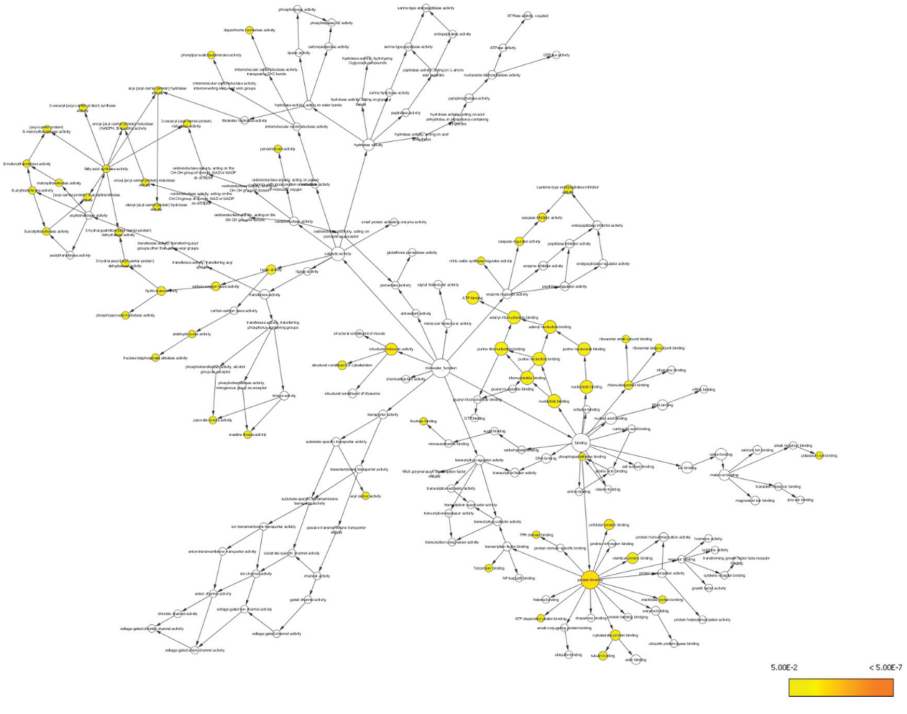


**Figure 8.** BiNGO results for molecular function, as visualized in Cytoscape (organism: *Homo sapiens*). Colored nodes indicate significant overrepresention. White nodes indicate insignificant overrepresention; they are included to show the colored nodes in the context of the GO hierarchy. The color key on the bottom right indicates the significance level of overrepresentation.

These molecular functions were found to involve a myriad of biological processes encompassing negative regulation of apoptosis (GO:43066), negative regulation of programmed cell death (GO:43069), negative regulation of cell death (GO:60548), ribosomal large subunit biogenesis (GO:42273), cytoskeleton organization (GO:7010), response to unfolded protein (GO:6986), multi-organism process (GO:51704), response to biotic stimulus (GO:9607), anti-apoptosis (GO:6916), and response to protein stimulus (GO:51789) (Figure 9).

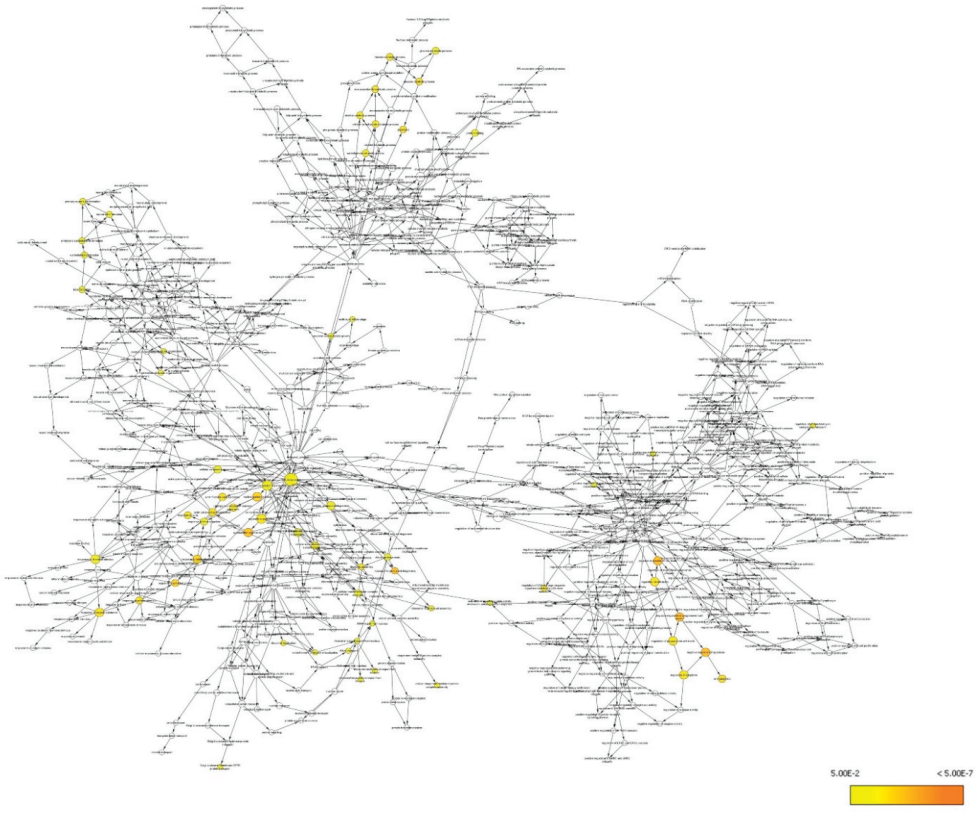


**Figure 9.** BiNGO results for biological process, as visualized in Cytoscape (organism: *Homo sapiens*). Colored nodes indicate significant overrepresention. White nodes indicate insignificant overrepresention; they are included to show the colored nodes in the context of the GO hierarchy. The color key on the bottom right indicates the significance level of overrepresentation.

The top ten enriched terms in all three categories were selected to elucidate the association between OSLP protection and $H_2O_2$ stress (Figure 10).

3.4.3. Systematic Pathway Enrichment Analysis

Reactome Pathways found that the differentially expressed proteins were significantly associated with the 25 pathways with the highest relevance ($p < 0.05$, Figure 11) out of the 80 identified pathways (see supplementary data, Pair A). These pathways were associated with 11 top-level pathway hierarchies, namely, signal transduction, vesicle-mediated transport, cellular responses to external stimuli, metabolism of proteins, cell cycle, neuronal system, autophagy, metabolism, developmental biology, hemostasis, and immune system (Table 5). At sub-level pathway hierarchy, they were seen to be involved in the signaling by Rho GTPases membrane trafficking, cellular responses to stress and HSF1-dependent transactivation, protein folding and post-translational protein modification, mitotic cell cycle, post-NMDA receptor activation events, activation of NMDA receptors, postsynaptic events, macroautophagy, metabolism of glucose and carbohydrates, nervous system development, response to elevated platelet cytosolic $Ca^{2+}$, and the innate immune system (Table 5).

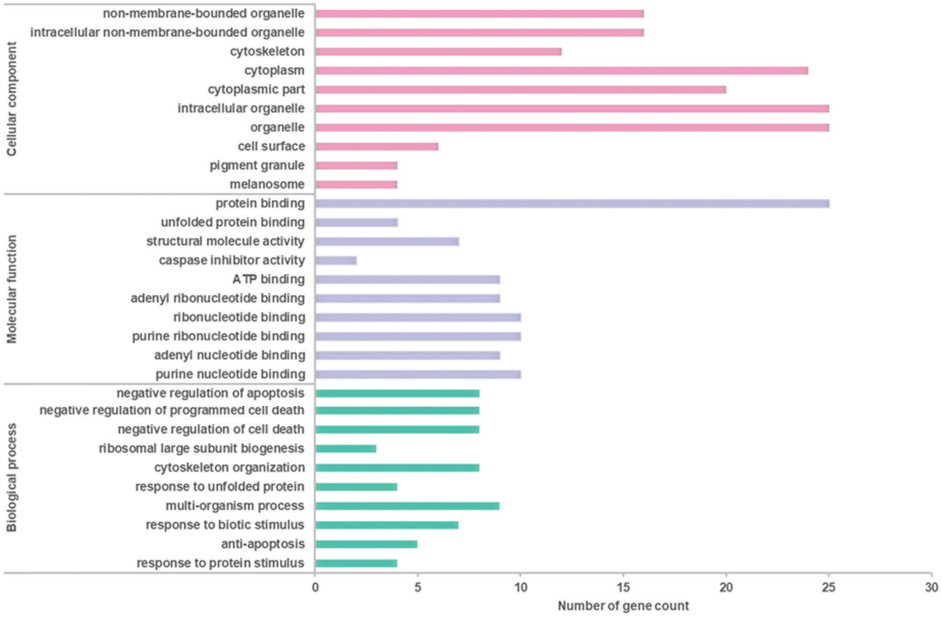


**Figure 10.** Classification of the top 10 enriched terms in cellular component, molecular function, and biological process annotated by BiNGO (organism: *Homo sapiens*; Pair B, $H_2O_2$ vs. Treatment). Hypergeometric test with Benjamini and Hochberg's false discovery rate (FDR) correction at $p < 0.05$.

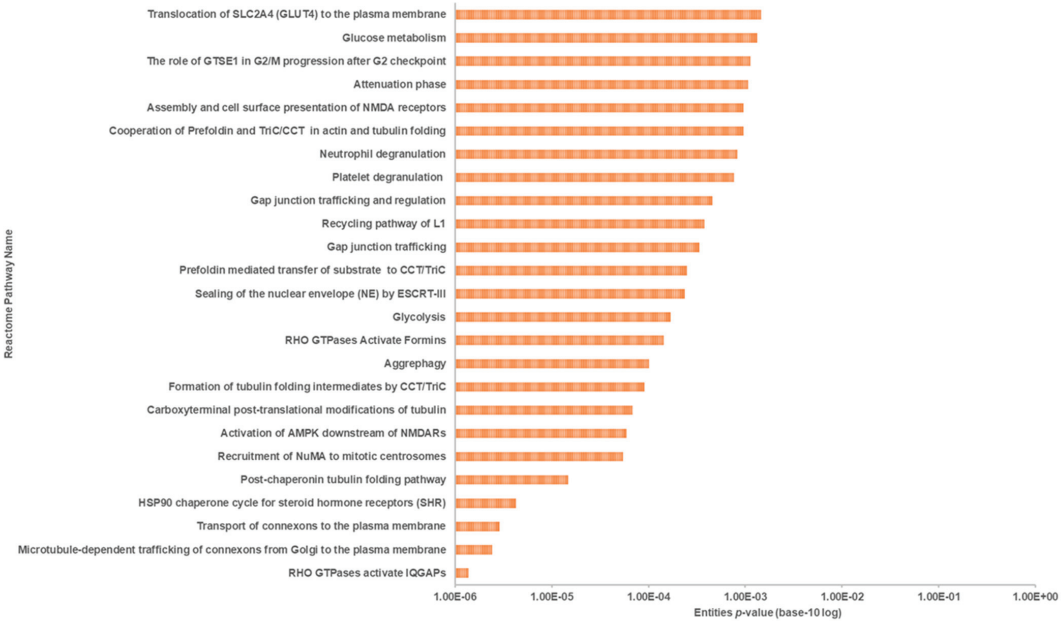


**Figure 11.** Classification of the 25 most relevant pathways sorted by false discovery rate (FDR) correction at $p < 0.05$ in the logarithmic scale (base 10) generated by the Reactome Pathway Browser (organism: *Homo sapiens*; Pair A, $H_2O_2$ vs. NC).

**Table 5.** Pathway hierarchy of the 25 most relevant pathways. Bold font indicates the top-level pathway hierarchy; bold and italic font indicates the sub-pathway hierarchy.

| Reactome Pathway Name | Reactome Pathway Identifier | Entities *p*-Value |
|---|---|---|
| **Signal transduction** | | |
| **Signaling by Rho GTPases** | | |
| RHO GTPases activate IQGAPs | R-HSA-5626467 | $1.38 \times 10^{-6}$ |
| RHO GTPases activate formins | R-HSA-5663220 | $1.45 \times 10^{-4}$ |
| **Vesicle-mediated transport** | | |
| **Membrane trafficking** | | |
| Microtubule-dependent trafficking of connexons from Golgi to the plasma membrane | R-HSA-190840 | $2.41 \times 10^{-6}$ |
| Transport of connexons to the plasma membrane | R-HSA-190872 | $2.87 \times 10^{-6}$ |
| Gap junction trafficking | R-HSA-190828 | $3.36 \times 10^{-4}$ |
| Gap junction trafficking and regulation | R-HSA-157858 | $4.56 \times 10^{-4}$ |
| Translocation of SLC2A4 (GLUT4) to the plasma membrane | R-HSA-1445148 | 0.001455 |
| **Cellular responses to external stimuli** | | |
| **Cellular responses to stress** | | |
| HSP90 chaperone cycle for steroid hormone receptors (SHRs) | R-HSA-3371497 | $4.24 \times 10^{-6}$ |
| Attenuation phase | R-HSA-3371568 | 0.001068 |
| **Metabolism of proteins** | | |
| **Protein folding** | | |
| Post-chaperonin tubulin folding pathway | R-HSA-389977 | $1.48 \times 10^{-5}$ |
| Formation of tubulin folding intermediates by CCT/TriC | R-HSA-389960 | $9.10 \times 10^{-5}$ |
| Prefoldin mediated transfer of substrate to CCT/TriC | R-HSA-389957 | $2.49 \times 10^{-4}$ |
| Cooperation of Prefoldin and TriC/CCT in actin and tubulin folding | R-HSA-389958 | $9.66 \times 10^{-4}$ |
| ***Post-translational protein modification*** | | |
| Carboxyterminal post-translational modifications of tubulin | R-HSA-8955332 | $6.85 \times 10^{-5}$ |
| **Cell cycle** | | |
| ***Cell cycle, mitotic*** | | |
| Recruitment of NuMA to mitotic centrosomes | R-HSA-380320 | $5.42 \times 10^{-5}$ |
| Sealing of the nuclear envelope (NE) by ESCRT-III | R-HSA-9668328 | $2.37 \times 10^{-4}$ |
| The role of GTSE1 in G2/M progression after G2 checkpoint | R-HSA-8852276 | 0.001135 |
| **Neuronal system** | | |
| ***Post N-methyl-D-aspartate (NMDA) receptor activation events*** | | |
| Activation of AMPK downstream of NMDARs | R-HSA-9619483 | $5.89 \times 10^{-5}$ |
| ***Activation of NMDA receptors and postsynaptic events*** | | |
| Assembly and cell surface presentation of NMDA receptors | R-HSA-9609736 | $9.66 \times 10^{-4}$ |
| **Autophagy** | | |
| ***Macroautophagy*** | | |
| Aggrephagy | R-HSA-9646399 | $1.02 \times 10^{-4}$ |
| **Metabolism** | | |
| ***Glucose metabolism*** | | |
| Glycolysis | R-HSA-70171 | $1.70 \times 10^{-4}$ |
| ***Metabolism of Carbohydrates*** | R-HSA-70326 | 0.001332 |
| Glucose metabolism | | |
| **Developmental biology** | | |
| ***Nervous system development*** | | |
| Recycling pathway of L1 | R-HSA-437239 | $3.81 \times 10^{-4}$ |
| **Haemostasis** | | |
| ***Response to elevated platelet cytosolic $Ca^{2+}$*** | | |
| Platelet degranulation | R-HSA-114608 | $7.68 \times 10^{-4}$ |
| **Immune system** | | |
| ***Innate immune system*** | | |
| Neutrophil degranulation | R-HSA-6798695 | $8.23 \times 10^{-4}$ |

In particular, to predict the protective mechanism of OSLP against $H_2O_2$ stress, the differentially expressed proteins in Pair B ($H_2O_2$ vs. OSLP treatment) were analyzed exclusively by Reactome Pathways. As per the analysis, the protein expression had a significant association with the 10 most relevant pathways ($p < 0.05$, Figure 12) out of the 56 pathways identified (see supplementary data, Pair B). They were interleukin-4 and interleukin-13 signaling (R-HSA-6785807), attenuation phase (R-HSA-3371568), formation of the cornified envelope (R-HSA-6809371), HSF1-dependent transactivation (R-HSA-3371571), HSP90 chaperone cycle for steroid hormone receptors (R-HSA-3371497), keratinization (R-HSA-6805567), influenza viral RNA transcription and replication (R-HSA-168273), resistance of ERBB2 KD mutants to sapitinib (R-HSA-9665244), resistance of ERBB2 KD mutants to trastuzumab (R-HSA-9665233), and resistance of ERBB2 KD mutants to afatinib (R-HSA-9665249). These pathways were associated with three top-level pathway hierarchies, encompassing the immune system, cellular responses to external stimuli, and developmental biology, and two disease pathways, namely, influenza infection and diseases of signal transduction by growth factor receptors and second messengers (Table 6).

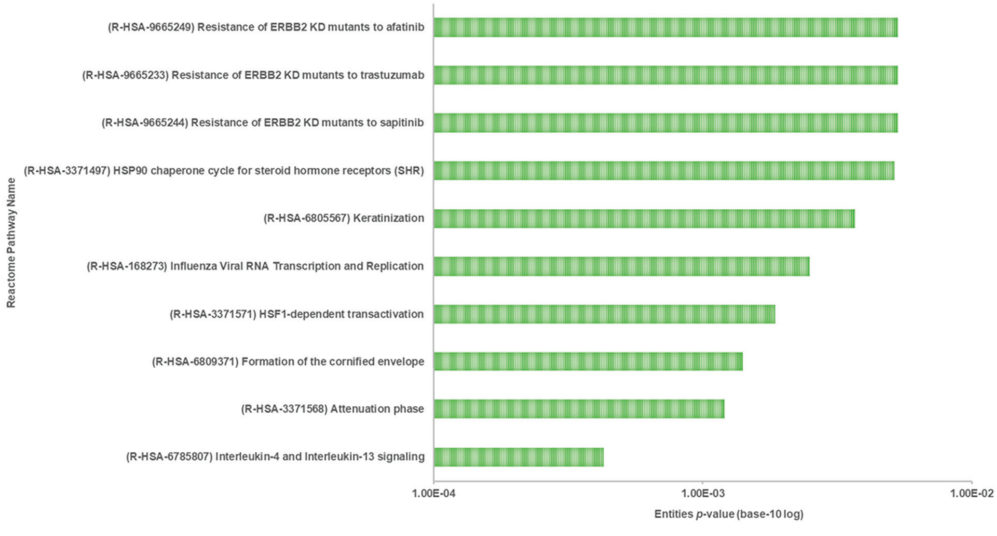


**Figure 12.** Classification of the 10 most relevant pathways sorted by false discovery rate (FDR) correction at $p < 0.05$ on the logarithmic scale (base 10) generated by the Reactome Pathway Browser (organism: *Homo sapiens*; Pair B, $H_2O_2$ vs. Treatment).

**Table 6.** Pathway hierarchy of the 10 most relevant pathways. Bold font indicates the top-level pathway hierarchy; bold and italic font indicates the sub-pathway hierarchy.

| Reactome Pathway Name | Reactome Pathway Identifier | Entities *p*-Value |
|---|---|---|
| **Immune system** | | |
| **Cytokine signaling in immune system** | | |
| Interleukin-4 and Interleukin-13 signaling | R-HSA-6785807 | $4.29 \times 10^{-4}$ |
| **Cellular responses to external stimuli** | | |
| **Cellular responses to stress** | | |
| HSF1-dependent transactivation | R-HSA-3371571 | 0.001867 |
| Attenuation phase | R-HSA-3371568 | 0.001204 |
| HSP90 chaperone cycle for steroid hormone receptors (SHRs) | R-HSA-3371497 | 0.005152 |
| **Developmental biology** | | |
| **Keratinisation** | | |
| Formation of the cornified envelope | R-HSA-6809371 | 0.001410 |
| Keratinisation | R-HSA-6805567 | 0.003672 |

**Table 6.** *Cont.*

| Reactome Pathway Name | Reactome Pathway Identifier | Entities *p*-Value |
|---|---|---|
| **Disease** | | |
| **Influenza infection** | | |
| Influenza Viral RNA Transcription and Replication | R-HSA-168273 | 0.002496 |
| **Diseases of signal transduction by growth factor receptors & second messengers** | | |
| Resistance of ERBB2 KD mutants to sapitinib | R-HSA-9665244 | 0.0053 |
| Resistance of ERBB2 KD mutants to trastuzumab | R-HSA-9665233 | 0.0053 |
| Resistance of ERBB2 KD mutants to afatinib | R-HSA-9665249 | 0.0053 |

Reactome is a database of reactions, pathways, and biological processes. It provides a graphical map showing signaling and metabolic molecules and their relationships. It is also an interactive interface that gives detailed information on components and their relationships to support data visualization, interpretation, and analysis (https://reactome.org/what-is-reactome dated 13th March 2020). Figures 13 and 14 show the two pathways, namely, attenuation phase (R-HSA-3371568) and HSP90 chaperone cycle for steroid hormone receptors (R-HSA-3371497), acting on cellular responses to stress. They were found in both Pairs A and B. Exclusively, Reactome Pathways has predicted interleukin-4 and interleukin-13 signaling (R-HSA-6785807) as the most relevant pathway in Pair B (Figure 15).

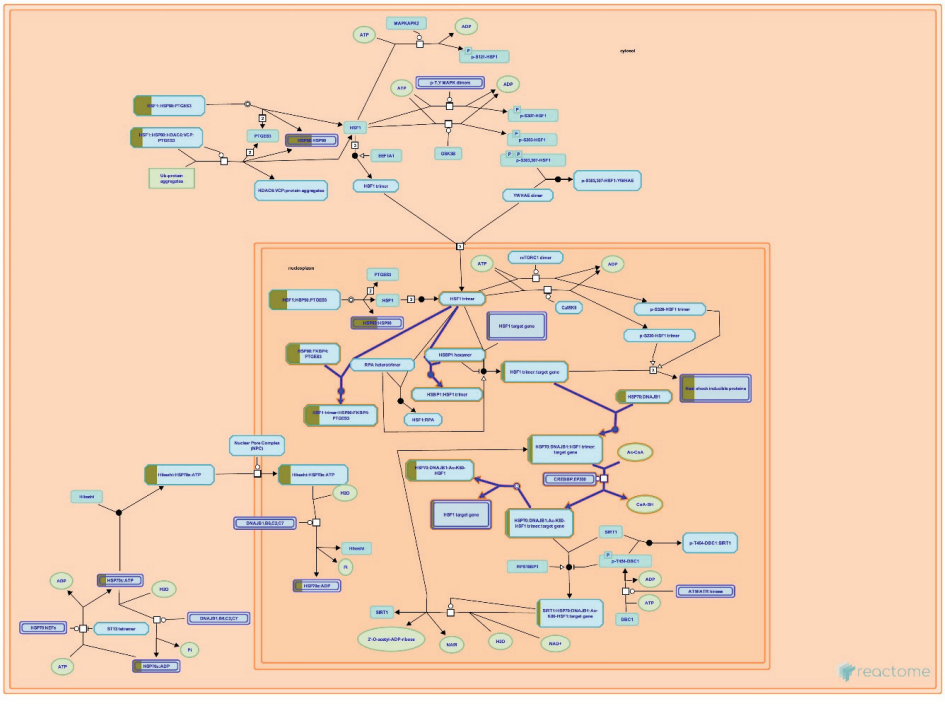


**Figure 13.** HSP90AA1 (also known as heat shock protein 90) and HSPA8 (also known as heat shock protein family A (Hsp70) member 8 or HSP70), highlighted in yellow, were mapped onto the attenuation phase pathway sorted by false discovery rate (FDR) correction at $p < 0.05$ on the logarithmic scale (base 10) generated by the Reactome Pathway Browser (organism: *Homo sapiens*).

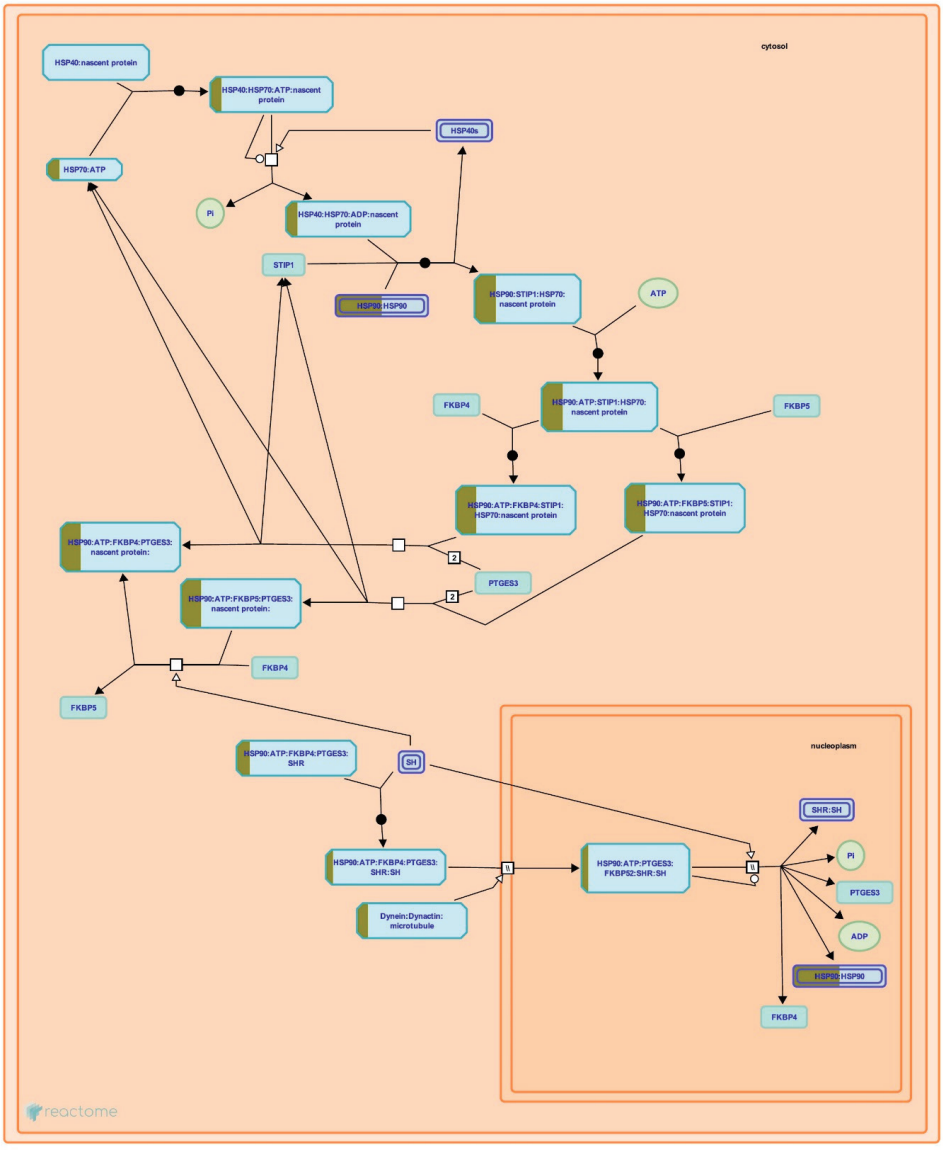


**Figure 14.** HSP90AA1 (also known as heat shock protein 90) and HSPA8 (also known as heat shock protein family A (Hsp70) member 8 or HSP70), highlighted in yellow, were mapped onto the HSP90 chaperone cycle for steroid hormone receptors (SHRs) pathway, sorted by false discovery rate (FDR) correction at $p < 0.05$ on the logarithmic scale (base 10) generated by the Reactome Pathway Browser (organism: *Homo sapiens*).

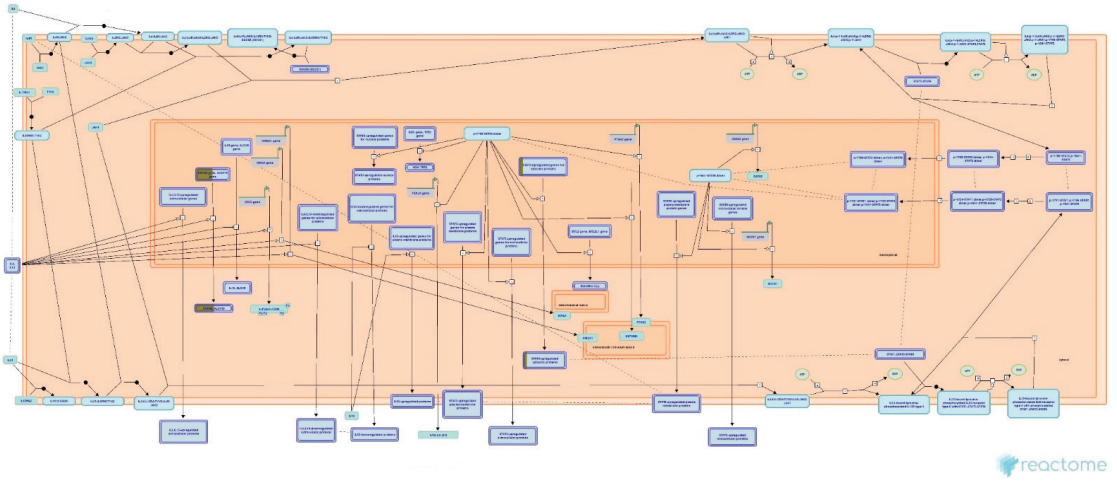


**Figure 15.** HSPA8 (also known as heat shock protein family A (Hsp70) member 8 or HSP70) and HSP90AA1 (also known as heat shock protein 90, as part of STAT3-upregulated genes for cytosolic proteins and STAT3-upregulated cytosolic proteins), highlighted in yellow, were mapped onto the signaling of interleukin-4 and interleukin-13 pathway, sorted by false discovery rate (FDR) correction at $p < 0.05$ on the logarithmic scale (base 10) generated by the Reactome Pathway Browser (organism: *Homo sapiens*).

## 4. Discussion

Evaluation of the cytotoxic effects of OSLPs on SH-SY5Y cells (24 and 48 h) in this study found that OSLP at concentrations of 25, 50, 125, 250, 500, and 1000 µg/mL did not challenge the survival of SH-SY5Y cells. Therefore, OSLP (25, 50, 125, 250, 500, and 1000) is considered safe for SH-SY5Y cells. In addition, the MNTD and MTD of OSLP at 24 h treatment were determined as 2000 and 4000 µg/mL, respectively. In contrast, the MNTD and MTD of OSLP at 48 h treatment were determined as 1000 and 2000 µg/mL, respectively. MNTD (the maximal non-toxic dose) represents the highest concentration that does not cause cytotoxic effects in a treated cell population, whilst the MTD (the minimal toxic dose) represents the lowest concentration that causes cytotoxic effects in a treated cell population [28]. On top of that, OSLP at 10 mg/mL has been found in this study to be potentially cytotoxic to SH-SY5Y cells. Based on these findings, OSLP (25, 50, 125, 250, 500, and 1000) is used in the evaluation of OSLP-protective effects on SH-SY5Y cells.

Hydrogen peroxide ($H_2O_2$) induction challenged the survival of SH-SY5Y cells. SH-SY5Y cell survival decreased when $H_2O_2$ concentrations increased. $H_2O_2$ at about 150 µM sufficiently inhibited the cell population by half. Concentrations higher than 250 µM were found to sufficiently inhibit the cell population by close to 90%. Based on these findings, the $IC_{50}$ in this study was determined at 150 µM, whereas the $IC_{90}$ was 250 µM and above. The half-maximal inhibitory concentration ($IC_{50}$) represents the dose that inhibits a cell population by half, while the maximal inhibitory concentration ($IC_{90}$) represents the dose that inhibits a cell population by 90% [29]. Therefore, 150 µM of $H_2O_2$ is used in the following evaluation of the protective effects of OSLP on SH-SY5Y cells.

The protective effects of OSLP were evaluated in $H_2O_2$-induced SH-SY5Y cells. $H_2O_2$ induction (150 µM) challenged the survival of SH-SY5Y cells. OSLP treatments exhibited protection against $H_2O_2$ induction in a concentration-dependent manner. OSLP at 125 µg/mL was found to be the lowest treatment dose showing protection against $H_2O_2$ stress. Pre-treatment with 125 µg/mL of OSLP increased the survival of SH-SY5Y cells (by about 30%) compared to the $H_2O_2$ group, although it did not attain statistical significance. Pre-treatments with OSLP at these three concentrations, 250, 500, and 1000 µg/mL, significantly increased the survival of SH-SY5Y cells, with an increase of 39%, 51%, and

57%, respectively, compared to the $H_2O_2$ group. In particular, pre-treatments with 500 and 1000 μg/mL of OSLP demonstrated apparent inhibitions of $H_2O_2$. Such observations suggest that OSLP at these concentrations (250 μg/mL or higher) could potentially inhibit the actions of $H_2O_2$ and, additionally, could promote the growth of SH-SY5Y cells. In line with the bright-field microscopic images obtained, OSLP pre-treatments at 250, 500, and 1000 μg/mL have seen improvements in cell architecture. OSLP-treated $H_2O_2$-induced SH-SY5Y cells showed reduced clumping and shrinkage (i.e., round up), with apparent neurite formations and pyramidal-shaped cells. In contrast, $H_2O_2$-treated cells showed shrinkage, round up, and clumping, all of which are indicative of unhealthy cell appearance, loss of cell viability, and progression towards death [20,30–33]. Additionally, $H_2O_2$-treated cells showed a decline in the population; in contrast, OSLP pre-treatments showed an increase in the cell population.

Taken together, the outcomes of in vitro assays collectively suggest that OSLP (250, 500, and 1000 μg/mL) could have neuroprotective potential with considerably low cytotoxic effects.

Proteomic analysis has identified a distinct protein expression pattern, where all the proteins are highly expressed in $H_2O_2$ (SH-SY5Y cells induced by 150 μM $H_2O_2$) compared to NC (SH-SY5Y cells without $H_2O_2$ induction and OSLP treatment). This observation is not seen in the OSLP-treated SH-SY5Y cells, with the majority of proteins expressed at lower levels compared to the $H_2O_2$-treated samples. Using functional annotation analysis, the top ten enriched terms in cellular components, molecular functions, and biological processes were identified (Figure 10). The ten selected enriched terms were significant associated with 25 cellular signaling pathways, as suggested by a Reactome Pathways analysis (Figure 11 and Table 5). Additionally, the Reactome Pathways analysis predicted the top ten cellular signaling pathways most likely modulated by OSLP treatment (Figure 12 and Table 6).

In the SH-SY5Y cells, $H_2O_2$ induction could have triggered cellular stress signaling via two main pathways: "attenuation phase" and "HSP90 chaperone cycle for steroid hormone receptors" (Figures 13 and 14). The modulations of these pathways are particularly related to two major heat shock proteins, HSPA8 (also known as heat shock protein family A (Hsp70) member 8 or HSP70) and HSP90AA1 (also known as heat shock protein 90), act together as machinery to modulate the folding of proteins. Studies have shown that most cellular proteins do not activate the HSP90/HSP70-based chaperone machinery for folding, stabilization, and trafficking under normal physiological conditions; following stress, the function of HSP90/HSP70-based chaperone machinery is disrupted [34–36]. The HSP90/HSP70-based chaperone machinery can influence a wide variety of client proteins and, thus, affect numerous important cellular pathways, such as protein conformational cycles, co-chaperone interactions, inter-domain communications, protein conformational stability, trafficking and turnover; signal transduction, intracellular transport [34,35,37,38], synaptic transmissions [39–42], and inflammation [36,43]. Additionally, studies have shown that activations of HSP70 and HSPB1 (also known as HSP27), following exposure to stress, manipulate the heat shock transcriptional response and its client proteins; under normal physiological conditions, these ATP-independent chaperones (HSP70 and HSPB1) provide a wide variety of protections. To name a few, these chaperones prevent the accumulation of improperly folded proteins, participate in the regulated degradation of misfolded proteins, protect the cytoskeleton, are involved in cellular metabolism, and decrease stress-induced apoptosis [44–46] in addition to preventing synaptic loss and neuronal death [47].

In this study, HSP90, HSP70, and HSPB1 had higher expressions in the $H_2O_2$ control (induced by $H_2O_2$ alone) compared to the normal control (without $H_2O_2$ induction). Therefore, it is suggested that both impaired the HSP90/HSP70-based chaperone machinery and that HSPB1 activation could have altered, direct or indirectly, a variety of cellular processes in the neuronal cells. In particular, these alterations include neuronal regulation in terms of growth, development, and death; neuronal architecture of cytoskeletons, cytoskeletal dynamics, and cytoskeletal protein expressions [34–36]; excitatory postsynaptic transmission activated by NMDA receptors; cellular metabolism, especially glucose and proteins; protein conformations; stabilization and post-translational modifications, as well

as inflammatory responses (Figure 11 and Table 5) [44–46]. Alterations, as such, are some common themes found in neurodegenerative diseases and neurological disorders.

In the SH-SY5Y cells, OSLP treatment might help buffer against cellular stress signaling chiefly via the "signaling of interleukin-4 and interleukin-13" (IL-4/-13 signaling, R-HSA-6785807) pathway (Figure 15). Within the CNS, HSPs are released from stressed or damaged cells, and they act as local "danger signals" that trigger inflammatory responses. OSLP might modulate the expression of IL-4/IL-13 by affecting the interaction of HSP90, with downstream targets such as HSP8 and the cytoplasmic protein arachidonate 15-lipoxygenase (ALOX15). In the expression of IL-4/-13, HSP90 is one of the genes for cytoplasmic proteins upregulated by signal transducer and activator of transcription 3 (STAT3). Via phosphorylation of STAT3 and signal transducer and activator of transcription 6 (STAT6), HSP8 participates in the downregulation of extracellular proinflammatory signal transducers, including ALOX15. Most likely, by modulating the "IL-4/-13 signaling" pathway, OSLP promotes the neuroprotective effects of IL-4 and IL-13, acting as anti-inflammatory cytokines [48,49], or IL-4 alone acts directly as a cytoprotective cytokine [50]. For instance, IL-4 and IL-13 induce the alternative activation of microglia (also known as the M2 state) to protect against neuronal damage in the hippocampus and the cortex in experimental models of ischemic stress [51,52]. Specifically, IL-13 alone has shown anti-inflammatory ability in a mouse model of cerebral ischemia [53]. In contrast, a study on humans with multiple sclerosis found high levels of IL-13-enhanced gamma-aminobutyric acid (GABA, the dominant inhibitory neurotransmitter) over glutamate transmission [54]. Otherwise, low levels of IL-4 in epileptic patients have been shown to decrease inflammation-related epilepsy [55,56].

Additionally, OSLP treatment might also protect against cellular-stress-mediated pathways, including "attenuation phase" (R-HSA-3371568) and "HSP90 chaperone cycle for steroid hormone receptors" (R-HSA-3371497) pathways (Figures 13 and 14). Via the "attenuation phase" pathway, OSLP might modulate the downstream interaction of HSP70 and its co-chaperone HSP40 with CoREST (transcriptional corepressor for repressor element 1-silencing transcription factor) at the negative-feedback loop. This negative feedback loop provides an important mechanism by which cells can regulate the activation and attenuation of heat shock factor 1 (HSF1) via the presence and concentration of HSPs in the cell. OSLP might also regulate SHR–protein interactions via the "HSP90 chaperone cycle for steroid hormone receptors" pathway. Upon the upstream activations of HSP40, HSP70, and stress-induced-phosphoprotein 1 (STIP1), respectively, HSP90 binds to the downstream co-chaperones FK506 binding protein 5 (FKBP51 and FKBP52) and prostaglandin E synthase 3 (PTGES3). The HSP90 and chaperone-mediated conformational changes are required to keep SHRs in a ligand-binding-competent state. In this regard, OSLP could have promoted the cytoprotective functions of HSPs as an alternative to neuroprotection [57]. For instance, HSPs and their respective co-chaperones facilitate native protein stabilization, translocation, re-folding, and degradation in response to stressful stimuli. HSP-based chaperone machinery not only ensures protein quality control but also prevents protein aggregation that would otherwise overwhelm the cell and lead to programmed cell death (apoptosis) or necrosis in unfavorable conditions [58,59]. In recent times, HSPs have demonstrated their ability to fine-tune inflammation in the CNS [43]. For instance, HSPs have been shown to assist in the protection of motor neurons and to prevent chronic inflammation after spinal cord injuries in animal models [60,61].

Last but not least, the changes in both KRT8 and KRT19 are also worthy of mention. They are keratins; KRT8 is a member of the type II keratin family, and KRT19 belongs to the type I family. The intermediate filament (IF) cytoskeleton of all epithelia is built from type I and type II keratins. Keratins not only maintain structural rigidity and stability, they also provide resistance to environmental stress [62]. In the presence of $H_2O_2$ stress, the keratin network organization in the cytoskeleton can be altered. The altered expression of keratins has an impact on the keratin network organization and has been associated

with inflammation, cellular stress, epithelial barrier defects, and higher sensitivity to tumor necrosis factor (TNF)-induced cell death [63–65].

Taken together, the protein expression study and bioinformatics analysis collectively suggest that OSLP could protect neuronal cells against inflammation and cellular stress. The neuroprotective potential of OSLP can be attributed to an assortment of proteins present in the crude. For instance, baicalein 7-O-glucuronosyltransferase and its glucoronosylated baicalein have been reported to possess anti-inflammatory, antioxidative, and neuroprotective [66] as well as anticonvulsive activities [67]; baicalin biosynthesized by baicalin-beta-D-glucuronidase has shown antioxidant activity [68,69]; rosmarinic acid biosynthesized by rosmarinate synthase have attracted interest for being anti-inflammatory, antioxidant, antiangiogenic, antitumor, antimicrobial [70] and antiseizure [71].

## 5. Concluding Remarks

The study suggests that OSLP could be a potential neuroprotective agent. Its neuroprotective potential is attributed to the ability of OSLP to modulate the "signaling of interleukin-4 and interleukin-13" pathway as the predominant mode of action and, thereby, activate anti-inflammatory cytokines to protect against proinflammatory responses under stress conditions. OSLP also modulates the "attenuation phase" and "HSP90 chaperone cycle for steroid hormone receptors" pathways to counteract HSP-induced damage under stress conditions. OSLP is, therefore, worthy of detailed investigations.

**Supplementary Materials:** The following are available online at https://www.mdpi.com/article/10.3390/life11060585/s1, Table S1: List of the total identified protein compositions of OSLP (both in-solution and in-gel digestions) using shotgun-ESI-LC-MS/MS approach. The annotations were retrieved from the databases of UniProtKB (http://www.uniprot.org/uniprot/, accessed on 19 June 2021) and NCBInr (https://www.ncbi.nlm.nih.gov/, accessed on 19 June 2021).

**Author Contributions:** Y.-S.C. was responsible for the design and execution of all the experiments and data analyses and the writing of the final manuscript. P.K.A. aided in supervision and provided monetary funds to the final manuscript. M.F.S. and I.O. contributed to the design of the study, supervised all aspects, provided critical feedback, and edited the final manuscript, as submitted. All authors have read and agreed to the published version of the manuscript.

**Funding:** This research was funded by the Global Asia in the 21st Century (GA21) Platform, Monash University Malaysia (research grant GA-HW-18-L04) and the NKEA EPP#1 Research Grant Scheme (NRGS) (NH1014D066), Ministry of Agriculture and Agro-based Industry, Malaysia.

**Institutional Review Board Statement:** Not applicable.

**Informed Consent Statement:** Not applicable.

**Data Availability Statement:** Data is contained within the article or supplementary material The data presented in this study are available in S1.

**Acknowledgments:** The authors would like to thank Kim-Sang Tang and Jey-Sern Tan for cell culture knowledge (School of Pharmacy), Syafiq Asnawi Zainal Abidin for ESI-LCMS/MS technical support (LC-MS laboratory of the Jeffrey Cheah School of Medicine and Health Sciences), and Brandon Kar-Meng Choo for providing a critical review of the final manuscript, as submitted, and unconditional support to our research.

**Conflicts of Interest:** The authors declare no conflict of interest. The funders had no role in the design of the study; in the collection, analyses, or interpretation of data; in the writing of the manuscript, or in the decision to publish the results.

## References

1. WHO. Neurological Disorders Public Health Challenges. *Scitech Book News* **2007**, *31*, 7–25.
2. Feigin, V.L.; Abajobir, A.A.; Abate, K.H.; Abd-Allah, F.; Abdulle, A.M.; Abera, S.F.; Abyu, G.Y.; Ahmed, M.B.; Aichour, A.N.; Aichour, I.; et al. Global, regional, and national burden of neurological disorders during 1990–2015: A systematic analysis for the Global Burden of Disease Study 2015. *Lancet Neurol.* **2017**, *16*, 877–897. [CrossRef]

3. Jellinger, K.A. Basic mechanisms of neurodegeneration: A critical update. *J. Cell. Mol. Med.* **2010**, *14*, 457–487. [CrossRef] [PubMed]
4. Vajda, F.J.E. Neuroprotection and neurodegenerative disease. In *Alzheimer's Disease*; Springer: Berlin/Heidelberg, Germany, 2004; pp. 235–243.
5. Lin, X.; Zhang, N. Berberine: Pathways to protect neurons. *Phytother. Res.* **2018**, *32*, 1501–1510. [CrossRef] [PubMed]
6. Rehman, M.U.; Wali, A.F.; Ahmad, A.; Shakeel, S.; Rasool, S.; Ali, R.; Rashid, S.M.; Madkhali, H.; Ganaie, M.A.; Khan, R. Neuroprotective Strategies for Neurological Disorders by Natural Products: An update. *Curr. Neuropharmacol.* **2019**, *17*, 247–267. [CrossRef] [PubMed]
7. Clark, A.I.; Vissel, B. Excess cerebral TNF causing glutamate excitotoxicity rationalizes treatment of neurodegenerative diseases and neurogenic pain by anti-TNF agents. *J. Neuroinflamm.* **2016**, *13*, 236. [CrossRef]
8. Lalkovičová, M.; Danielisová, V. Neuroprotection and antioxidants. *Neural Regen. Res.* **2016**, *11*, 865. [CrossRef]
9. Schapira, A.H. Neuroprotection in Parkinson's disease. In *Blue Books of Neurology*; Elsevier: Amsterdam, The Netherlands, 2010; pp. 301–320.
10. Adnyana, I.K.; Setiawan, F.; Insanu, M. From ethnopharmacology to clinical study of Orthosiphon stamineus Benth. *Int. J. Pharm. Pharm. Sci.* **2013**, *5*, 66.
11. Ameer, O.Z.; Salman, I.M.; Asmawi, M.Z.; Ibraheem, Z.O.; Yam, M.F. Orthosiphon stamineus: Traditional uses, phytochemistry, pharmacology, and toxicology. *J. Med. Food.* **2012**, *15*, 678–690. [CrossRef]
12. Chung, Y.S.; Choo, B.K.M.; Ahmed, P.K.; Othman, I.; Shaikh, M.F. A Systematic Review of the Protective Actions of Cat's Whiskers (Misai Kucing) on the Central Nervous System. *Front. Pharmacol.* **2020**, *11*, 692. [CrossRef]
13. Chung, Y.S.; Choo, B.K.M.; Ahmed, P.K.; Othman, I.; Shaikh, M. Orthosiphon stamineus Proteins Alleviate Pentylenetetrazol-Induced Seizures in Zebrafish. *Biomedicines* **2020**, *8*, 191. [CrossRef]
14. Aebersold, R.; Mann, M. Mass-spectrometric exploration of proteome structure and function. *Nature* **2016**, *537*, 347–355. [CrossRef] [PubMed]
15. Patterson, S.D.; Aebersold, R.H. Proteomics: The first decade and beyond. *Nat. Genet.* **2003**, *33*, 311–323. [CrossRef] [PubMed]
16. Fabregat, A.; Jupe, S.; Matthews, L.; Sidiropoulos, K.; Gillespie, M.; Garapati, P.; Haw, R.; Jassal, B.; Korninger, F.; May, B.; et al. The Reactome Pathway Knowledgebase. *Nucleic Acids Res.* **2018**, *46*, D649–D655. [CrossRef] [PubMed]
17. Fabregat, A.; Sidiropoulos, K.; Viteri, G.; Forner, O.; Marin-Garcia, P.; Arnau, V.; D'Eustachio, P.; Stein, L.; Hermjakob, H. Reactome pathway analysis: A high-performance in-memory approach. *BMC Bioinform.* **2017**, *18*, 142. [CrossRef] [PubMed]
18. Poonia, S.; Chawla, S.; Kaushik, S.; Sengupta, D. Pathway Informatics. In *Encyclopedia of Bioinformatics and Computational Biology*; Ranganathan, S., Nakai, K., Schonbach, C., Eds.; Academic Press: Oxford, UK, 2019; pp. 796–804.
19. Kovalevich, J.; Langford, D. Considerations for the Use of SH-SY5Y Neuroblastoma Cells in Neurobiology. *Methods Mol. Biol.* **2013**, *1078*, 9–21. [PubMed]
20. Shipley, M.M.; Mangold, C.A.; Szpara, M.L. Differentiation of the SH-SY5Y Human Neuroblastoma Cell Line. *J. Vis. Exp. JoVE* **2016**, 53193. [CrossRef]
21. Feeney, C.J.; Frantseva, M.V.; Carlen, P.L.; Pennefather, P.S.; Shulyakova, N.; Shniffer, C.; Mills, L.R. Vulnerability of glial cells to hydrogen peroxide in cultured hippocampal slices. *Brain Res.* **2008**, *1198*, 1–15. [CrossRef]
22. van der Vliet, A.; Janssen-Heininger, Y.M.W. Hydrogen peroxide as a damage signal in tissue injury and inflammation: Murderer, mediator, or messenger? *J. Cell. Biochem.* **2014**, *115*, 427–435. [CrossRef]
23. Wittmann, C.; Chockley, P.; Singh, S.K.; Pase, L.; Lieschke, G.J.; Grabher, C. Hydrogen Peroxide in Inflammation: Messenger, Guide, and Assassin. *Adv. Hematol.* **2012**, *2012*, 541471. [CrossRef]
24. Smaczniak, C.; Li, N.; Boeren, S.; America, T.; Van Dongen, W.; Goerdayal, S.S.; De Vries, S.; Angenent, G.C.; Kaufmann, K. Proteomics-based identification of low-abundance signaling and regulatory protein complexes in native plant tissues. *Nat. Protoc.* **2012**, *7*, 2144. [CrossRef]
25. Isaacson, T.; Damasceno, C.M.; Saravanan, R.S.; He, Y.; Catalá, C.; Saladié, M.; Rose, J.K. Sample extraction techniques for enhanced proteomic analysis of plant tissues. *Nat. Protoc.* **2006**, *1*, 769. [CrossRef]
26. Salem, M.A.; Jüppner, J.; Bajdzienko, K.; Giavalisco, P. Protocol: A fast, comprehensive and reproducible one-step extraction method for the rapid preparation of polar and semi-polar metabolites, lipids, proteins, starch and cell wall polymers from a single sample. *Plant Methods* **2016**, *12*, 45. [CrossRef]
27. Zhang, J.; Xin, L.; Shan, B.; Chen, W.; Xie, M.; Yuen, D.; Zhang, W.; Zhang, Z.; Lajoie, G.A.; Ma, B. PEAKS DB: De Novo sequencing assisted database search for sensitive and accurate peptide identification. *Mol. Cell. Proteom.* **2011**, *11*, M111-010587.
28. Chevret, S. Maximum Tolerable Dose (MTD). In *Wiley StatsRef: Statistics Reference Online*; Balakrishnan, N., Colton, T., Everitt, B., Piegorsch, W., Ruggeri, F., Teugels, J.L., Eds.; John Wiley & Sons: Chichester, UK, 2014.
29. Marques, J.; Vilanova, E.; Mourão, P.A.; Fernàndez-Busquets, X. Marine organism sulfated polysaccharides exhibiting significant antimalarial activity and inhibition of red blood cell invasion by Plasmodium. *Sci. Rep.* **2016**, *6*, 24368. [CrossRef]
30. Encinas, M.; Iglesias, M.; Liu, Y.; Wang, H.; Muhaisen, A.; Cena, V.; Gallego, C.; Comella, J.X. Sequential Treatment of SH-SY5Y Cells with Retinoic Acid and Brain-Derived Neurotrophic Factor Gives Rise to Fully Differentiated, Neurotrophic Factor-Dependent, Human Neuron-Like Cells. *J. Neurochem.* **2000**, *75*, 991–1003. [CrossRef] [PubMed]
31. Sree, N.V.; Sri, P.U.; Ramarao, N. Neuro-Protective Properties Of Orthosiphon Staminus (Benth) Leaf Methanolic Fraction Through Antioxidant Mechanisms On SH-SY5Y Cells: An In-Vitro Evaluation. *Int. J. Pharm. Sci. Res.* **2015**, *6*, 1115.

32. Forster, J.I.; Köglsberger, S.; Trefois, C.; Boyd, O.; Baumuratov, A.S.; Buck, L.; Balling, R.; Antony, P.M.A. Characterization of Differentiated SH-SY5Y as Neuronal Screening Model Reveals Increased Oxidative Vulnerability. *J. Biomol. Screen.* **2016**, *21*, 496–509. [CrossRef] [PubMed]
33. Zhang, Y.; Jiao, G.; Song, C.; Gu, S.; Brown, R.E.; Zhang, J.; Zhang, P.; Gagnon, J.; Locke, S.; Stefanova, R.; et al. An Extract from Shrimp Processing By-Products Protects SH-SY5Y Cells from Neurotoxicity Induced by Aβ25–35. *Mar. Drugs* **2017**, *15*, 83. [CrossRef]
34. Pratt, W.B.; Morishima, Y.; Peng, H.M.; Osawa, Y. Proposal for a role of the Hsp90/Hsp70-based chaperone machinery in making triage decisions when proteins undergo oxidative and toxic damage. *Exp. Biol. Med.* **2010**, *235*, 278–289. [CrossRef]
35. Picard, D. Heat-shock protein 90, a chaperone for folding and regulation. *Cell. Mol. Life Sci. CMLS* **2002**, *59*, 1640–1648. [CrossRef] [PubMed]
36. Sevin, M.; Girodon, F.; Garrido, C.; De Thonel, A. HSP90 and HSP70: Implication in Inflammation Processes and Therapeutic Approaches for Myeloproliferative Neoplasms. *Mediat. Inflamm.* **2015**, *2015*, 970242. [CrossRef] [PubMed]
37. Li, J.; Soroka, J.; Buchner, J. The Hsp90 chaperone machinery: Conformational dynamics and regulation by co-chaperones. *Biochim. Biophys. Acta BBA Mol. Cell Res.* **2012**, *1823*, 624–635. [CrossRef] [PubMed]
38. Stankiewicz, T.R.; Linseman, D.A. Rho family GTPases: Key players in neuronal development, neuronal survival, and neurodegeneration. *Front. Cell. Neurosci.* **2014**, *8*, 314. [CrossRef]
39. Chen, Y.; Wang, B.; Liu, D.; Li, J.J.; Xue, Y.; Sakata, K.; Zhu, L.Q.; Heldt, S.A.; Xu, H.; Liao, F.F. Hsp90 chaperone inhibitor 17-AAG attenuates Aβ-induced synaptic toxicity and memory impairment. *J. Neurosci.* **2014**, *34*, 2464–2470. [CrossRef]
40. Garcia, S.M.; Casanueva, M.O.; Silva, M.C.; Amaral, M.D.; Morimoto, R.I. Neuronal signaling modulates protein homeostasis in Caenorhabditis elegans post-synaptic muscle cells. *Genes Dev.* **2007**, *21*, 3006–3016. [CrossRef]
41. Gerges, N.Z.; Tran, I.C.; Backos, D.S.; Harrell, J.M.; Chinkers, M.; Pratt, W.B.; Esteban, J.A. Independent Functions of hsp90 in Neurotransmitter Release and in the Continuous Synaptic Cycling of AMPA Receptors. *J. Neurosci.* **2004**, *24*, 4758–4766. [CrossRef]
42. Zhang, Y.; Liu, J.; Luan, G.; Wang, X. Inhibition of the small GTPase Cdc42 in regulation of epileptic-seizure in rats. *Neuroscience* **2015**, *289*, 381–391. [CrossRef]
43. Dukay, B.; Csoboz, B.; Tóth, M.E. Heat-Shock Proteins in Neuroinflammation. *Front. Pharmacol.* **2019**, *10*, 920. [CrossRef]
44. Weeks, S.D.; Muranova, L.K.; Heirbaut, M.; Beelen, S.; Strelkov, S.V.; Gusev, N.B. Characterization of human small heat shock protein HSPB1 α-crystallin domain localized mutants associated with hereditary motor neuron diseases. *Sci. Rep.* **2018**, *8*, 688. [CrossRef]
45. Etienne-Manneville, S.; Hall, A. Rho GTPases in cell biology. *Nature* **2002**, *420*, 629–635. [CrossRef]
46. Henstridge, D.C.; Whitham, M.; Febbraio, M.A. Chaperoning to the metabolic party: The emerging therapeutic role of heat-shock proteins in obesity and type 2 diabetes. *Mol. Metab.* **2014**, *3*, 781–793. [CrossRef] [PubMed]
47. Taylor, J.P.; Hardy, J.; Fischbeck, K.H. Toxic proteins in neurodegenerative disease. *Science* **2002**, *296*, 1991–1995. [CrossRef] [PubMed]
48. Mori, S.; Maher, P.; Conti, B. Neuroimmunology of the Interleukins 13 and 4. *Brain Sci.* **2016**, *6*, 18. [CrossRef]
49. McCormick, S.; Heller, N.M. Commentary: IL-4 and IL-13 receptors and signaling. *Cytokine* **2015**, *75*, 38–50. [CrossRef] [PubMed]
50. Walsh, J.T.; Hendrix, S.; Boato, F.; Smirnov, I.; Zheng, J.; Lukens, J.R.; Gadani, S.; Hechler, D.; Gölz, G.; Rosenberger, K.; et al. MHCII-independent CD4+ T cells protect injured CNS neurons via IL-4. *J. Clin. Investig.* **2015**, *125*, 699–714. [CrossRef]
51. Yu, J.T.; Lee, C.H.; Yoo, K.Y.; Choi, J.H.; Li, H.; Park, O.K.; Yan, B.; Hwang, I.K.; Kwon, Y.G.; Kim, Y.M.; et al. Maintenance of anti-inflammatory cytokines and reduction of glial activation in the ischemic hippocampal CA1 region preconditioned with lipopolysaccharide. *J. Neurol. Sci.* **2010**, *296*, 69–78. [CrossRef]
52. Zhao, X.; Wang, H.; Sun, G.; Zhang, J.; Edwards, N.J.; Aronowski, J. Neuronal Interleukin-4 as a Modulator of Microglial Pathways and Ischemic Brain Damage. *J. Neurosci.* **2015**, *35*, 11281–11291. [CrossRef]
53. Kolosowska, N.; Keuters, M.H.; Wojciechowski, S.; Keksa-Goldsteine, V.; Laine, M.; Malm, T.; Goldsteins, G.; Koistinaho, J.; Dhungana, H. Peripheral Administration of IL-13 Induces Anti-inflammatory Microglial/Macrophage Responses and Provides Neuroprotection in Ischemic Stroke. *Neurotherapeutics* **2019**, *16*, 1304–1319. [CrossRef]
54. Rossi, S.; Mancino, R.; Bergami, A.; Mori, F.; Castelli, M.; De Chiara, V.; Studer, V.; Mataluni, G.; Sancesario, G.; Parisi, V.; et al. Potential role of IL-13 in neuroprotection and cortical excitability regulation in multiple sclerosis. *Mult. Scler. J.* **2011**, *17*, 1301–1312. [CrossRef]
55. Strauss, K.I.; Elisevich, K.V. Brain region and epilepsy-associated differences in inflammatory mediator levels in medically refractory mesial temporal lobe epilepsy. *J. Neuroinflamm.* **2016**, *13*, 270. [CrossRef]
56. Liu, H.; Prayson, R.A.; Estes, M.L.; Drazba, J.A.; Barnett, G.H.; Bingaman, W.; Liu, J.; Jacobs, B.S.; Barna, B.P. In vivo expression of the interleukin 4 receptor alpha by astrocytes in epilepsy cerebral cortex. *Cytokine* **2000**, *12*, 1656–1661. [CrossRef] [PubMed]
57. Wong, H.R. Endogenous Cytoprotective Mechanisms. In *NeuroImmune Biology*; Bertók, L., Chow, D.A., Eds.; Elsevier: Amsterdam, The Netherlands, 2005; pp. 49–65.
58. Miller, D.; Fort, P.E. Heat Shock Proteins Regulatory Role in Neurodevelopment. *Front. Neurosci.* **2018**, *12*, 821. [CrossRef] [PubMed]
59. Pratt, W.B.; Gestwicki, J.E.; Osawa, Y.; Lieberman, A.P. Targeting Hsp90/Hsp70-based protein quality control for treatment of adult onset neurodegenerative diseases. *Annu. Rev. Pharmacol. Toxicol.* **2015**, *55*, 353–371. [CrossRef] [PubMed]

60. Reddy, S.J.; La Marca, F.; Park, P. The role of heat shock proteins in spinal cord injury. *Neurosurg. Focus* **2008**, *25*, E4. [CrossRef]
61. Zhou, Z.B.; Huang, G.X.; Lu, J.J.; Ma, J.; Yuan, Q.J.; Cao, Y.; Zhu, L. Up-regulation of heat shock protein 27 inhibits apoptosis in lumbosacral nerve root avulsion-induced neurons. *Sci. Rep.* **2019**, *9*, 11468. [CrossRef]
62. Schwarz, P.E.; Gallein, G.; Ebermann, D.; Müller, A.; Lindner, A.; Rothe, U.; Nebel, I.T.; Müller, G. Global diabetes survey—an annual report on quality of diabetes care. *Diabetes Res. Clin. Pract.* **2013**, *100*, 11–18. [CrossRef]
63. Schwarz, N.; Windoffer, R.; Magin, T.M.; Leube, R.E. Dissection of keratin network formation, turnover and reorganization in living murine embryos. *Sci. Rep.* **2015**, *5*, 9007. [CrossRef]
64. Schreurs, O.; Karatsaidis, A.; Balta, M.G.; Grung, B.; Hals, E.K.; Schenck, K. Expression of keratins 8, 18, and 19 in epithelia of atrophic oral lichen planus. *Eur. J. Oral Sci.* **2020**, *128*, 7–17. [CrossRef]
65. Moll, R.; Divo, M.; Langbein, L. The human keratins: Biology and pathology. *Histochem. Cell Biol.* **2008**, *129*, 705–733. [CrossRef]
66. Wang, Z.L.; Wang, S.; Kuang, Y.; Hu, Z.M.; Qiao, X.; Ye, M. A comprehensive review on phytochemistry, pharmacology, and flavonoid biosynthesis of Scutellaria baicalensis. *Pharm. Biol.* **2018**, *56*, 465–484. [CrossRef] [PubMed]
67. Li, P.; Wang, X.; Zhang, J. Baicalein administration protects against pentylenetetrazole-induced chronic epilepsy in rats. *Trop. J. Pharm. Res.* **2018**, *17*, 293–298. [CrossRef]
68. Liu, P.-F.; Han, F.-G.; Duan, B.-B.; Deng, T.-S.; Hou, X.-L.; Zhao, M.-Q. Purification and antioxidant activities of baicalin isolated from the root of huangqin (Scutellaria baicalensis gcorsi). *J. Food Sci. Technol.* **2013**, *50*, 615–619.
69. Yin, F.; Liu, J.; Ji, X.; Wang, Y.; Zidichouski, J.; Zhang, J. Baicalin prevents the production of hydrogen peroxide and oxidative stress induced by Aβ aggregation in SH-SY5Y cells. *Neurosci. Lett.* **2011**, *492*, 76–79. [CrossRef]
70. Kim, G.D.; Park, Y.S.; Jin, Y.H.; Park, C.S. Production and applications of rosmarinic acid and structurally related compounds. *Appl. Microbiol. Biotechnol.* **2015**, *99*, 2083–2092. [CrossRef]
71. Choo, B.K.M.; Kundap, U.P.; Kumari, Y.; Hue, S.M.; Othman, I.; Shaikh, M.F. Orthosiphon stamineus Leaf Extract Affects TNF-α and Seizures in a Zebrafish Model. *Front. Pharmacol.* **2018**, *9*, 139. [CrossRef] [PubMed]

life

MDPI

*Article*

# Human Brain Lipidomics: Utilities of Chloride Adducts in Flow Injection Analysis

**Paul L. Wood [1,*], Kathleen A. Hauther [2], Jon H. Scarborough [3], Dustin J. Craney [4], Beatrix Dudzik [2], John E. Cebak [5] and Randall L. Woltjer [6]**

[1] Metabolomics Unit, College of Veterinary Medicine, Lincoln Memorial University, 6965 Cumberland Gap Pkwy, Harrogate, TN 37752, USA
[2] Anatomy Department, DeBusk College of Osteopathic Medicine, Lincoln Memorial University, 6965 Cumberland Gap Pkwy, Harrogate, TN 37752, USA; kathleen.hauter@lmunet.edu (K.A.H.); beatrix.dudzik@lmunet.edu (B.D.)
[3] Medicine Department, DeBusk College of Osteopathic Medicine, Lincoln Memorial University, 6965 Cumberland Gap Pkwy, Harrogate, TN 37752, USA; jon.scarborough@lmunet.edu
[4] Department of Psychiatry, Indiana University School of Medicine, 340 West 10th St, Indianapolis, IN 46202, USA; djcraney@iu.edu
[5] Neurology, Mayo Clinic, 5711 E. Mayo Blvd., Phoenix, AZ 85054, USA; cebak.john@mayo.edu
[6] Department of Pathology, Oregon Health Science University, 3181 SW Sam Jackson PK. Rd., Portland, OR 97239, USA; woltjer@ohsu.edu
* Correspondence: paul.wood@lmunet.edu

**Abstract:** Ceramides have been implicated in a number of disease processes. However, current means of evaluation with flow infusion analysis (FIA) have been limited primarily due to poor sensitivity within our high-resolution mass spectrometry lipidomics analytical platform. To circumvent this deficiency, we investigated the potential of chloride adducts as an alternative method to improve sensitivity with electrospray ionization. Chloride adducts of ceramides and ceramide subfamilies provided 2- to 50-fold increases in sensitivity both with analytical standards and biological samples. Chloride adducts of a number of other lipids with reactive hydroxy groups were also enhanced. For example, monogalactosyl diacylglycerols (MGDGs), extracted from frontal lobe cortical gray and subcortical white matter of cognitively intact subjects, were not detected as ammonium adducts but were readily detected as chloride adducts. Hydroxy lipids demonstrate a high level of specificity in that phosphoglycerols and phosphoinositols do not form chloride adducts. In the case of choline glycerophospholipids, the fatty acid substituents of these lipids could be monitored by $MS^2$ of the chloride adducts. Monitoring the chloride adducts of a number of key lipids offers enhanced sensitivity and specificity with FIA. In the case of glycerophosphocholines, the chloride adducts also allow determination of fatty acid substituents. The chloride adducts of lipids possessing electrophilic hydrogens of hydroxyl groups provide significant increases in sensitivity. In the case of glycerophosphocholines, chloride attachment to the quaternary ammonium group generates a dominant anion, which provides the identities of the fatty acid substituents under $MS^2$ conditions.

**Keywords:** flow infusion analysis; chloride adducts; ceramides; sphingolipids; glycerophosphocholines; human brain

**Citation:** Wood, P.L.; Hauther, K.A.; Scarborough, J.H.; Craney, D.J.; Dudzik, B.; Cebak, J.E.; Woltjer, R.L. Human Brain Lipidomics: Utilities of Chloride Adducts in Flow Injection Analysis. *Life* **2021**, *11*, 403. https://doi.org/10.3390/life11050403

Academic Editors: Jong Hyuk Yoon and Chiara Villa

Received: 1 April 2021
Accepted: 26 April 2021
Published: 28 April 2021

**Publisher's Note:** MDPI stays neutral with regard to jurisdictional claims in published maps and institutional affiliations.



## 1. Introduction

Ceramides have come under increasing scrutiny as potential biomarkers in a number of diseases [1]. However, lack of consistency in reported alterations of ceramide levels probably relates to both the selection of analytical methods and the quality of the biological specimens. In the case of Alzheimer's disease brain samples, large increases in ceramide levels have been reported with triple quadrupole-electrospray ionization (ESI)-mass spectrometry [2,3]. In contrast, triple quadrupole-ion trap ESI and Orbitap-ESI methods have reported small or no increases in cortical ceramides [4–7], suggesting that high-resolution

mass spectrometry provides more accurate measurements of these lipids. However, our flow infusion ESI lipidomics analytical platform [5,8] has been limited by weak $[M+H]^+$, $[M-H]^-$, and $[M+HCOO]^-$ ceramide signals.

To address this issue, we undertook an analysis [9] of the chloride adducts of ceramides and ceramide derivatives [10,11], and we observed 10- to 50-fold increases in sensitivity. While ceramide analysis was the focus of our method development, we also investigated other lipids to define the scope of chloride adducts and their utility in characterizing other lipids. In addition to the attachment to electrophilic hydrogens of hydroxyl groups of ceramides, we also investigated chloride attachment to tertiary and quaternary ammonium compounds, including glycerophosphocholines [10,12,13] and sphingomyelins [10,13] to monitor these lipids and to define the fatty acid substituents of glycerophosphocholines [9]. While lithiated adducts of glycerophosphocholines have been used to characterize the fatty acid substituents of these glycerophospholipids [14], it is our experience that lithiated adducts work well with analytical standards but lack consistency and sensitivity when used with biological samples. In contrast, the chloride adducts reliably allow the determination of fatty acid substituents of glycerophosphocholines in biological samples [9].

In this report, we present the utility of chloride adducts for improving lipidomics analysis of human tissues. Additionally, we contrasted the lipid profiles of cortical gray matter (GM) with that of subcortical white matter (WM) in the human frontal lobe postmortem brain tissue from cognitively intact subjects.

## 2. Materials and Methods

### *2.1. Human Brain Samples*

Postmortem frontal cortex tissues were provided to the Oregon Brain Bank by volunteer subjects who had enrolled in our studies of normal brain aging and were clinically evaluated in the Layton Aging and Alzheimer's Disease Center at Oregon Health and Science University and were found not to have clinically determined cognitive impairment (Clinical Dementia Rating = 0). Tissue acquisition and use followed institutional review board requirements (IRB 00001623). Frontal lobe tissue was flash frozen and stored at −80 °C for biochemical studies described here. Dissection of gray matter (GM) and white matter (WM) was conducted by the neuropathologist (RJW). This study included 6 males and 6 females aged 85 to 93 years.

### *2.2. Sample Preparation*

Frontal cortex gray matter (GM) or subcortical white matter (WM) samples were processed as described previously [5,8,9]. Detailed methods can be found in [9]. In 7 mL tubes, 30 to 80 mg of tissue were sonicated in 1 mL of methanol, containing stable isotope internal standards, and 1 mL of distilled water. The stable isotope internal standards included $[^{13}C_{16}]$Cer d18:1/16:0 ($[M+Cl]^-$ = 588.5356), $[^{13}C_3]$DG 36:2 ($[M+Cl]^-$ = 658.5179; $[M+NH_4]^+$ = 641.5819), $[^2H_{31}]$PC 34:1 ($[M+Cl]^-$ = 824.7359; $[M+H]^+$ = 790.7734), $[^{13}C_{40}]$PC 32:0 ($[M+Cl]^-$ = 808.6662; $[M+H]^+$ = 774.9036), and $[^2H_7]$SM d18:1/16:0 ($[M+Cl]^-$ = 768.7320; $[M+H]^+$ = 734.7694). Next, 2 mL of tert-butylmethylether was added and the samples shaken at room temperature and top speed (Fisher Multitube Vortexer) for 30 min prior to centrifugation at 4000× g for 30 min at room temperature. A total of 1 mL of the upper organic layer containing the lipids was phosphatidylcholines (PC) (Eppendorf Vacfuge Plus).

### *2.3. Lipidomics Analysis*

Brain lipids were characterized by flow infusion analysis (FIA) with electrospray ionization (ESI). FIA at 20 μL/minute was performed utilizing high-resolution (140,000 at 200 amu; <2 ppm mass error) data acquisition with an orbitrap mass spectrometer (Thermo Q Exactive; Thermo, Waltham, MA, USA), as reported previously [9]. The infusion solvent was 2-propanol:methanol:chloroform (8:4:4) + 5 mM ammonium chloride to optimize formation of $[M+Cl]^-$ anions of lipids. The FIA included a 30 s scan in the positive

ion mode followed by a 30 s scan in the negative ion mode, both with a mass range of 300–1200 amu.

In positive ESI, the $[M+H]^+$ cations of phosphatidylcholines, sphingomyelins, and hydroxysphingomyelins were monitored, along with the $[M+NH_4]^+$ cations of monoacylglycerols and diacylglycerols. In negative ion mode, the $[M-H]^-$ and potential $[M+Cl]^-$ anions of ceramides, hydroxyceramides, hexosylceramides, hexosylhydroxylceramides, phytoceramides, ceramide-phosphoethanolamines, monoacylglycerols, diacylglycerols, monogalactosyldiacylglycerols, phosphatidylcholines, sphingomyelins, and hydroxy-sphingomyelins were monitored.

At completion of the infusion, the syringe and tubing were flushed with 1 mL of methanol followed by 1 mL of hexane:ethyl acetate:chloroform (3:2:1) between each analysis.

Relative levels of individual lipids (signal intensity of endogenous lipid/signal intensity of a stable isotope internal standard) were calculated based on accurate masses obtained from the Lipid Maps database (lipidmaps.org) and identities validated by tandem mass spectrometry ($MS^2$). For $MS^2$ analysis, an isolation window of 0.4 amu and collision energies of 10, 20, and 30 NCE were used and the product ions were monitored with high resolution (140,000; <2 ppm mass error).

The $MS^2$ products of the chloride adducts of individual lipid classes are presented with each subsection of the Results and potential stable isotope internal standards are presented in Supplementary Table S2.

## 3. Results

### *3.1. Chloride Adducts: Assay Validation*

The repeatability of chloride adduct analysis was evaluated by 10 repeated injections of a brain GM extract daily for 5 days. Endogenous ceramide d18:1/16:0 and ceramide d18:1.24:1, along with the internal standard $[^{13}C_{16}]$ceramide d18:1/16:0, were monitored with less than 1 ppm mass error. The relative standard deviations (RSD) were less than 10% for intra-day assays and less than 20% for inter-day assays.

### *3.2. Chloride Adducts: Specificity*

Chloride ion adducts involve attachment to electrophilic hydrogens of hydroxyl groups [9]. In the cases of ceramides, hydroxyceramides, phytoceramides, hexosylceramides, lactosylceramides, and ceramide phosphoethanolamines we monitored 2- to 50-fold increases in sensitivity (Section 3.3; Supplementary Tables S1 and S2). In contrast to the weak $[M+H]^+$, $[M-H]^-$, and $[M+HCOO]^-$ ceramide signals, the chloride adducts were monitored as strong peak intensities. In the case of neutral lipids (i.e., monoacylglycerols and diacylglycerols) we did not monitor increased sensitivity but chloride adducts offer an alternative quantitation strategy when ion suppression occurs with the $[M+NH_4]^+$ cations (Section 3.4). Monogalactosyl diacylglycerols (MGDG) were not detectable in human brain as the $[M+NH_4]^+$ cations, but were routinely monitored as the chloride adducts $[M+Cl]^-$ and their identities were verified by $MS^2$ (Section 3.4).

With regard to the hexosylceramides, we did not monitor any distinction between the chloride adducts for galactosyl- vs., glucosyl-ceramide analytical standards such that these 2 lipid classes cannot be distinguished with FIA. With regard to glucosides, cholesterylglucoside formed a dominant chloride adduct (Section 3.5) while phosphatidylinositols did not form chloride adducts supporting the specificity of the chloride adducts we monitored. Similarly, while monoacylglycerols and diacylglycerols (Section 3.4) formed dominant chloride adducts, phosphatidylglycerols and bis(monoacylglyceryl)phosphates (BMP) did not (Section 3.4), again reinforcing the specificity of these adducts.

Other biomolecules we have monitored to form chloride adducts, involving the electrophilic hydrogens of hydroxyl groups, included fatty acyl ethanolamides (ethanolamide 18:0 = 362.2836; ethanolamide 20: = 382.2523); sphingosines (sphingosine = 334.2522; sphingosine D7 = 341.2962); and galactinol (376.1861).

Chloride attachment also occurs with quaternary ammonium compounds, including glycerophosphocholines and sphingomyelins [9,12,15]. In the case of sphingomyelins (Section 3.6) prevalent chloride adducts were monitored. A novel observation of our studies was the high sensitivity we observed for hydroxysphingomyelins. The $[M+H]^+$ cations of hydroxysphingomyelins were not detectable in the human brain samples we analyzed while the chloride adducts were consistently monitored (Section 3.6). Dominant chloride adducts of glycerophosphocholines were also observed. Another unique advantage of using chloride adducts over the use of $[M+H]^+$ cations is that the chloride adducts allow for $MS^2$ characterization of the fatty acid substituents of glycerophosphocholines (Section 3.7). The chloride adducts of oxidized glycerophosphocholines are also useful for monitoring these oxidation products. For example, PC 16:0/C5 aldehyde (POVPC; 628.3391) and PC 16:0/C5 acid (PGPC; 644.3340) are robust cations to monitor.

### *3.3. Ceramide Families*

Our analyses demonstrated that the relative levels of almost all ceramides, hydroxyceramides, hexosylceramides, hexosylhydroxyceramides, phytoceramides, and ceramide phosphoethanolamines were higher in the WM than the GM in the human frontal cortex (Figure 1). Our findings were consistent with previous reports of higher total ceramide levels in human brain WM [3]. These findings are encouraging and indicate that our modified analytical platform has the potential to clarify the roles of these sphingolipids as precursors for the structural lipids of myelin (i.e., sphingomyelins, sulfatides, and gangliosides). These ceramide families all formed dominant chloride adducts with analytical standards.

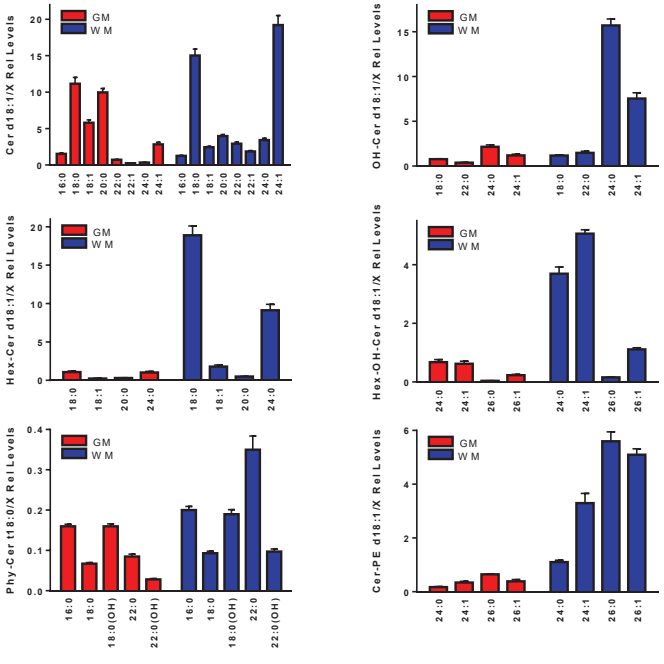


**Figure 1.** Ceramide families monitored in human frontal cortex gray matter (GM) and subcortical white matter (WM). These lipid families include ceramides (Cer), hydroxyceramides (OH-Cer), hexosylceramides (Hex-Cer), hexosylhydroxylceramides (Hex-OH-Cer), phytoceramides (Phy-Cer), and ceramide-phosphoethanolamines (Cer-PE). Relative levels (endogenous lipid peak intensity/peak intensity of a stable isotope internal standard) were corrected for wet weight differences. The internal standard for these determinations was 2 nmoles of $[^{13}C_{16}]$Cer d18:1/16:0. The specific masses utilized are summarized in Table 1. Mean ± SEM (N = 12).

**Table 1.** Exact masses, chloride adduct masses, and $MS^2$ anions for ceramides (Cer), hydroxy-ceramides (OH-Cer), phytoceramides (Phy-Cer), hexosyl-ceramides (Hex-Cer), hexosyl hydroxy-ceramides (Hex-OH-Cer), and ceramides phosphoethanolamines (CE-PE). Hex, hexose; PE, phosphoethanolamine; ppm, parts per million mass error.

| **Cer d18:1/x** | **Exact** | **$[M+Cl]^-$** | **Error (ppm)** | **$MS^2$ Product** | **$MS^2$ Anion** | **Error (ppm)** |
|---|---|---|---|---|---|---|
| 16:0 [$^{13}C_{16}$] | 553.5657 | 588.5356 | 0.35 | $[M-H]^-$ | 552.5584 | 0.67 |
| 16:0 | 537.5121 | 572.4819 | 0.24 | $[M-H]^-$ | 536.5048 | 1.18 |
| 18:0 | 565.5434 | 600.5132 | 1.1 | $[M-H]^-$ | 564.5361 | 0.64 |
| 20:0 | 593.5747 | 628.5445 | 0.53 | $[M-H]^-$ | 592.5674 | 0.75 |
| 20:1 | 591.5591 | 626.5289 | 0.23 | $[M-H]^-$ | 590.5518 | 0.68 |
| 22:0 | 621.6060 | 656.5758 | 0.18 | $[M-H]^-$ | 620.5987 | 1.05 |
| 22:1 | 619.5904 | 654.5602 | 0.31 | $[M-H]^-$ | 618.5831 | 0.91 |
| 24:0 | 649.6373 | 684.6071 | 0.32 | $[M-H]^-$ | 648.6300 | 0.30 |
| 24:1 | 647.6217 | 682.5915 | 0.15 | $[M-H]^-$ | 646.6144 | 0.45 |
| **OH-Cer d18:1/x** | **Exact** | **$[M+Cl]^-$** | **Error (ppm)** | **$MS^2$ Product** | **$MS^2$ Anion** | **Error (ppm)** |
| 18:0 | 581.5383 | 616.5082 | 0.47 | $[M-H]^-$ | 580.5310 | 0.34 |
| 22:0 | 637.6009 | 672.5708 | 0.018 | $[M-H]^-$ | 636.5936 | 0.45 |
| 24:0 | 665.6322 | 700.6021 | 0.11 | $[M-H]^-$ | 664.6249 | 0.26 |
| 24:1 | 663.6166 | 698.5864 | 0.25 | $[M-H]^-$ | 662.6093 | 0.051 |
| **Phy-Cer t18:0/x** | **Exact** | **$[M+Cl]^-$** | **Error (ppm)** | **$MS^2$ Product** | **$MS^2$ Anion** | **Error (ppm)** |
| 16:0 | 555.5226 | 590.4925 | 0.84 | $[M-H]^-$ | 554.5153 | 0.36 |
| 18:0 | 583.55396 | 618.5238 | 0.77 | $[M-H]^-$ | 582.5467 | 0.44 |
| 18:0(OH) | 599.5489 | 634.5187 | 0.016 | $[M-H]^-$ | 598.5416 | 0.39 |
| 22:0 | 639.6166 | 674.5864 | 0.37 | $[M-H]^-$ | 638.6093 | 0.78 |
| 22:0(OH) | 655.6115 | 690.5813 | 0.29 | $[M-H]^-$ | 654.6042 | 0.52 |
| **Hex-Cer** | **Exact** | **$[M+Cl]^-$** | **Error (ppm)** | **$MS^2$ Product** | **$MS^2$ Anion** | **Error (ppm)** |
| [D7] | 664.5619 | 699.5317 | 0.42 | | | |
| 18:0 | 727.5962 | 762.5660 | 1.1 | $[M-(Hex-H_2O)]^-$ | 564.5361 | 0.28 |
| 18:1 | 725.5806 | 762.5661 | 1.1 | $[M-(Hex-H_2O)]^-$ | 562.5205 | 0.45 |
| 20:0 | 755.6275 | 790.5973 | 0.98 | $[M-(Hex-H_2O)]^-$ | 592.5674 | 0.87 |
| 24:0 | 811.6901 | 846.6599 | 0.14 | $[M-(Hex-H_2O)]^-$ | 648.6299 | 0.94 |
| **Hex-OH-Cer** | **Exact** | **$[M+Cl]^-$** | **Error (ppm)** | **$MS^2$ Product** | **$MS^2$ Anion** | **Error (ppm)** |
| 24:0 | 827.6850 | 862.6548 | 0.29 | $[M-(Hex-H_2O)]^-$ | 664.6249 | 1.43 |
| | | | | $[M-Hex]^-$ | 646.61436 | 1.22 |
| 24:1 | 825.6693 | 860.6392 | 1.0 | $[M-(Hex-H_2O)]^-$ | 662.6092 | 0.40 |
| | | | | $[M-Hex]^-$ | 644.5987 | 0.24 |
| 26:0 | 855.7163 | 890.6861 | 0.42 | $[M-(Hex-H_2O)]^-$ | 692.6562 | 0.83 |
| | | | | $[M-Hex]^-$ | 674.6456 | 0.95 |
| 26:1 | 853.7006 | 888.6705 | 0.72 | $[M-(Hex-H_2O)]^-$ | 690.6405 | 0.65 |
| | | | | $[M-Hex]^-$ | 672.6300 | 0.50 |
| **Cer-PE** | **Exact** | **$[M+Cl]^-$** | **Error (ppm)** | **$MS^2$ Product** | **$MS^2$ Anion** | **Error (ppm)** |
| 24:0 | 772.6458 | 807.6156 | 1.3 | PE | 140.0118 | 1.1 |
| 24:1 | 770.6302 | 805.5999 | 1.2 | PE | 140.0118 | 1.0 |
| 25:0 | 786.6614 | 821.6313 | 0.10 | PE | 140.0118 | 1.3 |
| 25:1 | 784.6458 | 819.6156 | 0.72 | PE | 140.0118 | 1.2 |
| 26:0 | 800.6771 | 835.6469 | 0.024 | PE | 140.0118 | 1.1 |
| 26:1 | 798.6615 | 833.6313 | 0.26 | PE | 140.0118 | 1.3 |

Validation of these lipid identities were obtained via $MS^2$ analysis utilizing a 0.4 amu isolation window and acquisition with less than 2 ppm mass error of the product ions (Table 1). $MS^2$ analysis of ceramides, hydroxyceramides, and phytoceramides were characterized by product $[M-H]^-$ anions, while hexosylceramides yielded $[M-(hexose-H_2O)]^-$ anions, and hexosylhydroxyceramides yielded both $[M-(hexose-H_2O)]^-$ and $[M-hexose]^-$ product anions. Note that our FIA of hexosylceramides did not distinguish between galactosyl or glucosyl substituents. Ceramide-phosphoethanolamines yielded phosphoethanolamine as the product ion (Table 1; Supplementary Figure S1).

### *3.4. Neutral Lipids*

In our evaluation of potential chloride adducts of various lipids, we also noted strong adducts with the electrophilic hydrogens of the hydroxyl groups of monoacylglycerols (MG), diacylglycerols (DG), and monogalactosyl-diacylglycerols (MGDG) (Table 2, Supplementary Table S2). The chloride adducts of MGs and DGs, in brain samples, provided an approximate 1–2-fold increase in sensitivity compared the $[M+NH_4]^+$ cations. Human brain MGDGs, which we could not monitor in positive ESI, generated robust chloride adducts, with MGDG 34:1 constituting the major isoform.

Unfortunately, the $MS^2$ product ions of MGs and DGs did not yield structural information. In contrast, $MS^2$ analysis of the MGDGs generates the two fatty acid substituents indicating that human brain MGDG 34:1 is MGDG 18:0/16:1 (Table 2, Figure 2).

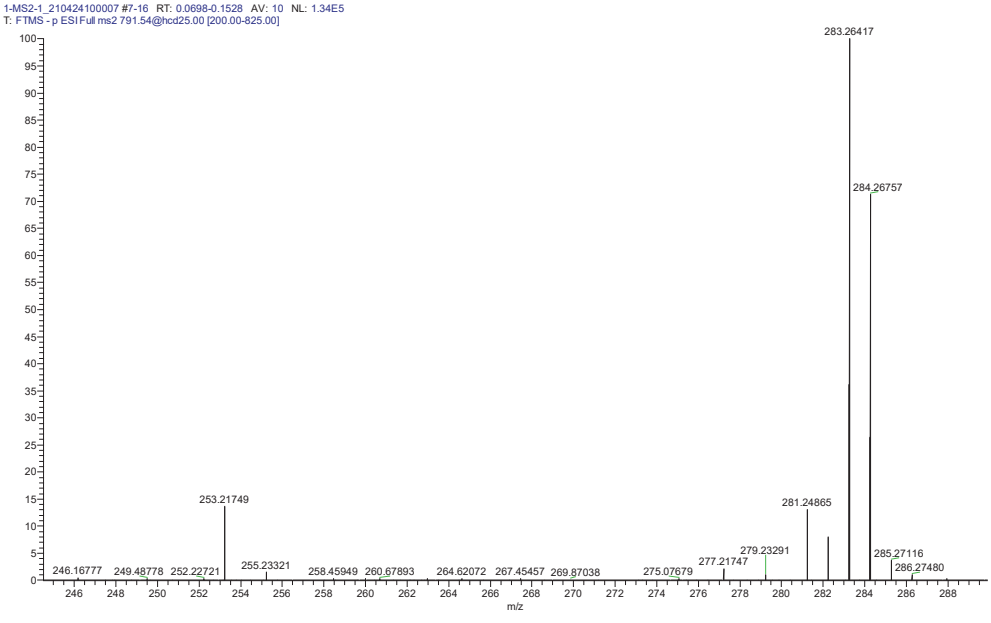


**Figure 2.** $MS^2$ spectrum for MGDG 34:1, clearly demonstrating that this is MGDG 16:1/18:0. Theoretical 16:1 = 253.21730 (0.76 ppm) and 18:0 = 283.2643 (0.61 ppm), also see Table 2.

MG relative levels in GM and WM were similar except for higher levels of MG 20:4 in the WM (Figure 3). In contrast most DGs were at higher levels in the WM (Figure 2). MGDG 34:1 was observed at higher levels in GM (Figure 4). MGDG 36:1 and 36:2 were also characterized in these samples (Table 2). MGDG synthesis has been reported for rat brain GM and WM [16–19] and MGDGs have been proposed as a biomarker of myelination [18]. However, to our knowledge our results represent the first characterization of specific MGDGs in human brain samples.

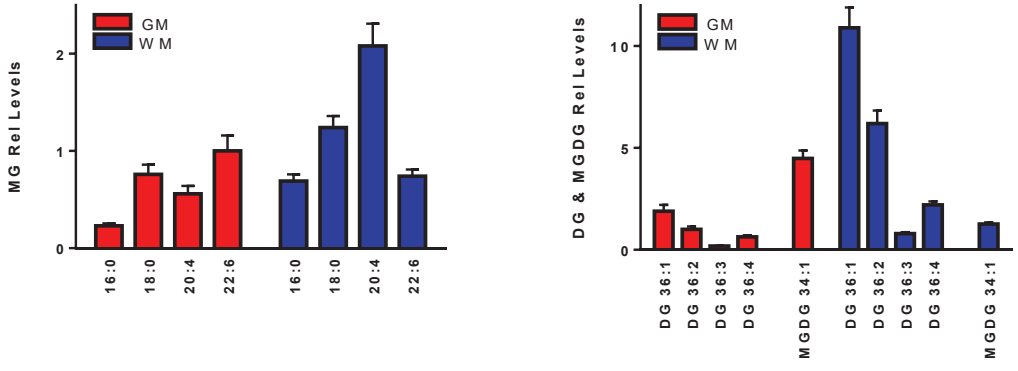


**Figure 3.** Monoacylglycerols (MG), diacylglycerols (DG), and monogalactosyl diacylglycerol 34:1 (MGDG) found in human frontal cortex gray matter (GM) and white matter (WM). The $MS^2$ spectrum for MGDG 34:1 is presented in Figure 3. Relative levels (endogenous lipid peak intensity/peak intensity of a stable isotope internal standard) were corrected for wet weight differences. The internal standard used for these determinations was 2 nmoles of [$^{13}C_3$]DG 36:2. The specific masses utilized are summarized in Table 2. Mean ± SEM (N = 12).

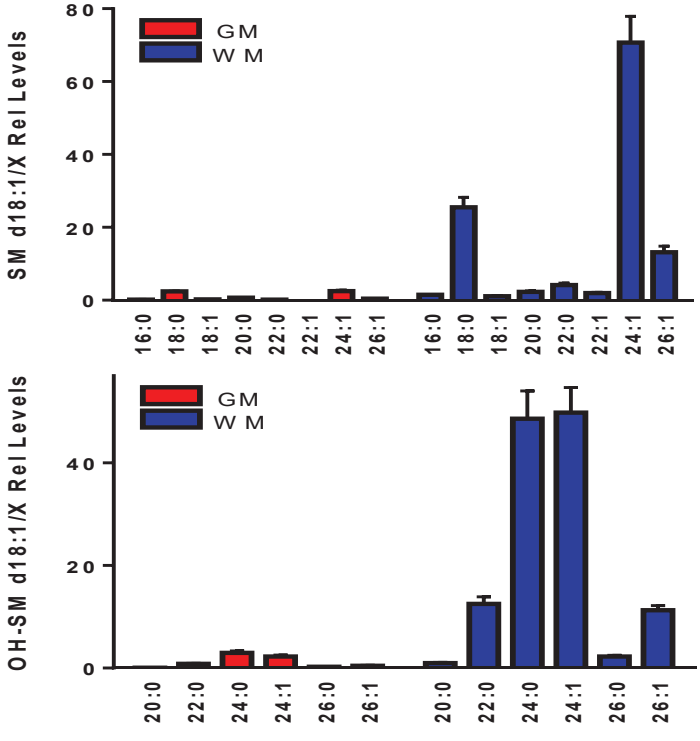


**Figure 4.** Sphingomyelins (SM) and hydroxysphingomyelins (OH-SM) found in human frontal cortical gray matter (GM) and subcortical white matter (WM). Relative levels (endogenous lipid peak intensity/peak intensity of a stable isotope internal standard) were corrected for wet weight differences. The internal standard used for these determinations was 10 nmoles of [$^2H_7$]SM d18:1/16:0. The specific masses utilized are summarized in Table 3. Mean ± SEM (N = 12).

**Table 2.** Exact masses and chloride adduct masses for monoacylglycerols (MG), diacylglycerols (DG), and monogalactosyldiacylglycerols (MGDGs) and $MS^2$ anions for MGDG. ppm, parts per million mass error.

| MG | Exact | $[M+Cl]^-$ | Error (ppm) | DG | Exact | $[M+Cl]^-$ | Error (ppm) |
|---|---|---|---|---|---|---|---|
| 18:1 [D5] | 361.3240 | 396.2939 | 0.73 | DG 36:2 [$^{13}C_3$] | 623.5480 | 658.5179 | 1.1 |
| 16:0 | 330.2770 | 365.2469 | 0.52 | 36:1 | 622.5536 | 657.5235 | 0.89 |
| 18:0 | 358.3083 | 393.2782 | 0.13 | 36:2 | 620.5379 | 655.5078 | 0.83 |
| 20:4 | 378.2770 | 413.2469 | 0.10 | 36:3 | 618.5223 | 653.4922 | 1.1 |
| 22:6 | 402.2770 | 437.2469 | 0.13 | 36:4 | 616.4910 | 651.4765 | 0.66 |
| **MGDG** | **Exact** | **$[M+Cl]^-$** | **Error (ppm)** | **$MS^2$ Product** | **$MS^2$ Anion** | | **Error (ppm)** |
| 34:1 | 756.5751 | 791.5450 | 0.76 | 16:1 | 253.2173 | | 1.02 |
| | | | | 18:0 | 283.2642 | | 0.38 |
| 36:1 | 784.6064 | 819.5763 | 0.69 | 18:0 | 283.2642 | | 0.60 |
| | | | | 18:1 | 281.2486 | | 0.12 |
| 36:2 | 782.5908 | 817.5606 | 0.77 | 18:1 | 281.2486 | | 0.12 |

**Table 3.** Exact masses, chloride adduct masses, and $MS^2$ anions for sphingomyelins (SM) and hydroxy-sphingomyelins (OH-SM). PC, phosphocholine; ppm, parts per million mass error.

| SM d18:1/x | Exact | $[M+Cl]^-$ | Error (ppm) | $MS^2$ Product | $MS^2$ Anion | Error (ppm) |
|---|---|---|---|---|---|---|
| 16:0 [D31] | 733.7621 | 768.7320 | 0.70 | $[M-CH_3]^-$ | 718.7386 | 0.87 |
| 16:0 | 702.5676 | 737.5374 | 0.33 | $[M-CH_3]^-$ | 687.5441 | 0.53 |
| 18:0 | 730.5988 | 765.5687 | 0.71 | $[M-CH_3]^-$ | 715.5753 | 0.55 |
| 18:1 | 728.5832 | 763.5531 | 0.94 | $[M-CH_3]^-$ | 713.5597 | 0.31 |
| 20:0 | 760.6458 | 795.6157 | 0.32 | $[M-CH_3]^-$ | 745.6223 | 0.82 |
| 22:0 | 786.6615 | 821.6313 | 0.83 | $[M-CH_3]^-$ | 771.6380 | 1.1 |
| 24:0 | 814.6928 | 849.6626 | 0.99 | $[M-CH_3]^-$ | 799.6693 | 0.24 |
| 24:1 | 812.6772 | 847.6469 | 0.32 | $[M-CH_3]^-$ | 797.6537 | 0.72 |
| 26:1 | 840.7085 | 875.6783 | 0.63 | $[M-CH_3]^-$ | 825.6850 | 0.96 |
| **OH-SM d18:1/x** | **Exact** | **$[M+Cl]^-$** | **Error (ppm)** | **$MS^2$ Product** | **$MS^2$ Anion** | **Error (ppm)** |
| 18:0 | 746.5938 | 781.5636 | 0.87 | $[M-CH_3]^-$ | 563.5242 | 1.3 |
| 20:0 | 774.6251 | 809.5949 | 0.70 | $[M-CH_3]^-$ | 591.5555 | 0.88 |
| 22:0 | 802.6564 | 837.6262 | 0.77 | $[M-CH_3]^-$ | 619.5868 | 0.50 |
| 22:1 | 800.6408 | 835.6106 | 0.76 | $[M-CH_3]^-$ | 617.5712 | 0.70 |
| 24:0 | 830.6877 | 865.6575 | 0.98 | $[M-CH_3]^-$ | 647.6180 | 0.10 |
| 24:1 | 828.6721 | 863.6419 | 0.73 | $[M-CH_3]^-$ | 645.6025 | 0.34 |
| 26:0 | 858.7190 | 893.6888 | 0.84 | $[M-CH_3]^-$ | 675.6494 | 0.56 |
| 26:1 | 856.7034 | 891.6732 | 0.86 | $[M-CH_3]^-$ | 673.6338 | 0.48 |

### *3.5. Glucosides (Glc)*

Cholesterylglucoside, which has been monitored in fibroblasts and gastric mucosa [20,21], formed a dominant chloride adduct (583.3775, 0.25 ppm)with an analytical standard, but was not detected in either the GM or WM samples of human frontal cortex.

One issue with FIA of lipids is that phosphatidylinositols (PtdIn) and phosphatidylglucosides (PtdGlc) are isobars that can only be individually characterized after prior chromatographic separation [21]. While we found that PtdIn do not form chloride adducts, no commercial standards of PtdGlc are available. We assume that these lipids should form chloride adducts but did not detect PtdGlc 18:0/20:0 (929.5215) in human brain samples. This specific lipid has been reported to be present in fetal rat brain developing astrocytes [20,21].

### *3.6. Sphingomyelins (SM) and Hydroxysphingomyelins (OH-SM)*

With our lipidomics analytical platform, we have easily monitored sphingomyelins as $[M+H]^+$ cations while hydroxysphingomyelins were most often below the threshold limit of detection as $[M+H]^+$ cations [4]. In contrast, the chloride adducts (Table 3) of both SM and OH-SM were detected in human brain samples (Supplementary Table S2). For the $MS^2$ analysis, SM were characterized by the generation of $[M\text{-}CH_3]^-$ anions while OH-SM generated [M-phosphocholine]$^-$ anions (Table 3). While there was no increase in sensitivity with the chloride adducts of sphingomyelins, hydroxysphingomyelins were detected while the [M+H]+ cations were not (Supplementary Table S2).

As reported by other investigators [19], we observed higher levels of SM d18:1/24:1 in the WM, compared to the GM (Figure 4). To our knowledge, we also report for the first time that higher relative levels of OH-SM are present in the cortical WM, compared to subcortical GM (Figure 4). OH-SMs have previously been characterized in human plasma [22], but not in brain.

### *3.7. Phosphatidylcholines (PC)*

As previously reported [9,11], PCs formed robust chloride adducts (Supplementary Table S2) which in turn allowed identification of the sn-1 and sn-2 fatty acid substituents with $MS^2$ (Table 4). The distribution of PCs was characterized by higher levels of PC 34:1, 36:1, and 36:2 in the WM (Figure 5). $MS^2$ analysis of PCs demonstrated that PC 32:1 was composed of a mixture of PC 14:0/18:0 and PC 16:0/16:1 (Table 4). Similarly PC 34:1 = PC 16:0/18:1; PC 36:2 = PC 18:1/18:1; PC 38:4 = PC 18:0/20:4 and PC 16:0/22:4; PC 38:6 = PC 16:0/22:6; and PC 40:6 = PC 18:0/22:6 (Supplementary Figure S2).

**Table 4.** Exact masses, cations, chloride adduct anions, and $MS^2$ anions for phosphatidylcholines (PC). ppm, parts per million mass error.

| PC | Exact | [M+H] | Error (ppm) | $[M+Cl]^-$ | Error (ppm) | $MS^2$ Product | $MS^2$ Anion | Error (ppm) |
|---|---|---|---|---|---|---|---|---|
| 28:0 [D54] | 729.8257 | 730.8330 | 0.78 | 764.7955 | 0.40 | 14:0 [D26] | 253.3649 | 0.61 |
| 34:1 [D31] | 789.7661 | 790.7734 | 0.86 | 824.7360 | 0.52 | 16:0 [D31] | 285.4213 | 0.54 |
| 32:1 | 731.5465 | 732.5537 | 0.10 | 766.5163 | 1.3 | 14:0 | 227.2016 | 0.17 |
| | | | | | | 18:1 | 281.2486 | 0.98 |
| | | | | | | 16:0 | 255.2329 | 0.39 |
| | | | | | | 16:1 | 253.2173 | 0.67 |
| 34:1 | 759.5778 | 760.5850 | 0.64 | 794.5476 | 1.3 | 16:0 | 255.2329 | 0.66 |
| | | | | | | 18:1 | 281.2486 | 0.67 |
| 36:1 | 787.6091 | 788.6163 | 0.94 | 822.5789 | 1.4 | 18:0 | 283.2643 | 0.44 |
| | | | | | | 18:1 | 281.2486 | 0.10 |
| 36:2 | 785.5931 | 786.6007 | 0.47 | 820.5633 | 1.1 | 18:1 | 281.2486 | 0.11 |
| 38:4 | 809.5931 | 810.6007 | 1.1 | 844.5633 | 1.2 | 18:0 | 283.2643 | 0.70 |
| | | | | | | 20:4 | 303.2329 | 0.82 |
| | | | | | | 16:0 | 255.2329 | 0.39 |
| | | | | | | 22:4 | 331.2642 | 0.36 |
| 38:5 | 807.5778 | 808.5851 | 0.85 | 842.5477 | 1.1 | 18:1 | 281.2486 | 0.53 |
| | | | | | | 20:4 | 303.2329 | 0.56 |
| 38:6 | 806.5622 | 806.5694 | 0.43 | 840.5320 | 1.3 | 16:0 | 255.2329 | 0.10 |
| | | | | | | 22:6 | 327.2329 | 0.27 |
| 40:6 | 833.5931 | 834.6007 | 0.12 | 868.5633 | 1.4 | 18:0 | 283.2643 | 0.10 |
| | | | | | | 22:6 | 327.2329 | 0.38 |

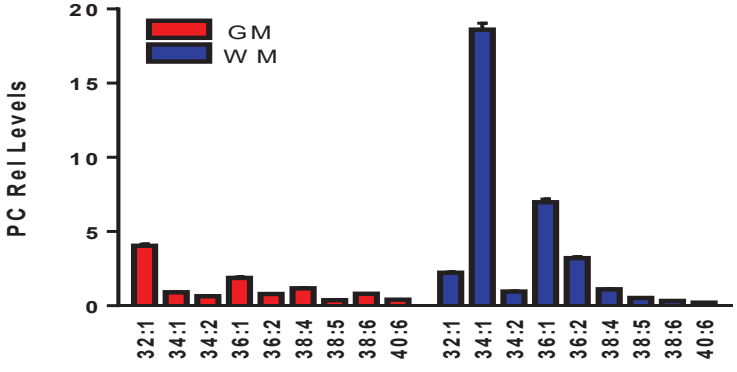


**Figure 5.** Phosphatidylcholines (PC) found in human frontal cortical gray matter (GM) and subcortical white matter (WM). Relative levels (endogenous lipid peak intensity/peak intensity of a stable isotope internal standard) were corrected for wet weight differences. The internal standard used for these determinations was 10 nanomoles of [$^{13}C_{40}$]PC 32:0. The specific masses utilized are summarized in Table 4. Mean ± SEM (N = 12).

## 4. Discussion

Sphingolipid metabolism is extremely complex in that ceramides act as mediators of signal transduction and as the precursors of critical structural molecules. These structural molecules include sphingomyelins, sulfatides, gangliosides, and ceramide phosphoethanolamines (PE-ceramides) which are present in both WM and GM, but are more heavily concentrated in WM (Figure 1). [12,13]. With FIA, coupled to high-resolution mass spectrometry, we observed that the chloride adducts of ceramides provided 2- to 50-fold (Supplementary Table S1) increases in sensitivity in brain samples compared to other adducts. Similarly, the chloride adducts of hydroxyceramides, hexosylceramides, hexosylhydroxyceramides, phytoceramides, and PE-ceramides were routinely monitored in the human brain samples we analyzed, in contrast to the $[M+H]^+$ or $[M-H]^-$ ions which were more susceptible to ion suppression.

Our previous studies of isolated human cells have shown that ceramides, hydroxyceramides, hexosylceramides, hexosylhydroxyceramides, phytoceramides, and PE-ceramides were present at higher concentrations in astrocytes and Schwan cells compared to neurons [9]. These cellular lipidomics analyses of the chloride adducts of sphingolipids provide critical information for evaluating the data obtained with intact postmortem brain tissues.

Members of the sphingomyelin synthase gene family exhibit PE-ceramide synthase activity [23] allowing for co-ordination of the biosynthesis of sphingomyelins and PE-ceramides required for myelin formation. However, biosynthesis of PE-ceramides also has been demonstrated in brain synaptic membranes suggesting a role in the ultrastructure of brain synapses [24]. Brain hydroxyceramides are predominantly α-hydroxyceramides which are precursors to galactosylceramides [25], which in turn are precursors to myelin sulfatides.

In contrast, lactosylceramides, which are concentrated in lipid rafts [26], were found at higher relative concentrations in human neurons [9]. Of interest are the findings that acid ceramidase deficiency results in elevated brain levels of lactosylceramides and may be associated with neuronal degeneration [27] and inflammatory processes [28]. To our knowledge these data are the first to characterize phytoceramides in human brain samples. This has potential clinical relevance since phytoceramides have been demonstrated to have neuroprotective properties [29,30].

In the case of sphingomyelins, the utilization of chloride adducts in our lipidomics analytical platform provided no increase in sensitivity over $[M+H]^+$ cations. However, hydroxysphingomyelins, which are present in the brain at lower concentrations, were undetectable as $[M+H]^+$ cations, but readily detectable as chloride adducts. To our knowl-

edge this is the first report of these sphingolipids in brain and further analyses of chloride adducts will allow further investigations of the roles of these lipids in brain function and disease. Hydroxysphingomyelins have been characterized in human plasma and have been found to be involved in regulating energy metabolism [31]. Our previous studies of isolated human cells have shown that while sphingomyelins were present at higher concentrations in astrocytes and Schwan cells, compared to neurons, hydroxysphingomyelins were at higher relative concentrations in neurons [9]. These data suggest that hydroxysphingomyelins may be involved in regulating neuronal energy metabolism. This is an intriguing interpretation since hydroxysphingomyelins are elevated in the cortex of Alzheimer's disease patients [32], who also demonstrate decreased glucose metabolism [33,34].

The chloride adducts of MGs and DGs provided sensitivity equal to that observed for the $[M+NH_4]^+$ cations. However, MGDGs, which were undetectable as $[M+NH_4]^+$ cations, were reliably monitored as chloride adducts. While MGDGs have been shown to be synthesized by hydroxyceramide galactosyltransferase [35] and proposed as biomarkers of myelination [18,19], to our knowledge these data are the first to characterize the specific MGDGs present in human brain. MGDG 34:1 (16:1/18:0) was the major constituent member of this lipid family with highest levels observed in gray matter.

A further advantage of the analysis of chloride adducts is found with phosphatidylcholines. These lipids are normally monitored as $[M+H]^+$ cations. However, $MS^2$ analysis only yields phosphocholine as the product ion. Analysis of the lithium or formate adducts of glycerophosphocholines has been reported to allow identification of the fatty acid substituents with $MS^2$. In our laboratory these methods work well with some analytical standards but are not useful in FIA of biological samples. $MS^2$ analysis of the chloride adducts of these lipids is extremely robust and allows definition of the fatty acid substituents [36] for human brain samples.

With regard to study limitations: (i) we did not monitor any gender differences in this study, but the small N of 6 per gender may limit such an interpretation; (ii) our data represent relative lipid concentrations, based on a small repertoire of internal standards; therefore, the next step will be to develop absolute quantitation utilizing analytical standards and the accompanying stable isotope analogs for key lipids.

## 5. Conclusions

FIA of the chloride adducts of sphingolipids, phosphatidylcholines, sphingomyelins, and neutral lipids provides an alternative analytical platform for the characterization of these lipids in human brain samples. In the case of sphingolipids, the chloride adducts of this complex lipid family provided enhanced sensitivity and detected significantly more lipids. With glycerophosphocholines, the chloride adducts enhanced our ability to determine the fatty acid substituents, in contrast to the $[M+H]^+$ ions, which upon fragmentation only generate phosphocholine as a product ion. The chloride adducts of sphingomyelins provide another means of validating the identities of individual sphingomyelins while hydroxysphingomyelins are more readily detected as chloride adducts. Mono- and diacylglycerols, as neutral lipids, are not always easily detected. The chloride adducts offer an alternative analytical strategy, with a greater number of diacylglycerols being detected.

In summary, we have demonstrated the utility of chloride adducts as a component of a lipidomics analytical platform for the examination of the brain lipidome. This approach should prove useful with other tissues and biofluids and for chromatographic methods of sample introduction, since no single platform can survey the entire lipidome.

**Supplementary Materials:** The following are available online at https://www.mdpi.com/article/10.3390/life11050403/s1, Figure S1: Phosphoethanolamine (theoretical mass of 240.0118; 0.071 ppm) $MS^2$ product of Cer-PE 24:0.; Figure S2: $MS^2$ spectrum for neocortical PC 40:6; Table S1: Raw peak intensities for ceramides in gray matter for the $[M+Cl]^-$ and $[M-H]^-$ anions.; Table S2: Lipids detected as chloride adducts compared to detection as [M-H]- anions, [M+H]+ cations, or [M+NH4]+ cations; Table S3: Masses and product ions of internal standards that form chloride adducts.

**Author Contributions:** P.L.W., J.E.C. and R.L.W. designed the study and provided the resources. K.A.H., J.H.S., D.J.C. and B.D. performed the analyses and data reduction. J.H.S. provided software development. P.L.W. wrote the first draft and all authors provided revisions. All authors have read and agreed to the published version of the manuscript.

**Funding:** This research was funded by Lincoln Memorial University and by NIA P30 AG066518 (Oregon Alzheimer's Disease Center).

**Institutional Review Board Statement:** Postmortem frontal cortex tissues were provided to the Oregon Brain Bank by volunteer subjects who had enrolled in our studies of normal brain aging and were clinically evaluated in the Layton Aging and Alzheimer's Disease Center at Oregon Health and Science University. Tissue acquisition and use followed institutional review board requirements (IRB 00001623).

**Informed Consent Statement:** All volunteers in this multiyear study provided informed consent.

**Data Availability Statement:** Raw data is available to qualified investigators upon request.

**Conflicts of Interest:** The Authors declare no conflict of interest.

## References

1. Kurz, J.; Parnham, M.J.; Geisslinger, G.; Schiffmann, S. Trends Ceramides as novel disease biomarkers. *Mol. Med.* **2019**, *25*, 20–32.
2. Cutler, R.G.; Kelly, J.; Storie, K.; Pedersen, W.A.; Tammara, A.; Hatanpaa, K.; Troncoso, J.C.; Mattson, M.P. Involvement of oxidative stress-induced abnormalities in ceramide and cholesterol metabolism in brain aging and Alzheimer's disease. *Proc. Natl. Acad. Sci. USA* **2004**, *101*, 2070–2075. [CrossRef] [PubMed]
3. Han, X.; Holtzman, D.M.; McKeel, D.W., Jr.; Kelley, J.; Morris, J.C. Substantial sulfatide deficiency and ceramide elevation in very early Alzheimer's disease: Potential role in disease pathogenesis. *J. Neurochem.* **2002**, *82*, 809–818. [CrossRef]
4. Chan, R.B.; Oliveira, T.G.; Cortes, E.P.; Honig, L.S.; Duff, K.E.; Small, S.A.; Wenk, M.R.; Shui, G.; Di Paolo, G. Comparative lipidomic analysis of mouse and human brain with Alzheimer disease. *J. Biol. Chem.* **2012**, *287*, 2678–2688. [CrossRef]
5. Wood, P.L.; Barnette, B.L.; Kaye, J.A.; Quinn, J.F.; Woltjer, R.L. Non-targeted lipidomics of CSF and frontal cortex gray and white matter in control, mild cognitive impairment, and Alzheimer's disease subjects. *Acta Neuropsychiatr.* **2015**, *27*, 270–278. [CrossRef] [PubMed]
6. Filippov, V.; Song, M.A.; Zhang, K.; Vinters, H.V.; Tung, S.; Kirsch, W.M.; Yang, J.; Duerksen-Hughes, P.J. Increased ceramide in brains with Alzheimer's and other neurodegenerative diseases. *Alzheimers Dis.* **2012**, *29*, 537–547. [CrossRef]
7. Hejazi, L.; Wong, J.W.; Cheng, D.; Proschogo, N.; Ebrahimi, D.; Garner, B.; Don, A.S.; Biochem, J. Mass and relative elution time profiling: Two-dimensional analysis of sphingolipids in Alzheimer's disease brains. *Biochem. J.* **2011**, *438*, 165–175. [CrossRef] [PubMed]
8. Wood, P.L. Non-targeted lipidomics utilizing constant infusion high resolution ESI mass spectrometry. In *Springer Protocols, Neuromethods: Lipidomics*; Humana Press: New York, NY, USA, 2017; Volume 125, pp. 13–19.
9. Wood, P.L.; Woltjer, R.L. Electrospray ionization high resolution mass spectrometry of the chloride adducts of steroids, mono- and oligo-saccharides, xyloglucans, ceramides, gangliosides, and phenols. In *Springer Protocols, Neuromethods: Metabolomics*; Human Press: New York, NY, USA, 2020; Volume 159, pp. 69–76.
10. Han, X.; Yang, K.; Gross, R.W. Multi-dimensional mass spectrometry-based shotgun lipidomics and novel strategies for lipidomic analyses. *Mass Spectrom. Rev.* **2012**, *31*, 134–178. [CrossRef]
11. Ostrinskaya, A.; Kelley, J.A.; Kunz, R.R. Characterization of nitrated sugar alcohols by atmospheric-pressure chemical-ionization mass spectrometry. *Rapid Commun. Mass Spectrom.* **2017**, *31*, 333–343. [CrossRef]
12. Zhu, J.; Cole, R.B. Formation and decompositions of chloride adduct ions. *J. Am. Soc. Mass Spectrom.* **2000**, *11*, 932–941. [CrossRef]
13. Leaptrot, K.L.; May, J.C.; Dodds, J.N.; McLean, J.A. Ion mobility conformational lipid atlas for high confidence lipidomics. *Nat. Commun.* **2019**, *10*, 985. [CrossRef]
14. Hsu, F.F.; Bohrer, A.; Turk, J.J. Formation of lithiated adducts of glycerophosphocholine lipids facilitates their identification by electrospray ionization tandem mass spectrometry. *Am. Soc. Mass Spectrom.* **1998**, *9*, 516–526. [CrossRef]
15. Wood, P.L.; Tippireddy, S.; Feriante, J.; Woltjer, R.L. Augmented frontal cortex diacylglycerol levels in Parkinson's disease and Lewy Body Disease. *PLoS ONE* **2018**, *13*, 0191815. [CrossRef]
16. Wenger, D.A.; Petitpas, J.W.; Pieringer, R.A. The metabolism of glyceride glycolipids. II. Biosynthesis of monogalactosyl diglyceride from uridine diphosphate galactose and diglyceride in brain. *Biochemistry* **1968**, *7*, 3700–3707. [CrossRef]
17. Wenger, D.A.; Subba Rao, K.; Pieringer, R.A. The metabolism of glyceride glycolipids. 3. Biosynthesis of digalactosyl diglyceride by galactosyl transferase pathways. *J. Biol. Chem.* **1970**, *245*, 2513–2519. [CrossRef]
18. Deshmukh, D.S.; Flynn, T.J.; Pieringer, R.A. The biosynthesis and concentration of galactosyl diglyceride in glial and neuronal enriched fractions of actively myelinating rat brain. *J. Neurochem.* **1974**, *22*, 479–485. [CrossRef] [PubMed]
19. Schmidt-Schultz, T.; Althaus, H.H. Monogalactosyl diglyceride, a marker for myelination, activates oligodendroglial protein kinase C. *J. Neurochem.* **1994**, *62*, 1578–1585. [CrossRef] [PubMed]

20. Ishibashi, Y.; Kohyama-Koganeya, A.; Hirabayashi, Y. New insights on glucosylated lipids: Metabolism and functions. *Biochim. Biophys. Acta.* **2013**, *1831*, 1475–1485. [CrossRef] [PubMed]
21. Hirabayashi, Y. A world of sphingolipids and glycolipids in the brain–novel functions of simple lipids modified with glucose. *Proc. Jpn. Acad Ser. B Phys. Biol. Sci.* **2012**, *88*, 129–143. [CrossRef] [PubMed]
22. Li, D.; Misialek, J.R.; Huang, F.; Windham, G.B.; Yu, F.; Alonso, A.J. Independent association of plasma hydroxysphingomyelins with physical function in the atherosclerosis risk in communities (ARIC) study. *Gerontol. A Biol. Sci. Med. Sci.* **2018**, *73*, 1103–1110. [CrossRef]
23. Ding, T.; Kabir, I.; Li, Y.; Lou, C.; Yazdanyar, A.; Xu, J.; Dong, J.; Zhou, H.; Park, T.; Boutjdir, M.; et al. All members in the sphingomyelin synthase gene family have ceramide phosphoethanolamine synthase activity. *J. Lipid Res.* **2015**, *56*, 537–545. [CrossRef]
24. Maurice, A.; Malgat, M. Evidence for the biosynthesis of ceramide-phosphoethanolamine in brain synaptic plasma membrane vesicles and in sciatic nerve microsomes from normal and Trembler mice. *Neurosci. Lett.* **1990**, *118*, 177–180. [CrossRef]
25. Alderson, N.L.; Rembiesa, B.M.; Walla, M.D.; Bielawska, A.; Bielawski, J.; Hama, H. The human FA2H gene encodes a fatty acid 2-hydroxylase. *J. Biol. Chem.* **2004**, *279*, 48562–48568. [CrossRef] [PubMed]
26. Iwabuchi, K.; Prinetti, A.; Sonnino, S.; Mauri, L.; Kobayashi, T.; Ishii, K.; Kaga, N.; Murayama, K.; Kurihara, H.; Nakayama, H.; et al. Involvement of very long fatty acid-containing lactosylceramide in lactosylceramide-mediated superoxide generation and migration in neutrophils. *Glycoconj. J.* **2008**, *25*, 357–374. [CrossRef]
27. Sikora, J.; Dworski, S.; Jones, E.E.; Kamani, M.A.; Micsenyi, M.C.; Sawada, T.; Le Faouder, P.; Bertrand-Michel, J.; Dupuy, A.; Dunn, C.K.; et al. Acid ceramidase deficiency in mice results in a broad range of Central Nervous System Abnormalities. *Am. J. Pathol.* **2017**, *187*, 864–883. [CrossRef] [PubMed]
28. Bodas, M.; Min, T.; Vij, N. Lactosylceramide-accumulation in lipid-rafts mediate aberrant-autophagy, inflammation and apoptosis in cigarette smoke induced emphysema. *Apoptosis* **2015**, *20*, 725–739. [CrossRef] [PubMed]
29. Lee, H.K.; Jang, J.Y.; Yoo, H.S.; Seong, Y.H. Neuroprotective effect of phytoceramide against transient focal ischemia-induced brain damage in rats. *Arch. Pharm. Res.* **2015**, *38*, 2241–2250. [CrossRef]
30. Jang, J.Y.; Lee, H.K.; Yoo, H.S.; Seong, Y.H. Phytoceramide ameliorates ß-amyloid protein-induced memory impairment and neuronal death in mice. *Arch. Pharm. Res.* **2017**, *40*, 760–771. [CrossRef]
31. Moreau, G.B.; Ramakrishnan, G.; Cook, H.L.; Fox, T.E.; Nayak, U.; Ma, J.Z.; Colgate, E.R.; Kirkpatrick, B.D.; Haque, R.; Petri, W.A., Jr. Childhood growth and neurocognition are associated with distinct sets of metabolites. *EBioMedicine* **2019**, *44*, 597–606. [CrossRef]
32. Varma, V.R.; Oommen, A.M.; Varma, S.; Casanova, R.; An, Y.; Andrews, R.M.; O'Brien, R.; Pletnikova, O.; Troncoso, J.C.; Toledo, J.; et al. Brain and blood metabolite signatures of pathology and progression in Alzheimer disease: A targeted metabolomics study. *PLoS Med.* **2018**, *15*, e1002482. [CrossRef]
33. Benvenutto, A.; Giusiano, B.; Koric, L.; Gueriot, C.; Didic, M.; Felician, O.; Guye, M.; Guedj, E.; Ceccaldi, M. Imaging Biomarkers of Neurodegeneration in Alzheimer's Disease: Distinct Contributions of Cortical MRI Atrophy and FDG-PET Hypometabolism. *J. Alzheimers Dis.* **2018**, *65*, 1147–1157. [CrossRef]
34. Riederer, I.; Bohn, K.P.; Preibisch, C.; Wiedemann, E.; Zimmer, C.; Alexopoulos, P.; Förster, S. Alzheimer disease and mild cognitive impairment: Integrated pulsed arterial spin-labeling MRI and $_{18}$F-FDG PET. *Radiology* **2018**, *288*, 198–206. [CrossRef] [PubMed]
35. Van der Bijl, P.; Strous, G.J.; Lopes-Cardozo, M.; Thomas-Oates, J.; van Meer, G. Synthesis of non-hydroxy-galactosylceramides and galactosyldiglycerides by hydroxy-ceramide galactosyltransferase. *Biochem. J.* **1996**, *317 Pt 2*, 589–597. [CrossRef]
36. Han, X.; Gross, R.W. Structural determination of picomole amounts of phospholipids via electrospray ionization tandem mass spectrometry. *J. Am. Soc. Mass Spectrom.* **1995**, *6*, 1202–1210. [CrossRef]

MDPI
St. Alban-Anlage 66
4052 Basel
Switzerland
Tel. +41 61 683 77 34
Fax +41 61 302 89 18
www.mdpi.com

*Life* Editorial Office
E-mail: life@mdpi.com
www.mdpi.com/journal/life

MDPI
St. Alban-Anlage 66
4052 Basel
Switzerland

Tel: +41 61 683 77 34
Fax: +41 61 302 89 18

www.mdpi.com


ISBN 978-3-0365-2603-4